Chemistry in the Environment

Advanced Ozonation Processes for Water and Wastewater Treatment

Active Catalysts and Combined Technologies

Edited by Hongbin Cao, Yongbing Xie,
Yuxian Wang and Jiadong Xiao

ROYAL SOCIETY OF CHEMISTRY

Advanced Ozonation Processes for Water and Wastewater Treatment

Active Catalysts and Combined Technologies

Chemistry in the Environment Series

Editor-in-chief:
Dionysios D. Dionysiou, *University of Cincinnati, USA*

Series editors:
Rajasekhar Balasubramanian, *National University of Singapore, Singapore*
Triantafyllos Kaloudis, *Athens Water Supply and Sewerage Company (EYDAP S.A.), Greece*
Rafael Luque, *University of Cordoba, Spain*

Titles in the series:
1: Graphene-based 3D Macrostructures for Clean Energy and Environmental Applications
2: Metallurgical Slags: Environmental Geochemistry and Resource Potential
3: Functional Hybrid Nanomaterials for Environmental Remediation
4: Emerging Nanotechnologies for Water Treatment
5: Biological Treatment of Industrial Wastewater
6: Advances in Functional Separation Membranes
7: Persulfate-based Oxidation Processes in Environmental Remediation
8: Advanced Ozonation Processes for Water and Wastewater Treatment: Active Catalysts and Combined Technologies

How to obtain future titles on publication:
A standing order plan is available for this series. A standing order will bring delivery of each new volume immediately on publication.

For further information please contact:
Book Sales Department, Royal Society of Chemistry, Thomas Graham House, Science Park, Milton Road, Cambridge, CB4 0WF, UK
Telephone: +44 (0)1223 420066, Fax: +44 (0)1223 420247
Email: booksales@rsc.org
Visit our website at www.rsc.org/books

Advanced Ozonation Processes for Water and Wastewater Treatment

Active Catalysts and Combined Technologies

Edited by

Hongbin Cao
Chinese Academy of Sciences, China
Email: hbcao@ipe.ac.cn

Yongbing Xie
Chinese Academy of Sciences, China
Email: ybxie@ipe.ac.cn

Yuxian Wang
China University of Petroleum, China
Email: yuxian.wang@cup.edu.cn

and

Jiadong Xiao
Shinshu University, Japan
Email: jdxiao_915@shinshu-u.ac.jp

ROYAL SOCIETY OF CHEMISTRY

Chemistry in the Environment Series No. 8

Print ISBN: 978-1-83916-389-0
PDF ISBN: 978-1-83916-573-3
EPUB ISBN: 978-1-83916-574-0
Print ISSN: 2516-2624
Electronic ISSN: 2516-2632

A catalogue record for this book is available from the British Library

The Royal Society of Chemistry is a charity, registered in England and Wales, Number 207890, and a company incorporated in England by Royal Charter (Registered No. RC000524), registered office: Burlington House, Piccadilly, London W1J 0BA, UK, Telephone: +44 (0) 20 7437 8656.

For further information see our website at www.rsc.org

Printed in the United Kingdom by CPI Group (UK) Ltd, Croydon, CR0 4YY, UK

Preface

Water is one of the most valuable resources on our Earth, and it ensures human survival and supports the development of human civilization. However, a safe and stable water supply has become intensively precious nowadays. The natural water body contains a large number of waste materials and/or by-products from human activities and industrial production, among which organics are one kind of typical pollutants in wastewater. Organic pollutants widely exist in municipal, industrial and agricultural wastewater, and they are toxic, persistent and easily transferred, posing a great challenge to in-depth decontamination. Even worse is the organic pollution from industrial wastewater in some developing countries.

Integrating advanced oxidation processes (AOPs) before or after biological degradation is one of the most effective strategies for organic wastewater treatment because of the merits of the fast and complete destruction of the aqueous organics into nontoxic products by the generated active species at relatively low cost. Until now, various AOPs have been developed, among which Fenton reaction and ozonation prove to be the most promising technologies for practical application. Ozonation can be operated in mild conditions without secondary pollution, yet ozone shows a selectivity in organics oxidation that hinders its broad application. To intensify ozonation efficiency, heterogeneous catalysts are fabricated, and a series of additional technologies/substances, such as photocatalysis, hydrogen peroxide, electric field, membrane and nanobubbles, are incorporated. The added chemicals or energy either greatly accelerates ozone transformation to reactive oxidative species or enhances the mass transfer of ozone, ultimately boosting efficiencies in organics mineralization and/or disinfection. These combined processes bring a new outlook to the traditional ozonation technologies, and this topic has received widespread attention all over the world,

Chemistry in the Environment Series No. 8
Advanced Ozonation Processes for Water and Wastewater Treatment: Active Catalysts and Combined Technologies
Edited by Hongbin Cao, Yongbing Xie, Yuxian Wang and Jiadong Xiao

Published by the Royal Society of Chemistry, www.rsc.org

especially in the field of wastewater treatment. It is the right time to popularize the state-of-the-art coupled ozonation technologies for advanced water and wastewater treatment.

For this book, we invited scientists from several countries who have been working on wastewater treatment with ozone for years to give a comprehensive and in-depth illustration of advanced ozonation processes for organic wastewater treatment. This book includes 12 chapters on intensified ozonation technologies and the corresponding mechanistic insights, which are catalytic ozonation processes with various heterogeneous catalysts (metal oxides, supported metal oxides and carbonaceous materials), ultraviolet- and visible-light-assisted photocatalytic ozonation, catalytic peroxone, electroperoxone, ultrasound-assisted catalytic ozonation, hybrid ceramic membrane–assisted catalytic ozonation and nanobubble-enhanced ozonation processes.

Addressing climate change has become a major concern of humankind and requires the mitigation of total carbon emissions by upgrading the heavy-emission processes. Coupled ozonation processes have demonstrated their superiority over time- and energy-consuming traditional processes in water decontamination. By summarizing their recent developments and the underlying mechanisms, this book is expected to facilitate the application of the effective coupled ozonation processes and stimulate the development of cost- and energy-efficient water purification technologies in order to create a sustainable future.

Hongbin Cao,
Yongbing Xie,
Yuxian Wang,
Jiadong Xiao

Foreword

In an era of continually accelerating industrial growth and global climate change, the necessity of controlling environmental pollution and increasing clean water availability has promoted the development of advanced water treatment technologies. Ozone is one of the most active, readily available and safest oxidizing agents, and it has been widely used for water purification and wastewater treatment since the operation of the first ozonation-based drinking water plant in Nice, France, in 1906.

The ozonation reaction is accomplished by direct ozone oxidation and indirect oxidation with *in situ* generated, highly oxidizing radical species typically including hydroxyl radicals, and the latter means is particularly powerful to mineralize a wide variety of micropollutants. Over the years, in order to improve the hydroxyl radical yield to ultimately attain a maximized overall efficiency, different types of active solid catalysts were designed, fabricated and applied in ozonation-based systems and various integrated technologies by combining ozonation with other oxidation processes (*e.g.*, photocatalytic/electrochemical oxidation, ultrasonic treatment, other oxidants that have been developed).

This book provides an overview of the most studied catalytic ozonation process and advanced ozone-integrated processes, some of which have been largely implemented for practical water treatment, given their proven efficacy, attractive economics and sustainability. The fundamental mechanism, kinetic modeling, operational conditions' impact on process performance, and economics are discussed. In particular, the book summarizes the synthesis methods, structure-property-performance relationships and stabilities of the best-in-class solid catalysts and provides examples of pilot-scale and full-scale plants as well as future research needs toward developing scalable applications in a real world for each process.

Chemistry in the Environment Series No. 8
Advanced Ozonation Processes for Water and Wastewater Treatment: Active Catalysts and Combined Technologies
Edited by Hongbin Cao, Yongbing Xie, Yuxian Wang and Jiadong Xiao

Published by the Royal Society of Chemistry, www.rsc.org

Most books available today concentrate on the general aspects of the typical catalytic ozonation process, seldom dealing with the best-in-class solid catalysts, advanced ozone-integrated processes and their applicable situations. This book, written by the leading scientists of the field from different nations, fills the gap. Anyone interested in the latest scientific and technological achievements in advanced ozonation processes, including water industry professionals, university professors, consulting scientists and engineers, and students, will find this book useful.

Prof. Jun Ma
Harbin Institute of Technology, China
E-mail: majunhit@126.com

Contents

Chemistry in the Environment Series No. 8
Advanced Ozonation Processes for Water and Wastewater Treatment: Active Catalysts and Combined Technologies
Edited by Hongbin Cao, Yongbing Xie, Yuxian Wang and Jiadong Xiao

Published by the Royal Society of Chemistry, www.rsc.org

CHAPTER 1

Heterogeneous Catalytic Ozonation over Metal Oxides and Mechanism Discussion

NA TIAN,[a] YULUN NIE,*[b] XIKE TIAN,[b] JIALU ZHU[b] AND DONG WU[b]

[a] School of Environmental Studies, China University of Geosciences, Wuhan, P.R. China; [b] Faculty of Materials Science and Chemistry, China University of Geosciences, Wuhan, P.R. China
*Email: ylnie@cug.edu.cn

1.1 Introduction

Nowadays, the catalytic ozonation process, which includes homogeneous and heterogeneous catalytic ozonation, is often regarded as a potential technology in water treatment due to its notable performance. Compared to single ozonation and homogeneous catalytic ozonation, heterogeneous catalytic ozonation could increase oxidation rate as well as mineralization degree and decrease the utilization efficiency of ozone, and it is characteristic of reclamation and lack of secondary pollution. Thus it is considered to be a promising wastewater treatment process. Various metal oxides, including typical transition metal oxides, other single-metal oxides and mixed metal oxides, have been widely adopted as heterogeneous catalysts in catalytic ozonation because of their excellent catalytic capability. A comprehensive summary of the application and mechanism in heterogeneous catalytic ozonation can provide theoretical support and guidance for designing and

Chemistry in the Environment Series No. 8
Advanced Ozonation Processes for Water and Wastewater Treatment: Active Catalysts and Combined Technologies
Edited by Hongbin Cao, Yongbing Xie, Yuxian Wang and Jiadong Xiao

Published by the Royal Society of Chemistry, www.rsc.org

choosing suitable catalysts to obtain higher removal efficiency in different kinds of wastewater. Therefore, the application and recent advances of various metal oxides in catalytic ozonation of organic contaminants in wastewater are summarized in this chapter. Moreover, their mechanism of heterogeneous catalytic ozonation by metal oxides, the reactive oxygen species and surface reaction process will also be discussed.

1.1.1 Typical Transition Metal Oxides as Ozonation Catalysts

Several typical transition metal oxides that are promising as alternative catalysts have been intensively exploited during the heterogeneous catalytic ozonation process, such as manganese oxides, iron oxides and cobalt oxides.[1–4] Advances in their possible application and relevant ozonation mechanisms are described here in detail.

1.1.1.1 Manganese Oxides

Manganese oxides possess different crystal structures (α-, β-, γ- *etc.*) and oxidation states (Mn^{2+}, Mn^{3+}, Mn^{4+} *etc.*); hence various manganese oxide catalysts including MnO_2, Mn_2O_3 and Mn_3O_4 have been applied for water and wastewater treatment during heterogeneous catalytic ozonation.[5–7] Numerous studies have been conducted on catalytic ozonation by manganese oxides in aqueous solution during the past decades. For instance, a manganese catalyst has been studied in the heterogeneous catalytic ozonation of phenol, indicating that hydroxyl radicals ($^{\bullet}OH$) generated from the manganese catalyst play a significant role in the oxidation of phenol.[5] Manganese catalysts in this study can react with ozone (O_3) and then undergo several steps to completely mineralize the phenol. The catalytic activity of Mn_2O_3 nanoparticles also has been investigated in the presence of ozone for the removal and decomposition of humic acids (HAs).[8] The results show that Mn_2O_3 with a higher point of zero charge exhibits effectively catalytic performance for ozone decomposition and HAs removal. Besides, Nawaz *et al.* have investigated several manganese oxides with controlled morphologies (including MnO_2, Mn_2O_3 and Mn_3O_4) for catalytic ozonation of phenolic compounds; it was ascertained that MnO_2 has greater catalytic activity than Mn_2O_3 and Mn_3O_4 since it possesses considerable electron transferability and a larger number of oxygen vacancies and hydroxyl groups on the surface.[9]

Among the various manganese oxides, MnO_2 has been proved to be the most efficient catalyst for the decomposition of ozone and degradation of organic pollutants in many studies. Apart from the oxidation states of manganese oxides, crystal structure is an important factor determining the activity of manganese oxides. The degradation of 4-nitrophenol (4-NP) by catalytic ozonation over various MnO_2 with six crystal phases (α-, β-, γ-, δ-, ε- and λ-MnO_2) have been studied, and the results indicate that there are various removal efficiencies of 4-NP in MnO_2 with different crystal structures.[10] Among them, α-MnO_2 is the most efficient catalyst for the catalytic ozonation of 4-NP,

in which the generated superoxide radicals ($^{\bullet}O_2^-$, 60.2%) are the primary reactive oxygen species (ROS), while singlet oxygen ($^1O_2$, 27.7%) contributes a little bit to 4-NP removal. In addition, three kinds of MnO_2 with tunneling structures, including α-MnO_2, β-MnO_2 and γ-MnO_2, have been synthesized and applied to catalytic ozonation in order to explore the effect of the crystal structure of MnO_2, indicating that the order of the catalytic capability by MnO_2 in heterogeneous catalytic ozonation is α-MnO_2 > γ-MnO_2 > β-MnO_2.[11] It is obvious that α-MnO_2 exhibits superior activity during catalytic ozonation due to its larger specific surface area, the lower average oxidation state of Mn and the higher density of oxygen vacancies. To investigate the effect of the crystal phase in the catalytic ozonation process, three types of MnO_2 (α-, β- and γ-MnO_2) have been developed by a uniform hydrothermal process and further investigated for the catalytic ozonation of phenol.[12] Compared with single ozonation, ROS with strong oxidation can be formed by the reaction between ozone and Mn–O bonds during the catalytic ozonation processes, which contributes to better oxidation efficiency. In addition, the increasing catalytic ozonation activity has been observed in the α-MnO_2/O_3 system with its enhanced surface active oxygen. The analysis confirmed that there were two critical factors for the enhanced catalytic activity of α-MnO_2: active surface oxygen and lattice oxygen. Also, the catalytic activities of β-MnO_2 and γ-MnO_2 are affected by the lattice oxygen and the bonded manganese of MnO_2.

According to previous studies, moderately acidic pH is of great benefit to the heterogeneous catalytic ozonation for organic contaminants removal by MnO_2 in an aqueous solution. The obvious indication is that the catalytic ozonation efficiency of oxalic acid significantly increases with the decreasing pH of the aqueous solution and that the appropriate range of pH is from 4.1 to 6.0 for the improvement of ozonation capability.[13] Therefore, the pH of the solution substantially influences the catalytic efficiency of manganese oxides, and the results acquired by heterogeneous catalytic ozonation over MnO_2 catalysts with different pH_{pzc} values are consistent with the reaction mechanism involving the formation of a surface manganese–oxalic acid complex. Similarly, a lack of catalytic activity occurred in different types of MnO_2 with a lower pH_{pzc} than that of the solution pH.

In addition, it has been concluded that the capabilities of manganese oxides in catalytic ozonation are dependent on morphology. In previous research, an α-MnO_2 nanotube and β-MnO_2 nanowires have been developed as ozonation catalysts and have revealed remarkable stability and catalysis for phenol degradation.[14,15] Compared to that of ozonation alone, the α-MnO_2 nanotube and β-MnO_2 nanowires remarkably accelerate the removal of phenol and chemical oxygen demand (COD). The degradation efficiency of phenol is up to approximately 94.9% in the presence of an α-MnO_2 nanotube, while there are increases of 38% and 27.1% on the degradation and mineralization efficiencies of phenol in the β-MnO_2 nanowires/ozone system, respectively. Petal-like δ-MnO_2 microspheres have been successfully synthesized and evaluated for efficiencies of catalytic ozonation for the degradation of bisphenol A (BPA) and ibuprofen (IBP).[16] The degradation

efficiencies of BPA and IBP in 20 min are 68.2% and 68.5%, respectively. Clearly, petal-like δ-MnO_2 microspheres have greater catalytic efficiencies than those of ozone alone and other heterogeneous catalytic commercial MnO_2/O_3 systems. In addition to the generation of $^{\bullet}OH$, the strong interaction between ozone and organic matters on the surface of metal oxide catalysts contributes to the rapid catalytic ozonation of organic compounds in the system of δ-MnO_2 microspheres and ozone.

Considering their unique structures with large specific surface areas and high porous properties, manganese oxides with hollow structures have been designated as an efficient ozonation catalyst with superior ozonation capability owing to the synergetic effect of adsorption and degradation for organic contaminant removal.[17] Three-dimensional α-MnO_2 porous hollow microspheres have been applied for the degradation of BPA in catalytic ozonation, and more than 90% degradation efficiency can be achieved within 30 min. This is higher than that of β-MnO_2 porous hollow microspheres and is attributed to the acceleration of the ROS generated rate (such as $^{\bullet}O_2^-$ and $^{\bullet}OH$), as well as to the more abundant lattice oxygen on the surface of α-MnO_2 porous hollow microspheres. Recently, α-MnO_2 with its mesoporous structure possesses a higher surface area and also shows the highest catalytic activity compared to those with lower surface areas. This indicates that the critical factors affecting the catalytic efficiencies of catalysts are the porous structure and specific surface areas in catalytic ozonation. For example, the mesoporous α-MnO_2 has been synthesized by using cetyltrimethylammonium bromide (CTAB), and studies on its catalytic ozonation activities for 4-NP degradation, compared with the MnO_2 synthesized with sodium dodecyl benzene sulfate (SDBS) as well as commercial MnO_2, have also been carried out.[18] Although 4-NP is completely degraded after 90 min during these catalytic ozonation processes, the removal efficiency of total organic carbon (TOC) is the highest in the mesoporous α-MnO_2/O_3 system. In this study, superoxide radicals are verified to have made a great contribution to the catalytic ozonation process, whereas hydroxyl radicals are not attributed to the removal of 4-NP. An ordered mesoporous β-MnO_2 has also been prepared by the nanocasting method and investigated for the catalytic degradation efficiency of phenol in the catalytic ozonation process.[19] There was an obviously great increase in phenol removal compared with the control MnO_2. In addition, mesoporous Mn_2O_3 has shown higher activity in benzene oxidation with ozone than commercial bulk Mn_2O_3 because of its higher surface area as well as its large number of oxygen vacancies and lattice oxygen.[20]

1.1.1.2 Iron Oxides

Owing to the abundant active sites and hydroxyl groups on their surface, iron oxides, including Fe_2O_3, Fe_3O_4 and FeOOH, with diverse structures and properties have been widely investigated in the catalytic ozonation process.[21–23] The outstanding performances in catalytic ozonation are attributed to the differences in their composition and crystal structures. For instance, FeOOH

possesses abundant hydroxyl groups on its surface, while Fe_3O_4 offers a superparamagnetic property. Furthermore, many Lewis acidic sites deposited on the surface of iron oxides can promote the decomposition of ozone into ROS. In previous studies, Trapido *et al.* have investigated and compared their catalytic ozonation of *m*-dinitrobenzene by different metal oxides as heterogeneous catalysts.[24] Their results have revealed that the catalytic capability of Fe_2O_3 is the highest of all others due to the additional ozone decomposition accomplished by accumulating the formation of ROS; these results indicate that iron oxides could be the most potent catalysts in *m*-dinitrobenzene ozonation. Recently, the transformation process of ozone on various iron oxides, including α-Fe_2O_3, α-FeOOH and Fe_3O_4, with different acid sites and hydroxyl groups has been investigated.[23] It has been shown that Lewis acid sites located on α-FeOOH and Fe_3O_4 are the active centers of catalytic ozonation, in which ozone molecules could substitute for the surface $^{\bullet}OH$ on the Lewis acid sites of iron oxides and directly interact with the iron ions in the surface of iron oxides, effectively decomposing into ROS and initiating the redox of iron ions.

Compared with various iron oxides, FeOOH has received significant attention and has become a promising heterogeneous catalyst in catalytic ozonation because of their extremely low solubility in water and more Lewis acid sites on their surface.[25–27] In addition, they are also efficient adsorbents for the removal of organic matter and inorganic ions in water. FeOOH, with a variety of crystal phases, is used to catalyze ozone for the degradation of contaminants, including goethite (α-FeOOH), akaganeite (β-FeOOH), lepidocrocite (γ-FeOOH) and feroxyhyte (δ-FeOOH). The comparison of catalytic activities of α-FeOOH in acidic and neutral conditions for the ozonation of oxalic acid (OA) has been carried out in Sui's work.[26] It was revealed that α-FeOOH could efficiently boost the formation of ROS ($^{\bullet}OH$) under acidic and neutral conditions, contributing to the improvement of the ozonation efficiency of OA by accelerating ozone decomposition. In this case, $^{\bullet}OH$ has been generated from ozone decomposition both in a neutral state (Fe–OH) and a positive charge state ($Fe–OH_2^+$) and performs as the main ROS in heterogeneous catalytic ozonation. In addition, different FeOOH catalysts, including SO_4^{2-}–FeOOH, Cl^-–FeOOH and NO_3^-–FeOOH, have been proposed and used for IBP removal in catalytic ozonation. Among them, the degradation efficiencies of IBP follow the order of SO_4^{2-}–FeOOH (40.2%) > NO_3^-–FeOOH (35.7%) > Cl^-–FeOOH (34.6%). The results reveal that the pH of the aqueous solution is a critical factor for the charge properties of surface hydroxyl groups on the interface of metal oxides. Because of the closeness of the pH_{pzc} value of SO_4^{2-}–FeOOH (7.12) to the pH of IBP solution (7.05), SO_4^{2-}–FeOOH presents a higher capacity than that of the other two FeOOH in catalytic ozonation. Moreover, SO_4^{2-}–FeOOH has possessed more hydroxyl groups than that of other catalysts, which can enhance its catalytic activity by the generation of $^{\bullet}OH$. Furthermore, ultra-small β-FeOOH nanorods are used as an effective catalyst to decompose ozone for the degradation of 4-chlorophenol (4-CP) in water.[27] Compared with ozonation alone, the degradation efficiency of 4-CP in heterogeneous catalytic ozonation has been significantly improved by adding

β-FeOOH catalyst. The removal efficiencies in the ozonation alone and heterogeneous catalytic ozonation system within 40 min are 67% and 99%, respectively. The high degradation efficiency of 4-CP in the β-FeOOH/O_3 system can be attributed to direct ozonation by ozone, the heterogeneous catalytic ozonation and homogeneous catalysis owing to β-FeOOH dissolution.

Although the redox transformation between Fe^{2+} and Fe^{3+} ions accelerates the generation of $^{\bullet}OH$ by directly decomposing ozone, iron ions dissolved and released from iron oxides could lead to secondary pollution in an aqueous environment. The recovery of the catalyst after catalytic ozonation and the release of iron ions restricts the reuse of the iron oxides in heterogeneous catalytic ozonation. Therefore, several studies have attempted to suppress the release of metal ions by improving the stability of the catalysts. Ferrocene, which is used as an efficient and recyclable heterogeneous catalyst, has been developed for catalytic ozonation since it is nontoxic and highly stable.[28] Once ferrocene is introduced to the ozonation system, amaranth can be almost completely degraded in 120 min, and TOC decreases significantly during the degradation. It has been demonstrated that the degradation of amaranth has been considerably improved in the ferrocene/O_3 system. Furthermore, there is little change in the degradation efficiencies of amaranth after several cycles, and ferrocene remains intact and undecomposed without any regeneration treatments, indicating that ferrocene as an alternative catalyst can be recyclable and remain highly efficient for catalyzing ozonation.

The development of magnetic iron oxides also can resolve the issue of catalyst recovery because it can be easily separated from the aqueous solution for further reuse. In addition to its magnetic property, Fe_3O_4 generally contains both Fe^{2+} and Fe^{3+} in the octahedral sites, which can remarkably accelerate electron transfer during the heterogeneous catalytic ozonation process. This unique property can be employed to facilitate the formation of ROS and further enhance catalytic ozonation efficiency. Thus in recent years, magnetic Fe_3O_4 has been fabricated by various methods and successfully applied as an efficient catalyst for the mineralization of organic contaminants in heterogeneous catalytic ozonation. In the research of Yin *et al.*, Fe_3O_4 nanoparticles have been prepared by a low-cost and green route and utilized in the catalytic ozonation of sulfamethoxazole (SMX).[29] It has been demonstrated that Fe_3O_4 nanoparticles can significantly boost the ozonation efficiency of SMX, which has been increased by 51% compared with ozonation alone. The increasing number of Lewis acid sites on the interface of the catalyst can be formed to interact with ozone for SMX degradation by adding Fe_3O_4 into the catalytic ozonation process, which is the easiest way to attack the targeted contaminants for greater catalytic efficiency in SMX removal. Furthermore, Fe_3O_4, with its ordered mesoporous structure, has been successfully synthesized and intensively studied for its catalytic capability in the heterogeneous ozonation process.[30] Compared to Fe_3O_4 nanoparticles synthesized by the conventional method, the ordered mesoporous Fe_3O_4 exhibits a superior capability for atrazine (ATZ) degradation in

heterogeneous catalytic ozonation. Homogeneous catalytic ozonation using the leached iron ions does not contribute to the degradation of ATX, which reveals that the heterogeneous catalytic ozonation promotes the generation of ROS and dominates the degradation of organic contaminants in the ordered mesoporous Fe_3O_4/O_3 system. In addition, the redox cycles between Fe^{2+} and Fe^{3+} that occurred in Fe_3O_4 contribute to the generation of $^{\bullet}OH$ which is the dominant ROS in ATZ degradation during the heterogeneous catalytic ozonation process.

1.1.1.3 Cobalt Oxides

Transition metal cobalt oxides also are the prevalent catalysts that have been proposed for heterogeneous catalytic ozonation. Co_3O_4 is a common form in cobalt oxide, and the improvement of organic contaminants mineralization has been achieved in the Co_3O_4/O_3 system owing to the formation of $^{\bullet}OH$ from ozone decomposition.[31–33] Many researchers have investigated the catalytic capability of Co_3O_4 as an alternative heterogeneous ozonation catalyst for the mineralization of organic contaminants; this indicates that the morphology and structure of cobalt oxide significantly affect its catalytic ozonation performance. Initially, Co_3O_4 nanoparticles with different average diameters have been synthesized, and their properties of catalytic ozonation have been investigated in the degradation of phenol.[34] The degradation efficiencies of phenol in aqueous solution have been studied in the absence and presence of Co_3O_4 nanoparticles during the ozonation process. The results indicate their dramatically catalytic capabilities for phenol mineralization, which denotes an alternative application as a heterogeneous ozonation catalyst in wastewater treatment. In a comparison of various Co_3O_4 nanoparticles with different average diameters, there is a slight increase in catalytic capabilities with decreasing average diameter, which is attributed to the better dispersion and higher surface area of Co_3O_4 with smaller sizes. It is further explained that these are important for catalysis efficiency.

Subsequently, two kinds of cobalt oxides, bulky Co_3O_4 and Co_3O_4 nanoparticles, were investigated to assess their catalytic activity, which indicated that Co_3O_4 nanoparticles exhibited superior ozonation efficiency in the mineralization of phenol compared with bulky Co_3O_4 and ozone alone.[35] There is a small negative effect on catalytic ozonation in the presence of *tert*-butyl alcohol, revealing that $^{\bullet}OH$ is the main ROS and that the catalytic reaction significantly depends on the surface properties of Co_3O_4 nanoparticles in heterogeneous catalytic ozonation for phenol degradation. In particular, the specific surface area, the number of hydroxyl groups and the good dispersibility of Co_3O_4 nanoparticles are beneficial for their higher catalytic efficiency than that of bulky Co_3O_4.

Compared with other metal oxides, Co_3O_4 not only exhibits an excellent catalytic activity but also possesses a high selectivity for catalytic products during heterogeneous catalytic ozonation. Ichikawa *et al.* have elucidated the catalytic ozonation activities of various metal oxide catalysts for the

ozonation decomposition of ammonia nitrogen in water.[36] Among these metal oxide catalysts, MgO and NiO have exhibited excellent catalytic activities, but they possess low selectivity to catalytic ozonation products, which necessitates producing a large amount of NO_3^-. Nevertheless, Co_3O_4, which is slightly less efficient than MgO and NiO, has a higher selectivity for gaseous products in all of those metal oxides. Thus Co_3O_4 is regarded as the optimal catalyst in catalytic ozonation under the comprehensive consideration of catalytic activity, selectivity and stability. Similarly, they have further investigated and found that the catalytic activity of Co_3O_4 can be greatly improved by repeated catalysis for the catalytic ozonation of ammonia nitrogen, which is primarily the reaction between the ammonium ion with hydroxyl groups and the formation of Co–NH_x groups on the Co_3O_4 surface.[37] Recently, the catalytic ozonation mechanism has been the subject of an intensive investigation involving the heterogeneous catalytic ozonation of ammonia nitrogen in the presence of Co_3O_4.[38] The results demonstrate that Co_3O_4 effectively promotes the formation of chloramines as ozonation products during the heterogeneous catalytic ozonation process.

Currently, there is a decreasing trend in catalytic ozonation by cobalt oxide alone. In recent decades, much investigation has been done on cobalt oxides with excellent behavior being supported on some catalysts, including other metal oxides and carbon materials and/or being combined with other oxides for catalytic ozonation.

1.1.1.4 Mechanism of Catalytic Ozonation

Heterogeneous catalytic ozonation involves the decomposition of ozone by various transition metal oxides; thus the reaction process and mechanisms are much more complicated. To a large extent, the efficiencies of heterogeneous catalytic ozonation are heavily dependent on the properties of the catalyst as well as on their surface structure. On the active sites of the catalyst's surface, organic pollutants can be adsorbed; these then form surface complexes with hydroxyl groups or ozone that can be decomposed to all kinds of ROS, including surface atomic oxygen (*O), $^{\bullet}O_2^-$ and $^{\bullet}OH$, on the surface of the catalysts. The decisive factor regarding the ozonation rate of metal oxides species and the removal efficiency of organic contaminants depends on the generated ROS involved in different reaction mechanisms. Several corresponding reaction mechanisms of heterogeneous catalytic ozonation have been carried out in previous investigations, including the radical mechanism, surface complexes theory, oxygen vacancies theory and the surface atomic oxygen mechanism.

According to previous studies performed on several transition metal oxides, catalytic ozonation mainly follows the radical oxidation pathways in some cases in which $^{\bullet}O_2^-$ and $^{\bullet}OH$ are the main ROS involved in the heterogeneous catalytic ozonation. The surface-bond and/or isolated hydroxyl groups on the surface of metal oxides can accelerate the decomposition of ozone, subsequently initiating the generation of strong oxidative ROS,

including $^{\bullet}O_2^-$, $^{\bullet}OH$ and even $^1O_2$. Specifically, this is greatly prone to the hydroxylation that occurred on the surface of metal oxides in the aqueous solution; the Brønsted acid sites can then be observed in these situations by delivering the protons from the surface hydroxyl groups on metal oxides. Meanwhile, diverse metal cations, as well as coordinately unsaturated oxygen, can be formed, which may be used at the Lewis acid and base centers for heterogeneous catalytic ozonation. Surface hydroxyl groups and these active centers deposited on the surface of metal oxides not only affect the adsorption of organic contaminants but also influence ozone decomposition during catalytic ozonation. Therefore, the Brønsted acid sites, as well as the Lewis acid and base sites, are regarded as the reactive centers of metal oxide catalysts for the degradation of organic contaminants in heterogeneous catalytic ozonation, which always reacts with ozone according to its electrophilic or nucleophilic property. Generally, ozone can combine primarily with the active centers on the surface of metal oxides and can then be decomposed into different radicals through a series of catalytic reactions (eqn (1.1)–(1.5)). The corresponding catalytic ozonation mechanisms by typical transition metal oxides are shown in Figure 1.1.

$$O_3 + Me\text{–}OH_2^+ \rightarrow Me\text{–}^{\bullet}OH^+ + HO_3^{\bullet} \quad (1.1)$$

$$2O_3 + Me\text{–}OH \rightarrow Me\text{–}^{\bullet}O_2^- + HO_3^{\bullet} + O_2 \quad (1.2)$$

$$Me\text{–}^{\bullet}OH^+ + H_2O \rightarrow Me\text{–}OH_2^+ + {}^{\bullet}OH \quad (1.3)$$

$$Me\text{–}^{\bullet}O_2^- + O_3 + H_2O \rightarrow Me\text{–}OH + O_2 + HO_3^{\bullet} \quad (1.4)$$

$$HO_3^{\bullet} \rightarrow {}^{\bullet}OH + O_2 \quad (1.5)$$

For example, Sun *et al.* have investigated the catalytic efficiency of OA in the MnO_x/O_3 system, in which $^{\bullet}OH$ is the primary ROS followed by the

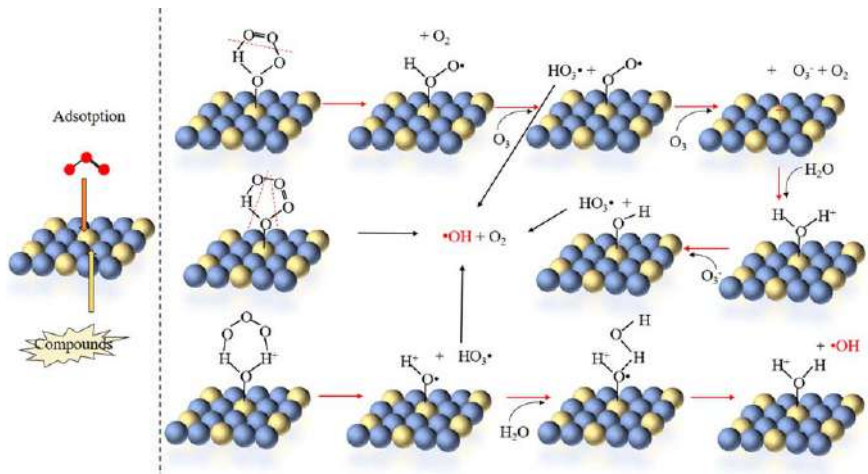

Figure 1.1 Possible radical catalytic ozonation mechanisms of metal oxides. Reproduced from ref. 1 with permission from Elsevier, Copyright 2019.

radical mechanism.[39] The protonated surface hydroxyl groups ($Mn–OH_2^+$) significantly promote the adsorption of OA and the generation of $^{\bullet}OH$ on the surface of MnO_x in catalytic ozonation, which can play a critical role in the catalytic capability of metal oxides catalysis. The superior degradation efficiency of OA can be achieved by adding the MnO_x because of an increasing number of surface hydroxyl groups generated on the surface of MnO_x. Furthermore, Sui *et al.* also have demonstrated that FeOOH as an efficient heterogeneous ozonation catalyst can effectively accelerate the generation of $^{\bullet}OH$ under acidic and neutral pH conditions and further improve the removal capability of OA by ozonation alone.[26] It is clear that all the protonated and neutral hydroxyl groups on the surface of typical metal oxides can be used as the active sites for decomposing ozone into $^{\bullet}OH$.

In addition, previous studies have shown that oxygen vacancy (OV), which is a 2-electron donor and is commonly distributed on the surface of transition metal oxides, is the major factor for organic contaminants removal during catalytic ozonation. Jia *et al.* have proposed the possible mechanism for ozone decomposition according to the involvement and recycling of oxygen vacancy deposited on the MnO_2.[11] First of all, ozone molecules combine with oxygen vacancy existing on the metal oxides' surface by withdrawing two electrons from oxygen vacancy to the oxygen atom of ozone when ozone contacts the ozonation catalyst. Thus an oxygen species (O^{2-}) in the oxygen vacancy site and an oxygen molecule that desorbs into the air can be generated, as described in eqn (1.6). Subsequently, the oxygen molecule and peroxide species (O_2^{2-}) are produced by the reaction of another ozone molecule with oxygen species (eqn (1.7)). As shown in eqn (1.8), O_2^{2-} finally decomposes to release an oxygen molecule and consequently recovers the oxygen vacancy, a reaction that can occur circularly in ozone decomposition.

$$O_3 + OV \rightarrow O_2 + O^{2-} \tag{1.6}$$

$$O_3 + O^{2-} \rightarrow O_2 + O_2^{2-} \tag{1.7}$$

$$O_2^{2-} \rightarrow O_2 + OV \tag{1.8}$$

Although the various catalytic reaction mechanisms have been introduced specifically, the process of catalytic ozonation by transition metal oxides is much more complicated and involves many reactions and reactive species. Generally, in many cases the outcome depends on the coexistence of various catalytic mechanisms during the catalytic ozonation processes.

1.1.2 Catalytic Ozonation over Other Single Metal Oxides

In addition to transition metal oxides, some other metal oxides are used as catalysts during the ozonation process. Aluminum, titanium, magnesium and calcium oxides have been the common ozonation catalysts in previous research. Their performances and possible mechanisms for heterogeneous catalytic ozonation of organic contaminants in water are briefly discussed next.

1.1.2.1 Aluminum Oxides

Aluminum oxides can be regarded as suitable and alternative catalysts for the mineralization of organic contaminants in heterogeneous catalytic ozonation, including Al_2O_3 and AlOOH.[40,41] Apart from their exceptional catalytic capabilities, some study has been conducted on the ability of γ-AlOOH and γ-Al_2O_3 to exhibit excellent stabilities due to the small amount of leaching of aluminum ions in the ozonation degradation of 2-isopropyl-3-methoxypyrazine (IPMP) from water.[42] The catalytic efficiency of IPMP by catalytic ozonation in the presence of γ-AlOOH and γ-Al_2O_3 is 94.2% and 90.0%, respectively. In the γ-AlOOH/O_3 system, the surface hydroxyl group on aluminum oxides also is a dominantly active center for ozone decomposition in the formation of $^{\bullet}OH$ during the heterogeneous catalytic ozonation of IPMP. While the surface complexes can be easily produced through physical adsorption between the ozone molecule and the catalyst surface in the heterogeneous catalytic ozonation over γ-Al_2O_3, they can further affect the capability of IPMP degradation. Based on these results, γ-AlOOH and γ-Al_2O_3 have exhibited different reaction mechanisms (shown in Figure 1.3). Therefore, a detailed introduction on the application of these two kinds of aluminum oxides in heterogeneous catalytic ozonation is presented here.

As we all know, there are both Lewis acid and basic sites (AlOH–H^+ and Al–OH) on the surface of γ-Al_2O_3 since it is an amphoteric solid; thus the number and structure of hydroxyl groups existing on the alumina surface determine its acidity and basicity. Similarly, these hydroxyl groups are of critical importance in ozone decomposition and ROS formation.[43] Generally, the number of basic sites decreases to some extent due to the adsorption of carboxylates after catalytic ozonation, while several investigations give evidence that the Lewis acid sites remain constant. Indeed, it has been recently reported that Al_2O_3 can decompose ozone by the heterogeneous catalytic ozonation and improve the generation of various ROS by the interaction between their hydroxyl groups and ozone. Ikhlaq *et al.* have demonstrated the mechanisms of catalytic ozonation for coumarin degradation on γ-alumina, and the results show that alumina is an efficient catalyst for coumarin removal by catalytic ozonation.[44] Catalytic ozonation for coumarin degradation follows a corresponding radical mechanism in the presence of alumina, and $^{\bullet}OH$ can be produced from the reaction between ozone and surface hydroxyl groups and is almost certainly involved in the heterogeneous catalytic ozonation process.

Some other studies have demonstrated that γ-Al_2O_3 reacts with O_3 to elevate the harvest of $^{\bullet}OH$ through various radical reactions involving $^{\bullet}O_2^-$ and/or ozonide radicals ($^{\bullet}O_3^-$), which contributes to the more efficient removal of carboxylic acids and 2,4-dimethylphenol (2,4-DMP) than ozonation alone.[45] There was clear observation of the degradation of 2,4-DMP within 25 min by the heterogeneous catalytic ozonation over γ-Al_2O_3. No adsorption of 2,4-DMP has occurred on γ-Al_2O_3, while an increase of 2,4-DMP oxidation can be observed after adding γ-Al_2O_3 in the ozonation process. Indeed, the removal efficiencies of TOC in single ozonation and in catalytic ozonation by

γ-Al_2O_3 is 14% and 46%, respectively. Similarly, the removal of COD has increased from 35% to 75% in the γ-Al_2O_3/O_3 system. Moreover, the catalytic effect of α-Al_2O_3 has been studied by several ozonation systems, indicating a crucial role of the active sites in catalytic ozonation. Although alumina is regarded as an inefficient adsorbent for BPA removal without ozone, there is an obvious increase in BPA mineralization, which can reach above 90% when alumina is joined in the ozonation system.[46] In another investigation, the results demonstrate that alumina remarkably promotes the degradation efficiency of NOM in the ozonation process.[47] In addition to the prominent adsorption property of alumina, the NOM removal efficiency in heterogeneous catalytic ozonation is twice as high as that of ozonation alone. In addition, there is no significant decline in the catalytic capability of alumina during the catalytic ozonation process with 62 cycles, which is attributed to the definite surface property of alumina.

Salla *et al.* have investigated and compared the performance of α-Al_2O_3 and MnO_2 for HAs removal in the catalytic ozonation process, indicating that α-Al_2O_3 exhibits better activity than MnO_2 for the catalytic ozonation of HAs.[8] Moreover, α-Al_2O_3 in a few amounts has been used as an alternative catalyst to degrade HAs in the ozonation process, and the catalytic reaction has taken place on the interface of α-Al_2O_3 by decomposing ozone into various ROS to further mineralize diverse organic contaminants. Also, γ-AlOOH is widely employed as an ozonation catalyst in the degradation of organic contaminants. For instance, the degradation of 2,4,6-trichloroanisole (TCA) has been investigated in the heterogeneous catalytic ozonation process with γ-AlOOH. This study demonstrated that the catalytic efficiency can achieve 80% within 10 min in catalytic ozonation when the initial concentration of TCA is 200 mg L^{-1}, whereas it is only 37.3% in ozonation alone.[43] In addition, γ-AlOOH as an effective catalyst has been further explored to remove 2-methylisoborneol (MIB), while the effect of adsorption occurring at the interface of γ-AlOOH also can be discussed for explaining the role of surface-active centers in γ-AlOOH (including acid and base sites) during heterogeneous catalytic ozonation.[48] The authors also discuss the mechanism of catalytic ozonation, in which surface hydroxyl groups of γ-AlOOH play a vital role in the adsorption and ozonation of MIB. The results of radical scavenger experiments have indicated that the surface hydroxyl groups determine the catalytic capability of γ-AlOOH in the ozonation process and that they are active sites of catalysts. In addition, the radical mechanism may be involved by exploring the pathway of catalytic ozonation by γ-AlOOH, in which the chemical adsorption occurs at the interface of γ-AlOOH by the interaction between surface hydroxyl groups and MIB. Owing to the competitive reaction on the interface, there are significant effects on ozone decomposition and ROS generation. Therefore, the adsorption occurring in the active centers can restrain the formation of ROS and inhibit the catalytic ozonation of MIB. An intensively study of the surface structure and property of ozonation catalysts would be beneficial for the in-depth understanding of the reaction mechanism in heterogeneous catalytic ozonation.

1.1.2.2 Titanium Oxides

As an inexpensive, efficient and notable catalyst, titanium dioxide (TiO_2) is used in a variety of technological fields, especially those having to do with energy and environment.[49] Generally, TiO_2 comes in two types, anatase and rutile, and has been intensely applied in photocatalysis due to its semiconductor characteristics and other properties. According to previous studies, TiO_2 effectively accelerates ozone decomposition into $^{\bullet}OH$ for the improvement of catalytic efficiency in organic contaminants removal in the heterogeneous catalytic ozonation, especially the rutile phase. In fact, TiO_2 exhibits superior capability in the catalytic ozonation of ATZ compared to ozonation alone.[50] There is a remarkable increase in ATZ degradation efficiency with the increase of the amount of TiO_2 and ozone, but it is clear that there is no influence on catalytic ozonation by the different initial concentrations of ATZ. Ninety-three percent degradation efficiency of ATZ can be achieved within 30 min in heterogeneous catalytic ozonation, whereas mineralization achieves 56% in the same conditions.

Another study compared the heterogeneous catalytic ozonation over TiO_2 catalyst with ozonation alone for the degradation of naproxen and carbamazepine, and the results reveal that two kinds of organic contaminants are completely removed within several minutes in catalytic ozonation.[51] Nevertheless, the degradation of naproxen and carbamazepine in ozone alone without TiO_2 catalyst takes some time, and only 50% mineralization can be reached in 20 min. In addition, the results show that the adsorption capacity of the catalyst significantly affects the ozonation efficiency, which is consistent with that of alumina previously mentioned. More hydroxyl radicals are generated from ozone decomposition for improving the mineralization degree in catalytic ozonation since the adsorption can take place on acid catalytic sites, especially in slightly acidic conditions. Moreover, the influences of ozonation and heterogeneous catalytic ozonation over TiO_2 on the structure and the amount of NOM have been studied and compared.[52] In the heterogeneous catalytic ozonation process, producing radicals is favorable in NOM degradation, which follows the radical mechanism. And the DOC removal efficiency in heterogeneous catalytic ozonation (up to 18%) is higher than that of ozonation alone (only 6%).

As we all know, there are abundant oxygen vacancies with Ti^{3+} atoms in the lattice of both anatase- and rutile-phase TiO_2. According to the oxygen vacancy theory, ozone molecules easily combine with oxygen vacancy on the TiO_2 surface by withdrawing two electrons from oxygen vacancy to the oxygen atom of ozone, which contributes to the generation of strong oxidative ROS for organic contaminants removal during catalytic ozonation. Also, the morphology and crystal phase of TiO_2 can be regarded as the primary influences on their catalytic capabilities in heterogeneous catalytic ozonation. Therefore, some research has been conducted on the effect of the morphology and crystal structure of TiO_2 on the catalytic ozonation of phenol.[53] It has been indicated that TiO_2, with its high specific surface area and

abundant surface hydroxyl groups, shows excellent catalytic activity for phenol removal in catalytic ozonation. Apart from the surface property, the crystal phase of TiO_2 exerts a great influence on its capability since TiO_2 with different crystal phases possesses various amounts of oxygen vacancy, which contributes to the performance of the heterogeneous catalytic ozonation. For instance, many surface hydroxyl groups are deposited on the rutile rather than other crystalline phases, and the degradation of phenol strongly relies on the concentration of surface hydroxyl groups. In conclusion, the mechanism of catalytic ozonation over TiO_2 catalyst is related to the adsorption capacity of the reaction intermediates on the Lewis acid sites of the TiO_2 surface and does not follow the pathway of radicals.

Furthermore, the crystal facet of TiO_2 also can severely influence their catalytic efficiencies of ozonation. For anatase TiO_2 catalyst, the thermodynamically stable (101) facet, rather than the more reactive (001) facet, dominates catalytic efficiency due to the rapid decrease of the surface with high reactivity during the crystal growth process as a result of the minimization of surface energy.[54] However, the catalytic activity of TiO_2 with exposed (001) facets could be enhanced through surface fluorination, and the ozonation efficiency of OA clearly can be accelerated by adding fluorinated TiO_2 catalyst.[55] Thus it can be deduced that two aspects, the high surface energy of (001) facets and the increased oxygen vacancies, contribute to the improved activity of fluorinated TiO_2 in the catalytic ozonation.

1.1.2.3 Magnesium and Calcium Oxides

Magnesium oxides and calcium oxides have always gathered much attention for catalytic ozonation as a result of their superior catalytic performances in organic contaminants degradation. In addition, magnesium and calcium oxides have a variety of advantages, including abundant surface basic sites, high insolubility, low toxicity, environmental friendliness and large specific surface area, which promote their application in heterogeneous catalytic ozonation.[56–60] First, MgO has been applied especially to the removal of COD and phenol from wastewater. The influence of certain factors on the efficiency of the catalytic ozonation also is evaluated, including MgO dosage, solution pH and the coexisting substance in the wastewater.[61] The experiment results reveal that 70% of the COD and 96% of the phenol are respectively removed at neutral pH in the MgO/O_3 system and that a synergistic efficiency for phenol degradation and COD removal can reach 39%. Meanwhile, the organic azo dye (Red 198) is degraded by the heterogeneous catalytic ozonation over MgO.[56] The catalytic efficiency of Red 198 has been greatly enhanced by adding MgO catalyst; thus the superior activity of heterogeneous catalytic ozonation leads to a shortened reaction time compared to single ozonation. It takes only 9 min to completely remove Red 198 in the heterogeneous catalytic ozonation, while the reaction time is about 30 min in ozonation alone. In the previous study, various metal oxides as the catalyst (such as Co, Ni, Fe, Sn, Mn, Cu, Mg and Al oxides) are evaluated for the ozonation of ammonia nitrogen in the presence

of Cl^-, indicating that MgO possesses the optimum catalytic activity for the decomposition of ammonia nitrogen.[36]

Due to the notable effects of surface area on its catalytic activity, the MgO catalyst synthesized by the conventional approach possesses a relatively large particle size and low specific surface area. Therefore, an increasing number of nano-sized MgO have been developed recently and applied for catalytic ozonation due to their controlled particle size and crystallinity. The use of a nano-sized MgO catalyst to degrade quinoline in wastewater has been investigated, and the results show that about 90.7% of quinolone can be effectively removed after 15 min.[62] It is also evidenced that the $^{\bullet}OH$ produced from ozone decomposition by the nano-sized MgO catalyst contributes to quinoline mineralization and that the partial adsorption occurring on the surface of nano-sized MgO can be ignored. In addition, mesoporous nanocrystalline MgO nanoparticles have been prepared by the hydrothermal or sol–gel approach and applied to improve the ozonation efficiency of acetaminophen, which indicates this MgO has superior catalytic activity in catalytic ozonation.[63] The functional groups on the MgO surface are crucial for boosting the ozone decomposition to $^{\bullet}OH$, in which the reaction between O_3 molecules and the hydroxyl groups can occur on the interface. The reaction between hydroxyl radical with acetaminophen molecules can also take place in the solution. In addition, MgO catalysts can adsorb the water molecules and dissociate them into hydroxyl radicals and hydrogen ions, thus enhancing the amount of $^{\bullet}OH$ in the heterogeneous catalytic ozonation process.

Indeed, the surface properties of catalysts, such as the exposed crystal facets, determine their active sites and markedly affect their catalytic performance in heterogeneous catalytic ozonation. Several MgO nanocrystals with different crystal facets of (111), (110), (100) and (200) have been synthesized and applied to investigate their reactivity in the catalytic ozonation of *Escherichia coli*.[64] Their catalytic capabilities follow the order of $MgO(111) > MgO(200) > MgO(110) > MgO(100)$, indicating that the crystal facets play a crucial role in catalytic activity. This is also evidenced by scavenger experiments in which $^{\bullet}OH$ detected in the heterogeneous catalytic ozonation was the main ROS in the $MgO(111)/O_3$ system, while more direct ozonation and a portion of $^{\bullet}O_2^-$ can be observed in other catalytic ozonation processes.

Calcium oxides are relatively inexpensive solids, which have a variety of properties and applications, certainly including wastewater treatment and remediation. Among them, CaO_2 can be regarded as a stable source of oxygen release depending on the pH of the solution since it can react with water molecules to generate hydrogen peroxide and calcium hydroxide.[65] In Izadifard's study, CaO_2 and CaO are used for catalyzing O_3 to degrade sulfolane, whose complete removal and TOC can be achieved within 40 and 150 min with CaO_2 and CaO, respectively.[66] The results demonstrate that both CaO_2 and CaO are available and alternative catalysts for heterogeneous catalytic ozonation treatment of wastewater contaminated with sulfolane. In addition, CaO exhibits greater activity than other metal oxides in the

catalytic ozonation of cinnamaldehyde since it has Brønsted acid sites.[59] Compared with the surface structure in a series of metal oxides, it is already clear that CaO possesses only trace Lewis acid sites but has a strong base site. According to its superior cinnamaldehyde conversion and benzaldehyde selectivity, CaO, with its strong base sites, can boost the ozone decomposition to various ROS, including $^{*}O$, $^{\bullet}OH$ and $^{\bullet}O_2^-$ *etc.* And the amount and property of different ROS generated from catalytic ozonation have strongly depended on reaction temperature.

1.1.2.4 Reaction Mechanism Discussion

The typical radical pathway is the primary mechanism of heterogeneous catalytic ozonation over different metal oxides for organic contaminants degradation. Generally, the free radicals, $^{\bullet}OH$ and $^{\bullet}O_2^-$, are regarded as the main ROS in the catalytic ozonation. Based on electron transfer, the catalytic ozonation can occur in the surface-active center of metal oxides by dissociating the O–O bond in ozone to generate various ROS for contaminants degradation. In Section 1.1.1.4, the mechanism of heterogeneous catalytic ozonation following the radical pathway has been discussed in detail.

In addition to radical oxidation, previous studies also have investigated the degradation pathway of carboxylates followed by non-radical oxidation in the heterogeneous catalytic ozonation process, which is attributed to intramolecular electron transfer.[67] Moreover, the pathway of organic degradation depends on the generated surface complex in the active sites deposited on the surface of metal oxides. Under certain conditions, organic matters in aqueous solution react with the adsorbed ozone molecules on the interface of metal oxides to generate the surface complexes that induce non-radical oxidation by intermolecular electron transfer instead of ozone decomposition. Thus the influence of solution pH (as well as pH_{pzc} of the catalyst and pK_a of the organics) on catalytic ozonation efficiency has been investigated in the non-radical pathways due to the significant effect on the adsorption of ozone and organics.

The possible ozonation pathways for the surface-complex reactions can be summarized in the following three cases (shown in Figure 1.2). First, organic matter can be chemisorbed on the surface of the metal oxide catalysts and can further react with ozone molecules leading to the generation of various ROS. Then ozone molecules are chemisorbed on the surface of the metal oxide catalysts, and the generated surface-ozone complexes can destroy the organic contaminants. Finally, organic matter and ozone molecules are chemisorbed on the surface of the metal oxide catalysts at the same time, and then the organic contaminants are degraded by intramolecular electron transfer.

For the degradation of organic contaminants *via* a surface complex mechanism, γ-Al_2O_3 has been investigated as a typical ozonation catalyst in the catalytic ozonation of 2-isopropyl-3-methoxypyrazine.[42] The results reveal that ozone molecules adsorbed on the γ-Al_2O_3 surface could either directly oxidize organic matter or decompose into free radicals for catalytic ozonation. However, the oxidation potential for direct ozone decomposition

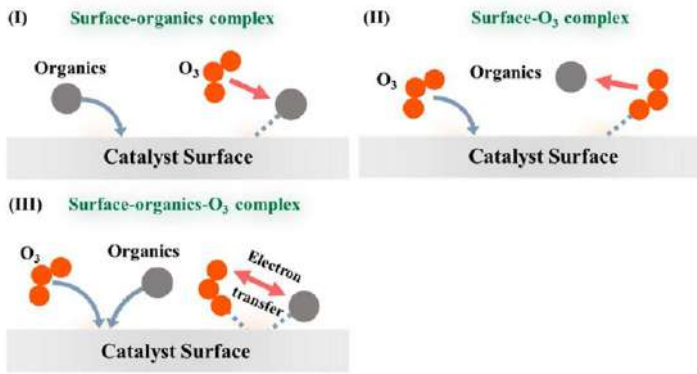

Figure 1.2 Possible surface-complex catalytic mechanisms of metal oxides. Reproduced from ref. 2 with permission from American Chemical Society, Copyright 2020.

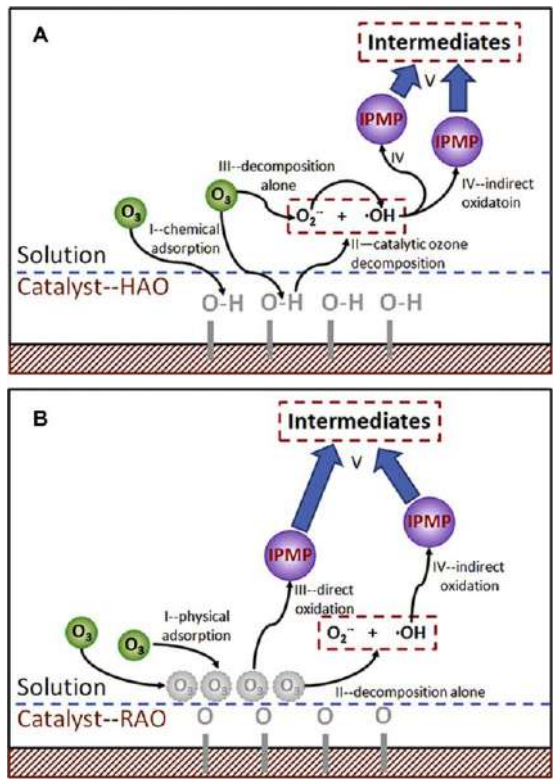

Figure 1.3 Proposed reaction pathways in catalytic ozonation by different alumina: (A) γ-AlOOH and (B) γ-Al_2O_3. Reproduced from ref. 42 with permission from Elsevier, Copyright 2013.

can be promoted by increasing the amount of the adsorbed ozone on the γ-Al_2O_3 surface. Clearly, it is especially difficult to achieve the complete mineralization of contaminants by this surface complex due to coexisting radical oxidation. Therefore, the surface complexes can acquire a mild oxidation potential for unsaturated organic matter degradation, but the mineralization of aliphatic acid cannot be realized.

Although different ozonation mechanisms have been involved in heterogeneous catalytic ozonation over various metal oxides catalysts, the ozonation efficiencies of catalysts depend to a large extent on their surface properties as well as on the solution pH, which dominate the surface active sites and ozone decomposition reactions in aqueous solutions. The physical and chemical properties of metal oxide catalysts must be preferentially considered when selecting the catalyst in the ozonation process, including the crystal size, surface area, crystal phase, surface groups and even surface active sites. Generally, hydroxyl groups situated on the metal oxide surface can behave as Brønsted acid sites, and Lewis acids and Lewis bases are special sites located on the metal cation and coordinatively unsaturated oxygen, respectively. Those active sites on the surface of metal oxide catalysts are responsible for catalytic efficiency in heterogeneous catalytic ozonation. The adsorption behavior of metal oxide catalysts is of great benefit to their activity of heterogeneous catalytic ozonation since the adsorption reaction is the preferential stage in the overall process; thus it must be taken into consideration to improve catalytic efficiency. All in all, the heterogeneous catalytic ozonation process certainly involves various reactions, including the adsorption, single ozonation, and catalytic ozonation of those metal oxides catalysts.

1.1.3 Mixed Metal Oxides for Catalytic Ozonation

An increasing number of mixed polymetallic oxides are used as the heterogeneous catalysts since they commonly possess greater catalytic capability and stability than those of monometallic oxides. Two typical representatives, perovskite and spinel-like oxides, have received increasing attention and possess good catalytic abilities in catalytic ozonation because of their availability, persistent structure, abundant metal valence states, controlled morphologies and various exposed defects.

1.1.3.1 Perovskites

As alternative catalysts, mixed metal oxides possessing the perovskite structure have been extensively utilized for catalytic ozonation of organic contaminants during the last two decades.[68–70] Generally, perovskites possess a formula of ABO_3, in which A usually represents the rare earth cation (the majority being La), and the B position has a transition metal cation. Perovskite catalysts can endure the replacement of both cation sites, in which the structural defects, including anionic and cationic vacancies, can be generated when the A position is substituted by lower-valence metal ions.

Subsequently, the oxidation state of metal ions is altered to maintain the electrical neutrality of perovskites, and the extensively available oxygen also can be formed with the increasing oxidation state of the B cation. The generated oxygen vacancies are responsible for promoting the catalytic activity in the ozonation process owing to the enhanced mobility of lattice oxygen. Thus the use of these perovskite catalysts has especially promoted applications involving ozone decomposition and has enhanced the catalytic ozonation rate of organic contaminants, even improving the mineralization degree during the ozonation process. To date, a series of perovskites ($LaMO_3$, M = Fe, Mn, Co, Cu, Ti and Ni) have been investigated as an effective alternative in the heterogeneous catalytic ozonation process for organic contaminants degradation.

Initially, the perovskite $LaTi_{0.15}Cu_{0.85}O_3$ has been successfully synthesized and evaluated for the catalytic ozonation of pyruvic acid, resulting in the formation of a refractory substance after catalytic ozonation.[71] The same perovskite was evaluated in the catalytic ozonation of different phenolic wastewaters, but no obvious changes were observed in this study according to the results regarding removal efficiency and mineralization degree.[72] There were no differences in single ozonation and heterogeneous catalytic ozonation for non-refractory wastewater. Thus the addition of perovskite can effectively dispose of those refractory organic contaminants in wastewater. It is evidenced that there was no improvement in the removal efficiency of pharmaceutical compounds when the catalysts were added into the single ozonation process in ultrapure water.[69] However, TOC removal is significantly increased in the presence of perovskite catalysts, especially for copper perovskite, where 90% of TOC removal could be achieved after 120 min. This is attributed to the formation of hydroxyl radicals resulting from the reaction of ozone molecules with hydrogen peroxide generated in the aromatic ring and unsaturated carbon bond-breaking. In addition, ozone decomposition occurred on the catalyst surface, especially copper perovskite, leading to efficient TOC removal.

Further investigation also has shown that a significant enhancement of catalytic capability is observed in the presence of perovskites with a different composition, which severely affects the catalytic property during the ozonation process. For instance, several lanthanum-based perovskites were carried out for the catalytic ozonation of organic contaminants.[73] $LaCoO_3$ has been supposed to be an efficient catalyst for organic contaminants as a result of the rapid ozonation rate, complete mineralization of organics and negligible metal leaching. It exhibits significant catalytic activity for benzotriazole (BZA) degradation, where complete degradation and about 71% of BrO_3^- inhibition can be achieved within 15 min.[70] While no catalytic activity for BZA degradation can be observed in the $LaFeO_3/O_3$ process, there is 73% of inhibition for the generation of BrO_3^-. In these cases, oxygen vacancies play a crucial role in the heterogeneous catalytic ozonation as a result of the ability to activate adsorbed species. It has been shown that H_2O_2 has an important but varied effect in different ozonation systems and combines with the surface hydroxyl groups to accelerate the BZA degradation and to

inhibit the generation of BrO_3^-. For other perovskites, $LaMnO_3$ also certainly exhibits catalytic performance, but it facilely suffers from the leaching of metal cations. Moreover, $LaMnO_3$ and $La_{0.8}Sr_{0.2}MnO_3$ perovskites have shown greatly inferior catalytic activity for ozone utilization in benzene oxidation than manganese monoxide, and La sites in perovskite accelerate the accumulation of less reactive by-product compounds on the catalysts.[74] In the case of manganese-based perovskite, ozone decomposition and organic contaminant degradation are decided by the catalyst composition.

Therefore, suitable modifications can be carried out to improve the properties of catalysts in catalytic ozonation. In Afzal's study, mesoporous nanocast $LaMnO_3$ and $LaFeO_3$ perovskites have been synthesized and applied effectively for 2-chlorophenol degradation in the heterogeneous catalytic ozonation process.[75] It has been demonstrated that nanocast perovskites, with their unique structure, exhibit higher catalytic efficiency than their uncast counterparts, as well as highly active Mn_3O_4 and Fe_2O_3. Based on various detailed analyses, it is evidenced that a neutrally charged surface (MnOH), as well as a protonated surface ($MnOH_2^+$), presented as more catalytically active than the deprotonated surface (MnO^-) in promoting ozone decomposition into $^{\bullet}OH$. Hence the generated $^{\bullet}OH$ rather than surface O_2^{2-}, $^*O$, $^{\bullet}O_2^-$ and $^1O_2$ is the primary ROS that contributes to the excellent activity in the heterogeneous catalytic ozonation process.

1.1.3.2 Spinel Oxides

Recently, some spinel oxides, with a general formula of AB_2O_4 in which A and B are metal ions, also are being extensively investigated for organic contaminants removal in heterogeneous catalytic ozonation systems owing to their superior catalytic activity, various valence states, and high stability.[76–80] All kinds of spinel oxides have been synthesized and applied to degrade the organic contaminants in catalytic ozonation. For instance, several magnetic spinel ferrites, including $CoFe_2O_4$, $CuFe_2O_4$, $NiFe_2O_4$ and $ZnFe_2O_4$, have been applied to dispose of shale gas in the heterogeneous catalytic ozonation.[81] It is obvious that these magnetic spinel oxides all offer attractive catalytic and recycling performance; their catalytic efficiencies follow the order of $CuFe_2O_4 > NiFe_2O_4 > CoFe_2O_4 > ZnFe_2O_4$. Their capacities of catalytic ozonation mainly rely on the surface property of these catalysts, and the proposed interaction pathway follows the typical radicals-involved process. Firstly, the ozone molecules can be adsorbed into the surface of the spinel ferrite and react with the surface functional groups to generate various radicals. In addition, the metal cations cycles in spinel oxides surface such as Fe^{2+}/Fe^{3+}, Cu^{2+}/Cu^+ and Co^{2+}/Co^{3+} significantly affect the generation of radicals. As shown in eqn (1.1)–(1.5), hydroxyl radicals could be finally produced by the series of chain reactions and then interact with the targeted organic matters for contaminants removal.

Furthermore, the same kinds of spinel oxides have been synthesized and investigated in the catalytic ozonation of oxalic acid.[82] In this study, 68.3% of

TOC could be removed within 120 min in the $CoFe_2O_4/O_3$ system, indicating $CoFe_2O_4$ has a more superior catalytic performance than others for oxalic acid mineralization. The reason for the excellent catalytic performance is that spinel oxides possess reducibility and electron-donating capacity; the order of catalytic activity is $CoFe_2O_4$, $NiFe_2O_4$, $CuFe_2O_4$ and $ZnFe_2O_4$. Similarly, the radical-based catalytic mechanisms and reaction pathways also can be proposed in the cases of spinel oxides, which include the interaction of ozone molecules with hydroxyl groups and metal ions on the surface of catalysts.

Due to the fascinating electromagnetic property, a large amount of research has been conducted on heterogeneous catalytic ozonation over magnetic spinel ferrite for easily recycling.[83–85] Magnetic spinel oxide crystals have a completely inverse spinel structure, where iron ions have occupied the tetrahedral and octahedral sites and all other metal ions (such as Ni, Cu, Co, Mn *etc.*) have located in the octahedral sites. For instance, Zhang *et al.* have prepared copper ferrite magnetic nanoparticles ($CuFe_2O_4$ MNPs) by the sol–gel approach for the catalytic ozonation of *N*,*N*-dimethylacetamide (DMAC).[86] The results have demonstrated that the removal efficiency of DMAC in the heterogeneous $CuFe_2O_4/O_3$ process (95.4%) is much higher than that of only $CuFe_2O_4$ catalyst (0%), ozonation alone (55.4%) and other heterogeneous Fe_2O_3/O_3 processes (32.1%). Hydroxyl groups on the surface of $CuFe_2O_4$ catalyst are the active sites and contribute to the ozone decomposition into $^{\bullet}OH$ as the dominant ROS in the $CuFe_2O_4/O_3$ process. Finally, a possible reaction mechanism in the $CuFe_2O_4/O_3$ process has been proposed according to research results, which mainly consists of ozonation alone as well as homogeneous and heterogeneous catalytic ozonation.

Magnetic $NiFe_2O_4$ as a catalyst also has been used for catalytic ozonation of di-*n*-butyl phthalate (DBP), and it has also been concluded that the surface hydroxyl groups as the catalytic active centers could boost $^{\bullet}OH$ generation.[87] Moreover, Ni^{2+} in the catalyst could facilitate electron transfer from the catalyst surface to induce ozone decomposition and enhance the formation of hydroxyl radicals, which lead to the improvement of DBP degradation. Additionally, magnetic $NiFe_2O_4$ could also be proposed for heterogeneous catalytic ozonation of phenol contaminants,[88] in which study, Lewis acid sites were indicated as catalytic reactive centers in the process. Therefore, the reasons for the superior catalytic activity of $NiFe_2O_4$ catalyst are not only the greater number of surface-active centers, including surface hydroxyl groups and Lewis acid sites, but also the enhanced interfacial electron transfer. Furthermore, the magnetic $NiFe_2O_4$ can be easily and efficiently separated from the heterogeneous catalytic system with an external magnet, making it promising for being an attractively separable catalyst in the heterogeneous catalytic ozonation of organic contaminants.

In addition, $ZnAl_2O_4$, another spinel-like ozonation catalyst, has been significantly reported to improve phenol degradation, in which the removal rate of phenol with a high concentration of 300 $mg\,L^{-1}$ can arrive at 73.4% within 60 min.[89] After recycling four times on the catalyst, there is a slight

decrease (only 5.7%) in the removal efficiency of phenol, illustrating the excellent reusability of $ZnAl_2O_4$ in the heterogeneous catalytic ozonation process. In addition to high reusability, $ZnAl_2O_4$ possesses brilliant stability since it can be extensively utilized in a wide pH range from 3.3 to 9.3, becoming a promising ozonation catalyst for wastewater treatment. These studies also imply that surface hydroxyl groups are the active sites and that $^{\bullet}OH$ is the main ROS in catalytic ozonation.[90]

For the spinel oxides, various metal cations possess different valence states, which can facilitate electron transfer on the catalyst surface for further boosting ozone decomposition to enhance oxidation efficiency.[91] To further study the catalytic mechanism, the degradation of dimethyl phthalate by CuFe-based spinel oxide as an ozonation catalyst has been evaluated, and the redox recycling of Fe^{2+}/Fe^{3+} and Cu^{+}/Cu^{2+} at the surface of the catalyst can accelerate electron transfer and $^{\bullet}OH$ generation. Similar results have been obtained in the degradation of organic dye by $CuAl_2O_4$ catalyzed ozonation, and almost 100% of the dye and 87.2% of the COD can be removed within 25 min at neutral pH in this heterogeneous catalytic ozonation process. It is worth mentioning that the catalytic reaction rate in heterogeneous ozonation is higher than that of other systems since the better textural properties and the higher density of active sites in $CuAl_2O_4$ (both Cu^{2+} and Al^{3+}) are critical for the degradation of the contaminants.

1.1.3.3 Mechanism of Catalytic Ozonation

The reaction mechanisms of catalytic ozonation over mixed metal oxides are more complex due to the distinctive structure of catalysts. For example, a large number of defective sites and active sites exist in mixed metal oxides, including oxygen vacancies, acid sites, and basic sites.[92] Also, metal cations that possessed diverse valence states on the catalyst surface are beneficial for redox cycling and electron transfer leading to the facile generation of ROS in catalytic ozonation.

Some studies have reported oxygen vacancies as the active centers of catalysis for radical-based oxidation in catalytic ozonation. In La-based perovskite, the lattice oxygen vacancies possess the capability to adsorb the ROS, which is crucial for catalytic efficiency in the ozonation process.[73] Similarly, it is observed that the oxygen vacancies and multivalence Mn of perovskite are at the Lewis acid sites, which are regarded as the active centers for ozone decomposition and the formation of $^{\bullet}OH$, $^{\bullet}O_2^{-}$, and $^{1}O_2$.[93] Generally, Lewis acid sites are covered by hydroxyl groups on the perovskite surface, which might mean that the reaction between ozone molecules with hydroxyl groups rather than with Lewis acid sites in the perovskite can preferentially occur.

According to previous studies, the overall heterogeneous mechanism of catalytic ozonation over mixed metal oxides is illustrated in Figure 1.4. Generally, the radical-based and non-radical mechanisms of catalytic ozonation have been proposed by the interaction of ozone with surface active

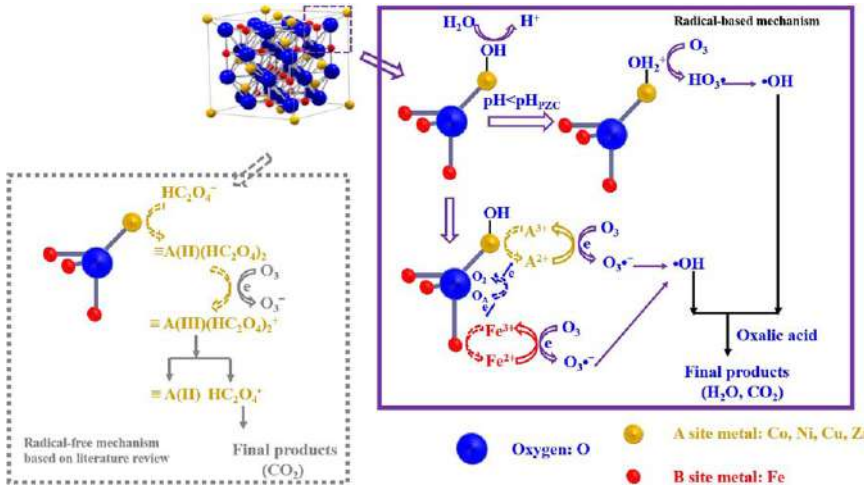

Figure 1.4 Catalytic mechanism of oxalic acid ozonation catalyzed by spinel ferrites. Reproduced from ref. 82 with permission from Elsevier, Copyright 2017.

sites on mixed metal oxides, which can accelerate the decomposition of ozone. The surface hydroxyl groups are primarily formed on account of the interaction between a water molecule and metal ions located in the A-site of mixed metal oxides. In some cases, the surface hydroxyl groups with positive charges are prone to be formed since the pH of the solution containing organic contaminants is basically lower than pH_{pzc} of spinel oxides. Then it can react with ozone molecules to generate the intermediate hydroozonide radicals ($HO_3^{\bullet}$) by electrostatic force, while $^{\bullet}OH$ is produced by the reaction of ozone molecules with hydrogen bonds. An electron transfer from the bivalent metal ion in the A site to ozone molecules can be observed, thus resulting in the generation of $^{\bullet}O_3^-$ and the trivalent metal ion in the A site. Also, $HO_3^{\bullet}$ as well as $^{\bullet}OH$ are formed by the reaction between the intermediate $^{\bullet}O_3^-$ and hydrogen ions in the solution. At the same time, the trivalent A site metal ion is reduced to its bivalent state by the lattice oxygen. It should be emphasized that the coexistence of iron ions with multiple valences and metal ions in the A site may accelerate the process of ozone decomposition.

On account of the ROS from catalytic activation of ozone molecules, heterogeneous catalytic ozonation processes have been evidenced to surpass single ozonation by the non-selective mineralization of contaminants with superior efficiency. In addition to $^{\bullet}OH$, other ROS such as $^{\bullet}O_2^-$ and $^1O_2$ can also be generated in catalytic ozonation, which contributes to the degradation of organic contaminants. Meanwhile, the pH dependence in ozone decomposition can be rationally regulated by the catalysts, adapting the effectiveness of ozonation to a wider pH range. For the heterogeneous catalytic ozonation over mixed metal oxides, the variable valence states of metal ions are responsible for the electron transfer, and the surface hydroxyl groups and oxygen vacancies of the catalysts can serve as Lewis acid sites for accepting electrons.

1.1.4 Summary

To sum up, a comprehensive understanding of the heterogeneous catalytic ozonation process over various metal oxides is provided in this chapter based on advanced research. The characteristics of heterogeneous ozonation catalysts have been proven to significantly affect their catalytic activities and efficiencies, such as their components, crystalline structure and morphology. Moreover, the heterogeneous catalytic ozonation mechanisms over various metal oxides have been summarized and analyzed in detail. In particular, active centers on the surface of different metal oxides are described respectively, including hydroxyl groups, metal cations, oxygen vacancies, acid sites and basic sites. Generally, the radical and/or non-radical degradation pathways including radical mechanism, surface complexes theory and oxygen vacancies mechanism are involved in the ozonation process.

Although numerous studies on heterogeneous catalytic ozonation have been investigated in the last decade, several limitations restrict the further applications of these metal oxide catalysts in water treatment, including the leaching of toxic metal ions and the reuse of solid catalysts separated from the aqueous solution. Hence developing environmental-friendly heterogeneous ozonation catalysts with excellent long-term stability is the key to accelerating the practical application of this technique. In this chapter, the metal oxides composed of natural abundant elements (Mg, Ca *etc*. instead of transition metals) have exhibited a satisfying ozonation performance, where the organic pollutants can also be completely degraded and mineralized. In addition, an in-depth understanding of the possible ozonation mechanism regarding metal oxides can provide theoretical support for properly designing and applying ozonation catalysts.

References

1. J. L. Wang and H. Chen, *Sci. Total Environ.*, 2020, **704**, 135249.
2. G. F. Yu, Y. X. Wang, H. B. Cao, H. Zhao and Y. B. Xie, *Environ. Sci. Technol.*, 2020, **54**(10), 5931.
3. J. Nawrocki, *Appl. Catal. B: Environ.*, 2013, **142–143**, 465.
4. B. Peng, W. J. Bao, L. L. Wei, R. D. Zhang, Z. J. Wang, Z. C. Wang and Y. Wei, *Petrol. Sci.*, 2019, **16**(4), 912.
5. S. Khuntia, M. K. Sinha and P. Singh, *Environ. Technol.*, 2019, 1.
6. J. Z. Hu, Y. M. Li, S. S. Nan, B. A. Yoza, Y. F. Li, Y. L. Zhan, Q. H. Wang, Q. X. Li, S. H. Guo and C. M. Chen, *Front. Chem.*, 2020, **8**, 80.
7. T. Gopi, G. Swetha, S. Chandra Shekar, C. Ramakrishna, B. Saini, R. Krishna and P. V. L. Rao, *Catal. Commun.*, 2017, **92**, 51.
8. J. S. Salla, N. Padoin, S. M. Amorim, G. Li Puma and R. F. P. M. Moreira, *J. Environ. Chem. Eng.*, 2020, **8**(2), 102780.
9. F. Nawaz, Y. B. Xie, J. D. Xiao, H. B. Cao, Z. A. Ghazi, Z. Guo and Y. Chen, *Catal. Sci. Technol.*, 2016, **6**(21), 7875.

10. F. Nawaz, H. B. Cao, Y. B. Xie, J. D. Xiao, Y. Chen and Z. A. Ghazi, *Chemosphere*, 2017, **168**, 1457.
11. J. B. Jia, P. Y. Zhang and L. Chen, *Appl. Catal. B: Environ.*, 2016, **189**, 210.
12. Y. M. Dong, K. Li, P. P. Jiang, G. L. Wang, H. Y. Miao, J. J. Zhang and C. Zhang, *RSC Adv.*, 2014, **4**(74), 39167.
13. R. Andreozzi, A. Insola, V. Caprio, R. Marotta and V. Tufano, *Appl. Catal. A: Gen.*, 1996, **138**, 75.
14. H. Zhao, Y. M. Dong, P. P. Jiang, G. L. Wang, J. J. Zhang, K. Li and C. Y. Feng, *New J. Chem.*, 2014, **38**(4), 1743.
15. Y. M. Dong, H. X. Yang, K. He, S. Q. Song and A. M. Zhang, *Appl. Catal. B: Environ.*, 2009, **85**(3–4), 155.
16. K. Luo, S. X. Zhao, Y. F. Wang, S. J. Zhao and X. H. Zhang, *New J. Chem.*, 2018, **42**(9), 6770.
17. X. Q. Tan, Y. F. Wan, Y. J. Huang, C. He, Z. L. Zhang, Z. Y. He, L. L. Hu, J. W. Zeng and D. Shu, *J. Hazard. Mater.*, 2017, **321**, 162.
18. F. Nawaz, Y. B. Xie, H. B. Cao, J. D. Xiao, Y. Q. Wang, X. H. Zhang, M. J. Li and F. Duan, *Catal. Today*, 2015, **258**, 595.
19. J. L. Zhang, T. Zhuang, S. J. Liu, G. C. Zhang and K. L. Huo, *J. Environ. Chem. Eng.*, 2020, **8**(4), 103967.
20. M. S. Jin, J. W. Kim, J. M. Kim, J. Jurng, G. N. Bae, J. K. Jeon and Y. K. Park, *Powder Technol.*, 2011, **214**(3), 458.
21. A. Ziylan and N. H. Ince, *Catal. Today*, 2015, **240**, 2.
22. L. Y. Yang, M. Sheng, Y. J. Li, W. B. Xue, K. Li and G. M. Cao, *Chemosphere*, 2020, **238**, 124639.
23. L. Q. Yan, J. S. Bing and H. C. Wu, *Sci. Rep.*, 2019, **9**(1), 14752.
24. M. Trapido, Y. Veressinina, R. Munter and J. Kallas, *Ozone Sci. Eng.*, 2005, **27**(5), 359.
25. Y. L. Nie, C. Hu, N. N. Li, L. Yang and J. H. Qu, *Appl. Catal. B: Environ.*, 2014, **147**, 287.
26. M. H. Sui, L. Sheng, K. X. Lu and F. Tian, *Appl. Catal. B: Environ.*, 2010, **96**(1–2), 94.
27. O. Oputu, M. Chowdhury, K. Nyamayaro, O. Fatoki and V. Fester, *J. Environ. Chem. Eng.*, 2015, **35**, 83.
28. K. A. Lin, T. Y. Lin, Y. C. Chen and Y. F. Lin, *Catal. Commun.*, 2017, **95**, 40.
29. R. L. Yin, W. Q. Guo, X. J. Zhou, H. S. Zheng, J. S. Du, Q. L. Wu, J. S. Chang and N. Q. Ren, *RSC Adv.*, 2016, **6**(23), 19265.
30. S. M. Zhu, B. Z. Dong, Y. H. Yu, L. J. Bu, J. Deng and S. Q. Zhou, *Chem. Eng. J.*, 2017, **328**, 527.
31. B. B. Xu, F. Qi, J. Z. Zhang, H. N. Li, D. Z. Sun, D. Robert and Z. L. Chen, *Chem. Eng. J.*, 2016, **284**, 942.
32. C. Hu, S. T. Xing, J. H. Qu and H. He, *J. Phys. Chem. C*, 2008, **112**, 5978.
33. A. Abdedayem, M. Guiza, F. J. R. Toledo and A. Ouederni, *Sep. Purif. Technol.*, 2017, **184**, 308.
34. Y. M. Dong, K. He, L. Yin and A. M. Zhang, *Nanotechnology*, 2007, **18**(43), 435602.

35. Y. M. Dong, G. L. Wang, P. P. Jiang, A. M. Zhang, L. Yue and X. M. Zhang, *B. Kor. Chem. Soc.*, 2010, **31**, 2830.
36. S.-i. Ichikawa, L. Mahardiani and Y. Kamiya, *Catal. Today*, 2014, **232**, 192.
37. L. Mahardiani and Y. Kamiya, *J. Jpn. Pet. Inst.*, 2016, **59**(1), 31.
38. P. A. Krisbiantoro, T. Togawa, L. Mahardiani, H. Aihara, R. Otomo and Y. Kamiya, *Appl. Catal. A: Gen.*, 2020, **596**, 117515.
39. Q. Q. Sun, L. S. Li, H. H. Yan, X. T. Hong, K. S. Hui and Z. Q. Pan, *Chem. Eng. J.*, 2014, **242**, 348.
40. Z. S. Ncanana and V. S. R. Rajasekhar Pullabhotla, *J. Environ. Chem. Eng.*, 2019, **7**(3), 103072.
41. P. Pocostales, P. Álvarez and F. J. Beltrán, *Chem. Eng. J.*, 2011, **168**(3), 1289.
42. F. Qi, B. Xu, Z. Chen, L. Feng, L. Zhang and D. Sun, *Chem. Eng. J.*, 2013, **219**, 527.
43. F. Qi, Z. L. Chen, B. B. Xu, J. M. Shen, J. Ma, C. Joll and A. Heitz, *Appl. Catal. B: Environ.*, 2008, **84**(3–4), 684.
44. A. Ikhlaq, D. R. Brown and B. Kasprzyk-Hordern, *Appl. Catal. B: Environ.*, 2012, **123–124**, 94.
45. J. Vittenet, W. Aboussaoud, J. Mendret, J. S. Pic, H. Debellefontaine, N. Lesage, K. Faucher, M. H. Manero, F. Thibault Starzyk, H. Leclerc, A. Galarneau and S. Brosillon, *Appl. Catal. A: Gen.*, 2015, **504**, 519.
46. R. Keykavoos, R. Mankidy, H. Ma, P. Jones and J. Soltan, *Sep. Purif. Technol.*, 2013, **107**, 310.
47. J. Nawrocki and L. Fijołek, *Appl. Catal. B: Environ.*, 2013, **142–143**, 533.
48. F. Qi, B. B. Xu, Z. L. Chen, L. Q. Zhang, P. Y. Zhang and D. Z. Sun, *Chem. Eng. J.*, 2010, **165**(2), 490.
49. D. Alrousan, A. Afkhami, K. Bani Melhem and P. Dunlop, *Water*, 2020, **12**(10), 2811.
50. Y. X. Yang, H. B. Cao, P. Peng and H. M. Bo, *J. Hazard. Mater.*, 2014, **279**, 444.
51. R. Rosal, A. Rodríguez, M. S. Gonzalo and E. García-Calvo, *Appl. Catal. B: Environ.*, 2008, **84**(1–2), 48.
52. J. J. Molnar, J. R. Agbaba, B. D. Dalmacija, M. T. Klasnja, M. B. Dalmacija and M. M. Kragulj, *Sci. Total Environ*, 2012, **425**, 169.
53. S. Song, Z. W. Liu, Z. Q. He, A. L. Zhang and J. M. Chen, *Environ. Sci. Technol.*, 2010, **44**, 3913.
54. H. G. Yang, C. H. Sun, S. Z. Qiao, J. Zou, G. Liu, S. C. Smith, H. M. Cheng and G. Q. Lu, *Nature*, 2008, **453**(7195), 638.
55. Z. Q. He, Q. L. Cai, F. Y. Hong, Z. Jiang, J. M. Chen and S. Song, *Ind. Eng. Chem. Res.*, 2012, **51**(16), 5662.
56. G. Moussavi and M. Mahmoudi, *Chem. Eng. J.*, 2009, **152**(1), 1.
57. H. L. Liu, L. Chen and L. Ji, *J. Hazard. Mater.*, 2019, **376**, 125.
58. Q. Wang, Z. C. Yang, B. Chai, S. Cheng, X. H. Lu and X. F. Bai, *RSC Adv.*, 2016, **6**(18), 14730.
59. J. F. Wu, T. M. Su, Y. X. Jiang, X. L. Xie, Z. Z. Qin and H. B. Ji, *Appl. Surf. Sci.*, 2017, **412**, 290.

60. J. He, W. C. Song, Z. Y. Gao and X. B. Huang, *Environ. Eng. Sci.*, 2020, **37**(6), 450.
61. G. Moussavi, A. Khavanin and R. Alizadeh, *Appl. Catal. B: Environ.*, 2010, **97**(1–2), 160.
62. H. Zhu, W. C. Ma, H. J. Han, Y. X. Han and W. W. Ma, *Chem. Eng. J.*, 2017, **327**, 91.
63. A. Mashayekh-Salehi, G. Moussavi and K. Yaghmaeian, *Chem. Eng. J.*, 2017, **310**, 157.
64. J. Chen, S. Xu, H. Yang, C. Au, S. H. Tian and Y. Xiong, *J. Chem. Technol. Biotechnol.*, 2018, **93**(6), 1648.
65. S. G. Lu, X. Zhang and Y. F. Xue, *J. Hazard. Mater.*, 2017, **337**, 163.
66. M. Izadifard, G. Achari and C. H. Langford, *Chemosphere*, 2018, **197**, 535.
67. T. Zhang and J. P. Croué, *Appl. Catal. B: Environ.*, 2014, **144**, 831.
68. W. J. Sun, H. Z. Wei, L. Y. An, C. Y. Jin, H. L. Wu, Z. A. Xiong, C. Y. Pu and C. L. Sun, *Appl. Catal. B: Environ.*, 2019, **245**, 20.
69. F. J. Beltrán, P. Pocostales, P. Alvarez, J. F. García Araya and O. Gimeno, *Ozone Sci. Eng*, 2010, **32**(4), 230.
70. Y. T. Zhang, Y. J. Xia, Q. W. Li, F. Qi, B. B. Xu and Z. L. Chen, *Sep. Purif. Technol.*, 2018, **197**, 261.
71. F. Rivas, M. Carbajo, F. Beltran, B. Acedo and O. Gimeno, *Appl. Catal. B: Environ.*, 2006, **62**(1–2), 93.
72. M. Carbajo, F. J. Beltrán, O. Gimeno, B. Acedo and F. J. Rivas, *Appl. Catal. B: Environ.*, 2007, **74**(3–4), 203.
73. C. A. Orge, J. J. M. Órfão, M. F. R. Pereira, B. P. Barbero and L. E. Cadús, *Appl. Catal. B: Environ.*, 2013, **140–141**, 426.
74. H. Einaga, N. Maeda and Y. Teraoka, *Appl. Catal. B: Environ.*, 2013, **142–143**, 406.
75. S. Afzal, X. Quan and J. L. Zhang, *Appl. Catal. B: Environ.*, 2017, **206**, 692.
76. J. Lu, X. D. Wei, Y. Chang, S. H. Tian and Y. Xiong, *J. Chem. Technol. Biotechnol.*, 2016, **91**(4), 985.
77. S. S. Sable, F. Medina and S. Contreras, *Appl. Catal. B: Environ.*, 2014, **150–151**, 30.
78. C. X. Fang, X. M. Gao, X. C. Zhang, J. H. Zhu, S. P. Sun, X. M. Wang, W. D. Wu and Z. X. Wu, *J. Colloid Interface Sci.*, 2019, **551**, 164.
79. J. S. D. Oliveira, J. D. S. Salla, R. C. Kuhn, S. L. Jahn and E. L. Foletto, *Mater. Res.*, 2018, **22**(1), e20180405.
80. F. Z. Zhang, C. H. Wei, Y. Hu and H. Z. Wu, *Sep. Purif. Technol.*, 2015, **156**, 625.
81. P. X. Liu, Y. M. Ren, W. J. Ma, J. Ma and Y. C. Du, *Chem. Eng. J.*, 2018, **345**, 98.
82. F. Z. Zhang, C. H. Wei, K. Y. Wu, H. T. Zhou, Y. Hu and S. Preis, *Appl. Catal. A: Gen.*, 2017, **547**, 60.
83. F. Qi, W. Chu and B. B. Xu, *Chem. Eng. J.*, 2015, **262**, 552.
84. F. Qi, W. Chu and B. B. Xu, *Chem. Eng. J.*, 2016, **284**, 28.
85. F. Qi, B. B. Xu and W. Chu, *J. Mol. Catal. A: Chem.*, 2015, **396**, 164.

86. H. Zhang, F. Z. Ji, Y. H. Zhang, Z. C. Pan and B. Lai, *Sep. Purif. Technol.*, 2018, **193**, 368.
87. Y. M. Ren, Q. Dong, J. Feng, J. Ma, Q. Wen and M. L. Zhang, *J. Colloid Interface Sci.*, 2012, **382**(1), 90.
88. H. Zhao, Y. M. Dong, G. L. Wang, P. P. Jiang, J. J. Zhang, L. N. Wu and K. Li, *Chem. Eng. J.*, 2013, **219**, 295.
89. H. Zhao, Y. M. Dong, P. P. Jiang, G. L. Wang, J. J. Zhang and C. Zhang, *Chem. Eng. J.*, 2015, **260**, 623.
90. Q. Z. Dai, Z. Zhang, T. T. Zhan, Z. T. Hu and J. M. Chen, *ACS Omega*, 2018, **3**(6), 6506.
91. Z. Y. Bai, Q. Yang and J. L. Wang, *Chem. Eng. J.*, 2016, **300**, 169.
92. X. K. Tian, J. L. Zhu, M. Tang, D. Wang, Y. L. Nie, L. Z. Yang, C. Dai, C. Yang and L. Q. Lu, *J. Hazard. Mater.*, 2021, **402**, 123475.
93. Y. X. Wang, L. L. Chen, H. B. Cao, Z. X. Chi, C. M. Chen, X. G. Duan, Y. B. Xie, F. Qi, W. Y. Song, J. Liu and S. B. Wang, *Appl. Catal. B: Environ.*, 2019, **245**, 546.

CHAPTER 2

Heterogeneous Catalytic Ozonation over Supported Metal Oxides

ZHAOKUN XIONG,[a,b] YANG LIU,[a,b] PENG ZHOU,[a,b] HENG ZHANG,[a,b] AND BO LAI*[a,b]

[a] State Key Laboratory of Hydraulics and Mountain River Engineering, College of Architecture and Environment, Sichuan University, Chengdu 610065, P.R. China; [b] Sino-German Centre for Water and Health Research, Sichuan University, Chengdu 610065, P.R. China
*Email: laibo@scu.edu.cn

Although tremendous efforts have been devoted to develop catalysts for heterogeneous catalytic ozonation, few catalysts can meet the requirements of the favorable catalysts: fast ozonation rate, high organic removal efficiency, long-term stability, good recyclability and easy separation from treated wastewater.[1] The highly efficient heterogeneous catalysts are usually composed of micro- or nanoscale particles to provide a large specific surface area and great number of active sites.[2–4] However, the small sizes of those particles make them difficult to separate and collect from wastewater. In order to increase the performance of metal oxides in catalyzing ozone, researchers often synthesize metal oxides on corresponding supports to increase the active sites and surface area of catalysts.[5–8] The dispersion of transition metals (Fe, Cu, Co, Mn, Ni, Ce, *etc.*) or oxides (Fe_3O_4, MnO_2, CeO_2, TiO_2, FeOOH, *etc.*) on porous hard supporters, such as Al_2O_3, TiO_2 and zeolites, is a common catalyst production

Chemistry in the Environment Series No. 8
Advanced Ozonation Processes for Water and Wastewater Treatment: Active Catalysts and Combined Technologies
Edited by Hongbin Cao, Yongbing Xie, Yuxian Wang and Jiadong Xiao

Published by the Royal Society of Chemistry, www.rsc.org

method.[9] The selection of the support, the active components of catalysts and the preparation of the catalysts affect the activity of a supported catalyst. Therefore, the suitable metal oxides and supported carrier have been widely investigated to meet the requirements of the industrial catalysts.

2.1 Typical Supported Metal Oxides as Ozonation Catalysts

2.1.1 Metal Oxides/Al_2O_3

The porous feature of Al_2O_3 can enhance the adsorption of pollutants, and the basic sites on the surface can promote the generation of hydroxyl radicals ($^{\bullet}OH$). In addition, Al_2O_3 has become one of the most typical supported metal oxides for ozone oxidation catalysts because of its low price, good machinery and stability.[10–12] The metal oxide supported on Al_2O_3 is usually prepared by dipping and drying, which has the advantages of simple operation and low cost.[13] These metal oxides include nickel oxide,[14,15] cobalt oxide[16,17] and manganese oxides.[18–20] After being loaded on Al_2O_3, the catalytic performance of these metal oxides was distinctly improved, and they are widely used to remove various refractory organic pollutants.

In the early days, the main focus was on a single metal oxide supported on Al_2O_3. In 2005, Einaga *et al.* studied the oxidation behavior of organic pollutants on Al_2O_3-supported manganese oxide in the presence of ozone.[21] The catalytic performance was related to the intermediate products formed on the surface of the catalyst. The sharp drop in activity was mainly due to the accumulation of intermediate compounds. Subsequently, they did a study on the effect of water vapor on the oxidation of benzene under the condition of ozone by Al_2O_3-supported manganese oxide.[22] Water vapor could effectively inhibit the accumulation of by-products on the surface of the catalyst, thereby inhibiting the deactivation of the catalyst. Moreover, Yang *et al.* studied the surface acidity and reactivity of β-FeOOH/Al_2O_3 to ozone-degrading drugs by *in situ* ATR-FTIR.[23] The Lewis acid sites on the material surface enhanced the binding of β-FeOOH and Al_2O_3. And their observations confirmed that the Lewis acid site was the active site of the reaction. Soltan *et al.* investigated the role of surface carboxylates in catalytic ozonation of acetone on alumina-supported manganese oxide.[24] Al_2O_3 reacted with adsorbed acetone to form a carboxylate intermediate. Then the carboxylate immediately migrated to the Mn site and reacted with the highly active atomic oxygen species produced by ozone decomposition.

In recent years, the synergy of bimetal oxides and even trimetal oxides has been extensively studied.[25–28] Chen *et al.* compared the effects of Ce, Mg and Mg–Ce oxides loaded onto Al_2O_3 on the catalytic ozone processes (COPs) for the oxidation of refractory oil refinery wastewater.[29] As shown in Figure 2.1(a), compared with Mg/Al_2O_3–COP, Ce/Al_2O_3–COP, Al_2O_3–COP and single ozonation, the removal rate of COD by Mg–Ce/Al_2O_3–COP increased by 4.7%, 4.1%, 6.0% and 17.5%, respectively. This result demonstrated the

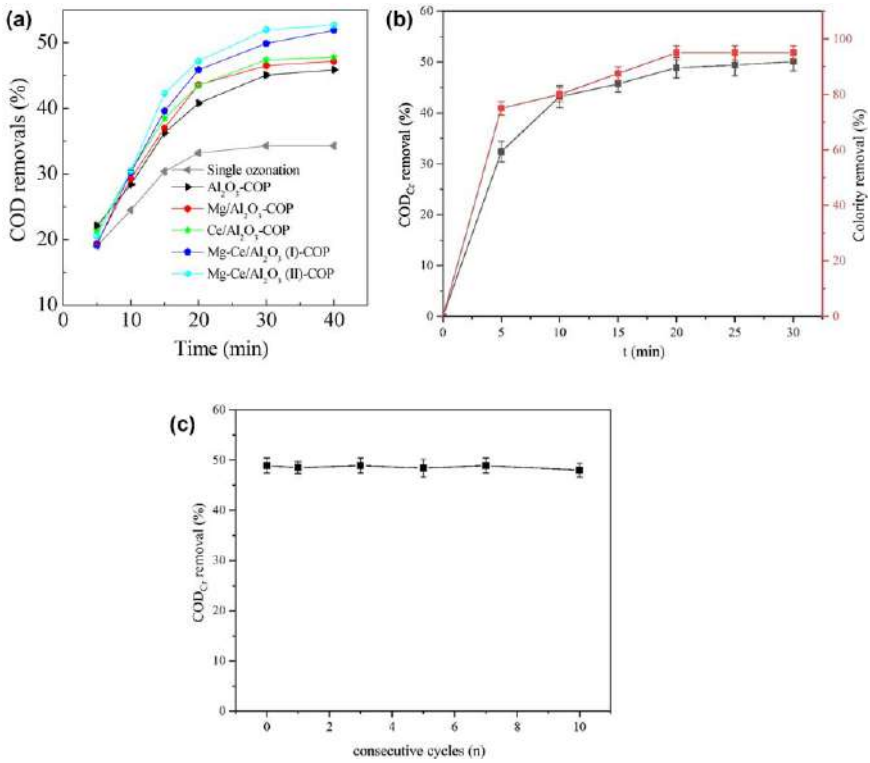

Figure 2.1 (a) COD removals for refractory oil refinery wastewater by single ozonation and various COPs systems. Reproduced from ref. 29 with permission from MDPI, Copyright 2017. (b) COD removal ratio and colority removal ratio under different reaction times. (c) COD removal ratio using Mn–Fe–Ce/c-Al_2O_3 catalyst in 10 consecutive cycles. Reproduced from ref. 25 with permission from Elsevier, Copyright 2020.

advantages of bimetallic oxides over monometallic oxides. In addition, Song *et al.* prepared Mn–Fe–Ce/γ-Al_2O_3 ternary catalyst by dipping and roasting in order to catalytic ozone oxidate dairy farming wastewater.[25,27] The removal rates of COD and chromaticity reached 48.9% and 95%, respectively (Figure 2.1(b)). It was particularly important that this catalyst had excellent stability. After ten cycles, the removal rate of COD was not significantly reduced (Figure 2.1(c)). Compared with single-metal oxides, multimetal oxides tended to have better catalytic performance. However, the synergistic mechanism of multimetal oxides and the issue of metal leaching should be considered further in the treatment of pollutants in wastewater.

2.1.2 Metal Oxides/TiO_2

TiO_2 is one of the most extensively studied materials in the field of photocatalysis.[30] It is also one of the most typically supported metal oxides for ozone oxidation catalysts, owing to its high chemical stability, biological

non-toxicity, low cost, porosity and other properties, coupled with its excellent catalytic performance for ozone.[31] Guo *et al.* used the impregnation method to prepare MnO_x–CeO_2/TiO_2.[31] By comparing the results of three catalysts (Mn–Ce/TiO_2-A, Mn–Ce/TiO_2-B, Mn–Ce/TiO_2-AB), the efficiency order of the ozone-catalyzed conversion of NO_x to HNO_3 was Mn–Ce/TiO_2-AB > Mn–Ce/TiO_2-B > Mn–Ce/TiO_2-A. The impregnation method was the most commonly used method for the synthesis of metal oxide loading, but when the metal loading was too high, sintering occurred during the calcination process. Valenzuela *et al.* explored the photochemical deposition method to deposit nickel nanoparticles on TiO_2.[32] This enabled reduction of the nickel precursor to a short time at room temperature. It was also a good direction to study the synergy of the two supported carriers to catalyze ozone because of the advantages of alumina and titania. Chen *et al.* synthesized TiO_2/Al_2O_3 by the dipping method and found that the TiO_2/Al_2O_3 catalyst was composed of approximately 10.0 wt% TiO_2 and 87.3 wt% Al_2O_3 and that TiO_2/Al_2O_3 was the most active.[33] Compared with Al_2O_3 catalyst, TiO_2/Al_2O_3 could achieve a higher total organic carbon (TOC) removal rate (98%), and the larger particle size was more conducive to recovery after the reaction.

2.1.3 Metal Oxides/Zeolites

As a porous frame structure, zeolite has the advantages of large specific surface area, developed pores and good reusability. It can selectively adsorb organic molecules in wastewater. In recent years, zeolite has been widely used to catalyze the ozone process.[34–36] Common zeolite types are 13X,[37–39] SBA-15,[40,41] ZSM-5,[42,43] MCM-41[44–46] and USY.[47,48]

Zhang *et al.* studied the effect of Ce-loaded natural zeolite on the catalytic ozone oxidation of penicillin G.[35] Quenching experiments proved that $^{\bullet}OH$ and superoxide radicals ($^{\bullet}O_2^-$) were the main active species (Figure 2.2(a)). The possible mechanism was proposed according to the quenching experiments (Figure 2.2(b)). The toxicity of the catalytic ozonation process was evaluated, and the highly toxic intermediates were decomposed into less toxic intermediates after 60 min of degradation. Their study indicated the application of Ce-loaded natural zeolite catalyst in the catalytic ozonation of penicillin G. Li *et al.* investigated the effect of modification methods (*in situ* synthesis and impregnation) and transition metal types (Cu and Co) on the catalytic ozonation of toluene by loading on MCM-41.[45] Compared with the impregnation method, the synthesis of copper oxide *in situ* was more likely to sinter and aggregate during the calcination process. Cobalt-modified catalysts had higher catalytic activity and stability compared with copper-modified catalysts. This excellent performance was attributed to the well-dispersed metal oxides and their strong ability to decompose and accumulate organic by-products on the catalyst surface. The optimal modification of different supports required specific metal oxides and synthesis methods. The investigation of optimal conditions was of great significance for practical applications.

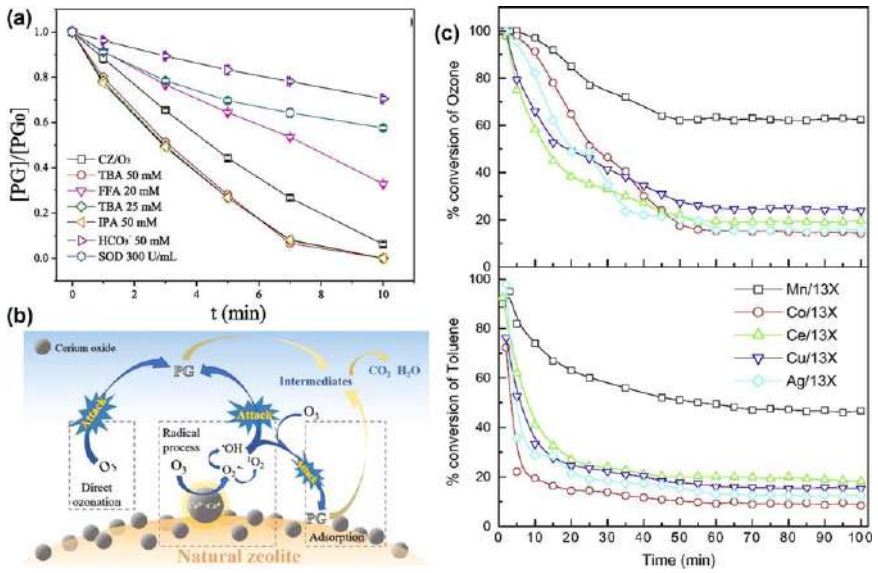

Figure 2.2 (a) Effect of scavengers on penicillin G removal efficiency in Ce-loaded natural zeolite catalytic ozonation system. (b) Reaction mechanism of penicillin G degradation in Ce-loaded natural zeolite catalytic ozonation system. Reproduced from ref. 35 with permission from Elsevier, Copyright 2019. (c) Change in the conversions of toluene and ozone with time on Mn/13X, Co/13X, Ce/13X, Ag/13X and Cu/13X catalysts. Reproduced from ref. 38 with permission from Elsevier, Copyright 2019.

Gopi *et al.* loaded different kinds of metal oxides on 13X zeolite to catalyze the oxidation of toluene by ozone.[38] The change in the conversions of toluene and ozone with time revealed that the activity was in the order of Mn/13X > Ce/13X > Cu/13X > Ag/13X > Co/13X and Mn/13X > Cu/13X > Ce/13X > Ag/13X > Co/13X, respectively (Figure 2.2(c)). They also found that the increase in temperature and humidity was beneficial to increase the activity and selectivity of catalytic ozone. Moreover, after the addition of water, the molar ratio of ozone to toluene consumption also decreased from 12 to 9.5, which indicated that adding water to the reaction stream could significantly reduce the amount of ozone required for oxidation and decomposition of carbon dioxide. Chen *et al.* studied the process of various ZSM-5 zeolite–supported metal (Ce, Fe or Mn) oxides to catalyze ozone oxidation to remove nitrobenzene in aqueous solution.[34] Compared with ZSM5 zeolite, the support of Ce, Fe or Mn oxides increased the catalytic activity, and Ce/NaZSM5-38 had the highest removal rate of TOC (86.3%). HZSM5-38 and NaZSM5-100 zeolites had a strong adsorption effect on nitrobenzene.

The combination of zeolite and Al_2O_3 will also get unexpected results. Bing *et al.* prepared Fe_2O_3/Al_2O_3@SBA-15 by the simple impregnation method.[40] The TOC removal rate could reach about 90% after 60 min of reaction. The characterization results showed that Al–O–Si was formed by Al^{3+} replacing

the hydrogen of the surface Si–OH group, which not only gave Al_2O_3 and Fe_2O_3 a higher dispersibility on SBA-15 but induced a large amount of surface Lewis acid sites. The synergistic effect of iron Lewis acid sites and alumina promoted the generation of surface-adsorbed $^{\bullet}OH$ and $^{\bullet}O_2^-$ and accelerated the oxidative degradation of ibuprofen.

2.1.4 Metal Oxides Supported on Other Porous Materials

In addition to these supports, many other porous materials are used as supports for supporting metal oxides. For example, SiO_2,[49–51] MnO_2,[52,53] CeO_2[54–56] and ZrO_2[57,58] have been widely used in the field of catalytic ozone oxidation. Einaga *et al.* loaded manganese oxide and manganese–copper oxide on SiO_2 to catalyze the oxidation of benzene by ozone.[49,50] Different metal precursors would affect the structure of the catalyst. Extended X-ray absorption fine structure (EXAFS) analysis showed that aggregated manganese oxide Mn_2O_3 would be formed when using manganese nitrate precursor to prepare the catalyst, whereas using manganese acetate precursor would form highly dispersed manganese oxide. For other heavy-loaded catalysts, the Mn/SiO_2 containing highly dispersed manganese sites prepared by manganese acetate precursor showed much higher performance than the catalyst prepared by manganese nitrate precursor. In addition, the catalytic activity of Cu–Mn mixed oxides rose with the increase of calcination temperature, which was related to the increase of the spinel-type Cu–Mn mixed oxide phase. Hu *et al.* loaded cobalt oxide on mesoporous zirconia and used it to catalyze ozonation of the herbicide 2,4-D.[57] The author proved that $^{\bullet}OH$ was the main reactive oxygen species. However, because cobalt is a heavy metal that is relatively harmful to the environment, its leaching problem should be paid more attention. Also, Ncanana *et al.* studied the degradation of cresol isomers by ozone oxidation under the catalyst of silica-supported nickel, iron, manganese and vanadium.[51]

Krisbiantoro *et al.* used palladium supported by cerium oxide as a highly active and selective catalyst to catalyze the oxidation and decomposition of ammonium ions in water by ozone.[54] Among the noble metals, Ru, Rh, Pd, Ag, Ir, Pt and Pd exhibited the highest activity and selectivity to gaseous compounds when catalyzing ozone to decompose NH_4^+ in water. The Pd carrier had a great influence on the catalytic performance, and CeO_2 was the most suitable carrier with high activity, selectivity and stability. In addition, Xing *et al.* also found that mesoporous cerium oxide, supported by manganese oxide catalytic ozone, could effectively oxidize sulfosalicylic acid.[55] As shown in Figure 2.3(a), Nawaz *et al.* prepared the mesoporous Fe_3O_4/MnO_2 composite material by the co-precipitation method.[52] Its catalytic ozone oxidation activity of *p*-cresol and *p*-chlorophenol mixture was much higher than those of Fe_3O_4 and MnO_2. At pH 9, it was proved to have the highest catalytic activity and the smallest amount of metal leaching. This experiment was of great significance for studying the synergy between different metal oxides.

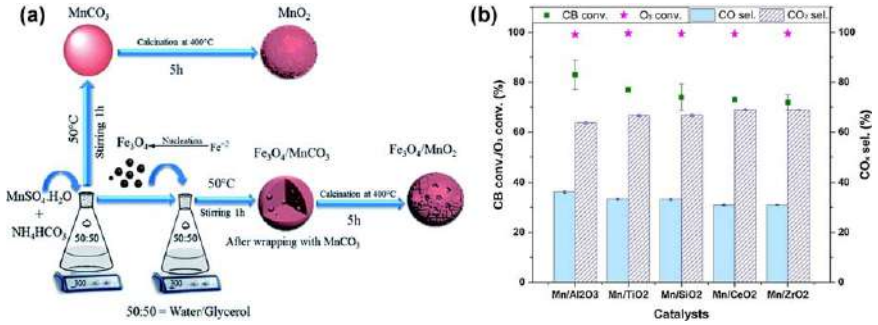

Figure 2.3 (a) Schematic illustration for the synthesis of Fe_3O_4/MnO_2. Reproduced from ref. 52 with permission from the Royal Society of Chemistry. (b) Catalytic performance of chlorobenzene ozonation over MnO_x with different supports. Reproduced from ref. 59 with permission from Elsevier, Copyright 2020.

The same metal oxides loaded on different carriers have different effects. Chen *et al.* used different supports (Al_2O_3, TiO_2, SiO_2, CeO_2, ZrO_2) to prepare a series of MnO_x-based catalysts.[59] As shown in Figure 2.3(b), the chlorobenzene conversion rate of the Mn/Al_2O_3 catalyst was the highest, reaching 82.92%. The conversion rate of other catalysts was in the order of $Mn/TiO_2 > Mn/SiO_2 > Mn/CeO_2 > Mn/ZrO_2$. In addition, Maddila *et al.* researched the degradation of trichlorophenol by using Ce–Zr on different metal oxides (Al_2O_3, SiO_2 and TiO_2) for catalytic ozonation.[60] SEM-EDX results illustrated that cerium–zirconia oxide was better dispersed on the surface of TiO_2 compared with Al_2O_3 and SiO_2 carriers. Also, they investigated the degradation of trichlorophenol by ozonation by using Ce–V on different metal oxides (Al_2O_3 and SiO_2).[61] Alkaline pH promoted the formation of $^{\bullet}OH$ in heterogeneous catalysts. Five percent $Ce–V/SiO_2$ catalyzed ozone oxidation could significantly increase the degradation rate of chloronitrophenol, and it was an effective method to remove chlorine, nitro and hydroxyl functions in organic compounds in water.

2.2 Effects of Operation Parameters on Catalytic Ozonation Efficiency

2.2.1 Initial pH

The pH value, a critical environmental parameter, is important in the catalytic ozonation system. It not only affects ozone mass transfer and decomposition but has effects on catalyst surface properties and the dissociation constant pK_a of contaminants. Aqueous hydroxide in alkaline conditions can boost ozone decomposition and promote the generation of $^{\bullet}OH$. Zhao *et al.* prepared Ag-doped nickel ferrite for the catalytic ozonation treatment of secondary biochemical effluent for papermaking wastewater.[6] They reported that the COD removal was enhanced with the increase of

initial pH in a sole ozone system. However, different from the sole ozone system, the highest removal efficiency was achieved around the pH of the point of zero charge (pH_{pzc}) of catalyst, which played an important role in promoting ozone decomposition and •OH production. When the pH condition was lower or higher than the pH_{pzc} of the catalyst, the catalyst surface presented a protonated or deprotonated state, causing the decrease of catalytic efficiency.

Zhang *et al.* synthesized a cerium-loaded natural zeolite (CZ) for catalytic ozonation of penicillin G. The effect of initial pH on penicillin G removal by the CZ catalytic ozonation system was evaluated.[35] Penicillin G removal efficiency was enhanced by increasing the initial pH from 3.0 to 4.5; then it changed slightly with the initial pH increasing from 4.5 to 5.0, and the removal efficiency dropped with the initial pH further increasing from 5.0 to 9.0. The apparent rate constant (k_{obs}) showed the same trend as the removal efficiency. As mentioned previously, OH^- could initiate ozone decomposition to generate •OH. Apart from the effect of OH^-, the pH_{pzc} of CZ was tested to be 5.4 in the experiments; when the initial pH was near pH_{pzc}, the removal efficiency of penicillin G reached the maximum.

In literature, OH^- could initiate ozone decomposition to generate •OH. As for pH effects on the catalyst surface property, the surface hydroxyl groups were the active sites for •OH production. The closer the pH came to the pH_{pzc} of the catalyst, the better performance the catalyst exhibited. Compared with the protonated or deprotonated form, the zero-charged surface of catalyst is mainly responsible for catalytic efficiency.

2.2.2 Ozone Dosage

Increasing ozone dosage can raise the dissolved ozone concentration in aqueous solution, which could facilitate the removal of contaminants since catalytic performance is usually proportional to the ozone concentration. Tong *et al.* synthesized a novel iron-doped SBA-16 mesoporous structure catalyst that showed efficient catalytic ozonation of diclofenac.[62] The effect of ozone dosage was discussed in this work. When the ozone dosage was 60 $mg\,h^{-1}$, the TOC removal rate reached 79.3%. Further increasing the ozone dosage to 80 and 100 $mg\,h^{-1}$ led to a higher TOC removal rate up to 82.5% and 88.8%, respectively. The increase of ozone dosage contributes little to TOC removal improvement, probably due to the limited active sites on the Fe–SBA-16 surfaces.

In the ozone catalytic oxidation system, the concentration of ozone dosage plays a crucial role in the amount of free radicals generated in the catalytic system, thereby causing the degradation of organic matter in wastewater. Sun *et al.* prepared a Fe–Mn@Bt catalyst used to deeply treat the biochemical tailwater of coal chemical wastewater for catalytic ozonation. When the ozone generation rate ranged from 0.5 $g\,h^{-1}$ to 2.5 $g\,h^{-1}$, the degradation performance of Fe–Mn@Bt ozone catalyst increased significantly with the growth of the ozone generation rate. When the amount exceeded 2.0 $g\,h^{-1}$, the removal

rate of the phenol and TOC in the wastewater rose very slowly. When the ozone concentration was low, it could be dissolved in water sufficiently and react with organic matter rapidly. The dissolved ozone in the water combined with the active sites in the Fe–Mn@Bt catalyst to catalyze the generation of free radicals with strong oxidative properties, and the capacity to remove the pollutant was significantly increased. However, the ozone dosage was not a restricting factor when the ozone flow rate was added excessively while the ozone concentration in the liquid phase had approached saturation.

Under normal circumstances, increasing ozone dosage leads to better catalytic performance. Nevertheless, from a practical point of view, it is not economically sound to perform catalytic ozonation by further increasing ozone dosage. Ozone utilization is the key factor in evaluating the activity of catalysts.

2.2.3 Catalyst Dosage

Catalyst dosage usually impacts catalytic performance. Increasing dosage mostly leads to rising efficiency at first and then a gradually slowing down at a certain concentration. Therefore, identifying the optimum catalyst dosage makes economic sense. Zhao *et al.* investigated catalytic activity in a series of catalyst concentrations (0–200 mg L^{-1}).[6] Catalytic efficiency was enhanced by increasing dosage from 0 to 100 mg L^{-1}. However, the further increase of catalyst dosage showed an unfavorable effect on degradation rate. The phenomenon was caused by the decrease of active sites owing to catalyst aggregation, and excessive leached Fe ions may act as a scavenger of $^{\bullet}OH$. Yan *et al.* prepared a complex catalyst, copper–oxygen–manganese/g-alumina (CMA), and explored the effect of CMA dosage on polyvinyl alcohol (PVA) removal.[63] With the increase of catalyst dosage from 0 to 100 mg L^{-1}, the removal rate of PVA increased rapidly to 88.1%. Afterward, the removal rate of PVA remained constant and even decreased slightly when the dosage was raised to 240 mg L^{-1}. The phenomenon had also been observed in other studies, possibly due to the aggregation of particles and the quenching of $^{\bullet}OH$ due to the excessive active sites.

In general, catalytic efficiency is usually boosted by increasing catalyst dosage at the very beginning. It is caused by the growing active sites provided in the reaction system. Up to a certain dosage, the efficiency no longer improves and tends to maintain a level or even fall back. Catalyst aggregation, which decreases exposed active sites or/and excessive catalyst quenching $^{\bullet}OH$, account for the phenomenon.

2.2.4 Initial Concentration of Contaminants

There is no doubt that the initial concentration of contaminants can affect the degradation efficiency of contaminants in the heterogeneous catalytic ozonation process with other experiment conditions staying the same. Generally, higher concentration decreases catalytic efficiency. Kruanak *et al.*

studied the initial concentration of contaminant during the degradation of 2,4,6-trichlorophenol in synthetic wastewater by catalytic ozonation using alumina-supported nickel oxides.[14] The results reported that as the initial concentration increased, the removal efficiency decreased due to the increasing amount of 2,4,6-trichlorophenol to react with ozone or •OH.

2.2.5 Reaction Temperature

Reaction temperature mainly affects the solubility of ozone and then weakens or enhances reaction efficiency. Yan *et al.* synthesized Si-doped α-Fe_2O_3 for the removal of nitrobenzene in aqueous solution. The effect of solution temperature on removal efficiency was studied at temperatures ranging from 15 °C to 35 °C.[7] Results showed that the removal efficiency of nitrobenzene under different reaction temperatures was discrepant and that the adsorption amounts of nitrobenzene under different temperatures were less than 3.5%. The removal efficiency increased from 74.2% to 82.0%, 85.0% and 94.5% with the reaction temperature ranging from 15 °C to 30 °C. And 72.5% of nitrobenzene can be rapidly degraded within 2 min under a reaction temperature of 30 °C. Further increasing the reaction temperature from 30 °C to 35 °C decreased the removal efficiency from 94.5% to 88.0% at 20 min, which showed a negative effect on the catalytic process. Chen *et al.* prepared MnO_x/SBA-15 for norfloxacin degradation by catalytic ozonation and discussed temperature effects on degradation efficiency.[64] The TOC removal efficiency increased with temperature from 5 °C to 25 °C. However, when the temperature continued to climb to 30 °C, its mineralization rate decreased, possibly due to the reduction of ozone solubility in solution. The increase of temperature would accelerate the mass transfer rate of norfloxacin onto the catalyst and enhance the reaction rate of ozone and •OH with the norfloxacin.

Reaction temperature is an important factor for the behavior of ozone in a catalytic system. Within a befitting range, increasing reaction temperature can positively increase the activation molecules and promote the degradation of contaminants. Simultaneously, ozone shows a lower solubility in water with the increasing of temperature.

2.2.6 Coexisting Ions in Water

Coexisting ions are of vital importance to the ozone oxidation process in aqueous condition. Levanov *et al.* studied ozone catalysis reaction with chloride ions by metal ions in an acidic medium.[65] The results showed that VO^{2+}, Fe^{3+}, Co^{2+} and Cu^{2+} ions catalyze the reaction of ozone with Cl^- in an acidic medium, whereas Al^{3+}, Cr^{3+}, Cr^{2+}, Ni^{2+}, Zn^{2+}, Sn^{4+} and Ce^{3+} ions do not have a catalytic effect. Those phenomena can be explained in two ways. On one hand, metal ions in a higher oxidation state can be formed in oxidation with ozone. These can oxidize the chloride ion by transferring charge. On the other hand, a catalytic complex that decomposes with the liberation of chlorine can be formed by coordination catalysis. Trapido *et al.* studied

the effects of coexisting ions on ozone performance for the degradation of *m*-dinitrobenzene.[66] The work reported that with dissolved ions of Fe^{2+}, Mn^{2+}, Cu^{2+}, Ni^{2+}, Co^{2+}, V^{5+}, Cr^{3+} and Mo^{6+}, the ozonation catalytic efficiency was promoted significantly. Wang *et al.* selected bicarbonate (HCO_3^-), phosphate (PO_4^{3-}) and sulfate (SO_4^{2-}) as inorganic anions to investigate the influence on phthalic acid degradation in the O_3/CeO_2 and O_3/FeOOH systems.[67] The results showed that HCO_3^- scarcely affected the phthalic acid degradation in the O_3/CeO_2 system while significantly influencing the O_3/FeOOH system. PO_4^{3-} and SO_4^{2-}, which are good at chelation, curbed the removal of phthalic acid notably in the O_3/CeO_2 system. It could be deduced that phthalic acid was mainly degraded by $^{\bullet}OH$ oxidation in the O_3/FeOOH system and by complexation in the O_3/CeO_2 system.

As mentioned previously, coexisting ions in the aqueous ozonation process strongly affect the reaction process. When metal ions were added into the solution, the routine of generating $^{\bullet}OH$ changes. Electron transfer between the different valence states of metal ions can promote the production of $^{\bullet}OH$, or coordination catalysis happens. However, inorganic anions affect the catalytic process differently. If the reaction system mainly eliminates the pollutant by generating $^{\bullet}OH$, some inorganic anions, such as HCO_3^-, can clearly inhibit the catalytic process. If complexation plays a dominant role in the degradation process, inorganic anions such as PO_4^{3-} and SO_4^{2-} competitively adsorb on the catalyst surface to occupy the active sites and restrain the catalytic process.

2.3 Catalytic Reaction Mechanisms

To date, supported metal oxides in catalytic ozonation for the degradation of organic pollutants have been widely investigated. Unfortunately, despite increasing research efforts in the field of catalytic ozonation and the introduction of new catalysts, the specific catalytic reaction mechanism has not been widely recognized. In particular, there is a lack of understanding of catalyst activity and deactivation. Various reaction mechanisms have been proposed. Frequently, the same catalysts studied by different research groups, sometimes contradictory results. The performance of catalytic ozonation depends largely on the surface properties of the catalyst, but the reaction process and mechanism are complex, particularly concerning supported metal oxides. Therefore, the catalytic active sites and proposed catalytic reaction mechanisms need to be intensively summarized and discussed.

2.3.1 The Circumstance of Radical and Non-radical Pathways

It is well-known that heterogeneous catalytic ozonation can proceed *via* two major pathways to degrade pollutants: direct molecular ozone reactions and the adsorption of O_3 and/or pollutants on the surface of the catalyst leading to ozone dissociation and the generation of reactive oxygen species (ROS, *e.g.* $^{\bullet}OH$, $^{\bullet}O_2^-$ or singlet oxygen [$^1O_2$]).[68,69] Radicals oxidation relying on $^{\bullet}OH$ and/or $^{\bullet}O_2^-$ from O_3 decomposition on the active sites of catalysts has been recognized as

the dominant pathway for the degradation of pollutants. To identify the generation of radicals, quenching experiments, chemical probes and electron paramagnetic resonance (EPR) analyses have been utilized. Quenching experiments have been widely applied to investigate the generated radical species and the contribution of corresponding radicals by evaluating the inhibitory degree of degradation efficiency in the presence or absence of radical scavengers such as *tert*-butanol (TBA), isopropanol (IPA), methanol, *p*-benzoquinone (*p*-BQ), *etc.* Apart from selecting the appropriate chemical scavengers, the concentration of scavengers also needs to be noted based on the competition between the target organic pollutants and chemical scavengers to react with ROS.[70] Besides, the improper selection of the radical scavengers and design of the quenching experiments often cause mistakes or misinterpretations of the results.[69] For example, the competitive reactions between the scavengers and the target radicals and other oxidants can mislead the interpretation of the quenching results.[69] Steady-state ROS concentration can also be quantitatively detected by means of chemical probe methods. Typically, benzoic acid is employed as a probe compound for the capture of $^{\bullet}OH$ in order to quantify the yield of $^{\bullet}OH$.[71] Benzoic acid can react with $^{\bullet}OH$ to produce three isomers of hydroxyl benzoic acid. Total hydroxybenzoic acid yield is calculated from this ratio by measuring *p*-HBA.[70] Also, *p*-chlorobenzoic acid, terephthalic acid and coumarin can be applied to quantitatively examine the steady-state concentration of generated $^{\bullet}OH$.[1,27,72] Nitro blue tetrazolium (NBT) was selected as a qualitative indicator of $^{\bullet}O_2^-$ as it could be reduced by $^{\bullet}O_2^-$ ($k = [5.8–6.0] \times 10^4\ M^{-1}\ s^{-1}$) to form purple product, which exhibits a maximum absorption region at 530 nm.[70,73] In addition, the adoption of chemical scavengers to determine the contribution of ROS, spin trapping agents can be used to directly quantify ROS by detecting the by-products through EPR. 5,5-Dimethyl-1-pyrrolidine *N*-oxide (DMPO) is a frequently used spin trapping agent in the EPR for $^{\bullet}OH$ and $^{\bullet}O_2^-$ identification *via* the formation of specific adducts. Thereinto, DMPO–OH is a typical 4-line EPR spectrum with the relative intensity ratio of 1 : 2 : 2 : 1 due to the equivalent hyperfine splitting constants of $\alpha_N = \alpha_H = 14.9$ G.[74] Also, DMPO can be applied as a spin trapping agent for $^{\bullet}O_2^-$ with six characteristic peaks of DMPO–OOH in EPR spectrum.[73] It should be emphasized that the adoption of organic solvent such as absolute ethanol and/or dimethyl sulfoxide (DMSO) as the reaction medium instead of ultrapure water can prolong the half-life of $^{\bullet}O_2^-$ as well as act as the scavenger for $^{\bullet}OH$.[70,75]

Li *et al.* fabricated the Mn–Fe–Ce/γ-Al_2O_3 ternary catalyst by the impregnation roasting method to catalyze ozone for dairy farming wastewater treatment.[27] The catalyst was found to significantly influence the generation of $^{\bullet}OH$. EPR and coumarin fluorescence techniques were applied to qualitatively and quantitatively investigate the generation of $^{\bullet}OH$. As shown in Figure 2.4(a), the generation of $^{\bullet}OH$ in the Mn–Fe–Ce/γ-Al_2O_3/O_3 system as OOM (O_3–OH^- metals) due to the electrons in OH^- were transferred to the metals, and O_3 was attracted to the surface hydroxyl groups.[27] Bing *et al.* prepared the Fe_2O_3/Al_2O_3@SBA-15 catalyst to highly effective mineralize ibuprofen in the presence of ozone.[40] Mechanism analysis found that the chemisorbed O_3 was

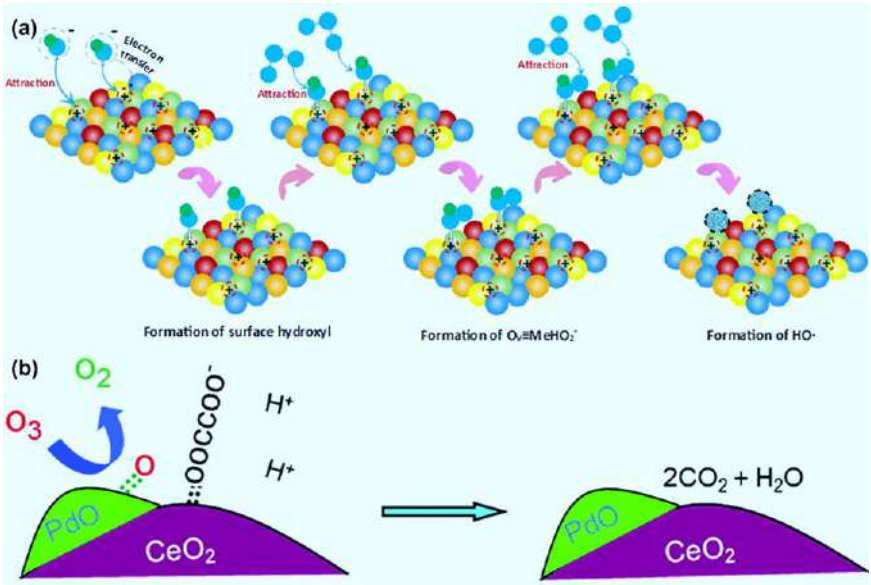

Figure 2.4 (a) Proposed OOM model of the Mn–Fe–Ce/γ-$Al_2O_3 + O_3$ system. Reproduced from ref. 27 with permission from American Chemical Society, Copyright 2020. (b) The proposed mechanisms of PdO/CeO_2 for catalytic ozonation of oxalate. Reproduced from ref. 77 with permission from American Chemical Society, Copyright 2011.

decomposed into surface atomic oxygen species at the Lewis acid sites of Al^{3+} while it was converted into surface-adsorbed $^{\bullet}OH_{ads}$ and $^{\bullet}O_2^-$ at the Lewis acid sites of Fe^{3+}.[40] The combination of both Lewis acid sites of Fe^{3+} and Al^{3+} onto the catalyst could promote the generation of $^{\bullet}OH_{ads}$ and $^{\bullet}O_2^-$.

Recently, non-radical oxidation processes relying on surface complexes, surface-adsorbed activated oxygen species or $^1O_2$ oxidation have been found as the alternative degradation pathways in heterogeneous catalytic ozonation.[69,76] Zhang *et al.* found that cerium-supported palladium oxide (PdO/CeO_2) at a low palladium loading was an efficient catalyst in catalytic ozonation of oxalate not relying on $^{\bullet}OH$ oxidation.[77] As shown in Figure 2.4(b), the oxalate molecule was adsorbed on the surface of the CeO_2 of the catalyst forming surface complexes, and O_3 was adsorbed on the PdO of the catalyst and further decomposed into surface atomic oxygen (*O), surface peroxide (*O_2) and O_2 gas in sequence.[77] In addition, the CeO_2 support also enhanced the conglutination and decomposition of O_3 on the surface of PdO. The strong affinity probably increased the stability of the surface atomic oxygen against the fast reaction with ozone forming peroxide. Whereafter, the same group developed the CuO/CeO_2 catalyst to significantly enhance oxalate degradation in reaction with ozone.[56] They uncovered a novel catalytic ozonation pathway that depended on neither acid assistance nor radical oxidation. In addition, the hybrid mechanisms consisting of radical and

non-radical pathways were found by Chen *et al.* CuO_x, supported on mesoporous alumina microsphere catalysts with hierarchical structures, were fabricated to boost catalytic ozonation for the degradation of phenol wastewater. The quenching experiments and EPR analysis indicated that $^{\bullet}O_2^-$, $^1O_2$ and $^{\bullet}OH$ were the predominant reactive species.

It is still challenging to precisely and quantitatively estimate the contribution of the radical and non-radical pathways in total oxidation. Moreover, since the complicated mechanisms of non-radical processes remain ambiguous and controversial, more attention should be paid to designing more efficient catalysts and exploring deep mechanisms in order to investigate the intrinsic catalytic sites, improve their stabilities and exploit the full potential of these properties.[70]

2.3.2 Identification of Catalytic Active Sites

Surface hydroxyl groups, Lewis acid sites, structural defects and surface functionalities have been suggested as potential catalytic active sites for catalytic O_3 activation to produce radicals.[69] However, identification of catalytic active sites is still ambiguous even for similar heterogeneous catalytic ozonation systems. For heterogeneous catalytic ozonation over supported metal oxides, the complicated structure of catalysts and the interfacial reaction make it not so easy to identify the precise catalytic active sites. As shown in Figure 2.5(a), H_2O molecules strongly adsorbed on the metal oxides surface when the metal oxide catalyst was introduced into aqueous solution. Then the adsorbed H_2O always dissociated into OH^- and H^+, forming the surface hydroxyl groups with surface cations and oxygen anions, respectively.[78,79] Ozone molecules in aqueous solution interacted with the surface–OH_2^+ existing on the surface of the catalyst due to electrostatic forces and/or hydrogen bonding due to their resonance structures, resulting in the radical chain reactions and promoting $^{\bullet}OH$ generation.[78] Sun *et al.* investigated the catalytic ability and mechanisms of SBA-15-supported manganese oxide (MnO_x/SBA-15) for the degradation of oxalic acid. The adsorption of oxalic acid and $^{\bullet}OH$ initiation on the protonated surface hydroxyl groups (Mn–OH_2^+) are the two key factors that enhance the degradation of oxalic acid.[80] Mn–OH_2^+ groups were the active sites for ozone molecules decomposing into $^{\bullet}OH$ according to the investigation of radical scavengers and pH_{pzc}. It happens that, in a similar case, mesoporous Mn–CeO_x/γ-Al_2O_3 catalyst was practicably fabricated *via* a facile impregnation–calcination method. The protonated surface hydroxyl groups of S–OH_2^+ on Mn–CeO_x/γ-Al_2O_3 were the active sites for ozone decomposition to generate $^{\bullet}OH$ and $^{\bullet}O_2^-$.[81] The oxygen vacant sites derived from electron transfer from O_{latt} to Ce^{4+} and Mn^{4+} can promote ozone molecules adsorption (Figure 2.5(b)). Water molecules are adsorbed onto the surface of Lewis acid sites when Mn–CeO_x/γ-Al_2O_3 are introduced into solution and then dissociate into the protonated surface hydroxyl groups (S–OH_2^+). Subsequently, the surface complex S–OH_2^+–O_3 was formed by the interaction of aqueous ozone molecules with Brønsted acid S–OH_2^+ *via* hydrogen bonding and/or

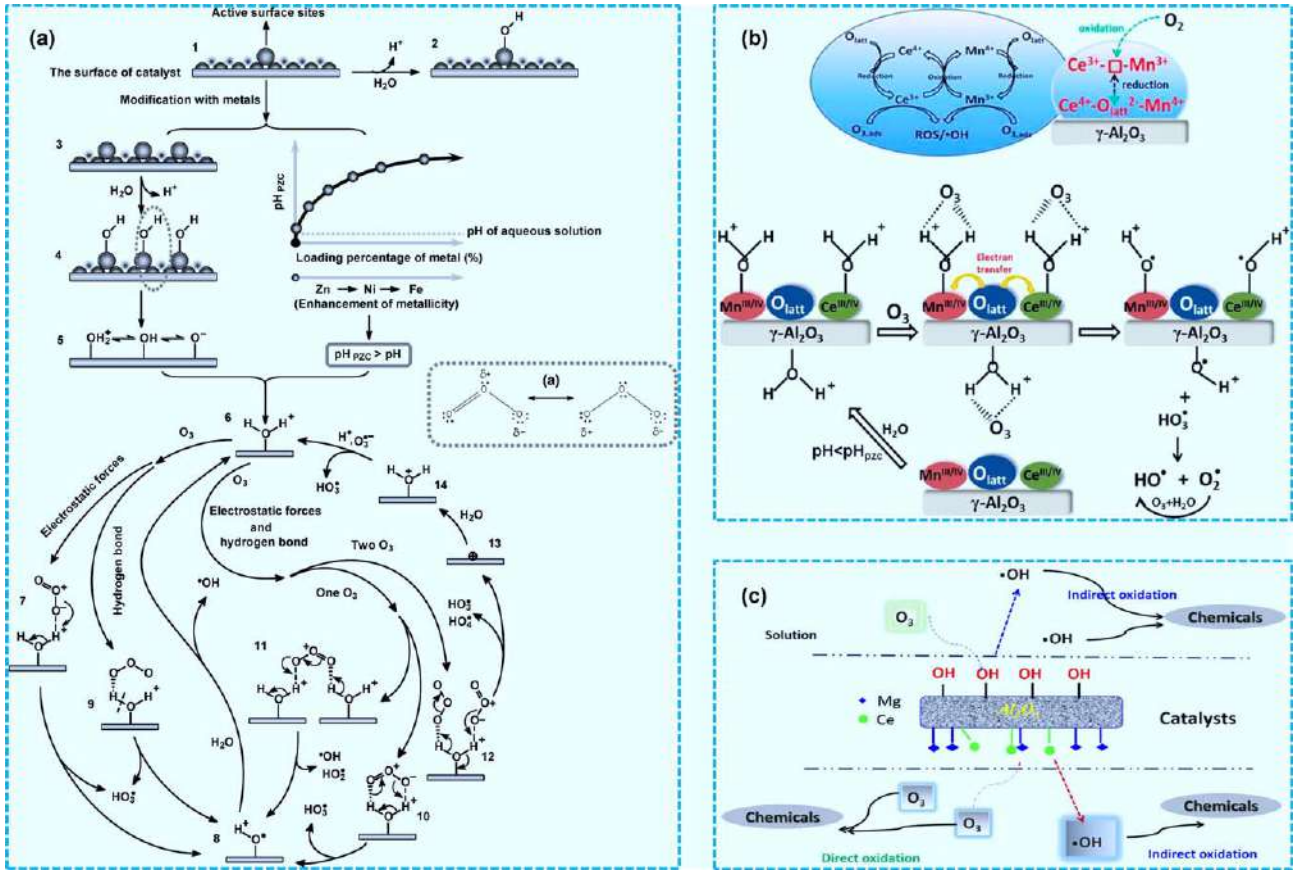

Figure 2.5 (a) Proposed enhancement mechanism of ozone decomposition on the surface of CH-supported metals. Reproduced from ref. 78 with permission from American Chemical Society, Copyright 2009. (b) Schematic illustrations of the synergistic effect of Mn–CeO_x component and a probable mechanism of Mn–CeO_x/γ-Al_2O_3-catalyzed ozonation. Reproduced from ref. 81 with permission from American Chemical Society, Copyright 2018. (c) Proposed ozonation mechanisms of chemicals in RPRW upon metal oxide–loaded Al_2O_3 catalysts. Reproduced from ref. 29 with permission from MDPI, Copyright 2017.

electrostatic forces and was then transformed into $^{\bullet}OH$ and $^{\bullet}O_2^-$ through radical chain reactions (Figure 2.5(b)).[81] Chen *et al.* found that surface hydroxyl groups (–OHs) were the dominant catalytic active sites on Al_2O_3 in the Mg–Ce oxide-loaded Al_2O_3 catalytic ozonation system.[29] As shown in Figure 2.5(c), the metal oxide–loaded Al_2O_3 catalysts provided a platform for the adsorption of chemicals and/or ozone molecules, resulting in the dissociation of ozone and the generation of $^{\bullet}OH$.

Moreover, Lewis acid sites,[23,40] metal ions[56,82] and/or metal oxides[13,77] also have been explored as the catalytic active sites in heterogeneous catalytic ozonation over supported metal oxides. The representative studies on the supported metal oxides catalytic ozonation systems for illustrating the catalytic active sites and the dominant radicals were summarized in Table 2.1.

2.3.3 Mechanism Analysis by Theoretical Calculation

Theoretical calculation based on density functional theory (DFT) is a powerful tool to predict and/or confirm the possible reaction mechanism of heterogeneous catalytic ozonation. The surface energy of the α-MnO_2 adsorption energy of ozone on the oxygen vacancy of α-MnO_2 and the adsorption energy of a S atom in CH_3SH on oxygen vacancy of α-MnO_2 with different exposed facets are shown in Figure 2.6(a).[83] The DFT calculation results indicated that the (310) facets possess higher surface energy than other facets and feature the construction of oxygen vacancies, thus facilitating the adsorption and activation of ozone into intermediate peroxide species (O^{2-}/O_2^{2-}) and reactive oxygen species ($^{\bullet}O_2^-$ or $^1O_2$).[83] Yang *et al.* adopted DFT to deepen comprehension of the adsorption behavior of CH_3SH over the CuO/MnO_2 interface in catalytic ozonation.[53] As shown in Figure 2.6(b), the CH_3SH molecule can be steadily adsorbed on CuO(111) in two different configurations with higher adsorption energies than that of MnO_2. In addition, Figure 2.6(c) demonstrates that the DFT calculated energy barriers of ozone activation by V_O–MnO_2 in CuO/V_O–MnO_2. The calculation results of the energy profile of the ozone activation by V_O–MnO_2 in 5CuO/V_O–MnO_2 in a humid atmosphere revealed that the larger number of oxygen vacancies in 5CuO/V_O–MnO_2 enable more O_3 molecules to convert into $^{\bullet}OH$ and $^{\bullet}O_2^-$ and rapidly react with CH_3SH. Also, Chen *et al.* developed the DFT calculation to explore the ozonation activity on the surface of faceted CeO_2.[84] It revealed that ozone activation on O-(1 0 0) leads to ozone decomposition into a surface oxygen atom and an oxygen, while ozone physisorption occurs without decomposition on O-(1 1 0) and O-(1 1 1). The tendency order of ozone decomposition was (1 0 0) > (1 1 0) > (1 1 1), and the theoretical results were in accord with the experimental data of bromate inhibition efficiencies.

Furthermore, the degradation pathway of organic contaminants can also be investigated and predicted by DFT calculation. According to Fukui's frontier orbit theory, the nucleophilic reaction easily occurs in dense places of the highest occupied molecular orbital (HOMO), and the electrophilic reaction tends to occur in the dense places of the lowest unoccupied

Table 2.1 Catalytic active sites and involved ROS in supported metal oxides for catalytic ozonation.

Catalyst	Pollutants	ROS	Catalytic active site	Ref.
Fe_2O_3/Al_2O_3@SBA-15	Ibuprofen	$^{\bullet}OH$ and $^{\bullet}O_2^-$	Lewis acid sites of Fe^{3+}	40
CuO/CeO_2	Oxalate	No-radical	Cu(II)	56
Cerium oxides loaded natural zeolite	Penicillin G	$^{\bullet}OH$ and $^{\bullet}O_2^-$	Surface hydroxyl groups	35
MnO_x/SBA-15	Oxalic acid	$^{\bullet}OH$	Surface hydroxyl groups ($Mn–OH_2^+$)	80
Ce, Mg, and Ce–Mg oxides–loaded Al_2O_3	Petroleum refinery wastewater	$^{\bullet}OH$	Surface hydroxyl groups	29
β-FeOOH/Al_2O_3	Ibuprofen Ciprofloxacin	$^{\bullet}OH$	Surface Lewis acid sites	23
$CuFe_2O_4$/sepiolite	Quinoline	$^{\bullet}OH$ and $^{\bullet}O_2^-$	Surface hydroxyl groups and Lewis acid sites	8
$NiFe_2O_4$–NiO/NF	Methyl orange nitrobenzene	$^{\bullet}OH$ and $^{\bullet}O_2^-$	Lewis acid sites	1
SD-CuO_x@Al_2O_3	Phenol	$^{\bullet}O_2^-$, $^1O_2$ and $^{\bullet}OH$	Surface hydroxyl groups and CuO_x	13
ZSM-5 zeolites loaded with metallic (Ce, Fe, or Mn) oxides	Nitrobenzene	$^{\bullet}OH$	Surface Si–O bonds and/or Si–O(H)–Al structures	34
PdO/CeO_2	Oxalate	Surface atomic oxygen (*O), surface peroxide ($^*O_2$)	PdO	77
Mn/Al_2O_3, Cu/Al_2O_3 and Mn–Cu/Al_2O_3	Benzotriazole	$^{\bullet}OH$	Lewis acid sites	12
Mn–CeO_x/γ-Al_2O_3	Bromaminic acid	$^{\bullet}OH$ and $^{\bullet}O_2^-$	Surface hydroxyl groups $S–OH_2^+$	81
PdO/CeO_2	Pyruvic acid	No-radical	Lewis acid sites	94
PdO/CeO_2	Pyruvic acid	$^{\bullet}O$	Pd (II)	82
Fe oxides/MCM-41	*p*-Chlorobenzoic acid	$^{\bullet}OH$	Iron oxide	95
Alumina-supported Mn and Cu oxides	Refinery wastewater	$^{\bullet}OH$	Surface hydroxyl groups	96

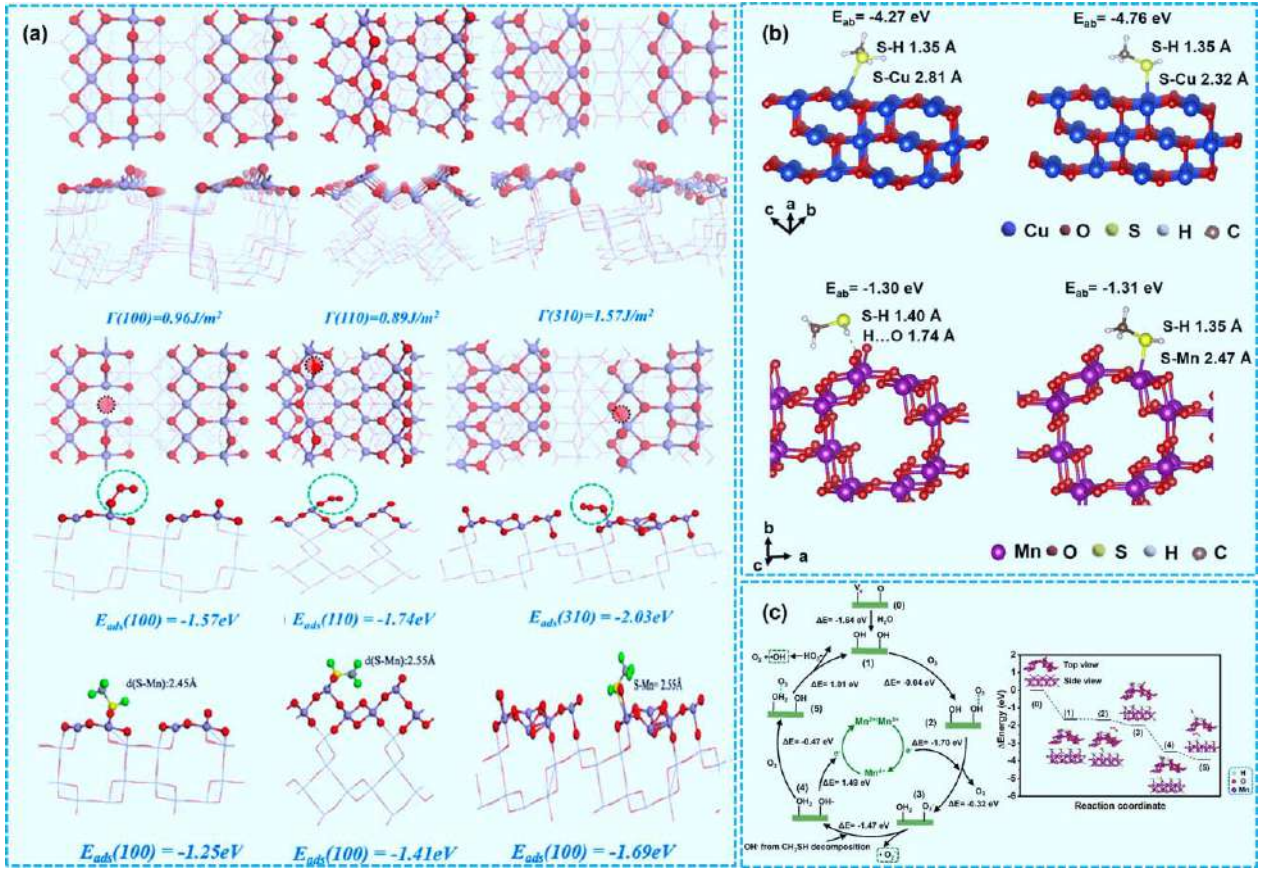

Figure 2.6 (a) Surface energy of α-MnO_2, adsorption energy of O_3 on oxygen vacancy of α-MnO_2 and adsorption energy of S atom in CH_3SH on oxygen vacancy of α-MnO_2 with different exposed facets. Red sphere stands for oxygen atom, and violet sphere stands for manganese atom. Reproduced from ref. 83 with permission from American Chemical Society, Copyright 2020. (b) Schematic states of adsorbed CH_3SH group on CuO (111) surface and on V_O–MnO_2 (100) surface. Reproduced from ref. 53 with permission from Elsevier, Copyright 2020. (c) DFT calculated energy barriers of ozone activation by V_O–MnO_2 in CuO/V_O–MnO_2. Schematic process states and energy profile of ozone activation by V_O–MnO_2 in 5CuO/V_O–MnO_2 under humid atmosphere. Reproduced from ref. 53 with permission from Elsevier, Copyright 2020.

molecular orbital (LUMO).[70,85] Turkay *et al.* adopted frontier (HOMO/LUMO) orbitals to discuss donor–acceptor interaction between substance and catalyst, and the calculation results revealed that the $[CuO + O_3 + H_2O]$ reaction system was found to be more appropriate for CuO-catalyzed ozonation with regard to energy level.[86]

These results indicated that DFT calculation has progressively become an important working tool in exploiting the possible mechanism and degradation pathway of organic pollutants in catalytic ozonation process. However, it remains a major challenge in the theoretical community to improve its accuracy and efficiency. Further investigations should employ more appropriate DFT methods to improve its accuracy and efficiency.

2.4 Practical Applications

Although the total amount of industrial wastewater has been decreasing year by year under the strict requirements of state and scientific control, it still occupies a large proportion of the total amount of environmental pollution sources and an important position in current pollution control work.[36,87] The application of ozonation technology in this field has a noticeable effect and relatively simple technological process.[6,19] At present, a big part of the wastewater treatment facilities are still adopting the traditional wastewater treatment technology. Along with the development of the industry, traditional technology has been unable to meet the demand for wastewater treatment. As an advanced oxidation technology, catalytic ozonation has a good treatment effect, simple operation and bare secondary pollution.[6,88] It has a good application prospect in the in-depth treatment of industrial wastewater. Strengthening the research in this field can provide better guidance for industrial wastewater treatment and environmental protection work. Herein, Heterogeneous catalytic ozonation over supported metal oxides in engineering applications was discussed.

At present, the catalysts used in industrial wastewater treatment can be divided into homogeneous catalysts and heterogeneous catalysts. Due to various defects such as unstable chemical composition, short duration of use, and prone to recontamination, homogeneous catalysts are not widely promoted in actual use, so the relevant research proportion is relatively low.[89] For heterogeneous catalysts, the current researches mainly focus on two aspects: one is transition metal oxides. The second is supported catalyst. Transition metal oxides also have many unsolvable problems in chemical mechanisms such as acid resistance and solubility resistance.[1,61] Therefore, the research mainly focuses on supported catalysts in practical applications. The carriers include Al_2O_3, ceramics and other novel chemical carriers. The study of heterogeneous catalysts composed of transition metals mainly focuses on Mn, Fe and Cu. By studying these metals in various aspects, considering the impact on the ecological environment, economic cost and other factors, Mn and Fe have a more comprehensive range of applications in practical applications.[25,30,90]

2.4.1 Application Case

In catalytic ozonation processes, Al_2O_3-supported catalysts usually have stable structures but relatively low surface activity, while carbon-supported catalysts are the opposite. Wei *et al.* designed a Ni-induced C–Al_2O_3-framework ($_{Ni}$CAF) and reinforced it with a Cu–Co bimetal to create an efficient catalyst (CuCo/$_{Ni}$CAF) with a core–multishell structure.[91] The pilot-scale demonstration of CuCo/$_{Ni}$CAF-catalyzed ozonation revealed a 120% increase in ozone-utilization efficiency ($\Delta COD/\Delta O_3 = 2.12$) compared to that of sole ozonation (0.96) (Figure 2.7(a)). During the treatment of crude carbolic acid wastewater at a COD of ~130 mg L^{-1} and an HRT of 30 min, a 15.2%–46.3% decrease in COD residue in the effluent could be observed in catalytic ozonation compared with that of sole ozone. CuCo/NiCAF demonstrated good and steady performance during long-term operation (Figure 2.7(b)). In addition, massive destruction or elimination of aromatic groups occurred in the catalytic ozonation processes. These results imply both excellent performance and structural stability of CuCo/$_{Ni}$CAF, which could be useful for practical application.

Figure 2.8(a)–(c) was the pilot-scale units for catalytic ozonation. A unique core–multishell structure could be observed for CuCo/$_{Ni}$CAF. Based on the EDS-mapping analysis, C, Cu, Co and Ni were successfully introduced inside the pore channels of the Al_2O_3 substrate. Simultaneously, the enrichment of C and Cu elements near the catalyst edge resulted in a core–multishell appearance within the section. The $_{Ni}$CAF-supported catalysts showed the best TOC removal performance. Besides, CuCo/$_{Ni}$CAF exhibited the highest efficiency in $^{\bullet}OH$ production (R_{ct} of 1.02×10^{-8}), which was 76% greater than CuCo/$_{Ni}$A (5.78×10^{-9}) and 20-fold higher than ozone alone (4.80×10^{-10}). The synergisms resulting from carbon–Al_2O_3, carbon–metal, and metal–metal interactions could contribute to its high performance during catalytic ozonation. The authors used a pilot-scale reactor with a fixed bed filled with CuCo/$_{Ni}$CAF catalysts to further demonstrate the potential for engineering applications. In contrast, a reactor without catalysts was used to determine benchmarks.

In addition, as shown in Figure 2.8(d), two different two-stage ozone oxidation towers were designed to evaluate the potential of practical application of as-prepared Mn–CeO_x/γ-Al_2O_3 catalysts, which can be easily prepared on a large scale through an impregnation–pelletizing–calcination method with the commercial industrial alumina as support.[81] The established system exhibited excellent catalytic ozonation performance in the oxidative degradation of pharmaceutical and chemical industry wastewater.

2.4.2 Limitations in Practical Applications

2.4.2.1 The Lower Efficiency of Mineralization

In current practical engineering applications, due to the different industrial wastewater types and the technical limitations of catalyst types, there is a big difference between the overall mineralization rate of catalytic ozone and the

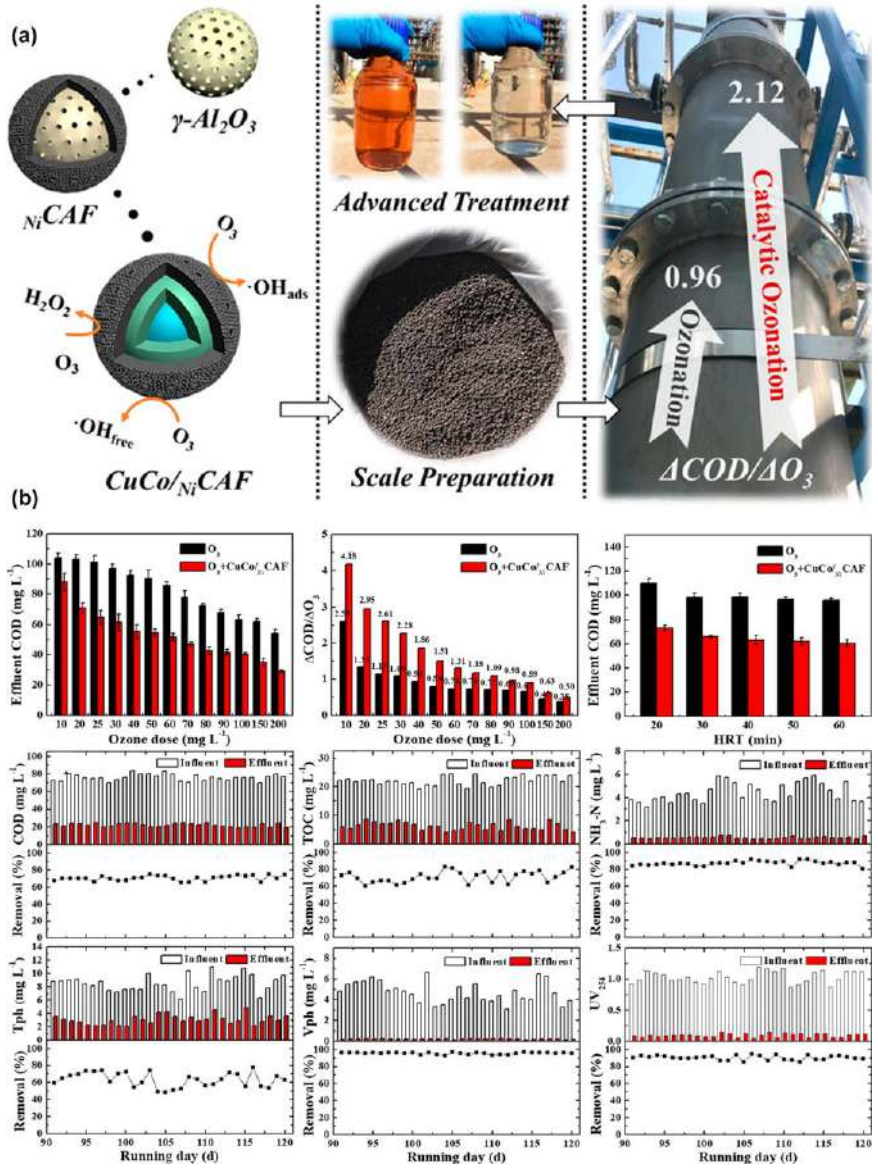

Figure 2.7 (a) Schematic of the integrated mechanisms of the CuCo/NiCAF catalyzed ozonation process. (b) Effects of ozone dosage (HRT 30 min) and hydraulic retention time (ozone dosage 25 mg L^{-1}) during the treatment of crude carbolic acid. Conditions: feed COD ≈ 130 mg L^{-1}, pH 6–7; Long-term water quality indexes before and after catalytic ozonation of coal-gasification wastewater (secondary effluent) (the following six figures). Influent: COD 70–80 mg L^{-1}, TOC 20–25 mg L^{-1}, NH_3–N 3–6 mg L^{-1}, T_{ph} 6–11 mg L^{-1}, V_{ph} 2–7 mg L^{-1}, UV_{254} 1–1.5, pH 6.5–7.0, SS < 20. Conditions: ozone dosage 25 mg L^{-1}, HRT 30 min, feed flux 200 L h^{-1}. Reproduced from ref. 91 with permission from American Chemical Society, Copyright 2019.

Figure 2.8 Pilot-scale units for catalytic ozonation: (a) coagulation sedimentation and cartridge filtration, (b) oxygen generator, ozone generator, and ozone detector and gas flowmeters, and (c) a pair of cylinder column reactors for ozone reactions (the left one filled with CuCo/NiCAF, the right one empty for blank control). Reproduced from ref. 91 with permission from American Chemical Society, Copyright 2019. (d) Photographs of the large-scale production of Mn–CeO_x/γ-Al_2O_3 catalysts and two-stage ozone oxidation towers for the pilot-scale catalytic ozonation of real wastewater. Reproduced from ref. 81 with permission from American Chemical Society, Copyright 2018.

actual requirements. Generally, the rate of increase is only about 10%–30%.[30,92] The lower efficiency has a strong limitation on the popularization and application of catalytic ozone technology, making its overall engineering application level relatively low.

2.4.2.2 The Lower Reuse Rate

Whether the catalyst can be reused directly determines the cost of catalytic ozonation in engineering applications. In practical application, the preparation method of the catalyst determines its stability. No matter which preparation method is adopted, the catalyst activity will gradually decrease

with increasing reactions, thus reducing industrial wastewater's treatment effect. To maintain the catalytic ozonation effect continuously, it is necessary to increase capital investment and increase the overall operating cost.

2.4.2.3 Dependent on Solution pH

Under acidic conditions, catalytic ozonation has a relatively weak effect.[8,93] For industrial wastewater with acidity, especially strongly acidic industrial wastewater containing heavy metal ions, the effect should also be considered as well as the overflow of metal ions in the treatment process. Therefore, the application of catalytic ozonation technology in this field also has significant limitations.

2.5 Summary

Catalytic ozonation technology can alone effectively solve the limitations of weak ozonation and selectivity. By improving the ozone utilization rate, reducing ozone dosage and improving the mineralization effect, the feasibility of the deep treatment of refractory industrial wastewater in terms of technical and economic indexes can be realized. In line with the principle of no secondary pollution to industrial wastewater and the realization of catalyst reuse, the current mainstream way to catalyze ozone in industrial wastewater is to use heterogeneous catalytic oxidation of supported catalysts containing transition metals. The development and preparation of more stable, durable efficient and inexpensive catalysts is the desired direction. To further broaden the application scope of catalytic ozonation technology in industrial wastewater, the coupling of the catalytic ozone and the biological unit can be considered to improve biodegradability and to reduce biotoxicity as the primary catalytic objectives, as well as to reduce operating cost by reducing ozone dosage. In addition, the organic combination of and coordination between catalytic ozone and traditional water treatment units must also meet the inevitable trend-related and technical requirements of current industrial wastewater treatment and upgrading. Finally, although the catalytic ozone oxidation technology in engineering application has many limitations, its technological level also needs improvement. Nevertheless, through the in-depth study of related aspects, further incorporating the adjacent technology research, transforming enterprise-level operating facilities in governance and enhancing treatment effects all still play a role in practical, broad market application perspective.

Acknowledgements

The authors would like to acknowledge the financial support from National Natural Science Foundation of China (No. 52070133) and National Key Research and Development Program of China (Grant No. 2021YFA1202500).

References

1. C. Feng and P. Diao, *Appl. Surf. Sci.*, 2021, **541**, 148683.
2. F. Qi, W. Chu and B. Xu, *Chem. Eng. J.*, 2016, **284**, 28.
3. J. Zhang, Y. Wu, L. Liu and Y. Lan, *Sep. Purif. Technol.*, 2015, **151**, 318.
4. L. Yuan, J. Shen, Z. Chen and X. Guan, *Appl. Catal. B Environ.*, 2016, **180**, 707.
5. J. Wang and H. Chen, *Sci. Total Environ.*, 2020, **704**, 135249.
6. J. Zhao, J. Cao, Y. Zhao, T. Zhang, D. Zheng and C. Li, *J. Environ. Sci.*, 2020, **97**, 75.
7. P. Yan, J. Shen, L. Yuan, J. Kang, B. Wang, S. Zhao and Z. Chen, *Sep. Purif. Technol.*, 2019, **228**, 115766.
8. D. Liu, C. Wang, Y. Song, Y. Wei, L. He, B. Lan, X. He and J. Wang, *Chemosphere*, 2019, **227**, 647.
9. Z. Ma, L. Zhu, X. Lu, S. Xing, Y. Wu and Y. Gao, *Sep. Purif. Technol.*, 2014, **133**, 357.
10. S. M. He, P. C. Luan, L. H. Mo, J. Xu, J. Li, L. Q. Zhu and J. S. Zeng, *Bioresources*, 2018, **13**, 3686.
11. Y. Chen, C. M. Chen, B. A. Yoza, Q. X. Li, S. H. Guo, P. Wang, S. J. Dong and Q. H. Wang, *Pet. Sci.*, 2017, **14**, 605.
12. B. Roshani, I. McMaster, E. Rezaei and J. Soltan, *Sep. Purif. Technol.*, 2014, **135**, 158.
13. H. Chen, C. Fang, X. Gao, G. Jiang, X. Wang, S. P. Sun, W. Duo Wu and Z. Wu, *J. Colloid Interface Sci.*, 2021, **581**, 964.
14. K. Kruanak and C. Jarusutthirak, *J. Environ. Chem. Eng.*, 2019, **7**, 102825.
15. M. Stoyanova, P. Konova, P. Nikolov, A. Naydenov, S. Christoskova and D. Mehandjiev, *Chem. Eng. J.*, 2006, **122**, 41.
16. P. Konova, M. Stoyanova, A. Naydenov, S. Christoskova and D. Mehandjiev, *Appl. Catal., A*, 2006, **298**, 109.
17. P. Pocostales, P. Álvarez and F. J. Beltrán, *Chem. Eng. J.*, 2011, **168**, 1289.
18. F. Lin, Z. Wang, Q. Ma, Y. Yang, R. Whiddon, Y. Zhu and K. Cen, *Appl. Catal. B Environ.*, 2016, **198**, 100.
19. E. Rezaei, J. Soltan, N. Chen and J. R. Lin, *Chem. Eng. J.*, 2013, **214**, 219.
20. R. Rosal, M. S. Gonzalo, A. Rodriguez and E. Garcia-Calvo, *J. Hazard. Mater.*, 2010, **183**, 271.
21. H. Einaga and S. Futamura, *Appl. Catal. B Environ.*, 2005, **60**, 49.
22. H. Einaga and S. Futamura, *J. Catal.*, 2006, **243**, 446.
23. L. Yang, C. Hu, Y. Nie and J. Qu, *Appl. Catal. B Environ.*, 2010, **97**, 340.
24. M. Aghbolaghy, J. Soltan and R. Sutarto, *Chem. Eng. Res. Des.*, 2017, **128**, 73.
25. J. Li, W. Song, Z. Yu and Q. Li, *Arabian J. Chem.*, 2020, **13**, 3724.
26. C. M. Chen, B. A. Yoza, Y. D. Wang, P. Wang, Q. X. Li, S. H. Guo and G. X. Yan, *Environ. Sci. Pollut. Res.*, 2015, **22**, 5552.
27. J. Y. Li, W. F. Song, X. C. Mao, Q. H. Li and Z. F. Yu, *J. Phys. Chem. C*, 2020, **124**, 13215.
28. S.-P. Tong, R. Shi, H. Zhang and C.-A. Ma, *J. Hazard. Mater.*, 2011, **185**, 162.

29. C. M. Chen, Y. Chen, B. A. Yoza, Y. H. Du, Y. X. Wang, Q. X. Li, L. P. Yi, S. H. Guo and Q. H. Wang, *Catalysts*, 2017, **7**, 72.
30. B. Wang, H. Zhang, F. F. Wang, X. G. Y. Xiong, K. Tian, Y. B. Sun and T. T. Yu, *Catalysts*, 2019, **9**, 241.
31. L. Guo, F. Meng, Y. Zeng, Y. Jia, F. Qian, S. Zhang and Q. Zhong, *Mol. Catal.*, 2020, **493**, 111095.
32. J. L. Rodríguez, M. A. Valenzuela, F. Pola, H. Tiznado and T. Poznyak, *J. Mol. Catal. A: Chem.*, 2012, **353–354**, 29.
33. Y. H. Chen, D. C. Hsieh and N. C. Shang, *J. Hazard. Mater.*, 2011, **192**, 1017.
34. C. Chen, X. Yan, B. A. Yoza, T. Zhou, Y. Li, Y. Zhan, Q. Wang and Q. X. Li, *Sci. Total Environ.*, 2018, **612**, 1424.
35. J. Zhang, Z. Xiong, J. Wei, Y. Song, Y. Ren, D. Xu and B. Lai, *Chem. Eng. J.*, 2020, **383**, 123144.
36. A. L. Petre, J. B. Carbajo, R. Rosal, E. Garcia-Calvo and J. A. Perdigón-Melón, *Chem. Eng. J.*, 2013, **225**, 164.
37. T. Gopi, G. Swetha, S. C. Shekar, C. Ramakrishna and A. K. Gupta, *J. Environ. Chem. Eng.*, 2017, **5**, 4031.
38. T. Gopi, G. Swetha, S. C. Shekar, R. Krishna, C. Ramakrishna, B. Saini and P. V. L. Rao, *Arabian J. Chem.*, 2019, **12**, 4502.
39. C. Ramakrishna, S. C. Shekar, A. K. Gupta, B. Saini, R. Krishna, G. Swetha and T. Gopi, *J. Environ. Chem. Eng.*, 2017, **5**, 1484.
40. J. S. Bing, C. Hu, Y. L. Nie, M. Yang and J. H. Qu, *Environ. Sci. Technol.*, 2015, **49**, 1690.
41. R. Huang, H. Yan, L. Li, D. Deng, Y. Shu and Q. Zhang, *Appl. Catal. B Environ.*, 2011, **106**, 264.
42. Y. Shu, M. He, J. Ji, H. Huang, S. Liu and D. Y. C. Leung, *J. Hazard. Mater.*, 2019, **364**, 770.
43. H. Huang, X. Ye, W. Huang, J. Chen, Y. Xu, M. Wu, Q. Shao, Z. Peng, G. Ou, J. Shi, X. Feng, Q. Feng, H. Huang, P. Hu and D. Y. C. Leung, *Chem. Eng. J.*, 2015, **264**, 24.
44. E. Rezaei and J. Soltan, *Chem. Eng. J.*, 2012, **198–199**, 482.
45. M. Li, K. N. Hui, K. S. Hui, S. K. Lee, Y. R. Cho, H. Lee, W. Zhou, S. Cho, C. Y. H. Chao and Y. Li, *Appl. Catal. B Environ.*, 2011, **107**, 245.
46. Z. Jeirani and J. Soltan, *J. Water Process. Eng.*, 2016, **12**, 127.
47. R. Yang, P. Han, Y. Fan, Z. Guo, Q. Zhao, Y. Wang, S. Che, S. Lin and R. Zhu, *Chemosphere*, 2020, **247**, 125864.
48. H. Einaga, Y. Teraoka and A. Ogata, *J. Catal.*, 2013, **305**, 227.
49. H. Einaga, N. Maeda, S. Yamamoto and Y. Teraoka, *Catal. Today*, 2015, **245**, 22.
50. H. Einaga, S. Yamamoto, N. Maeda and Y. Teraoka, *Catal. Today*, 2015, **242**, 287.
51. Z. S. Ncanana, N. J. Sadgrove and V. S. R. Rajasekhar Pullabhotla, *Catal. Today*, 2020, **358**, 284.
52. F. Nawaz, Y. B. Xie, J. D. Xiao, H. B. Cao, Y. P. Li and D. Zhang, *RSC Adv.*, 2016, **6**, 29674.

53. J. Yang, Y. Huang, Y.-W. Chen, D. Xia, C.-Y. Mou, L. Hu, J. Zeng, C. He, P. K. Wong and H.-Y. Zhu, *Nano Today*, 2020, **35**, 100944.
54. P. A. Krisbiantoro, T. Togawa, K. Kato, J. Zhang, R. Otomo and Y. Kamiya, *Catal. Commun.*, 2021, **149**, 106204.
55. S. Xing, X. Lu, J. Liu, L. Zhu, Z. Ma and Y. Wu, *Chemosphere*, 2016, **144**, 7.
56. T. Zhang, W. Li and J.-P. Croué, *Appl. Catal. B Environ.*, 2012, **121–122**, 88.
57. C. Hu, S. T. Xing, J. H. Qu and H. He, *J. Phys. Chem. C*, 2008, **112**, 5978.
58. S. T. Xing, C. Hu, J. H. Qu, H. He and M. Yang, *Environ. Sci. Technol.*, 2008, **42**, 3363.
59. G. Y. Chen, Z. Wang, F. W. Lin, Z. M. Zhang, H. D. Yu, B. B. Yan and Z. H. Wang, *J. Hazard. Mater.*, 2020, **391**, 122218.
60. S. Maddila, V. D. B. C. Dasireddy, E. O. Oseghe and S. B. Jonnalagadda, *Appl. Catal. B Environ.*, 2013, **142–143**, 129.
61. S. Maddila, V. Dasireddy and S. B. Jonnalagadda, *Appl. Catal. B Environ.*, 2014, **150**, 305.
62. X. Tong, Z. Li, W. Chen, J. Wang, X. Li, J. Mu, Y. Tang and L. Li, *J. Colloid Interface Sci.*, 2020, **578**, 461.
63. Z. C. Yan, J. X. Zhu, X. Y. Hua, D. P. Liang, D. M. Dong, Z. Y. Guo, N. Zheng and L. W. Zhang, *J. Cleaner Prod.*, 2020, **272**, 122856.
64. W. Chen, X. Li, Z. Pan, S. Ma and L. Li, *Sep. Purif. Technol.*, 2017, **173**, 99.
65. A. V. Levanov, I. V. Kuskov, K. B. Koiaidarova, A. V. Zosimov, E. E. Antipenko and V. V. Lunin, *Kinet. Catal.*, 2005, **46**, 138.
66. M. Trapido, Y. Veressinina, R. Munter and J. Kallas, *Ozone: Sci. Eng.*, 2005, **27**, 359.
67. Q. Wang, Z. Yang and H. Xu, *Chin. J. Environ. Eng.*, 2017, **11**, 2113.
68. J. Nawrocki and B. Kasprzyk-Hordern, *Appl. Catal. B Environ.*, 2010, **99**, 27.
69. G. Yu, Y. Wang, H. Cao, H. Zhao and Y. Xie, *Environ. Sci. Technol.*, 2020, **54**, 5931.
70. Z. Xiong, Y. Jiang, Z. Wu, G. Yao and B. Lai, *Chem. Eng. J.*, 2020, **421**, 127863.
71. S. H. Joo, A. J. Feitz, D. L. Sedlak and T. D. Waite, *Environ. Sci. Technol.*, 2004, **39**, 1263.
72. M. Cho, H. Chung, W. Choi and J. Yoon, *Water Res.*, 2004, **38**, 1069.
73. M. Hayyan, M. A. Hashim and I. M. AlNashef, *Chem. Rev.*, 2016, **116**, 3029.
74. M. Kubo, K. Sekiguchi, N. Shibasaki-Kitakawa and T. Yonemoto, *Res. Chem. Intermed.*, 2012, **38**, 2191.
75. J. Yan, J. Peng, L. Lai, F. Ji, Y. Zhang, B. Lai, Q. Chen, G. Yao, X. Chen and L. Song, *Environ. Sci. Technol.*, 2018, **52**, 14302.
76. Z. Sun, L. Zhao, C. Liu, Y. Zhen and J. Ma, *Environ. Sci. Technol.*, 2019, **53**, 10342.
77. T. Zhang, W. Li and J. P. Croue, *Environ. Sci. Technol.*, 2011, **45**, 9339.
78. L. Zhao, Z. Sun and J. Ma, *Environ. Sci. Technol.*, 2009, **43**, 4157.
79. T. Zhang and J. Ma, *J. Mol. Catal. A: Chem.*, 2008, **279**, 82.

80. Q. Sun, L. Li, H. Yan, X. Hong, K. S. Hui and Z. Pan, *Chem. Eng. J.*, 2014, **242**, 348.
81. Z. Wu, G. Zhang, R. Zhang and F. Yang, *Ind. Eng. Chem. Res.*, 2018, **57**, 1943.
82. W. Li, Z. Qiang, T. Zhang, X. Bao and X. Zhao, *J. Mol. Catal. A: Chem.*, 2011, **348**, 70.
83. C. He, Y. Wang, Z. Li, Y. Huang, Y. Liao, D. Xia and S. Lee, *Environ. Sci. Technol.*, 2020, **54**, 12771.
84. X. Chen, H. Yang, C. Au, S. Tian, Y. Xiong and Y. Chang, *Chem. Eng. J.*, 2020, **390**, 124480.
85. K. Fukui, T. Yonezawa and H. Shingu, *J. Chem. Phys.*, 1952, **20**, 722.
86. O. Turkay, H. Inan and A. Dimoglo, *Sep. Purif. Technol.*, 2014, **134**, 110.
87. A. K. H. Al jibouri, J. N. Wu and S. R. Upreti, *Can. J. Chem. Eng.*, 2019, **97**, 67.
88. J. Liu, L. Ke, J. Liu, L. Sun, X. Yuan, Y. Li and D. Xia, *J. Hazard. Mater.*, 2019, **371**, 42.
89. S. Maddila, V. Dasireddy and S. B. Jonnalagadda, *Appl. Catal. B Environ.*, 2013, **138**, 149.
90. P. Liu, G. Wei, H. He, X. Liang, H. Chen, Y. Xi and J. Zhu, *Appl. Surf. Sci.*, 2019, **464**, 287.
91. K. Wei, X. Cao, W. Gu, P. Liang, X. Huang and X. Zhang, *Environ. Sci. Technol.*, 2019, **53**, 6917.
92. M. Sui, J. Liu and L. Sheng, *Appl. Catal. B Environ.*, 2011, **106**, 195.
93. C. V. Rekhate and J. K. Srivastava, *Chem. Eng. J. Adv.*, 2020, **3**, 100031.
94. W. Li, Z. Qiang, T. Zhang and F. Cao, *Appl. Catal. B Environ.*, 2012, **113–114**, 290.
95. R. Huang, B. Lan, Z. Chen, H. Yan, Q. Zhang, J. Bing and L. Li, *Chem. Eng. J.*, 2012, **180**, 19.
96. F. Deng, S. Qiu, C. Chen, X. Ding and F. Ma, *Ozone: Sci. Eng.*, 2015, **37**, 546.

CHAPTER 3

Catalytic Ozonation over Composite Metal Oxides

RODRIGO PEREIRA CAVALCANTE AND
RENATO FALCAO DANTAS*

School of Technology, University of Campinas–UNICAMP, Paschoal Marmo, 1888, CEP 13484-332, Limeira, SP, Brazil
*Email: renatofalcaod@ft.unicamp.br

3.1 Introduction

Ozone (O_3) is a powerful oxidizer extensively used in the treatment of water and effluents for disinfection purposes, due to its ability to inactivate resistant pathogenic microorganisms, such as *Escherichia coli*, *Salmonella* and *Bacillus* sp. where conventional chlorine-based disinfectants can fail and/or may contribute to the preferred selection of chlorine-resistant bacteria.[1,2] Also, it is well-known that ozone can react with various contaminants in different environmental compartments, such as secondary wastewater effluents.[3,4] However, it is also well reported that ozone has a selective oxidation character, leading to very limited mineralization and in many cases to the formation of toxic by-products.[5] In contrast, ozone-refractory organic compounds are eliminated to a certain extent by hydroxyl radicals ($^{\bullet}OH$) that are formed by the decomposition of O_3 in water.[6,7]

Unlike the direct reaction by ozone, which is selective, it is known that $^{\bullet}OH$ radicals are characterized by being non-selective and reacting quickly (rate constants varying between 10^7 and 10^{10} L mol^{-1} s^{-1})[8] with practically

Chemistry in the Environment Series No. 8
Advanced Ozonation Processes for Water and Wastewater Treatment: Active Catalysts and Combined Technologies
Edited by Hongbin Cao, Yongbing Xie, Yuxian Wang and Jiadong Xiao

Published by the Royal Society of Chemistry, www.rsc.org

all organic compounds, leading to the complete breakdown of these molecules and even reaching high levels of mineralization.

As the generation of •OH radicals during ozone reactions is relatively low, additional alternatives are investigated in order to increase the production of •OH radicals, leading to ozonation processes being considered, such as advanced oxidation processes (AOPs) or AOPs-like processes.[6,9] In this sense, several strategies are applied in the ozonation processes to form different types of ozone-based AOPs. This involved the addition of hydrogen peroxide (H_2O_2) to the ozonation process (known as the peroxone process), ozonation at high pH (O_3/HO^-), as well as the combination of ozone with ultraviolet radiation (UV) and/or catalyst (catalytic ozonation).[6,10] The processes using H_2O_2 and UV radiation have some limitations for practical applications, such as residual H_2O_2 and high energy consumption for UV lamp operation.[5]

Among ozone-based treatment processes, catalytic ozonation is gaining prominence in the field of drinking water and wastewater treatment. The main advantage of this technology is related to the increase in the generation of active species, mainly •OH radicals, which consequently increase the rate of degradation of recalcitrant compounds and especially decreases the number of toxic by-products due to the improvement in the degree of mineralization.[11] The encouragement of catalysts use in ozonation is due to the reduction of operating costs, since it does not require additional energy costs such as operating the UV lamp and/or costs related to pH adjustment and control.[10] In addition, it is well described that the application of catalytic ozonation results in a significant decrease in ozone consumption.[12]

Ozone decomposition in the presence of catalysts is subdivided into two categories depending on the physical nature of the catalyst used.[10,12–14] When transition metal ions are employed in solution, catalytic ozonation is considered to be homogeneous; however, if solid catalysts are involved, such as solid metal oxides or noble metals supported on alumina, silica, activated carbon, *etc.*, the process is known as heterogeneous catalytic ozonation. In summary, several types of catalysts are effective for ozonation, especially transition metals[13,15] such as Fe^{2+}, Fe^{3+}, Mn^{2+}, Cu^{2+}, Co^{2+}, Zn^{2+} and Cr^{3+}. Among the solid catalysts, carbon materials, metal oxides (*e.g.* MnO_2, TiO_2, Al_2O_3, Fe_2O_3, WO_3 and CeO_2) and supported metal oxides (*e.g.* Cu–Al_2O_3, Cu–TiO_2, Ru–CeO_2, Fe_2O_3/Al_2O_3 and TiO_2/Al_2O_3) are frequently mentioned in applications of catalytic ozonation.[5,12,16,17] Physical properties such as the particle size, porosity, morphology and composition of the catalysts are fundamental parameters that influence catalytic activity.

In the last decades, the application of composite materials in catalytic ozonation has received significant attention from the scientific community. Composite materials are classified as materials that are manufactured from two or more constituent substances with distinct properties.[18] The combination of these materials develops some new characteristics to the resulting material, which were not present in the individual materials. It can give them higher recyclability, stability and performance in ozone decomposition. Their use can increase ozonation efficiency at the same time it reduces drawbacks of

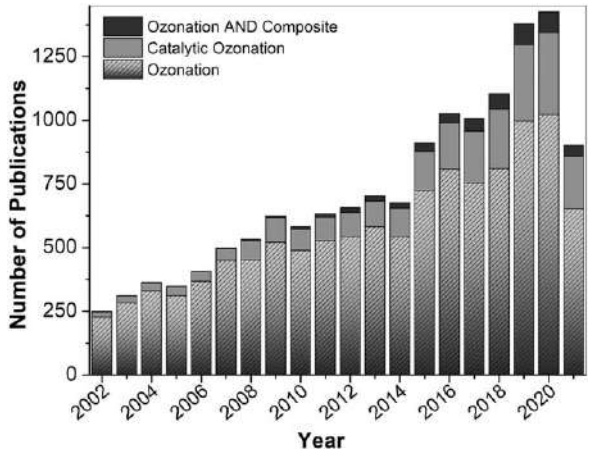

Figure 3.1 Number of publications per year related to ozonation, catalytic ozonation and catalytic ozonation using composite materials carried out in the ISI Web of Science database, using the following search keywords separately: ''ozonation,'' ''catalytic ozonation.'' ''ozonation and composites.'' Data from https://www.webofknowledge.com/, accessed July 26, 2021.

heterogeneous catalytic ozonation. Consequently, composite materials are good alternatives to perform catalytic ozonation; thus the number of publications related to the application of these composite materials in catalytic ozonation has been increasing continuously over the last years. Figure 3.1 presents a histogram showing the evolution of the number of publications per year that address the application of composite materials in ozonation. For comparison, the graph also shows the number of publications reported using ''ozonation'' or ''catalytic ozonation'' as a search keyword.

Different types of oxide composites have been used to explore their feasibility for catalytic ozonation application, such as Mn-based composite oxide,[19,20] composite metal oxide–loaded alumina,[21] magnetic Fe_3O_4@SiO_2@$Mg(OH)_2$ composite,[22] pure zeolites and doped with metals,[23–25] perovskites,[26,27] spinel oxides.[28,29] Among the types of composite materials, composite mixed oxides with perovskite- and spinel-type structures are attractive catalysts of continuous interest to the scientific community and have been investigated in catalytic ozonation due to their promising physicochemical properties for application in catalytic processes.[30,31] Sections 3.2 and 3.3 present basic knowledge along with a critical review of composite materials with perovskite-type and spinel-type mixed oxides use for catalytic ozonation applied for water and wastewater treatment. Other natural minerals commonly used in catalytic ozonation are also reported.

3.2 Perovskite-type Catalysts

Perovskite oxide-based catalysts are successfully applied in different processes, including supercapattery applications,[32] sensors,[33] cathode

materials,[34] thermoelectric technology,[35] solar cells,[36] electrocatalytic activity toward the oxygen evolution reaction[37] and catalytic and photocatalytic activity for removal of pollutants.[38,39] In particular, perovskite-type oxides appear as a class of catalysts with potential for application in catalytic ozonation. These materials exhibit excellent properties that may be responsible for catalytic improvement such as (1) high stability under severe conditions and at high temperature, which facilitates the application of catalytic ozonation in real samples such as wastewater treatment; (2) a high degree of stabilization of transition metals in their respective oxidation states; and (3) high oxygen mobility.[40,41]

These perovskite class catalysts are a group of inorganic compounds that have the general chemical formula ABO_3, where A indicates a metal belonging to the group of alkali metals, beryllium, magnesium and rare earth metals and B is a transition metal cation, normally titanium, niobium, tantalum or manganese.[13,40,41] The name of the group comes from the natural mineral perovskite $CaTiO_3$.[13] In the ABO_3 structure, the A-site cation is 12-fold coordinated and the B-site cation is 6-fold coordinated with oxygen anions.[42] These types of materials are susceptible to substitution of both cations without alteration in the crystalline structure.[43] It is described in the literature that the catalytic performance of a perovskite oxide is related to the B-site transition metal element.[44] When the oxidation state of the B cation increases, the redox reaction generates greater amounts of available oxygen, that is, it increases the lattice oxygen mobility, and, as a result, the overall oxidation activity is increased.[43] On the other hand, the substitution of metals at A-sites does not directly affect catalytic activity; however, depending on the type of cation in the A-site, it can affect the electronic structure and change the oxidation state of the transition metal cation, thus introducing its effect on catalytic activity in an indirect way.[43,44]

Therefore, one of the advantages of perovskite structures is the possibility of regulating the composition, changing either the A or the B cations or partially replacing each cation with others of different sizes or oxidation states, resulting in perovskite with the general formula $A_{1-x}A'_xB_{1-y}B'_yO_{3\pm\delta}$.[45] Thus the oxidation state of the B-site cation and the oxygen vacancy content can be controlled, consequently enabling the correlation of the physicochemical properties with the catalytic performance of the materials.[42]

The types of perovskite catalysts that have been used for catalytic ozonation are shown in Table 3.1. Among the 14 works found using perovskite oxides for application in ozonation, only one did not use lanthanum (La) as an A-site metal. Lanthanides are commonly used in position A in a perovskite oxide because of their crystalline structure that benefits the exposure of active sites.[46] Among the lanthanide-based perovskites that have been applied in ozonation so far, it can be seen from the distribution shown in Table 3.1 that $LaTi_{1-x}Cu_xO_3$, with an emphasis on $LaTi_{0.15}Cu_{0.85}O_3$[11,14,47–49] was the most used and demonstrated high catalytic efficiency.

The first publications on catalytic ozonation with perovskites, reported in 2006, were developed by the same research group.[11,14,47] First, the authors

Table 3.1 Catalytic ozonation of pollutants in water and wastewater by perovskites.[a]

No.	Catalysts (Cat.)	Synthetic Methods	Pollutants/water matrix	Reaction parameters	Catalytic efficiency (%)/ time (min)	Comments/additional information	Refs.
1	$LaTi_{0.15}Cu_{0.85}O_3$	Citrate decomposition	Pyruvic acid (PA)/ ultrapure water	$[PA] = 5.0\times10^{-3}$ mol L^{-1}, $[O_3] = 50$ mg L^{-1}, $[Cat.] = 1.0$ g L^{-1}, $T = 20$ °C	Total removal of pyruvic acid after 150 min	Ozone dose, catalyst concentration and temperature influenced the degradation	Rivas *et al.*[47]
2	$LaTi_{1-x}Cu_xO_3$ ($x = 0.15, 0.22, 0.40, 0.60, 0.85$) and $LaTi_{1-x}Co_xO_3$ ($x = 0.60, 0.85$)	Citrate decomposition	Pyruvic acid (PA)/ ultrapure water	$[PA] = 5.0\times10^{-3}$ mol L^{-1}, $[O_3] = 50$ mg L^{-1}, $[Cat.] = 1.0$ g L^{-1}, pH = 6.0, $T = 20$ °C	$LaTi_{0.15}Cu_{0.85}O_3$ and $LaTi_{0.15}Co_{0.85}O_3$: = 80% removal of pyruvic acid in 120 min	Perovskites catalysts did show significant catalytic activity to increase the ozonation of pyruvic acid	Carbajo *et al.*[14]
3	$LaTi_{0.15}Cu_{0.85}O_3$	Citrate decomposition	Gallic acid (GA)/pure water	$[GA] = 1.0\times10^{-3}$ mol L^{-1}, $[O_3] = 5$ mg L^{-1}, $[Cat.] = 2.5$ g L^{-1}, pH = 3.5, $T = 20$ °C.	$O_3 + LaTi_{0.15}Cu_{0.85}O_3 = 90\%$ mineralization in 180 min. O_3 alone = 35% at the same time.	Several series of experiments carried out at different operating conditions.	Carbajo *et al.*[11]
4	$LaTi_{0.15}Cu_{0.85}O_3$	Citrate decomposition	Mixture of three phenols (tyrosol, gallic acid and syringic acid)	$[COD]_0 = 1200$ mg L^{-1}, $[O_3] = 50$ mg L^{-1}, $[Cat.] = 0.1$ g L^{-1}, pH = 3.0, $T = 20$ °C	> 90% mineralization/ 300 min	Concentration of perovskites did show no appreciable influence for values above 0.1 g L^{-1}	Carbajo *et al.*[48]
5	$LaTi_{0.15}Cu_{0.85}O_3$	Citrate decomposition	Pyruvic acid (PA)/ ultrapure water	$[PA] = 5.0\times10^{-3}$ mol L^{-1}, $[O_3] = 50$ g m^{-3}, $[Cat.] = 1.0$ g L^{-1}, $T = 20$ °C.	O_3 = above 20% of degradation after 180 min. O_3/perovskite = complete removal in about 120 min.	Using the combination of the oxidants O_3/UV/ perovskite the pyruvic acid is eliminated in just 45 min.	Rivas *et al.*[49]
6	Copper or cobalt perovskites ($LaTi_{0.15}Me_{0.85}O_3$ with Me as Cu or Co)	Citrate decomposition	Sulfamethoxazole (SULFA)/ultrapure water	$[SULFA] = 30$ mg L^{-1}, $[O_3] = 20$ mg L^{-1}, $[Cat.] = 0.3$ g L^{-1}, pH = 7.0, $T = 20$ °C	TOC removal in 120 min: O_3 + copper perovskite = 85%; O_3 + cobalt perovskite = 60%; single ozonation = 28%	Low pH has a negative effect when perovskite-type catalysts are used because of metal leaching	Beltrán *et al.*[50]
7	Copper or cobalt perovskites ($LaTi_{0.15}Me_{0.85}O_3$ with Me as Cu or Co)	Citrate decomposition	Diclofenac (DCF) and 17α-Ethynylstradiol (EST)/ultrapure water and domestic wastewater	Ultrapure water: $[DCF] = 30$ mg L^{-1}, $[EST] = 9$ mg L^{-1}, $[O_3] = 20$ mg L^{-1}, $[Cat.] = 0.1$ g L^{-1},	TOC removal in 120 min: DCF in ultrapure water: O_3 + cobalt or copper perovskite = 80 or 95% in	During ozone processes of domestic wastewater, the presence of cobalt perovskite catalyst does not allow any	Beltrán *et al.*[51]

				pH = 7.0 and 2.0, $T = 20$ °C Domestic wastewater spiked up with DCF and EST: $T = 20$ °C. $[TOC]_0 = 30\ mg\ L^{-1}$, $[COD]_0 = 80\ mg\ L^{-1}$, pH = 7.0	120 min. ozonation alone = 40% EST in ultrapure water: ozonation alone = 55% in 120 min; O_3 + perovskite = about 85% (regardless of the type of perovskite) Domestic wastewater = 60% in 120 min using copper catalyst	improvement of the oxidation rate	
8	La-containing perovskites ($LaFeO_3$; $LaNiO_3$; $LaCoO_3$; $LaMnO_3$; $LaFe_xCu_{1-x}O_3$ and $LaAl_xCu_{1-x}O_3$, $x = 0.9$ and 0.7)	Citrate method	Oxalic acid (OA) and CI Reactive Blue 5/pure water	$[OA] = 1\ mmol\ L^{-1}$, $[dye] = 50\ mg\ L^{-1}$, $[O_3] = 50\ g\ m^{-3}$, $[Cat.] = 0.14\ mg\ mL^{-1}$, $pH_{oxalic\ acid} = 3.0$, $pH_{dye} = 5.5$	$O_3 + LaCoO_3$: complete removal of oxalic acid after around 60 min and an almost complete mineralization of dye after 180 min Single O_3: 70% mineralization after 180 min	$LaMnO_3$ presented the best performance; however, metal leaching was observed during catalytic ozonation	Orge *et al.*[43]
9	Mesoporous nanocast perovskites (NC-$LaMnO_3$ and NC-$LaFeO_3$)	Nanocasting technique	2-Chlorophenol (2-CH)/pure water	$[2\text{-CH}] = 50\ mg\ L^{-1}$, $[O_3] = 12\ mg\ L^{-1}$, $[Cat.] = 0.3\ g\ L^{-1}$	TOC removal in 75 min: O_3 alone = 25%; O_3 + NC-$LaMnO_3$ = 80%; O_3 + NC-$LaFeO_3$ = 68%	Uncast counterpart perovskites (CA-$LaMnO_3$ and CA-$LaFeO_3$), were also prepared and all showed lower efficiencies than the NC-$LaMnO_3$ and NC-$LaFeO_3$	Afzal *et al.*[52]
10	Bismuth ferrite ($BiFeO_3$) magnetic	Thermal decomposition	Oxalic acid (OA) solution and norfloxacin (NFX) solution	$[OA] = [NFX] = 10\ mg\ L^{-1}$, $[Cat.] = 0.2\ mg\ L^{-1}$, $[O_3] = 75\ mg\ h^{-1}$, $T = 25$ °C	OA = 8.6% degradation in single O_3 after 60 min. O_3 + $BiFeO_3$ = 27.9% NFX = O_3 alone: about 37.9% of TOC removal in 120 min; O_3 + $BiFeO_3$: 39.1%.	A photocatalytic ozonation mechanism for $BiFeO_3$ was proposed.	Yin *et al.*[26]
11	$LaFeO_3$ and $LaCoO_3$	Sol–gel method	Benzotriazole (BZA)/pure water and bromate (BrO_3^-)	$[BZA] = 10\ mg\ L^{-1}$, $[Br^-] = 100\ \mu g\ L^{-1}$, $[O_3] = 2\ mg\ L^{-1}$,	O_3 or O_3 + $LaFeO_3$: = complete degradation of BZA in 20 min.	$LaFeO_3$ showed no catalytic activity for BZA degradation but inhibited	Zhang *et al.*[53]

Table 3.1 (*Continued*)

No.	Catalysts (Cat.)	Synthetic Methods	Pollutants/water matrix	Reaction parameters	Catalytic efficiency (%)/ time (min)	Comments/additional information	Refs.
				[Cat.] = 0.5 g L^{-1}, pH = 6.4	O_3 + $LaCoO_3$: complete degradation of BZA in 15 min and about 71% BrO_3^- inhibition	the generation of BrO_3^- by 73%	
12	$LaCoO_3$	Sol–gel method	Benzotriazole (BZ)/ Wastewater samples	[BZ] = effluent spiked with benzotriazole (100 mg L^{-1}) and Br^- (100 mg L^{-1}). [O_3] = 1.0 mg L^{-1}, [Cat.] = 0.25 g L^{-1}, pH = 7.39	O_3 = complete degradation of benzotriazole after 20 min with a reaction kinetic constant of 0.1462 min^{-1} O_3 + $LaCoO_3$ = complete degradation after 20 min with significant increase of kinetic constant (0.2141 min^{-1})	$LaCoO_3$ catalytic ozonation promoted the reduced the formation of aldehydes and oxalic acid as important toxic by-products in the sole ozonation.	Zhang *et al.*[54]
13	Combination of perovskite oxide ($LaCoO_3$, LCO) and graphitic carbon nitrite (g-C_3N_4, CN): CN/LCO	Sol–gel method	Benzotriazole (BZ)/ pure water	[BZ] = 10 mg L^{-1}, [O_3] = 1.0 mg L^{-1}, [Cat.] = 0.25 g L^{-1}, pH = 6.4	The highest removal efficiency was observed when CN/LCO-400 was used (k_{obs} was 0.0820 min^{-1})	The better degradation efficiency of BZA was observed in CN/LCO-400 catalytic ozonation, which indicated that the optimal calcination temperature was 400 °C	Zhang *et al.*[27]
14	Lanthanum manganite perovskites composites ($LaMn_4O_x$)	Modified co-precipitation method	Oxalic acid (OA) and 1*H*-benzotriazole (BTA)/pure water	[OA] = 50 mg L^{-1}, [BTA] = 50 mg L^{-1}, [O_3] = 20 mg L^{-1}, [Cat.] = 0.2 g L^{-1}, pH = 6.8, T = 25 °C	OA = O_3 alone: less than 10% of removal after 60 min; O_3 + $LaMn_4O_x$: complete removal in 45 min BTA = O_3 alone: complete removal in 60 min; O_3 + $LaMn_4O_x$: complete removal in 30 min	The hierarchical structure favored the catalytic activities of lanthanum manganite perovskites composites	Wang *et al.*[55]

[a]TOC = total organic carbon; COD = chemical oxygen demand

evaluated the catalytic ozonation of pyruvic acid, a common by-product formed after ozonation of aromatic compounds, in the presence of the perovskite $LaTi_{0.15}Cu_{0.85}O_3$.[47] The mechanistic studies developed indicated that a reaction occurs on the catalyst surface, after subsequent reaction products are formed and desorb to bulk solution. Continuing these studies, the researchers evaluated the ozonation of pyruvic acid using $LaTi_{1-x}Cu_xO_3$ and $LaTi_{1-x}Co_xO_3$ peroskovites[14] synthesized with different proportions of the transition metal. In the same year, another pioneering study developed by the authors was the application of $LaTi_{0.15}Cu_{0.85}O_3$ in the catalytic ozonation of gallic acid.[11] In the following year, the authors published a paper that demonstrated the application of the same catalyst to evaluate efficiency in the catalytic ozonation of a mixture of three phenols (tyrosol, gallic acid and syringic acid).[48] Furthermore, in that same work, the catalyst was tested in the remediation of real effluents from a wine distillery industry and two processes related to olive oil and table olive manufacturing.

Subsequently, Beltran *et al.*[50,51] studied combined ozone and copper or cobalt perovskites ($LaTi_{0.15}Me_{0.85}O_3$ with Me as Cu or Co) to assess the mineralization degree of pharmaceutical compounds by using sulfamethoxazole,[50] diclofenac[51] and 17α-ethynylstradiol[51] as model compounds. The increase in mineralization was highly significant in the presence of perovskite when compared to single ozonation, regardless of the pharmaceutical to be removed (see results in Table 3.1). It is worth mentioning that catalytic ozonation was also efficient for the mineralization of organic matter from a domestic effluent enriched with the drugs diclofenac and 17α-ethynylstradiol.

Three years after the work developed by Beltran *et al.*[50,51] in 2013, the work developed by Orge *et al.*[43] was highlighted. In this research, non-substituted perovskites ($LaFeO_3$, $LaNiO_3$, $LaCoO_3$ and $LaMnO_3$) and substituted perovskites ($LaFe_xCu_{1-x}O_3$ and $LaAl_xCu_{1-x}O_3$, $x = 0.9$ and 0.7) were employed as efficient catalysts for the removal of oxalic acid and dye CI Reactive Blue 5. More recently, in 2017, Afzal *et al.*[52] in their research work, synthesized mesoporous perovskites type NC-$LaMnO_3$ and NC-$LaFeO_3$, where NC was the acronym used by the authors to represent the mesoporous materials. Mesoporous materials have high surface areas, and it is well reported that the increase in surface area increases the catalytic response. The researchers synthesized these mesoporous materials in order to increase the catalytic response of perovskites in ozonation applications. As a target compound, the researchers chose 2-chlorophenol, which is considered a priority pollutant. The synthesized perovskites showed a comparatively high catalytic activity in terms of mineralization in the ozonation of 2-chlorophenol in relation to the other conventional perovskites (see summary in Table 3.1). From a detailed study carried out by the researchers to discuss the mechanism of catalytic ozonation of NC-$LaMnO_3$ perovskite, $^{\bullet}OH$ radicals were the dominant reactive oxygen species contributed to high catalytic activity.

Perovskite type $BiFeO_3$ magnetic nanoparticles were evaluated by Yin *et al.*[26] for catalytic and photocatalytic ozonation using oxalic acid and norfloxacin as model compounds. In this case, $BiFeO_3$ has low activity for

the catalytic activation of ozone. However, under visible light irradiation, a high increase in catalytic activity was obtained. The authors attributed this increase to the synergy between photocatalysis and ozonation that resulted from the recombination inhibition of the photo-generated electron–hole pairs and the improved yield of $^{\bullet}OH$ radicals.

Zhang *et al.*[53] investigated benzotriazole removal in catalytic ozonation with two perovskites, $LaCoO_3$ and $LaFeO_3$, as catalysts and investigated the minimization of bromate (BrO_3^-) formation in the presence of the perovskites. It is worth noting here that it is extremely important to investigate the generation of BrO_3^- (anion classified as a potential carcinogen to humans) in ozonation processes. In another study, Zhang *et al.*[54] evaluated the performance of catalytic ozonation in the presence of $LaCoO_3$ in a comprehensive manner and in real conditions, including a real matrix derived from effluents of primary and secondary clarifiers in a municipality's wastewater. They investigated the degradation of benzotriazole as a typical emerging pollutant, the reduction of bromate, and the ability of the system to remove precursors from disinfection by-products. The results obtained by the researchers showed that catalytic ozonation in the presence of perovskite-type $LaCoO_3$ improved the removal of contaminant and organic matter from the effluent. Advantageously, $LaCoO_3$ catalytic ozonation has shown an ability to remove toxic halogenated organic by-products, aldehydes and the disinfection by-product precursors.

In particular, the hierarchically clustered microsphere structure of the perovskites could enable the active sites to be highly exposed and consequently favor catalytic activities. Wang *et al.*[55] synthesized a series of hierarchical lanthanum manganite perovskites composites ($LaMn_4Ox$) with non-stoichiometric compositions and evaluated the catalytic ozonation activities of the as-synthesized perovskites using oxalic acid and 1*H*-benzotriazole as the target pollutants. The hierarchical structure favored the catalytic activities of these lanthanum manganite perovskites. From the various mechanistic studies carried out by the authors, it was proven that oxygen vacancies, the Mn^{3+}/Mn^{4+} redox centers and the surface hydroxyl groups were the potential active sites for ozone decomposition in the presence of $LaMn_4Ox$. Reactive oxygen species, among them $^{\bullet}OH$ radicals, superoxide ($^{\bullet}O_2^-$) and singlet oxygen ($^1O_2$), also contributed to catalytic activity in $LaMn_4Ox$ catalytic ozonation. In this catalytic system, the authors proposed that the produced $^{\bullet}O_2^-$ and $^1O_2$ might originate from the ozone-dissociated products on oxygen vacancies, while $^{\bullet}OH$ might stem from O_3 adsorbed onto Mn sites and/or surface hydroxyl groups. The mechanism of catalytic ozonation with perovskites is still a challenge for chemists, and there are not many detailed studies, demonstrating the need to explore this field.

3.3 Spinel-like Oxide-type Catalysts

The combination of two single-cation oxides to form two-cation oxide with spinel structure is a strategy to improve the properties of this material

compared to its binary oxide's counterparts, among them stability, electronic, magnetic and optical properties.[56–58] The interesting properties of these oxides enhance their use as a catalyst in several applications, with emphasis on catalytic ozonation, discussed in this chapter.

Spinel oxides are typically known as mixing metal oxides with the stoichiometric chemical formula AB_2O_4, where A and B represent divalent and trivalent metallic ions, respectively.[57,58] Spinel oxides are being widely used as non-noble catalysts in catalytic ozonation. The catalytic performance of AB_2O_4 nanoparticles in ozonation processes is practically studied using aluminate and ferrite spinel oxides. Spinel ferrites with the general formula $MeFe_2O_4$ (Me = Ni, Cu, Mn, Zn, Co) are widely studied for their catalytic applications in ozonation as they have the advantages of easy recovery, good stability and high activity.[15] The use of ferrites also makes it possible to recover the catalyst at the end of the process, allowing reuse and consequently reducing operating costs and facilitating application in full-scale effluents.

Table 3.2 presents a summary of the catalytic performance of pure and doped ferrite spinel oxides for application in catalytic ozonation used to remove contaminants such as di-*n*-butyl phthalate, phenacetin, phenol in pure water and wastewater.

Di-*n*-butyl phthalate (DBP), a common member of phthalate esters, is one of the most reported compounds to evaluate the effectiveness of the use of spinel ferrites in ozonation. The first study reporting the use of magnetic porous ferrospinel materials for the removal of DBP in catalytic ozonation was carried out by Ren *et al.*[59] In this research, magnetic porous ferrospinel $NiFe_2O_4$ was prepared by a sol–gel method. According to the results summarized in Table 3.2, the presence of the catalyst showed more than 60% increase in the rate of DBP degradation (in 30 min of reaction), compared to ozonation alone. In the work of Zhao *et al.*,[60] $NiFe_2O_4$ nanomaterials were prepared by two different methods. $NiFe_2O_4$ synthesized by the hydrothermal method significantly increased the removal of phenol (around 16% compared to ozonation alone), while the catalyst synthesized by the calcined method was non-effective. This was due to differences in the properties of the catalysts that showed differences in interaction with ozone.

Qi *et al.*[61,62,64] published a series of three scientific articles in the years 2015–2016 using copper, *manganese and nickel* spinel ferrites, for application in the catalytic ozonation of phenancentin, a non-opioid analgesic and antipyretic agent. The catalytic activity of copper ferrite, $CuFe_2O_4$, for the removal of NO_x and *N*,*N*-dimethylacetamide (a widely used industrial solvent) *via* the catalytic ozonation process was also investigated by Zhao *et al.*[66] and Zhang *et al.*,[69] respectively. $CuFe_2O_4$ showed high activity for application in catalytic ozonation, as observed in results shown in Table 3.2. The main problem with the application of these metals in catalytic ozonation is leaching, which can cause secondary pollution due to their toxicity.[15] However, as demonstrated by the results obtained by the researchers,[64,66,69] the magnetism of spinel ferrites favors recycling, which can be used to separate it from the solution for reuse and consequently reduce the problems of

Table 3.2 Catalytic ozonation of pollutants in water and wastewater by undoped (No. 1–12) and doped (No. 13–18) spinel ferrites.

No.	Catalysts (Cat.)	Synthetic methods	Pollutants/water matrix	Reaction parameters	Catalytic efficiency (%)/time (h or min)	Comments/additional information	Refs.
1	$NiFe_2O_4$	Sol–gel process	Di-*n*-butyl phthalate (DBP)/deionized water	[DBP] = 0.5 mg L^{-1}, [O_3] = 5 mg L^{-1}, [Cat.] = 0.01 g L^{-1}, pH = 7.7. T = 25 °C.	Single ozonation = 25% of removal in 10 min, and 42% after 60 min. O_3 + $NiFe_2O_4$ = almost 100% removal in 30 min	$NiFe_2O_4$ catalytic ozonation followed a •OH radical-type mechanism	Ren *et al.*[59]
2	$NiFe_2O_4$	Hydrothermal method ($NiFe_2O_4$–H) and calcined method ($NiFe_2O_4$–C)	Phenol/deionized water	[Phenol] = 300 mg L^{-1}, [O_3] = 0.75 mg min^{-1}, [Cat.] = 1.0 g L^{-1}, pH = 6.5 ± 0.1, T = 20.0 ± 1.0 °C	Phenol removal in 60 min: Sole ozonation = 38.9%; O_3 + $NiFe_2O_4$–H = 55.2%	$NiFe_2O_4$–C was non-effective	Zhao *et al.*[60]
3	$CuFe_2O_4$	Co-precipitation-calcination method	Phenacetin (PNT)/ distilled-deionized water and wastewater treatment plant effluent	[DBP] = 0.2 mmol L^{-1}, [O_3] = 0.36 mg L^{-1} or 3.85 mg L^{-1}, [Cat.] = 2.0 g L^{-1}, pH = 7.72	(1) Sole ozonation [0.36 mg L^{-1}] = 95% of PNT removal in 30 min. (2) sole ozonation [3.85 mg L^{-1}] = complete removal in 5.0 min (3) O_3 + $CuFe_2O_4$ = The total reaction time was reduced by half to obtain the same removal (4) the effluent of wastewater treatment: did not show some negative effect on the performance of catalytic ozonation	In sole ozonation, the molecular ozone was reacted with phenacetin fast, but it was less effective for phenacetin's mineralization	Qi *et al.*[61]
4	$MnFe_2O_4$ and $NiFe_2O_4$	Co-precipitation-calcination method	Phenacetin (PNT)/ distilled-deionized water	[PNT] = 0.2 mmol L^{-1}, [O_3] = 0.36 mg L^{-1}, [Cat.] = 2.0 g L^{-1}, pH = 7.72	Sole ozonation = 29.36% of TOC removal in 3 h In the presence of a catalyst, the mineralization increased to 60%, regardless of the catalyst selection	All catalysts showed a weak heavy metal leaching; catalysts can be reused many times	Qi *et al.*[62]

5	$ZnFe_2O_4$ (ZFO)	Hydrothermal (ZFO-H) and citrate sol–gel methods (ZFO-C)	Phenol/ultrapure water and biologically treated coking wastewater (BTCW)	Ultrapure water: [phenol] = 300 mg L^{-1}, [O_3] = 14 ± 1 mg L^{-1}, [Cat.] = 1.0 g L^{-1}, pH = 6.38 BTCW: [O_3] = 31 ± 1 mg L^{-1}, [Cat.] = 1.0 g L^{-1}, pH = 7.0 ± 0.5	Sole ozonation = 63.4% of phenol removal in 30 min O_3 + ZFO-H = 92.6% after 30 min O_3 + ZFO-C = no increment of removal was obtained BTCW: TOC removal in 60 min = 23.4% (sole O_3); 27.9% (O_3 + ZFO-C); 35.8% (O_3 + ZFO-H)	The effect of TBA as radical scavenger demonstrated the predominant role of ozone in non-catalytic ozonation, whereas •OH notably prevailed in catalytic ozonation	Zhang *et al.*[63]
6	$CuFe_2O_4$ (CFO) and CFOH (precursor of copper ferrite)	CFO: Co-precipitation-calcination method; CFOH: same procedure without the calcination step	Phenacetin (PNT)/ distilled-deionized water	[PNT] = 0.2 mmol L^{-1}, [O_3] = 0.36 mg L^{-1} or 3.85 mg L^{-1} [Cat.] = 2.0 g L^{-1}, pH = 7.72	TOC removal in 180 min: Sole O_3 [3.85 mg L^{-1}] = about 30%; O_3 [3.85 mg L^{-1}]/CFOH = about 90%	Better performance and mineralization of PNT in catalytic ozonation by CFOH were observed, which was dominated by the surface reaction	Qi *et al.*[64]
7	$MgFe_2O_4$	Sol–gel combustion process	Acid Orange II (AOII)/ simulated wastewater	[AOII] = 50 mg L^{-1}, [O_3] = 5.0 mg L^{-1} [Cat.] = 0.1 g L^{-1}.	O_3 + $MgFe_2O_4$ = 94.1% of AOII removal after 40 min and 48.1% of TOC removal in 80 min (4.74 times that in O_3 alone)	The degradation of AOII using other spinel ferrites, among them $NiFe_2O_4$, $MnFe_2O_4$, and $CuFe_2O_4$ as catalysts were investigated for comparisons	Lu *et al.*[65]
8	$CuFe_2O_4$	Hydrothermal method	Simulated flue gas (mixing N_2 and NO gas (5% (v/v), balanced with N_2))	[NO_x] = 450 mg L^{-1}, [O_3] = 2.8 mg L^{-1}, Cat. = 200 mg, pH = 6.38	O_3 + $CuFe_2O_4$ = 83% NO_x removal	A possible mechanism for the catalytic ozonation of NO_x was proposed	Zhao *et al.*[66]
9	AFe_2O_4 (A = Co, Ni, Cu, and Zn)	Citrate sol–gel method	Oxalic acid (OA)/ ultrapure water	[OA] = 5 mmol L^{-1}, [O_3] = 14 ± 1 mg L^{-1}, [Cat.] = 1.0 g L^{-1}, pH = 2.30 ± 0.02	TOC removal in 120 min: single ozonation = 4.7%; O_3 + $CoFe_2O_4$ = 68.3%; O_3 + $ZnFe_2O_4$ = 8.5%; O_3 + $CuFe_2O_4$; O_3 + $NiFe_2O_4$ = 15%	The mechanism of oxalic acid ozonation catalyzed by spinel ferrites have been proposed	Zhang *et al.*[67]
10	$MeFe_2O_4$ (Me = Cu, Co, Ni, Zn)	Auto combustion reaction method	Shale gas produced water (PW)	PW = 1.0 L, mixing gas = flow rate of 0.8 L min^{-1}, O_3 = 1.0 mg L^{-1} min^{-1}, [Cat.] = 0.15 g L^{-1},	COD removal of PW in 24 h: (i) O_3 alone: less than 200 mg L^{-1} COD removal; O_3 + $CuFe_2O_4$ = 572 mg L^{-1}; O_3 + $NiFe_2O_4$ = 530 mg L^{-1};	The catalytic performance of catalysts was ranked as $CuFe_2O_4$ > $NiFe_2O_4$ > $CoFe_2O_4$ > $ZnFe_2O_4$	Liu *et al.*[68]

Table 3.2 (*Continued*)

No.	Catalysts (Cat.)	Synthetic methods	Pollutants/water matrix	Reaction parameters	Catalytic efficiency (%)/time (h or min)	Comments/additional information	Refs.
				$T = 25 \pm 2$ °C, pH = 10.2 ± 0.2	$O_3 + CoFe_2O_4 = 503$ mg L^{-1}; $O_3 + ZnFe_2O_4 = 413$ mg L^{-1} of COD removal		
11	$CuFe_2O_4$	Sol–gel combustion method	*N*,*N*-dimethylacetamide (DMAC)/deionized water	[DMAC] = 200 mg L^{-1}, $[O_3] = 4.6$ mg L^{-1}, [Cat.] = 30 g L^{-1}, pH = 6.7. $T = 25 \pm 1$ °C	COD and TOC removal in 120 min: sole O_3: COD = 11.1%, TOC = 6.8%; $O_3 + CuFe_2O_4$: COD = 30.1%, TOC = 22.3%	The performance of $O_3 + CuO$ process for the DMAC degradation was much stronger than that of $O_3 + CuFe_2O_4$ process, but the leaching concentration of Cu^{2+} in $O_3 + CuO$ process was about 10 times than that of $O_3 + CuFe_2O_4$ process	Zhang *et al.*[69]
12	$CoFe_2O_4$	Sol–gel combustion technique	Clofibric acid (CA)/deionized water	[CA] = 0.1 mmol L^{-1}, $[O_3] = 5.1$ mg min^{-1}, [Cat.] = 0.2 g L^{-1}, pH ~ 4.0, $T = 25 \pm 2$ °C	CA removal in 30 min: sole O_3 = 64%; $O_3 + CoFe_2O_4$ = 98.7% TOC removal in 120 min: sole ozonation = 29.8%. $O_3 + CoFe_2O_4$ = 72.7%	The $O_3 + CoFe_2O_4$ was efficient for the oxidation of other contaminants (2,4-dichlorophenol and bisphenol A) and it also performed well in removing CA in river, lake and tap water	Cai *et al.*[70]
13	Bi-doping $MnFe_2O_4$ ($Mn_{1-x}Bi_xFe_2O_4$, $x = 0$, 0.005, 0.01, 0.02, 0.05)	Sol–gel process	Di-*n*-butyl phthalate (DBP)/deionized water	[DBP] = 0.05 mg L^{-1}, $[O_3] = 0.3$ mg L^{-1}, [Cat.] = 0.01 g L^{-1}, pH = 6.9. $T = 25 \pm 1$ °C	DBP removal in 60 min: sole O_3 = 33%; O_3 + Bi-doping catalysts: follows the order of $Mn_{0.95}Bi_{0.05}Fe_2O_4$ (more than 70% removal) > $Mn_{0.98}Bi_{0.02}Fe_2O_4$ > $Mn_{0.99}Bi_{0.01}Fe_2O_4$ > $Mn_{0.995}Bi_{0.005}Fe_2O_4$ > $MnFe_2O_4$	$O_3 + Mn_{0.95}Bi_{0.05}Fe_2O_4$ exhibits the highest efficiency on removal of DBP, which is about twice higher than degradation of ozone alone	Ren *et al.*[71]
14	Graphene oxide doping $MnFe_2O_4$ (rGO-$MnFe_2O_4$, rGO = mass ratio: 1%, 5%, 10%)	Electrospinning method	Di-*n*-butyl phthalate (DBP)/deionized water	[DBP] = 0.5 mg L^{-1}, $[O_3] = 0.40$ mg min^{-1}, [Cat.] = 0.01 g L^{-1}, pH = 7.0, $T = 20 \pm 2$ °C	DBP removal in 60 min: sole O_3 = 32%; O_3 + 5% rGO-$MnFe_2O_4$ = 87%	In 5% rGO-$MnFe_2O_4$/O_3 system, $^{\bullet}OH$ is the main radicals and chemisorbed oxygen groups act as extremely important active sites in the catalytic reaction	Ren *et al.*[72]

15	Ag-doped $MnFe_2O_4$ (Ag molar loading of 0.2, 0.5, 1, 2, and 5%)	Sol–gel process	Di-*n*-butyl phthalate (DBP)/deionized water	[DBP] = 0.5 mg L^{-1}, O_3 = 0.68 mg min^{-1}, [Cat.] = 10 mg L^{-1}, pH = 7.3, $T = 25 \pm 2$ °C	DBP removal in 60 min: sole O_3 = 30%; O_3 + 0.5% Ag/$MnFe_2O_4$ = 75.3%	Experiments showed an important role of surface hydroxyl groups to promote the ozone decomposition and •OH radical production	Wang *et al.*[73]
16	$CuFe_2O_4$ loaded on natural sepiolite ($CuFe_2O_4$/SEP)	Citrate sol–gel method	Quinoline/deionized water and biologically treated coking wastewater	Ultrapure water: [quinoline] = 50 mg L^{-1}, O_3 = 1.0 L min^{-1}, [Cat.] = 1.0 g L^{-1}, pH = 6.8	Quinoline (TOC removal in 30 min): sole O_3 = 16.8%; O_3 + $CuFe_2O_4$ = 55.8%; O_3 + $CuFe_2O_4$/SEP = 90.3% Biologically treated coking wastewater (TOC removal in 60 min): sole O_3 = 19.99%; O_3 + $CuFe_2O_4$/SEP = 57.81%	Mechanistic studies indicated that •OH and $^{\bullet}O_2^-$ were the main reactive species in the ozonation in the presence of $CuFe_2O_4$/SEP	Liu *et al.*[74]
17	Mn-doped $ZnFe_2O_4$ ($Mn_xZn_{1-x}Fe_2O_4$, $x = 0$, 0.2, 0.5, 0.8)	Sol–gel process	Di-*n*-butyl phthalate (DBP)/deionized water	[DBP] = 0.5 mg L^{-1}, [O_3] = 0.5 mg min^{-1}, [Cat.] = 0.01 g L^{-1}, pH = 7.0, $T = 20 \pm 2$ °C.	DBP removal in 30 min: Sole O_3 = 36%; O_3 + $ZnFe_2O_4$ = 50.5%; O_3 + $Mn_{0.5}Zn_{0.5}Fe_2O_4$ = 91.7%.	The surface hydroxyl groups were the main active sites for $Mn_xZn_{1-x}Fe_2O_4$ in the catalytic ozonation process. •OH was the primary species responsible for DBP degradation	Zhao *et al.*[75]
18	Ag-doped $NiFe_2O_4$ ($Ag_{2x}Ni_{1-x}Fe_2O_4$, $x = 0$, 0.01, 0.02, 0.03, 0.05)	Sol–gel method	Papermaking wastewater	[O_3] = 5 mg L^{-1}, [Cat.] = 0.1 g L^{-1}, $T = 25 \pm 2$ °C	COD removal in 60 min: Sole O_3 = 23%; O_3 + $NiFe_2O_4$ = 53%; O_3 + $Ag_{0.02}Ni_{0.99}Fe_2O_4$ = 58%; O_3 + $Ag_{0.04}Ni_{0.98}Fe_2O_4$ = 62%; O_3 + $Ag_{0.06}Ni_{0.97}Fe_2O_4$ = 65%; O_3 + $Ag_{0.1}Ni_{0.95}Fe_2O_4$ = 70%	Ag and Ni worked as the active sites and the efficient cycling of electron between Ag and Ni enhanced the decomposition of ozone and generated more •OH radicals	Zhao *et al.*[76]

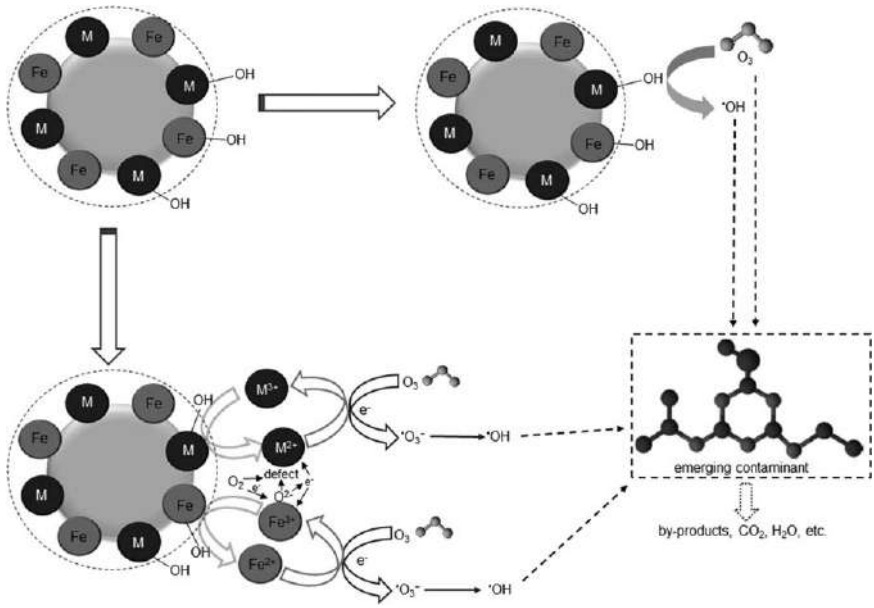

Figure 3.2 Scheme illustrating the possible mechanism for ozonation process in the presence of ferrite spinel oxides catalysts.

secondary pollution. In general, mechanistic studies indicate that the high density of surface hydroxyl groups and oxygen vacancies promotes the generation of •OH radicals, which is the main active species responsible for the efficiency of the application of spinel oxides in catalytic ozonation.

It is also found in the literature (see Table 3.2) that the magnetic nanoparticles of $ZnFe_2O_4$,[63,67,68] $MgFe_2O_4$[65] and $CoFe_2O_4$[67,68,70] are catalytically active in the ozonation of emerging organic contaminants.

Based on the possible reaction mechanisms for catalytic ozonation with different ferrite spinel oxides proposed by Zhang *et al.*,[67,69] as proposed by Cai *et al.*[70] and complemented with the results obtained by Lu *et al.*,[65] a possible general mechanism for catalytic ozonation by spinel ferrites is illustrated in Figure 3.2. From the discussions held by the researchers, a possible explanation for the mechanism is described here: (1) Superficial M–OH groups formed due to the adsorption of water molecules on the active sites of the metal oxide[70] (eqn (3.1)). (2) Then, the dissolved ozone adsorbed on the surface of the catalyst and interaction with the hydroxyl groups on the surface occurred, resulting in the generation of •OH radicals[69] (eqn (3.2)–(3.4)). (3) In addition, the transfer of an electron from the bivalent A-site metal ion to ozone generated the radical $^{\bullet}O_3^-$ and trivalent A-site metal ion. This radical reacts with H^+ in solution, generating $HO_3^{\bullet}$ and finally •OH radicals. Simultaneously, oxidized trivalent metals are reduced by lattice oxygen, regenerating their bivalent state.[67]

$$\equiv M^{2+} + H_2O \rightarrow \equiv M^{2+} - OH + H^+ \tag{3.1}$$

$$\equiv M^{2+}\text{–}OH + 2O_3 \rightarrow \equiv M^{2+}\text{–}{}^{\bullet}O_2{}^{-} + HO_3{}^{\bullet} + O_2 \quad (3.2)$$

$$HO_3{}^{\bullet} \rightarrow {}^{\bullet}OH + O_2 \quad (3.3)$$

$$\equiv M^{2+}\text{–}{}^{\bullet}O_2{}^{-} + O_3 + H_2O \rightarrow \equiv M^{2+}\text{–}OH + HO_3{}^{\bullet} + O_2 \quad (3.4)$$

More recently (2016), some researchers have focused on the modification of ferrite spinel oxides for application in catalytic ozonation. Generally, the addition of a metal dopant can significantly increase the catalytic properties of ferrites and of spinel oxides in general due to changes in the properties of catalysts, such as increased surface area, particle size distribution, ion distribution, formation of porous oxides and surface morphology.[71] In addition, metal-doped catalysts have more Lewis acid sites on the surface, which hold more hydroxyl groups on the surface and consequently increase the generation of active species.[76]

The first work using spinel ferrite doped for ozonation applications was reported by Ren *et al.*[71] In this study, Bi-doping spinel ferrite $Mn_{1-x}Bi_xFe_2O_4$ was applied in the catalytic ozonation of DBP, and it was found that the introduction of Bi into $MnFeO_4$ improved the catalytic DBP decomposition due to decreased crystallite size and the increased surface hydroxyl site concentration of $MnFe_2O_4$. In the literature (see Table 3.2), there are reported works applying spinel ferrites doped with Ag and Mn for application in ozonation. More specifically, the effectiveness of Ag-doped $MnFe_2O_4$[73] and Mn-doped $ZnFe_2O_4$[75] as catalysts for the ozonation of DBP degradation and Ag-doped $NiFe_2O_4$[76] for catalytic ozonation of secondary effluents of papermaking wastewater are highlighted.

Table 3.3 represents the review of other spinel oxides that have been applied in the catalytic ozonation process. From the presented works, it is possible to observe that aluminate spinel oxides, specifically cobalt,[77] copper[78,80,83] and zinc[79,82] aluminates, are generally used in catalytic ozonation. Aluminate spinels have been reported to be good catalysts for application in catalytic ozonation (see Table 3.3 No. 1–4, 6, 7). For example, Xu *et al.*[83] studied the catalytic ozonation of the common azo dyes, CI Acid Orange 7 using $CuAl_2O_4$-based mixed oxides, obtaining a high rate of dye decomposition (96% of removal) and an increase of about 47% in the removal of COD compared to ozonation alone. Recently, Chen and Wang[85] reported a spinel cobaltite $NiCo_2O_4$ as the catalyst for the ozonation of sulfamethazine (SMT), an antibiotic widely used in veterinary practice.

In summary, to the best of our knowledge, Tables 3.2 and 3.3 show the spinel oxides that have been used so far for application in catalytic ozonation.

3.4 Other Natural Minerals

Many natural minerals have been used in the field of water treatment by the catalytic ozonation process due to their low cost and ready availability. The most common natural minerals used as catalysts in ozonation processes are shown in Figure 3.3(a) and (b) and Table 3.4, which include goethite,[90]

Table 3.3 Review of other types of spinel oxides used in the catalytic ozonation process.[a]

No.	Catalysts (Cat.)	Synthetic methods	Pollutants/water matrix	Reaction parameters	Catalytic efficiency (%)/time (h or min)	Comments/additional information	Refs.
1	Co/Al_2O_3 (Co/Al_2O_3-X-Y °C-Z%, X = calcination atmosphere (nitrogen, N, or air, A), Y = calcination temperature (500 to 800 °C) and Z = weight percentage of cobalt (0.5 to 5%)).	Incipient wetness impregnation method	Pyruvic acid (PA)/ deionized water	[PA] = 5 mmol L^{-1}, [O_3] = 40 mg L^{-1}, [Cat.] = 0.01 g L^{-1}, pH = 2.5, T = 20 °C	DOC removal in 120 min: Sole O_3 = 5.5%; $O_3 + Al_2O_3$ = 41.1%; $O_3 + Co/Al_2O_3$-A-500 °C-2% = 90.2%	All the Co/Al_2O_3 catalysts prepared showed good stability as the percentage of cobalt leached out was rather low	Álvarez *et al.*[77]
2	$CuAl_2O_4$ and $Cu_xMg_{1-x}Al_2O_4$ (x = 0.75, 0.5, 0.25)	Co-precipitation method	Clofibric acid (CFA)/ deionized water	[CFA] = 100 mg L^{-1}, [O_3] = 1.2 g h^{-1}, [Cat.] = 0.5 g L^{-1}, T = 25 ± 2 °C	TOC removal in 6 h: Sole O_3 = about 40%; $O_3 + CuAl_2O_4$ = 83%; $O_3 + Cu_{0.75}Mg_{0.25}Al_2O_4$ = 85%	The fast disappearance of CFA in less than 15 min was observed, as with spinel catalysts	Sable *et al.*[78]
3	$ZnAl_2O_4$	Hydrothermal method	Phenol/deionized water	[Phenol] = 300 mg L^{-1}, [O_3] =: 0.75 mg min^{-1}, [Cat.] = 1.0 g L^{-1}, pH = 6.4 ± 0.1, T = 25 ± 0.5 °C	Phenol removal in 60 min: sole O_3 = about 50%; $O_3 + ZnAl_2O_4$ = 73.4%	In the presence of $ZnAl_2O_4$, ozone transformed into high active •OH radicals	Zhao *et al.*[79]
4	$CuAl_2O_4$ and $Cu_{0.75}Mg_{0.25}Al_2O_4$	Co-precipitation method	Clofibric acid (CFA)/ deionized water	[CFA] = 100 mg L^{-1}, [O_3] = 1.2 g h^{-1}, [Cat.] = 0.5 g L^{-1}	TOC removal in 2 h: sole O_3 = 28.1%; $O_3 + CuAl_2O_4$ = 50%; $O_3 + Cu_{0.75}Mg_{0.25}Al_2O_4$ = 55.3%	The surface hydroxyl groups and Lewis acid sites are responsible for promoting the generation of •OH radicals	Sable *et al.*[80]
5	Ordered mesoporous Fe_3O_4	Nanocasting route	Atrazine (ATZ)/ ultrapure water	[ATZ] = 5.0 μmol L^{-1}, [O_3] = 0.1 mmol L^{-1}, [Cat.] = 0.2 g L^{-1}, pH = 6.54, T = 25 ± 2 °C	ATZ removal after 10 min: sole O_3 = 9.1%; $O_3 + Fe_3O_4$ = 82%	A mechanism based on the redox cycles of Fe^{2+}/Fe^{3+} and •OH radical was proposed	Zhu *et al.*[81]

6	$ZnAl_2O_4$	Hydrothermal ($ZnAl_2O_4$-H), sol–gel ($ZnAl_2O_4$–S), and coprecipitation ($ZnAl_2O_4$–C) methods	5-Sulfosalicylic acid (SSal)/ultrapure water	[SSal] = 500 mg L^{-1}, $[O_3]$ = 5.0 mg min^{-1} or 10.0 mg min^{-1}, mg min^{-1}, [Cat.] = 0.2 g L^{-1}, pH = 7	SSal removal after 60 min: sole O_3 = 49.4%; O_3 + $ZnAl_2O_4$-H = 64.8%; O_3 + $ZnAl_2O_4$-S = 61.7%; O_3 + $ZnAl_2O_4$-C = 59% COD removal after 60 min: sole O_3 = 33.2%; O_3 + $ZnAl_2O_4$-H = 46.2%; O_3 + $ZnAl_2O_4$-S = 38.8%; O_3 + $ZnAl_2O_4$-C = 36.6%	•OH radicals were the main active oxidative species in catalytic ozonation	Dai *et al.*[82]
7	$CuAl_2O_4$	Conventional citric acid complexation method	C. I. Acid Orange 7 (AO7)/deionized water	[AO7] = 100 mg L^{-1}, $[O_3]$ = 10.06 mg min^{-1}, [Cat.] = 0.5 g L^{-1}, pH = 6.54	AO7 in 25 min: sole O_3 = 76.4%; O_3 + $CuAl_2O_4$ = 96.0% COD removal in 120 min: sole O_3 = 40%; O_3 + $CuAl_2O_4$ = 87.2%	Combination of Al and Cu was found highly effective to catalyze ozone and form reactive radicals (adsorbed •OH and few $•O_2^-$)	Xu *et al.*[83]
8	γ-Al_2O_3 doped with different metals M alone or in mixture (M = Mg, Ca, Zn, Fe, Ba, Zr, Cu, Co, Ni, Ce, Ti, with 0.05 < M/Al < 0.5 molar ratio)	Incipient wetness deposition or by direct sol–gel	Synthetic mixture representative of a produced water (water coming naturally during oil or gas extraction)	Synthetic mixture: pH = 3.3–4.3, TOC = 216 mg L^{-1}, COD = 668 mg O_2 L^{-1}, $[O_3]$ = 5 g Nm^{-3}, [Cat.] = 5.0 g L^{-1}, T = 30 °C	TOC removal: O_3 + Mg/γ-Al_2O_3 Mg/Al(0.2/1), O_3 + Cu/Mg/Al_2O_3 Cu/Mg/Al (0.2/0.2/1), O_3 + Mg/γ-Al_2O_3 Mg/Al (0.1/1) = >90% after 2 h and 95% after 5 h	Among the catalysts, Mg-doped alumina with molar ratio Mg/Al = 0.1, 0.2 prepared by incipient wetness deposition were the more efficient catalysts	Xu *et al.*[84]
9	$NiCo_2O_4$	Hydroxide coprecipitation and thermal decomposition	Sulfamethazine (SMT)/deionized water	[SMT] = 20 mg L^{-1}, $[O_3]$ = 4.5 mg min^{-1}, [Cat.] = 0.05 g L^{-1}, pH = 5.2	TOC removal in 60 min: sole O_3 = ~11%; O_3 + $NiCo_2O_4$ = 34.1%	$NiCo_2O_4$ could accelerate the generation of •OH, which was responsible for the improvement of TOC removal	Chen and Wang[85]

[a]DOC = dissolved organic carbon.

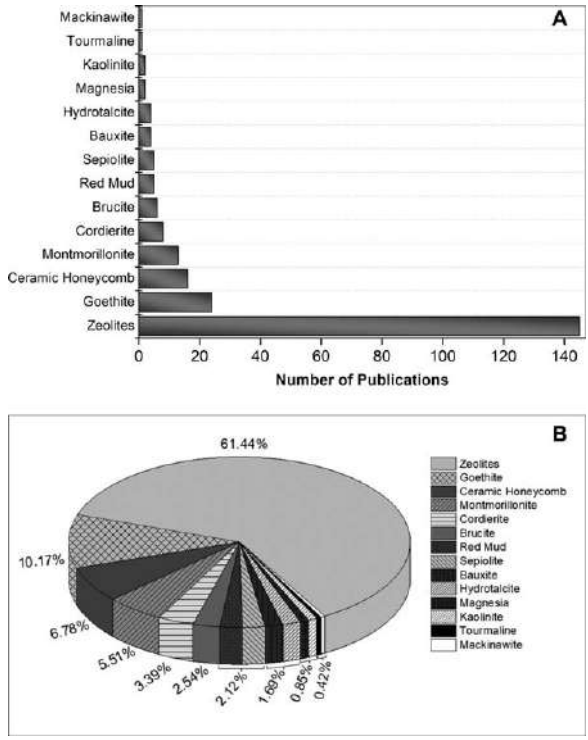

Figure 3.3 (a) Distribution of the number of publications on the catalytic activity of the most common minerals in ozonation. (b) Comparison of the use of catalysts in ozonation in percentages for the minerals shown in graph (a). Data taken from ISI Web of Science database using the keyword ''catalytic ozonation'' and the name of each mineral shown on the *y*-axis of the graph. Data from https://www.webofknowledge.com/, accessed July 27, 2021.

ceramic honeycomb,[91,98] red mud,[95] montmorillonite,[96] zeolites.[25,104] These minerals can accelerate ozone decomposition leading to the production of more $^{\bullet}$OH radicals on the surface of mineral catalysts[107] and are used pure or modified with metals or metal oxides in order to increase the catalytic response. Figure 3.3(b) shows that zeolites are the most used minerals in catalytic ozonation, representing 61.44% of the publications in relation to the catalysts presented here. Ceramic honeycomb is a stable material and has also been used to improve the efficiency of ozonation processes.[98] The use of goethite, montmorillonite and red mud are also significant but are less explored compared to zeolites and ceramic honeycomb. In addition to these minerals, bauxite, sepiolite and brucite, along with others of lesser significance (see Figure 3.3), are also found for few application studies in catalytic ozonation.

Zeolites have been used successfully in catalytic ozonation to remove various pollutants, including pharmaceuticals,[24,25] leachate,[104] nitrobenzene,[108]

Table 3.4 Application of catalytic ozonation with minerals.

Catalysts	Pollutants	Catalytic efficiency (%)	Refs.
Brucite	Active brilliant red X-3B dye	89% degradation in 10 min	Dong *et al.*[86]
Brucite, magnesia	Nitrobenzene and aniline	>95% of nitrobenzene and aniline degradation in 120 min	Dong *et al.*[87]
De-aluminated Y zeolite	Phenol	87.5% degradation in 45 min	Dong *et al.*[88]
Brucite, magnesia	Phenol	Brucite: 55% increase in degradation in 15 min; Magnesia: 91% increase in 15 min.	He *et al.*[89]
Goethite	Nitrobenzene	65% of nitrobenzene degradation in 20 min	Zhang and Ma[90]
Mn–ceramic honeycomb	Nitrobenzene	74% of nitrobenzene degradation in 15 min	Zhao *et al.*[91]
Cordierite-supported copper	Nitrobenzene	77.9% of degradation after 20 min	Zhao *et al.*[92]
Bauxite	2,4,6-Trichloroanisole	86.0% of degradation after 10 min	Qi *et al.*[93]
Calcined magnetite	Reactive Red-120 dye	84.5% of degradation in 10 min	Moussavi *et al.*[94]
Red mud	Nitrobenzene	67.17% of degradation in 40 min	Qi *et al.*[95]
Fe^{2+}-montmorillonite	Sulfamethoxazole antibiotic	98–99% COD removal in 20 min	Shahidi *et al.*[96]
Cobalt-loaded red mud	Bezafibrate	>80% of bezafibrate removal in 30 min	Xu *et al.*[97]
MgO/ceramic honeycomb	Acetic acid	81.6% of degradation in 30 min	Shen *et al.*[98]
Natural mackinawite	*N*,*N*-Dimethylacetamide	96.6% of degradation after 20 min	Peng *et al.*[99]
Tourmaline	Atrazine herbicide	98% of degradation after 10 min	Wang *et al.*[100]
Zeolite 4A	Paracetamol	90.68% removal efficiency in 60 min	Ikhlaq *et al.*[25]
Kaolinite	*p*-Nitrophenol	89% of degradation after 8 min	Ma *et al.*[101]
Natural and plasma-treated goethite	Sulfasalazine antibiotic	96.05% of degradation in 40 min (plasma-treated goethite using nitrogen)	Pelalak *et al.*[102]
Cerium-loaded zeolite	Penicillin G antibiotic	99.5% of degradation in 15 min	Zhang *et al.*[24]
Sepiolite	Caffeine	96% of degradation in 10 min	Savun-Hekimoğlu *et al.*[103]
Natural zeolite	Landfill leachate	66% COD removal in 120 min	AlGburi *et al.*[104]
Montanit300® zeolite	Orange II dye	91% TOC removal in 240 min	Inchaurrondo *et al.*[105]
Mg/Al hydrotalcite	2,4-Dichlorophenoxyacetic acid herbicide	68% COD removal in 60 min	Tian *et al.*[106]

dyes,[105,109] and surfactants.[110] Some of these works[24,105,108,110] discussed the mechanisms involved in catalytic ozonation and point out that zeolites are responsible for ozone decomposition leading to the production of •OH radicals. As described by Valdés *et al.*,[109] zeolites are known to exhibit both Lewis acidic sites (such as acidic OH groups) and basic sites (such as basic oxygen atoms or alkaline metal clusters) on their surfaces that can effectively convert aqueous ozone into reactive radicals. Valdés *et al.* reported in their works[109,111] that the use of zeolites increased the decomposition rates of ozone, leading to a greater generation of free radicals. In the case of modified zeolites, the ozone decomposition capacity is probably increased by increasing Lewis acid sites. For example, Zhang *et al.*[24] studied the mechanism of catalytic ozonation for the removal of penicillin G using cerium-loaded natural zeolite as the catalyst. They found that •OH and $^{\bullet}O_2^-$ radicals were the dominant reactive oxygen species that belong to the penicillin G degradation mechanism. In summary, the main points addressed by the mechanism proposed by Zhang *et al.*[24] were (1) part of the contaminant could be adsorbed on the porous surface of the catalyst, leading to degradation *in situ* during the process of catalytic ozonation; (2) the cerium dopant can participate in redox reactions triggering radical reactions, producing •OH radicals; and (3) direct ozonation can contribute to the degradation of the drug.

However, some other studies have suggested a non-radical mechanism. Ikhlaq *et al.* proposed in his works[25,112,113] that the catalytic ozonation of organic pollutants using ZSM-5 zeolites (a type of zeolite that contains high silica content) occurred *via* adsorption of pollutant on the surface of zeolites, followed by their reactions with molecular ozone in a four-step cycle, consisting of (1) adsorption, (2) surface reaction, (3) desorption of by-products and (4) surface regeneration. Therefore, it is important to investigate the mechanism of different types of zeolites.

Another mineral used as a catalyst for ozonation is ceramic honeycomb, mainly investigated by Zhao and collaborators,[91,114–117] who are among the main research groups that applied O_3/ceramic honeycomb and O_3/modified ceramic honeycomb processes for the degradation of organic contaminants, with emphasis mainly on the removal of nitrobenzene, a compound commonly used in industrial processes, including the production of pesticides, dyes and explosives. The results presented from these studies showed that the presence of ceramic honeycombs significantly increased the ozonation degradation rate of nitrobenzene compared to ozonation alone. Zhao *et al.*[114] found that the nitrobenzene removal increased from 45% to 69.5% in the presence of ceramic honeycombs and led to 49.6% of total organic carbon (TOC) removal compared to 31.7% in ozonation alone. The process was found to proceed *via* a radical-type mechanism, and ceramic honeycomb was responsible for accelerating the ability to generate •OH radicals, initiated by the surface of the catalyst. In addition, the modification of ceramic honeycomb with Mn, Cu and K ions increased the catalytic ozonation of nitrobenzene, resulting from a significant increase in its surface area and the ability to initiate the generation of •OH radicals.[115]

The same group[91] also demonstrated that the degradation of nitrobenzene is accelerated in the presence of Mn–ceramic honeycomb as the catalysts, and mechanistic studies indicated that the loading of Mn caused an increase of pH at the point of zero charge (pH_{pzc}) and that the enhancement of the density of surface hydroxyl groups, which were responsible for accelerating the decomposition of ozone leading to the generation of •OH radicals.

Goethite (FeOOH) mineral[90] was also used as the catalyst in the ozonation of nitrobenzene. With this catalyst, 65% removal of nitrobenzene was obtained in 20 min of reaction (see Table 3.4). The removal increment was about two times higher than in ozonation alone and was due to the generation of more •OH radicals from the decomposition of the ozone induced by the uncharged surface hydroxyl groups of FeOOH. Another mineral catalyst, red mud, which is an abundant waste product from the aluminum industry, was also studied by Qi *et al.*[95] for degradation of nitrobenzene, reaching 67.17% removal of the contaminant in 20 min under conditions considered ideal. The authors performed experiments on inhibiting •OH radicals, and it was proven that these radicals participate in red mud catalytic ozonation.

Many other catalysts have shown excellent performance in catalytic ozonation (see Table 3.4 and Figure 3.3); however, they are still little explored. Recently, Savun-Hekimoğlu *et al.*[103] tested low-cost natural clay mineral sepiolite for the degradation and mineralization of caffeine by catalytic ozonation. The catalytic ozonation with sepiolite provided 96% of caffeine removal and 30% mineralization during 10 min and 60 min reaction, respectively, while 72% degradation and 18% mineralization were obtained by ozonation alone during equivalent reaction times.

3.5 Concluding Remarks and Future Trend

The combination of catalysts and ozonation aims to solve the problems found in ozonation alone, mainly to increase the degradation of organic pollutants in water and to reduce the generation of toxic by-products by increasing mineralization. These processes also stand out for normally requiring a lower dose of ozone and a shorter reaction time when compared to ozonation alone. The application of composite materials for this purpose has been highlighted due to interesting physical and chemical properties that present high performance in ozone decomposition.

This chapter summarized the different research endeavors dedicated to the use of composite materials with an emphasis on perovskite and spinel oxides for application in catalytic ozonation to remove organic contaminants in water and wastewater. We focused mainly on showing all the applications of these materials for catalytic ozonation, as well as discussing the mechanisms involved.

For a better understanding, we divided this section into three blocks:

3.5.1 Perovskite Oxides

For application in catalytic ozonation, perovskite with lanthanide as a metal in position A stands out. In all these studies, using La-containing perovskites, mainly of the type $LaTi_{0.15}Cu_{0.85}O_3$, showed that they were effective for the removal of different contaminants in water. Benzotriazole, pyruvic acid and oxalic acid have been the most studied contaminants, but there is also an application for the removal of drugs (diclofenac, sulfamethoxazole and norfloxacin), phenols and gallic acid.

3.5.2 Spinel Oxide

Some types of spinel oxides have demonstrated great applicability in catalytic ozonation, due to their low cost, high reactivity and low toxicity. Among them, Fe-based catalysts are the most often employed since these catalysts present the additional advantages of easy removal from the reaction medium and recovery provided by their magnetic properties. Mechanistic studies have demonstrated a mechanism based on radicals, including the interaction of ozone with surface hydroxyl groups and surface metal ions. We could see that the doping of spinel ferrites increased catalytic activity. Some researchers have also demonstrated the use of aluminate spinel oxides in catalytic ozonation with excellent efficiency due to their superlative textural properties and high density of active sites (hydroxyl groups and Lewis acidity).[83]

3.5.3 Natural Minerals

As presented in this chapter (Section 3.4), several natural minerals are explored in catalytic ozonation, due to their low cost and ready availability with emphasis on zeolites and ceramic honeycomb. Zeolites have the advantages of high surface area, well-developed pores and perfect reusability,[24] which makes them promising for application in catalytic ozonation. As discussed in this chapter, there are contradictions regarding the catalytic mechanism. Some studies reported that zeolites are responsible for the decomposition of aqueous ozone leading to the generation of $^{\bullet}OH$ radicals, while other studies have shown a non-radical mechanism. Other minerals (Table 3.4 and Figure 3.3) are also applied for catalytic ozonation; however, there are not many studies in the literature with these catalysts.

Some important points related to future trends can be summarized.

In general, a significant number of studies are found in the literature for the catalysts presented here. These studies are on a laboratory scale, and various parameters inherent to the processes were investigated, such as catalyst concentration, ozone dose, pH, catalyst reuse potential. However, few studies have evaluated the effect of the water matrix, taking the work to a more realistic scenario. Nevertheless, more catalytic ozonation studies are required to treat real effluents, such as secondary effluent from wastewater treatment plants, industrial effluents like distilleries, pulp and paper,

petrochemicals. Another point of paramount importance that has been little explored in the works found in the literature is the application of experimental design to evaluate the various parameters involved in the process of catalytic ozonation.

Future studies should be focused on the identification of intermediates and the assessment of the toxicity of by-products, since the generation of toxic by-products causes inefficiency in the process, especially when the reduction in TOC is low, as seen in most studies presented here. It is also extremely important to evaluate the cost:benefit ratio of catalytic ozonation since the high efficiency and low cost make the process attractive for the remediation of wastewater.

Recently, research is focused on the development of new nanocomposites containing spinel or perovskite oxides combined with other materials, such as carbon materials, zeolites and clay minerals. As reported in Table 3.1, Zhang *et al.*[27] studied catalytic ozonation of benzotriazole using the coupling of graphitic carbon nitride (g-C_3N_4) and perovskite oxide ($LaCoO_3$). As another example, in the work carried out by Liu *et al.*,[74] the researchers evaluated the mineralization of quinoline and biologically treated coking wastewater using spinel ferrite $CuFe_2O_4$ loaded on natural sepiolite.

The use of composite materials for application in catalytic ozonation, given their potential, should attract more attention in research and become promising materials for the treatment of wastewater.

Acknowledgements

The authors thank the financial support of the Fundação de Amparo à Pesquisa do Estado de São Paulo FAPESP [2019/26210-8; 2014/17774-1], project CAPES/COFECUB [88881.191742/2018-00] and Conselho Nacional de Desenvolvimento Científico e Tecnológico CNPq [308914/2017-1].

References

1. W. Ding, W. Jin, S. Cao, X. Zhou, C. Wang, Q. Jiang, H. Huang, R. Tu, S.-F. Han and Q. Wang, *Water Res.*, 2019, **160**, 339.
2. U. V. Gunten, *Water Res.*, 2003, **37**, 1469.
3. J. A. Malvestiti, A. Cruz-Alcalde, N. López-Vinent, R. F. Dantas and C. Sans, *Appl. Catal., B*, 2019, **259**, 118104.
4. J. Gomes, R. Costa, R. M. Quinta-Ferreira and R. C. Martins, *Sci. Total Environ.*, 2017, **586**, 265.
5. H. M. Jalali, *Phys. Chem. Res*, 2017, **5**, 1.
6. M. Sillanpää, M. C. Ncibi and A. Matilainen, *J. Environ. Manage.*, 2018, **208**, 56.
7. L. Rizzo, S. Malato, D. Antakyali, V. G. Beretsou, M. B. Đolić, W. Gernjak, E. Heath, I. Ivancev-Tumbas, P. Karaolia, A. R. L. Ribeiro, G. Mascolo, C. S. McArdell, H. Schaar, A. M. T. Silva and D. Fatta-Kassinos, *Sci. Total Environ.*, 2019, **655**, 986.

8. B. A. Wols and C. H. M. Hofman-Caris, *Water Res.*, 2012, **46**, 2815.
9. D. B. Miklos, C. Remy, M. Jekel, K. G. Linden, J. E. Drewes and U. Hübner, *Water Res.*, 2018, **139**, 118.
10. J. Wang and H. Chen, *Sci. Total Environ.*, 2020, **704**, 135249.
11. M. Carbajo, F. J. Beltrán, F. Medina, O. Gimeno and F. J. Rivas, *Appl. Catal. B*, 2006, **67**, 177.
12. B. Kasprzyk-Hordern, M. Ziółek and J. Nawrocki, *Appl. Catal. B*, 2003, **46**, 639.
13. J. Nawrocki and B. Kasprzyk-Hordern, *Appl. Catal. B*, 2010, **99**, 27.
14. M. Carbajo, F. J. Rivas, F. J. Beltrán, P. Alvarez and F. Medina, *Ozone: Sci. Eng.*, 2006, **28**, 229.
15. C. V. Rekhate and J. K. Srivastava, *CEJ Adv.*, 2020, **3**, 100031.
16. D. Shahidi, R. Roy and A. Azzouz, *Appl. Catal., B*, 2015, **174–175**, 277.
17. G. Boczkaj and A. Fernandes, *Chem. Eng. J.*, 2017, **320**, 608.
18. N. Pal, *Adv. Colloid Interface Sci.*, 2020, **280**, 102156.
19. J. Xu, Y. Li, M. Qian, J. Pan, J. Ding and B. Guan, *Appl. Catal., B*, 2019, **256**, 117797.
20. C. Fei, D. Li, X. Mao, Y. Guo and W. Jing, *J. Chem. Eng.*, 2018, **26**, 1862.
21. Y. Chen, C.-M. Chen, B. A. Yoza, Q. X. Li, S.-H. Guo, P. Wang, S.-J. Dong and Q.-H. Wang, *Pet. Sci.*, 2017, **14**, 605.
22. J. Wu, Q. Sun and J. Lu, *J. Environ. Chem. Eng.*, 2020, **8**, 104318.
23. J. Kim, E. E. Kwon, J. E. Lee, S.-H. Jang, J.-K. Jeon, J. Song and Y.-K. Park, *J. Hazard. Mater.*, 2021, **403**, 123934.
24. J. Zhang, Z. Xiong, J. Wei, Y. Song, Y. Ren, D. Xu and B. Lai, *Chem. Eng. J.*, 2020, **383**, 123144.
25. A. Ikhlaq, S. Waheed, K. S. Joya and M. Kazmi, *Catal. Commun.*, 2018, **112**, 15.
26. J. Yin, G. Liao, J. Zhou, C. Huang, Y. Ling, P. Lu and L. Li, *Sep. Purif. Technol.*, 2016, **168**, 134.
27. Y. Zhang, Q. Li, Y. Long, J. Zou, Z. Song, C. Liu, L. Liu, F. Qi, B. Xu and Z. Chen, *Appl. Catal., B*, 2019, **254**, 569.
28. S. Hou, S. Jia, J. Jia, Z. He, G. Li, Q. Zuo and H. Zhuang, *J. Environ. Manage.*, 2020, **267**, 110615.
29. C. Li, F. Jiang, D. Sun and B. Qiu, *Chem. Eng. J.*, 2017, **325**, 624.
30. S. A. Hosseini and M. C. Alvarez-Galvan, *J. Taiwan Inst. Chem. Eng.*, 2016, **61**, 261.
31. J. Zhu and A. Thomas, *Appl. Catal. B*, 2009, **92**, 225.
32. M. P. Harikrishnan, A. J. C. Mary and A. C. Bose, *Electrochim. Acta*, 2020, **362**, 137095.
33. Q. Rong, Y. M. Zhang, J. C. Hu, H. P. Wang, Z. Q. Zhu, J. Zhang and Q. Liu, *Mater. Res. Bull.*, 2020, **132**, 111006.
34. H. Li and Z. Lü, *Electrochim. Acta*, 2020, **361**, 137054.
35. P. Rajasekaran, Y. Kumaki, M. Arivanandhan, M. M. S. I. Khaleeullah, R. Jayavel, H. Nakatsugawa, Y. Hayakawa and M. Shimomura, *Physica B Condens. Matter.*, 2020, **597**, 412387.

36. M. De Bastiani, A. S. Subbiah, E. Aydin, F. H. Isikgor, T. G. Allen and S. De Wolf, *Mater. Horiz.*, 2020, **7**, 2791.
37. C. B. Njoku, B. P. Doyle, E. Carleschi and R. J. Kriek, *Electroanalysis*, 2020, **32**, 1.
38. H. Chen, J. Motuzas, W. Martens and J. C. D. da Costa, *Appl. Catal., B*, 2018, **221**, 691.
39. L. E. Verduzco, R. Garcia-Díaz, A. I. Martinez, R. A. Salgado, F. Méndez-Arriaga, S. A. Lozano-Morales, M. Avendaño-Alejo and K. P. Padmasree, *Dyes Pigm.*, 2020, **183**, 108743.
40. M. L. Rojas-Cervantes and E. Castillejos, *Catalysts*, 2019, **9**, 230.
41. A. Kumar, B. Prasad and K. K. Garg, *Process. Saf. Environ.*, 2021, **147**, 162.
42. J. Zhu, H. Li, L. Zhong, P. Xiao, X. Xu, X. Yang, Z. Zhao and J. Li, *ACS Catal.*, 2014, **4**, 2917.
43. C. A. Orge, J. J. M. Órfão, M. F. R. Pereira, B. P. Barbero and L. E. Cadús, *Appl. Catal., B*, 2013, **140–141**, 426.
44. J. Miao, X. Duan, J. Li, J. Dai, B. Liu, S. Wang, W. Zhou and Z. Shao, *Chem. Eng. J.*, 2019, **355**, 721.
45. S. Royer, D. Duprez, F. Can, X. Courtois, C. Batiot-Dupeyrat, S. Laassiri and H. Alamdari, *Chem. Rev.*, 2014, **114**, 10292.
46. Y. Wang, Z. Chi, C. Chen, C. Su, D. Liu, Y. Liu, X. Duan and S. Wang, *Appl. Catal., B*, 2020, **272**, 118972.
47. F. J. Rivas, M. Carbajo, F. J. Beltrán, B. Acedo and O. Gimeno, *Appl. Catal., B*, 2006, **62**, 93.
48. M. Carbajo, F. J. Beltrán, O. Gimeno, B. Acedo and F. J. Rivas, *Appl. Catal., B*, 2007, **74**, 203.
49. F. J. Rivas, M. Carbajo, F. J. Beltrán, O. Gimeno and J. Frades, *J. Hazard. Mater.*, 2008, **155**, 407.
50. F. J. Beltrán, P. Pocostales, P. M. Álvarez and F. López-Piñeiro, *Appl. Catal., B*, 2009, **92**, 262.
51. F. J. Beltrán, P. Pocostales, P. Alvarez, J. F. García-Araya and O. Gimeno, *Ozone Sci. Eng.*, 2010, **32**, 230.
52. S. Afzal, X. Quan and J. Zhang, *Appl. Catal., B*, 2017, **206**, 692.
53. Y. Zhang, Y. Xia, Q. Li, F. Qi, B. Xu and Z. Chen, *Sep. Purif. Technol.*, 2018, **197**, 261.
54. Y. Zhang, Y. An, C. Liu, Y. Wang, Z. Song, Y. Li, W. Meng, F. Qi, B. Xu, J.-P. Croue, D. Yuan and A. Ikhlaq, *Water Res.*, 2019, **166**, 115026.
55. Y. Wang, L. Chen, H. Cao, Z. Chi, C. Chen, X. Duan, Y. Xie, F. Qi, W. Song, J. Liu and S. Wang, *Appl. Catal., B*, 2019, **245**, 546.
56. N. A. Masmali, Z. Osman and A. K. Arof, *Ceram. Int.*, 2021, **47**, 2949.
57. M. A. Rafiq, A. Javed, M. N. Rasul, M. Nadeem, F. Iqbal and A. Hussain, *Mater. Chem. Phys.*, 2021, **257**, 123794.
58. V. S. Kirankumar and S. Sumathi, *Mater. Today Chem.*, 2020, **18**, 100355.
59. Y. Ren, Q. Dong, J. Feng, J. Ma, Q. Wen and M. Zhang, *J. Colloid Interface Sci.*, 2012, **382**, 90.

60. H. Zhao, Y. Dong, G. Wang, P. Jiang, J. Zhang, L. Wu and K. Li, *Chem. Eng. J.*, 2013, **219**, 295.
61. F. Qi, W. Chu and B. Xu, *Chem. Eng. J.*, 2015, **262**, 552.
62. F. Qi, B. Xu and W. Chu, *J. Mol. Catal. A: Chem.*, 2015, **396**, 164.
63. F. Zhang, C. Wei, Y. Hu and H. Wu, *Sep. Purif. Technol.*, 2015, **156**, 625.
64. F. Qi, W. Chu and B. Xu, *Chem. Eng. J.*, 2016, **284**, 28.
65. J. Lu, X. Wei, Y. Chang, S. Tian and Y. Xiong, *J. Chem. Technol. Biotechnol.*, 2016, **91**, 985.
66. W. Zhao, S. Zhang, J. Ding, Z. Deng, L. Guo and Q. Zhong, *J. Mol. Catal. A: Chem.*, 2016, **424**, 153.
67. F. Zhang, C. Wei, K. Wu, H. Zhou, Y. Hu and S. Preis, *Appl. Catal., A*, 2017, **547**, 60.
68. P. Liu, Y. Ren, W. Ma, J. Ma and Y. Du, *Chem. Eng. J.*, 2018, **345**, 98.
69. H. Zhang, F. Ji, Y. Zhang, Z. Pan and B. Lai, *Sep. Purif. Technol.*, 2018, **193**, 368.
70. C. Cai, X. Duan, X. Xie, S. Kang, C. Liao, J. Dong, Y. Liu, S. Xiang and D. D. Dionysiou, *J. Hazard. Mater.*, 2021, **410**, 124604.
71. Y. Ren, Y. Chen, T. Zeng, J. Feng, J. Ma and W. A. Mitch, *Chem. Eng. J.*, 2016, **283**, 662.
72. Y. Ren, H. Zhang, H. An, Y. Zhao, J. Feng, L. Xue, T. Luan and Z. Fan, *J. Colloid Interface Sci.*, 2018, **526**, 347.
73. Z. Wang, H. Ma, C. Zhang, J. Feng, S. Pu, Y. Ren and Y. Wang, *Chem. Eng. J.*, 2018, **354**, 42.
74. D. Liu, C. Wang, Y. Song, Y. Wei, L. He, B. Lan, X. He and J. Wang, *Chemosphere*, 2019, **227**, 647.
75. Y. Zhao, H. An, G. Dong, J. Feng, Y. Ren and T. Wei, *Appl. Surf. Sci.*, 2020, **505**, 144476.
76. J. Zhao, J. Cao, Y. Zhao, T. Zhang, D. Zheng and C. Li, *J. Environ. Sci.*, 2020, **97**, 75.
77. P. M. Álvarez, F. J. Beltrán, J. P. Pocostales and F. J. Masa, *Appl. Catal., B*, 2007, **72**, 322.
78. S. S. Sable, F. Medina and S. Contreras, *Appl. Catal., B*, 2014, **150–151**, 30.
79. H. Zhao, Y. Dong, P. Jiang, G. Wang, J. Zhang and C. Zhang, *Chem. Eng. J.*, 2015, **260**, 623.
80. S. S. Sable, P. P. Ghute, D. Fakhrnasova, R. B. Mane, C. V. Rode, F. Medina and S. Contreras, *Appl. Catal., B*, 2017, **209**, 523.
81. S. Zhu, B. Dong, Y. Yu, L. Bu, J. Deng and S. Zhou, *Chem. Eng. J.*, 2017, **328**, 527.
82. Q. Dai, Z. Zhang, T. Zhan, Z. -T. Hu and J. Chen, *ACS Omega*, 2018, **3**, 6506.
83. Y. Xu, Z. Lin, Y. Zheng, J. -P. Dacquin, S. Royer and H. Zhang, *Sci. Total Environ.*, 2019, **651**, 2585.
84. R. Xu, H. Nabet, A. Breton, P. Baldoni-Andrey, N. Lesage, T. Cacciaguerra, V. Hulea, F. Fajula and A. Galarneau, *Pet. Chem.*, 2020, **60**, 858.

85. H. Chen and J. Wang, *Chemosphere*, 2021, **268**, 128840.
86. Y. Dong, K. He, B. Zhao, Y. Yin, L. Yin and A. Zhang, *Catal. Commun.*, 2007, **8**, 1599.
87. Y. Dong, K. He, L. Yin and A. Zhang, *Catal. Lett.*, 2007, **119**, 222.
88. Y. Dong, H. Yang, K. He, X. Wu and A. Zhang, *Appl. Catal., B*, 2008, **82**, 163.
89. K. He, Y. M. Dong, Z. Li, L. Yin, A. M. Zhang and Y. C. Zheng, *J. Hazard. Mater.*, 2008, **159**, 587.
90. T. Zhang and J. Ma, *J. Mol. Catal. A: Chem.*, 2008, **279**, 82.
91. L. Zhao, J. Ma, Z.-Z. Sun and X.-D. Zhai, *Appl. Catal., B*, 2008, **83**, 256.
92. L. Zhao, Z. Sun, J. Ma and H. Liu, *Environ. Sci. Technol.*, 2009, **43**, 2047.
93. F. Qi, B. Xu, Z. Chen, J. Ma, D. Sun, L. Zhang and F. Wu, *J. Hazard. Mater.*, 2009, **168**, 246.
94. G. Moussavi, R. Khosravi and N. R. Omran, *Appl. Catal. A Gen.*, 2012, **445–446**, 42.
95. F. Qi, H. Li, B. Xu and D. Sun, *J. Nanosci. Nanotechnol.*, 2014, **14**, 6984.
96. D. Shahidi, A. Moheb, R. Abbas, S. Larouk, R. Roy and A. Azzouz, *J. Hazard. Mater.*, 2015, **298**, 338.
97. B. Xu, F. Qi, J. Zhang, H. Li, D. Sun, D. Robert and Z. Chen, *Chem. Eng. J.*, 2016, **284**, 942.
98. T. Shen, Q. Wang and S. Tong, *Ind. Eng. Chem. Res.*, 2017, **56**, 10965.
99. J. Peng, J. Yan, Q. Chen, X. Jiang, G. Yao and B. Lai, *Chemosphere*, 2018, **210**, 831.
100. D. Wang, H. Xu, J. Ma, X. Lu, J. Qi and S. Song, *Chem. Eng. J.*, 2018, **354**, 113.
101. W. Ma, J. Hu, B. A. Yoza, Q. Wang, X. Zhang, Q. X. Li, S. Guo and C. Chen, *Appl. Clay Sci.*, 2019, **175**, 159.
102. R. Pelalak, R. Alizadeh and E. Ghareshabani, *J. Hazard. Mater.*, 2020, **392**, 122269.
103. B. Savun-Hekimoğlu, Z. Eren and N. H. Ince, *Environ. Prog. Sustainable Energy*, 2021, **40**, e13552.
104. H. R. AlGburi, H. A. Aziz, H. M. Zwain and A. F. M. Noor, *Environ. Eng. Sci.*, 2021, **38**(7), 635.
105. N. Inchaurrondo, C. di Luca, G. Žerjav, J. M. Grau, A. Pintar and P. Haure, *Catal. Today*, 2021, **361**, 24.
106. X. Tian, J. Zhu, M. Tang, D. Wang, Y. Nie, L. Yang, C. Dai, C. Yang and L. Lu, *J. Hazard. Mater.*, 2021, **402**, 123475.
107. P. Fu, X. Lin, L. Wang and Y. Ma, *Appl. Clay Sci.*, 2020, **198**, 105834.
108. C. Chen, X. Yan, B. A. Yoza, T. Zhou, Y. Li, Y. Zhan, Q. Wang and Q. X. Li, *Sci. Total Environ.*, 2018, **612**, 1424.
109. H. Valdés, R. F. Tardón and C. A. Zaror, *Chem. Eng. J.*, 2012, **211–212**, 388.
110. J. Rivera-Utrilla, M. Sánchez-Polo, M. I. Bautista-Toledo and J. D. Méndez-Díaz, *Chem. Eng. J.*, 2012, **180**, 204.

111. H. Valdés, V. J. Farfána, J. A. Manoli and C. A. Zaror, *J. Hazard. Mater.*, 2009, **165**, 915.
112. A. Ikhlaq, D. R. Brown and B. Kasprzyk-Hordern, *Appl. Catal., B*, 2013, **129**, 437.
113. A. Ikhlaq and B. Kasprzyk-Hordern, *Appl. Catal., B*, 2017, **200**, 274.
114. L. Zhao, J. Ma and Z.-Z. Sun, *Appl. Catal. B*, 2008, **79**, 244.
115. L. Zhao, J. Ma, Z.-Z. Sun and X.-D. Zhai, *J. Hazard. Mater.*, 2009, **161**, 988.
116. L. Zhao, J. Ma, Z.-Z. Sun and H. Liu, *Appl. Catal., B*, 2009, **89**, 326.
117. L. Zhao, W. Ma, S. Lu and J. Ma, *Sep. Purif. Technol.*, 2019, **210**, 167.

CHAPTER 4

Catalytic Ozonation over Activated Carbon-based Materials

ZHENG-QIAN LIU,* JIA-YING LI AND SHU-TING LI

School of Environmental Science and Engineering, Huazhong University of Science and Technology, Wuhan 430074, P.R. China
*Emails: zhengqianliu@126.com; zhengqianliu@hust.edu.cn

4.1 Activated Carbon

Ozonation is widely used in drinking water and wastewater treatment, however, it has the disadvantages of selectivity oxidation and oxidation efficiency easily affected by the water matrix (*e.g.* carbonate).[1] Therefore, various heterogeneous catalysts[2,3] have been developed to overcome these disadvantages of ozonation alone,[4] and some catalysts have been used in full-scale applications.[5,6] Among these heterogeneous catalysts, activated carbon (AC) has not only a large specific surface area but also good stability in acidic and basic media, which has received extensive attention in the past two decades.[7–10] To the best of our knowledge, AC was used as the catalyst to treat contaminated groundwater during the earliest full-scale application of heterogeneous catalytic ozonation in 1992.[6]

4.1.1 Adsorption or Catalysis During Ozonation with AC?

As Nawrocki said, only when the effect of ozonation with a catalyst to remove the target organic compound exceeds the combined effect of ozonation alone

Chemistry in the Environment Series No. 8
Advanced Ozonation Processes for Water and Wastewater Treatment: Active Catalysts and Combined Technologies
Edited by Hongbin Cao, Yongbing Xie, Yuxian Wang and Jiadong Xiao

Published by the Royal Society of Chemistry, www.rsc.org

and adsorption of the catalyst under the same experimental conditions can we discuss the catalytic role of the catalyst during ozonation.[11] As far as AC is concerned, Asgari *et al.* observed that the degradation efficiency of pentachlorophenol for AC catalytic ozonation is slightly higher than that of the combination of ozonation alone and AC adsorption.[12] Vatankhah *et al.* found in the AC catalytic ozonation of secondary municipal wastewater effluent for the removal of micropollutants, additional degradation effect could be only obtained for meprobamate, sucralose and tris(2-chloroethyl) phosphate among the investigated 13 micropollutants compared to the superposition effect of ozonation alone and AC adsorption.[9] However, not every researcher is as lucky as Asgari *et al.*[12] or Vatankhah *et al.*[9] since AC usually has good adsorption performance for many organic pollutants. Hadavifar *et al.* found that the performance on chemical oxygen demand (COD) or color removal for AC catalytic ozonation is even lower than the superposition effect of ozonation alone and AC adsorption for initial pH from 2 to 10, and this is due to the excellent adsorption performance on alcohol distillery wastewater of AC.[13] Therefore, it often encounters the dilemma that the effect of AC catalytic ozonation is not as good as the superposition effect of ozonation alone and AC adsorption (see Figure 4.1). In this case, it is easy to cause controversy because some researchers believe that there is a catalytic effect, while others think that there is none. A simple method is to replace a target pollutant that AC cannot easily adsorb, such as oxalic acid.[14] However, this method is only suitable for activity testing during the development of catalysts in the laboratory. When you need to test the feasibility of the catalytic ozonation for treating actual wastewater (Figure 4.1), this method is no longer applicable.

A good method is to simultaneously conduct ozonation alone, AC adsorption and AC catalytic ozonation experiments in continuous mode. According to the results obtained during the treatment of a food processing secondary effluent, although the total organic carbon (TOC) removal by AC catalytic ozonation is less than the combined effect of ozonation alone and AC adsorption at the beginning of the reaction, after 180 min of continuous operation, the TOC removal by AC adsorption suddenly dropped to close to zero due to the saturation of the AC adsorption. In this case, the catalytic activity of AC could be confirmed since the TOC removal by AC catalytic ozonation and ozonation alone was still about 36% and 20%, respectively.[16] It should be noted that this experiment cannot fully prove the catalytic activity of AC because it ignores the difference between the adsorption of intermediates and the adsorption of raw wastewater on the AC surface. In addition, most of the laboratory researches are in batch or semi-batch mode, so other methods are needed to solve this problem.

4.1.1.1 Adsorption of Target Organic Compound on the AC Surface

In order to distinguish whether the better TOC removal is only due to the superposition of AC adsorption and ozonation alone or not, we have tried to

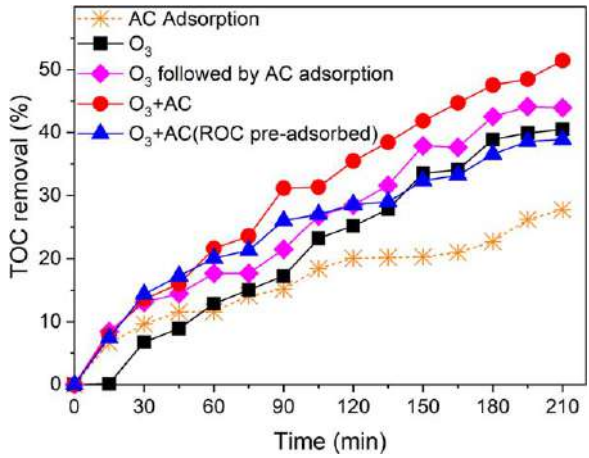

Figure 4.1 TOC removal by O_3, AC adsorption, O_3 followed by AC adsorption and ozonation in the presence of AC with or without CG-ROC adsorbed. (Experimental conditions: ozone gas concentration: 20 mg min^{-1}; AC dose: 1.5 g L^{-1}; initial pH: 9; temperature: 20 °C.) (Note: For the experiment of O_3 followed by AC adsorption, O_3 was conducted first through continuous bubbling ozone into a 1.0 L CG-ROC solution, and then 15 mL of the solution was taken out during different reaction times, and 5 mL of the solution was diluted to determine the TOC after O_3. The remaining ozone in the 10 mL residual solution is removed by nitrogen purge first, and the subsequent adsorption experiment was carried out by the addition of 15 mg of AC to the solution for the same time as adopted for O_3, and then the AC was removed by filtration before the TOC measurement, and the obtained TOC is the result of the combined effect of O_3 and subsequent AC adsorption. For the experiment of AC with CG-ROC pre-adsorbed, 1.5 g AC was dosed into a 1.0 L CG-ROC solution (TOC: 113.8 mg L^{-1}) with an initial pH 9 for 210 min 20 °C, and then the obtaining AC with pre-adsorbed CG-ROC was used for ozonation of CG-ROC [TOC: 113.8 mg L^{-1}].) Reproduced from ref. 15 with permission from Elsevier, Copyright 2020.

perform the adsorption pretreatment of AC in reverse osmosis concentrate (ROC) first (its adsorption time is the same as that of catalytic ozonation) and then AC with ROC pre-adsorbed was separated through filtration after adsorption, and subsequently this AC was used as a catalyst directly for an experiment of ozonation of ROC.[15] As shown in Figure 4.1, AC with ROC pre-adsorbed or not has a similar activity on TOC removal during ozonation of ROC within the first 75 min. As the reaction time was prolonged, the TOC removal during ozonation in the presence of AC with ROC pre-adsorbed is gradually lower than that without ROC pre-adsorbed. This is because the pre-adsorbed organic matter begins to desorb from its surface with the organic matter removal of the ROC in solution.[15]

Moussavi *et al.*[17] first separated the AC after reaction, dried it, then eluted the amoxicillin adsorbed on the AC surface using a mixture of acetonitrile and phosphate buffer solution, and subsequently measured the amoxicillin

concentration in the eluate to determine the contribution of adsorption to its removal. The results show that whether it is the original or NH_4Cl-treated AC, the contribution on amoxicillin removal by the adsorption is less than 17% compared to that by catalysis.

4.1.1.2 Adsorption of Intermediates on the AC Surface

As mentioned, when the removal of TOC or COD instead of the target pollutant is used as an indicator of catalytic ozonation activity, the removal of intermediates by adsorption on the AC surface needs to be considered.[11] This is because the catalytic activity on TOC or COD removal may only be an illusion caused by the adsorption of intermediates on the AC surface.

In order to clarify this point, Beltrán *et al.* used the maximum concentration of the intermediates during ozonation alone as the initial concentration to investigate the adsorption performance of AC on intermediates[18] and then used these results to estimate the contribution of adsorption during ozonation of polyphenol compounds with AC.[18,19]

Chen *et al.* found that the catalytic activity upon COD removal during the ozonation of heavy oil refinery wastewater in the presence of MnO_x supported on AC is less than that of AC. This may be due to the better adsorption performance of AC for wastewater. However, the catalytic activity of MnO_x/AC is higher than that of AC from the second use, and as the number of repeated uses increases, the difference between the COD removed in the process of ozonation with MnOx/AC and the process of ozonation with AC will become larger and larger, until the final difference is constant. The authors believe that this is the catalytic activity of the supported MnO_x since the adsorption of catalyst on COD removal will decrease with the increasing of the number of reuses.[20] In the same way, as AC adsorption reaches saturation after repeated use, the difference in COD between AC catalytic ozonation and ozonation alone also reflects the catalytic activity of AC for ozonation of heavy oil refinery wastewater.

As suggested by Nawrocki,[11] we conducted an experiment of ozonation alone followed by AC adsorption during the investigation of ozonation of ROC derived from coal gasification wastewater. We first performed an ozonation-alone experiment and determined the TOCs at different reaction times, then conducted the adsorption experiment after AC addition for the same reaction time without ozone, and measured the corresponding TOC again. The difference between the two measured TOCs indicates the adsorption performance of AC for intermediates (Figure 4.1). Interestingly, unlike AC's efficient adsorption of raw ROC (27.8% TOC removal in 210 min), the adsorption after oxidation by ozonation alone can only increase TOC removal by 3%–4% after 60 min.[15] This may be due to the fact that the hydrophobic components in effluent organic matter (EfOM, the main component of ROC) are progressively transformed into hydrophilic components during ozonation alone,[21] which is unfavorable to the adsorption of AC. A similar phenomenon was also observed in the investigation of the adsorption of intermediates during ozonation of diclofenac with AC.[22]

Please keep in mind that the intermediates of ozonation alone and AC catalytic ozonation will definitely be different, so the adsorption in the process of ozonation alone followed by AC adsorption does not completely represent AC adsorption during catalytic ozonation. However, since the concentrations of intermediates of AC catalytic ozonation are usually lower than that of ozonation alone,[19,23] the contribution of adsorption on TOC or COD removal during the AC catalytic ozonation should not exceed that of AC adsorption in the process of ozonation alone followed by AC adsorption. Soares *et al.* conducted a similar experiment under a continuous operation in a column; that is, the treatment effects of textile effluent and dye solutions by AC catalytic ozonation and ozonation alone, followed by AC adsorption, were compared to determine whether AC has a catalytic effect.[24]

In general, if some of the adsorption experiments on target organic compounds and intermediates just mentioned are investigated reasonably, whether the increase in organic compound removal with the presence of AC is a catalysis or a simple superposition of ozonation alone and AC adsorption could be more clearly understood.

4.1.2 Influence of Chemical Properties, Texture Characteristics and Impurities

As early as 2002, Rivera-Utrilla and Sanchez-Polo's research showed that the surface basicity, macroporous volume and mineral impurities of commercial AC all play a role in the ozonation of 1,3,6-naphthalenetrisulphonic acid.[25] As presented in Figure 4.2, various surface functional groups, including the lactone, carboxyl, carbonyl, phenolic hydroxyl, pyrrole and pyridine groups, are usually presented on the surface of carbon materials.[26] A high basicity of AC usually has a higher catalytic activity in promoting ozone decomposition[30] and pollutant degradation;[16,25,27] therefore, many researchers use various methods to treat AC to increase its surface basicity for promoting its catalytic activity.[17,27–29] Unfortunately, these basic groups (such as pyrrole groups) on the AC surface are expected to be easily exhausted during ozonation, leading to a quick decrease in AC activity.[1,16] However, it was suggested that phenolic hydroxyl on the AC surface could promote ozone decomposition into $^{\bullet}OH$,[30] thus resulting in improvement on pollutant removal.[31] Due to the continuous changes of the surface properties of AC during ozonation, it is generally accepted that AC is not a real catalyst but rather an initiator and/or promoter that accelerates ozone decomposition to generate $^{\bullet}OH$ since 2005.[1,28,30,32]

Carbon materials usually have porous structures and large specific surface areas. Some researchers have suggested that there is no close relationship between the ozone adsorption on the AC surface and the specific surface area of AC, but ozone adsorption may depend on pore diffusion.[28,30] Oxalic acid degradation was found to increase for the AC with a larger specific surface area,[27] while Rivera-Utrilla and Sanchez-Polo found no clear relationship between the degradation rate of 1,3,6-naphthalenetrisulphonic acid

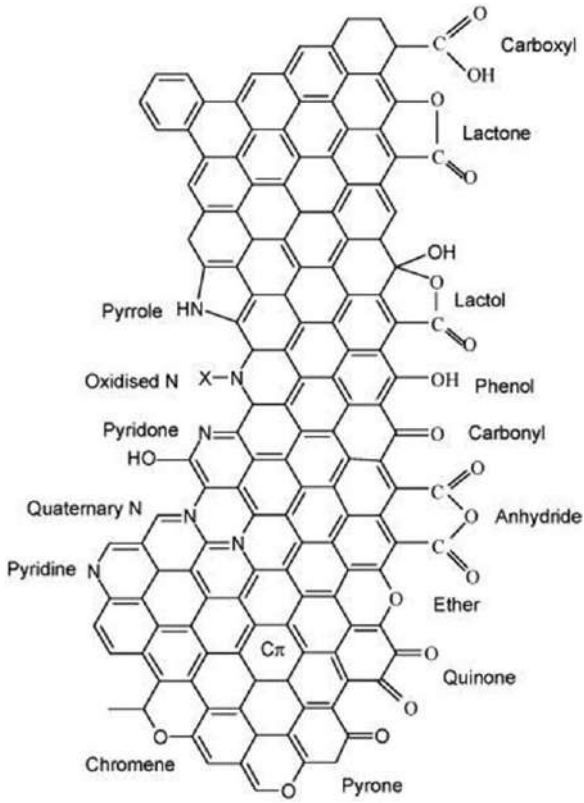

Figure 4.2 Nitrogen and oxygen surface groups on carbon. Reproduced from ref. 26 with permission from Elsevier, Copyright 2009.

and the specific surface area of AC.[25] Certainly, a high macroporosity of AC could reduce the diffusion of ozone and/or pollutant, favor the contact between active sites on the AC surface and ozone and/or pollutant, and then enhance the ozonation of the pollutant.[25]

As far as the mineral impurities in AC are concerned, in contrast to Rivera-Utrilla and Sanchez-Polo's opinion that the mineral impurities in AC promote the ozone decomposition to generate highly reactive oxygen species,[25] Alvárez *et al.* believe that the mineral impurities may promote the decomposition of H_2O_2 on the AC surface instead of promoting ozone decomposition, which certainly would result in a decrease in the amount of H_2O_2 entering the solution.[30] Nawrocki and Fijołek believe that the mineral impurities in AC would dissolve during ozonation, which would affect the pH of the solution, so that the improvement in ozone decomposition may be caused by the increase in the solution pH, not necessarily the initiation or promotion of AC. Therefore, the authors suggested that demineralization treatment for AC should be conducted to avoid its interference when investigating the possible catalytic role of AC in ozonation.[32]

4.1.3 Influence of Water Matrix

4.1.3.1 Chloride and Sulfate

As environmental protection policies are becoming stricter, more and more advanced oxidation processes (AOPs) (such as catalytic ozonation, Fenton) are used for the advanced treatment of wastewater,[33] especially for industrial wastewater.[34] Unlike conventional municipal wastewater, these industrial wastewaters usually contain high concentrations of chloride and sulfate.[34] Chloride has been regarded as a typical $^{\bullet}OH$ scavenger under acidic conditions (eqn (4.1)–(4.3)).[35] It is interesting that the presence of 0.8 mM chloride or sulfate has a negative effect on the phenazone degradation during ozonation alone at pH 7, and the authors speculated that this may be due to the less active $^{\bullet}Cl_2^-$ and $^{\bullet}SO_4^-$ generated from the reactions between these ions and $^{\bullet}OH$.[36] However, based on our results of kinetic model calculations, the total contribution of $^{\bullet}Cl_2^-$, $^{\bullet}SO_4^-$, $^{\bullet}Cl$ and $^{\bullet}ClO$ on the EfOM degradation is less than 0.6% during ozonation of ROC in a basic condition.[15]

$$Cl^- + {}^{\bullet}OH \rightarrow ClOH^{\bullet -} \quad k_1 = 4.3\times10^9\ M^{-1}\,s^{-1} \tag{4.1}$$

$$ClOH^{\bullet -} \rightarrow Cl^- + {}^{\bullet}OH \quad k_2 = 6.1\times10^9\ s^{-1} \tag{4.2}$$

$$ClOH^{\bullet -} + H^+ \rightarrow {}^{\bullet}Cl + H_2O \quad k_3 = 2.1\times10^{10}\ M^{-1}\,s^{-1} \tag{4.3}$$

$$ClOH^{\bullet -} + Cl^- \rightarrow {}^{\bullet}Cl_2^- + OH^- \quad k_4 = 1.0\times10^5\ M^{-1}\,s^{-1} \tag{4.4}$$

$$Cl^- + {}^{\bullet}Cl \rightarrow {}^{\bullet}Cl_2^- \quad k_5 = 6.5\times10^9\ M^{-1}\,s^{-1} \tag{4.5}$$

$$^{\bullet}Cl_2^- \rightarrow Cl^- + {}^{\bullet}Cl \quad k_6 = 1.1\times10^5\ s^{-1} \tag{4.6}$$

As for AC catalytic ozonation, the presence of chloride leads to a decrease in the specific surface area of AC, and perhaps this is the reason why a high chloride concentration reduces the adsorption capacity of AC.[37] The addition of 50 mM chloride was found to have no effect on formic acid removal during AC catalytic ozonation at pH 3.0, and the authors believe that this may be due to this reaction's involving carbon-based radicals that are not easily captured by chloride.[38] As the NaCl concentration was increased from 5 to 50 $g\,L^{-1}$ during the Reactive Blue 194 oxidation, the UV_{254} abatement was changed only slightly by ozonation alone, while it is interesting that the UV_{254} abatement increased significantly during AC catalytic ozonation. The authors believe that this may be caused for two reasons: One is that the increase in NaCl concentration promotes the aggregation of dye, thereby promoting its adsorption on AC; the other is the conversion of $^{\bullet}OH$ into more selective chlorine radicals, and these chlorine radicals have a stronger affinity for pollutants with electron-rich functional groups.[39]

4.1.3.2 Bicarbonate and Carbonate

Bicarbonate and/or carbonate could react with $^{\bullet}OH$ generated by ozone decomposition to form $^{\bullet}CO_3^-$ with lower activity, which is detrimental to the degradation of pollutants.[1] It is reported that the presence of 9.43 mM carbonate has almost no effect on COD removal for the ozonation of the effluent of a pulp and paper mill with or without AC; however, the adverse effect of the presence of carbonate on COD removal may be offset by the promotion caused by the increase of initial pH from 7.3 to 8.5 with the addition of carbonate.[40] Some researchers even found that the degradation efficiency of phenol increased with the increase of carbonate concentration during ozonation of sludge-based biochar, and the authors also believe that the increase in pH caused by the addition of carbonate is one of the reasons.[41] In fact, the change in pH caused by carbonate may have a very significant impact on phenol degradation. It is well-known that the pH of the solution will drop rapidly with prolonged reaction time[41] due to the generation of intermediates (such as small molecular organic acids) during the ozonation of phenol.[1,34] The more carbonate is added, the stronger its buffering effect on the pH of solution will be, and the higher the second rate constant will be of the reaction between ozone and phenol.[1,34] Since the degradation efficiency of pollutants usually increases with the increase of pH during ozonation,[1] the influence of added carbonate on the pH of the solution is necessarily a concern if there is no buffer.

ROC and some industrial wastewater often contain relatively high concentrations of carbonate.[33,34] This may have a significant impact on ozonation alone at high pH because sometimes the ozonation of industrial wastewater may even be conducted at initial pH 11 to achieve a high COD removal.[42] In our previous work, the TOC removal was significantly delayed in the initial reaction stage during the treatment of ROC by ozonation alone at an initial pH 11.[34] According to the pK_a ($pK_{a1} = 6.35$ and $pK_{a2} = 10.33$), the proportion of carbonate in ROC is about 82% at initial pH 11, and the reaction rate of $^{\bullet}OH$ reacting with carbonate to form $^{\bullet}CO_3^-$ is nearly two orders of magnitude higher than that with bicarbonate (eqn (4.7) and (4.8)).[1] This means that, although more $^{\bullet}OH$ are expected to be generated at pH 11 during ozonation alone, they may also be quickly scavenged by the large amount of carbonate present in the ROC to generate $^{\bullet}CO_3^-$ with lower reactivity, and this leads to the slow TOC removal at the beginning of the reaction. Our kinetic calculation results also show that a high concentration of $^{\bullet}CO_3^-$ is generated at the beginning of the reaction.[15]

$$HCO_3^- + {}^{\bullet}OH \rightarrow {}^{\bullet}CO_3^- + H_2O \quad k_7 = 8.5\times10^6\ M^{-1}\,s^{-1} \tag{4.7}$$

$$CO_3^{2-} + {}^{\bullet}OH \rightarrow {}^{\bullet}CO_3^- + OH^- \quad k_8 = 3.9\times10^8\ M^{-1}\,s^{-1} \tag{4.8}$$

However, no remarkable effect on the TOC removal was observed during AC catalytic ozonation at initial pH 11 because it is believed that the reaction between $^{\bullet}OH$ and organic matter mainly occurs on the carbon surface.[43] A slight

reduction in COD and TOC was observed with the addition of 26.9 mM and 9.4 mM bicarbonate and/or carbonate during the treatment of the real landfill leachate[4] and the dye wastewater[44] with AC catalytic ozonation, respectively.

4.1.4 Deactivation and Regeneration of Activated Carbon

4.1.4.1 Deactivation of Activated Carbon

Rivera-Utrilla and Sanchez-Polo suggested that the surface basic groups and mineral impurities of commercial AC play a major role in the ozonation of organic matter.[25] Nawrocki and Fijołek believed that these mineral impurities contained in commercial AC, especially alkaline elements, are easily dissolved during ozonation.[32] Clearly these mineral impurities dissolved in the ozonation can no longer play a catalytic role in subsequent use, and they may show activity on the transformation of ozone into •OH only once. Certainly, these mineral impurities cannot be restored through AC regeneration.

In the absence of pollutant, a relatively high TOC was observed at the initial stage of AC catalytic ozonation in batch mode, especially in the case of a basic AC, and Rivera-Utrilla and Sanchez-Polo believe that this is due to ozone attacking AC to produce soluble organic matter.[25] Our previous study has also shown that the TOC increases with the extension of the reaction time during AC catalytic ozonation without pollutant in semi-batch mode.[14] It is interesting that the oxalic acid concentration increased gradually with the extension of the reaction time during the ozonation of oxalic acid with AC in the presence of *tert*-butanol (*t*BA), and the authors believe that this increase was caused by the oxidative attack of some functional groups on the AC surface by ozone.[29] During the AC catalytic ozonation, the basic groups on its surface continue to decrease, while the acidic groups continue to increase with the extension of the oxidation time.[30] Therefore, it is generally believed that AC is not a real catalyst but an initiator and/or promoter that accelerates ozone decomposition to generate •OH.[1,30,32]

AC with high basicity generally has higher activity in promoting ozone decomposition[30] and organic matter degradation.[25] However, with the continuous increase in the number of reuses, the basic groups on the AC surface gradually decrease, and the acidic groups gradually increase, resulting in a continuous decrease in the rate of ozone decomposition. The rate of AC decomposing ozone is reduced by more than 30% after 200 reuses.[30] After 20 hours of continuous operation, a significant reduction in degradation performance was observed for all investigated micropollutants during AC catalytic ozonation of secondary municipal wastewater effluent, and a fourfold increase in the ratio of O and C on the AC surface was found according to XPS analysis. The authors believe that this is due to the significant increase in acidic groups on the AC surface.[9] In addition, the specific surface area of AC also decreased by about 10% after 20 hours of continuous use.[9] Furthermore, the pretreatment of AC with ozone in the gas phase[28] or nitric acid[29] will cause a significant decrease in its specific surface area.

Certainly, it was found that the slightly acidic AC is more difficult to deactivate than the basic AC.[16] Wei *et al.* also found that the phenol in wastewater can more effectively compete with ozone compared to oxalic acid, thereby reducing the conversion of carbonyl groups on the AC surface being oxidized by ozone to carboxyl groups.[23] However, the gradual acidification of the surface of AC is inevitable during ozonation, resulting in a gradual decrease in its activity, and then it still needs to be regenerated after a period of use.

4.1.4.2 Regeneration of Activated Carbon

Bakht Shokouhi *et al.* found that the color removal efficiency decreases from 94% to 70% after 65 repeated use of AC during the ozonation of Reactive Blue 194, and the specific surface area of multi-used AC is also reduced by about 223 $m^2 g^{-1}$ compared with the raw AC. Subsequently, this multi-used AC was regenerated through ozonation with organic matter for 10 h *in situ*, and then the color removal efficiency can be restored to 88%, but the recovery of the specific surface area of this regenerated AC is not significant.[39] Sanchez-Polo *et al.* found that the specific surface area of AC significantly decreases from 1075 to 632 $m^2 g^{-1}$ after 120 min pretreatment with ozone in gas phase.[28] Cao *et al.* observed that the specific surface area of AC after nitric acid pretreatment dropped drastically from 1128 to 232 $m^2 g^{-1}$, while its specific surface area increased to 1023 $m^2 g^{-1}$ after subsequent amination pretreatment.[29] The authors believe that this is because the nitric acid treatment did not cause the collapse of the micropores, but the generated acidic groups blocked the entrance of the micropores and prevented the inaccessibility of N_2 molecules, which caused a significant underestimation of the specific surface area.[28,29] These acidic groups could be eliminated or changed after subsequent amination pretreatment, and then the specific surface area could be recovered.[29] In addition, Wang *et al.* used the pyrolysis method to regenerate the AC saturated with the effluent of the biological treatment of the dyeing and finishing wastewater and found that this regenerated AC still exhibited a high activity on COD removal during ozonation of the effluent of the biological treatment of the dyeing and finishing wastewater.[45]

The electroperoxone (E-peroxone) process was proposed by Wang's group in 2013, which combines conventional ozonation and *in situ* generation of hydrogen peroxide at the cathode for water and wastewater treatment.[46] They found that the adsorption capacity of powdered AC saturated with rhodamine B could be restored by more than 90% through the regeneration by either ozonation or E-Proxone but that the complete mineralization of desorbed rhodamine B can be achieved only by E-Proxone regeneration.[47] Furthermore, if using an activated carbon fiber (ACF) as the cathode in the E-peroxone process, not only can ACF significantly increase the apparent reaction rate for the nitrobenzene degradation by E-peroxone, but also the surface basic groups of ACF could increase slightly after 100 times of repeated use.[48] However, similarly to AC catalytic ozonation, ACF has a significant decrease in basic groups and a remarkable increase in acidic groups after 100 times of repeated use.[48]

Wang's group also found that the combination of ozonation and the three-dimensional electrochemical process can not only improve TOC removal during the pharmaceutical wastewater treatment but also achieve the *in situ* regeneration of granular AC electrode.[49] Wang *et al.* found that the activity of AC in the catalytic ozonation decreases relatively quickly, that the number of basic groups on the AC surface decreases by more than 50%, and that the number of acidic groups increases by nearly 50% after 20 times of repeated use. However, in the combination of the ozonation and three-dimensional electrochemical process, the activity of AC is relatively stable, and the numbers of surface acidic groups and basic groups are almost unchanged after 50 times of repeated use.[50]

4.2 Activated Carbon-supported Metal Oxides

Ma *et al.* prepared amorphous manganese dioxide supported on the AC surface through the direct redox reaction of $KMnO_4$ and AC, and they used this as the catalyst in the ozonation of nitrobenzene. This was the first article in catalytic ozonation about AC-supported metal oxide.[51] Since then, various AC-supported single-metal oxides (CeO_x, FeO_x, CoO_x, CuO_x, MnO_x, ZnO, TiO_x, MgO) and bimetallic oxides are widely used in catalytic ozonation, especially from the last decade.

4.2.1 Single-metal Oxides

4.2.1.1 Cerium Oxide

Orge *et al.* prepared the cerium oxide–AC composites using the precipitation method and investigated its catalytic activity on the degradation of oxalic acid, oxamic acid and CI Reactive Blue 5 during ozonation.[52] A rod-like CeO_2@AC catalyst was prepared by Feng *et al.* using hydrothermal treatment and calcination, and it has a performance on oxalic acid removal similar to that of cerium oxide–AC composites; however, the TOC is not increased with prolonged reaction time during the ozonation of CeO_2@AC without organic pollutant compared to the increase of TOC during the ozonation of AC or cerium oxide–AC composites. It also has a good stability in ozonation with a trace amount of leached cerium.[53]

However, in most studies, cerium oxide is used as the active component and loaded on AC to prepare a supported catalyst in the last decade (Table 4.1). Gonçalves *et al.* found that the highly dispersed cerium oxide on AC catalyst has a better performance compared to a cerium oxide–AC composite with a similar composition. They also found that different precursors also have different effects on the activity of the prepared catalyst; the catalysts prepared from precursor $Ce(NO_3)_3$ and $(NH_4)_2[Ce(NO_3)_6]$ favor the removal of aniline and oxalic acid, respectively.[54]

Many studies have shown that the reaction mechanism of Ce/AC catalytic ozonation is similar to that of AC, which involves the $^{\bullet}OH$ oxidation on the

Table 4.1 Ozonation of pollutant in the presence of AC supported cerium oxide.

Catalyst	Organic pollutants	Highlights	Ref.
20% CeO_2/AC	Oxalic acid and aniline	Ce^{3+} species on the surface are the active sites for promoting ozone decomposition to formation $^{\bullet}OH$, and then its amount dominates the activity of catalyst during ozonation.	54
0.2%–1% Ce/AC	Pyrene and fluoranthene	Compared to ozonation alone and AC catalytic ozonation, the degradation efficiencies of pyrene and fluoranthene could be significantly improved using 0.3% Ce/AC catalyst.	55
20% CeO_2/AC	Sulfamethoxazole	TOC removal during ozonation with CeO_2/AC is slightly higher than that of CeO_2/CNT (carbon nanotube), which may be due to the higher adsorption capacity of CeO_2/AC.	56
0.5%–2% Ce/AC	*p*-Toluenesulfonic acid	COD removal efficiency is 50.8%, 62.4% and 74.1% for the degradation of *p*-toluenesulfonic acid by ozonation alone, AC and 1% Ce/AC catalytic ozonation, respectively.	59
20% CeO_2/AC	Bezafibrate	TOC removal during ozonation with CeO_2/AC is higher than that of CeO_2/CNT.	57
5% Ce/AC	Oxytetracycline	TOC removal efficiency is 9.1%, 17.5% and 46.0% for the oxytetracycline degradation by ozonation alone, AC and Ce/AC catalytic ozonation, respectively.	60
Ce/AC	*p*-Chlorobenzoic acid, ROC	Ce/AC has a high activity on the ozonation of *p*-chlorobenzoic acid in water and mineralization of organic compounds in ROC derived from a municipal wastewater treatment plant.	58

catalyst surface and in the bulk solution simultaneously. The active sites of catalysis for ozone decomposition are not only from the AC surface but also from the cerium oxide supported on AC.[54–57] Ce^{3+} species on the AC surface are recognized as the active sites for promoting ozone decomposition to form $^{\bullet}OH$, and then the amount of Ce^{3+} species dominates the activity of catalysis during ozonation.[54–56,58] Liu *et al.* suggested that the mineral impurities in the AC are helpful to fluoranthene removal during ozonation with Ce/AC catalyst.[55]

4.2.1.2 Iron Oxide

Iron oxides and supported iron oxides have been widely used in ozonation.[61] The review on iron oxides and supported iron oxides has been systematically reviewed a few years ago,[61] so this section will not be expanded in detail (Table 4.2). Yuan *et al.* found that the solution pH has a significant effect on formate degradation by Fe/AC catalytic ozonation and that the presence of

Table 4.2 Ozonation of pollutant in the presence of AC-supported iron oxide.

Catalyst	Organic pollutants	Highlights	Ref.
0.2%–10% Fe/AC	Omethoate	Omethoate degradation efficiency is 37.6%, 58.0% and 82.4% for ozonation alone, AC and 5% Fe/AC catalytic ozonation, respectively, and only less than 7% of omethoate removal by the adsorption of AC or 5% Fe/AC.	62
5%–35% Fe/AC	Heavy oil refining wastewater	COD removal efficiency during ozonation of Fe/AC is significantly higher than that of AC due to its greater •OH formation.	67
5.6% Fe/AC	Crystal Violet	COD removal efficiency is 41% and 57% for ozonation alone and 5% Fe/AC catalytic ozonation, respectively.	68
15%–30% Fe/AC	Dibutyl phthalate	A highest degradation efficiency was achieved at initial pH 8 during ozonation of dibutyl phthalate with 15% iron loading among all the experimental conditions.	63
Fe_3O_4/PAC	High saline petrochemical wastewater	The order for the degradation of organic compounds is Fe_3O_4/PAC catalytic ozonation > PAC catalytic ozonation > Fe_3O_4 catalytic ozonation > ozonation alone.	64
48.7% γ-Fe_2O_3/PAC	Alizarin Red S	The mineralization of Alizarin Red S is 13%, 25% and 40% for ozonation alone, PAC and Fe_2O_3/PAC catalytic ozonation, respectively.	69
0.11–11.2% Fe_2O_3/AC	Oxalic acid	The oxalic acid removal is 3.2%, 79.6% and 89.2% for ozonation alone, PAC and 1.12% Fe_2O_3/PAC catalytic ozonation, respectively.	65
14% Fe/AC	ROC from coal gasification wastewater	Solution pH, ozone dose and catalyst dose have positive effects on ozonation of ROC with Fe/AC, and high salinity has a negative impact on the TOC removal.	70
0.1% Fe/AC	Formate	The solution pH would change the properties of catalyst surface and speciation of iron oxide and then affect the ozone decomposition to generate reactive oxygenated radicals, which in turn affects the formate degradation.	38
FeO_x/AC	Industrial phenolic wastewater	Reaction rate constant in TOC removal is 0.008, 0.013 and 0.023 min^{-1} for microbubble ozonation alone, AC and FeO_x/AC catalytic microbubble ozonation, respectively.	66

Fe/AC is only effective for the ozonation of formate at pH 3.0, which does not lead to an improvement in either the degradation rate or the extent of ozonation of formate at pH 7.3 and 8.5, indicating that only the protonated iron oxide active sites on the surface can promote ozone decomposition to generate reactive oxygen radicals. The main oxidant produced is •OH at pH

3.0 during Fe/AC catalytic ozonation.[38] In addition, the degradation of formate during Fe/AC catalytic ozonation mainly occurs on the interface between solid and liquid and/or in bulk solution, and the formate adsorption is not necessary for the overall oxidation reactions.[38] Ling *et al.* suggested that the ferrihydrite particles on the surface act as the main active sites for ozone decomposition in order to generate •OH during the ozonation of omethoate with Fe/AC and that the catalytic activity of Fe/AC is obtained mainly at pH 7.0–8.0 due to the nearly neutral surface charge of the Fe/AC.[62] Huang *et al.* believe that the improvement in dibutyl phthalate degradation is likely due to the promoting of ozone decomposition to generate •OH on the Fe/AC surface.[63] The major COD removal mechanisms include the Fe_3O_4/PAC adsorption and the •OH oxidation reactions occurring both on the catalyst surface and in the bulk solution according to the effect of •OH scavenger.[64] Li *et al.* believe that the hydroxyl groups on the Fe_2O_3/AC surface play an important role in the ozonation of oxalic acid and that the oxalic acid removal follows a •OH oxidation reaction mechanism.[65] In addition, after FeO_x/AC catalytic microbubble ozonation of industrial phenolic wastewater for 60 min, the BOD_5/COD increases from 0.31 to 0.76 and the acute biotoxicity is reduced by 79.2%.[66]

4.2.1.3 Other Metal Oxides

As shown in Table 4.3, various metal oxides (CoO_x, CuO, MnO_x, TiO_2, ZnO and MgO) have been used as an active component support AC, and the catalytic activity of these catalysts is investigated during the ozonation of pollutants. The catalytic activity of TiO_2/AC catalysts obtained by different preparation methods also varies significantly. Ferreiro *et al.* found that both the oxidation rate of aniline and the degree of mineralization decrease in the following order: TiO_2/AC prepared by precipitation method > AC > TiO_2/AC prepared by wet impregnation method > TiO_2/AC prepared by hydrothermal method during ozonation.[71]

Faleh *et al.* believe that the oxalic acid removal mainly occurs on the AC surface since both ozone and oxalic acid could be adsorbed and reacted on the surface and that the Co(III) species may be generated by the redox reaction between cobalt and AC and may promote ozone decomposition into •OH.[72]

4.2.2 Bimetallic Oxides

To improve catalytic activity and/or stability, loading of bimetallic and even multi-metallic oxides on some supports was sometimes used.[5,78] Lü *et al.* found that the catalytic activity on TOC removal during ozonation of 2,4-dichlorophenoxyacetic acid in the presence of Fe–Ni/AC (72%) is higher than that of Fe/AC (60%) or Ni/AC (62%).[79] Unfortunately, the other four papers only compared the activity of AC-supported bimetallic catalyst with the AC

Table 4.3 Ozonation of pollutant in the presence of other AC-supported metal oxides.

Catalyst	Organic pollutants	Highlights	Ref.
1%–10% Co/AC	Oxalic acid	Oxalic acid removal efficiency is 25%, 77% and 91% for ozonation alone, AC and 5% Co/AC catalytic ozonation, respectively.	72
2%–12% CuO/AC	Nitrobenzene	Reaction rate constant in nitrobenzene degradation is 0.0063, 0.0076 and 0.0109 min^{-1} for ozonation alone, AC and 12% Cu/AC catalytic ozonation, respectively.	73
MnO_x/AC	Heavy oil refinery wastewater	Activity on COD removal for AC in ozonation at the first use is higher than that of MnO_x/AC, while MnO_x/AC has higher activity from the second use.	20
2.1%–9.1% TiO_2/AC	Aniline	TiO_2, formed *in situ* using alcoholic $TiCl_4$ precursor solutions on AC, has a better performance in aniline degradation than that of TiO_2/AC prepared by immersion impregnation or hydrothermal method.	71
TiO_2/AC	Aniline	A three-phase mathematical model reaction was proposed to describe the stages of gas–liquid transfer, catalyst adsorption and oxidation in the bulk solution and on the catalyst surface.	74
ZnO/AC	Metronidazole	The presence of phosphate significantly inhibits the metronidazole degradation due to the high tendency of phosphate to be combined with functional groups on the catalyst surface.	75
ZnO/AC	Dibutyl phthalate in goat whey solution	The degradation efficiency of dibutyl phthalate in goat whey solution decreases in the following order: ZnO/AC catalytic ozonation > ZnO catalytic ozonation > ozonation alone	76
0.5%–10% MgO/AC	Phenol	COD removal efficiency is 21.3%, 15.1% and 83.5% for ozonation alone, MgO/AC adsorption and 1% MgO/AC catalytic ozonation, respectively.	77

but did not provide the comparison results of the activity of the two single-metal oxides supported on AC (Table 4.4).

According to the finding that *t*BA strongly inhibits 2,4-dichlorophenoxyacetic acid degradation, it is suggested that ozonation of 2,4-dichlorophenoxyacetic acid in the presence of Fe–Ni/AC follows a $^{\bullet}OH$ oxidation mechanism.[79] Li *et al.* believe that the presence of MnO_2–Co_3O_4/AC catalyst could accelerate the aqueous ozone decomposition into $^{\bullet}OH$ and then promote the degradation of the refractory pollutants in incineration leachate. As confirmed by ESR, $^{\bullet}OH$ are considered to be the main active free radicals in ozonation alone and MnO_2–Co_3O_4/AC catalytic ozonation.[80] The reason why $^{\bullet}OH$

Table 4.4 Ozonation of pollutant in the presence of AC-supported bimetallic oxides.

Catalyst	Organic pollutants	Highlights	Ref.
Fe_2O_3–CeO_2/AC	Sulfamethoxazole	TOC removal efficiency is 37%, 78% and 86% for ozonation alone, AC and Fe_2O_3/CeO_2/AC catalytic ozonation, respectively	82
0.22% Fe–Ni/AC	2,4-Dichlorophenoxyacetic acid	TOC removal efficiency is 34%, 8%, 50%, 60%, 62% and 72% for ozonation alone, Fe–Ni/AC adsorption, AC, Fe/AC, Ni/AC and Fe–Ni/AC catalytic ozonation, respectively	79
Fe–Mn/AC	Methyl orange	TOC removal efficiency is 18.0%, 31.0% and 42.5% for ozonation alone, AC and Fe–Mn/AC catalytic ozonation, respectively	83
Fe–Ni/AC	Phenol	$^{\bullet}O_2^-$ was suggested to play a key role in the phenol degradation, while other radicals were not important according to the experiments of radical scavenging.	84
MnO_2–Co_3O_4/AC	Incineration leachate	COD removal efficiency is 21%, 5%, 5%, 27% and 30% for ozonation alone, AC adsorption, Mn–Co/AC adsorption, AC and Mn–Co/AC catalytic ozonation, respectively	80

is also the main active free radical in ozonation alone may be related to the fact that many organic compounds with aromatic structure in the incineration leachate can trigger ozone decomposition to generate $^{\bullet}OH$.[1,81]

As the number of reuses increases, the TOC removal efficiency decreases slightly during ozonation of 2,4-dichlorophenoxyacetic acid in the presence of Fe–Ni/AC catalyst. Lü *et al.* believe that the variation of the specific surface area of Fe–Ni/AC catalyst during repeated use may be the main reason, since it decreases from 519.68 to 401.54 $m^2 g^{-1}$ after three uses, and some composite oxides of Fe–Ni particles were expected to spall during the ozonation of 2,4-dichlorophenoxyacetic acid in the presence of Fe–Ni/AC due to the partial oxidation of the AC surface by ozone.[79] A similar phenomenon was observed during the ozonation of papermaking wastewater in the presence of Fe/AC catalyst, and the specific surface area of Fe/AC catalyst also decreased from 825 to 786 $m^2 g^{-1}$ after five uses.[40]

The loading of metal oxides usually causes significant changes in the specific surface area of carbon materials. After AC loaded 12% Cu by impregnation, the specific surface area of the Cu/AC catalyst increased from 926.7 to 1040 $m^2 g^{-1}$ for the increase in calcination temperature from 350 °C to 550 °C, which the authors believe is mainly caused by the development of the porosity of the catalyst under difference calcination temperatures. Also,

the performance in nitrobenzene adsorption improved for AC with the copper loading.[73] Nasseh *et al.* also found that the specific surface area of AC significantly increased from 284 to 442 $m^2 g^{-1}$ after coating with ZnO nanoparticles by the deep-coating methodology.[75] However, the loading of metal oxides usually leads to a decrease in the specific surface area of the catalyst.[40,58,70] Chen *et al.* found that the COD removal efficiency during the ozonation of heavy oil refinery wastewater in the presence of MnO_x/AC is less than that of AC for the first use, which may be due to the better adsorption performance of AC for wastewater because the specific surface area of AC decreased from 1143.3 to 975.6 $m^2 g^{-1}$ after MnO_x loading.[20] The remarkable reduction of the specific surface area of AC is more likely to occur at a high metal oxide loading, and about 19% and 31% reductions of the specific surface area of AC were observed with 30%[63] and 48.7%[69] Fe loading, respectively. Except for *in situ* formed amorphous MnO_x,[85] the specific surface area is usually small for metal oxide compared to carbon materials. Therefore, if the weight ratio of the metal oxide in the AC-supported catalyst is taken into consideration, the specific surface area may not change drastically after metal oxide loading in most cases.

As previously mentioned, the activity reduction of metal oxide supported on AC may be diverse. For example, the active sites on the AC-supported metal oxide catalyst may be covered by pollutants, oxidation intermediates or water matrix, or the metal oxides may leach during ozonation, or the metal oxide may spall during ozonation due to the partial oxidation of the AC surface by ozone. As observed by Wang *et al.* during the treatment of actual bio-treated dyeing and finishing wastewater in a continuous mode, the COD removal during ozonation in the presence of AC could be enhanced 14%–25% with the loading of iron oxide; however, this improvement effect by Fe/AC can only last for less than 2 d, and the catalytic activity of AC can be maintained for at least 20 d.[45] Therefore, the activity and stability of AC-supported metal oxide catalysts is an important issue that deserves more attention.

4.3 Biochar-based Materials

4.3.1 Biochar

Various biomass materials (such as pistachio hull, sewage sludge and petroleum sludge) are used to prepare biochar for catalytic ozonation (Table 4.5). No catalytic activity on oxalic acid removal is found for the sludge-based carbon using KOH or H_2SO_4 as the activated agent, while a high catalytic activity is observed for the sludge-based carbon using $ZnCl_2$ as the activated agent, the authors believe that this is due to the fact that the specific surface area of sludge-based carbon activated by KOH (99 $m^2 g^{-1}$) or H_2SO_4 (68 $m^2 g^{-1}$) is much lower than that activated by $ZnCl_2$ (363 $m^2 g^{-1}$).[86] The specific surface area of biochar increases with the pyrolysis temperature, which is 0.4, 39.1 and 95.9 $m^2 g^{-1}$ for the pyrolysis temperature of 500, 700 and 900 °C, respectively, while the catalytic activity on phenol degradation

Table 4.5 Ozonation of pollutant in the presence of biochar.

Source of biochar	Preparation conditions	Highlights	Ref.
Pistachio hull	Pyrolysis at 500 °C in air	$S_{BET} = 2.85\ m^2\,g^{-1}$, $pH_{pzc} = 11.5$, macroporous, the decolorization of Reactive Red 198 by ozonation alone, biochar adsorption and biochar catalytic ozonation are about 20%, 20% and 98%, respectively.	89
Sewage sludge	Pyrolysis at 700 °C in N_2 using $ZnCl_2$ as activation agent, and inorganic impurities removed by HCl	$S_{BET} = 363\ m^2\,g^{-1}$, $pH_{pzc} = 3.8$, mesoporous, the oxalic acid removal by biochar catalytic ozonation is 45.4% higher than that of the superposition of ozonation alone and biochar adsorption.	86
Sewage sludge and corncob (1 : 1, w/w)	Pyrolysis at 600 °C using $ZnCl_2$ as activation agent, and inorganic impurities removed by HCl	$S_{BET} = 712.8\ m^2\,g^{-1}$, the Ibuprofen degradation by biochar catalytic ozonation is slightly higher than that of the superposition of ozonation alone and biochar adsorption.	92
Coking wastewater treatment sludge	Pyrolysis at 300, 500, 700 or 900 °C in N_2	$S_{BET} = 39.1\ m^2\,g^{-1}$ for pyrolysis at 700 °C, the phenol degradation by biochar catalytic ozonation is much higher than that of the superposition of ozonation alone and biochar adsorption.	41
Sewage sludge	Pyrolysis at 500, 600, 700 or 800 °C in N_2	Hydroquinone degradation efficiency during ozonation with biochar heat-treated at 700 °C is higher than that of biochar pretreatment by HNO_3.	87
Petroleum sludge	Pyrolysis at 850 °C in N_2 using $ZnCl_2$ as activation agent	$S_{BET} = 143\ m^2\,g^{-1}$, the TOC removal (53.5%) during ozonation of petroleum refinery wastewater with biochar is twice that of ozonation alone (26.9%).	88

for the pyrolysis temperature of 700 °C is comparable to that for 900 °C.[41] However, the higher the pyrolysis temperature of sludge-based carbon is in the range of 500–800 °C, the higher the catalytic activity on hydroquinone degradation will be.[87]

The specific surface areas are 143, 561 and 569 $m^2\,g^{-1}$ for the raw petroleum sludge biochar, the biochar pretreatment with HNO_3 and the biochar pretreatment with both HNO_3 and NaOH, respectively. It is found that TOC removal during ozonation with biochar is significantly higher than that of the combination of ozonation alone and biochar adsorption, while TOC removal during ozonation with biochar pretreatment with HNO_3 or with both HNO_3 and NaOH is lower than or comparable to that of the

combination of ozonation alone and biochar adsorption. The authors believe that the surface functional carbon groups, Si–O structures, and metal oxides of biochar promote the ozone decomposition to generate •OH for mineralizing petroleum contaminants.[88] Xu *et al.* also suggested that Fe^{2+} and Fe^{3+} in the sludge-based carbon may act as active sites to improve its catalytic activity according to the results of Mössbauer spectrum.[87] *t*BA has no effect on oxalic acid removal during ozonation in the presence of sludge-based carbon.[86] Moussavi and Khosravi also found that *t*BA has no effect on the decolorization of Reactive Red 198 during ozonation in the presence of biochar, while the presence of 5 mM phosphate changes the decolorization rate of Reactive Red 198 from 95% to 45% in 30 min, and the authors believe that this may be caused by the strong bonding of phosphate to surface groups;[89] however, this phenomenon usually occurs in ozonation with metal oxide catalyst.[90] Certainly, if the mainly active sites of biochar used by Moussavi and Khosravi[89] are surface hydroxyl groups, the presence of phosphate is expected to have a significant effect on the catalytic activity of biochar since phosphate could prevent •OH formation by covering the Lewis acid sites.[91]

Some researchers have compared the catalytic activity of biochar with commonly used commercial AC. Moussavi and Khosravi found that the decolorization of Reactive Red 198 during ozonation in the presence of biochar and AC catalytic ozonation is about 98% and 44% in 60 min, respectively.[89] Hydroquinone degradation efficiency during ozonation with biochar heat-treated at 700 °C is higher than that of commercial coal AC.[87] Although the specific surface area of sludge-corncob AC (712.8 $m^2 g^{-1}$) is lower than that of coconut shell AC (835.6 $m^2 g^{-1}$), apricot shell AC (962.9 $m^2 g^{-1}$) or coal AC (1030.5 $m^2 g^{-1}$), the degradation efficiency of ibuprofen during ozonation with sludge-corncob AC is higher than that of coconut shell AC, apricot shell AC or coal AC.[92] This may be caused by the more basic functional groups of sludge-corncob AC. However, Wen *et al.* observed that oxalic acid removal during ozonation with sludge-based carbon and AC is 81.2% and 98.7% in 40 min, respectively.[86]

Some researchers are also concerned about the stability of biochar in ozonation. The stability of heat-treated biochar at 700 °C is poor stability during ozonation, and the degradation efficiency of phenol is reduced from 95.4% in the first use to 59.3% in the fourth use.[41] The organic carbon dissolved in the distilled water of the 1.0 $g L^{-1}$ raw sludge, or the biochar heat-treated at 300 °C is in the range of 130–140 $mg L^{-1}$, and it decreases to less than 3.5 $mg L^{-1}$ for the heat-treated biochar at no less than 500 °C. Meanwhile, the leaching of Co^{2+}, Fe^{3+}, Ni^{2+}, Cu^{2+} and Mn^{2+} is also observed for raw sludge and the biochar heat-treated at 300 °C.[41] Chen *et al.* also found that TOC removal decreases with repeated use of petroleum sludge-based biochar during ozonation and that the leaching of metal ion was also observed after the first use, while the TOC removal efficiency for ozonation with petroleum sludge-based biochar after the fifth reuse is still higher than that of ozonation alone.[88]

In addition, in order to investigate the relationship between the surface functional groups of carbon materials and their catalytic activity, Boehm titration[93] is often used to quantitatively determine the various functional groups on the surface of carbon materials. However, the multiple steps of Boehm titration are conducted in various ways by different research groups, making these results difficult to compare. Therefore, Andreas Olsson's research group standardized the Boehm titration procedure in 2010 to minimize errors.[94,95] It should be noted that the relatively high content of impurities (such as oxides, silica and alumina) in biochar may cause obvious interference in determining functional groups on biochar surface using Boehm titration, so it needs to be pretreated with NaOH and HCl before Boehm titration.[96]

4.3.2 Biochar-supported Metal Oxides

As shown in Tables 4.5 and 4.6, the specific surface area of biochar prepared without adding activator is usually not large, and it ranges from 2.85 to 95.9 $m^2 g^{-1}$, which may be related to different raw materials.[41,89] The specific surface area of biochar activated by different activators is very different, and the specific surface area of sludge-based carbon activated by $ZnCl_2$ (18.3 $m^2 g^{-1}$) or H_2SO_4 (51.9 $m^2 g^{-1}$) is much lower than that activated by $ZnCl_2 + H_2SO_4$ (179.9 $m^2 g^{-1}$).[97] While Wen *et al.* found that the specific surface area of sludge-based carbon prepared by $ZnCl_2$ activator is more than three times that of other activators (KOH or H_2SO_4).[86]

Some researchers have found that metal oxides have only a slight effect on the specific surface area of biochar,[98,99] while some researchers have found that metal oxide loading reduces the specific surface area of biochar by more than 15%.[100,101] It is interesting that the specific surface area of biochar (87.4 $m^2 g^{-1}$) increases significantly with the loading of either MnO_x (109.8 $m^2 g^{-1}$) or FeO_x (99.8 $m^2 g^{-1}$); this may be due to the fact that these catalysts have not undergone the pyrolysis process but are only formed by the redox reaction between biochar and $KMnO_4$ or K_2FeO_4.[85] Lu *et al.* found that not only the specific surface area of ferromagnetic sludge-based AC decreases with the increase of the amount of iron loading (940.9 $m^2 g^{-1}$ for 2.3% Fe, 936.7 $m^2 g^{-1}$ for 4.3% Fe and 880.6 $m^2 g^{-1}$ for 9.5% Fe) but also the catalytic activity gradually decreases with the increase of Fe loading. This may be caused by the continuous agglomeration of iron oxide on the biochar surface with the increase of iron loading.[102] The adsorption of pollutants may also significantly reduce the specific surface area of biochar; MnO_x/biochar and FeO_x/biochar decreased by 36.1%, 32.9% and 34.0% due to the adsorption of pollutants, although it can be recovered up to 89.1%, 96.5% and 91.2% after 60 min ozonation, respectively.[101]

Catalytic ozonation can significantly improve the biodegradability of wastewater. The BOD_5/COD of biologically pretreated papermaking wastewater is 0.16, 0.27, 0.35 and 0.46 for untreated wastewater, ozonation alone, biochar catalytic ozonation and MnO_x/biochar catalytic ozonation,

Table 4.6 Ozonation of pollutant in the presence of biochar-supported metal oxides.

Source of biochar	Biochar preparation	Biochar supported metal oxide preparation	Highlights	Ref.
Supported iron oxide				
Sewage sludge	Pyrolysis at 700 °C in N_2 using $ZnCl_2$ as activation agent, and inorganic impurities removed by HCl	Wet impregnation with $Fe(NO_3)_3$ and pyrolysis at 600 °C in N_2	S_{BET} decrease from 398.6 to 339.1 $m^2 g^{-1}$ with the 7.51% Fe loading, the COD removal for biologically pretreated Lurgi coal gasification wastewater by ozonation alone, biochar and Fe/biochar catalytic ozonation is about 42.1%, 54.3% and 73.7%, respectively	101
Sewage sludge and corncob (1 : 1, w/w)	Pyrolysis at 600 °C using $ZnCl_2$ as activation agent, and inorganic impurities removed by HCl	Co-precipitation with $FeCl_3$ and $FeSO_4$ and dried at 50 °C	S_{BET} decrease from 941.0 to 940.9 $m^2 g^{-1}$ with the 2.3% Fe loading, the *p*-chlorobenzoic acid degradation by biochar catalytic ozonation is slightly lower than that of the superposition of ozonation alone and biochar adsorption	102
Cow dung	Pyrolysis at 800 °C in N_2	*In situ* precipitation oxidization using $FeSO_4$ and dried at 60 °C	S_{BET} decrease from 55.1 to 20.6 $m^2 g^{-1}$ with the Fe_3O_4 loading, the COD removal efficiency reached 74% during ozonation of biologically pretreated coal gasification wastewater in the presence of catalyst	100
Commercial biochar	Not mentioned	Impregnation with K_2FeO_4 and dried	Atrazine degradation efficiency by ozonation alone and FeO_x/biochar catalytic ozonation is 48.1% and 100%, respectively	85
Supported manganese oxide				
Sewage sludge	Pyrolysis at 700 °C in N_2 using $ZnCl_2$ as activation agent, and inorganic impurities removed by HCl	Wet impregnation with $Mn(NO_3)_2$ and pyrolysis at 600 °C in N_2	S_{BET} decrease from 398.6 to 327.5 $m^2 g^{-1}$ with the 15.23% Mn loading, the COD removal for biologically pretreated Lurgi coal gasification wastewater by ozonation alone, biochar and Mn/biochar catalytic ozonation is 42.1%, 54.3% and 78.1%, respectively	101
Commercial biochar	Not mentioned	Impregnation with $KMnO_4$, and dried	Atrazine degradation efficiency by ozonation alone and MnO_x/biochar catalytic ozonation is 48.1% and 83%, respectively	85

Table 4.6 (*Continued*)

Source of biochar	Biochar preparation	Biochar supported metal oxide preparation	Highlights	Ref.
Sewage sludge	Pyrolysis at 550 °C in N_2 using $ZnCl_2$, H_2SO_4, and $ZnCl_2 + H_2SO_4$ as activation agent, and inorganic impurities removed by HCl	Wet impregnation with $KMnO_4$ and pyrolysis at 550 °C in N_2	Oxalic acid removal efficiency by ozonation alone and 30% MnO_x/biochar catalytic ozonation at pH 3.5 is 10.3% and 92.2%, respectively	97
Rice straw	Impregnated into the H_3PO_4 solution and dried at 80 °C	Wet impregnation with $Mn(NO_3)_2$ and pyrolysis at 550 °C in N_2	S_{BET} decrease from 917.6 to 901.1 $m^2 g^{-1}$ with 11.8% Mn loading, COD removal efficiency by ozonation alone and MnOx/biochar catalytic ozonation is 45.5% and 75.5%, respectively	98
Piggery residue	Pyrolysis at 550 °C	Impregnation with $MnSO_4$ and $KMnO_4$, and dried	S_{BET} decrease from 16.27 to 16.09 $m^2 g^{-1}$ with the Mn loading, COD removal efficiency by ozonation alone, biochar and MnO_x/biochar catalytic ozonation is 24.0%, 31.6% and 36.9%, respectively	99
Supported cobalt oxide				
Olive stones	Carbonization at 600 °C and then activated using steam as oxidizing agent at 850 °C	Impregnation with $CoSO_4$ and pyrolysis at 550 °C in N_2	S_{BET} decrease from 734.2 to 721.9 $m^2 g^{-1}$ with the 5% Co loading, TOC removal efficiency by ozonation alone, biochar and CoO_x/biochar catalytic ozonation is 24%, 45% and 65%, respectively	103

respectively.[98] The BOD_5/COD of biologically pretreated coal gasification wastewater also increased from 0.04 to 0.52 after Fe_3O_4/biochar catalytic ozonation. The authors believe that this is due to the electron transfer between Fe^{2+} and Fe^{3+} in Fe_3O_4 and the improved •OH formation through the reaction of active sites and ozone; the •OH reaction mechanism is confirmed by ESR.[100] Tian *et al.* also believed, by means of radical scavenger experiment and ESR analysis, that the •OH is the main active species during ozonation with MnO_x/biochar or FeO_x/biochar.[85] Nitrobenzene degradation is proposed as the improvement of the •OH formation on the CoO_x/biochar surface according to the effect of •OH scavengers.[103]

Despite finding only trace amounts of iron and manganese during ozonation of atrazine with MnO_x/biochar or FeO_x/biochar, the atrazine degradation efficiency decreases 23.9% and 24.3% for MnO_x/biochar or FeO_x/biochar after four uses.[85] The leaching of iron is more remarkable than that of manganese during repeated use, while no remarkable difference was found on the catalytic activity of the prepared MnO_x/biochar or FeO_x/biochar catalysts after ten uses.[101] Lu *et al.* found that the adsorption capacity and catalytic activity on the *p*-chlorobenzoic acid degradation decrease only slightly during ozonation with ferromagnetic sludge-based AC after six uses.[102] Zhuang *et al*. observed that the COD removal efficiency decreased by only 4.1% during the ozonation of papermaking wastewater with MnO_x/biochar after 20 uses, indicating that the catalyst has a good stability.[98]

4.4 Reaction Mechanisms

4.4.1 Brief Description of Several Viewpoints

4.4.1.1 Adsorption Mechanism

Sánchez-Polo *et al.* observed that the adsorption rate of atrazine on AC was faster than its oxidation rate by ozone; therefore, the authors believed that atrazine removal during the AC catalytic ozonation is mainly caused by its adsorption on the AC surface.[104] This is because AC usually has better adsorption performance for hydrophobic micropollutants.

It should be noted that adsorption may not play a major role in organic matter removal for the ozonation of wastewater with AC. The concentration of organic matter in wastewater is relatively high, and the hydrophobicity of the organic matter usually decreases significantly[21] due to the longer oxidation time compared with that in drinking water treatment, which is not conducive to the adsorption of the oxidation products on the AC surface. As mentioned, 27.8% of TOC removal can be achieved for ROC treatment by AC adsorption in 210 min; however, only 3%–4% TOC can be obtained by AC adsorption for ROC after treating by ozonation for more than 60 min.[15]

In general, if the pollutant concentration is low and its hydrophobicity is also strong, then adsorption may play an important role in this pollutant's removal during AC catalytic ozonation.

4.4.1.2 Direct Ozonation Reaction Mechanism

Beltrán *et al.* proposed a two-stage reaction mechanism during ozonation of polyphenols (gallic acid, tyrosol and syringic acid) in the presence of AC, that is, the first-stage direct molecular ozone reaction mechanism involving the oxidation of polyphenols and the second-stage hydroxyl radical reaction mechanism involving the oxidation of intermediates.[105] Since they found that there is no dissolved ozone in the initial stage of the reaction (15–60 min), this means that the gas–liquid ozone reacts with polyphenols directly and quickly in solution,[105] and that these reactions may be due to the ozone attack on aromatic rings through electrophilic substitution and 1,3-cycloaddition reaction.[1] Beltrán *et al.*[105] found that the second-order reaction rate constants of these three polyphenols and ozone are all above $5\times10^4\ M^{-1}\ s^{-1}$, which means that the prerequisite for the direct molecular ozone reaction is that the reaction between ozone and organic matter is relatively fast. Lee *et al.*[106] also found in the ozonation of secondary municipal wastewater effluent for the removal of micropollutants, the contribution of direct ozone oxidation in the degradation of micropollutants exceeded 80% when the second-order reaction rate constants of ozone and micropollutants exceeded $10^5\ M^{-1}\ s^{-1}$.

4.4.1.3 Free Radicals

Logemann and Annee[4] believe that the AC-catalytic ozonation is not a reaction of $^{\bullet}OH$ but a reaction mechanism of the surface-bound oxygen-containing free radicals ($O^{\bullet}$, $^{\bullet}O_2^-$ and $^{\bullet}O_3^-$)[6] oxidizing the organic matter adsorbed on the AC surface. Jans and Hoigné believe that AC is a catalyst in ozonation, which reacts with ozone to generate $^{\bullet}OH$.[107] More and more researchers agree that AC catalytic ozonation follows the $^{\bullet}OH$ reaction mechanism.[108] However, the basic groups on the AC surface continue to decrease, while the acidic groups continue to increase with the extension of ozonation, which in turn leads to the decrease of its performance on pollutant degradation during ozonation with AC.[28] Therefore, it is generally believed that AC is not a real catalyst but an initiator and/or promoter that accelerates the ozone decomposition to generate $^{\bullet}OH$.[1,28,30,108]

4.4.2 Reactive Oxygen Species and Intermediates Formation

4.4.2.1 Superoxide Radical Formation

Organic matter can still be efficiently degraded in the condition of a low pH 3.5 or a high concentration of $^{\bullet}OH$ scavenger carbonate;[4] therefore, in 1997, Kaptijn believed that the free radicals that oxidize organic matter in the AC catalytic ozonation are surface-bound oxygen-containing free radicals ($O^{\bullet}$, $^{\bullet}O_2^-$ and $^{\bullet}O_3^-$).[6] In 2005, Sánchez-Polo *et al.*[28] further confirmed the existence of $^{\bullet}O_2^-$ in the AC catalytic ozonation by detecting the product of the rapid reaction of tetranitromethane and $^{\bullet}O_2^-$ ($k=2\times10^9\ M^{-1}\ s^{-1}$); the higher the concentration of pyrrole groups was on the AC surface, the more $^{\bullet}O_2^-$ will

be generated during ozonation, but the pyrrole groups will be quickly consumed due to its rapid reaction with ozone ($k = 5.8 \times 10^5$ M^{-1} s^{-1}).[109]

Using 5,5-dimethyl-pyrrolineoxide (DMPO) as a $^{\bullet}O_2^-$ trapping agent, the existence of $^{\bullet}O_2^-$ during ozonation with powder AC was confirmed since the DMPO-$^{\bullet}O_2^-$ signal was detected by electron spin resonance (ESR), while $^{\bullet}O_2^-$ can be generated more effectively during ozonation with CNT.[43]

In recent years, many researchers have adopted *p*-benzoquinone as a $^{\bullet}O_2^-$ scavenger[2,41,110] because of the rapid reaction between *p*-benzoquinone and $^{\bullet}O_2^-$ ($k = 9.8 \times 10^8$ M^{-1} s^{-1}).[2] But it should be noted that the rate of direct reaction between ozone and *p*-benzoquinone is not slow ($k = 2.5 \times 10^3$ M^{-1} s^{-1}).[111] In order to effectively scavenge the $^{\bullet}O_2^-$ generated during the reaction, it is usually necessary to add excess *p*-benzoquinone. If the ozone dose is limited or the target pollutant is an ozone refractory, the decrease in the degradation efficiency of the target pollutant with the addition of *p*-benzoquinone is not necessarily caused by the capture of $^{\bullet}O_2^-$ by *p*-benzoquinone. It may also be caused by the additional consumption of ozone with the addition of *p*-benzoquinone through competing with the target pollutant. Recently, Wang's group proved that in the case of a certain dosage of ozone, the decomposition rate of ozone will increase as the ratio of *p*-benzoquinone to ozone increases, which leads to a gradual decrease in the degradation of target compound.[112] The authors suggested that the addition of trace $^{\bullet}O_2^-$ probe compound (such as chloroform) is a good choice for the quantitative determination of $^{\bullet}O_2^-$ generated in the catalytic ozonation, since the presence of trace $^{\bullet}O_2^-$ probe compound has no noticeable effect on the reaction mechanism of catalytic ozonation.[112] In addition, the consumption of $^{\bullet}OH$ caused by the reaction of $^{\bullet}OH$ and *p*-benzoquinone ($k = 1.2 \times 10^9$ M^{-1} s^{-1})[112] is also not conducive to achieving the target pollutant degradation, which may be another issue that needs attention.

4.4.2.2 Hydroxyl Radical Formation

Many researchers have reported the role of singlet oxygen ($^1O_2$) in the degradation of organics during photocatalysis and persulfate-based AOPs.[2,113] In recent years, researchers have also found that $^1O_2$ is generated during ozonation with graphene-based, manganese-based or perovskite catalysts.[2,110] To the best of our knowledge, there is no report that $^1O_2$ plays a role in the degradation of organics during ozonation with AC.

Jans and Hoigné found that AC can accelerate the transformation of dissolved ozone to $^{\bullet}OH$ and believe that this is an AOP comparable to the combination of ozone and H_2O_2 in 1998.[107] Sánchez-Polo *et al.* found that the activity of AC catalytic ozonation is lower than that of the combination of ozone and OH^- or H_2O_2 in synthetic water, but the activity on the pollutant degradation is similar for all three ozone-based AOPs (AC, OH^-, and H_2O_2) in the actual water with the existence of $^{\bullet}OH$ scavenger bicarbonate/carbonate.[104] Furthermore, the existence of $^{\bullet}OH$ during ozonation with powder AC was demonstrated since the typical characteristic peaks of DMPO-$^{\bullet}OH$ with

an intensity ratio of 1 : 2 : 2 : 1 was detected by ESR, while its •OH concentration was found to be much less than that of ozonation with CNT.[43]

In fact, most researchers deduce the role of •OH in AC catalytic ozonation based on the effect of *t*BA on the degradation efficiency of pollutants, since *t*BA is a typical •OH scavenger due to its very slow reaction with ozone (3×10^{-3} M^{-1} s^{-1})[114] and fast reaction with •OH (6×10^{8} M^{-1} s^{-1}).[115]

4.4.2.3 Hydrogen Peroxide Formation

It is reported that a very small amount of H_2O_2 is generated during ozone decomposition in the absence of pollutant in acidic conditions.[116,117] It is also observed that a small amount of H_2O_2 is formed in aqueous solution with the presence of AC and dissolved oxygen because the dissolved oxygen can be reduced by the oxygen-containing groups (such as quinone and chromene) on the AC surface (eqn (4.9)).[118] In fact, the direct oxidation of organic matter by ozone involves the breaking of the aromatic ring or the Criegee mechanism of ozone attacking double bonds, which may also generate hydrogen peroxide.[1,119] H_2O_2 was found to be generated during ozonation of gallic acid with or without AC, and the H_2O_2 concentration formed during ozonation with AC was lower than that in ozonation alone. The authors believe that this was because AC more effectively promotes the H_2O_2 decomposition to generate •OH for promoting the degradation of saturated carboxylic acids.[18]

$$C^{*}_{Red} + \frac{1}{2}O_2 + H_2O \rightarrow C^{*}_{OX} + H_2O_2 \qquad (4.9)$$

It is generally accepted that the H_2O_2 formation during AC catalytic ozonation is mainly related to the π electron of basal planes,[25] basic oxygen-containing groups (such as quinone and chromene)[25,30] and phenolic groups[30] on the AC surface. Nawrocki's group found that the AC heat-treated in a hydrogen atmosphere has a significant increase in the H_2O_2 concentration produced during ozonation. The authors believe that this is because the heat treatment eliminates oxygen-containing groups, thereby removing the hindrance of ozone from attacking the double bond on the AC surface.[120] Furthermore, Nawrocki's group also observed that the lower the pH was, the larger the amount of H_2O_2 usually generated. This is because the ozone and H_2O_2 in the solution will be more stable at low pH and will not easily decompose to generate •OH. Therefore, a relatively high H_2O_2 concentration would not be expected for the case of pH > 5, and the authors believe that H_2O_2 could not be the source of •OH during AC catalytic ozonation under this condition.[120] However, Alvárez *et al.* found that AC promotes ozone decomposition more significantly under neutral and basic pH than under that in acidic conditions, and the authors believe that the promotion of ozone decomposition only comes from the reactions between adsorbed/non-adsorbed ozone and some surface groups and mineral impurities of AC at acidic pH due to the very high pK_a (11.6) of H_2O_2. While at a neutral and

basic pH, besides the accelerating ozone decomposition on the AC surface, H_2O_2 dissociates into HO_2^- in solution, thereby promoting the dissolved ozone decomposition in solution (eqn (4.10) and (4.11)).[30]

$$H_2O_2 \xleftrightarrow{pK_a = 11.6} H^+ + HO_2^- \quad (4.10)$$

$$HO_2^- \rightarrow \cdots \rightarrow {}^{\bullet}OH \quad (4.11)$$

$^{\bullet}$OH may generate on the AC surface due to the ozone decomposition, but its populations are extremely short-lived (10^{-9} s)[121] due to its extremely high reactivity with AC and/or the pollutant adsorbed on the AC surface, resulting in the impossible diffusion of generated $^{\bullet}$OH from the AC surface into the solution.[30] The concentration of $^{\bullet}$OH generated by the ozone decomposition on the AC surface depends on how fast the ozone is transferred from the aqueous solution to the carbon surface. The generated $^{\bullet}$OH may react with ozone or interact with one another to form H_2O_2,[122] while it is reported that the active site on the carbon surface that initiates the decomposition of H_2O_2 may be the same as that of ozone.[123] In this case, H_2O_2 that has not decomposed on the AC surface may desorb into the solution and may be detected.[120] In addition, different from Rivera-Utrilla and Sanchez-Polo's opinion that the mineral impurities in AC promote the ozone decomposition to generate highly reactive oxygen species,[25] Alvárez *et al.* believe that the mineral impurities may promote the decomposition of H_2O_2 on the AC surface instead of promoting ozone decomposition, and certainly this will result in a decrease in the amount of H_2O_2 entering the solution.[30]

4.4.3 Hydroxyl Radical Mechanism

$^{\bullet}$OH plays an important role in the degradation of pollutants during AC catalytic ozonation, as recognized by more and more researchers.[11,108,124,125] However, *t*BA can effectively scavenge the $^{\bullet}$OH only in the bulk solution but cannot effectively quench the $^{\bullet}$OH adsorbed on the AC surface due to the very weak adsorption of *t*BA on the surface of carbon materials.[30,126,127] According to the effect of *t*BA on the degradation efficiency of pollutants, different researchers have debated whether the $^{\bullet}$OH oxidation occurs in the bulk solution[126] or on the AC surface.[128]

4.4.3.1 Bulk Solution Reaction

Beltrán's group found that *t*BA hardly adsorbed on the AC surface within 150 min and that it also has no impact on the oxalic acid adsorption on the AC surface, indicating that *t*BA can only quench the $^{\bullet}$OH generated in the solution, not on the AC surface. The presence of *t*BA significantly inhibited TOC removal during AC catalytic ozonation, and so it is suggested that the reaction between oxalic acid and $^{\bullet}$OH occurs in the bulk solution.[126] Jans and Hoigné also believed that the reaction between $^{\bullet}$OH and pollutant occurs in the aqueous

solution.[107] Gu *et al.* observed that the *t*BA has a slight and remarkable effect on the *p*-nitrophenol degradation at pH 4.0 and 10.0, respectively. The authors believe that this is due to the different degradation mechanisms of *p*-nitrophenol at pH 4.0 and pH 10.0. AC adsorption plays a major role in the *p*-nitrophenol degradation at pH 4.0, while •OH oxidation in the solution plays an important role in the *p*-nitrophenol degradation at pH 10.0.[129]

4.4.3.2 Surface and Bulk Solution Reactions

Pereira's group found that the *t*BA has no effect on the oxalic acid removal at pH 3.0 but that it inhibits the ozonation of oxalic acid with AC or AC pre-treated by HNO_3, similarly to the same reaction with the absence of *t*BA at pH 7.0. Therefore, the authors believe that the oxidation of oxalic acid or oxamic acid by •OH generated in AC catalytic ozonation will occur simultaneously on the AC surface and in the bulk solution. The contribution of the bulk solution reaction in the degradation of pollutants depends on the surface properties of the AC, the pollutants and the pH of solution.[128]

Many researchers have investigated the adsorption of *t*BA on carbon materials, and all studies have found that *t*BA scarcely adsorbs on the surface of carbon materials (Table 4.7).[30,126,127,130,131] Furthermore, Alvárez *et al.* found that although some *t*BA is eventually adsorbed on the AC surface, its

Table 4.7 Adsorption of *t*BA on the surface of carbon materials and its impact on pollutant degradation.

Carbon	Experimental conditions	Highlights	Ref.
Granular AC ($1.25\ mg\,L^{-1}$)	Adsorption of 1 mM *t*BA on AC with or without 8 mM oxalic acid at pH 2.5	*t*BA adsorption on AC surface <2% within 150 min, and *t*BA has no impact on the oxalic acid adsorption on the AC surface.	126
Granular AC ($4.0\ g\,L^{-1}$)	Adsorption of 1–10 mM *t*BA on AC at pH 7 (phosphate buffer)	*t*BA adsorption on AC surface ~12% within 10 d, and *t*BA has significant impact on the ozone decomposition rate on AC surface.	30
CNT ($0.1\ g\,L^{-1}$)	Adsorption of 1 mM *t*BA on CNT with or without 1 mM oxalic acid at pH 3.0	*t*BA adsorption on CNT surface <2% within 40 min, and *t*BA has no effect on the oxalic acid adsorption on CNT surface.	127
Powder AC (0.1 or $0.5\ mg\,L^{-1}$)	Adsorption of 1–100 mM *t*BA on AC with 0.5 mM oxalic acid at pH 7 (Phosphate buffer)	*t*BA adsorption on AC surface ~2% for the 100 mM *t*BA dose, and the total amount of tBA adsorption on AC surface is relatively high (2 mM).	130
Granular AC ($2.0\ g\,L^{-1}$) or super-fine powdered AC ($1.0\ g\,L^{-1}$)	Adsorption of 1 mM *t*BA on AC with 1 μM *p*-chlorobenzoic acid	*t*BA adsorption on AC surface <10% within 20 min	131

adsorption rate on the AC surface is much slower compared with the ozone decomposition rate.[30] If ozone decomposes on the AC surface to generate •OH, it is difficult for *t*BA to effectively scavenge •OH due to the scarce adsorption of *t*BA on the AC surface. On the contrary, since *t*BA mainly exists in the bulk solution, it can very effectively scavenge the •OH derived from the ozone decomposition in bulk solution. Therefore, the reaction mechanism in which the surface reactions and the bulk solution reactions occur simultaneously is generally accepted for AC catalytic ozonation.[27,29,38,58,127,130–132]

The more *t*BA is added in the solution, the higher the •OH scavenging will be. However, it should be noted that too much *t*BA may bring other side effects. Cao's group found that the presence of 1 mM or 10 mM *t*BA has no effect on the oxalic acid removal during ozonation with 0.5 g L^{-1} powder AC; however, it is interesting that the addition of 100 mM *t*BA affects the oxalic acid removal to a certain extent. A reasonable explanation is that although *t*BA adsorbs scarcely on the AC surface, the *t*BA adsorbed on the AC surface can reach about 2 mM for the addition of 100 mM *t*BA in solution, which may occupy some active sites originally involved in the surface catalytic reaction.[130] In addition, Li *et al.* observed that the presence of *t*BA not only did not inhibit the pyruvic acid degradation during Pd/CeO_2 catalytic ozonation but slightly promoted it. The authors believe the reasons are as follows. One is that the pyruvic acid degradation mainly occurs on the Pd/CeO_2 surface, so the addition of *t*BA would not reduce its degradation efficiency, and the other is that the addition of *t*BA will inhibit the ozone decomposition in the solution, thereby increasing the dissolved ozone concentration in water and then slightly promoting the pyruvic acid degradation.[133]

Therefore, the *t*BA scavenger dose should meet the minimum dose principle that can meet the requirement of the •OH scavenging efficiency (*e.g.* 90% or 95%). Certainly, the appropriate *t*BA dose can be deduced through the influence of different concentrations of *t*BA on the pollutant degradation.[130,134] In fact, since the second rate constant of the reaction between *t*BA and •OH is known to be 6×10^8 M^{-1} s^{-1},[115] if the second rate constant of the reaction between pollutant and •OH is known, the required concentration of •OH scavenger *t*BA can be directly calculated by eqn (4.12) and (4.13) according to the requirement of the •OH scavenging efficiency.[135]

$$R = \frac{k_{\bullet OH,tBA} \times C_{tBA}}{k_{\bullet OH,Pollutant} \times C_{Pollutant} + k_{\bullet OH,tBA} \times C_{tBA}} \tag{4.12}$$

Where *R* is the scavenging efficiency of •OH in bulk solution, which is usually 90%, 95% or even higher. It should be noted that the eqn (4.13) is based on the assumption that synthetic water contains only *t*BA and pollutant and that the reaction between water matrix (such as bicarbonate/carbonate) and •OH needs to be considered for an actual water.

And then the required C_{tBA} can be expressed as:

$$C_{tBA} = \frac{R \times k_{\bullet OH,Pollutant}}{(1-R)k_{\bullet OH,tBA} \times C_{Pollutant}} \tag{4.13}$$

It should also be noted that the excessive addition of *t*BA will also adversely affect the exploration of the reaction mechanism. Wang's group observed that the ozone decomposition rate during ozonation with MnO_2 catalyst is remarkably reduced to an even lower rate during ozonation alone with the presence of a high concentration of *t*BA,[112] and the authors believe that this is because the presence of high concentration of *t*BA will capture all the primary •OH without producing $•O_2^-$ during ozonation alone, thus preventing the occurrence of radical chain reactions.[1] Taking into account that the addition of trace •OH probe compound (such as *p*-chlorobenzoic acid[136] or deethylatrazine[137]) will not have a significant impact on the reaction mechanism of catalytic ozonation, the authors recommend that the addition of •OH probe compound is more suitable for the investigation of the reaction mechanism than *t*BA.[112,138] Actually, this method had been adopted by the von Gunten's group as early as 15 years ago to detect the •OH concentration during AC catalytic ozonation,[28,104]

Cao's group observed that the effect of *t*BA on AC catalytic ozonation gradually decreases with the increase of AC dose, indicating that the •OH oxidation in the bulk solution plays a smaller and smaller role in oxalic acid removal, until the •OH oxidation in the bulk solution disappears completely when the AC dose exceeds 0.2 $g\,L^{-1}$. The authors believe that this may be caused by the quenching of •OH in the bulk solution by AC.[130] In fact, there is another possible explanation: the dissolved ozone in the solution tends to zero during the reaction when the AC dose is more than 0.2 $g\,L^{-1}$, which makes it difficult to generate •OH in the bulk solution. Cao's group also found that different basic groups have different effects on the proportion of •OH oxidation on the AC surface or in bulk solution for oxalic acid removal and that the pyrrole groups and pyridine groups on the AC surface may directly or indirectly facilitate the •OH oxidation in the bulk solution, while other basic sites (*e.g.* basal planes and basic oxygen-containing groups) promote oxalic acid removal through •OH oxidation on the AC surface.[27]

Chen *et al.* changed the granular AC from 863 μm to 1 μm superfine powder AC by ball milling, which increased the external specific surface area and the sum of the volume of mesopores and macropores by 190% and 563%, respectively, and then led to change in the contribution of surface reaction on the oxalic acid removal from 61% to 96%. Meanwhile, the authors believe that the changes in surface oxidation and basic value of AC caused by ball milling also play an important role in improving its catalytic activity.[131] However, Biernacki *et al.* believe that not only the external surface plays an important role in the ozone decomposition with granular AC, since the active sites on the external surface are too limited to meet the requirements of ozone decomposition.[122]

7-Hydroxycoumarin, a hydroxylation product obtained by attacking coumarin with •OH, was used as a •OH marker. Zhang *et al.* creatively proposed to detect the generation of •OH in the surface region using fluorescence

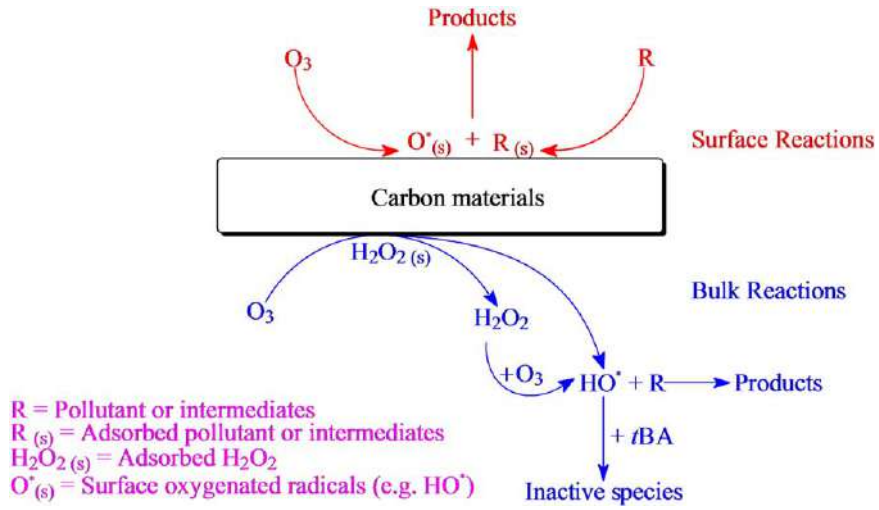

Figure 4.3 Illusion of the mainly reaction mechanism for the pollutant degradation during ozonation in the presence of carbon materials. Reproduced from ref. 127 with permission from Elsevier, Copyright 2009.

microscopy image analysis, and the abundance of •OH in the surface region was at least 1000 times higher than that of the bulk solution during CNT catalytic ozonation. Although the abundance of •OH on the surface region in AC catalytic ozonation is significantly lower than that of CNT, it is still significantly higher than that in the bulk solution.[43]

Based on these results and discussion, it can be concluded that •OH plays an important role in the AC catalytic ozonation and that the pollutant oxidation by •OH occurs simultaneously on the AC surface and in the bulk solution. As shown in Figure 4.3, as far as the reactions in bulk solution are concerned, the •OH for the degradation of the pollutant and/or intermediates could be produced in two ways. The first way is to assume that AC initiates dissolved ozone decomposition and transforms into •OH in bulk solution. The second way is that ozone reacts with some functional groups on the AC surface to form adsorbed H_2O_2, and then some H_2O_2 may diffuse into the solution and react with dissolved ozone to form •OH in the bulk solution. As for the reactions on the AC surface, the ozone adsorbed on the AC surface decomposes to generate surface-oxygenated radicals (such as •OH), which can oxidize the pollutant and/or intermediates adsorbed on the AC surface.[127]

Although most researchers use AC as a catalyst for ozonation of pollutant, the mechanisms obtained vary significantly in different works. Some authors believe that the •OH reactions mainly occur on the AC surface, while other authors believe that the major •OH reactions occur in the bulk solution. The factors affecting the changes in these mechanisms are not yet clear, which may be related to the complexity of surface reactions. As we know, surface

reaction involves the adsorption of ozone and pollutant and/or intermediates, surface reaction and desorption. The surface charging of AC is related to the pH of the solution and the pH_{pzc} of AC,[139] which may have a significant impact on the adsorptions of ozone and pollutant and/or intermediates, surface reaction and desorption. Similarly, the nature of pollutants, the surface modification of AC, the structure and specific surface area of AC, mineral impurities of AC, *etc.* may all have a certain impact on its reaction mechanism. Therefore, more systematic and in-depth investigation is needed in the future.

For metal oxide-supported catalysts using AC as a support, the reaction mechanism may be different from that of AC catalytic ozonation. Even if it still follows the $^{\bullet}OH$ mechanism of surface reaction and bulk solution reaction simultaneously, the loading of different metal oxides may also bring different effects on the mechanism. Yuan *et al.* observed that the addition of *t*BA has no effect on formate removal during ozonation with AC, whereas it has a significant effect on formate removal during ozonation with AC-supported iron oxide, and the authors believe that the major oxidation reaction of formate does not occur on the AC surface after iron oxide loading.[38] Xu *et al.* found that the loading of Ce on AC leads to the decrease of the contribution of surface reactions in the *p*-chlorobenzoic acid degradation from 64.4% to 8.6%.[58]

4.5 Practical Applications

As mentioned, many studies have reported that the toxicity of organic substances has been significantly reduced after ozonation of AC, AC-supported catalysts, biochar or biochar-supported catalysts. However, the acute toxicity increases from 98.3 to 146.5 μg $HgCl_2\,L^{-1}$ during AC catalytic ozonation of the effluent of the biological treatment of the dyeing and finishing wastewater, but its toxicity can be significantly reduced to 13.1 μg $HgCl_2\,L^{-1}$ after subsequent biological AC treatment.[45]

The earliest full-scale application of heterogeneous catalytic ozonation was reported using AC as the catalyst for the treatment of a contaminated groundwater in 1992.[6] In the past roughly three decades, AC as a catalyst or catalyst support has been used in the full-scale applications of actual water and wastewater treatment, especially in industrial wastewater treatment in China in the last decade. However, there are almost no articles about the full-scale application of AC catalytic ozonation. Full-scale application data for about three months from July 6 to September 30, 2020, is shown in Figure 4.4 for ozonation of the wastewater from a fine chemical industry park in the presence of AC-supported iron oxide. The COD of the influent varies from 35 to 40 mg L^{-1}, and the COD of the effluent is usually around 20 mg L^{-1} after the catalytic ozonation for 20 min with the 30 mg L^{-1} ozone dose. The $\Delta O_3/\Delta COD$ varies within the range of 1.5–2 mg O_3 mg^{-1} COD, which is economically acceptable for the refractory wastewater treated by heterogeneous catalytic ozonation in the full-scale application.

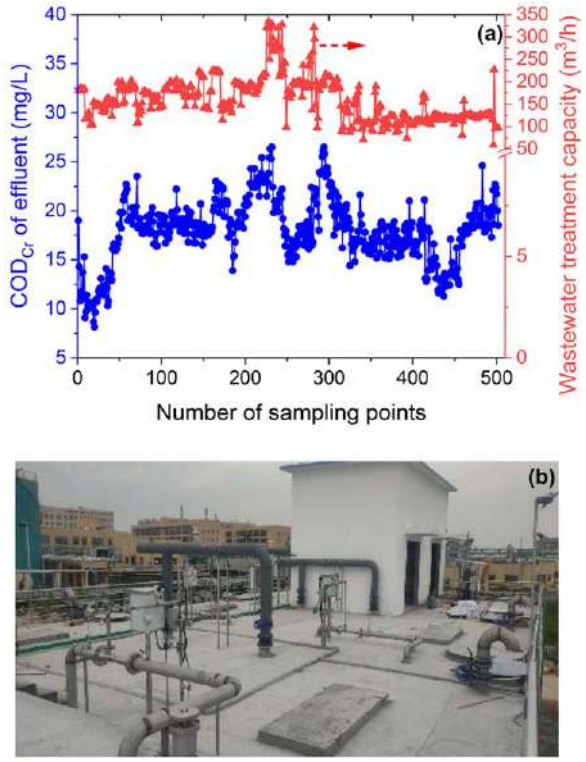

Figure 4.4 (a) Variations of COD_{Cr} of effluent and wastewater treatment capacity. (b) Full-scale application of ozonation of the wastewater from a fine chemical industry park in the presence of AC-supported iron oxide. Reaction conditions: ozone gas concentration: 30 mg L^{-1}; COD_{Cr} of influent: 35–40 mg L^{-1}; reaction time: 20 min.

Acknowledgements

The authors are very grateful to Dr. Xintao Li of Beijing OriginWater Technology Co., Ltd for providing the data and picture of a full-scale application of catalytic ozonation. The authors appreciate the work done by master student Chenxi Huang and undergraduate Shenglan Gong on the collection and classification of literature.

References

1. C. von Sonntag and U. von Gunten, *Chemistry of Ozone in Water and Wastewater Treatment: From Basic Principles to Applications*, IWA Publishing, London, 2012.
2. G. Yu, Y. Wang, H. Cao, H. Zhao and Y. Xie, *Environ. Sci. Technol.*, 2020, **54**, 5931–5946.
3. C. V. Rekhate and J. K. Srivastava, *Chem. Eng. J. Adv.*, 2020, **3**, 100031.
4. F. P. Logemann and J. H. J. Annee, *Water Sci. Technol.*, 1997, **35**, 353–360.

5. Z.-Q. Liu, B.-J. Han, G. Wen, J. Ma, S.-J. Wang, R.-G. Zha, L.-P. Shen and C. Wang, *J. Environ. Eng.*, 2014, **140**, A5013002.
6. J. P. Kaptijn, *Ozone: Sci. Eng.*, 1997, **19**, 297–305.
7. J. Wang and H. Chen, *Sci. Total Environ.*, 2020, **704**, 135249.
8. O. Rozas, C. Baeza, K. Nunez, A. Rossner, R. Urrutia and H. D. Mansilla, *Sci. Total Environ.*, 2017, **590–591**, 430–439.
9. H. Vatankhah, S. M. Riley, C. Murray, O. Quinones, K. X. Steirer, E. R. V. Dickenson and C. Bellona, *Chemosphere*, 2019, **234**, 845–854.
10. M. Alameddine, Z. T. How and M. Gamal El-Din, *Sci. Total Environ.*, 2021, **770**, 144679.
11. J. Nawrocki, *Appl. Catal., B*, 2013, **142–143**, 465–471.
12. G. Asgari, F. Samiee, M. Ahmadian, A. Poormohammadi and B. solimanzadeh, *Appl. Water Sci.*, 2017, **7**, 393–400.
13. M. Hadavifar, H. Younesi, A. A. Zinatizadeh, F. Mahdad, Q. Li and Z. Ghasemi, *J. Environ. Manage.*, 2016, **170**, 28–36.
14. Z.-Q. Liu, J. Ma and Y.-H. Cui, *Carbon*, 2008, **46**, 890–897.
15. Z.-Q. Liu, C. Huang, J.-Y. Li, J. Yang, B. Qu, S.-Q. Yang, Y.-H. Cui, Y. Yan, S. Sun and X. Wu, *J. Cleaner Prod.*, 2021, 124951.
16. P. M. Alvarez, J. P. Pocostales and F. J. Beltran, *J. Hazard. Mater.*, 2011, **185**, 776–783.
17. G. Moussavi, A. Alahabadi and K. Yaghmaeian, *Chem. Eng. Res. Des.*, 2015, **97**, 91–99.
18. F. J. Beltrán, J. F. García-Araya and I. Giráldez, *Appl. Catal., B*, 2006, **63**, 249–259.
19. I. Giráldez, J. F. García-Araya and F. J. Beltrán, *Ind. Eng. Chem. Res.*, 2007, **46**, 8241–8247.
20. C. Chen, L. Wei, X. Guo, S. Guo and G. Yan, *Fuel Proc. Technol.*, 2014, **124**, 165–173.
21. P. Jin, X. Jin, V. A. Bjerkelund, S. W. Osterhus, X. C. Wang and L. Yang, *Water Res.*, 2016, **88**, 643–652.
22. F. J. Beltran, P. Pocostales, P. Alvarez and A. L. Oropesa, *J. Hazard. Mater.*, 2009, **163**, 768–776.
23. K. Wei, Z. Wang, C. Ouyang, X. Cao, P. Liang, X. Huang and X. Zhang, *Water Res.*, 2020, **173**, 115536.
24. O. S. G. P. Soares, P. C. C. Faria, J. J. M. Órfão and M. F. R. Pereira, *Sep. Sci. Technol.*, 2007, **42**, 1477–1492.
25. J. Rivera-Utrilla and M. Sanchez-Polo, *Appl. Catal., B*, 2002, **39**, 319–329.
26. J. L. Figueiredo and M. F. R. Pereira, *Catal. Today*, 2010, **150**, 2–7.
27. L. Xing, Y. Xie, H. Cao, D. Minakata, Y. Zhang and J. C. Crittenden, *Chem. Eng. J.*, 2014, **245**, 71–79.
28. M. Sánchez-Polo, U. von Gunten and J. Rivera-Utrilla, *Water Res.*, 2005, **39**, 3189–3198.
29. H. Cao, L. Xing, G. Wu, Y. Xie, S. Shi, Y. Zhang, D. Minakata and J. C. Crittenden, *Appl. Catal., B*, 2014, **146**, 169–176.

30. P. M. Alvárez, J. F. García-Araya, F. J. Beltrán, I. Giráldez, J. Jaramillo and V. Gómez-Serrano, *Carbon*, 2006, **44**, 3102–3112.
31. J. Feng, B. Xing and H. Chen, *J. Environ. Manage.*, 2019, **237**, 114–118.
32. J. Nawrocki and L. Fijołek, *Appl. Catal., B*, 2013, **142–143**, 307–314.
33. M. Umar, F. Roddick and L. Fan, *Crit. Rev. Environ. Sci. Technol.*, 2014, **45**, 193–248.
34. Z.-Q. Liu, L. You, X. Xiong, Q. Wang, Y. Yan, J. Tu, Y.-H. Cui, X.-Y. Li, G. Wen and X. Wu, *Chemosphere*, 2019, **222**, 696–704.
35. G. G. Jayson, B. J. Parsons and A. J. Swallow, *J. Chem. Soc. Faraday Trans.*, 1973, **69**, 1597–1607.
36. H. F. Miao, M. Cao, D. Y. Xu, H. Y. Ren, M. X. Zhao, Z. X. Huang and W. Q. Ruan, *Chemosphere*, 2015, **119**, 326–333.
37. F. Fang and H. Han, *Ozone: Sci. Eng.*, 2018, **40**, 275–283.
38. Y. Yuan, G. Xing, S. Garg, J. Ma, X. Kong, P. Dai and T. D. Waite, *Water Res.*, 2020, **177**, 115785.
39. S. Bakht Shokouhi, R. Dehghanzadeh, H. Aslani and N. Shahmahdi, *J. Water Proc. Eng.*, 2020, **35**, 101188.
40. S. He, J. Li, J. Xu and L. Mo, *BioResources*, 2016, **11**, 8396–8408.
41. F. Zhang, K. Wu, H. Zhou, Y. Hu, P. Sergei, H. Wu and C. Wei, *J. Environ. Manage.*, 2018, **224**, 376–386.
42. C. X. Wen, H. Wang, L. C. Wang, Z. Y. Lou, Z. Y. Sun and Z. Zhou, *J. Clean. Prod.*, 2019, **240**, 118194.
43. S. Zhang, X. Quan, J.-F. Zheng and D. Wang, *Water Res.*, 2017, **122**, 86–95.
44. P. C. C. Faria, J. J. M. Órfão and M. F. R. Pereira, *Appl. Catal., B*, 2009, **88**, 341–350.
45. W. L. Wang, H. Y. Hu, X. Liu, H. X. Shi, T. H. Zhou, C. Wang, Z. Y. Huo and Q. Y. Wu, *Chemosphere*, 2019, **231**, 369–377.
46. S. Yuan, Z. Li and Y. Wang, *Electrochem. Commun.*, 2013, **29**, 48–51.
47. S. Liu, Y. Wang, B. Wang, J. Huang, S. Deng and G. Yu, *J. Cleaner Prod.*, 2017, **168**, 584–594.
48. X. Zhang, Y. Zhou, C. Zhao, Z. Sun, Z. Zhang, Z. A. Mirza, G. Saylor, J. Zhai and H. Zheng, *Chem. Eng. J.*, 2016, **304**, 129–133.
49. J. Zhan, Z. Li, G. Yu, X. Pan, J. Wang, W. Zhu, X. Han and Y. Wang, *Sep. Purif. Technol.*, 2019, **208**, 12–18.
50. T. Wang, Y. Song, H. Ding, Z. Liu, A. Baldwin, I. Wong, H. Li and C. Zhao, *Chem. Eng. J.*, 2020, **394**, 124852.
51. J. Ma, M.-H. Sui, Z.-L. Chen and L.-N. Wang, *Ozone: Sci. Eng.*, 2004, **26**, 3–10.
52. C. A. Orge, J. J. M. Órfão and M. F. R. Pereira, *Appl. Catal., B*, 2011, **102**, 539–546.
53. J. Feng, X. Zhang, J. Fu and H. Chen, *Catal. Commun.*, 2018, **110**, 28–32.
54. A. Gonçalves, J. Silvestre-Albero, E. V. Ramos-Fernández, J. C. Serrano-Ruiz, J. J. M. Órfão, A. Sepúlveda-Escribano and M. F. R. Pereira, *Appl. Catal., B*, 2012, **113–114**, 308–317.
55. L. Hao, D. Huiping and S. Jun, *J. Mol. Catal. A: Chem.*, 2012, **363**, 101–107.
56. A. G. Gonçalves, J. J. M. Órfão and M. F. R. Pereira, *J. Environ. Chem. Eng.*, 2013, **1**, 260–269.

57. A. G. Goncalves, J. J. Orfao and M. F. Pereira, *Environ. Technol.*, 2015, **36**, 776–785.
58. X. Xu, Z. Xia, L. Li, Q. Huang, C. He and J. Wang, *Molecules*, 2019, **24**, 4365.
59. Q. Dai, J. Wang, J. Chen and J. Chen, *Sep. Purif. Technol.*, 2014, **127**, 112–120.
60. Z.-Q. Liu, Y.-H. Cui, M.-Y. Wang, Y.-J. Zheng, Z.-X. Zhong, X.-H. Wu, Z. Wang and B.-P. Zhang, *Environ. Eng. Manage. J.*, 2016, **15**, 2231–2237.
61. J. Wang and Z. Bai, *Chem. Eng. J.*, 2017, **312**, 79–98.
62. W. Ling, Z. Qiang, Y. Shi, T. Zhang and B. Dong, *J. Mol. Catal. A: Chem.*, 2011, **342–343**, 23–29.
63. Y. Huang, C. Cui, D. Zhang, L. Li and D. Pan, *Chemosphere*, 2015, **119**, 295–301.
64. M. Ahmadi, B. Kakavandi, N. Jaafarzadeh and A. Akbar Babaei, *Sep. Purif. Technol.*, 2017, **177**, 293–303.
65. X. Li, W. Chen and L. Li, *Ozone: Sci. Eng.*, 2018, **40**, 448–456.
66. S. Deng, L. Jothinathan, Q. Cai, R. Li, M. Wu, S. L. Ong and J. Hu, *Water Res.*, 2021, **190**, 116687.
67. C. Chen, H. Chen, X. Guo, S. Guo and G. Yan, *J. Ind. Eng. Chem.*, 2014, **20**, 2782–2791.
68. J. Wu, H. Gao, S. Yao, L. Chen, Y. Gao and H. Zhang, *Sep. Purif. Technol.*, 2015, **147**, 179–185.
69. B. Kamarehie, A. Jafari, M. Ghaderpoori, M. Amin Karami, K. Mousavi and A. Ghaderpoury, *Chem. Eng. Commun.*, 2018, **206**, 898–908.
70. F. Fang and H. Han, *Ozone: Sci. Eng.*, 2018, **40**, 275–283.
71. C. Ferreiro, N. Villota, J. I. Lombraña and M. J. Rivero, *J. Cleaner Prod.*, 2019, **228**, 1282–1295.
72. S. Faleh, M. Guiza and A. Ouederni, *Ozone: Sci. Eng.*, 2018, **41**, 274–285.
73. A. Abdedayem, M. Guiza and A. Ouederni, *C. R. Chim*, 2015, **18**, 100–109.
74. C. Ferreiro, N. Villota, J. I. Lombraña and M. J. Rivero, *Water*, 2020, **12**, 3448.
75. N. Nasseh, F. S. Arghavan, S. Rodriguez-Couto, A. Hossein Panahi, M. Esmati and T. J. A-Musawi, *Adv. Powder Technol.*, 2020, **31**, 875–885.
76. J. Zhang, L. Liu, H. Shi, X. Li and X. Zhang, *Environ. Technol. Innovation*, 2020, **20**, 101165.
77. L. Zhou, S. Zhang, Z. Li, X. Liang, Z. Zhang, R. Liu and J. Yun, *J. Water Proc. Eng.*, 2020, **36**, 101168.
78. Y. J. Hou, J. Ma, Z. Z. Sun, Y. H. Yu and L. Zhao, *J. Environ. Sci.*, 2006, **18**, 1065–1072.
79. X. Lü, Q. Zhang, W. Yang, X. Li, L. Zeng and L. Li, *RSC Adv.*, 2015, **5**, 10537–10545.
80. C. Li, F. Jiang, D. Sun and B. Qiu, *Chem. Eng. J.*, 2017, **325**, 624–631.
81. Y. Liu, J. Jiang, J. Ma, Y. Yang, C. Luo, X. Huangfu and Z. Guo, *Water Res.*, 2015, **68**, 750–758.
82. J. Akhtar, N. S. Amin and A. Aris, *Chem. Eng. J.*, 2011, **170**, 136–144.
83. S. Tang, D. Yuan, Q. Zhang, Y. Liu, Q. Zhang, Z. Liu and H. Huang, *Environ. Sci. Pollut. Res. Int.*, 2016, **23**, 18800–18808.
84. Y. Yang, X. Shi, M. Zhao, S. Chu and J. Xiao, *Catalysts*, 2020, **10**, 1123.

85. S. Q. Tian, J. Y. Qi, Y. P. Wang, Y. L. Liu, L. Wang and J. Ma, *Water Res.*, 2021, **193**, 116860.
86. G. Wen, Z.-H. Pan, J. Ma, Z.-Q. Liu, L. Zhao and J.-J. Li, *J. Hazard. Mater.*, 2012, **239–240**, 381–388.
87. J. Xu, Y. Yu, K. Ding, Z. Liu, L. Wang and Y. Xu, *Water Sci. Technol.*, 2018, **77**, 1410–1417.
88. C. Chen, X. Yan, Y. Xu, B. A. Yoza, X. Wang, Y. Kou, H. Ye, Q. Wang and Q. X. Li, *Sci. Total Environ.*, 2019, **651**, 2631–2640.
89. G. Moussavi and R. Khosravi, *Bioresour. Technol.*, 2012, **119**, 66–71.
90. M. Sui, L. Sheng, K. Lu and F. Tian, *Appl. Catal., B*, 2010, **96**, 94–100.
91. J. Feng, Y. Yang, H. Chen and X. Zhang, *Water Sci. Technol.*, 2017, **2017**, 58–65.
92. H. Wang, L. Zhang, F. Qi, X. Wang, L. Li and L. Feng, *J. Nanosci. Nanotechnol.*, 2014, **14**, 7266–7271.
93. H. P. Boehm, *Carbon*, 1994, **32**, 759–769.
94. S. L. Goertzen, K. D. Thériault, A. M. Oickle, A. C. Tarasuk and H. A. Andreas, *Carbon*, 2010, **48**, 1252–1261.
95. A. M. Oickle, S. L. Goertzen, K. R. Hopper, Y. O. Abdalla and H. A. Andreas, *Carbon*, 2010, **48**, 3313–3322.
96. L. Tsechansky and E. R. Graber, *Carbon*, 2014, **66**, 730–733.
97. Y. Huang, Y. Sun, Z. Xu, M. Luo, C. Zhu and L. Li, *Sci. Total Environ.*, 2017, **575**, 50–57.
98. H. Zhuang, J. Guo and X. Hong, *Pol. J. Environ. Stud.*, 2018, **27**, 451–457.
99. Z. Luo, D. Wang, W. Zeng and J. Yang, *Sci. Total Environ.*, 2020, **734**, 139448.
100. S. Hou, S. Jia, J. Jia, Z. He, G. Li, Q. Zuo and H. Zhuang, *J. Environ. Manage.*, 2020, **267**, 110615.
101. H. Zhuang, H. Han, B. Hou, S. Jia and Q. Zhao, *Bioresour. Technol.*, 2014, **166**, 178–186.
102. S. Lu, Y. Liu, L. Feng, Z. Sun and L. Zhang, *Environ. Sci. Pollut. Res. Int.*, 2018, **25**, 5086–5094.
103. A. Abdedayem, M. Guiza, F. J. R. Toledo and A. Ouederni, *Sep. Purif. Technol.*, 2017, **184**, 308–318.
104. M. Sanchez-Polo, E. Salhi, J. Rivera-Utrilla and U. von Gunten, *Ozone: Sci. Eng.*, 2006, **28**, 237–245.
105. F. J. Beltrán, I. Giráldez and J. F. García-Araya, *Ind. Eng. Chem. Res.*, 2008, **47**, 1058–1065.
106. Y. Lee, D. Gerrity, M. Lee, A. E. Bogeat, E. Salhi, S. Gamage, R. A. Trenholm, E. C. Wert, S. A. Snyder and U. von Gunten, *Environ. Sci. Technol.*, 2013, **47**, 5872–5881.
107. U. Jans and J. Hoigné, *Ozone: Sci. Eng.*, 1998, **20**, 67–90.
108. J. Nawrocki and B. Kasprzyk-Hordern, *Appl. Catal., B*, 2010, **99**, 27–42.
109. R. Flyunt, A. Leitzke, G. Mark, E. Mvula, E. Reisz, R. Schick and C. von Sonntag, *J. Phys. Chem. B*, 2003, **107**, 7242–7253.
110. Y. Wang, X. Duan, Y. Xie, H. Sun and S. Wang, *ACS Catal.*, 2020, **10**, 13383–13414.
111. E. Mvula and C. von Sonntag, *Org. Biomol. Chem.*, 2003, **1**, 1749–1756.

112. Y. Guo, Y. Zhang, G. Yu and Y. Wang, *Appl. Catal., B*, 2021, **280**, 119418.
113. J. Lee, U. von Gunten and J. H. Kim, *Environ. Sci. Technol.*, 2020, **54**, 3064–3081.
114. J. Hoigné and H. Bader, *Water Res.*, 1983, **17**, 173–183.
115. B. Ervens, S. Gligorovski and H. Herrmann, *Phys. Chem. Chem. Phys.*, 2003, **5**, 1811–1824.
116. K. Sehested, H. Corfitzen, J. Holcman and E. J. Hart, *J. Phys. Chem. A*, 1998, **102**, 2667–2672.
117. I. Fábián, *Pure Appl. Chem.*, 2006, **78**, 1559–1570.
118. E. Ahumada, H. Lizama, F. Orellana, C. Suárez, A. Huidobro, A. Sepúlveda-Escribano and F. Rodríguez-Reinoso, *Carbon*, 2002, **40**, 2827–2834.
119. Y. Pi, J. Schumacher and M. Jekel, *Water Res.*, 2005, **39**, 83–88.
120. L. Fijołek, A. Malaika, W. Biernacki and J. Nawrocki, *Ozone: Sci. Eng.*, 2018, **41**, 128–136.
121. S. Zhang, X. Quan and D. Wang, *Environ. Sci. Technol.*, 2018, **52**, 8701–8711.
122. W. Biernacki, L. Fijołek and J. Nawrocki, *Ozone: Sci. Eng.*, 2018, **41**, 296–311.
123. G. I. Razdyakonova, O. A. Kokhanovskaya and V. A. Likholobov, *Radioelectron. Nanosyst. Inf. Technol.*, 2015, **7**, 180–190.
124. S. P. Ghuge and A. K. Saroha, *J. Environ. Manage.*, 2018, **211**, 83–102.
125. S.-J. Yuan and X.-H. Dai, *Environ. Sci.:Nano*, 2017, **4**, 17–26.
126. F. J. Beltran, F. J. Rivas, L. A. Fernandez, P. M. Alvarez and R. Montero-de-Espinosa, *Ind. Eng. Chem. Res.*, 2002, **41**, 6510–6517.
127. Z.-Q. Liu, J. Ma, Y.-H. Cui and B.-P. Zhang, *Appl. Catal., B*, 2009, **92**, 301–306.
128. P. C. C. Faria, J. J. M. Órfão and M. F. R. Pereira, *Appl. Catal., B*, 2008, **79**, 237–243.
129. L. Gu, X. Zhang and L. Lei, *Ind. Eng. Chem. Res.*, 2008, **47**, 6809–6815.
130. L. Xing, Y. Xie, D. Minakata, H. Cao, J. Xiao, Y. Zhang and J. C. Crittenden, *J. Environ. Sci.*, 2014, **26**, 2095–2105.
131. T. Chen, W. Gu, G. Li, Q. Wang, P. Liang, X. Zhang and X. Huang, *Front. Environ. Sci. Eng.*, 2017, **12**, 6.
132. Z.-Q. Liu, J. Ma, Y.-H. Cui, L. Zhao and B.-P. Zhang, *Appl. Catal., B*, 2010, **101**, 74–80.
133. W. Li, Z. Qiang, T. Zhang and F. Cao, *Appl. Catal., B*, 2012, **113–114**, 290–295.
134. Z.-Q. Liu, J. Ma, Y.-H. Cui, L. Zhao and B.-P. Zhang, *Sep. Purif. Technol.*, 2011, **78**, 147–153.
135. Z.-Q. Liu, J. Tu, Q. Wang, Y.-H. Cui, L. Zhang, X. Wu, B. Zhang and J. Ma, *Sep. Purif. Technol.*, 2018, **200**, 51–58.
136. M. S. Elovitz and U. von Gunten, *Ozone: Sci. Eng.*, 1999, **21**, 239–260.
137. J. Yang, J. Li, W. Dong, J. Ma, T. Li, Y. Yang, J. Li and J. Gu, *Chem. Eng. J.*, 2016, **295**, 443–450.
138. Y. Guo, J. Zhan, G. Yu and Y. Wang, *Water Res.*, 2021, 116927.
139. L. Radovic, C. Moreno-Castilla and J. Rivera-Utrilla, *Carbon Materials as Adsorbents in Aqueous Solutions* Dekker, Inc., New York, 2001.

CHAPTER 5

Catalytic Ozonation over Nanocarbon Materials

YA LIU[a,b] AND YUXIAN WANG*[a]

[a] State Key Laboratory of Heavy Oil Processing, State Key Laboratory of Petroleum Pollution Control, China University of Petroleum–Beijing, Beijing 102249, China; [b] School of Chemical Engineering and Advanced Materials, The University of Adelaide, Adelaide, SA 5005, Australia
*Email: yuxian.wang@cup.edu.cn

5.1 Introduction

Thanks to their highly active and environmentally benign nature and in the interest of avoiding the secondary contamination by toxic metal leaching, carbonaceous materials, especially the nanocarbons, have been developed as promising alternatives to conventional transition/noble metals and oxides in the past two decades.[1] In recent years, fruitful contributions have been made to metal-free purification systems, especially for catalytic ozonation in advanced material design, mechanistic investigation, theoretical computations and applications in practical water treatment.[2–4] Additionally, breakthroughs in carbon structure and surface functionalities and their correlations to catalytic ozonation, as well as advances in the fundamental understanding of materials properties and catalytic mechanism, have been achieved. Nevertheless, the bottlenecks are the economical production of high-performance nanocarbons with robust structures and the improved utilization efficiency of ozone.

In this chapter, we showcase the road map of the development of reaction-oriented nanocarbons, unraveling the intrinsic active sites in carbocatalytic

Chemistry in the Environment Series No. 8
Advanced Ozonation Processes for Water and Wastewater Treatment: Active Catalysts and Combined Technologies
Edited by Hongbin Cao, Yongbing Xie, Yuxian Wang and Jiadong Xiao

Published by the Royal Society of Chemistry, www.rsc.org

ozonation, the identification of reactive oxygen species (ROS), reaction intermediates and reaction pathways. Additionally, critical issues and future directions are proposed in the implementation of nanocarbon-catalyzed ozonation for real-world wastewater treatment.

5.2 Carbon Nanotube-based Metal-free Nanocarbons

Carbon nanotubes (CNTs) are one-dimensional carbon nanomaterials and can be regarded as a single piece of graphene rolled up to form a tubular structure. According to the number of carbon nanotube layers, they can be classified as single-wall carbon nanotubes (SWCNTs) and multiwall carbon nanotubes (MWCNTs), as shown in Figure 5.1. MWCNTs are formed by two or more SWCNTs with different diameters surrounding the same hollow shaft, and the distance between two adjacent lattices is about 0.34 nm. The mesoporous structure of CNTs with a large external specific surface area (SSA) facilitates the dispersion of the active components on the catalyst, helps reduce the influence of the mass transfer and diffusion of the reactants in the liquid phase and promotes the interaction between the organic matter and the catalyst, thereby contributing to the improvement of catalyst activity. In recent years, CNTs as well as their surface-engineered derivatives have been widely used as heterogeneous catalysts to catalyze ozonation in aqueous solutions to degrade organic pollutants.

Catalytic activities of CNTs can be significantly influenced by their surface chemistries. Previous studies reported that O_3 oxidation will induce certain changes in the number and types of oxygen-containing functional groups on the surface of nanocarbons, thus altering the physical and chemical properties of CNTs, which in turn affect their catalytic activities. Based on this consideration, Liu *et al.* studied the effect of ozonation pretreatment on the surface properties of MWCNTs and explored its effect on the catalytic activity of MWCNTs with oxalic acid as the target organic pollutant.[5] Based on the Boehm titration results, it can be found that with the increase of O_3 oxidation pretreatment time, the number of basic functional groups on the surface of MWCNTs continues to decrease, while the number of acidic functional groups increases rapidly. In addition, after ozonation pretreatment, the SSA and mesoporous volume of MWCNTs increased slightly.

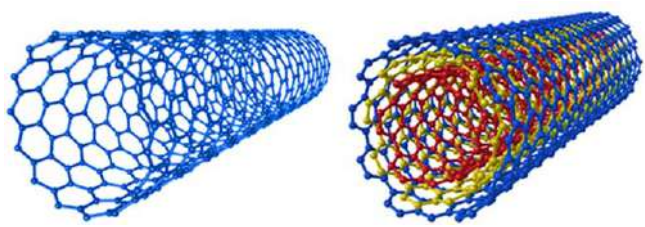

Figure 5.1 Schematic illustration of SWCNTs (left) and MWCNTs (right) structure.

Compared with untreated MWCNTs, the catalytic activity of MWCNTs was significantly reduced after O_3 oxidation pretreatment. And the catalytic activity of MWCNTs decreases with the increase of O_3 pretreatment time. This is consistent with the changing trend of the treated MWCNT surface groups (Table 5.1). Therefore, the loss of MWCNT activity after ozonation pretreatment is mainly due to the increase of acidic functional groups and the decrease of basic functional groups. The mechanism of catalytic ozonation using the O_3-treated MWCNTs was further explored by the quenching tests with *tert*-butanol (TBA) as the quenching agent. The addition of TBA reduced the removal rate of oxalic acid (OA); however, it did not fully quench the reaction. Meanwhile, a trivial effect on OA adsorption on the surface of MWCNTs with the addition of TBA was observed. Based on these results, it was suggested that a $^{\bullet}OH$-based free radical mechanism, involving both surface reactions on MWCNTs and reactions in the aqueous bulk, was responsible for OA degradation, as schematically shown in Figure 5.2.

In a subsequent study, Liu *et al.* further investigated the influence of heat treatment temperature and atmosphere on catalytic ozonation activities of MWCNTs by annealing them in N_2 and H_2 at different temperatures.[6] Table 5.2 summarizes the changes in the physical and chemical properties of the MWCNT surface after different pretreatments. After HNO_3 pretreatment, the pH point of zero charge (pH_{pzc}) of the MWCNTs decreased significantly. This was due to the decrease of basic functional groups on the surface of MWCNTs and the increase of acidic functional groups (lactone, phenol, carboxyl). Compared with MWCNT-HNO_3, under N_2 or H_2 atmosphere heat treatment, the number of acidic functional groups on the MWCNT surface was significantly reduced, and the number of basic functional groups was significantly increased, resulting in a significant increase in the pH_{pzc} of the treated MWCNTs.

For catalytic ozonation activities, MWCNTs treated with a higher heat treatment temperature (950 °C) exhibited higher catalytic activities. And the H_2-treated MWCNTs showed higher activities than the N_2-treated ones. Further analysis found that the pH_{pzc} of MWCNTs had a linear relationship with the rate constant of OA degradation. It was proposed that the reducing property of H_2 decreased the population of acidic groups on MWCNTs and increased the basic properties and thus enhanced the activity. Therefore, a higher number of the basic groups on the surface of MWCNTs induced a

Table 5.1 Influence of MWCNTs ozonation pretreatment time on its physical and chemical properties. Reproduced from ref. 5 with permission from Elsevier, Copyright 2009.

Sample	S_{BET} ($m^2 g^{-1}$)	Acidity ($\mu mol\, g^{-1}$)			Basicity ($\mu mol\, g^{-1}$)	pH_{pzc}
		Carboxyl	Lactone	Phenol		
Untreated	117.5	70	14	37	163	6.1
O_3 (10 min)	125.1	196	67	39	70	3.9
O_3 (120 min)	129.2	238	98	61	29	3.6

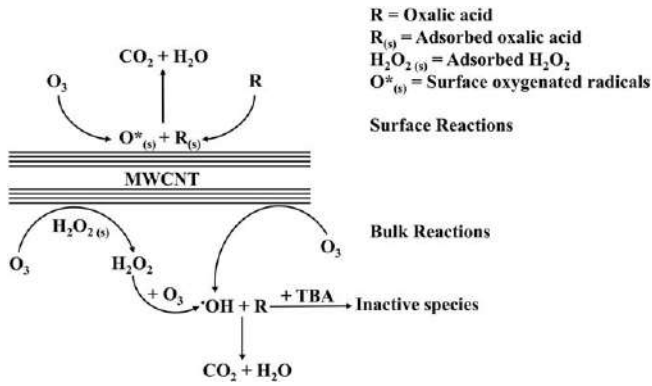

Figure 5.2 The clearer version of the image is provided. acid in aqueous solution. Reproduced from ref. 5 with permission from Elsevier, Copyright 2009.

Table 5.2 Physical and chemical properties of CNTs under different pretreatment methods. Reproduced from ref. 6 with permission from Elsevier, Copyright 2010.

Sample	S_{BET} ($m^2 g^{-1}$)	Acidity ($\mu mol\ g^{-1}$)			Basicity ($\mu mol\ g^{-1}$)	pH_{pzc}
		Carboxyl	Lactone	Phenol		
Commercial MWCNTs	118	70	14	37	163	6.1
MWCNT-HNO_3	125	307	91	63	14	2.9
MWCNT-N_2-450	123	—	19	56	87	6.2
MWCNT-N_2-950	119	—	—	—	193	8.9
MWCNT-H_2-450	121	—	—	34	111	7.4
MWCNT-H_2-950	115	—	—	—	208	9.2

greater pH_{pzc} value, which promoted the catalytic ozonation activity. Goncalves *et al.* also reported similar results, *i.e.* the low acidic nature of the MWCNTs promoted the catalytic ozonation process of degradation of aliphatic acids.[7]

However, contradictory results have been reported by Qu *et al.*[8] and Oulton *et al.*[9] Qu *et al.* functionalized CNTs with different contents of carboxylic groups and reported that a higher number of carboxylic groups on the surface of CNTs resulted in greater catalytic ozonation activity for indigo decolorization.[8] Oulton further synthesized a CNTs/ceramic membrane filter and evaluated its catalytic ozonation activity for the removal of several ozone recalcitrant species, such as *para*-chlorobenzoic acid, atrazine and ibuprofen,[9] and reported that the surface oxygen functionalities resulted from the HNO_3 treatment are the potential active sites for O_3 decomposition and $^{\bullet}OH$ formation.

Heteroatom doping in the carbon framework can significantly enhance the catalytic activity of nanocarbons. Introduction of heteroatoms such as N, P and B into the carbon framework redistributes the charge density around the doping elements and results in the changes in sp^2 carbon band structure

because of the difference in electronegativity. On the other hand, heteroatom doping will change the Fermi energy level on the surface of the material, improve the electron transfer efficiency and enhance the catalytic activity and stability of the carbon materials. Restivo *et al.* synthesized N-, S-, and O-doped CNTs by chemical and thermal treatments and evaluated their catalytic ozonation activities for OA removal (Figure 5.3).[10] In this study, it is reported that thermal annealed N-doped CNTs utilizing urea as the precursor obtained a greater catalytic activity than the untreated CNTs, while the CNTs treated by other methods, such as CNT-N by HNO_3 boiling and CNT-S by concentrated H_2SO_4, exhibited inferior activities to the untreated CNTs. The authors proposed that these modification methods introduced a redundant number of acidic surface groups on the surface of CNTs, which were detrimental to the adsorption and decomposition of O_3 necessary to generate the highly effective ROS.

Soares *et al.* further used melamine and urea as nitrogen precursors to synthesize N-doped CNTs by ball milling and evaluated the influence of ball milling methods (dry and wet) on catalytic ozonation activities of the N-doped CNTs.[11] XPS results suggested that different nitrogen contents (0.2%–4.8%) were doped on the surface of CNTs, and the samples were prepared with melamine as the precursor obtained higher nitrogen contents than the samples prepared with urea. Moreover, all of the as-synthesized samples obtained nearly neutral pH_{pzc} (6.4–6.8). For catalytic ozonation activities, CNTs (CNT-BM-M-DT) prepared by dry treatment with melamine

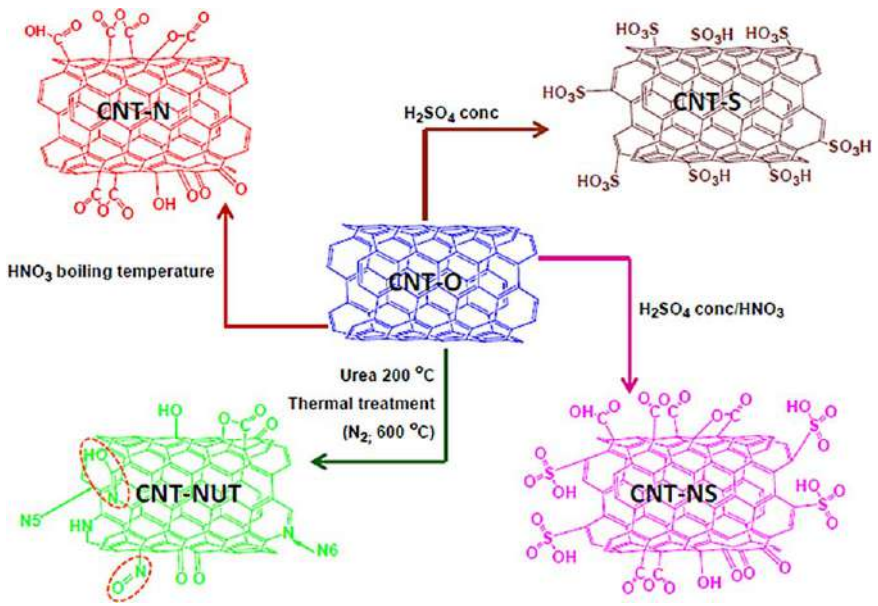

Figure 5.3 Schematic illustration of carbon nanotubes functionalized with O-, S-, and N-containing surface groups. Reproduced from ref. 10 with permission from Elsevier, Copyright 2014.

displayed a higher removal rate of OA than the ball-milled CNTs (CNT-BM) sample. This indicates that N-containing functional groups on the surface of CNTs introduced by dry treatment ball milling improved the catalytic ozonation activity. In addition, the effect of heat treatment at 600 °C after ball milling treatment on catalyst performance was also investigated. Under this heat temperature, the melamine-induced N-containing functional groups were removed. As expected, the catalytic activity of the CNTs without heat treatment (CNT-BM-M-DT-w/oTT) was lower than the untreated sample.[12] This further proves that the N-containing functional groups introduced on the CNTs through the decomposition of melamine during the heat treatment at 600 °C played an important role in the catalytic ozonation and degradation of OA.

Fluorine (F) is the most negatively charged element with an electronegativity of 3.98, which is much higher than N (3.04) and O (3.44). Compared with N- or O-doping, F-doping can generate a relatively high positive charge density on adjacent C atoms because of the strong electron-withdrawing ability of F, which further accelerates ozone activation. Wang *et al.* used HF as the precursor of F and synthesized F-CNTs with different F contents.[13]

The effect of F-CNTs with the same F content in catalytic ozonation and degradation of OA is shown in Figure 5.4(a). F-doped CNTs demonstrated a better catalytic ozonation activity than non-F-doped CNTs, and F-CNTs-0.45 that were synthesized with the HF concentration of 0.45 M obtained the highest activity. Additionally, synthesized F-CNTs-0.45 achieved a superior catalytic ozonation activity to most of the prevailing metal-based catalytic ozonation materials (Figure 5.4(b)). It should be noted that with the increase of F content, the catalytic activity of F-CNTs first increased and then decreased, which may be related to the interdependence between catalytic performance and the dispersibility of F-CNTs in the aqueous medium. The dispersibility of the catalyst can play a vital role in the liquid-phase catalysis

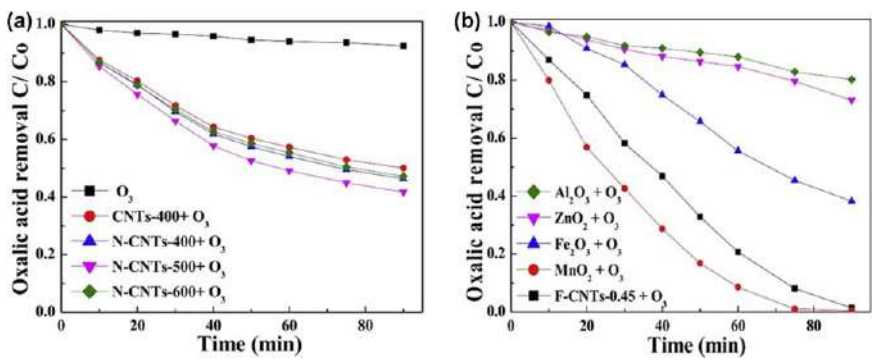

Figure 5.4 The effect of (a) F-CNTs with different F content and (b) various metal-based catalysts on the catalytic ozonation degradation of oxalic acid. Reaction conditions: initial pH: 2.8; initial concentration of oxalic acid: 2 mmol L^{-1}; ozone concentration: 4 mg min^{-1}; catalyst dosage: 0.05 g L^{-1}. Reproduced from ref. 13 with permission from Elsevier, Copyright 2018.

process, which dominates the mass transfer process. The dispersibility of F-doped CNTs is worse than that of the original CNTs because of the hydrophobicity of the C–F bond. Therefore, it is necessary to synthesize F-CNT catalysts with high dispersibility to further improve the catalytic activity.

In this study, electron paramagnetic resonance (EPR) experiments were further carried out with 5-*tert*-butoxycarbonyl-5-methyl-1-pyrroline-*N*-oxide (BMPO) and 2,2,6,6-tetramethyl-4-piperidone hydrochloride (TEMP) as free radical spin trapping agents to investigate the ROS generated in the catalytic ozonation process. The results suggested that $^{\bullet}O_2^-$ and $^1O_2$ are the main ROS in the process of catalytic ozonation and degradation of OA and that the doping of F can promote the generation of $^{\bullet}O_2^-$. XPS analysis revealed that, compared with the original F-CNTs, the content of carbonyl groups (C=O) in the used F-CNTs decreased from 4.5% to 3.2%, while the carboxyl group (–C=O) content increased from 1.7% to 6.6%. In addition, compared with the original F-CNTs-0.45, the pH_{pzc} of the used F-CNTs-0.45 is slightly lower, which is consistent with its catalytic performance for O_3. These results indicate that the surface acid-base groups of carbon materials may play an important role in the catalytic ozonation process. However, the pH_{pzc} of the F-doped CNTs was quite similar to those of the undoped CNTs, so more critical factors might be dominating catalytic activity. Changes in the surface electronic properties of carbon nanotubes caused by F-doping might also play a crucial role in their catalytic properties. Compared with the original F-CNTs-0.45, the content of sp^2 C–C and delocalized π system in the used F-CNTs-0.45 was significantly reduced. Therefore, the delocalized π system in F-CNTs could be the predominant active sites since the delocalized π electrons within the graphene basal plane are closely related to the electron transfer ability of the catalyst.

5.3 Graphene-based Metal-free Nanocarbons

Graphene is a two-dimensional carbon nanomaterial with a periodic honeycomb lattice structure formed by a single layer of carbon atoms with sp^2 hybrid orbitals.[14] The carbon atoms in graphene form a fairly strong σ bond with adjacent carbon atoms, while the remaining unbonded p-orbital electrons form delocalized π bonds across the entire layer in a perpendicular direction to the graphene plane. π electrons can move freely in the plane, endowing graphene with good electrical conductivity. In addition, graphene with high SSA facilitates the adsorption of substances and the exposure of catalytic active sites. Therefore, graphene and graphene-based materials are environmentally friendly alternatives to the metal-based materials as wastewater treatment and environmental remediation catalysts.

In terms of environmental remediation, graphene-based materials are also widely used in the fields of persulfate catalysis, photocatalysis, electrocatalysis and catalytic ozonation, showing excellent catalytic activity for organics removal.[15–17] Not only does graphene completely avoid the secondary pollution problem caused by the dissolution of metal ions, but also the surface

defect sites and oxygen-containing functional groups in graphene can be acted as active sites to catalyze the decomposition of oxides into highly active oxidation species. Meanwhile, the doping of non-metallic heteroatoms in the graphene structure can further improve catalytic performance and stability. However, the synthesis cost of highly active graphene-based nanocarbon materials is relatively high, the synthesis steps are complicated and the yield is low. It is of great significance to seek a simple, economical and efficient method for the synthesis of nanocarbides.

Oxidation of graphite is one of the most effective methods to achieve large-scale production of graphene. However, chemical groups such as carboxyl (–COOH), hydroxyl (–OH), carbonyl (–C=O) and epoxy (C–O–C) will be introduced. The presence of these groups alters the bonding mode between carbon atoms, leading to a dramatic decline in the conductivity of graphene and thus affecting the excellent properties of graphene.[18] Therefore, in order to obtain better physical and chemical properties, graphene oxide (GO) needs to be reduced, and the product obtained after reduction is reduced graphene oxide (rGO). During the pyrolysis process, the oxygen-containing functional groups will volatilize and escape as the pyrolysis temperature rises, thereby peeling off the stacked graphite flakes to restore the 2D morphology and corresponding physical and chemical properties. In addition, due to the exfoliation of graphite flakes, the SSA and pore volume of rGO also increase significantly *via* thermal reduction, which is conducive to the adsorption of substances and the improvement of catalytic activity. Therefore, rGO is widely used in the research of catalytic ozonation.

In recent years, our group performed a series of studies on rGO-based nanocarbons with different reduction methods. Moreover, the catalytic ozonation mechanism, as well as the generated ROS for the degradation of organic contaminants, has been elucidated. In a pioneer study, rGO was obtained by the thermal reduction of GO, which was synthesized *via* the modified Hummers method from commercially obtained graphite.[19] In this study, rGO that was annealed in the air at 300 °C was denoted as rGO-300, while rGO heated in and N_2 atmosphere at 700 °C was labeled as rGO-700. SEM observations suggested that the removal of oxygen-containing functional groups on the surface of rGO resulted in the exfoliation of graphene oxide nanosheets compared with GO. GO had a wrinkled and silk-like structure, while rGO exhibited highly exfoliated graphene nanosheets. At the same time, some aggregated and wrinkled structures were observed at the ends of rGO nanosheets since the samples produced more defect sites after heat treatment at higher temperatures.[20]

The exfoliation of GO nanosheets increased the SSA of the sample. After thermal reduction, the functional groups on the surface of the sample disappeared, and the BET surface area of rGO-300 and rGO-700 increased from 40.3 to 305.4 and 265.4 $m^2 g^{-1}$, respectively. In addition, the heat treatment also increased the total pore volume and average pore diameter of the sample. The I_D/I_G value in Raman spectroscopy is typically used to reflect the degree of graphitization of carbon materials.[21] After thermal reduction,

the I_D/I_G values of rGO-300 and GO did not change much (0.84 *versus* 0.86), indicating that low-temperature thermal reduction in the air will not produce more defect sites on the graphene layer. The I_D/I_G value of rGO-700 was calculated to be 0.98, indicating that more defect sites were formed on the partially aggregated edge.

In a *para*-hydroxylbenzoic acid (PHBA) solution with an initial pH of 3.5, the catalytic ozonation performance of graphene was investigated. Although rGO-300 and rGO-700 had larger SSA, the adsorption of PHBA was negligible. The pH_{pzc} of rGO-300 and rGO-700 were 4.7 and 4.9, respectively, indicating that they were positively charged in a solution with a pH of 3.5. PHBA has a pK_a value of 4.85, which mainly exists in the form of molecules in the solution. Therefore, the catalysts had low physical adsorption capacities for PHBA. rGO-300 and rGO-700 obtained similar catalytic activities in PHBA removal and completely degraded PHBA within 30 min, and the removal rates of total organic carbon (TOC) were significantly increased from 25% to 95%, which indicated that rGO could effectively activate ozone molecules to produce active species. Although rGO-700 obtained a higher defective level than rGO-300, it had a smaller number of oxygen-containing groups than rGO-300. The comparable catalytic activity of rGO-300 and rGO-700 might be caused by both defect sites and oxygen-containing groups.[20,22]

Apart from thermal reduction, we also investigated the effect of microwave reduction on the catalytic activity of rGO, and the sample synthesized by microwave reduction was denoted as MWI-rGO. To compare, Argon-rGO was synthesized under Ar annealing at 700 °C. From the SEM images (Figure 5.5), MWI-rGO obtained a greater exfoliation level. Moreover, the SSA of MWI-rGO was higher than that of Argon-rGO (734 and 654 $m^2 g^{-1}$). This is because the microwave method can generate higher heat instantaneously, resulting in a greater degree of exfoliation of the graphite sheet. In addition, the pore volume of MWI-rGO was also larger than that of argon-rGO (5.05 and 4.81 $cm^3 g^{-1}$). XPS results also showed that there was less residual oxygen on the rGO after microwave treatment, which further proved that microwave reduction would lead to better peeling of GO and produce abundant bare edges.

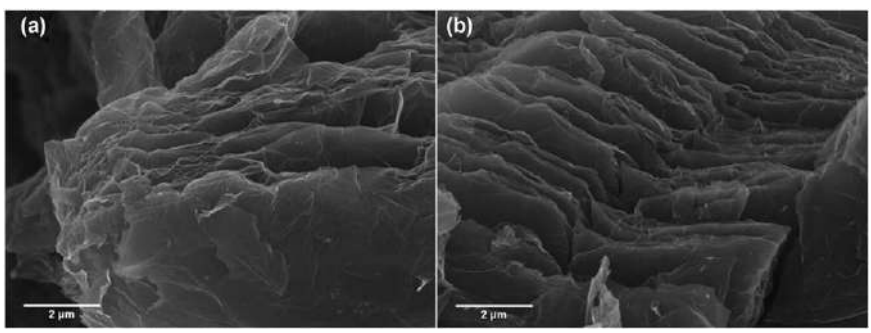

Figure 5.5 The SEM images of (a) Argon-rGO and (b) MWI-rGO. Reproduced from ref. 23 with permission from Elsevier, Copyright 2019.

This work investigated the catalytic performance of these graphene-based catalysts by evaluating their catalytic ozonation activities for both 4-nitrophenol (4-NP) and OA degradation. For both MWI-rGO and Argon-rGO, 4-NP was completely degraded within 20 min with more than 80% of TOC mineralization within 60 min. MWI-rGO demonstrated a higher degradation efficiency and TOC mineralization rate for 4-NP than argon-rGO. Similar trends were observed when OA was used as the target pollutant, further indicating that microwave reduction was more effective than high-temperature pyrolysis. EPR combined with Raman observations found that microwave pyrolysis formed more structural defect sites, such as armchair and zigzag edges. These defects had delocalized electrons and dangling bonds, which were beneficial to adjust the surface reactivity of the adsorbed reactants, thereby improving the catalytic potential of ozone decomposition into ROS.

In a subsequent study, we further employed graphite that was obtained from the anode of waste lithium-ion battery (LIB) as the precursor to synthesized GO.[24] And three kinds of rGO samples were prepared by the thermal reduction method, chemical reduction method[25] and hydrothermal method,[15] labeled as LIB-rGO, LIB-rGO-C and LIB-rGO-H, respectively. Commercial graphite was also used as the carbon precursor, and the same preparation process as LIB-rGO was used, denoted as C-rGO. The Raman spectra showed that the I_D/I_G ratios of LIB-rGO, LIB-rGO-C and LIB-rGO-H were 0.93, 1.05 and 1.25, respectively. Therefore, the degree of defects of these three materials was LIB-rGO-H > LIB-rGO-C > LIB-rGO. By comparing the catalytic ozonation activity of these three materials, it was found that the degree of defects directly affected the catalytic activity. More defect sites resulted in the better catalytic activity (Figure 5.6). LIB-rGO-H had higher defect sites and SSA than LIB-rGO, and its first-order reaction rate constant was higher. Therefore, this work preliminarily indicated that structural defects (vacancies and defect edges) on rGO were the main active sites for ozone activation.

Doping of metal-free heteroatoms can improve the electrochemical catalytic activity, hydrophilicity and selectivity of carbon materials.[26,27] In the field of environmental remediation, Sun *et al.* found that doping nitrogen atoms into rGO and carbon nanotubes could significantly improve the adsorption capacity and catalytic activity of persulfate.[28,29] Yin *et al.* synthesized N-doped rGO (NGO) and P-doped rGO (PGO) utilizing GO as the carbon precursor.[30] Ammonium nitrate and ammonium dihydrogen phosphate were employed as nitrogen and phosphorus precursors, respectively. The catalytic ozonation activities of the as-synthesized samples were evaluated by measuring the sulfamethoxazole (SMX) degradation rates. In order to explore the effect of heteroatom doping on the structure and properties of rGO, Raman spectroscopy was used to characterize the defects and disorder of carbon materials. The higher D band intensity achieved by rGO, NGO and PGO suggested the increased disorder level with N- and P-doping. The corresponding I_D/I_G of rGO, NGO and PGO was 0.868, 0.987, and 0.898, respectively. XPS results revealed that pyrrole N was the main N species

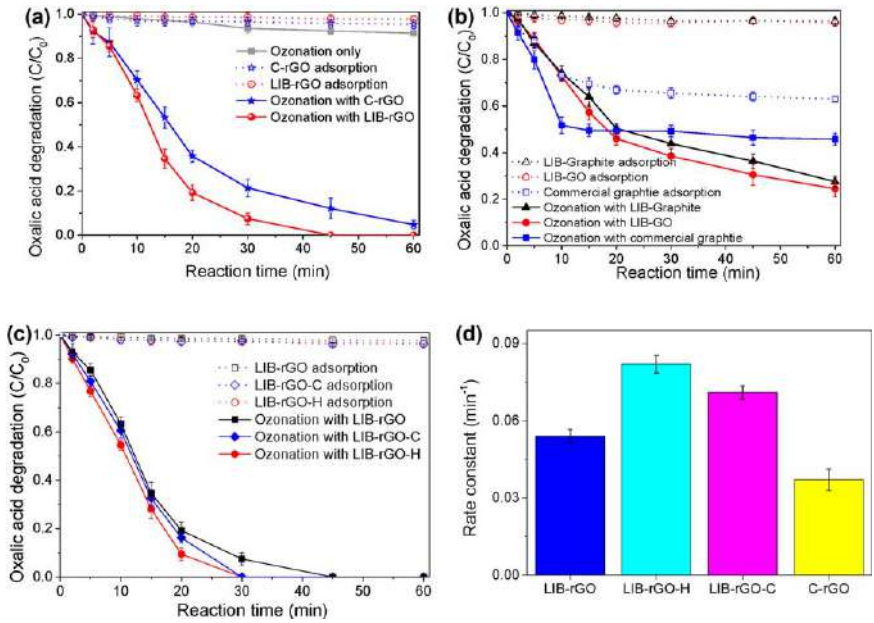

Figure 5.6 (a) OA removal in ozonation, adsorption and catalytic ozonation with different materials. (b) OA adsorption and degradation over different LIB-rGO materials. (c) OA adsorption and degradation over various materials. (d) Reaction rate constant for LIB-rGO made from different methods in OA degradation. Reaction conditions: $[OA]_0$: 50 mg L^{-1}; catalyst loading: 0.1 g L^{-1}; ozone flow rate: 100 mL min^{-1}; ozone concentration: 50 mg L^{-1}; temperature: 25 °C; initial pH: 3.0. Reproduced from ref. 24 with permission from Elsevier, Copyright 2019.

within the NGO structure. PGO obtained a higher P-doping content (9.86%), mainly in the form of P–O bonds.

For catalytic ozonation activities, the degradation rates of SMX after 5 min of treatment by using rGO, NGO and PGO were 83%, 95% and 99%, respectively. It showed that NGO and PGO had higher catalytic ozonation activity than rGO. It was speculated that the doped N and P atoms with lone pairs of electrons destroyed the original sp^2 carbon structure and generated more defect sites. The promoted adsorption of O_3 molecules and the electron transfer between the graphene basal plane and the adsorbed O_3 significantly improved the efficiency of the catalytic ozonation process.

Song *et al.* evaluated the catalytic ozonation efficiency of nitrogen-doped, phosphorus-doped, boron-doped and sulfur-doped rGO (N-, P-, B-, S-rGO) for the degradation of benzotriazole (BZA) and *p*-chlorobenzoic acid (PCBA).[31] Moreover, the catalytic active sites and ROS of the process were systematically analyzed. In this study, GO was synthesized by the Hummers method, and N-, P-, B- and S-rGO were synthesized through further thermal annealing using melamine, phosphoric acid, boric acid and anhydrous sodium sulfate as the N, P, B, and S precursors, respectively. rGO obtained the

largest SSA (273.3 $m^2 g^{-1}$) and pore volume (0.83 $cm^3 g^{-1}$). Doping of heteroatoms reduced the SSA of rGO, which might be due to the stacking of graphitic layers after doping. Among the doped rGO, N-rGO had the highest SSA (136.2 $m^2 g^{-1}$). N-rGO, P-rGO and B-rGO exhibited excellent performance in the catalytic ozonation of BZA and PCBA. The calculated k_{obs} showed that the order of catalytic activity was N-rGO > P-rGO > B-rGO > rGO > S-rGO. N-, P- and B-doping significantly improved the catalytic ozonation activity of rGO; however, S-doped exerted an adverse effect. It was speculated that integrating S atoms within the graphene basal plane destroyed the stability of graphene during ozonation, with the observed partial performance improvement caused by surface adsorption.

By conducting the quantitative structure–activity relationship (QSAR) analysis, the potential active sites on the doped rGO for catalytic ozonation were proposed. It was suggested that surface oxygen functionalities, the doped metal-free heteroatoms, and the delocalized π electrons within the sp^2 graphene lattice were catalytically active for O_3 adsorption and decomposition. Among these active sites, the electron transfer mechanism induced by the free electrons on the doped rGO was the predominant step for O_3 activation. The detailed mechanism is schematically illustrated in Figure 5.7.

5.4 Other Types of Metal-free Nanocarbons

Nanocarbons have been proved to be catalytically active in energy conversion, electrochemical applications and environmental remediations. However, their synthesis is often cost-intensive, complicated and low-yield,

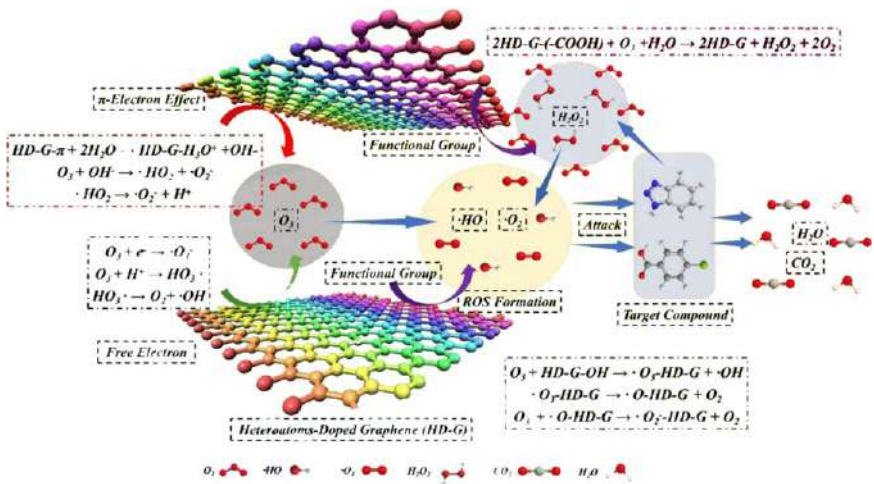

Figure 5.7 Schematic illustration of O_3 activation mechanisms using metal-free-doped rGO as catalysts. Reproduced from ref. 31 with permission from American Chemical Society, Copyright 2019.

which hindered their wide application. In recent years, synthesis of nanocarbons from cost-efficient precursors has attracted widespread attention. Wang *et al.* used β-cyclodextrin and melamine as precursors to synthesize an N-doped layered graphite carbon material catalyst by a one-step pyrolysis method and to evaluate its catalytic ozonation activity for decontamination of organic pollutants.[32] In accordance with mass ratios of melamine and β-cyclodextrin, the as-synthesized materials were denoted as N1C-1100 and N3C-1100.

The involvement of melamine in the precursors induced the formation of layered structures. Moreover, with the increase in N/C ratio of the precursors, higher SSA resulted. Specifically, the SSA (78.9 $m^2 g^{-1}$) of N3C-1100 is 2.6 times that of N1C-1100 (29.6 $m^2 g^{-1}$). Additionally, ordered graphitic lattice with the interlayer spacing of 0.38 nm was discerned in HRTEM observation, which was larger than that of the pristine graphene (0.34 nm). The extended interlayer spacing indicated the successful doping of N atoms within the graphene basal plane. The doped N atoms also broke the internal strain balance of the pristine graphene lattice and induced the formation of bent layers.

Catalytic ozonation activities of the as-synthesized materials were evaluated by using OA as the target pollutant, which is fairly resistant to O_3 attack. For catalytic ozonation using the sample without adding melamine as the precursor (CD-1100) as the catalyst, only 18% of the initial OA was removed after 1 h treatment (Figure 5.8(a)). N-doping significantly enhanced the catalytic activity. N1C-1100 obtained a greater catalytic activity than the undoped CD-1100, resulting in 70% of OA removal after 90 min. For N3C-1100, complete OA removal was achieved within 45 min. The reusability of N3C-1100 was evaluated using a four-run catalytic ozonation test (Figure 5.8(b)). A slight deactivation was noticed after four cycles of usage. Compared with the unused N3C-1100, the SSA and pore volume of the used catalyst slightly decreased, suggesting the deactivation may be caused by the

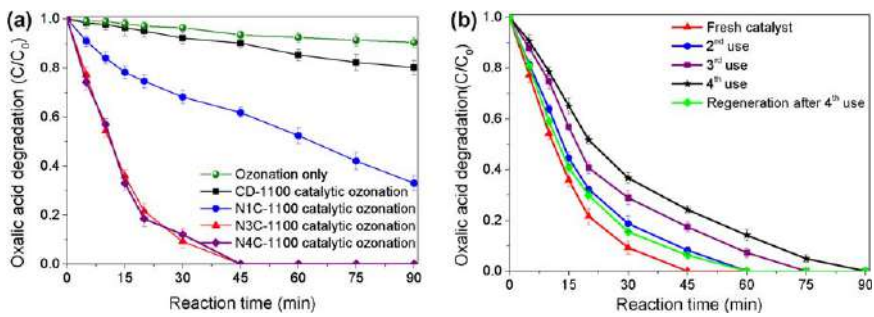

Figure 5.8 (a) Catalytic ozonation of oxalic acid using different catalysts. (b) Stability tests for N3C-1100. Reaction conditions: catalyst dosage: 0.1 $g L^{-1}$; [oxalic acid]$_0$: 50 $mg L^{-1}$; ozone flow rate: 100 $mL min^{-1}$; ozone concentration: 25 $mg L^{-1}$; temperature: 25 °C; initial pH: 3.2. Reproduced from ref. 32 with permission from Elsevier, Copyright 2019.

blockage of active sites or the physical changes on the surface. A mild heat treatment was conducted to regenerate the used catalysts, and it was discovered that the catalytic activity was dramatically restored, and OA could be completely removed after 60 min.

Previous studies revealed that defect sites played a critical role in carbocatalysis as delocalized electrons, and carbon dangling bonds may provide high chemical potential. Although similar defective levels were observed for N3C-600, N3C-800, and N3C-1100 by the Raman spectra (Figure 5.9(a)), the slightly higher I_D/I_G of N3C-600 did not result in the best catalytic activity, which could be ascribed to the redistribution of charge density caused by N-doping or the existence of other more effective active sites. N-doped sites may be the dominant active sites for promoting the catalytic activity because N-doping can stimulate electron transfer from adjacent C atoms owing to the higher electronegativity of N. The relationship between the relative amounts of N-doping types of different samples obtained from XPS analysis and their corresponding pseudo-first-order reaction rate constants is shown in Figure 5.9(b). It is found that the catalytic activity of this material is proportional to the graphite N content. To further illustrate the catalytic activity enhancement resulting from graphitic N, the turnover frequency (TOF) of the catalysts was estimated based on the OA degradation efficiency

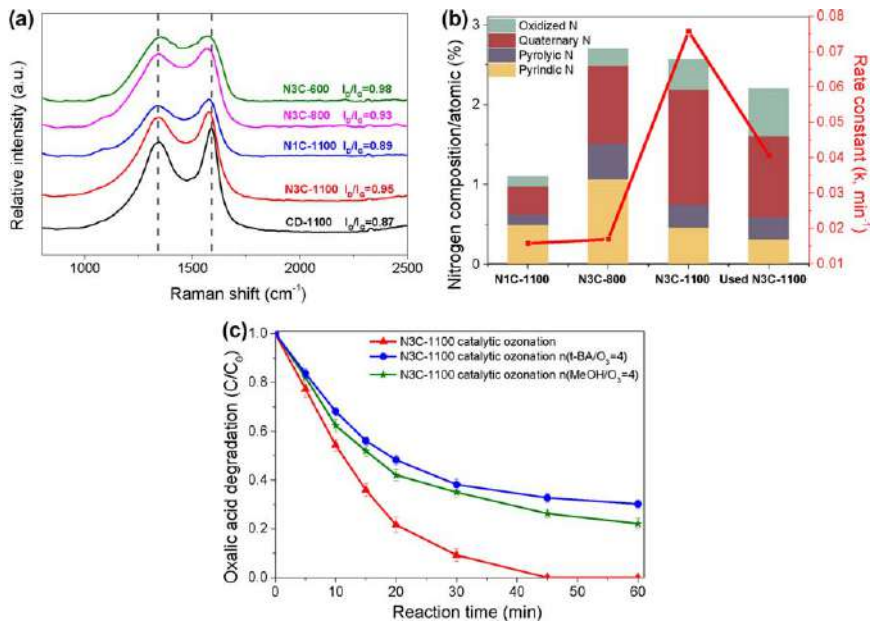

Figure 5.9 (a) Raman spectra of the as-prepared carbonaceous materials. (b) N species composition *versus* pseudo-first-order reaction rate. (c) Radical quenching during N3C-1100 catalytic ozonation. Reaction conditions: catalyst dosage: 0.1 g L^{-1}; $[\text{oxalic acid}]_0$: 50 mg L^{-1}; ozone flow rate: 100 mL min^{-1}; ozone concentration: 25 mg L^{-1}; temperature: 25 °C; initial pH: 3.2. Reproduced from ref. 32 with permission from Elsevier, Copyright 2019.

and their BET surface areas. The TOFs for N3C-600, N3C-800 and N3C-1100 were calculated to be 4.4×10^{-4}, 1.4×10^{-3}, and 1.9×10^{-3} $s^{-1}\,m^{-2}$, respectively. Thus a higher graphitic N content promoted the catalytic activity and corresponding TOF for OA removal.

To investigate the generated ROS and their contributions to OA degradation, quenching tests were performed. Addition of TBA and methanol only resulted in a minor inhibitory effect, suggesting the contribution of $^{\bullet}OH$ (Figure 5.9(c)). The partial inhibition also indicated that N3C-1100 may initiate nonradical reaction pathway which did not rely on $^{\bullet}OH$ or $^{\bullet}O_2^-$.

Apart from layered nanocarbons, 3D nanocarbons with large SSA and porous structure not only facilitated mass transfer in multiphase reactions but also maximized the exposure of reaction sites. Wang *et al.* used low-cost α-cyclodextrin (α-CD) as a carbon precursor and co-pyrolyzed with Co ions to synthesize a non-metallic 3D mesoporous material (CPG) with an embedded carbon nanotube structure.[33] According to the amount of cobalt precursor (0.25 g, 0.5 g and 1 g), the synthesized products were marked as CPG-0.5, CPG-1 and CPG-2, respectively. The synthesized material prepared by the single α-CD according to this process is denoted as CD-1000.

Compared with the prevailing catalytic ozonation materials such as nonmetal commercial graphite, rGO, CNTs and metal-based $LaMnO_3$ perovskite,[34] CPG-2 obtained the highest catalytic activity (Figure 5.10(a) and (b)). The enhanced catalytic activity of CPG-2 may be originated from the increase of SSA and the multilayer embedded nanotubes in the graphitic carbon structure. The pseudo-first-order reaction rate constant of CPG-2 was calculated to be four times higher than CD-1000 (Figure 5.10(c)). The reusability of CPG-2 is shown in Figure 5.10(d). After four repeated uses, only slight deactivation was observed, indicating that the catalyst achieved a good stability.

In order to study the ROS produced by CD-1000 and CPG-2 in the process of catalytic ozone oxidation of OA, EPR tests were performed. From Figure 5.11(a), it can be seen that the signal intensity of the DMPO–$^{\bullet}OH$ adduct of CPG-2 was higher than that of CD-1000, indicating that CPG-2 generates more $^{\bullet}OH$. To distinguish the signal of $^{\bullet}O_2^-$, methanol was added to quench $^{\bullet}OH$ (Figure 5.11(b)). The amount of $^{\bullet}O_2^-$ in the CPG-2/O_3 system was significantly greater than that of CD-1000/O_3. TEMP was employed as the spin trapping agent to detect the possible generation of $^1O_2$ (Figure 5.11(c)). The signal intensity of CPG-2 was higher, indicating that a higher amount of $^1O_2$ was generated.

The results of the quenching experiments are shown in Figure 5.11(d). The addition of methanol (MeOH) or carbonate anion (HCO_3^-) to the reaction solution had an inhibitory effect on the degradation of OA, indicating the contribution of $^{\bullet}OH$ to OA degradation. After adding *para*-benzoquinone (*p*-BQ), the OA degradation curve almost overlapped with that after adding MeOH, suggesting $^{\bullet}O_2^-$ was insignificant to degradation of OA. Moreover, to further differentiate the contribution of surface-adsorbed oxygen atoms to OA destruction, NaN_3 (2 mM), MeOH (2 mM) and *p*-BQ (0.5 mM) were added simultaneously to the reaction solution. With the addition of these

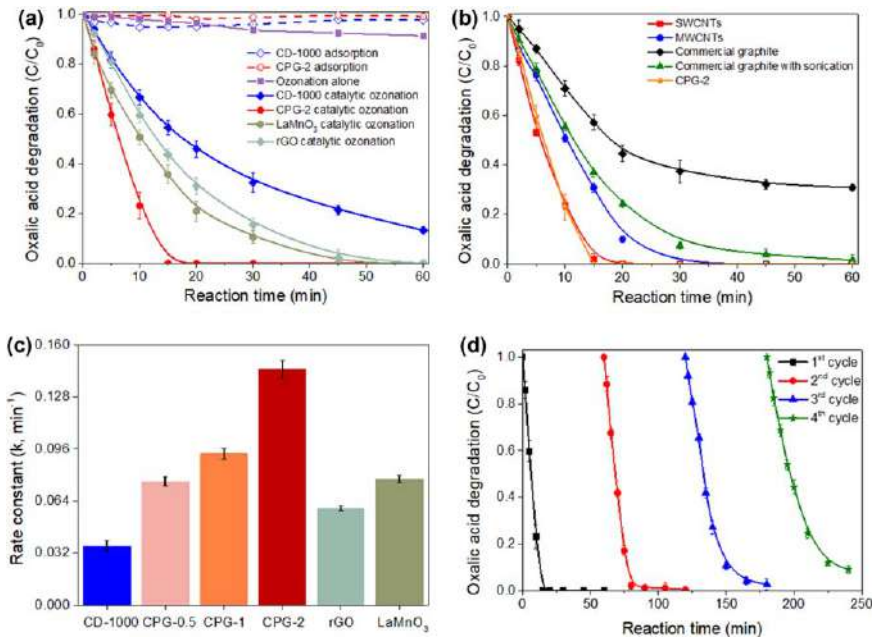

Figure 5.10 (a and b) Oxalic acid removal by different treatments. (c) Comparison of pseudo first-order inverse rates of different catalysts. (d) Four-cycle reusability test. Reaction conditions: catalyst dosage = 0.1 g L^{-1}; $[OA]_0$: 50 mg L^{-1}; ozone flow rate = 100 mL min^{-1}; ozone concentration = 25 mg L^{-1}; temperature = 25 °C. Reproduced from ref. 33 with permission from Elsevier, Copyright 2019.

scavengers, more than 95% of the initial OA decomposed in 60 min, suggesting the dominant role of surface-adsorbed oxygen atoms in the CPG-2/O_3 catalytic system. Therefore, these results indicate that in addition to free radical oxidation and singlet oxygen oxidation, the reaction process also includes non-radical oxidation based on surface oxidation.

Sun *et al.* also synthesized nitrogen-doped nanocarbon hollow spheres (NHCs) using polydopamine (PDA) as a precursor, and the hollow sphere morphology was validated by both SEM and TEM observations.[35] To evaluate the catalytic ozonation activities of the as-prepared NHCs, ketoprofen (KTP) was used as the target pollutant. Increasing the calcination temperature, which helped improved activity. NHC[8] synthesized at 800 °C obtained the highest catalytic activity; however, further elevating the calcination temperate decreased the catalytic activity. The stability of the NHC[8] was also evaluated. Minor deactivation was observed after the third usage, and the catalytic activity can be restored by the reannealing process.

EPR experiments and quenching tests were further performed to evaluate the possible generated ROS and their contributions to KTP degradation. A higher intensity of DMPO–$^{\bullet}$OH adduct was observed when NHC[8] was employed as the catalysts, suggesting that a greater amount of $^{\bullet}$OH was produced.

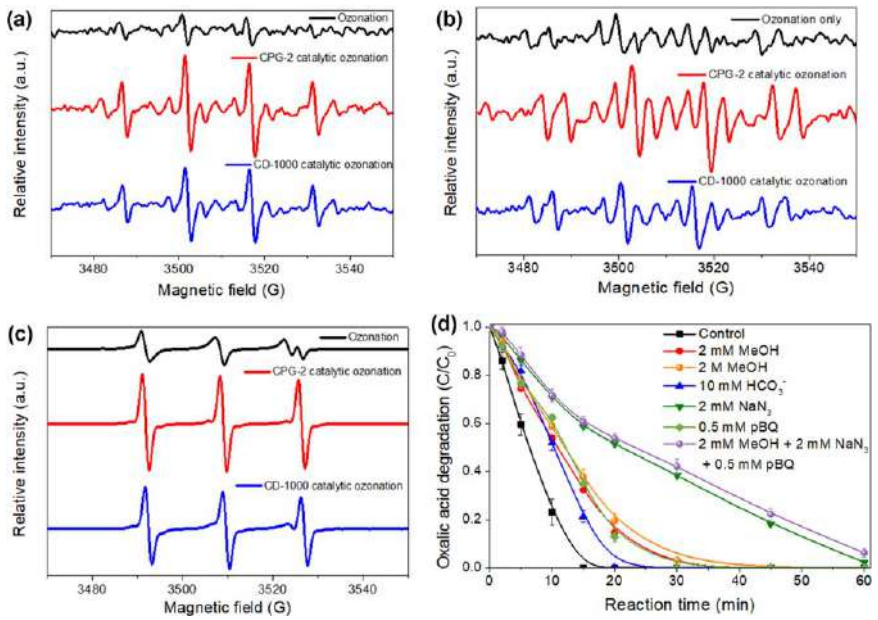

Figure 5.11 (a) EPR test using DMPO as a spin trapping agent. (b) EPR test using DMPO as a spin trapping agent and methanol (1 M). (c) EPR test using TEMP as a spin trapping agent. (d) Quenching tests with CPG-2 as catalyst. Reaction conditions: ozone flow rate: 100 mL min^{-1}; ozone concentration: 25 mg L^{-1}; temperature: 25 °C. Reproduced from ref. 33 with permission from Elsevier, Copyright 2019.

However, a negligible EPR signal for $^{\bullet}O_2^-$ was observed for all samples. Methanol was further added to differentiate the $^{\bullet}O_2^-$ signal. However, strong peaks of 5,5-dimethyl-2-oxo-pyrroline-1-oxyl (DMPOX) were observed with the occurrence of DMPO–$^{\bullet}$OOH signal, indicating DMPO might be directly oxidized by the surface-confined active species. Moreover, minor quenching effects resulted when TBA was added as the $^{\bullet}$OH scavenger, suggesting the degradation of KTP might follow a non-radical oxidation scheme.

The study further correlated the amount of oxygen-containing functional groups, defect sites and types of N-doping with the catalytic activities. Scattered correlations were established between the types of the oxygen-containing functional groups and the rate constants. Meanwhile, a negative correlation between the defective level (I_D/I_G) of the sample and the intensity of DMPO–$^{\bullet}$OH indicates that the defect sites in the O_3/NHCs system might not promote the production of more $^{\bullet}$OH. Nevertheless, positive correlations were observed when correlating the types of N-dopants and the intensity of DMPO–$^{\bullet}$OH. Therefore, the *in situ* doped N atoms are the catalytically active sites of NHCs, while the degradation of KTP is based on the synergy between the radical oxidation of $^{\bullet}$OH and the non-radical reaction of internal electron transfer.

The as-proposed mechanism of NHC-catalyzed ozonation for the degradation of KTP is schematically illustrated in Figure 5.12. Both nonradical oxidation

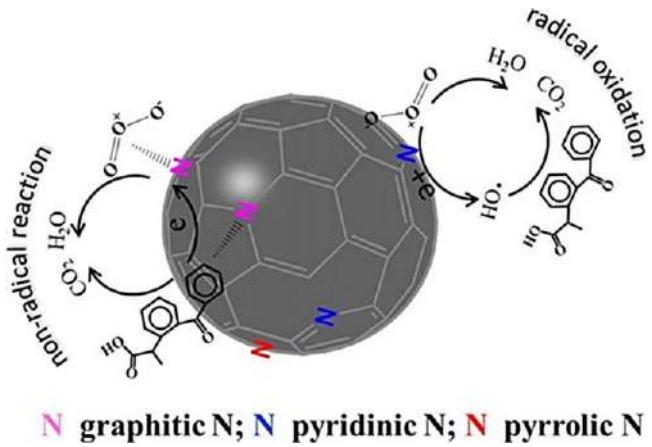

Figure 5.12 Schematic illustration on mechanism ozonation of ketoprofen (KTP) catalyzed by NHCs. Reproduced from ref. 35 with permission from American Chemical Society, Copyright 2019.

relying on the intra-electron transfer between the surface-adsorbed O_3 molecules and organics and the •OH-dominated radical oxidation were responsible for KTP destruction, and the doped N species were critical for ruling the oxidation pathways. For nonradical oxidation, the doped graphitic N in the frame of graphitic carbon modulated the electron structures of the adjacent carbon atoms by enhancing their charge densities and thus facilitated the adsorption of O_3 molecules. In addition, the delocalized conjugated system between lone electron pairs of doped N atoms and the adjacent sp^2 hybridized carbon framework promoted the localized electron transfer process. Therefore, graphitic N functioned as the "electron-mobility" region accelerating the electron-transfer between the adsorbed O_3 and KTP and induced a nonradical oxidation. Meanwhile, radical-based oxidation was observed on pyridinic N and pyrrolic N sites. The edging-located or the defect-located pyridinic N and pyrrolic N obtained high activity since their lone pair electrons were not confined by the adjacent carbon atoms. Consequently, these sites acted as the "radical-generation" regions where O_3 molecules could be catalytically decomposed into •OH.

As a 2D material, graphitic carbon nitride (g-C_3N_4) has been widely employed as the efficiency photocatalysts energy conversion and environmental remediations. However, several studies reported that g-C_3N_4 demonstrated poor activities when employed in catalytic ozonation for removal of organic contaminants.[32,36] For instance, Xiao *et al.* used *p*-hydroxybenzoic acid as the target pollutant to evaluate the catalytic activity of g-C_3N_4 in the photocatalytic ozonation reaction and reported the marginal catalytic ozonation activity of g-C_3N_4 in *p*-hydroxybenzoic acid without light irradiation.[37] Nevertheless, Song *et al.* synthesized two types of g-C_3N_4 with melamine and urea as the precursors and reported that g-C_3N_4 could efficiently activate ozone to produce ROS for degradation of refractory organic compounds such as 4-chlorobenzoic acid (*p*-CBA) and benzotriazole (BZA).[38] Observed from

SEM images, the as-synthesized g-C_3N_4 had a layered stacked structure with folded edges. After catalytic ozonation, the layered structure of g-C_3N_4 was retained, proving the good structural stability of g-C_3N_4.

Catalytic ozonation activities in organic removal and bromate elimination by utilizing different layered nanocarbon materials were evaluated by utilizing the as-synthesized g-C_3N_4 catalysts. The results showed that, although the catalytic ozonation activities of the two types of g-C_3N_4 were lower than those of GO and rGO, they achieved greater rate constants than ozonation alone. EPR tests combined with the radical quenching tests suggested that both $^{\bullet}OH$ and $^{\bullet}O_2^-$ were generated during the catalytic ozonation process and that $^{\bullet}OH$ dominated ROS in g-C_3N_4 catalytic ozone oxidation. Additionally, compared to g-C_3N_4 synthesized from melamine (M-g-C_3N_4), g-C_3N_4 synthesized from urea (U-g-C_3N_4) obtained higher concentrations in the generated $^{\bullet}OH$ and $^{\bullet}O_2^-$, which further explained the higher catalytic activity of U-g-C_3N_4.

To investigate the active sites on g-C_3N_4, this study further analyzed the changes of the surface chemistries of g-C_3N_4 before and after the reaction through EPR experiments. For fresh M-g-C_3N_4, a sharp resonant peak ($g = 2.001$) with high intensity was observed, ascribed to the π conjugate structure of the *s*-triazine units. The fresh U-g-C_3N_4 demonstrated a similar EPR signal profile but with a lower intensity than the M-g-C_3N_4. Based on the EPR observations, M-g-C_3N_4 obtained more delocalized electrons and a higher defective level (nitrogen vacancies) than U-g-C_3N_4. After catalytic ozonation, the number of delocalized electrons in both M-g-C_3N_4 and U-g-C_3N_4 decreased, indicating the participation of structural defects and delocalized electrons in catalytic ozonation.

5.5 Active Sites on Metal-free Nanocarbons

In catalytic ozonation, active sites on the carbocatalysts are of great importance to determine the interactions with the O_3 molecules and organic contaminants, thus influencing the ROS production and remediation efficiency.[1,39,40] Therefore, obtaining the fundamental knowledge on the intrinsic nature of the active sites on the nanocarbons would help evaluate the catalytic activities of the nanocarbon and establish synthesis protocols for manipulating the desired active sites for the specified catalytic reactions.

5.5.1 Carbon Framework and Dimensional Effect

The highly graphitic sp^2 carbon network with delocalized π electrons of the nanocarbons has been recognized as one of the potential active sites for ozone activation. The delocalized π networks significantly increase the mobility of the electrons that participate in the redox reactions for O_3 activation and the oxidation of organics.[31] The enhanced electron transfer might also induce a synergistic effect with the adjacent active sites, thereby promoting the catalytic activity of the nanocarbons.[17] Meanwhile, the delocalized π networks also develop a strong affinity toward the electrophilic binding with

O_3 molecules.[41] The π–π interactions or charge transfer interactions expedite the adsorption of aromatic organics.[42]

The dimensional effects of the nanocarbons can also exert a profound effect on catalytic ozonation activities. As 1D carbon-organized structures, carbon nanotubes (CNTs), including single-walled CNTs (SWCNTs), multiwalled CNTs (MWCNTs) and their derivatives, have been broadly utilized in the activation of O_3 for the decontamination of wastewater.[9,43] The diameter, helicity and curvature of the CNTs regulate the electronic properties owing to the 1D feature.[44,45] They also enhanced structural stability with resistance to chemical abrasion, envisioning the possibility of long-term operation in highly oxidative environments. Additionally, surface chemistries of the CNTs can also be facilely manipulated to achieve the optimum types and contents for ROS generation. Additionally, the nanoconfinement effect accelerating chemical reactions can be taken advantage of by the tubular structure of CNTs, which act as the microreactors.[46] As the 2D structure, graphene—especially the pristine graphene, which is made of single-layered sp^2 hybridized carbon atoms—takes on outstanding electronic properties because of the highly delocalized π networks.[14] However, the difficulties in a scaled-up synthesis block its further application. Reduced graphene oxide (rGO), which is synthesized from the reduction of graphene oxide (GO) possessing overabundant oxygen functionalities. is one alternative.[47] Developing porous graphitic nanocarbons with 3D structures with the exposure of mesopores and macropores is a promising strategy to shorten the mass diffusion length, enhance the interactions with the active sites and accelerate the reaction kinetics.[48–50] In recent years, various 3D porous graphitic nanocarbons such as hierarchical nanocarbons, layered nanocarbons and hollow carbon microspheres have been synthesized and employed as the efficient catalyst for catalytic ozonation for removal of organic contaminants.

5.5.2 Surface Oxygen Functionalities

Surface oxygen groups are the inherent functionalities on the nanocarbons originating from the materials fabrications.[51] The existence of the surface oxygen groups alters the surface properties of the nanocarbons and the electronic properties by affecting the electron charge distribution and thus influences the interactions of the surface of nanocarbons with the organic contaminants and O_3. Nevertheless, it is quite challenging to differentiate the separated roles of surface oxygen groups in catalytic ozonation reactions because of their coexistence as well as the complexity of the surface properties of the nanocarbons.

5.5.2.1 Hydroxyl/Phenolic Groups

The mildly electron-donating hydroxyl groups could increase the electron density of the carbon basal plane and facilitate the electrophilic interaction with the O_3 for its catalytic decomposition to produce ROS.[52,53] The hydroxyl group as well as the oxidizing product-ketonic group would function as the

redox pairs for O_3 activation.[52] Furthermore, the presence of hydroxyl groups enhances the water dispersibility of nanocarbons by increasing the hydrophilicity, which promoted the mass transfer process.

5.5.2.2 Ketone Groups/Quinone Groups

Located at the structural defects or edges of the graphene framework, the electron-rich –C=O group can be significant in O_3 activation. The Lewis basic character of the lone-paired electrons within –C=O groups supply extra electrons to the bonded O_3 for its activation to generate $^{\bullet}O_3^-$ a promoter for radical chain reactions. Additionally, the lone-paired electrons can also activate the conjugated π networks in the sp^2 carbon matrix.[54] For instance, in the catalytic ozonation of PHBA degradation with rGO as the catalysts, the activities of rGO samples with similar defective levels but different compositions of surface oxygen functionalities were evaluated.[19] It was discovered that the electron-rich –C=O groups promoted O_3 activation by the electron transfer process and that rGO with a higher content of –C=O demonstrated a greater activity. Similar results were also reported in a g-C_3N_4/O_3 system.[31] It has been found that the great content of surface –C=O group was oxidized to –COOH during the catalytic ozonation process, suggesting the dominating role of –C=O in O_3 activation.

5.5.2.3 Carboxyl Groups

The existence of C=O within the carboxyl group also increases the charge density and facilitates the interaction with O_3 *via* the electron transfer process.[31] Alternatively, carboxylates can also be destructed by O_3 and serve as the initiator for radical chain reactions.[55]

It is noteworthy that although surface oxygen functionalities can contribute to O_3 activation, it is unfavorable to anchor the excess amount of oxygen functionalities on the surface of the nanocarbons. The overabundant oxygen functionalities will (1) occupy the edges or the defective sites, which are also critical active sites for O_3 activation; (2) obstruct the electron mobilities *via* steric hindrance; and (3) decrease the reductive degree of the carbon lattice, which determines the charge transport capacity toward the redox reactions. It is thus suggested that the types as well as the populations of the surface oxygen functionalities should be tuned precisely.

5.5.3 Edging and Structural Defects

Edging sites and structural defects are inherent point defects in nanocarbons and have gained much research attention because of their enhanced effect on surface reactivities arising from the variations in electronic properties by deviating the homogeneity of the carbon network with high chemical potentials and the existence of abundant unpaired electrons. Edging sites (for both carbene-type C atoms at zigzag edges and carbine-like C atoms in armchair

edges) obtain a great affinity to covalent bonds, and the subsidiary dangling bonds can promote radical chain reactions.[57,58] Furthermore, electron transfer can be significantly improved on the edging sites rather than on the basal plane, which boosts catalytic reactions.[59] Previous studies reported that the high exposure of the edging sites in nanocarbon accelerated the activation of O_3 for ROS production (Figure 5.13(a) and (b)).[9,24,31] Moreover, activities of the incorporated heteroatoms or oxygen functionalities can be further enhanced when they are located within the proximity of edging sites or vacancies.[60,61] Density functional theory (DFT) calculations suggested that higher adsorption energies and more elongated l_{O-O} would result when an O_3 molecule was placed around the hydroxyl groups located at the zigzag and armchair configurations rather than on the basal plane.[24]

Structural defects arising from the nonhexagonal rings or a random point mismatch destroy the perfection of the graphene lattice and break up the conjugated π networks by creating unpaired electrons.[62] Additionally, the charge distribution of C atoms near the defective sites can also be altered, resulting in the promoted affinities for binding with O_3. DFT simulation results suggested that when O_3 was placed near the zigzag edge, armchair edge and the structural vacancy, its peroxide bond within O_3 molecule would be broken and evolved a surface-adsorbed atomic O ($^*O_{ad}$) and a free peroxide species ($O_{2\ free}$) (Figure 5.13(c)–(f)). The corresponding adsorption energies were −5.69, −3.88 and −4.64 eV accordingly, which were much higher than the cases in which O_3 was located adjacent to the surface oxygen functionalities.[24]

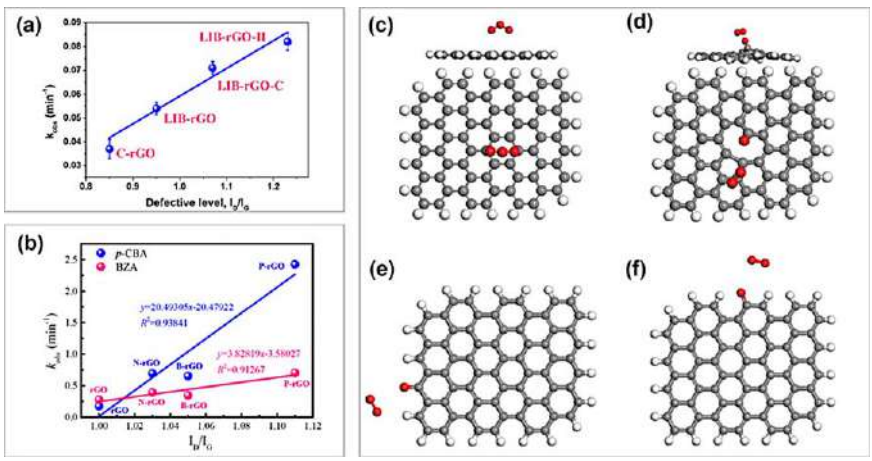

Figure 5.13 (a) Relationship between defective level of various rGO samples and the pseudo-first-rate constants for catalytic ozonation of 4-nitrophenol degradation. (b) Relationship between defective level of various doped rGO samples and the pseudo-first-rate constants for catalytic ozonation of *p*-chlorobenzoic acid and benzotriazole degradation. (c) DFT simulations of O_3 adsorption on basal plane, (d) structure edge, (e) zigzag edge, and (f) armchair edge of graphene. Reproduced from ref. 56 with permission from American Chemical Society, Copyright 2020.

5.5.4 Heteroatom Dopants

Nonmetallic atoms such as B, N, F, P and S with different electronegativities (χ) to the C atom can be doped into the graphene lattice as the point defects to break the stable delocalized π electrons and redistribute the electronic density (Figure 5.14).[63] The electron relocalization induced by heteroatom doping also changes the local density of states (DoS) of the graphene lattice and results in the variation in the work function.[64]

5.5.4.1 N-doping

The large electronegativity difference between N and C (χ, 3.07 *versus* 2.55) induces a significant relocation of the charge density on the graphene lattice and a notable influence on the mobility of electrons,[32,65] resulting in enhanced interactions with O_3 molecules. The significantly improved electronic properties, making the N-doping the prevailing doping strategy in catalytic ozonation to increase the catalytic activity.[16,23,30,31,35,66] In fact, the pyridinic N can offer a p electron to the delocalized π networks of the carbon matrix and thus enhance electron-donating behavior.[67]

Apart from activating O_3 for its catalytical decomposition to produce ROS, N-doping sites can also induce the direct oxidation of the adsorbed organic by the direct electron transfer process. The ortho-located C atoms

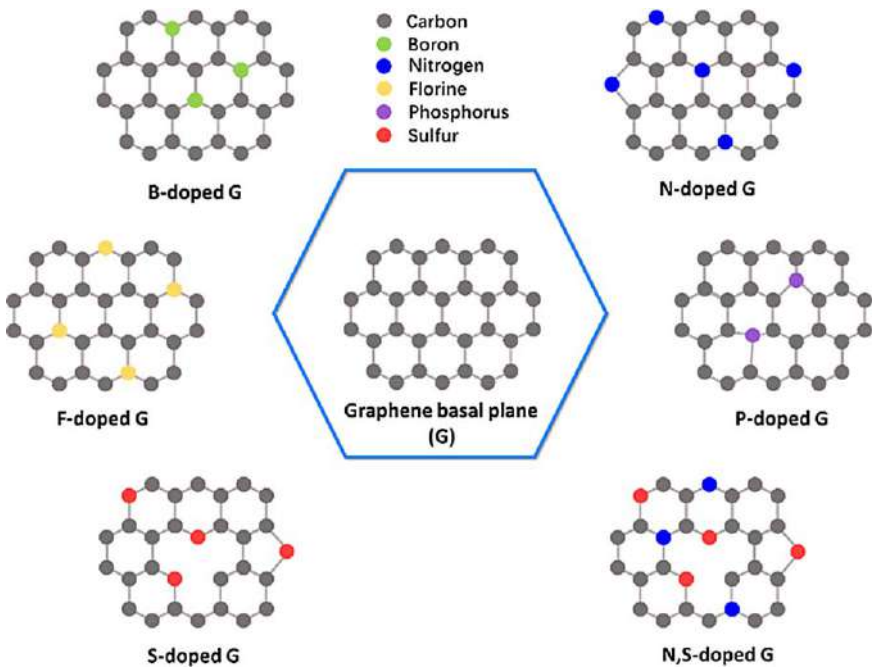

Figure 5.14 Heteroatom doping in the graphene. Reproduced from ref. 56 with permission from American Chemical Society, Copyright 2020.

adjacent to the quaternary N were reported to obtain much higher electronic densities near the Fermi level than the C atoms on the basal plane, which induced an electronic structure similar to the d band of transition metals and endowed these C atoms with a strong affinity toward the nucleophilic interactions with O_3.[35,68] Additionally, the conjugated system formed between the lone pair electrons of the quaternary N and the sp^2-hybridized carbon framework accelerated electron mobilities. As a result, regions around quaternary N facilitated nonradical oxidation *via* the enhanced electron transfer process from the adsorbed O_3 to organics without the generation of radicals.

5.5.4.2 *B-doping/P-doping*

Doping the graphene lattice with boron or phosphorus atoms can induce a different scenario from doping with nitrogen atoms because of the smaller electronegativities of B/P atoms than that of C atoms. As a result, positive-charged B-doping or P-doping sites are formed by polarizing the paired covalent electrons toward C atoms.[69] Theoretically, the strong electron-withdrawing capability of the doped B/P atoms introduced a high local spin density to the carbon basal plane,[70] favoring the electrophilic interaction with the O_3 molecules and the π–π interaction with the aromatic pollutants. B-doping sites also facilitate the electron transfer from the graphitic carbon π electrons to the adsorbed O_3 molecules.[71,72] Furthermore, a higher defective level will be expected for P-doping than B-doping because of the larger atomic size of P atoms over B atoms. In B-rGO/O_3 for degradation of benzotriazole and *p*-CBA, B-doping only gave rise to marginal improvements in both degradation efficiency and TOC mineralization rates compared to the undoped rGO.[31] However, P-doping significantly improved the degradation rates of organics, obtaining a similar catalytic activity to the N-doped rGO.[30,31] The enhanced delocalized π networks and the higher defective level induced by P-doping are responsible for the activity improvement.[30]

5.5.4.3 *S-doping/F-doping*

Doping S and F atoms within the graphene lattice can be more challenging than the others because of the much larger atomic size of S than that of C and the chemical inertness of F.[72] Successful S-doping usually induces an increased number of defective sites, which is similar to P-doping.[73,74] However, little or even negative doping effects were reported for S-doping due to the atomic size-effect that encumbered the electron transfer.[4,16,31] For F-doping, the large difference in electronegativity endows C atoms adjacent to the F dopants' high positive charge densities, which are in favor of the nucleophilic interactions with O_3.[75] In F-doped CNT–catalyzed ozonation for OA degradation, the covalent C–F bonds were reported to form at the sp^3-hybridized C sites rather than on the sp^2 hybridizations.[13] The selectively doped F atoms retained the integrity of the delocalized π networks on the graphene lattice, facilitating the activation O_3 by the electron transfer

process. Moreover, the positively charged C atoms adjacent to F atoms induced the nucleophilic activation of O_3.

In addition to single-atom doping, co-doping with different heteroatoms have been suggested as an effective strategy to further boost the catalytic activities of the carbon materials in environmental remediations and energy conversions because of the synergistic effects associated with synergistic electronic interactions between the co-doped heteroatoms and the adjacent C atoms.[4,76,77] Future studies can take the advantage of these synergistic effects to improve the catalytic activities of nanocarbon in catalytic ozonation for aqueous organics degradation.

5.6 Active Sites on Supported Nanocarbons

Integrating metal components on nanocarbons is another strategy to increase the catalytic activities of nanocarbons by the synergistic effects between the metals and nanocarbons. The electron-donating d-orbital electrons of the integrated metal components regulate their electronic properties such as spin structures and work functions to improve the charge transfer (Figure 5.15(a)–(c)).[78,79] Geometric effects related to the intrinsic structural characters of nanocarbons and the crystallographic/shape variations of metal components can be induced to enhance mass transfer and facilitate the exposure of the highly active facets.[80] Additionally, the appearance of complexing structures at the metal–carbon boundaries are also catalytically active. As already mentioned, surface defective sites, nonmetallic heteroatom dopants and surface oxygen functionalities on the graphitic carbon basal plane can act as the potential sites for anchoring the metal components *via* the improved metal–carbon interactions and the corresponding charge transfer (Figure 5.15(d)).[81] Comprehensive understanding on the interactions of the metal components on nanocarbons is critical for surface engineering of the nanocarbons to improve catalytic activity. On the other hand, the metal@carbon hybrids are appealing for practical heterogeneous reactions. The nanoscale catalysts can be easily recycled in the presence of an external magnet or a magnetic field because of the loaded paramagnetic transition metal species, addressing the long existing problem of secondary contamination due to the loss of nanomaterials.

5.7 Methods to Probe the Active Sites on Nanocarbons

Variable control is one of the most prevailing methods to investigate active sites based on the activity evaluation of a series of catalysts with a specified parameter gradient changed.[54,82] Nevertheless, it is quite demanding to alter the population of the specified types of the active sites without influencing the others. Another methodology is the employment of analogs with single or limited types of the proposed active sites on the bulk nanocarbons as the alternative catalysts. It can be achieved either by utilizing the discrete organic molecules with the same functional groups that were proposed as the active

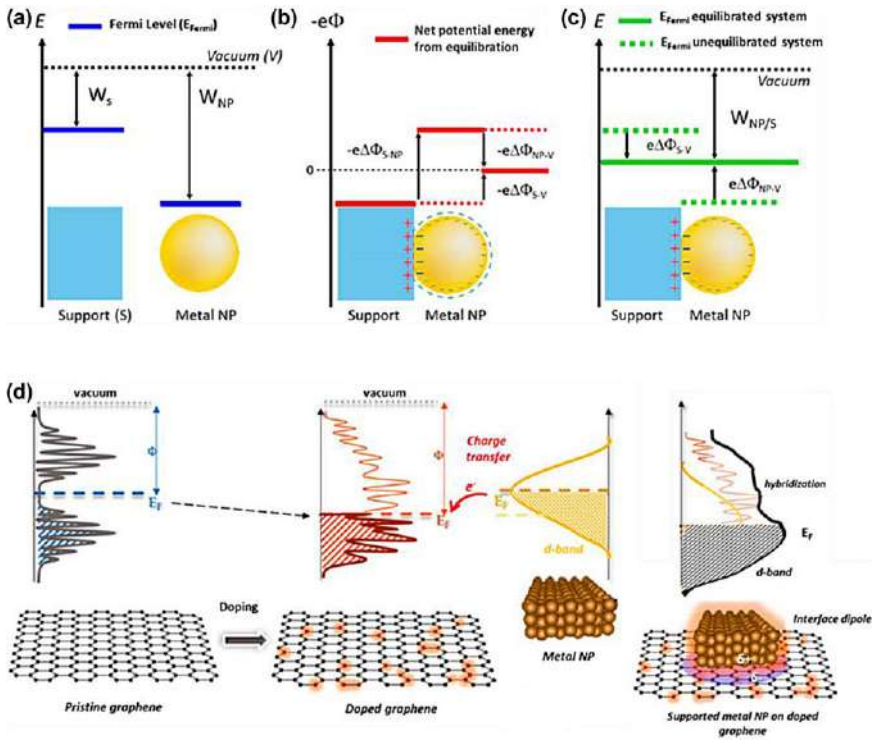

Figure 5.15 Schematic illustrations of variations in electronic properties after metal loading. (a) Work functions of the isolated support and NP. (b) Illustration of the additional net electrostatic energy contribution $(-e)\ \Phi$ resulting from electronic equilibration. An outer surface charge on the NP is necessary to account for the difference $\Phi_{NP\text{-}V}$ of the net electrostatic potential levels in a vacuum and inside the NP, respectively. (c) The equilibrated system is characterized by a common Fermi level and work function $W_{NP/S}$. (d) Effect of the introduction of heteroatoms in the nanocarbon support on metal NP–nanocarbon support interactions. Reproduced from ref. 56 with permission from American Chemical Society, Copyright 2020.

sites on the nanocarbons or the carbon allotropes with a much simpler structure than the bulk nanocarbon catalysts. Apart from these methods, post-treatments of the nanocarbons that selectively mask the specified types of the active sites have been suggested as the credible method for assessing the active sites.[83] The inhibition in catalytic activities demonstrated the participation of the masked active sites in catalytic reaction and *vice versa*. However, the accurate and complete removal of a specified type of the active sites without affecting the others is quite challenging because of the limited selectivity of the post treatments. As a result, the conventional application of this methodology is to compare the variations in morphology, surface chemistries and structures of the deactivated catalysts with the fresh ones.[3,84] By correlating the variation factors with the catalytic activities *via* quantitative

structure–activity relationship (QSAR) analysis, the dominant active sites can be discovered.

Characterization including morphology observation, surface chemistry analysis and structural analysis by employing advanced characterization techniques can help obtain the basic physiochemical information of the nanocarbons. In addition, theoretical computations such as calculations with density functional theory (DFT) have been applied as a powerful method to investigate the intrinsic nature of the active sites and the reaction pathways. By constructing rational and suitable models in atomic level, the electronic states of the catalysts can be visualized and a comprehensive understanding of the reaction mechanism can be achieved by simulating the interactions between the reactants and the proposed active sites on the catalysts.[20]

5.8 Oxidation Pathways in Metal-free Nanocarbon Catalyzed Ozonation

Catalytic ozonation can induce two types of oxidations of the aqueous organics: O_3 direct oxidation and indirect oxidation by the produced ROS *via* the catalytic dissociation of O_3 on the active sites of the nanocarbons or O_3 self-dissociation. However, for O_3 direct oxidation, the previously mentioned selective oxidation ability of O_3 is only capable of attacking organics with unsaturated carbon bonds and results in partial mineralization.[85,86] Additionally, the limited solubility of O_3 further hinders its interaction with the aqueous organic pollutants.[86] Hence it is of great importance to focus on the indirect oxidation pathways by the produced ROS.

5.8.1 Radical-based Oxidations

5.8.1.1 $^{\bullet}$OH-based Oxidations

Two routes have been reported for $^{\bullet}$OH generation in catalytic ozonation: ozone self-decomposition and catalytic O_3 decomposition. O_3 is quite sluggish in producing $^{\bullet}$OH in acidic environment with the pseudo first reaction rate constant (k) of 1.1×10^{-4} M^{-1} s^{-1} (eqn (5.1)),[87] yet its self-decomposition is remarkably influenced by the solution pH. The alkaline activated $HO_2^{\bullet}$/$^{\bullet}O_2^-$ performs as a critical linker for the formation of $^{\bullet}$OH, as discussed in the following section. It is worth noting that the amount of $^{\bullet}$OH generated from O_3 self-decomposition in both acidic and basic environments is quite limited with respect to achieving an efficient treatment.

$$O_3 + H_2O \rightarrow 2^{\bullet}OH + O_2, \quad k = 1.1\times10^{-4}\ M^{-1}\,s^{-1} \tag{5.1}$$

Catalytic O_3 decomposition on the active sites of the nanocarbons plays a critical role in $^{\bullet}$OH production. The enhanced electron transfer on the active sites facilitates the catalytic activation of O_3 to initiate the chain reactions.

The following equations (eqn (5.2)–(5.4)) describe the possible interactions between O_3 and the carbon surface, as well as the subsequent activation process for •OH generation. During the catalytic ozonation, these interactions might alter the surface chemistries of the nanocarbons, resulting in the passivation of the catalysts.[5,19,35] Moreover, the carbon framework could be dissociated by the O_3 and the produced ROS into soluble organics, leading to the increase of dissolved TOC.[33,88] Therefore, some studies reported that the carbon surface acted more like the initiator or promoter for O_3 decomposition rather than like the true catalyst.[89,90]

$$O_3 + S \leftrightarrow O_3 - S \tag{5.2}$$

$$O_3 - S \leftrightarrow O - S + O_2 \tag{5.3}$$

$$O - S + H^+ \leftrightarrow {}^{\bullet}OH + S \tag{5.4}$$

Degradation or mineralization of organic pollutants by the generated •OH can occur in the bulk solution and/or on the surface of the catalysts depending on the whether the generated •OH was released from the surface of the catalyst into the aqueous bulk or was still adsorbed on the surface (Figure 5.16(a)). Radical quenching test employing TBA as the scavenger has been suggested as an effective method to differentiate the place where the organics are degraded since TBA hardly adsorbs on the surface of the carbon-based materials and achieves a fast reaction rate with the •OH (6×10^8 M^{-1} s^{-1}) in the aqueous bulk. For mineralization of organics in the aqueous bulk, the generated •OH was released from the active sites and

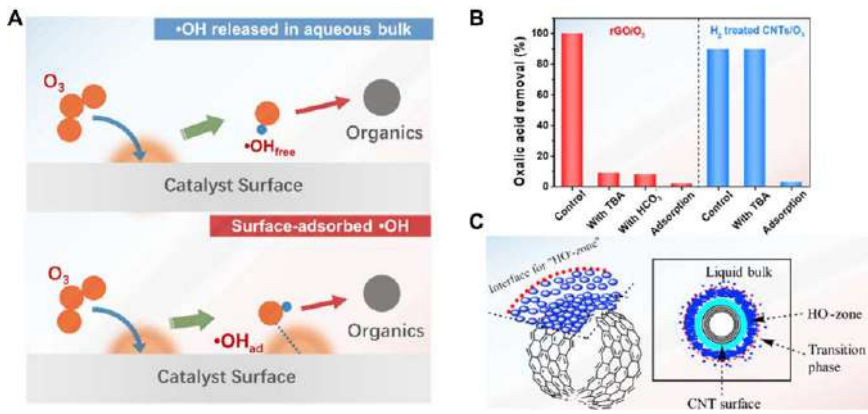

Figure 5.16 (A) Schematic illustration of the mineralization of organic by •OH in the aqueous bulk and on the surface of the nanocarbons; (B) Quenching tests for oxalic acid degradation in the bulk solution (rGO/O_3, red) and on the surface of nanocarbons (H_2 treated CNTs/O_3, blue); (C) Schematic illustration of •OH generation on the surface or around the surface region of CNTs. Reproduced from ref. 56 with permission from American Chemical Society, Copyright 2020.

reacted with the non-adsorbed organics, and the presence of TBA can rapidly react with $^{\bullet}OH$, and significantly inhibited the destruction of organics (Figure 5.16(b)).[90,91] The generated $^{\bullet}OH$ can also adsorb on the surface of the catalyst and achieve the oxidation process. In MWCNTs/O_3 systems, the presence of TBA partially inhibited or had no influence on the degradation of the organics; however, the variation in O_3 consumption rates and the suppression of the reaction by adding bicarbonates that quench $^{\bullet}OH$ both in the aqueous bulk and on the surface of the catalysts validated the generation of $^{\bullet}OH$.[5,43,92–94] Fluorescence microscopy image (FMI) analysis with coumarin as the $^{\bullet}OH$ probe can be utilized to visualize the $^{\bullet}OH$ produced and accumulated within a surface region of the CNTs by observation of the fluorescence oxidation product of 7-hydroxylcoumarion.[41] It was found that the catalytic degradation of the organics occurred on the surface of CNTs and the solid–liquid interphase (Figure 5.16(c)), and the radical abundance within the solid–liquid interface was calculated to be at least 1000 times greater than that in the bulk solution.

5.8.1.2 $^{\bullet}O_2^-$ Mediated Oxidations

$HO_2^{\bullet}/^{\bullet}O_2^-$ are the key radical chain reaction intermediates. $HO_2^{\bullet}$ can be generated by $^{\bullet}OH$ activation of O_3 (eqn (5.5)), and it dissociates into $^{\bullet}O_2^-$ when the solution pH is greater than 4.8 (eqn (5.6)).[87] In alkaline solution, O_3 can be activated by the ambient OH^- to form $HO_2^{\bullet}/^{\bullet}O_2^-$ (eqn (5.7)). Additionally, the delocalized π electron donated by the sp^2 frame of the nanocarbon also facilitated $^{\bullet}O_2^-$ formation.[31] $HO_2^{\bullet}/^{\bullet}O_2^-$ can demonstrate a reducing capability (E^0 ($O_{2aq}/^{\bullet}O_2^-$) = − 0.18 V) or an oxidizing capability (E^0 ($^{\bullet}O_2^-/H_2O_2$) = 1.44 V) based on the evolution pathways. As a reductive radical, $^{\bullet}O_2^-$ can act as the chain carrier pairs accelerating the radical chain reactions for $^{\bullet}OH$ generation (eqn (5.8)–(5.11)).[41,95] The reductive property of $^{\bullet}O_2^-$ is helpful in restoring the oxidation states of the metal/oxygen redox couples, which are the key active sites in catalytic ozonation.[95] $HO_2^{\bullet}/^{\bullet}O_2^-$, with its mild oxidation potential, can directly oxidize aqueous organics with low oxidation barriers.[19,31] As a result, $^{\bullet}O_2^-$ has been regarded as the dominant ROS for *p*-CBA degradation.

$$O_3 + {}^{\bullet}OH \rightarrow O_2 + HO_2^{\bullet} \tag{5.5}$$

$$HO_2^{\bullet} \leftrightarrow {}^{\bullet}O_2^- + H^+, \quad pK_a = 4.8 \tag{5.6}$$

$$O_3 + OH^- \rightarrow HO_2^{\bullet} + {}^{\bullet}O_2^-, \quad k = 70\ M^{-1}\,s^{-1} \tag{5.7}$$

$$^{\bullet}O_2^- + O_3 \rightarrow {}^{\bullet}O_3^- + O_2 \tag{5.8}$$

$$^{\bullet}O_3^- + H_2O \rightarrow HO_3^{\bullet} + OH^-, \quad k = 5.2\times10^{10}\ M^{-1}\,s^{-1} \tag{5.9}$$

$$HO_3^{\bullet} \rightarrow {}^{\bullet}OH + {}^{\bullet}O_2^-, \quad k = 1.1\times10^{5}\ M^{-1}\,s^{-1} \tag{5.10}$$

$$2{}^{\bullet}O_2^- + HO_2^{\bullet} + H_2O \rightarrow H_2O_2 + O_2 + OH^- \tag{5.11}$$

5.8.2 Nonradical Oxidations

Apart from radical-based oxidations, nonradical oxidations depending on the surface-confined activated species or singlet oxygen ($^1O_2$) have been recently reported as the alternative pathways for the degradation of the organics in nanocarbon-catalyzed ozonation (Figure 5.17(a)). For the nonradical oxidations, adding the prevailing alcohol-based or inorganic quenching agents usually has negligible inhibition effect on degradation efficiency. Varying the adsorption of O_3 and target pollutants on the surface of the nanocarbons by altering the solution pH or adding surface reaction quenchers could tremendously affect catalytic efficiency since the degradation process occurs on the surface of the catalysts by the interactions between the surface-adsorbed activated species from O_3 dissociation and the adsorbed organics.[96,97]

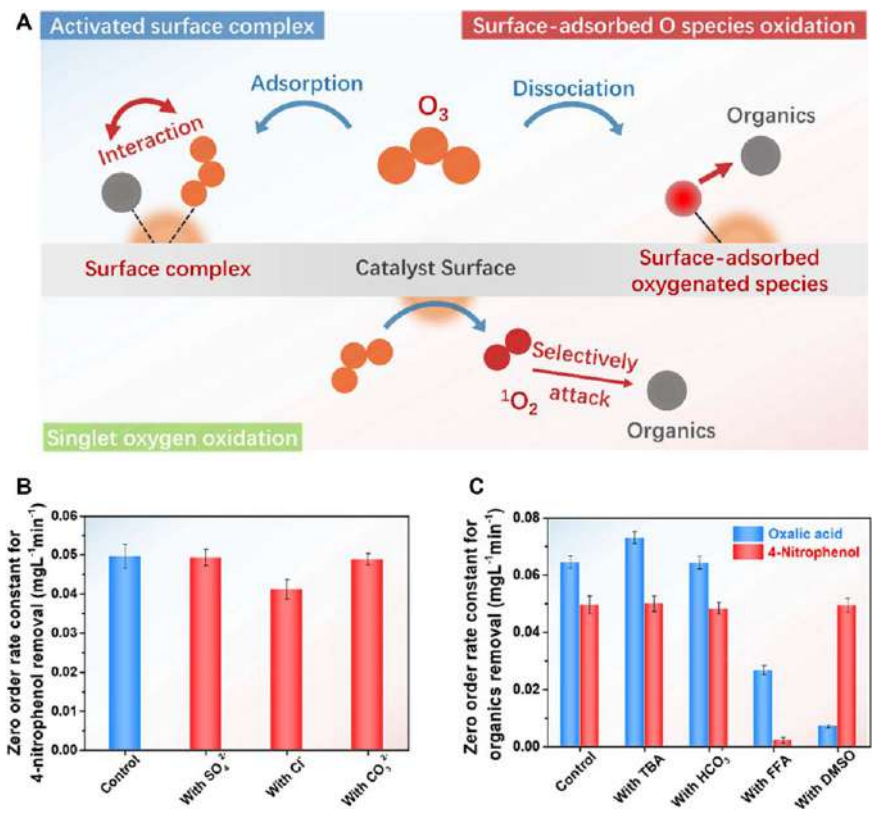

Figure 5.17 (A) Schematic illustration of various types of nonradical oxidations; (B) Effect of inorganic anions on nonradical oxidations; (C) Demonstration of the selective oxidation of the nonradical species by zero-order rate constants for oxalic acid (blue) and 4-nitrophenol removals (red). Reproduced from ref. 56 with permission from American Chemical Society, Copyright 2020.

5.8.2.1 *Nonradical Oxidations by Surface-adsorbed Activated Species*

Two types of surface-adsorbed activated species have been discovered to be responsible for degradation of the organics in nanocarbon-catalyzed ozonation: surface O_3 complexing structure and surface-adsorbed atomic oxygen ($^*O_{ad}$). For the formation of surface O_3, the O_3 molecule was chemically adsorbed on the surface active sites without decomposition, which drastically increased the oxidation potential of the surface of the catalyst.[35,98–102] Destruction of the adsorbed organics *via* the intramolecular electron transfer process was thus expected by forming the complexing or bridging structure with surface O_3 because of its high oxidation potential. During this process, the sp^2 carbon with delocalized π electrons serves as an electron tunnel to accelerate charge transportation.

Surface-adsorbed atomic oxygen ($^*O_{ad}$) has been reported as another dominant surface-adsorbed activated species for the destruction of organics in nanocarbon-catalyzed ozonation.[96,103] The high oxidation potential of $^*O_{ad}$ (2.43 V), which is comparable to that of $^\bullet$OH, enables the mineralization of the recalcitrant organics with high reaction energy barriers. For layered N-doped nanocarbon catalyzed ozonation, a multistrategy evaluation based on quenching tests (*in situ* EPR, *in situ* Raman and DFT simulation) was performed to prove the role of $^*O_{ad}$ in the degradation of oxalic acid.[32]

5.8.2.2 *Nonradical Oxidation by $^1O_2$*

$^1O_2$ as the by-product of the chain reactions has also been considered as another nonradical species, and thus the occurrence of the $^1O_2$-nonradical oxidations is often in accompanied by radical-based oxidation.[34,95,104,105] The following equations (eqn (5.12)–(5.14)) describe the typical generation pathways of $^1O_2$, where $^*O_2$ denotes the surface-adsorbed peroxide or free peroxide from O_3 dissociation products.[106,107] It is worth noting that $^1O_2$, with its mild oxidation potential (E_0 ($^1O_2/^\bullet O_2^-$) = 0.81 V, NHE), is a highly selective oxidant that reacts exclusively with unsaturated organics *via* electrophilic addition and electron abstraction, yet it is incapable of degrading the aliphatic acids with saturated carbon bonds. Therefore, $^1O_2$ demonstrates a limited oxidation capability that can only degrade a specified range of target pollutants, and it is erroneous to correlate TOC abatement with the contribution of $^1O_2$.

$$^*O_2 \xrightarrow{\text{electron transfer}} {}^1O_2 \tag{5.12}$$

$$^\bullet O_2^- + HO_2^\bullet + H^+ \rightarrow H_2O_2 + {}^1O_2 \tag{5.13}$$

$$^\bullet O_2^- + {}^\bullet OH \rightarrow {}^1O_2 + OH^- \tag{5.14}$$

5.8.2.3 *Engineering Outlooks of Nonradical Oxidations*

For the treatment of real wastewater containing abundant inorganic anions, the efficiency of radical-based systems could be dramatically impacted because of the radical-scavenging nature of the inorganic anions and background matters. In practical application, either the treatment time was extended or a higher amount of O_3 and/or catalysts was dosed to achieve a satisfactory purification efficiency. Nevertheless, the existence of inorganic anions in high concentrations negligibly influences the nonradical oxidations that are based on the surface-adsorbed ROS and $^1O_2$ (Figure 5.17(b)).[32,33] Therefore, the nonradical systems broaden the "sweet zone" of the catalytic ozonation treatment by intensifying its treatment compatibility. However, the nonradical systems are selective and substrate dependent: The surface-adsorbed ROS with strong oxidation potentials tend to react with the aliphatic compounds in saturated carbon bonds, while $^1O_2$ with a moderate redox capacity would preferentially attack phenolics with unsaturated carbon bonds together with O_3 molecules (Figure 5.17(c)). As a result, in the case of phenolics treatment, the degradation rate of carbocatalytic ozonation is slower than that of the $^{\bullet}$OH-based system because of the relatively lower oxidation potentials of $^1O_2$ and O_3 than $^{\bullet}$OH, whereas the subsequent mineralization processes are accelerated owing to the participation of surface-adsorbed ROS.

Figure 5.18 summarizes the O_3 dissociation mechanism in the formation and evolution of diverse ROS. Direct ozone oxidation is favorable for the destruction of unsaturated organics, while O_3 is dissociated over nanocarbons to produce ROS with high oxidation potentials, which are responsible for the complete mineralization of contaminants. The free and surface-confined hydroxyl radicals would non-selectively attack the organics. $^{\bullet}O_2^-$ manifests either a reductive capability as a key linker for the formation of other ROS or a mild oxidative potential for oxidizing less recalcitrant organics. H_2O_2, as the annihilation product of $^{\bullet}O_2^-$, is a critical index to indirectly quantify the concentration of $^{\bullet}O_2^-$. The activated surface O_3 complex and $^*O_{ad}$ are

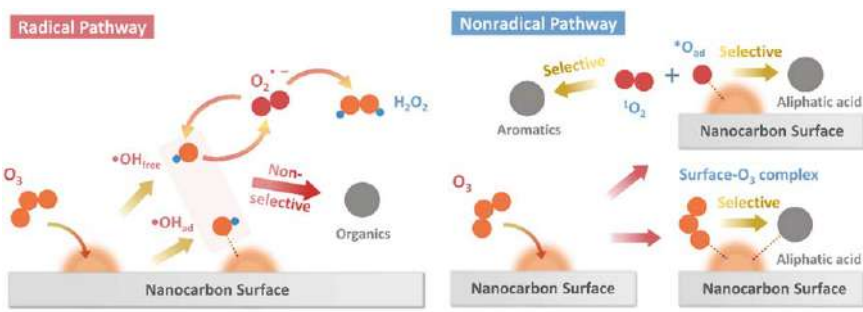

Figure 5.18 Schematic illustration of both radical and nonradical oxidation pathways *via* O_3 dissociation on the surface of nanocarbons towards the formation and evolution of diverse ROS. Reproduced from ref. 56 with permission from American Chemical Society, Copyright 2020.

nonradical ROS with high oxidation potentials, and they involve particular selectivity toward aliphatic acids against aromatics. Similar to $^{\bullet}O_2^-$, $^1O_2$ is often detected in catalytic ozonation with a mild oxidation potential, which facilitates the oxidation of electron-rich aromatics.

5.8.3 Identification of the Types of ROS and Evaluation of Their Roles

The electron paramagnetic resonance (EPR) or the electron spin resonance (ESR) technique with the aid of spin trapping agents has been employed as the most definitive method to demonstrate the existence of the ROS and to differentiate their types owing to characteristic EPR signals of the radical adducts from the reactions between the generated ROS and the specific spin trapping agents.[108,109] Apart from EPR/ESR measurement, in situ characterization techniques such as in situ Raman and in situ diffuse reflectance infrared Fourier transform spectroscopy (DRIFTS) as well as probe methods can be employed to identify and evaluate the role of ROS

5.8.3.1 Identification and Evaluation of Roles of $^{\bullet}OH$

For $^{\bullet}OH$ identification, prevailing spin trapping agents such as 5,5-dimethyl-pyrroline-*N*-oxide (DMPO) and 5-*tert*-butoxycarbonyl-5-methyl-1-pyrroline-*N*-oxide (BMPO) have been utilized because of their high stabilities as well as their strong and distinguishable EPR signals of the adducts.[32] Figure 5.19(a) and (b) demonstrates the characteristic EPR signals for the DMPO–$^{\bullet}OH$ and BMPO–$^{\bullet}OH$ adducts. 5,5-Dimethyl-2-oxo-pyrroline-1-oxyl (DMPOX) signals with the peak intensity ratio of 1 : 2 : 1 : 2 : 1 : 2 : 1 might be observed, which can be probably ascribed to the over-oxidation of the DMPO.[110,111]

Quenching tests can be conducted to evaluate the contributions of the generated ROS to the removal of organic pollutants. The ideal radical quenchers or scavengers employed in catalytic ozonation should obtain a high selectivity against the particular ROS, yet they should be quite inert against the attack from other ROS or O_3 to avoid the occurrence of competitive reactions. Aliphatic alcohols with small molecular weights such as *tert*-butanol (TBA) and methanol have been widely employed as the $^{\bullet}OH$ scavenger because of their fast reaction rates with $^{\bullet}OH$ (6×10^8 $M^{-1}s^{-1}$ and 3×10^9 $M^{-1}s^{-1}$) and high recalcitrance against O_3 (both $<3\times10^{-3}$ $M^{-1}s^{-1}$).[112] Different from methanol, TBA is only capable of quenching the $^{\bullet}OH$ in the bulk solution and cannot react with the $^{\bullet}OH$ on the surface of the catalysts.[113,114] It is worth noting that the presence of TBA reduces the surface tension of the aqueous solution, increasing the dispersion of gaseous O_3 within the aqueous solution by producing numerous fine bubbles and therefore enhancing the ozone mass transfer.[34] Inorganic scavengers such as carbonate (CO_3^{2-}, 3.9×10^8 $M^{-1}s^{-1}$) and bicarbonate (HCO_3^-,

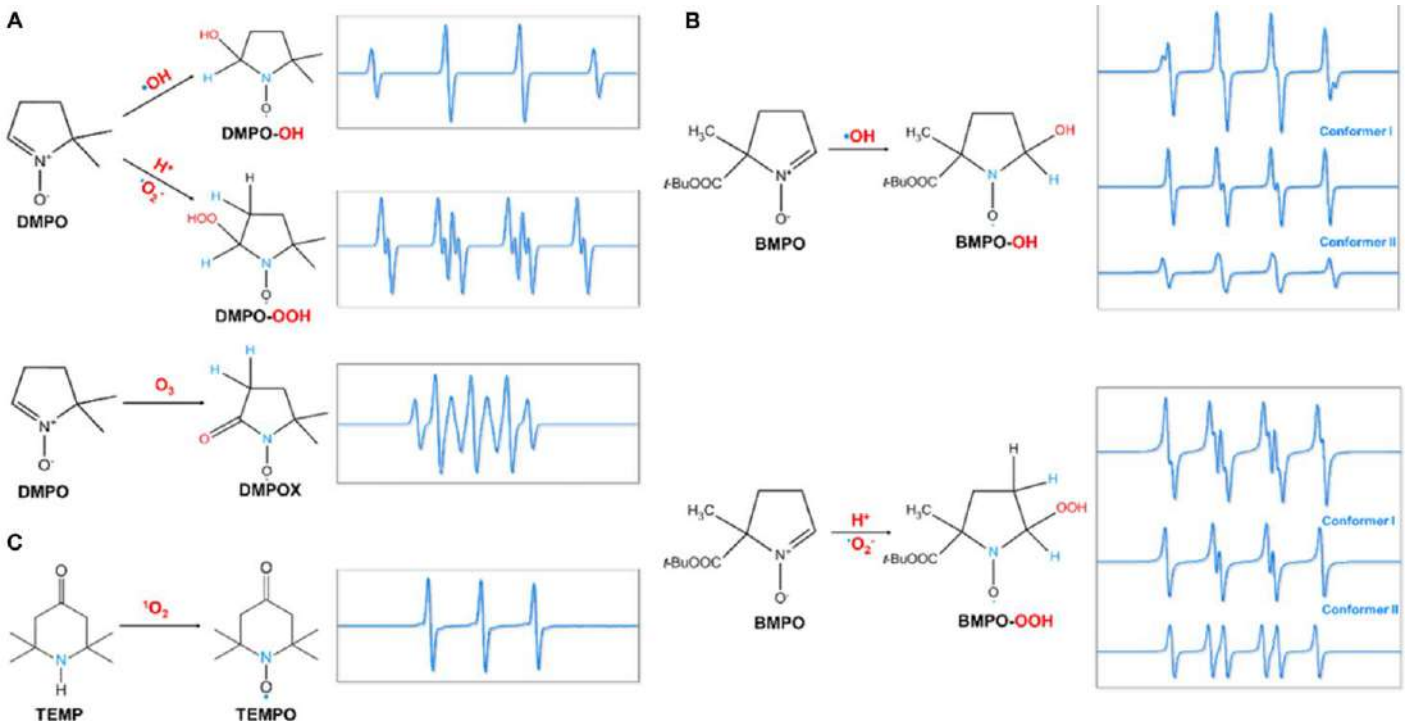

Figure 5.19 (A) Structures and simulated EPR signals of DMPO–$^{\bullet}$OH and DMPO–$^{\bullet}$OOH adducts formed by trapping $^{\bullet}$OH and $^{\bullet}O_2^-$ radicals with DMPO and DMPOX formed by oxidation of DMPO with O_3; (B) Structures and EPR signals of BMPO–$^{\bullet}$OH and BMPO–$^{\bullet}$OOH adducts formed by trapping $^{\bullet}$OH and $^{\bullet}O_2^-$ radicals with BMPO; (C) Structures and EPR signals of TEMPO adducts formed by trapping $^1O_2$ with TEMP. Reproduced from ref. 56 with permission from American Chemical Society, Copyright 2020.

$8.5\times10^6\ M^{-1}\ s^{-1}$) anions can also be utilized in catalytic ozonation to evaluate the role of $^{\bullet}OH$ in TOC mineralization, which alcohol-based scavengers cannot achieve.[115]

5.8.3.2 *Identification and Evaluation of Roles of $HO_2^{\bullet}/^{\bullet}O_2^-$*

In catalytic ozonation, the identification of $HO_2^{\bullet}/^{\bullet}O_2^-$ and determination of its role for organics degradation can be more demanding than that of $^{\bullet}OH$ since the generation of $HO_2^{\bullet}/^{\bullet}O_2^-$ is often accompanied by the production of other ROS with higher oxidation potentials such as $^{\bullet}OH$ and $^1O_2$.[19,116,117] In EPR measurements, the peak intensities of the DMPO–$^{\bullet}OOH$ and BMPO–$^{\bullet}OOH$ adducts were much inferior to those of $^{\bullet}OH$-adducts. Moreover, the characteristic signals for $^{\bullet}OOH$-adducts and $^{\bullet}OH$-adducts overlap. Alcohols can be added into the reaction solution as $^{\bullet}OH$ scavengers to shield the strong $^{\bullet}OH$-adduct peaks. The characteristic signals with $a_N = 14.2$ G, $a_H{}^{\beta} = 11.4$ G, and $a_H{}^{\gamma1} = 1.2$ G can be accounted for by the DMPO–$^{\bullet}OOH$ (Figure 5.19(a)). Nevertheless, the produced DMPO–$^{\bullet}OOH$ adducts with the half-life time ($t_{1/2}$) of 45 s is unstable and can be decayed into DMPO–$^{\bullet}OH$.[111] In addition, the carbon-centered radicals such as $^{\bullet}CH_3$, arising from the oxidation of the added alcohols by $^{\bullet}OH$ might be generated and further disturb the identification of DMPO–$^{\bullet}OOH$ adducts. BMPO can be employed as a better alternative to DMPO for $^{\bullet}O_2^-$ trapping owing to the much longer half-life of BMPO–$^{\bullet}OOH$ adduct ($t_{1/2} = 23$ min).

Organic probes such as *para*-benzoquinone (*p*-BQ) and 4-chloro-7-nitrobenzo-2-oxa-1,3-dizole (NBD-Cl) have been employed as a $HO_2^{\bullet}/^{\bullet}O_2^-$ scavenger in catalytic ozonation.[13,31,116,118–120] However, the quenching results are sometimes debatable. $^{\bullet}OH$ reacts quickly with *p*-BQ as a nonselective ROS, while its influence can be reduced by adding $^{\bullet}OH$ scavengers. Meanwhile, *p*-BQ possesses similar reaction rates with $HO_2^{\bullet}/^{\bullet}O_2^-$ and with O_3 ($9.8\times10^8\ M^{-1}\ s^{-1}$ *versus* $2.5\times10^8\ M^{-1}\ s^{-1}$),[121] which results in competitive reactions. Moreover, the overdosage of *p*-BQ further depletes the dissolved O_3 and misdirects the quenching results. Similar issues also exist in the application of NBD-Cl. Therefore, precise control of the quenching agent's dosage and careful interpretation of the quenching results are required.

5.8.3.3 *Identification and Evaluation of Roles of $^1O_2$*

As one of the nonradical species, $^1O_2$ can also be detected by EPR measurement with 2,2,6,6-tetramethyl-4-piperidone hydrochloride (TEMP) as the spin trapping agent.[34,105] The occurrence of the characteristic EPR signals of three lines with identical peak intensities and the hyperfine coupling of $a_N = 13.4$ G confirms the formation of 4-hydroxyl-2,2,6,6-tetramethyl-4-piperidone-N-oxyl (TEMPO), which is the oxidation product of TEMP by $^1O_2$ (Figure 5.19(c)).[106] However, other ROS such as $^{\bullet}OH$, $HO_2^{\bullet}/^{\bullet}O_2^-$ and the photo-induced holes (h^+) produced in photocatalysis can also oxidize TEMP

to generate TEMPO.[106,122–124] A multistrategy evaluation is thus suggested for identifying $^1O_2$.

The effect of $^1O_2$ on the organic pollutant removal can be evaluated by adding furfuryl alcohol (FFA) as the scavenger owing to the fast reaction rate (1×10^8 $M^{-1}s^{-1}$).[125] Noteworthily, FFA is also an effective $^{\bullet}OH$ scavenger (1×10^9 $M^{-1}s^{-1}$).[126,127] The influence of $^{\bullet}OH$ needs to be excluded by the corresponding quenching tests when evaluating the contribution of $^1O_2$. Sodium azide (NaN_3) has also been employed as the $^1O_2$ quenching agents (2×10^9 $M^{-1}s^{-1}$).[128] However, azide anion with a strong reducing potential also obtains high reaction rates with O_3 (2.5×10^6 $M^{-1}s^{-1}$) and $^{\bullet}OH$. The inlet O_3 can be quickly depleted if NaN_3 is overdosed, and the results would be deviated because of the hindered generation of ROS. Moreover, solution pH needs to be adjusted when NaN_3 is added because of the high alkalinity of N_3^-; otherwise, alkaline activation of O_3 is induced. Therefore, careful attention is required when employing NaN_3 as the $^1O_2$ scavenger. The isotopic kinetic solvent effect can be taken advantage of when differentiating the role of $^1O_2$ by replacing the reaction medium to D_2O. The lifetime of $^1O_2$ becomes 20-fold longer in D_2O than that in H_2O (3 μs *versus* 68 μs), and the reaction activity of $^1O_2$ is also enhanced in D_2O.[129]

5.8.3.4 *Identification and Evaluation of the Roles of Surface-adsorbed Species*

Identification of the nonradical surface-adsorbed species might be more complicated than that of the radicals because of transient formation and fast evolutions. Coloration, fluorescence and chemiluminescence approaches have been applied to demonstrate the presence of $^{\bullet}OH$, $HO_2^{\bullet}/^{\bullet}O_2^-$ and $^1O_2$ in different catalytic reaction systems.[41,130–132] *In situ* surface-based characterization techniques are thus required for their differentiation. *In situ* Raman spectroscopy can be employed to investigate the types of the surface-adsorbed species from O_3 dissociation.[32,133,134] In accordance with Oyama *et al.*, the characteristic peaks occurring at the Raman shift of 580 and 1020 cm^{-1} can be ascribed to the $^*O$, while the peak generated at 884 cm^{-1} confirms the adsorbed peroxide species.[134] Isotopic substitution of $^{16}O_3$ by $^{18}O_3$ further reveals the evolution pathway of the surface-adsorbed activated species. The active surface complexing structures and the surface-adsorbed species can be analyzed by *in situ* diffuse reflectance infrared Fourier transform spectroscopy (DRIFTS).[135] Recently, electrochemical analysis has been employed to investigate the surface-based nonradical reactions in persulfate activation.[2,136,137] By measuring the open-circuit potentials with/without the addition of different persulfates and the target pollutants, it is discovered that the formation of the carbon-persulfate surface complexes was critical for the nonradical oxidations.[136]

For assessing the contribution of surface-absorbed ROS, quenching agents such as dimethylsulfoxide (DMSO) and potassium iodide (KI) with high affinities to the surface of the catalysts can be employed.[84,138] However, the fast

reaction rate between KI and O_3 (1×10^8 M^{-1} s^{-1}) encumbers its application. Though DMSO obtains a sluggish reaction rate with O_3 (0.4162 M^{-1} s^{-1}),[139] it also reacts quickly with $^{\bullet}OH$ besides the surface-adsorbed ROS. The contribution of $^{\bullet}OH$ requires its exclusion when interpreting quenching results.

5.8.4 Critical Issues in Determination of the Oxidation Pathways

A multistrategy combining the results from different evaluations is recommended for proposing and determining the oxidation pathways. In some early studies, the proposed reaction pathways were not solid since they were derived based merely on the simple radical quenching tests with TBA as the quenching agent and/or analyzing the variation in O_3 consumption rate. The validations by the results of other evaluation techniques, such as EPR, *in situ* Raman and the employment of other quenching agents, are missing. On the basis of this review, the slight inhibition with the addition of TBA might also be ascribed to the occurrence of non-radical reactions relying on the surface-adsorbed activated species such as $^{*}O_{ad}$ and surface O_3 complexing structures.

On the other hand, attention should also be paid to the actual oxidation potentials of the generated ROS for the degradation and mineralization of the target organics. Though ROS with weak oxidation potentials, such as $^{\bullet}O_2^-$ and $^1O_2$, might be detected in the catalytic ozonation systems, it is unrealistic to expect these ROS to act as the dominant reactive species for the degradation of organics with a high energy barrier of reaction, such as aliphatic acids. They might behave more like the critical linkers that initiate or promote the chain reactions rather than contributing to the degradation of the organics. The misuse of quenching agents or misinterpretation of quenching results might also misdirect the determination of the dominant reactive species, since some of the quenchers did not achieve the single selectivity toward the specified ROS or induce the competitive reactions against other oxidants. In light of the results from the previous findings, $^1O_2$ with a mild oxidation potential usually obtains a high oxidation tendency toward the organics with unsaturated carbon bonds and electron-rich functionalities because of its electrophilic nature. $^{*}O_{ad}$, with a higher oxidation potential (2.43 V), was more favorable to the degradation of recalcitrant pollutants such as aliphatic acids than the unsaturated organics, while the high oxidation potential of $^{\bullet}OH$ endows its non-selective oxidation capability.

5.9 Conclusions and Perspectives

To conclude, surface-engineered nanocarbon materials with different dimensions have been developed as efficient ozonation catalysts for wastewater remediation. The versatility of the nanocarbons facilitates in-depth investigation of the interactions of O_3 and organics on their active sites by surface and morphology control, post-functionalization or creating discrete organic molecules containing analogous active sites on the nanocarbons. Defective sites,

including intrinsic defects (such as vacancies, edges and topological defects) and impurity defects of heteroatom dopants as well as surface functionalities, are the key active sites for catalytic ozone decomposition to produce ROS. Additionally, the synergies between the active sites are critical to further boost catalytic activity by governing electronic properties, regulating the adsorption behaviors of the reactants and tuning electron-transfer capacity. The interactions of O_3 on the active sites of the nanocarbons can induce the conventional $^{\bullet}OH$-based oxidation pathway, which can occur either in the aqueous bulk or on the surface of the nanocarbons. Meanwhile, $^{\bullet}O_2^-$ can also be produced as the reaction intermediate and serves as the chain carrier pairs for promoting $^{\bullet}OH$ or directly oxidizing vulnerable aromatic organics. However, the oxidation capability of $^{\bullet}O_2^-$ is still debatable since it can be mildly reductive or mildly oxidative. On the other hand, nonradical oxidation pathways relying on the surface-adsorbed activated species and/or $^1O_2$ might also be induced. By manipulating the types and configuration of the active sites, the reactive species and reaction pathways of the nanocarbon/O_3 system can be controlled, herein providing an oxidation system with a tunable redox potential and capacity. Additionally, a ''substrate-dependent'' oxidation regime was discovered to manifest specific selectivity to the organic contaminants because of the difference in oxidation potentials of the ROS. The discovery of the non-radical pathway in nanocarbon-based catalytic ozonation significantly broadens the applications of the AOP's technology for treating the real wastewater with the coexistence of a myriad of inorganic anions and/or organic matters. Notably, careful attention should be paid to the interpretation of EPR spectra and to the results of quenching tests for identifying ROS and evaluating their roles, since the employed spin trapping agents and the scavengers might not be ''single-selective'' to the specified ROS. Multiple strategies are thus recommended for assessing the ROS with weak oxidation potential. For transient surface-adsorbed activated species, *in situ* or *operando* techniques can be employed.

Acknowledgements

The authors greatly appreciate the financial supports from the National Natural Science Foundation of China (No. 21978324), Beijing Natural Science Foundation (No. 8192039) and Science Foundation of China University of Petroleum, Beijing (No. 2462020YXZZ034).

References

1. X. Duan, H. Sun and S. Wang, *Acc. Chem. Res.*, 2018, **51**, 678.
2. W. Ren, L. Xiong, G. Nie, H. Zhang, X. Duan and S. Wang, *Environ. Sci. Technol.*, 2020, **54**, 1267.
3. X. Duan, Z. Ao, L. Zhou, H. Sun, G. Wang and S. Wang, *Appl. Catal., B*, 2016, **188**, 98.
4. X. Duan, K. O'Donnell, H. Sun, Y. Wang and S. Wang, *Small*, 2015, **11**, 3036.

5. Z. Liu, J. Ma, Y. Cui and B. Zhang, *Appl. Catal., B*, 2009, **92**, 301.
6. Z. Liu, J. Ma, Y. Cui, L. Zhao and B. Zhang, *Appl. Catal., B*, 2010, **101**, 74.
7. A. G. Gonçalves, J. L. Figueiredo, J. J. Órfão and M. F. Pereira, *Carbon*, 2010, **48**, 4369.
8. R. Qu, B. Xu, L. Meng, L. Wang and Z. Wang, *Water Res.*, 2015, **68**, 316.
9. R. Oulton, J. P. Haase, S. Kaalberg, C. T. Redmond, M. J. Nalbandian and D. M. Cwiertny, *Environ. Sci. Technol.*, 2015, **49**, 3687.
10. J. Restivo, R. P. Rocha, A. M. T. Silva, J. J. M. Órfão, M. F. R. Pereira and J. L. Figueiredo, *Chin. J. Catal.*, 2014, **35**, 896.
11. O. Soares, R. Rocha, A. Gonçalves, J. L. Figueiredo, J. Órfão and M. F. R. Pereira, *Appl. Catal., B*, 2016, **192**, 296.
12. O. Soares, R. P. Rocha, A. Gonçalves, J. L. Figueiredo, J. Órfão and M. F. R. Pereira, *Carbon*, 2015, **91**, 114.
13. J. Wang, S. Chen, X. Quan and H. Yu, *Chemosphere*, 2018, **190**, 135.
14. A. K. Geim and K. S. Novoselov, *Nat. Mater.*, 2007, **6**, 183.
15. H. Sun, S. Liu, G. Zhou, H. M. Ang, M. O. Tadé and S. Wang, *ACS Appl. Mater. Interfaces*, 2012, **4**, 5466.
16. M. Pedrosa, L. M. Pastrana-Martínez, M. F. R. Pereira, J. L. Faria, J. L. Figueiredo and A. M. T. Silva, *Chem. Eng. J.*, 2018, **348**, 888.
17. S. Navalon, A. Dhakshinamoorthy, M. Alvaro and H. Garcia, *Chem. Rev.*, 2014, **114**, 6179.
18. M. J. McAllister, J.-L. Li, D. H. Adamson, H. C. Schniepp, A. A. Abdala, J. Liu, M. Herrera-Alonso, D. L. Milius, R. Car and R. K. Prud'homme, *Chem. Mater.*, 2007, **19**, 4396.
19. Y. Wang, Y. Xie, H. Sun, J. Xiao, H. Cao and S. Wang, *ACS Appl. Mater. Interfaces*, 2016, **8**, 9710.
20. X. Duan, Z. Ao, H. Sun, S. Indrawirawan, Y. Wang, J. Kang, F. Liang, Z. H. Zhu and S. Wang, *ACS Appl. Mater. Interfaces*, 2015, **7**, 4169.
21. C. H. Choi, S. H. Park and S. I. Woo, *ACS Nano*, 2012, **6**, 7084.
22. X. Duan, H. Sun, J. Kang, Y. Wang, S. Indrawirawan and S. Wang, *ACS Catal.*, 2015, **5**, 4629.
23. Y. Wang, H. Cao, C. Chen, Y. Xie, H. Sun, X. Duan and S. Wang, *Chem. Eng. J.*, 2019, **355**, 118.
24. Y. Wang, H. Cao, L. Chen, C. Chen, X. Duan, Y. Xie, W. Song, H. Sun and S. Wang, *Appl. Catal., B*, 2018, **229**, 71.
25. S. Stankovich, D. A. Dikin, R. D. Piner, K. A. Kohlhaas, A. Kleinhammes, Y. Jia, Y. Wu, S. T. Nguyen and R. S. Ruoff, *Carbon*, 2007, **45**, 1558.
26. B. Frank, J. Zhang, R. Blume, R. Schlögl and D. S. Su, *Angew. Chem., Int. Ed.*, 2009, **48**, 6913.
27. J. Zhang, X. Liu, R. Blume, A. Zhang, R. Schlögl and D. S. Su, *Science*, 2008, **322**, 73.
28. H. Sun, C. Kwan, A. Suvorova, H. M. Ang, M. O. Tadé and S. Wang, *Appl. Catal., B*, 2014, **154**, 134.
29. H. Sun, Y. Wang, S. Liu, L. Ge, L. Wang, Z. Zhu and S. Wang, *Chem. Commun.*, 2013, **49**, 9914.

30. R. Yin, W. Guo, J. Du, X. Zhou, H. Zheng, Q. Wu, J. Chang and N. Ren, *Chem. Eng. J.*, 2017, **317**, 632.
31. Z. Song, M. Wang, Z. Wang, Y. Wang, R. Li, Y. Zhang, C. Liu, Y. Liu, B. Xu and F. Qi, *Environ. Sci. Technol.*, 2019, **53**, 5337.
32. Y. Wang, L. Chen, C. Chen, J. Xi, H. Cao, X. Duan, Y. Xie, W. Song and S. Wang, *Appl. Catal., B*, 2019, **254**, 283.
33. Y. Wang, J. Xi, X. Duan, W. Lv, H. Cao, C. Chen, Z. Guo, Y. Xie and S. Wang, *J. Hazard. Mater.*, 2020, **384**, 121486.
34. Y. Wang, L. Chen, H. Cao, Z. Chi, C. Chen, X. Duan, Y. Xie, F. Qi, W. Song, J. Liu and S. Wang, *Appl. Catal., B*, 2019, **245**, 546.
35. Z. Sun, L. Zhao, C. Liu, Y. Zhen and J. Ma, *Environ. Sci. Technol.*, 2019, **53**, 10342.
36. J. Yin, G. Liao, D. Zhu, P. Lu and L. Li, *J. Photochem. Photobiol., A*, 2016, **315**, 138.
37. F. Yang, M. Zhao, Z. Wang, H. Ji, B. Zheng, D. Xiao, L. Wu and Y. Guo, *RSC Adv.*, 2014, **4**, 58325.
38. Z. Song, Y. Zhang, C. Liu, B. Xu, F. Qi, D. Yuan and S. Pu, *Chem. Eng. J.*, 2019, **357**, 655.
39. X. Duan, H. Sun, Z. Shao and S. Wang, *Appl. Catal., B*, 2018, **224**, 973.
40. J. Yu, H. Feng, L. Tang, Y. Pang, G. Zeng, Y. Lu, H. Dong, J. Wang, Y. Liu, C. Feng, J. Wang, B. Peng and S. Ye, *Prog. Mater. Sci.*, 2020, **111**, 100654.
41. S. Zhang, X. Quan, J. F. Zheng and D. Wang, *Water Res.*, 2017, **122**, 86.
42. S. Navalon, A. Dhakshinamoorthy, M. Alvaro, M. Antonietti and H. García, *Chem. Soc. Rev.*, 2017, **46**, 4501.
43. X. Fan, J. Restivo, J. J. M. Órfão, M. F. R. Pereira and A. A. Lapkin, *Chem. Eng. J.*, 2014, **241**, 66.
44. S. Iijima, *Nature*, 1991, **354**, 56.
45. H. Dai, *Surf. Sci.*, 2002, **500**, 218.
46. X. Pan and X. Bao, *Acc. Chem. Res.*, 2011, **44**, 553.
47. D. Chen, H. Feng and J. Li, *Chem. Rev.*, 2012, **112**, 6027.
48. D. Yu, K. Goh, H. Wang, L. Wei, W. Jiang, Q. Zhang, L. Dai and Y. Chen, *Nat. Nanotechnol.*, 2014, **9**, 555.
49. Y. Xue, Y. Ding, J. Niu, Z. Xia, A. Roy, H. Chen, J. Qu, Z. L. Wang and L. Dai, *Sci. Adv.*, 2015, **1**, e1400198.
50. J. Zhao, Y. Jiang, H. Fan, M. Liu, O. Zhuo, X. Wang, Q. Wu, L. Yang, Y. Ma and Z. Hu, *Adv. Mater.*, 2017, **29**, 1604569.
51. D. R. Dreyer, S. Park, C. W. Bielawski and R. S. Ruoff, *Chem. Soc. Rev.*, 2010, **39**, 228.
52. F. Bernat-Quesada, J. C. Espinosa, V. Barbera, M. Álvaro, M. Galimberti, S. Navalón and H. García, *ACS Sustainable Chem. Eng.*, 2019, **7**, 17443.
53. Y. Yoon, H. Oh, Y. T. Ahn, M. Kwon, Y. Jung, W. K. Park, T. M. Hwang, W. S. Yang and J. W. Kang, *Catal. Today*, 2017, **282**, 77.
54. X. Duan, H. Sun, Z. Ao, L. Zhou, G. Wang and S. Wang, *Carbon*, 2016, **107**, 371.
55. C. D. Vecitis, T. Lesko, A. J. Colussi and M. R. Hoffmann, *J. Phys. Chem. A*, 2010, **114**, 4968.

56. Y. Wang, X. Duan, Y. Xie, H. Sun and S. Wang, *ACS Catal.*, 2020, **10**, 13383.
57. M. Acik and Y. J. Chabal, *Jpn. J. Appl. Phys.*, 2011, **50**, 070101.
58. F. Banhart, J. Kotakoski and A. V. Krasheninnikov, *ACS Nano*, 2011, **5**, 26.
59. W. Yuan, Y. Zhou, Y. Li, C. Li, H. Peng, J. Zhang, Z. Liu, L. Dai and G. Shi, *Sci. Rep.*, 2013, **3**, 2248.
60. A. Shen, Y. Zou, Q. Wang, R. A. W. Dryfe, X. Huang, S. Dou, L. Dai and S. Wang, *Angew. Chem., Int. Ed.*, 2014, **53**, 10804.
61. P. P. Sharma, J. Wu, R. M. Yadav, M. Liu, C. J. Wright, C. S. Tiwary, B. I. Yakobson, J. Lou, P. M. Ajayan and X. Zhou, *Angew. Chem., Int. Ed.*, 2015, **54**, 13701.
62. S. T. Skowron, I. V. Lebedeva, A. M. Popov and E. Bichoutskaia, *Chem. Soc. Rev.*, 2015, **44**, 3143.
63. L. Dai, Y. Xue, L. Qu, H.-J. Choi and J.-B. Baek, *Chem. Rev.*, 2015, **115**, 4823.
64. R. Garg, N. K. Dutta and N. R. Choudhury, *Nanomaterials*, 2014, **4**, 267.
65. D. Usachov, A. Fedorov, O. Vilkov, B. Senkovskiy, V. K. Adamchuk, L. V. Yashina, A. A. Volykhov, M. Farjam, N. I. Verbitskiy, A. Grüneis, C. Laubschat and D. V. Vyalikh, *Nano Lett.*, 2014, **14**, 4982.
66. O. S. G. P. Soares, R. P. Rocha, A. G. Gonçalves, J. L. Figueiredo, J. J. M. Órfão and M. F. R. Pereira, *Appl. Catal., B*, 2016, **192**, 296.
67. X. Liu and L. Dai, *Nat. Rev. Mater.*, 2016, **1**, 16064.
68. W. Li, Y. Gao, W. Chen, P. Tang, W. Li, Z. Shi, D. Su, J. Wang and D. Ma, *ACS Catal.*, 2014, **4**, 1261.
69. L. Zhang, Y. Shi, Y. Wang and N. R. Shiju, *Adv. Sci.*, 2020, **7**, 1902126.
70. X. Kong, Q. Chen and Z. Sun, *Chem. Phys. Chem.*, 2013, **14**, 514.
71. L. Yang, S. Jiang, Y. Zhao, L. Zhu, S. Chen, X. Wang, Q. Wu, J. Ma, Y. Ma and Z. Hu, *Angew. Chem., Int. Ed.*, 2011, **50**, 7132.
72. J. P. Paraknowitsch and A. Thomas, *Energy Environ. Sci.*, 2013, **6**, 2839.
73. X. Ma, G. Ning, Y. Wang, X. Song, Z. Xiao, L. Hou, W. Yang, J. Gao and Y. Li, *Electrochim. Acta*, 2018, **269**, 83.
74. S. Yang, L. Zhi, K. Tang, X. Feng, J. Maier and K. Müllen, *Adv. Funct. Mater.*, 2012, **22**, 3634.
75. M. Wu, C. Cao and J. Z. Jiang, *Nanotechnology*, 2010, **21**, 505202.
76. B. Dai, K. Chen, Y. Wang, L. Kang and M. Zhu, *ACS Catal.*, 2015, **5**, 2541.
77. Y. Zheng, Y. Jiao, L. H. Li, T. Xing, Y. Chen, M. Jaroniec and S. Z. Qiao, *ACS Nano*, 2014, **8**, 5290.
78. G. Pacchioni, *Phys. Chem. Chem. Phys.*, 2013, **15**, 1737.
79. G. Pacchioni and H.-J. Freund, *Chem. Soc. Rev.*, 2018, **47**, 8474.
80. Y. Wang, Y. Xie, H. Sun, J. Xiao, H. Cao and S. Wang, *J. Hazard. Mater.*, 2016, **301**, 56.
81. H. Terrones, R. Lv, M. Terrones and M. S. Dresselhaus, *Rep. Prog. Phys.*, 2012, **75**, 062501.
82. Y. Wang, Z. Ao, H. Sun, X. Duan and S. Wang, *Appl. Catal., B*, 2016, **198**, 295.
83. W. Qi, W. Liu, B. Zhang, X. Gu, X. Guo and D. Su, *Angew. Chem., Int. Ed.*, 2013, **52**, 14224.

84. S. Zhu, X. Huang, F. Ma, L. Wang, X. Duan and S. Wang, *Environ. Sci. Technol.*, 2018, **52**, 8649.
85. U. von Gunten, *Water Res.*, 2003, **37**, 1443.
86. B. Kasprzyk-Hordern, M. Ziolek and J. Nawrocki, *Appl. Catal., B*, 2003, **46**, 639.
87. B. Kasprzyk-Hordern, M. Ziółek and J. Nawrocki, *Appl. Catal., B*, 2003, **46**, 639.
88. T. Du, A. S. Adeleye, T. Zhang, N. Yang, R. Hao, Y. Li, W. Song and W. Chen, *Environ. Sci.: Nano*, 2019, **6**, 2484.
89. M. Sánchez-Polo, U. von Gunten and J. Rivera-Utrilla, *Water Res.*, 2005, **39**, 3189.
90. P. M. Alvárez, J. F. García-Araya, F. J. Beltrán, I. Giráldez, J. Jaramillo and V. Gómez-Serrano, *Carbon*, 2006, **44**, 3102.
91. F. J. Beltrán, F. J. Rivas, L. A. Fernández, P. M. Álvarez and R. Montero-de-Espinosa, *Ind. Eng. Chem. Res.*, 2002, **41**, 6510.
92. Z. Liu, J. Ma, Y. Cui, L. Zhao and B. Zhang, *Appl. Catal., B*, 2010, **101**, 74.
93. Y. Yoon, J. Moon, M. Kwon, Y. Jung, S. Kim and J.-W. Kang, *Ozone: Sci. Eng.*, 2014, **36**, 465.
94. A. G. Gonçalves, J. L. Figueiredo, J. J. M. Órfão and M. F. R. Pereira, *Carbon*, 2010, **48**, 4369.
95. Y. Zhang, Q. Li, Y. Long, J. Zou, Z. Song, C. Liu, L. Liu, F. Qi, B. Xu and Z. Chen, *Appl. Catal., B*, 2019, **254**, 569.
96. J. Bing, C. Hu and L. Zhang, *Appl. Catal., B*, 2017, **202**, 118.
97. F. J. Beltrán, B. Acedo, F. J. Rivas and O. Gimeno, *Ozone: Sci. Eng.*, 2005, **27**, 159.
98. R. C. Martins and R. M. Quinta-Ferreira, *Appl. Catal., B*, 2009, **90**, 268.
99. X. Liu, Z. Zhou, G. Jing and J. Fang, *Sep. Purif. Technol.*, 2013, **115**, 129.
100. Q. Dai, J. Wang, J. Yu, J. Chen and J. Chen, *Appl. Catal., B*, 2014, **144**, 686.
101. A. Ikhlaq, S. Waheed, K. S. Joya and M. Kazmi, *Catal. Commun.*, 2018, **112**, 15.
102. Z. Ma, L. Zhu, X. Lu, S. Xing, Y. Wu and Y. Gao, *Sep. Purif. Technol.*, 2014, **133**, 357.
103. T. Zhang, W. Li and J.-P. Croué, *Environ. Sci. Technol.*, 2011, **45**, 9339.
104. S. Zhang, X. Quan and D. Wang, *Environ. Sci. Technol.*, 2018, **52**, 8701.
105. Y. Wang, Y. Xie, H. Sun, J. Xiao, H. Cao and S. Wang, *Catal. Sci. Technol.*, 2016, **6**, 2918.
106. Y. Nosaka and A. Y. Nosaka, *Chem. Rev.*, 2017, **117**, 11302.
107. A. D. Bokare and W. Choi, *Environ. Sci. Technol.*, 2015, **49**, 14392.
108. Y. Wang, H. Sun, X. Duan, H. M. Ang, M. O. Tadé and S. Wang, *Appl. Catal., B*, 2015, **172**, 73.
109. X. Duan, H. Sun, Y. Wang, J. Kang and S. Wang, *ACS Catal.*, 2015, **5**, 553.
110. J. Xiao, Q. Han, H. Cao, J. Rabeah, J. Yang, Z. Guo, L. Zhou, Y. Xie and A. Brückner, *ACS Catal.*, 2019, **9**, 8852.
111. H. Zhao, J. Joseph, H. Zhang, H. Karoui and B. Kalyanaraman, *Free Radical Biol. Med.*, 2001, **31**, 599.

112. G. V. Buxton, C. L. Greenstock, W. P. Helman and A. B. Ross, *J. Phys. Chem. Ref. Data*, 1988, **17**, 513.
113. T. Turan-Ertas and M. D. Gurol, *Chemosphere*, 2002, **47**, 293.
114. J. Xiao, Y. Xie, H. Cao, Y. Wang, Z. Guo and Y. Chen, *Carbon*, 2016, **107**, 658.
115. J. Ma and N. J. D. Graham, *Water Res.*, 2000, **34**, 3822.
116. F. Nawaz, H. Cao, Y. Xie, J. Xiao, Y. Chen and Z. A. Ghazi, *Chemosphere*, 2017, **168**, 1457.
117. F. Nawaz, Y. Xie, J. Xiao, H. Cao, Z. A. Ghazi, Z. Guo and Y. Chen, *Catal. Sci. Technol.*, 2016, **6**, 7875.
118. A. Ikhlaq, D. R. Brown and B. Kasprzyk-Hordern, *Appl. Catal., B*, 2013, **129**, 437.
119. F. Nawaz, Y. Xie, H. Cao, J. Xiao, Y. Wang, X. Zhang, M. Li and F. Duan, *Catal. Today*, 2015, **258**, 595.
120. J. Zhang, Y. Wu, C. Qin, L. Liu and Y. Lan, *Chemosphere*, 2015, **141**, 258.
121. E. Mvula and C. von Sonntag, *Org. Biomol. Chem.*, 2003, **1**, 1749.
122. P. Bilski, K. Reszka, M. Bilska and C. F. Chignell, *J. Am. Chem. Soc.*, 1996, **118**, 1330.
123. R. Poupko and I. Rosenthal, *J. Phys. Chem.*, 1973, **77**, 1722.
124. T. A. Konovalova, J. Lawrence and L. D. Kispert, *J. Photochem. Photobiol., A*, 2004, **162**, 1.
125. F. E. Scully and J. Hoigné, *Chemosphere*, 1987, **16**, 681.
126. E. A. Betterton and D. Craig, *J. Air Waste Manage. Assoc.*, 1999, **49**, 1347.
127. J. Catalán, C. Díaz and L. Barrio, *Chem. Phys.*, 2004, **300**, 33.
128. A. Jawad, X. Lu, Z. Chen and G. Yin, *J. Phys. Chem. A*, 2014, **118**, 10028.
129. C. Schweitzer and R. Schmidt, *Chem. Rev.*, 2003, **103**, 1685.
130. H. Goto, Y. Hanada, T. Ohno and M. Matsumura, *J. Catal.*, 2004, **225**, 223.
131. H. Wu, Q. Song, G. Ran, X. Lu and B. Xu, *TrAC, Trends Anal. Chem.*, 2011, **30**, 133.
132. K. Naito, T. Tachikawa, M. Fujitsuka and T. Majima, *J. Phys. Chem. C*, 2008, **112**, 1048.
133. S. Gong, Z. Xie, W. Li, X. Wu, N. Han and Y. Chen, *Appl. Catal., B*, 2019, **241**, 578.
134. W. Li, G. V. Gibbs and S. T. Oyama, *J. Am. Chem. Soc.*, 1998, **120**, 9041.
135. J. Wu, T. Su, Y. Jiang, X. Xie, Z. Qin and H. Ji, *Appl. Surf. Sci.*, 2017, **412**, 290.
136. W. Ren, G. Nie, P. Zhou, H. Zhang, X. Duan and S. Wang, *Environ. Sci. Technol.*, 2020, **54**, 6438.
137. L. Tang, Y. Liu, J. Wang, G. Zeng, Y. Deng, H. Dong, H. Feng, J. Wang and B. Peng, *Appl. Catal., B*, 2018, **231**, 1.
138. S. Zhu, X. Li, J. Kang, X. Duan and S. Wang, *Environ. Sci. Technol.*, 2019, **53**, 307.
139. J. J. Wu, M. Muruganandham and S. H. Chen, *J. Hazard. Mater.*, 2007, **149**, 218.

CHAPTER 6

UVA Photocatalytic Ozonation of Water Contaminants

F. J. BELTRÁN* AND O. GIMENO

Departamento de Ingeniería Química y Química Física, Instituto Universitario de Investigación del Agua, Cambio Climático y Sostenibilidad, Universidad de Extremadura, 06006 Badajoz, Spain
*Email: fbeltran@unex.es

6.1 Introduction

At the end of the 1980s, the significant improvement of analytical equipment allowed the identification of many organic compounds (pesticides, polynuclear aromatics, *etc.*) in different water environments.[1–3] Previously, in the 1970s, other potentially toxic compounds such as trihalomethanes or halocarboxylic acids were detected in finished drinking water.[4,5] More recently, as a result of their extensive use for therapeutic purposes or personal care, numerous pharmaceuticals and hygienic products were identified in municipal wastewater treatment plants.[6–8] The immediate consequence of all these findings was that scientists started the search for technologies able to remove these compounds from water. Toward this end, technologies such as advanced oxidation processes (AOP) were appearing to clean water environments.[9–11] AOPs are usually a combination of one, two or three agents (chemical oxidants, radiation, catalysts, *etc.*) to generate hydroxyl free radicals, short-lived species with high oxidizing power only below that of fluorine and atomic oxygen.[12] Two of these AOPs are ozonation and UV photocatalytic oxidation. Applied separately, they can generate hydroxyl radicals, with an

Chemistry in the Environment Series No. 8
Advanced Ozonation Processes for Water and Wastewater Treatment: Active Catalysts and Combined Technologies
Edited by Hongbin Cao, Yongbing Xie, Yuxian Wang and Jiadong Xiao

Published by the Royal Society of Chemistry, www.rsc.org

intensity (or concentration) that depends on such experimental conditions as pH and organic content of the water, among others. This chapter deals with these two technologies when used together to constitute a third one called UV photocatalytic ozonation (PhCatOz). This chapter focuses on the use of radiation sources of wavelengths between 300 and 400 nm, which is currently called UVA radiation. In the next two sections, a brief introduction of both AOPs, individually considered, is first presented.

6.2 Ozonation of Water Contaminants

Ozone is an allotropic form of oxygen with three atoms linked to form a hybrid in resonance having a variable electronic distribution in the molecule. This allows ozone to react with organics in different ways such as 1,3-dipolar addition to a carbon double bond (Criegge mechanism),[13] constituted by a mechanism initiated by the simultaneous attack of oxygen at the edges of the ozone molecule positively and negatively charged or by substitution reactions on groups negatively or positively charged, such as the known electrophilic aromatic substitution reactions. These latter ways of action are significantly important when aromatic compounds with activating substituents groups (hydroxyl in phenols, amine in aniline, *etc.*) are present in the water to be treated as, for instance, in the case of many pharmaceuticals. However, ozone has another way of reaction through hydroxyl radicals that are formed from its decomposition when there are no fast reacting compounds in water or when these compounds are in a very low concentration (at ppb level or less), as is the case of pharmaceuticals in municipal wastewater. This is why ozonation is an AOP. However, the initial reaction of the ozone decomposition mechanism has a low rate constant, 70 or 140 $M^{-1}\,s^{-1}$, depending on different authors,[14,15] which makes ozonation a weak AOP because of the low concentration of hydroxyl radicals it generates by itself. The first reactions of the ozone mechanism are:

$$O_3 + OH^- \rightarrow HO_2^- + O_2 \tag{6.1}$$

In reaction (6.1), no free radicals are formed, but hydrogen peroxide results as shown next. In 1987, Glaze and coworkers[9] reported their studies on the combinations of ozone and hydrogen peroxide or UVC radiation (perozone and photolytic ozone processes, respectively). The initial reactions of these AOP are:

$$O_3 + HO_2^- \rightarrow HO_2^{\bullet} + {}^{\bullet}O_3^- \tag{6.2}$$

and

$$O_3 + H_2O \xrightarrow{h\nu} H_2O_2 + O_2 \tag{6.3}$$

Hydrogen peroxide generated in reaction (6.2) continues with reaction (6.1) and with the photolysis of hydrogen peroxide:

$$H_2O_2 \xrightarrow{h\nu} 2^{\bullet}OH \tag{6.4}$$

Therefore, from ozone photolysis, hydroxyl radicals are formed through two routes, though reaction (6.2) always predominates in the photolytic ozone process.[16] Then O_3/H_2O_2 and O_3/UV were the first two ozone-combined AOPs investigated. In photolytic processes, in addition to pH, the importance of parameters such as the quantum yield and absorption coefficient of ozone and hydrogen peroxide have to be kept in mind. Radiations of wavelength higher than 325 nm are useless since ozone does not absorb at these wavelengths, but with UVA of higher energy ($\lambda < 325$ nm), UVB and especially UVC, the generation of hydroxyl radicals significantly increases.[17] Something similar applies to hydrogen peroxide photolysis.[18] In ozonation systems, ozone decomposition is accelerated by the increase of pH to form more hydrogen peroxide and increase the rate of reaction (6.2), the true initial reaction of ozone processes. Substances present in water play three different roles in an ozone system: initiators, promoters and scavengers of ozone decomposition.[14] An *initiator* is hydrogen peroxide since when it reacts with ozone directly, it generates free radicals, specifically the hydroperoxide and ozonide ion radicals as shown in reaction (6.2). These free radicals eventually lead to the formation of hydroxyl radicals, especially at a pH higher than 4.8, a pK of equilibrium between $HO_2^{\bullet}$ and the superoxide ion radical $^{\bullet}O_2^{-}$. In addition to hydrogen peroxide, other organics act as initiators, such as diclofenac, one of the most abundant pharmaceuticals identified in municipal wastewater.[19] *Promoters* are compounds that, while reacting with the hydroxyl radical, form the hydroperoxide radical or some peroxy radicals that propagate the mechanism chain. Finally, *scavengers* are substances whose reaction with hydroxyl radicals terminates the mechanism chain. Natural scavengers are, for example, carbonates. Scavengers are one of the disadvantages of using AOPs because their presence reduces the hydroxyl radicals available to react with micropollutants. Another ozone AOP is catalytic ozonation, wherein the presence of catalysts accelerates the decomposition of ozone through different mechanisms that depend on the type of catalyst and organics to be removed.[20] This kind of ozone process, however, cannot always be cataloged as an AOP since reactions responsible for organic removal can be direct reactions through complex formation.[21] Also, combinations of ozone with ultrasound (which in fact is another sort of photolytic ozonation) or with a catalyst and light (photocatalytic ozonation) are more recent AOPs. The last one is the object of this review. In spite of being an old process (it harkens to the end of the nineteenth century), the importance of ozonation is shown in the multiple works published in the last 30 years. According to the Scopus data base, nearly 3000 papers on water ozonation have been published just from 2015.

6.3 Photocatalytic Oxidation of Water Contaminants

Studies on photocatalytic oxidation started in the 1960s with the works of Fujishima and coworkers on the conversion of solar energy by photoelectrical cells.[22] They used TiO_2 since, in addition to being a cheap and stable material, this semiconductor is recommended for processes of photoinduced

hydrophilicity. Both processes can simultaneously develop on the same TiO_2 surface, although, depending on composition and processing, only one of them can be favored. Returning to the first step of photoelectrical cells, Fujishima *et al.*[23] tried to reproduce the natural photosynthesis of plants that oxidizes water to produce oxygen and to reduce carbon dioxide to produce hydrogen. They called their process solar photoelectrolysis of water splitting that consisted of one TiO_2 electrode connected to a counter-electrode of Pt. Both electrodes were submerged in cells separated by an ionic conductor.[24] The TiO_2 electrode was exposed to solar light, and the following reactions developed:

TiO_2 excitation:

$$TiO_2 \xrightarrow{2h\nu} 2h^+ + 2e^- \tag{6.5}$$

Oxygen formation at the TiO_2 electrode:

$$H_2O + 2h^+ \rightarrow 0.5O_2 + 2H^+ \tag{6.6}$$

Hydrogen formation at the Pt electrode:

$$2H^+ + 2e^- \rightarrow H_2 \tag{6.7}$$

Fujishima *et al.*[23] observed that this process developed, regardless of radiation intensity provided the energy of the incident radiation was higher than that of the band gap of the catalyst. The excitation of the catalyst is the initial step of photocatalytic oxidation. In this AOP, hydroxyl radicals are mainly formed in the valence band of the catalyst when holes from reaction (6.5) oxidize water to give hydroxyl radicals. The process depends on the band gap of the catalyst, the energy of incident radiation and the energy of the valence and conduction bands of the catalyst. Thus the energy of the valence band must be more positive than the one of the $^{\bullet}OH/H_2O$ system (2.27 eV), and the energy of the conduction band more negative than the one of $O_2/^{\bullet}O_2^-$ system (−0.28 eV). A few catalysts, TiO_2 among them, fulfill these requirements. Thus TiO_2 presents energies of +2.53 eV and −0.52 eV in its valence and conduction bands, respectively. The problem is its high band gap: 3.2 eV makes visible light useless in exciting TiO_2. However, the energy of radiation lower than 385 nm, that is, UVA, UVB and UVC radiation, is valid for the process. In addition to reaction (6.5), with previous requirements, the main reactions of the photocatalytic oxidation system are the oxidation of adsorbed water or hydroxyl groups to form hydroxyl radicals.

$$TiO_2 - H_2O(OH-) + h^+ \rightarrow TiO_2 - {}^{\bullet}OH \tag{6.8}$$

and oxygen reduction by capturing electrons:

$$O_2 + e^- \rightarrow {}^{\bullet}O_2^- \tag{6.9}$$

The superoxide ion radical formed in reaction (6.9) leads to hydrogen peroxide:

$$^{\bullet}O_2^- + H^+ \rightarrow HO_2^{\bullet} \tag{6.10}$$

and

$$2HO_2^{\bullet} \rightarrow H_2O_2 + O_2 \quad (6.11)$$

though these last two reactions depend on the organic composition of water, since the superoxide ion radical also has some oxidizing power. Another important negative step in photocatalytic oxidation is the electron–hole recombination that inhibits the reaction rate:

$$h^+ + e^- \rightarrow TiO_2 + \text{energy} \quad (6.12)$$

As indicated for ozonation, photocatalytic oxidation is another AOP of high use in water environmental studies. The Scopus data base reports nearly 1000 publications (most of them research papers) in the last five years. Radiation sources, the nature of catalysts, the influence of variables such as organic concentration, pH, intensity of radiation are the basis of most of these publications.[25,26]

6.4 Photocatalytic Ozonation

As can be deduced from the main reactions of ozonation and photocatalytic oxidation mechanisms, the simultaneous presence of ozone, radiation and a semiconductor catalyst with the right properties related to valence and conduction band energies and band gap should increase the rate of hydroxyl radical formation with new initial steps. First, when TiO_2 is the catalyst, in addition to oxygen, ozone and hydrogen peroxide can also trap electrons from the conduction band of TiO_2 since the redox potential of H_2O_2/H_2O and O_3/H_2O is more positive, 1.35 and 2.07 eV, respectively, than the energy of the conduction band of TiO_2, −0.52 eV. This means there are similar reactions to reaction (6.9) between oxygen and electrons:

$$O_3 + e^- \rightarrow {}^{\bullet}O_3^- \quad (6.13)$$

$$H_2O_2 + e^- \rightarrow {}^{\bullet}OH + OH^- \quad (6.14)$$

and the ozonide ion radical to eventually yield more hydroxyl radicals:

$${}^{\bullet}O_3^- + H^+ \rightarrow HO_3^{\bullet} \quad (6.15)$$

$$HO_3^{\bullet} \rightarrow {}^{\bullet}OH + O_2 \quad (6.16)$$

Note that hydrogen peroxide is a key oxidant in ozone systems. In photocatalytic ozonation of organic compounds there is no need to add hydrogen peroxide because this is formed from direct ozone reactions, as happens with diclofenac ozonation[27] as an example. In fact, when the organics are initiators of ozone decomposition, hydrogen peroxide is formed, and hence reaction (6.14) is another means of hydroxyl radical formation.

Now that the mechanism of photocatalytic ozonation has been described, one can better understand why this AOP is more effective than single ozonation and photocatalytic oxidation systems and why there is a synergism between these two processes. Some works have already checked this

synergism, simply by determining the pseudo first-order rate constants of the three processes and observing that the ratio of the rate of photocatalytic ozonation was higher than the sum of the rates of single ozonation and photocatalytic oxidation (see Section 6.5.7).

Although the number of publications about photocatalytic ozonation is lower than those of the single processes (Scopus reports nearly 150 during the last five years), this AOP still attracts the attention of many researchers, especially in preparing catalysts that can be easily separated from water or be active under visible light. On the other hand, the higher energy of UVB and UVC radiations makes the oxidation rates of micropollutants more efficient when using ozone and catalysts. However, in this chapter only UVA radiation is reviewed focusing on works reported in the last five years since other reviewing works have been published in 2015 and earlier.[28–30] The reason for the preferential study of UVA radiation photocatalytic ozone processes is the lower cost of UVA lamps against the more expensive UVC lamps and also the possibility of using UVA LEDs as the radiation source, minimizing the cost of the process regarding duration and maintenance.[31–33]

6.5 UVA Photocatalytic Ozonation

In this process, lamps or light-emitting diodes (LEDs) are the source of radiation. UVA radiation extends from about 300 to 400 nm, and radiations with wavelengths between 300 and 325 nm activate not only TiO_2 but also ozone and hydrogen peroxide that still undergo photolysis to generate more hydroxyl free radicals. Also, solar radiation reaching Earth belongs to this category though only about 5% falls in the UVA range. In any case, for catalysts such as TiO_2, solar radiation specifically falls in the UVA photocatalytic ozonation category since TiO_2 is not active under visible light.

Because the mechanism of this process has already been explained in previous sections, here the review deals with different aspects of the process such as catalyst nature, radiation source, organics treated, influence of variables, kinetics, *etc.* This work reviews research articles of the last five years because the literature already reports reviews published before 2015. These works are listed with their main characteristics in Table 6.1.

6.5.1 Catalysts

Catalysts, radiation source and ozone are the main agents of UVA PhCatOz. There are two types of UVA photocatalytic ozonation depending on the catalyst used: dissolved in water or as a solid material. For the first group, homogeneous photocatalytic ozonation, as far as we know, in the last five years, only one work has been published.[90] In this case, the catalyst was iron sulfate applied with ozone and UVC radiation to treat hospital wastewater containing 83 target pharmaceutical contaminants. Homogeneous photocatalysis presents the problem of catalyst separation, though when iron salts are used, the inconvenience is minimized due to the high permissible

Table 6.1 Works on UVA photocatalytic ozonation of water contaminants.[a]

Catalysts	Target pollutants	Reactor and radiation source	Ozonation conditions	Process performance	Ref.
TiO_2 nanotubes $C_{cat} = 0.1–0.3\ g\,L^{-1}$	PAHs in offshore water (1–10 $\mu g\,L^{-1}$)	Agitated Amber bottle (500 mL) UVA LED 365 nm	0.12 $L\,min^{-1}$ 0.6–1.8 O_3 $mg\,min^{-1}$ $pH_0 = 7.68$ 4.25 $mW\,cm^{-2}$ at 34 V and 9.93 $mW\,cm^{-2}$ at 36 V	In 10 min total phenol removal In 40 min total PAH removal Intermediates, toxicity, biodegradability	34
TiO_2 nanotubes supported on Ti foils	Parabens (UP and MWW) (1 $mg\,L^{-1}$ each)	2 L semibatch tank with quartz tubes for UVA lamps 365 nm and Sunlight	Gas flow: 0.2 $L\,min^{-1}$ pH = 7.2 5.75×10^{-7} Einstein^{-1} Ls^{-1}	In 15 min total paraben removal with O_3 In 10 min total paraben removal with O_3/cat/light TOD. Toxicity	35
TiO_2/Fe_3O_4/activated carbon composite $C_{cat} = 0.4\ g\,L^{-1}$	Pharmaceuticals (2 $mg\,L^{-1}$ each) SEMWW and synthetic wastewater	Solar box. Xe lamp. λ: 300–800 nm 550 $W\,m^{-2}$ Semibatch reactor V = 300 mL	$pH_0 = 7.5–7.8$ 20 $L\,h^{-1}$ flowrate, 10 $mg\,L^{-1}$ O_3 3.86×10^{-7} Einstein^{-1} $L\,s^{-1}$	Total removal of pharmaceuticals in less than 30 min with PhCatOz. 40% removal with O_2/Light/cat PhCatOz: 45–50% DOC removal in 2 h O_2/Light/cat: 35–40% DOC removal in 2 h	36
P25 TiO_2 1 $g\,L^{-1}$	Methylene blue (3.5×10^{-5} M) in sea water with 20%–30%–40% salt concentration	Medium pressure Hg lamp 1.27 L semibatch column	30–60 $mg\,L^{-1}$ O_3 in gas 94 $\mu W\,cm^{-2}$	PhCatO_3: 93% MB removal in 40 min O_3: 90 and 75% MB removal in 40 min (UP and sea water Synergism effect. Pseudo first-order kinetics	37
TiO_2/Fe_3O_4 0.1–2 $g\,L^{-1}$	Ceftazide (CFT) 10–50 $mg\,L^{-1}$	1 L semibatch column with recirculated water 30 W UVA lamp	O_3: 1.7 to 3.7 $mg\,min^{-1}$	15 min: CFT removal: 100% TOC: 75% PhCatOz; 50.6% O_3; 34.6% O_2/UVA/Cat at pH = 11 (best pH) Pseudo first-order kinetics. Scavenger effects	38

10% N–TiO_2 70–140 mg L^{-1}	5 Paraben mixture (50 mg L^{-1}) River and SMWW	2 L semibatch tank with quartz tubes for UVA lamps 365 nm	Gas flow: 0.2 L min^{-1} pH = 7.2 5.75 × 10^{-7} Einstein $^{-1}$ L s^{-1}	Effects of salts and water matrix TOD, Phytotoxicity	39
P25 TiO_2 10–500 mg L^{-1}	Primidone (PRM) 13 mg L^{-1}	Semibatch tank plus UVA led (365 nm) cylindrical reactor with recirculation	pH: 5–6 10 mg L^{-1} O_3; gas flowrate: 15 L h^{-1} 3.92×10^{-5} Einstein $^{-1}$ L s^{-1}	Non-ideal flow study. Mechanism and kinetic modeling for TOC removal TOC removal: 90% PhCatOz; 20% O_3	40
Fe_3O_4/TiO_2/ Graphene 0.5 g L^{-1}	Cotinine in UPW and mixture of pharmaceuticals (0.5 mg L^{-1} each) in SEMWW	Solar box. 1500 W Xe lamp. λ: 300–800 nm Semibatch reactor V = 500 mL	pH 5 30 L h^{-1}, 10 mg L^{-1} O_3 550 W m^{-2}	PhCatOz: 65 min: 100% CTN and 2 h: 80% TOC removals In SEMWWM: 65% TOC removal. Measurements of R_{HOO3}, RCT. Catalyst reuse and stability	41
γFe_2O_3/AC 0.5 g L^{-1}	Azo dye: Ponceau 4R 50 mg L^{-1}	500 mL semibatch tank. Sunlight	3.33 mg min^{-1} O_3 35.4 W m^{-2}	Pseudo first-order kinetics. Influence of water matrix. Best AOPs for color removal: PhCatOz + H_2O_2, O_3: 100% removal in 60 min	42
Me–TiO_2: 0.7 g L^{-1} Me: Au, Ag, Pt, Pd	Parabens mixture 10 mg L^{-1} each	Semibatch tanks with UVC, UVA lamps and sun light with CPC reactor	0–8 mg L^{-1} O_3 0–70 mg L^{-1} H_2O_2 UVC:1.06 × 10^{-5} UVA: 5.75 × 10^{-7} and solar light: 2.6×10^{-4} units: Einstein $^{-1}$ L s^{-1};	Mineralization, biodegradability and toxicity and cost assessment. Pseudo first-order kinetics. Different AOPs	43
0.35–0.52% TiO_2/ Glass Raschig ring 1.26–3.08% TiO_2/ Ceramic foams	DEET (20 mg L^{-1} in UPW and 1 mg L^{-1} in SEMWW)	Solar box. Xe lamp. λ: 300–800 nm Semibatch reactor V = 170 mL	15 L h^{-1} 15 mg L^{-1} O_3 pH_0 = 6 550 W m^{-2}	100 min 100% DEET removal and 40% DOC removal with PhCatOz UPW. Effects of salts. Catalyst reused.	44
TiO_2/Glass beads	Organics in seawater aquarium	Fixed bed photocatalytic reactor and 350–400 nm UVA black light lamp	8 L h^{-1} 1.5 mg min^{-1} O_3 24 W m^{-2}	Growth of the hard and soft corals and the disappearance of most of cyanobacteria from the rear wall with PhCatOz Bromate control. PhCatOz cycles	45

Table 6.1 (*Continued*)

Catalysts	Target pollutants	Reactor and radiation source	Ozonation conditions	Process performance	Ref.
WO_3/spongy alginate beads	Textile wastewater COD: 1970 mg L^{-1} BOD: 540 mg L^{-1} TD = 11 300 mg L^{-1}	Membrane reactor/ semibatch photocatalytic reactor (5 L). 16 W visible light	1–5 mg h^{-1} O_3 Residence time: 2–5 h $pH_0 = 8.2$ pHf = 7.9	Membrane flux and fouling. Color and COD removal (95% PhCatOz). Sludge effect. Higher membrane flux with PhCatOz	46
Magnetic nanoparticles/ Carbon 0.5 g L^{-1}	Oxamic acid, blue dye5, aniline, metolachlor Between 89,05 and 283 mg L^{-1}	Semibatch reactor Medium pressure Hg lamp (365, 405, 436, 546, 578 nm)	9 L h^{-1} 50 mg L^{-1} O_3	Oxamic acid only nearly 90% removed with PhCatOz. Presence of carbon in catalyst improved the removal. TOC from other organics removed 80%–90% with PhCatOz	47
P25 TiO_2 0.1 g L^{-1}	Acetamiprid (0.1 mg L^{-1}) in 4 SEMWW with COD: 14.9 – 70.5 mg L^{-1} DOC: 13.3–21.7 mg L^{-1}	1.5 L Semibatch reactor; 3 black light lamps (350–400 nm)	18 L h^{-1} 10 mg L^{-1} pH = 7.7–8.0 5,47 mW cm^{-2}	Determination of TOD and R_{HOO3}. Two mass transfer steps. Lower cost in PhCatOz processes.	48
TiO_2/carbon dots 1 g L^{-1}	Ciprofloxacin 10 mg L^{-1}	Semibatch rotary reactor. 350 W Xe lamp (290 nm) simulating solar light	0.9 L h^{-1} 4.7 mg L^{-1} O_3 $pH_0 = 7$	6% C in catalyst best composite for PhCatOz. Mechanism and intermediates detected. Effects of salts	49
Cd–ZnO 0–1 g L^{-1}	Textile dyeing WW COD: 1120–1480 mg L^{-1} BOD_3: 98–130 mg L^{-1}	Semibatch reactor. 15 W 365 nm UVA lamp	0 to 9.5 mg min^{-1} O_3 $pH_0 = 7$ (buffered)	0.2 g L^{-1} best catalyst concentration. TOC removal in 4 h: 90% with PhCatOz, 30% with O_3 or Cat/light. Poor reusability	50
0.16% TiO_2/glass Raschig rings	12 Pharmaceuticals in SEMWW mg L^{-1} and ng L^{-1} levels DOC: 22–26 mg L^{-1} IC: 70–74 mg L^{-1}	Continuous flow packed bed reactor with water recirculation and 4 10 W UVA LED (360 nm)	15 mL min^{-1} 20 mg L^{-1} O_3 pH = 7.6	Non ideal flow study. Fast removal of organics. Direct ozonation: most important oxidation way.	51

TiO_2/Fe_3O_4/AC 0.375–0.75 $g\,L^{-1}$	COD: 12.2 $mg\,L^{-1}$ Industrial WW, 2.1 $mg\,L^{-1}$ SEMWW	Biological tank followed by semibatch AOP reactor with 1500 W Xe lamp (300–800 nm)	20 $L\,h^{-1}$ 20–30 $mg\,L^{-1}$ O_3 $pH_0 = 7.5$ 550 $W\,m^{-2}$	Biological tank: 50% COD removal (7 h) Intermediates detected. Toxicity. Biodegradability enhanced by AOP processes. COD removal in 5 h: 48% PhCatOz, 23% O3. Good catalyst reusability	52
TiO_2 (80–240 $mg\,L^{-1}$), Fe(III) (2.5–7 $mg\,L^{-1}$)	Pharmaceuticals in SEMWW 0.01–0.1 $mg\,L^{-1}$ each DOC: 13 $mg\,L^{-1}$	200 L pilot plant CPC solar reactor	0.57 $L\,min^{-1}$ 1.2 $mg\,L^{-1}$ O_3 5% H_2O_2/Fe(III) $pH_0 = 7.9$; 38.2 $W\,m^{-2}$	Different solar AOP. Removal of organics: 0.7–1.1,0.9–1.0, 1.1–1.3, and 1.4–1.9 $mgO_3\,mg^{-1}$ DOC for antibiotics, estrogens, and acidic and neutral pharmaceuticals, respectively. Higher TOC removal with PhCatOz. Toxicity	53
P25 TiO_2/Fe(III) 0.2 $g\,L^{-1}$	Phenol, oxalic acid 100 $mg\,L^{-1}$ each	0.5 L semibatch reactor and Xe lamp (200–400 nm)	6.9 $L\,h^{-1}$ 27 $mg\,L^{-1}$ O_3 320 $mW\,cm^{-2}$	Intermediate identification. TOC removal (phenol): 90% PhCatOz; 32% in sequential O_3 + PhCat. For oxalic acid removal: Only PhCatOz in 10 min. Mechanism, synergism.	54
Various TiO_2 (4.13%–5.36%) on foamed Al_2O_3	2 Surfactants (32–4 $mg\,L^{-1}$), 1 textile dye and phenol (25 $mg\,L^{-1}$ each) in UP and WW	Semibatch packed bed photoreactor with 3 UVA lamps (360 nm)	1.4 $mg\,L^{-1}$ Dissolved O_3 $pH_0 = 4.9$ 4 $mW\,cm^{-2}$	Total TOC removal between 2 (dye) and 3 h (surfactants) with PhCatOz. 90% TOC removal in WW with PhCatOz. Synergism.	55
P25 TiO_2 0.25 $g\,L^{-1}$	Carbamazepine 200 $\mu g\,L^{-1}$	4 L Semibatch reactor in a black wooden box and 4 black light lamps (350–400 nm)	35 $L\,h^{-1}$ 13 $mg\,L^{-1}$ O_3 1.4×10^{-6} Einstein s^{-1}	Light inhibition *V. Fischeri*. Mortality/immobility and chronic reproduction bioassays of *D. Magna*	56

Table 6.1 (*Continued*)

Catalysts	Target pollutants	Reactor and radiation source	Ozonation conditions	Process performance	Ref.
Me–TiO_2 Me = Au, Ag, Pd, Pt 70 mg L^{-1}	5 parabens 10 mg L^{-1} each	2 L Semibatch reactor with 3 UVA lamps (365 nm)	O_3 data given as TOD 5.75×10^{-7} Einstein^{-1} Ls^{-1}	Toxicity with *V. Fischeri* and *C. fluminea* (clams). Best and worst catalysts: Ag/TiO_2 and Au/TiO_2, respectively. TOD measurements. Intermediates. Energy consumption	57
TiO_2 and Me–TiO_2 Me = Ag, Cu, Fe 0.1–1 g L^{-1}	Waterborne pathogens (*Escherichia coli, Salmonella, Shigella and Vibrio cholera*) in SEMWW (COD: 32 mg L^{-1})	0.7 L Semibatch reactor with UVA lamp (366 nm) 1 tube solar CPC	20.83 mg L^{-1} min^{-1} O_3	Bacterial inactivation efficiency, post-disinfection regrowth and synergism studies. Bacterial cells irreparably damaged with PhCatOz. Ag–TiO_2 best catalyst	58
Cellullose fibers/ TiO_2 (4 g)/zeolite/ Silica	Flumequine and Claritromycine 10 to 40 mg L^{-1}	Falling (staircase) film reactor with 3 UVA lamps (365 nm) with water recirculation	Water: 70–150 L h^{-1} 0–6 mmol L^{-1} H_2O_2 O_3 conc. and gas flow rate not given 14.5–28 W m^{-2}	Effect of UVA intensity. Langmuir kinetics. Scavenger effect. Slight rate increases by adding H_2O_2 (UVA/cat/H_2O_2) and ozone (PhCatOz) and both. Intermediate identification.	59
C_3N_4 and nanostructured C_3N_4 (100 mg L^{-1})	Oxalic acid, Melamine, phenol, tiophene (1 mM), BPA 50 mg L^{-1})	0.4 L semibatch reactor with simulated solar light	6 L h^{-1} 45 mg L^{-1} O_3 0.42 W cm^{-2}	DFT study. ROS determination. Catalyst stability. Measurements of TOC, NO_3^- with and without organics presence	60
$gC_3N_4/FeVO_4$ $gC_3N_4/FeO_4/Fe@NH_2$ Biochar 0.5 g L^{-1}	Methyl-paraben, *o*-chlorophenol 20 mg L^{-1} each	0.5 L batch reactor exposed to sunlight	$pH_0 = 3$–11 10^{-4} M initial dissolved O_3	Lower band gap than TiO_2. Catalyst reusability. Cytotoxicity. Adsorption kinetics. Pseudo first-order kinetics for AOP. Measurements of H_2O_2	61

				formed. Scavenger effect. Mechanism of reactions.	
TiO_2, MWCNT, P25 TiO_2/MWCNT 0.5 $g\,L^{-1}$	Aniline 1 mM	0.25 L semibatch reactor with medium-pressure mercury lamp and glass filter (366, 436 and 546 nm	9 $L\,h^{-1}$ 50 $mg\,L^{-1}$ O_3 43 $mW\,cm^{-1}$; 1.61×10^{-7} $Einstein^{-1}\,L\,s^{-1}$	Pseudo first-order kinetics. 100% removal in 9 min with PhCatOz and CatOz. Similar mineralization with different catalysts in PhCatOz and much higher than O_3 or CatOz	62
TiO_2/glass beads	180 L coral reef aquarium water with small marine organisms and 34 $g\,L^{-1}$ sea salts	Semibatch recirculated reactor with black light lamp (350–400 nm)	10 $L\,h^{-1}$ 24 $W\,m^{-2}$	Cycles of ozonation and photocatalysis: bromate reduction, organics removal.	63
TiO_2, Me–TiO_2 Me: Cu, Ag, Fe 0.5 $g\,L^{-1}$	Phenol in UPW and SEMWW 5 $mg\,L^{-1}$	0.7 L Semibatch cylindrical photoreactor with UVA lamp and 1 tube CPC solar photoreactor	20.8 $mg\,L^{-1}\,min^{-1}$ O_3 gas	Electrical energy per order, average oxidation state, cytotoxicity. Better figures for PhCatOz. Better catalysts Ag or Fe/TiO_2: 7–8 $kW\,m^3\,order^{-1}$. Slight decrease in catalyst activity.	64
0.16% TiO_2/Glass Raschig rings	Different bacteria in Surface water and MWW COD: 29–95 $mg\,L^{-1}$ BOD: 5–25 $mg\,L^{-1}$	Continuous (0.9 $L\,h^{-1}$) Semibatch flow packed bed reactor with water recirculation (5.4 $L\,h^{-1}$) and 2 UVA LED (382 nm)	9 $L\,h^{-1}$ 50 $mg\,L^{-1}$ O_3 gas 450 $W\,m^{-2}$	Bacteria present in regrowth after disinfection with Oz, UVA and PhCatOz. Effects on DNA. Similar structure of bacterial community after 3 days storage of treated samples.	65
TiO_2 nanotubes	2,4-D and MCPA pesticides 20 $mg\,L^{-1}$	1.5 L semibatch ozone reactor followed by a tubular fixed bed UVA LED (365 nm) photoreactor	30–120 $L\,h^{-1}$ 4.7 $mg\,L^{-1}$ dissolved O_3 after 3 min $pH_0 = 5.4$ (2,4-D), 8.5 (MCPA) 17.3 $mW\,cm^{-2}$	60 min: 100% 2,4D removal by PhCatOz, 80% Oz, 30% PhCat. 90%–95% removal in commercial pesticide in 2 h by PhCatOz. MCPA: 60 min 100% removal by PhCatOz and Oz. 40% by PhCat	66
TiO_2/glass beads 0.1 g TiO_2	Nitrophenol (NP) in saline wastewater with different metal ions 0.05–1.16 $g\,L^{-1}$ and 33 $g\,L^{-1}$ NaCl	Semibatch ozone reactor plus a Cylindrical fixed bed 125 W UVA LED (365 nm) photoreactor	12.3 $L\,h^{-1}$ 0.095–1.65 $mg\,L^{-1}$ O_3 gas	Langmuir adsorption kinetics. Similar NP removals due to Oz and PhCatOz. Total removal of NP with PhCatOz + AC adsorption. Synergism	67

Table 6.1 (*Continued*)

Catalysts	Target pollutants	Reactor and radiation source	Ozonation conditions	Process performance	Ref.
	WW TOC: 74–100 mg L^{-1}	(plus GAC column in some case)		effects depend on the ratio between the rate of PhCatOz and amount of AC.	
TiO_2, Me–TiO_2 Me: Cu, Ag, Fe 0.5 g L^{-1}	Phenol (5 mg L^{-1}) in SEMWW DOC: 20 mg L^{-1} COD: 42 mg L^{-1}	0.7 L Semibatch cylindrical photoreactor with 150 W UV lamp and 1 tube CPC solar reactor	pH 6 20.8 mg L^{-1} min^{-1} O_3 gas UV lamp: 70 mW cm^{-2}	Langmuir kinetics. Synergism effect. Phenol removal: 5%, 15% and 95% by Oz, PhCat and PhCatOz, respectively, in 60 min. Fe–TiO_2 best catalyst for mineralization: 90% in 2 h	68
TiO_2/Carbon supported on PTFE membrane 2 mg TiO_2 cm^{-2}	Methylene blue 3×10^{-5}–9×10^{-5} M	Continuous tubular membrane photoreactor externally exposed to UVA light (365 nm)	0.12 L h^{-1} O_3 gas concentration not given Light intensity: 5–10 mW cm^{-2}	MB removal 25 min: approx. 98%, 73% and 42% with PhCatOz, Oz and PhCat, respectively. Release of SO_4^{2-}. Pseudo first-order kinetics	69
TiO_2 nanotube electrode	Textile wastewater COD: 153 mg L^{-1} OC: 550 mg L^{-1} Color: 1080 mgPtCo L^{-1}	Semibatch photochemical reactor with UV lamp (315 nm) DSA cathode in some case	60–240 L h^{-1} 1.11–2.91 gO_3 h^{-1} $pH_0 = 8$ 0.128 mW cm^{-2}	Photoelectrochemical catalytic ozonation performed better than the other AOP included PhCatOz. Synergism and electrical energy per order estimation	70
P25 TiO_2, TiO_2 and TiO_2/MWCNT	*Tert*-buthylazine 5 mg L^{-1}	Solar box. Xe lamp. λ: 300–800 nm 0.25 L Semibatch reactor V = 170 mL	20 L h^{-1} 10 mg L^{-1} O_3 gas $pH_0 = 6.1$ 581 W m^{-2} (UV–Vis) 62 W m^{-2} (UVA)	Freundlich isotherm analysis. AC bed breakthrough curves. Results also with UVC lamp. Organic removal in 40 min: 80% Oz, 93% Sun/Oz, 100% PhCatOz (P25 and TiO_2 cat), 90% PhCatOz (TiO_2/MWCNT) but mainly due to adsorption. Loss of activity in reused TiO_2/MWCNT cat. RCT, mechanism and intermediates.	71

0.16% TiO_2/glass Raschig rings	Priority pollutants, CECs and bacteria in MWW and Surface Water Different concentrations from $mg\,L^{-1}$ to $ng\,L^{-1}$	Continuous ($0.9\,L\,h^{-1}$) semibatch flow packed bed reactor with water recirculation ($5.4\,L\,h^{-1}$) and 2 UVA LED (382 nm)	$0.9\,L\,h^{-1}$ $50\,mg\,L^{-1}$ O_3 gas	Removal of micropollutants. Antibiotic resistance genes(ARG) and antibiotic resistance bacteria (ARB). qPCR analysis. Microbial inactivation and reanimation. PhCatOz the most efficient AOP to remove organics and microbial loads including ARG.	72
Fe(III): $2.8\,mg\,L^{-1}$ Fe_3O_4: $150\,mg\,L^{-1}$ P25 TiO_2: $0.25\,g\,L^{-1}$	Nine pharmaceuticals ($200\,\mu g\,L^{-1}$ each) in PEMWW	Biological oxidation reactor (HRT = 7 h) followed by 5 L CPC solar reactor	$34.8\,L\,h^{-1}$ $13\,L\,h^{-1}$ O_3 gas pH 3 for Fe catalyst runs pH 7 for TiO_2 runs 30–40 $kJ\,L^{-1}$ accumulated energy	Biological oxidation: Partial remove of some pharmaceuticals. Total removal of caffeine and acetominophen: AOP: PhCatOz best AOP for TOC removal. In Fenton processes, H_2O_2 is not added but generated.	73
2 gC_3N_4 catalysts $1\,g\,L^{-1}$	Oxalic acid 1 mM	0.45 L Semibatch reactor exposed to UV light (200–400 nm) and also with visible light (420–800 nm)	$6\,L\,h^{-1}$ 5–60 $mg\,L^{-1}$ O3 gas $365\,mW\,cm^{-2}$	Catalyst optical properties. Effects of scavengers. Oxalic acid removal: 0% CatOz, 20% PhCat (UV light), 100% PhCatOz (UV light). Poorer results with visible light.	74
nanoTiO_2 coated on quartz tubes $0.393\,g\,L^{-1}$	Tire cord wastewater COD = 450–500 $mg\,L^{-1}$ BOD5 = 80–100 $mg\,L^{-1}$ TSS = 120–360 $mg\,L^{-1}$	Continuous cylindrical reactor with a UVA lamp (365 nm)	$300\,L\,h^{-1}$ H_2O_2: 10 mM pH 3, 7, 11 $60\,mW\,cm^{-2}$	2.3 $gO_3\,gCOD^{-1}$. Response surface method applied with COD, reaction time and initial pH as variables. Cycles of aeration and ozonation. BOD/COD. ANOVA results. Intermediates. Effect of adding H_2O_2	75

Table 6.1 (*Continued*)

Catalysts	Target pollutants	Reactor and radiation source	Ozonation conditions	Process performance	Ref.
TiO_2 on montmorillonite 0.005–0.08 $g\,L^{-1}$	Ciprofloxacin 5–25 $mg\,L^{-1}$	Semibatch cylindrical reactor with 8W UVA lamp (315–400 nm) in axially situated	1–6 $L\,h^{-1}$ 5 $mg\,L^{-1}$ O_3 gas	Comparison with other AOP: Removal in 30 in: 90% PhCatOz, 70% UVA/Cat, 70% O_3. Synergism. Scavenger effect. Intermediates. Mechanism. Reusability. Effect of water matrix	76
P25 TiO_2 0.005–0.5 $g\,L^{-1}$	Clopyralid, picloram, triclopyr 5 and 20 $mg\,L^{-1}$	1 L cylindrical reactor with 4 external UVA black lamps (350–400 nm)	30 $L\,h^{-1}$ 50 $mg\,L^{-1}$ 1–14 $\times$ 10^{-7} $Einstein^{-1}\,Ls^{-1}$	Comparison with other AOP. Better process: PhCatOz. Kinetics of UVC/H_2O_2. Influence of variables. Chloride and nitrate determination. Reusability. Eco-toxicity bioassays with *Daphnia parvula* and *Culex pipiens* larvae	77
P25 TiO_2 0.5 $g\,L^{-1}$	Amoxicilin and diclofenac (0,1 mM each) and 35 micropollutants in real MWW at $\mu g\,L^{-1}$ and $ng\,L^{-1}$ level	Semibatch cylindrical reactor with UVA/visible lamp ($\lambda > 300$ nm)	9 $L\,h^{-1}$ 50, 70, 90 $mg\,L^{-1}$	Little differences for remove DCF and AMX with O_3, PhCatOz. Important differences in TOC removal with phCatOz as better process. Growth inhibition of *Escherichia coli* DSM 1103 and *Staphylococcus aureus* DSM 1104	78
MWCN–TiO_2 0.2 $g\,L^{-1}$	Four pharmaceuticals 10 $mg\,L^{-1}$	1 L semibatch glass cylindrical reactor and solar chamber and Xe lamp ($\lambda > 300$ nm)	20 $L\,h^{-1}$ 6 $mg\,L^{-1}$ O_3 gas pH 3 to 9 Lamp: 550 $W\,m^{-2}$	Catalyst characterization. Mineralization measured as TOC and inorganic anions (F^-, Cl^-, NO_3^-, NH_4^+, $SO_4^{=}$. Some adsorption noted. TOC removal: 63% in PhCatOz. Catalyst reusability.	79

Fe(III)(2.8 mg L^{-1}) and TiO_2 (0.2 g L^{-1})	Six pharmaceuticals (0.2 mg L^{-1} each) in SEMWW(COD: 59 BOD5: 10 mg L^{-1})	5 Tube CPC reactor with solar light	40 L h^{-1} 13 mg L^{-1} O_3 gas pH 3 (Fenton processes) Solar light: 33 kJ L^{-1} accumulated energy	AOP comparison. Pseudo first-rate constants. Time for 99% organic removal. Phenolics intermediates. Ecotoxicity. Energy cost. Biodegradability. Hydroxyl radical exposure.	80
Fe(III) (2.8 mg L^{-1}) and Fe_3O_4 (0.15 g L^{-1})	BPA and five pharmaceuticals (0.1 mg L^{-1} each) in synthetic WW (TOC: 20, COD: 56 BOD5: 14 mg L^{-1})	Semibatch agitated tank with two external UVA black light lamps (365 nm)	35 L h^{-1} 13 mg L^{-1} O_3 gas pH 3 (buffered) and pH 7 Lamps: 7.05×10^{-5} Einstein^{-1} Ls^{-1}	Direct ozonation as main oxidation way. RCT to predict organic concentration with time. TOC and COD % removals of 80 and 90, respectively, with PhCatOz. Biodegradability increase after ozone processes. Ecotoxicity	81
TiO_2, (P25), Nb_2O_5, SnO_2, WO_3, Fe_2O_3, In_2O_3, and $BiVO_4$, 2 g L^{-1}	Oxalic acid: 10 mM	Semibatch agitated tank with Xe lamp (360–470 nm)	32 L h^{-1} 14 mg L^{-1} O_3 gas pH 2.1 200 mW	TOC removal: Efficacy of catalysts with PhCatOz: $TiO_2 > WO_3 > In2O_3 > BiVO_4 > SnO_2PNb_2O_5 > Fe_2O_3$ With visible light: WO_3 best catalyst	82
TiO_2/ceramic plates on the four walls of photoreactor	Phenazopyridine (PzP) 25 mg L^{-1}	2 L semibatch rectangular glass reactor with UVA lamp (354 nm)	1–10 L h^{-1} 0.3–5 mg L^{-1} dissolved O_3 pH 7	Influence of variable on PzP removal. Mechanism. Synergism. Formation of H_2O_2. Scavengers. Intermediates. Ecotoxicity	83
As in [73]	Three pharmaceuticals	As in [73]	As in [73]	Central composite design. Mechanism. Intermediates.	84
As in [71]	As in [71]	As in [71]	[71]	AOP comparison, synergism, ozone demand, energy requirements. Kinetics.	85
0.5%–0.8% B–TiO_2	Four pesticides	As in [71]	10 L h^{-1}		86

Table 6.1 (*Continued*)

Catalysts	Target pollutants	Reactor and radiation source	Ozonation conditions	Process performance	Ref.
0.33 $g\,L^{-1}$	5 $mg\,L^{-1}$ each		5 $mg\,L^{-1}$ O_3 gas 550 $W\,m^{-2}$	Catalyst characterization. AOP comparison: Better efficiency of B-TiO_2 than TiO_2. No differences in ozone processes to remove the organics. TOC removal %: 20 in O_3, 45 in PhOz and 70–80 in PhCatOz. Reusability.	
CeO_2 0.25 $g\,L^{-1}$	*N*,*N*-Diethyl-meta-toluamide 5 $mg\,L^{-1}$	As in [71]	15 $L\,h^{-1}$ 10 $mg\,L^{-1}$ O_3 gas $pH_0 = 6$ 550 $W\,m^{-2}$	Catalyst characterization. AOP comparison: DEET: no removal with PhCat and similar removal rate in ozone processes. TOC removal, %: 19 in O_3, 24 in CatOz, 47% SolarCatOz and 80% in PhCatOz. H_2O_2 formation.	87
P25 TiO_2 and WO_3 0.25 $g\,L^{-1}$	Primidone 0.5 $mg\,L^{-1}$ in UPW 0.5 $mg\,L^{-1}$ in SEMWW (COD: 47, BOD5: 11, TOC: 14 in $mg\,L^{-1}$)	As in [71]	20 $L\,h^{-1}$ 10 $mg\,L^{-1}$ O_3 gas $pH_0 = 6$ 550 $W\,m^{-2}$	Organic removal similar in both water matrices. WO_3 poor catalytic effect in SEMWW. AOP comparison: TOC removal increase with PhCatOz. Scavengers study. Intermediates. Mechanism. Ecotoxicity	88
MOF = MIL-100(Fe) 1 $g\,L^{-1}$	Three pharmaceuticals and one pesticide	As in [71]	0.25–2.5 g H_2O_2/gMOF 0–0.25 gO_3/gMOF	Catalyst characterization. Activity and stability in different oxidizing conditions (solar light, ozone, H_2O_2). Fast organics degradation but organic part of catalyst leaches. Not recommended for water treatment.	89

[a]From 2015.

concentration of this metal in water, about 0.3 mg L^{-1}. This chapter is addressed to heterogeneous photocatalytic ozonation, where catalysts of different natures or compositions have been used. In all these works, an important part is dedicated to characterizing the catalyst. Characterization techniques allow catalyst properties to be known. These properties are related to crystal phases present and aspects such as crystallinity; crystal size (X-ray refraction spectrometry, XRD); textural characteristics of external and internal areas, pores size distribution, *etc.* (N_2 adsorption–desorption isotherms, N2-AD, mercury porosimetry); morphological features and microstructure (scanning and transmission electron microscopies, SEM, TEM, or their high-resolution means: HRSEM, HRTEM, the former used, in some cases, to energy disperse X-ray spectroscopy, EDS, for elemental composition of catalysts and its elements); atomic surface composition or chemical state of elements (X-ray photoelectron spectroscopy, XPS); optical properties such as wavelength range of absorbed radiation and band gap (UV–visible diffuse reflectance spectroscopy, UV–vis DRS); surface-active functional groups in catalysts (Fourier transform infrared spectroscopy, FTIR); thermal catalyst stability (thermogravimetric analysis, TA); magnetic properties (superconducting quantum interference device magnetometer, SQUID); adsorption potential (pH of point of zero charge, pH_{pzc}); thickness of metal catalysts on support (wavelength dispersive X-ray fluorescence, WDXRF); effectiveness of coating technique (atomic force microscopy, AFM); elemental composition (elemental analyzer, EA); C hybridization in carbon materials (Raman spectroscopy, RM); metal determination (inductive coupled plasma with mass spectrometry, ICP MS); and photochemical charge separation and transfer process (electrochemical impedance spectroscopy, EIS). Table 6.2 shows the number of works quoted in Table 6.1 that have used these techniques. As can be seen, XRD, SEM, N2-AD

Table 6.2 Catalyst characterization techniques and number of UVA photocatalytic ozonation works that have used them.

Characterization techniques	Number of works quoted in Table 6.1
XRD	25
SEM	25
N2-AD	22
XPS	18
UVvisDRS	13
TEM, HRTEM	11
SEM-EDS	8
FTIR	8
SQUID	6
pH_{pzc}	6
TA	6
WDXRF	4
AFM	3
EA	2
RM	2
ICP MS	2
EIS	1

and XPS are the most used of these techniques due to the important properties they allow to be identified. These properties are intimately related to the activity, stability and selectivity of catalysts.

Among catalysts, TiO_2 is the most common material (see Table 6.1). Several reasons have already been reported many times, such as low cost, high stability, capability of being linked to other metals, non-metals, metal oxides, carbon materials, *etc.* As a consequence, nearly all researchers have focused their attention on heterogeneous PhCatOz and TiO_2 as catalyst, used in different forms: in powder,[40] as nanotubes,[34] fibers,[59] doped with some other metal such as Au, Ag, Pt[43,54,57] or non-metal such as nitrogen,[39] linked to other metal oxides,[38] supported on other materials such as glass, aluminum foam, activated carbon, membranes,[36,51,55,65,69] or being part of metal organic frameworks,[89] *etc.* These TiO_2 catalysts were prepared for two main reasons: First is to make TiO_2 active under visible light; due to the high band gap that TiO_2 presents (3.2 eV), only radiations lower than 385 nm can be valid to excite it. Second, it can be magnetized or supported on some porous or non-porous materials[36,38,52] to facilitate its separation from water once used. Some important aspects of these works are highlighted here. Very recently, TiO_2 nanotube arrays have been prepared for application in photocatalytic oxidation. According to Ye *et al.*,[91] this catalyst organization presents large surface area and high stability, and it can easily be recovered for subsequent reuse. After being first applied on the photocatalytic oxidation of metoprolol, a pharmaceutical beta-blocker, it was used to remove hazardous compounds such as polycyclic aromatic hydrocarbons from offshore produced water.[34] These nanotubes present diameters between 75 and 100 nm and a thickness of about 42 nm. This tube structure facilitates the charge transfer reducing the electron–hole recombination reaction and increasing the quantum yield of the catalyst.[92] A composite of TiO_2 and multi-wall carbon nanotube (MWCNT) has been used to remove aniline.[62] According to Orge *et al.*,[62] the role of the MWCNT phase in the composite catalyst can be due to three possible routes: (1) dispersing media for TiO_2 nanoparticles, (2) co-adsorbent, and (3) photosensitizer. The first means of action is promoted when TiO_2 particles are simultaneously generated during the synthesis of the composite catalyst so that chemical groups at the surface of the CNT may act as anchoring points to TiO_2 nanoparticles. In this way, electron–hole recombination is reduced, and photosensitization is promoted. In other works,[43,54,57] metals (Ag, Pt, Pd, Au, Cu and Fe) were doped to TiO_2. These works report that indirect/direct band gaps of pure TiO_2 (3.27 eV/3.38 eV) were reduced to 3.00 eV from 3.22 eV, to 2.74 eV from 3.23 eV, to 2.59 eV from 3.19 eV and to 2.5 eV from 3.13 eV for TiO_2–Ag, TiO_2–Pt, TiO_2–Au and TiO_2–Pd (all 0.5 wt%), respectively, from pure TiO_2, thus enhancing the absorption of visible light.

For catalyst synthesis, some different methods were followed. In some of them, TiO_2–Pt, TiO_2–Pd and TiO_2–Ag were prepared by UV reduction of chloride salts of Pt^{4+}, Pd^{2+} and Ag^{+} in TiO_2 (P25) suspension, while, in others, TiO_2–Au was prepared by the sol–gel method[43] or UV-reduction of Pt^{4+}, Pd^{2+} and Ag^{+} ions in a titanium dioxide suspension through

photodecomposition.[57] Another form of improving TiO_2 absorption of light is doping with non-metals. These dopants also interact with the electronic molecular orbitals and reduce the band gap to increase the absorption of TiO_2 in the visible or solar spectrum range. As an example, Fernandes *et al.*[39] used a N–TiO_2 catalyst to increase the removal of parabens. They prepared their catalyst from titanium(IV) isopropoxide (97%) and ammonium hydroxide as a titanium precursor and doping agent, respectively, to finally obtain a ratio of 10% (w/w) of N. Another group of important TiO_2-derived catalysts are those incorporating a magnetic material.[36,38,47,49] Representative of this group is the work of Chávez *et al.*[36] The catalyst used was based on a magnetically activated carbon material (Fe_3O_4/AC). The carbon part provides high surface area that makes these catalysts suitable for AOP. In Chávez's work,[36] TiO_2 (anatase) was incorporated into the Fe_3O_4/AC structure to yield hybrid materials with high photocatalytic performance under solar radiation. The synthesis method is shown in detail by Quiñones *et al.*[93] Figure 6.1 shows a typical XRD pattern of the magnetic catalyst.

Another example is TiO_2-based catalysts as supported catalysts.[41,44,51,71,75] The material supporting the catalyst should be porous to increase the specific surface, but its main function is to serve for easy separation from water. A specific example of this type of catalyst is the work of Rodriguez *et al.*,[44] wherein a TiO_2/alumina foam and TiO_2/glass ring materials were used to remove DEET from water. Another similar work was reported by Chávez *et al.*,[51] wherein TiO_2 was also supported on glass Raschig rings to remove contaminants of emerging concern (pharmaceuticals) from a real secondary urban wastewater effluent (see Section 6.5.3). Other materials used as support were montmorillonite (MMT)[76] and ceramics.[83,84] The first material allows a high dispersion of TiO_2 particles into layered MMT structures that lead to the stabilization of TiO_2 particles and allows for many molecules to have easier access to the surface of TiO_2 crystals. Other ceramics used were obtained through sol–gel dip-coating procedures to immobilize TiO_2 nanoparticles on ceramic plates.[83] Thus organically modified silica (ormosil) was used as hydrophobic binder. The coating solution (constituted by methanol, TiO_2 nanoparticles and methyltrimethoxysilane) was adjusted to achieve the required TiO_2/ormosil weight ratio of 0.240.

Recently, a new TiO_2 composite is being investigated: graphene oxide/TiO_2 (GO/TiO_2).[94] Graphene discovered in 2004 can be considered a 2D material that can be formed from strong oxidation of graphite[95] that first yields graphite oxide. This oxide still keeps the 3D form of graphite, but it contains numerous oxygen groups such as carboxylic, hydroxyl, epoxide, *etc.*[96] In a second step, graphite oxide is exfoliated with ultrasound radiation to form a similar oxide but containing fewer than ten layers of a honeycomb structure of sp^2 carbon atoms. This oxide is called graphene oxide. In PhCatOz, among the many properties GO presents, electrical conductivity is used to avoid the electron–hole recombination process, thus increasing the formation rate of hydroxyl radicals. Some molecular orbital of GO presents potential redox between those of the valence and conduction bands of TiO_2, facilitating the

transition of electrons to this GO orbital and then being conducted away to avoid recombination (see reaction (6.12) and Figure 6.1[97]). Because GO/TiO_2 composites are prepared for visible light PhCatOx or PhCatOz, this AOP process is not commented in this chapter.

In relation to catalysts different from TiO_2, graphitic carbon nitride (g-C_3N_4 composites), other metal oxides,[46,50,82,88] magnetite,[42,47] Cd/ZnO or metal/ZnS, graphene/Fe_3O_4[41,50] can be cited. Likely, gC_3N_4 composites[60,61,74] deserve special consideration due to their activity as metal-free photocatalysts. These catalysts can easily be synthesized through direct polymerization of cheap feedstocks. They present a very narrow band gap of 2.7 eV, which permits the absorption of visible light.[98] Also, g-C_3N_4 exhibits high thermal and chemical stability due to the presence of a tri-s-triazine ring structure. For instance, Xiao *et al.*[74] prepared GCN-T and GCN-D composites by direct polycondensation of dicyandiamide and thiourea, respectively. They were applied to both UV and visible light photocatalytic ozonation of oxalic acid (OA) and *p*-hydroxybenzoic acid (PHBA). The work was aimed to show a high synergy between ozonation and photocatalytic oxidation (see later Section 6.5.7). Another group of

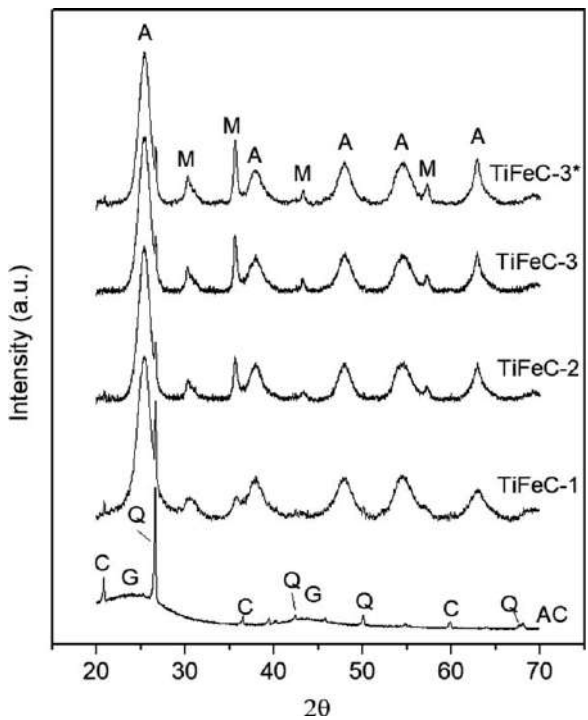

Figure 6.1 XRD patterns of the AC support and some TiFeC catalysts. Crystalline phases detected: anatase (A), magnetite/maghemite (M), graphite (G), quartz (Q), cristoballite (C). TiFeC-3* represents catalyst TiFeC-3 after being used in ten consecutive photocatalytic ozonation runs. Reproduced from ref. 93 with permission from Elsevier, Copyright 2014.

catalysts tested in photocatalytic ozonation are metal organic frames which are materials based on the coordination of metal ions or clusters and organic linkers. These components make possible the synthesis of composites with tunable properties valid for different applications.[99] Properties such as a well developed and ordered porous structure, large surface areas, flexible framework or UV–visible light response make some of them good for water purification both with adsorption or with different advanced oxidation processes (AOPs).[100] However, their stability in water or in the presence of strong oxidants is a matter of controversy. In a recent paper, Chávez *et al.*[89] studied this problem with MIL-100Fe composed of iron nodes and 1,3,5-benzenetricarboxylate (H3BDC or trimesic acid, TMA) as a bridging ligand (chemical formula $Fe_3O(H_2O)_2(F/OH)\{C_6H_3(COO)_3\}_2 \cdot nH_2O$ with $n \sim 14.5$). It was observed that stability depended on the conditions of use. At high doses of ozone or hydrogen peroxide with radiation, a large mass loss of the catalyst was observed, and moderate stability was obtained in less severe conditions. However, in any case, MIL-100(Fe) presented surface oxidation/decarboxylation. Figure 6.2 shows how this catalyst is effective in PhCatOz processes to remove a series of emerging contaminants and simultaneously to release the organic linker, trimesic acid. The final conclusion is that this material is not very appropriate for PhCatOz processes.

The stability of catalysts is linked to their activity, and this property is often studied by researchers carrying out repetitive runs with the same amount of catalyst and fresh solutions of the organics studied. In most cases, high activity is reported, regardless of the catalyst used, organics treated and radiation source.

6.5.2 Radiation Sources

UVA PhCatOz works mainly using three types of radiation sources emitted between 300 and 400 nm: UVA lamps, UVA LEDs, solar simulators (with Xe lamps provided with filters) and solar radiation. Solar simulators are also used without visible light filter so that an electromagnetic radiation spectrum similar to that of the Sun is applied.

Regarding the use of lamps, for example, Oropesa *et al.*[56] used four 15 W black light lamps (Lamp 15 TBL HQ Power TM Velleman®) placed in the corners inside a 50×30×30 cm black wooden box. These lamps emit radiation in the range of 350–400 nm centered at ~370 nm with an incident photon flux of 1.4×10^{-6} Einstein s^{-1}. Mecha *et al.*[58,68] worked with a medium-pressure mercury lamp (Heraeus TQ 150W), placed axially in a quartz immersion tube with a light intensity of 70 m Wcm^{-2}. Gmurek *et al.*[43] applied to their reacting system three black light, blue glass lamps, with the maximum emission of 365 nm with an incident intensity of 5.75×10^{-7} Einstein $L^{-1}\,s^{-1}$ (8.9 $W\,m^{-2}$).

UVA LEDs are used for their lower cost and energy consumption compared to lamps due to long duration and being more environmentally attractive (they are mercury-free devices). Examples of the use of UVA LED can be seen

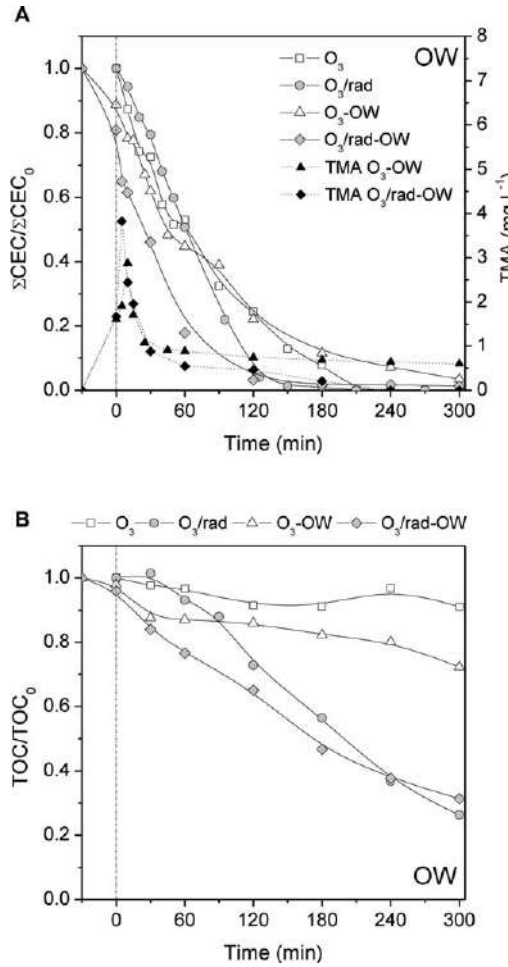

Figure 6.2 (a) Removal of CECs and TMA released into the reaction medium by different ozonation processes using MIL-100(Fe)-OW as catalyst. (b) TOC removal by different ozonation processes. Experimental conditions: $V = 0.25$ L; $pH_0 = 4.8$ (free); $T = 25$–40 °C; simulated solar irradiance (if applied) $= 550$ W m^{-2}; gas flow rate $(O_2/O_3) = 10$ L h^{-1}; gas inlet O_3 concentration $= 6$ mg L^{-1}; initial CECs concentration $= 10$ mg L^{-1} each; initial TOC concentration $= 26$ mg L^{-1}; MOF dose (if applied) $= 0.2$ g L^{-1}. Reproduced from ref. 89 with permission from Elsevier, Copyright 2021.

in several works.[34,40,51,72] For instance, Moreira *et al.*[40,72] and Chávez *et al.*[51] used two 10 W UV LEDs (15.5 mm×23 mm), with main emission at 382 nm and long service life (intensity remains above 70% after 10 000 h work). According to the authors, 382 nm was chosen as a compromise between the cost of LEDs (increasing when the emission wavelength decreases) and the possibility of achieving an overlap between the LED's main emission wavelength and the TiO_2 absorption spectrum. In a more recent work, Liu *et al.*[34]

used ten UV-LEDs mainly emitting at 365 nm. Light intensity was between 4.25 mW cm^{-2} and 9.93 mW cm^{-2}. Figueredo *et al.*[40] used six 3 W LEDs (LZ4-04UV00), each with maximum emission at 365 nm. The photon flux per unit volume, in this case, was 3.92×10^{-5} Einstein $L^{-1} s^{-1}$. As can be deduced, wavelengths of about 390 nm are approximately the limit above which TiO_2 is non-active as a catalyst due to its large band gap.

However, the most used radiation source is solar simulator or direct solar light with different reactor configurations (see Section 6.5.3). Regarding solar simulators, in nearly all cases a Xe lamp, the literature reports many works.[41,49,52,58,68,74,82] For instance, Mano *et al.*[82] used a 300 W Xe lamp with an IR cutoff filter. The incident light power was about 200 mW covering a wavelength range of 360 nm $< \lambda <$ 470 nm. They also worked with visible light irradiation with a second cutoff filter ($\lambda > 410$ nm). In another work,[74] the same system was used but this time without UVB–UVC filter so that the wavelength of radiation extended from 200 to 400 nm. In this case, the aqueous solution was irradiated with an average radiant flux of 365 mW cm^{-2}. Chávez *et al.*[41,52] and Alvarez *et al.*[71] irradiated their solutions with a solar box (Suntest CPS, Atlas) provided with a 1500 W Xe lamp and cutoff filters ($\lambda = 300$–800 nm, irradiation intensity 550 W m^{-2}). Zeng *et al.*[49] simulated solar light with a 350 W xenon lamp with 290 nm cut-off filters. Xiao *et al.*[60] simulated sunlight with an AM 1.5G solar simulator that supplied a 0.42 W cm^{-2} light intensity.

Direct solar radiation is also one of the most used radiation sources in UVA PhCatOz (see Table 6.1). In Section 6.5.3, more details about the experimental reactor solar system are given. In some cases, data about the radiation intensity are given with coordinates of the place where experiments were done,[42] with the latitude,[53,73,80,85] the time of year[43] or the average irradiance.[43,58]

6.5.3 Reactor Type

The third important factor of UVA PhCatOz is the reactor type. This depends on the radiation source to be applied, *i.e.* lamps, LEDs or directly from the sun, and how the catalyst is charged. In most cases, the reactors work in a semi-batch way by continuously feeding mixtures of ozone–oxygen or ozone–air and with the water to be treated charged or recirculating by a pump through another tank to ensure good mixing conditions.[35,38,40] When lamps are used, the simplest form of photoreactor was a tank provided with the necessary inlets and outlets for gas, sampling, *etc.*, a quartz plate as a tap and a lamp above the tank.[83] However, the main reactor configuration utilized is the cylindrical tank provided with a borosilicate or quartz well axially situated in the center where the lamp is placed.[39,47,76] This well can also have a jacket in which water or a filtering solution is run to avoid some radiation wavelength from the lamp reaching the water problem or simply for thermostatic purposes. In some cases, regardless of the presence of the inside lamp, the reactor was also surrounded by some other lamps to reinforce the intensity of the light.[56,77,81] In other cases, the inside walls were coated with the catalyst, as in Fathinia and Khataee[83] and Fathia *et al.*,[84] where four

ceramic plates were installed on the four walls of the reactor with the surface of the ceramic plates coated with TiO_2 nanoparticles. In some other cases, the reactor tank without any central lamp was situated inside a box, and the inside box walls were covered with aluminum foil to increase light reflection back to the tank.[56] The tanks worked as slurry reactors when the catalyst was charged in powder form[37,40,48,50,56,74] or as a catalytic fixed bed when, for instance, the catalyst was supported on some materials such as glass beads or rings.[45,67] A variation of this type of reactor was constituted by three lamps equidistantly inserted in their corresponding wells inside the cylindrical tank and around a positioned foam Al_2O_3 monolith with immobilized TiO_2.[55] Another configuration of the cylindrical tank with the inside lamp axially centered is the one provided with a series of quartz tubes surrounding the lamp well and containing the catalyst (TiO_2) coated on glass beads.[75]

An interesting type of reacting system is that combining photocatalysis, ozone and membranes. An example of this kind is the optofluidic membrane microreactor.[69] This is a parallelepipedic chamber where two opposing walls are polydimethylsiloxane (PDMS) covers. Inside the chamber, a membrane facing both PDMS walls and prepared from carbon paper divided the chamber in the liquid reaction zone and the gas reaction zone. TiO_2 impregnated the membrane facing the liquid zone, while the other membrane side had been treated with PTFE to ensure the hydrophobicity of the membrane favoring the gas–liquid separation. The lamp is located in front of the PDMS cover in contact with the liquid reaction zone. In this way, the ozone gas circulates through one of the compartments while diffusing through the membrane to the liquid reaction zone. In this zone, radiation incises and excites the TiO_2 supported on the membrane[69] while reacting with ozone.

Another type of reactor of increasing importance is one that allocates LEDs. In this group, there are also different possible configurations: LEDs are submerged and situated in glass columns inside the reactor tank,[34] or the tank is placed inside a box with UVA LED placed in the box wall.[51] Also, reacting systems are constituted by a sequential reactor consisting of a perfectly mixed ozonation tank followed by an UVA LED photoreactor tube.[40] In this latter case, the glass photoreactor tube was above a platform where LEDs oriented toward the tube were equidistantly situated, as shown in Figure 6.3.

Similar to this was a sequential ozonation tank and LED photoreactor tube where the catalyst was a TiO_2 fixed bed.[66] Another, UVA LED reactor configuration was used here,[51] consisting of a glass-packed bubble column filled with glass rings (coated with TiO_2), a recirculating loop and eight 10 W UVA LEDs positioned along the column as shown in Figure 6.4.

Photoreactors used with solar simulation or when direct solar radiation is used constituted another important group. With solar-simulated radiation, the photochemical reactor, a tank of different geometrical forms, with inlet and outlet for the gas and a sampling port, is placed inside a chamber or solar simulator where a Xe lamp is also situated above the tank (Figure 6.5).

The lamp is surrounded by a transparent film filter to avoid radiation lower than 300 nm to reach the tank so that only UVA–visible radiation is

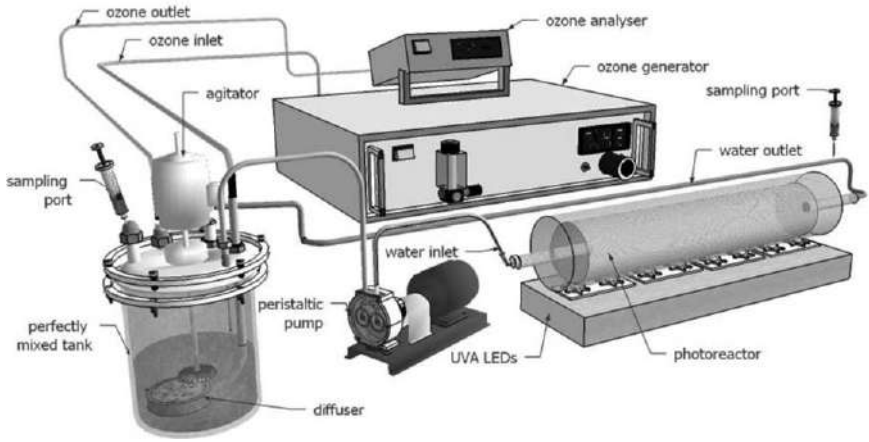

Figure 6.3 Experimental setup of a UVA LED photocatalytic ozonation reacting system. Reproduced from ref. 40 with permission from the Royal Society of Chemistry.

used.[36,79,86–88] The spectrum of this Xe lamp radiation is practically coincident with that of the Sun reaching the Earth's surface,[36] as shown in Figure 6.6.

When direct solar radiation is used, the simplest configuration is the tank or tube exposed to the Sun.[61] In these cases, a reactor tube is usually utilized. However, a better configuration that is used is constituted by the photoreactor tube provided with some gas inlet, a tank as water reservoir connected to a gas separation unit and a pump that recirculates the water problem through the system. In most cases, the photoreactor section consists of several tubes connected in series and placed above anodized aluminum reflectors usually oriented to the south and tilted at an angle equal to the latitude of the place. The system is also provided with a broadband UV radiometer tilted at the same angle as that of the photoreactor tubes to measure the instantaneous solar and accumulated UV light absorbed. This kind of system is called a compound parabolic collector (CPC) and has been used in some works.[53,73,80] Figure 6.7 shows an example of this solar photoreactor.

Finally, another interesting reacting system that can be used with solar radiation or UVA lamps has been reported.[41] The reactor is called the falling film photoreactor since it is formed by a staircase where the falling water forms a thin film while receiving radiation from above from UVA lamps or the Sun. Six regular steps of the same dimensions (depth/height/width: 6 cm/6 cm/25 cm) are covered with the TiO_2 (0.18 m^2: 72 cm×25 cm corresponding approximately to 4 g of catalyst). The system allows high catalyst surface and improves oxygenation of the waste solution.

6.5.4 Organics Studied and Water Matrices

A high variability of organic compounds have been treated with UVA PhCatOz, as Table 6.1 shows. This is likely due to the high oxidation power

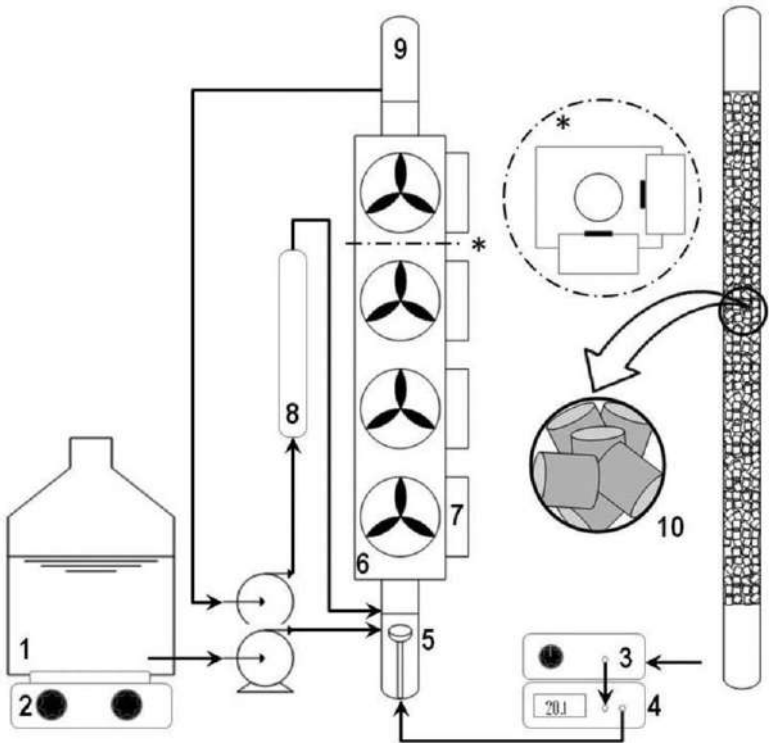

Figure 6.4 UVA LED photoreactor system with a packed bed column (TiO_2 supported on glass Raschig rings) and a recirculating system: (1) reservoir, (2) magnetic stirrer, (3) ozone generator, (4) ozone analyzer, (5) ceramic diffuser, (6) box of LEDs, (7) fan, (8) loop column, (9) packed column, and (10) glass-coated or uncoated rings. From A.M. Chávez, A.R. Ribeiro, N.F.F. Moreira, A.M. T. Silva, A. Rey, P.M. Álvarez and F.J. Beltrán, "Removal of Organic Micropollutants from a Municipal Wastewater Secondary Effluent by UVA-LED Photocatalytic Ozonation," *Catalysts* 2019, 9, 472. Reproduced from ref. 51, https://doi.org/10.3390/catal9050472, under the terms of the CC BY 4.0 license https://creativecommons.org/licenses/by/4.0/.

of hydroxyl radicals and ozone. The first one reacts unselectively with organics regardless of their molecular structure, and the second one due to its selective capacity to attack compounds with specific functional groups in their molecules.[101] For instance, phenols and many pharmaceutical compounds present in their molecules are candidate groups for removal from water by means of the sole action of ozone reactions.

The compounds named in Table 6.1 have been studied because they entail environmental issues so that the nature of the water matrix where they are usually found is also studied. Particularly, due to the unselective character of hydroxyl radical oxidation, studies of the PhCatOz of organics in a real water matrix results fundamentally in discerning the scavenging effect of other

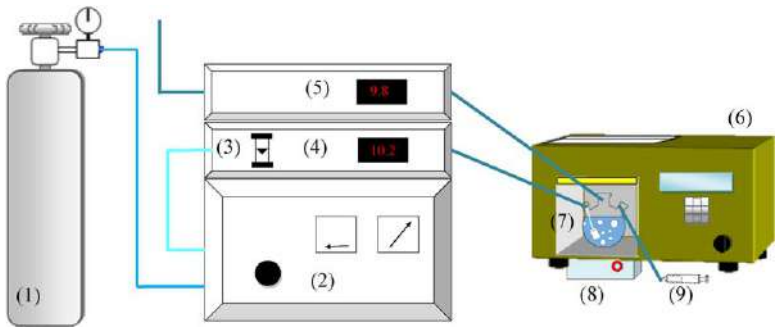

Figure 6.5 Experimental setup used for catalytic tests: (1) oxygen bottle, (2) ozone generator, (3) flow meter, (4) ozone inlet analyzer, (5) ozone outlet analyzer, (6) solar box, (7) reactor, (8) magnetic stirrer, (9) sampling port. Reproduced from ref. 36 with permission from Elsevier, Copyright 2020.

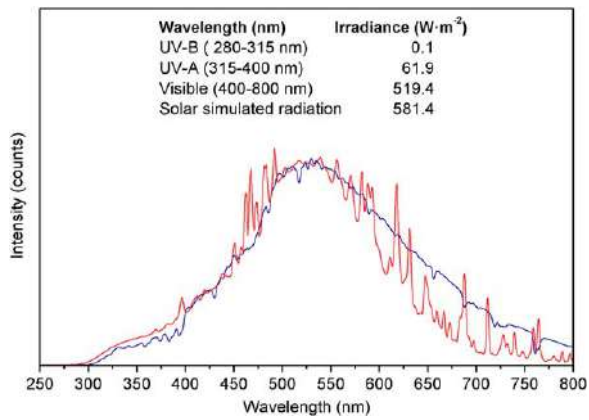

Figure 6.6 Natural and simulated solar radiation (blue and red lines, respectively). Cumulative irradiance and photon flux at given wavelength regions. Reproduced from ref. 36 with permission from Elsevier, Copyright 2020.

non-targeting substances present in the water. Carbonates are a clear example of this because they consume hydroxyl radicals, and their presence decreases or even inhibits real contaminant oxidation (see Section 6.5.6). Therefore, works dealing with surface water,[72] groundwater,[76] aquacultural water,[45,69] seawater[45,67] and municipal[35,36,44,48,53,72,73] and industrial[46,50,58,64,65,70,75,79–81] wastewater have been the subject of study.

Among organics, the most treated are contaminants of emerging concern, that is, pharmaceuticals and personal care products.[35,36,38–40,43,49,51,53,57,59,72,79–81] As far as personal care products are concerned, parabens removal is of the highest interest.[35,39,43,57,61] Parabens are widely used as antimicrobial and preservatives in many pharmaceutical and personal care products, and their toxic character and carcinogenic potential have also already been tested.[102,103] They have also been classified as potential endocrine disruptor compounds since they can

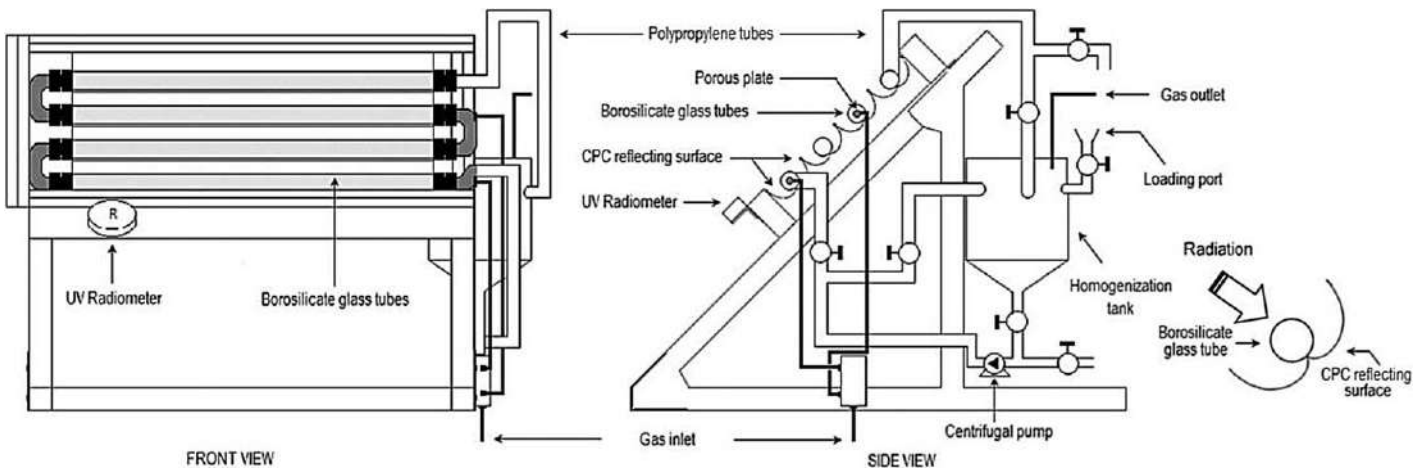

Figure 6.7 Scheme of CPC photoreactor. Reproduced from ref. 85 with permission from Elsevier, Copyright 2015.

interfere with animal and human hormonal systems.[104] Also, herbicides,[76,77] phenols[54,61,64,68] and dyes[47,55,69] constitute another group that has attracted the attention of researchers, although to a lesser extent. Finally, other less studied contaminants have been detergents[55] and polynuclear aromatic hydrocarbons.[34] Low-molecular-weight carboxylic acids, such as oxalic, formic or oxamic acids, have also been selected because they are simple molecules and usually final products of ozonation and AOP.[74,82] With the PhCatOz of these simple molecules, the presence of intermediates is avoided, and the activity of some new synthesized catalysts can be better clarified as well as the mechanism steps of the process. Another issue of relevance, as far as disinfection by-products formation is concerned, is the presence of bromide ions in water that, while being ozonated, leads to bromate formation, a suspected carcinogenic. Then Parrino *et al.*[105] studied the possibility PhCatOz to improve the oxidation rate and to reduce bromate formation. In their work, they used formic acid as the model compound to check this possibility. Finally, another issue treated in PhCatOz studies is the problem of antibiotic resistant bacteria (ARB), antibiotic resistant genes (ARG)[72] and pathogen removal and regrowth.[58,65] In these works,[58,65,72] the importance of PhCatOz to improve disinfection processes and the removal of ARB and ARG is developed under different experimental conditions. For instance, Moreira *et al.*[72] checked the importance of PhCatOz to remove different groups of cultivable microorganisms and housekeeping (16S rRNA) and antibiotic resistant or related genes (intI1, blaTEM, qnrS, sul1). Becerra-Castro *et al.*[65] observed the bacterial community composition of secondarily treated urban wastewater and of surface water collected in a drinking water treatment plant by comparing results before and three days after disinfection with ultraviolet radiation, ozonation or photocatalytic ozonation. In their work they assessed the dynamics of the bacterial communities during regrowth after disinfection. Finally, Mecha *et al.*[58] treated PhCatOz to inactivate waterborne pathogens (*Escherichia coli*, *Salmonella* sp., *Shigella* sp. and *Vibrio cholerae*) in synthetic water and secondary municipal wastewater effluents (see more about disinfection in Section 6.5.11.3).

6.5.5 AOP Comparison, Influence of Variables

Different variables govern the performance of UVA PhCatOz—concentration of catalyst, ozone and organics, intensity of incident radiation and wavelength or energy supplied to the catalyst and ozone, *etc.*—but the first step to check the benefits of this process is carrying out a comparison with other AOPs. This is often what papers dealing with UVA PhCatOz first do. For that reason, before beginning the functional evaluation of influence of variables, there is a comparison of several treatment processes: Photolysis, adsorption, ozonation, photolytic ozonation, catalytic ozonation, photocatalytic oxidation and photocatalytic ozonation to degrade organic contaminants.[36,66,71,76] When comparing different AOPs, especially considering their application in large-scale water treatment, degradation efficiency is among the most crucial parameters. It relates the required energy, oxidant or catalyst dose to the efficacy of the treatment.

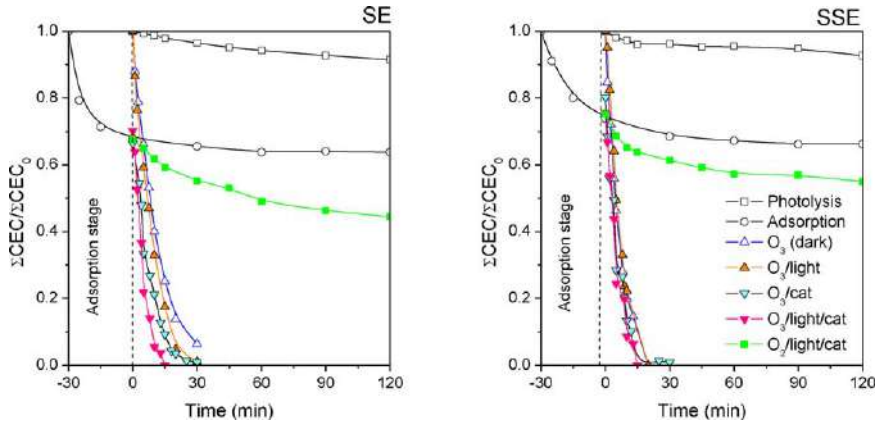

Figure 6.8 Removal of CECs from SE (secondary effluent) and SSE (synthetic secondary effluent) by different treatment processes. Experimental conditions: volume = 0.75 L; pH = 7.5–8.5; T = 35 40 °C; simulated solar irradiance (if applied) = 550 W m^{-2}; catalyst dose (if applied) = 0.4 g L^{-1}; ozone dosage (if applied) = 3.3 mg min^{-1}. Reproduced from ref. 36 with permission from Elsevier, Copyright 2020.

Amongst the various processes, as a rule of thumb, adsorption and photolysis have no significant contribution in the removal of contaminants; low degradation rates are observed with PhCatOx (in the absence of ozone), while PhCatOz presents the highest rates.[66] Ozone-based processes generally achieve complete conversion of some pollutants, as is the case of many contaminants of emerging concern (CECs)[36,79] (see Figure 6.8).

As far as mineralization is concerned, despite the higher degradation rates of individual organics with ozone technologies, PhCatOz and single ozonation lead to the highest and lowest TOC removal, respectively[36,43,54,66,79] (see Figure 6.9).

Such improvement in oxidation efficiency is thought to be primarily due to the increase of OH exposure since ozone is capable of trapping photocatalytically generated electrons more efficiently than oxygen, avoiding, therefore, the recombination of electron–hole pairs. The mineralization of recalcitrant organic compounds is the final goal of AOPs. The importance of the mineralization of organic pollutants arises from the fact that occasionally intermediates formed during degradation processes have higher toxicity than the parent compounds. Furthermore, combining ozone and photocatalysis processes improves toxicity removal.[43] PhCatOz is, among the technologies studied by several authors, the one that usually presents the highest rate of mineralization and toxicity removal.

Main experimental conditions of UVA PhCatOz involve the aspects discussed next.

6.5.5.1 Photocatalyst Dosage

The photocatalyst dose for optimal operation is a parameter that is thoroughly evaluated in research articles. It is evident that this parameter is

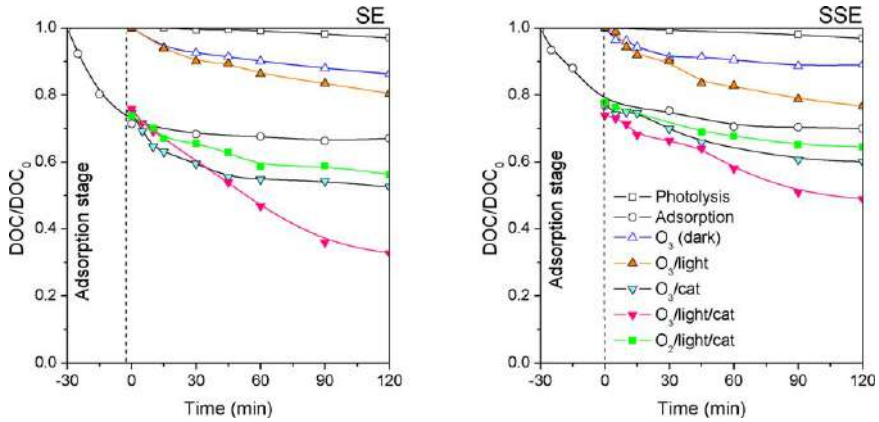

Figure 6.9 DOC removal from SE (secondary effluent) and SSE (synthetic secondary effluent) by different treatment processes. Experimental conditions: volume = 0.75 L; pH = 7.5–8.5; T = 35–40 °C; simulated solar irradiance (if applied) = 550 W m^{-2}; catalyst dose (if applied) = 0.4 g L^{-1}; ozone dosage (if applied) = 3.3 mg min^{-1}. Reproduced from ref. 36 with permission from Elsevier, Copyright 2020.

directly related to capital amounts in terms of the cost of semiconductor materials required for water purification. As a rule of thumb, the increase of catalyst dosage produces an enhancement in the degradation efficiency up to a certain value. Then removal rates slightly decrease, in consonance with the existence of an optimum concentration (as experimental observations suggest).[68,76] High loading of catalysts can increase solution opacity and significantly decrease light penetration depth. This effect may induce dead zones where the catalyst is not photoactivated due to light hindering. Further, the excessive mass of catalysts may induce particle aggregation, which significantly diminishes the active surface area.

6.5.5.2 *Role of pH*

The pH of the solution is one of the most important parameters in photocatalytic reactions because it may affect the surface charge properties of the semiconductor, the substrate structure and consequently the equilibrium adsorption (adsorption of contaminants onto photocatalyst surfaces is a key step in photocatalytic processes). Therefore, this parameter is usually chosen as one of the main process variables investigated in the UVA PhCatOz process. The effect of the initial pH on the degradation efficiency of organics in PhCatOz is studied normally in the pH 3–11 range,[68,76] though research efforts have arrived at different results in some cases. Working at a pH where ozone is mostly in molecular form usually leads to the best results. In this way, ozone is capable of extracting electrons from the conduction band of the catalyst, thereby reducing the unsuccessful electron–hole recombination. Nevertheless, a near neutral pH has been the most recommended to improve PhCatOz performance.[68]

6.5.5.3 Initial Pollutant Concentration

Generally, the degradation rates of organic contaminants are increased when the initial concentration is augmented. The increase in the oxidation rates can be attributed to the quantitative increase of collisions among the generated hydroxyl radicals and organic molecules when their concentrations increase.[76,83]

6.5.5.4 Effect of Influent Ozone Gas Concentration

According to the related literature data, the increase in the ozone concentration in the inlet gas results in a more effective removal of organic compounds in both PhCatOz and ozonation.[83] Thus the effect of influent ozone gas concentration on PhCatOz of organic pollutants was investigated by several authors at a fixed pH and at constant concentrations of organics and catalyst. Results show that the PhCatOz degradation rate of contaminants increases as the initial ozone gas concentration rises[66] as a consequence of the enhanced absorption of ozone molecules. Stabilization of the photogenerated positive holes on the photocatalyst surface was a result of PhCatOz, which favors the reaction between photogenerated electrons and adsorbed ozone molecules and the adsorption of pollutants on the positively charged photocatalyst surface.[76]

6.5.6 Ozone Consumption, R_{ct}, R_{HOO3}, Scavengers

Related to studies of mechanism and kinetics are those aspects concerning the presence of scavengers, hydroxyl radical and ozone exposures and ozone consumption. Information from them can be of importance to establish some steps of the mechanism and then the kinetics of the UVA PhCatOz process. Some of these aspects are represented by parameters such as R_{CT} or R_{HOO3}.[106–108] In this section, a brief resume is presented about what literature reports on these parameters. More information can be found in works listed in Table 6.1.

Among ozone processes (ozonation alone or single ozonation, catalytic ozonation, photolytic ozonation and photocatalytic ozonation), the amount of ozone consumed per unit of organic carbon consumed is always lower in UVA PhCatOz process, indicating that, in spite of being a system with more agents to add or feed, it presents lower cost for the use of ozone.[41,85] Another parameter in a similar role is the transfer of ozone dose (TOD), which is obtained from eqn (6.17):[106,107]

$$\mathrm{TOD} = \int_o^t \frac{v_g}{V}\left[C_{O_3 ge} - C_{O_3 go}\right] dt \tag{6.17}$$

where V is the reactor volume, v_g is the gas flow rate and $C_{O_3 ge}$ and $C_{O_3 go}$ the concentrations of ozone in the gas at the entrance and exit of the reactor, respectively. TOD has been calculated as a way of measuring the

concentration of hydroxyl radicals as indicated next.[41,48,57] The concentration of hydroxyl radicals results are fundamental to estimating the importance of the free radical oxidation pathway or as a tool to measure the synergism of PhCatOz (see Section 6.5.7). Also, the kinetic rate term of any compound subjected to an advanced oxidation process contains this concentration, which has to be known in order to solve the corresponding mass balance of the kinetic model (see Section 6.5.9). It could be said that the classical way of measuring the hydroxyl radical concentration is through the hydroxyl radical exposure, which can be obtained from eqn (6.18):[108]

$$\int C_{HO} dt = \frac{\ln\left(\frac{M}{M_o}\right)}{k_{HOM}} \tag{6.18}$$

where the left side of this equation is the hydroxyl radical exposure. The right term represents the ratio between (1) the logarithm of remaining dimensionless concentration of a probe compound M that does not directly react with ozone or absorb radiation of the wavelength emitted by the radiation source and (2) the rate constant of the reaction between this compound and hydroxyl radicals. The values of this integral are estimations of the hydroxyl radical concentration.[41,80] For instance, Chávez *et al.*[41] calculated the hydroxyl radical exposure for different ozone processes by using cotinine, an alkaloid found in tobacco and main metabolite of nicotine that fulfills the indicated requirements when UVA–visible radiation is applied. Also, the concentration of hydroxyl radicals at any time can be obtained from numerical derivation of eqn (6.18). Figure 6.10 shows as an example the changes of hydroxyl radical exposure and hydroxyl radical concentration with the corresponding times[41] for some ozone processes, including UVA PhCatOz using a solar simulator with a Xe lamp and a magnetic graphene titania catalyst.

As can be seen from Figure 6.10, UVA PhCatOz presents the highest values of both parameters, confirming that it is the most powerful AOP among the processes studied.[41]

The ratio between the hydroxyl radical and ozone exposures, called R_{CT} after Elovitz and von Gunten,[108] represents the yield of hydroxyl radicals, another parameter usually obtained in ozone processes to estimate the importance of the free radical oxidation way:

$$R_{CT} = \frac{\int_0^t C_{HO} dt}{\int_0^t C_{O_3} dt} \tag{6.19}$$

In Chávez *et al.*,[41] values of R_{CT} for PhCatOz were 13- to 38-fold those of single ozonation, confirming PhCatOz as a more powerful oxidation process. R_{CT}, however, depends on the ozone dose applied, and the values can change with different conditions of ozone supply. To solve this, Kwon *et al.*[106] and

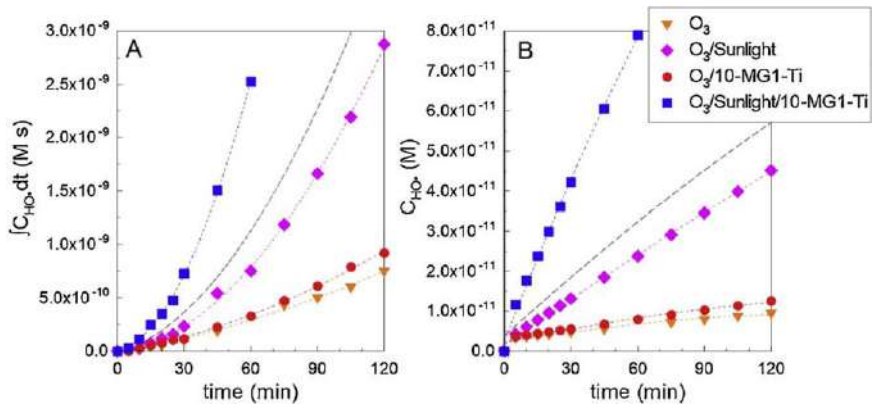

Figure 6.10 Evolution with (a) time of the hydroxyl radical exposure and (b) its concentration for different technologies combining simulated sunlight, ozone and the photocatalyst 10-MG1-Ti. Dashed gray line: sum of photolytic and catalytic ozonation. Experimental conditions: volume = 500 mL; pH = free (initially 5.7 ± 0.4); $Q_{GAS} = 30\ L\,h^{-1}$; $C_{O_3 inlet} = 10\ mg\,L^{-1}$ (if required); C10-MG1-Ti = 0.5 $g\,L^{-1}$ (if required); CCTN, 0 = 10 $mg\,L^{-1}$. Reproduced from ref. 41 with permission from Elsevier, Copyright 2020.

then Cruz-Alcalde *et al.*[107] proposed the $R_{HO,O3}$ concept, which is the hydroxyl radical exposure per TOD:

$$R_{HOO3} = \frac{\int_0^t C_{HO} dt}{TOD} \tag{6.20}$$

For instance, in Chávez *et al.*,[41] R_{HOO3} values were 3.37–7.6 times higher in PhCatOz than in single ozonation for the systems of Figure 6.10.

In order to clarify or establish the action of some radical oxygen species (ROS), the hydroxyl radicals included, or the effect on the specific surface area of the photocatalyst, during studies of ozonation processes such as PhCatOz, some substances are fed to the aqueous solution being investigated. These substances are called scavengers since they react with some of these ROS or adsorb on the catalyst surface, diminishing the number of active sites where ozone or compounds can be adsorbed to react and inhibiting the oxidation rate of pollutants or organics present in the water. Carbonates and phosphates are usually applied scavengers belonging to both groups. Table 6.3 presents a list of scavenging substances and their role (reacting with some ROS or reducing the catalyst surface area) that have recently been used in PhCatOz studies.

Among scavengers, *t*-butanol is likely the most used to trap hydroxyl radicals, since it is practically inert to ozone attack and does not absorb UVA–visible radiation. However, its role as hydroxyl radical scavenger has been questioned because its presence decreases the surface tension of the water and then increases the specific surface area of ozone–oxygen or ozone–air

Table 6.3 Scavengers often used in PhCatOz processes.

Scavenger name and reference	Short live species undergoing reaction or step affected
CO_3,[2–36,41,48] EDTA[59]	Hydroxyl radical
$PO_4H_2^-$,[76] NO_3^-,[76] Cl^-[76,83]	
t-Butanol,[38,60,61,76,83] Isopropanol[59]	
F-,[76,83] SO_4^{2-}[76]	Adsorption
SO_4,[2–76] NO_3^-,[76] Cl^-,[76,83] I^-[76]	Holes
Oxalate[38,49]	
EDTA[61,76]	
I-,[76] CrO_4,[2–49] CCl_4[59]	Electrons
Benzoquinone,[49,76] L-ascorbic acid,[76] $CHCl_3$,[76] N_2,[38] 4-hydroxy-2,2, 6,6-tetramethylpiperidinyloxy[61]	Superoxide ion radical

bubbles during ozonation processes when applied at high concentration ($>10^{-2}$ M).[109] This increase means that the volumetric mass transfer of ozone from the gas to the water also increases, favoring the absorption rate of ozone and the amount of available dissolved ozone. Thus, on one hand, *t*-butanol reacts with hydroxyl radicals decreasing the pollutant reaction rate when the hydroxyl radical oxidation is important as in PhCatOz. On the other hand, if supplied at high concentration, it increases the pollutant oxidation rate since more ozone is available to be decomposed in hydroxyl radicals.

6.5.7 Synergism

It is well-known that the combination of various advanced oxidation processes (AOPs) may result in an enhanced generation of oxidative species and consequently in accelerating the degradation and mineralization of refractory organic pollutants. As said previously, single photocatalysis and single ozonation have great potential in wastewater treatment. Nevertheless, when used individually, these processes have some drawbacks that limit their effectiveness in the degradation of organic pollutants. Photocatalysis is a relatively slow process because of its low oxidation rate. Ozonation, in spite of its two means of oxidation, leads to a partial oxidation to mineralize the organic content of the water (1) by molecular ozone reactions, highly selective, and (2) by hydroxyl radicals coming from ozone decomposition that results in a low concentration of these species. Partial oxidation leads to the formation of carboxylic acids as end products that cannot be further oxidized; therefore, complete mineralization is not achieved. These disadvantages make the individual application of these processes to treat polluted water economically undesirable. PhCatOz has appeared to overcome these shortcomings.[68] Therefore, coupling heterogeneous photocatalysis and ozonation produces hydroxyl radicals more successfully than ozonation or photocatalytic oxidation, resulting in higher reaction rates and avoiding the formation of toxic by-products.[67] As a result, the degradation rate of PhCatOz is higher than the sum of the degradation rates of ozonation and PhCatOx, indicating the presence of a synergistic effect between these two processes.

This synergism is due to an increased generation of the reactive oxygen species (ROS), mainly hydroxyl radicals, which is probably the result of the following: (1) photocatalytically induced decomposition of ozone in non-selective hydroxyl radicals, (2) the decreased recombination rate of electrons and positive holes on the photocatalyst surface and (3) the action of dissolved ozone as an electron acceptor (ozone is a more powerful oxidant than oxygen, and it can quickly capture the strong reducing electrons upon CB of the photocatalysts). The synergism notably reduces the time needed for the degradation and mineralization of pollutants, which is an important factor to make the process practically viable.[66] Therefore, photocatalytic ozonation can be considered a truly desirable candidate for different practical applications, such as aquaculture and waste and drinking water treatment.

6.5.8 Mechanisms of Reactions

Two types of mechanisms are explained or developed in understanding how UVA PhCatOz works: the basic mechanism involving the initiation, propagation and termination reactions of free radical chains, as presented in a simplified manner in Sections 6.2–6.4, and the mechanism of formation and removal of intermediates detected through chromatographic techniques (HPLC/MS, GC/MS, *etc.*). Although the fundamentals of the free radical mechanism are well understood, many works still deal with it in an attempt to justify the results they have obtained,[38,76] the role of catalysts they have used,[49,76] the intermediates they identified,[83] the action of scavengers[38,49,57,76] upon the removal of organics treated and the improvement of reaction rates observed compared to ozone-free photocatalytic oxidation.[76,77] Also, in some works the authors attempt to deepen and clarify some steps.[49] An important conclusion highlighted in some of these works derived from the radical chain mechanism is the number of electrons needed to produce one hydroxyl radical, which is one in the PhCatOz process against three in the PhCatOx process.[77] In Hassani *et al.*,[76] the steps concerning the reactions of superoxide ion radicals with electrons in the metal network of montmorillonite that allows the increase in the rate of ciprofloxacin removal, the compound studied, are included in the classical mechanism. In Yang *et al.*,[110] electron paramagnetic resonance (EPR), in addition to some classical scavengers, was used to deduce the action of ROS such as the hydroxyl radical, superoxide ion radical and singlet oxygen. In the experiments, 5,5-dimethyl-1-pyrroline (DMPO) and 2,2,6,6-tetramethyl-4-piperidinol (TEMP) were chosen as spin trapping agents, respectively. Xie *et al.*,[54] while studying the PhCatOz of phenol and oxalic acid with Fe^{3+}/TiO_2 catalyst, proposed different steps involving iron species to complete the radical chain PhCatOz process and explain their evolution in water. Zeng *et al.*,[49] in their work with TiO_2–carbon dots, concluded that electrons on the surface of carbon dots are trapped by ozone and oxygen in order to generate ROS that eventually led to HO radicals to remove ciprofloxacin. Their main conclusions are the three roles of carbon dots: (1) increase light absorption, (2) very high electron transfer and (3) electron storage capacity.

Intermediates identified in some works,[54,57,62,83,84] on the other hand, facilitated the establishment of a mechanism of molecular species and the nature of the reactions between steps. For instance, in Gomes *et al.*,[57] PhCatOz of parabens was studied with different metal noble titania catalysts. From intermediates formed, the authors proposed hydroxylation as the most significant reaction pathway and hydroquinone, 4-HBA, 3,4-diHBA and 2,4-diHBA as the most commonly identified by-products from reactions with ozone, hydroxyl radical and photocatalytic oxidation. In Yang *et al.*,[110] from intermediate identification and the aid of scavengers, a mechanism of reactions involving parent compound and intermediates was proposed. Fathinia *et al.*,[84] from the identification of intermediates of the PhCatOz of three pharmaceuticals, reported that the oxidation process is initiated by the simultaneous demethylation and hydroxylation of parent compounds, followed by formation of first identified intermediates. Subsequent steps are the non-selective attack of HO to yield carboxylic acids such as acetic acid and low-molecular-weight compounds such as carbodiimide. The final products are carbon dioxide and water. In the case of PhCatOz of phenazopyridine with TiO_2–ceramic plates and UVA light, Fathinia and Kathaee[83] report that the formation of intermediates can be justified by the break of the azo bond followed by a subsequent opening of benzene rings to form compounds such as pentadecanoic acid or methyl formamide, compounds that are not detected during single ozonation. With this, the authors reinforce the importance of PhCatOz *versus* ozonation. Orge *et al.*,[62] by studying aniline removal with TiO_2/carbon composites, focused on the formation of recalcitrant oxamic and oxalic acids. They also discussed the formation of nitrogen compounds, NO_3^- and NH_4^+, which are formed in higher concentration during PhCatOz compared to the other oxidation systems applied. As a final example, Lou *et al.*,[59] in their work on PhCatOz of flumequine and clarithromycin, report the breaking of one N-containing ring to yield intermediates that remain more than 2 h in the aqueous medium. They also report decarboxylation as a main initial step which is due to the reaction of an $RCOO^-$ group with generated holes in the valence band of TiO_2 to form one carbon dioxide molecule.

6.5.9 Kinetics

The ultimate step of studying processes such as AOP is the establishment of a kinetic model that predicts the level of degradation that any pollutant in water can reach under certain experimental conditions. However, due to the complex nature of a wastewater mixture, this study usually applies to global parameters that characterize water contamination as the chemical oxygen demand (COD) or total organic carbon (TOC). The proposal of a kinetic model previously requires the knowledge about a mechanism of reactions to derive the rate equation of the main species present in water. These rate equations contain the rate constants of the reaction mechanism steps, and, in ozonation systems, the volumetric mass transfer coefficient, liquid

holdup of the gas–liquid contactor used, the gas–liquid equilibrium and perfect law constants. In the presence of light and catalysts, quantum yields of pollutants and catalysts and adsorption equilibria data are also needed. For these reasons, some papers have, among their objectives, determined these rate constant parameters. In the presence of UVA light, pollutants such as most pharmaceuticals do not absorb light, so there is no worry about their quantum yields. Ozone and even hydrogen peroxide, however, do absorb and photolyze, though weakly, in radiation with wavelengths between 300 and 335 nm. Then, in PhCatOz, the main agent that absorbs radiation is the catalyst. The energy of radiation it absorbs is limited by the corresponding band gap (3.2 eV for anatase TiO_2, which means an active catalyst until radiations of about 385 nm). To make more active TiO_2, for example with visible light, some doping materials are used such as some containing N, S, noble metals or combined with other oxides such as WO_3, carbon materials such as C_3N_4, *etc.* These PhCatOz processes in the exclusive presence of visible light will be treated in another chapter. In addition to quantum yields, the dispersion and absorption coefficients of catalysts are also necessary.[111,112] With all this information and the geometry of the reactor, a radiation transfer equation[113,114] has to be solved and the results applied to the kinetic model of PhCatOz. In spite of the importance of these radiation parameters, as far as we know, there is scarce information in literature with only a few works working on photocatalytic oxidation[115] kinetic modeling. Regarding PhCatOz, in most of the papers that address the kinetics limit, their study is to determine apparent pseudo first-order rate constants just to show how much higher they are compared to those of single ozonation or photocatalytic oxidation. For instance, Zeng *et al.*,[49] in spite of presenting a mechanism of reactions similar to that treated in Section 6.5.8, limited their kinetic study to calculate pseudo first-order rate constants in PhCatOz of ciprofloxacin at different pH values and in the presence of different salts, scavengers, *etc.* With these rate constants, they showed the importance of some steps of the mechanism and the action of reacting oxygen species. Kumar *et al.*[61] worked on adsorption, followed by photocatalytic oxidation and PhCatOz of methyl paraben (MP) and orthochlorophenol (oCP) with some g-C_3N_4/$FeVO_4$ catalysts and solar radiation. They first studied the adsorption isotherms with Langmuir and Freundlich equations, and finally the kinetics of AOP processes studied was reduced to fitting experimental concentrations of MP and oCP to apparent pseudo first-order kinetics. Values of the first-order rate constants showed the apparent importance of the ozone-photocatalytic system compared to the other ozone-free oxidation or adsorption systems. Mecha *et al.*[68] reportd results on the PhCatOz of a secondary wastewater effluent with TiO_2 and noble metal–doped TiO_2 catalysts with solar radiation and UV lamp emitting radiation at different wavelengths from UVC to UVA. They used the Langmuir–Hinshelwood equation to model the photocatalytic degradation of phenol doped to the wastewater that finally reduced to simple pseudo first-order kinetics. Also, TOC was taken as a lumped parameter for the kinetic study. They also indicated that the

apparent rate constant was the sum of the contributions of direct ozone reaction, hydroxyl free radical reaction, photocatalytic reaction due to photons and direct photolysis. However, only the total apparent rate constant was reported. Orge *et al.*[62] studied the removal of aniline by PhCatOz with different catalysts (see Table 6.1) and a medium-pressure mercury vapor lamp. They also assumed pseudo first-order kinetics for the different AOP studied. Catalytic ozonation resulted in the best AOP applied since it leads to higher first-order rate constants for all catalysts used except when using P25 TiO_2. For this case, PhCatOz was the faster oxidation process to remove aniline from water.

In other works, a more rigorous kinetics was presented combining non-ideal flow and kinetic studies. In this sense, Quiñones *et al.*[85] published results of the AOP of a mixture of six pharmaceuticals doped to a secondary municipal wastewater in the presence and absence of sunlight. The AOP studied involve Fe^{3+}/H_2O_2/ozone/solar light (pH 3) and TiO_2/ozone/solar light (pH 7) and their corresponding simpler processes such as single ozonation, TiO_2/solar light photocatalytic oxidation, *etc.* Their oxidation system was a CPC reactor fed with ozone and connected to a tank for recirculation purposes. A perfectly mixed flow was adopted, and the kinetic model was applied to TOC as a lumped parameter. They applied rate equations with different contributing terms for direct photolysis, direct ozone reaction, hydroxyl radical reactions due to free radicals coming from ozone reactions and from the Fenton reaction. The kinetic model for TOC removal in both PhCatOz systems was:[85]

For Fe^{3+}/H_2O_2/ozone/solar light at pH 3:

$$-\frac{\mathrm{dTOC}}{\mathrm{d}t} = \left[k_{\mathrm{T}_2} C_{\mathrm{Fe(III)}} C_{\mathrm{H_2O_2}} + k_{\mathrm{D}} C_{\mathrm{O_3}} + k_{\mathrm{T}_3} C_{\mathrm{O_3}}\right]\mathrm{TOC} \tag{6.21}$$

where first, second and third terms of the right-hand side of eqn (6.21) correspond to the photo-Fenton reaction, TOC–ozone direct reaction and indirect TOC–ozone reaction, due to the fraction of hydroxyl radicals that comes from ozone decomposition initiation–promotion steps, respectively.

For TiO_2/ozone/solar light at pH 7:

$$-\frac{\mathrm{dTOC}}{\mathrm{d}t} = \left[k_{\mathrm{UV}} + \frac{k_i C_{\mathrm{O_3}}}{1 + \sum_i K_i C_i} + k_{\mathrm{D}} C_{\mathrm{O_3}} + k_{\mathrm{T}_3} C_{\mathrm{O_3}}\right]\mathrm{TOC} \tag{6.22}$$

where the first and second terms of the right-hand side of eqn (6.22) correspond to the contributions of direct TOC photolysis (usually negligible) and ozone photocatalytic reaction on the catalyst surface considering a Langmuir kinetics, respectively. The authors explain that after some transformation and at the conditions they investigated, both TOC mass balance equations reduce to first-order kinetics. Also, eqn (6.21) and (6.22) were applied to single processes such as ozonation alone or solar photo-Fenton oxidation, and their

corresponding second-order rate constants were also obtained. For example, apparent second-order rate constants for solar photo-Fenton (pH 3), single ozonation, photolytic ozonation and TiO_2/ozone/solar light (the three latter at pH 7) were found to be 4.34×10^5, 7.39×10^2, 1.13×10^4 and 1.3×10^4 M^{-1} min^{-1}, respectively. For TiO_2/solar light a value of 4.28×10^{-3} min^{-1} was found for the apparent pseudo first-order rate constant. In another work, Figueredo *et al.*[40] first studied the type of flow through the photocatalytic system, a glass borosilicate tube externally illuminated with UVA LEDs (see Figure 6.3). The tube was connected to a perfectly mixed tank where water was ozonated and recirculated with a pump through the tube. The non-ideal flow study indicated that the residence time distribution function of the tubular photoreactor corresponded to one of a series of four equally sized perfectly mixed tanks. The authors studied the ozonation, photolytic ozonation and photocatalytic ozonation of primidone by assuming a mechanism of reactions. They modeled the time variation of TOC, as surrogate parameter, ozone concentrations in the gas and water and hydrogen peroxide. Because of the different reactivity of compounds formed during ozonation, they assumed four different TOCs. The corresponding TOC values were changing with time so that some reaction steps of the mechanism were proposed to justify the removal and formation of these TOCs with time. The actual TOC was the sum of the four TOCs assumed. On this basis, mass balance equations, corresponding to the four perfectly mixed tanks in series, were established in accordance with the non-ideal flow of the reacting system. In these equations, some parameters were initially unknown and later obtained after fitting experimental and calculated results of TOCs and concentrations of ozone (gas and water) and hydrogen peroxide. The model predicts that the direct ozone reactions were mainly responsible for TOC removal. Another example can be seen in the work of Chávez *et al.*,[51] who conducted the PhCatOz of real municipal secondary wastewater where concentrations of pharmaceuticals were at $\mu g\,L^{-1}$ level (ciprofloxacin was the compound identified at the highest concentration, 4.25 $\mu g\,L^{-1}$). The reacting system consisted of a fix bed of TiO_2 supported on Raschig rings illuminated with external UVA LEDs connected to a second column for recirculation purposes (see Figure 6.4). In this case, tracer experiments permitted the determination of the residence time distribution function which allowed the reacting system to be assumed as an ideal perfectly mixed reactor. The authors applied concepts of the kinetics of gas–liquid reactions and determined the Hatta number of the direct reactions of ozone with the pharmaceuticals.[101] Values of Ha were always lower than 1, indicating that the kinetic regime of the direct ozonation was slow and that a possible competition with hydroxyl free radical oxidation could be at play. With rate constant values of hydroxyl radical–pharmaceutical reactions, they established the conditions of PhCatOz so that the process could be controlled by direct or hydroxyl radical reactions. The presence of natural scavengers in wastewater, such as carbonates, was a key factor so that the higher the scavenger concentration was, the lower the importance of the free radical mechanism was to remove pharmaceuticals at their actual concentration in wastewater. For instance, for the

secondary wastewater effluents they treated, they reported scavenging factors (the product of the rate constant of hydroxyl radical–scavenger reaction and scavenger concentration) of 6.7×10^5 and 8.2×10^5 s^{-1}, and they concluded that compounds such as bezafibrate, isoproturon, metoprolol, tramadol and venlafaxine could be better removed with PhCatOz compared to single ozonation if the mass transfer coefficient were at least of 0.12 s^{-1}.[51] For compounds such as carbamazepin, fluoxetin, clarithromycin, diclofenac, among others, the direct ozone reaction is the main oxidation step so that single ozonation is enough to remove these compounds from water under the conditions investigated.

6.5.10 Energy and Cost

Other important questions are those concerning the use of energy and cost analysis, as commented on in this section.

6.5.10.1 Energy Use

Energy consumption is a critical parameter to analyze the viability of the photocatalytic treatment, and it is closely related to the wattage of the lamp. In order to determine energy requirements, figures-of-merit on the use of electrical energy recommended by IUPAC were employed by researches working on UVA- and solar-based processes.[64] The most important design parameter in AOP systems is the amount of energy applied to produce enough hydroxyl radicals. The figures of merit assume that contaminants undergo pseudo first-order kinetics, due to their low concentration.

For the energy efficiency of AOPs, electrical energy per order (EEO) is often chosen as a figure of merit. EEO is defined as the electrical energy in kW h required to remove a pollutant by one order of magnitude in a unit of volume, *i.e.* 90%, in 1 m^3 of water. EEO can be calculated from eqn (6.23) for batch or from eqn (6.24) for flow-through operation:

$$\mathrm{EEO} = \frac{Pt1000}{V\log\left(\frac{C_\mathrm{i}}{C_\mathrm{f}}\right)},\ \mathrm{kw\,hm^{-3}order^{-1}} \tag{6.23}$$

$$\mathrm{EEO} = \frac{P1000}{Q\log\left(\frac{C_\mathrm{i}}{C_\mathrm{f}}\right)},\ \mathrm{kwhm^{-3}order^{-1}} \tag{6.24}$$

where P is the rate power in kW to the AOP system, t is the time of treatment in h, V is the volume of treated aqueous solution in L, Q is the flow rate in $m^3\,h^{-1}$, and C_i and C_f are the concentrations of contaminant at the initial time and time t, respectively, for batch systems and entrance and outlet concentrations for flow systems, respectively. Also, 1000 is a conversion factor (1000 L m^{-3}). In the case of UVA PhCatOz, the power input is the sum of the energy input of the ozone generation, the UVA lamp or LEDs and the power supply.[70]

For solar-driven systems, the cost is dominated by the capital investment in the collector, and the efficiency is best described in terms of irradiated area. Collector area per order, A_{CO} ($m^2\,m^{-3}\,order^{-1}$), is the collector area needed to obtain one-order-magnitude degradation of a given contaminant per unit of volume receiving a ''standardized'' incident solar fluence rate of 1000 $W\,m^{-2}$ over a period of 1 h. It is calculated from eqn (6.25):[64]

$$A_{CO} = \frac{A_t E_S}{V \log \frac{C_i}{C_f}} \tag{6.25}$$

where A_t is the collector area, and E_s is the average solar irradiance over the time for a given treatment.

Another standard figure of merit estimated in several studies is electrical energy per mass (EEM), which is defined as the electric energy in kWh that brings about the degradation of a unit mass (*e.g.* 1 kg) of a contaminant in polluted water.[116] The EEM is also necessary for the comparison and evaluation of the electric-energy-driven AOPs:

$$EEM = \frac{rC_{O_3}Q + P}{F(\gamma_i - \gamma_f)} \tag{6.26}$$

where r is the energy requirement for mass of O_3 production from oxygen; C_{O_3} is the gas ozone concentration in the influent gas ($mg\,L^{-1}$); Q is the flow rate of the influent gas ($L\,min^{-1}$); F is the flow rate of the water ($m^3\,h^{-1}$); γ_i and γ_f are the organic concentrations in the influent and effluent ($mg\,L^{-1}$) water, respectively; and P is the power of UV lamp.

Gmurek *et al.* 2019[43] calculated the specific energy consumption (SEC), that is, the amount of electrical energy consumption (kWh) per unit mass of COD (in lab scale). In ozone-based processes, SEC is calculated with eqn (6.27):

$$SEC_{O_3} = \frac{Pt + r\mathrm{TOC}}{V(\mathrm{COD_i} - \mathrm{COD_f})} \tag{6.27}$$

where P is the nominal electric power (kW) of the photochemical system, t is the reaction time (h), r is the energy requirement per mass for O_3 production (15 $kW\,h\,kg^{-1}$ O_3)[117] and V is the volume (L) of the solution in the reactor.[43]

In case of oxidants or catalysts, the ''stored electric energy'' of a compound can be calculated based on prices for electric energy (price per kW h) and the respective compound (price per kg).

6.5.10.2 Process Cost Analysis

Cost evaluation is an important step when deciding the industrial implementation of a treatment technology. When choosing the best method for wastewater treatment, some significant factors should be taken under

consideration including economy, effluent quality goals, ongoing regulatory framework and operationality, among others. In real AOP applications, the economic issue is often seen as the most relevant factor since these technologies are electric-energy-intensive. Accordingly, electric energy tends to account for the main operating cost.[70] Therefore, economic analysis must be considered before process development and scale-up.

To evaluate the possibility of using this technology in further studies with real industrial effluents, it is important to perform a cost analysis of the process to determine whether it is applicable in a real case scenario. Several authors have followed a simple methodology performed by Gagol and coworkers[118] to determine the chemicals and energy cost. The cost of effluent treatment by UVA PhCatOz depends on a number of factors, including the volume of an effluent, the kind and concentration of contaminants or the desired effectiveness of degradation. These calculations include the treatment time needed for complete oxidation, cost of oxidants/or catalysts used and cost of electric energy. Also, equipment and maintenance cost per year, respectively, were summed.[119] Quiñones *et al.*[80] presented this simplified economic comparison of operating costs, taking into account experimental conditions used throughout their investigation. Thus two criteria were used: (1) operating costs to reach complete removal of pollutants and (2) operating costs to remove 20% of the TOC of the secondary effluent.[70]

6.5.11 Other Aspects

In addition to the items discussed in previous sections, other aspects concerning the PhCatOz of water pollutants are toxicity, the bromate issue and disinfection problems.

6.5.11.1 Toxicity

One important aspect about the application of AOPs is the possible formation of toxic intermediates or by-products that could be even more toxic than the compounds initially present in the samples. Thus several research works reported the significance of analyzing the relationship between intermediates formed during UVA PhCatOz and the overall toxicity of the wastewater treated effluent. Based on these relationships, the main toxic compounds could be identified so that effluent toxicity is diminished effectively before the effluent is discharged to the water environment.[34]

To cover a wide range of trophic levels, different species such as *Vibrio fischeri* (bacteria), *Corbicula fluminea* (clam) and *Lepidium sativum* (plant) were used.[57] Additional toxicity bioassays employed by some authors are assessed by using acute *Daphnia magna* (microcrustacean)[56,80] and the marine bacterium *Photobacterium phosphoreum*[53] where the toxicity unit was correlated to the EC_{50}. García-Cambero *et al.*[120] proved the zebrafish model for toxicity evaluations. According to these authors, the initial stages (embryos) have been used in various applications including toxicity tests of

individual or mixtures of emerging contaminants, sediment and sediment extracts and evaluations of complex mixtures like sewage effluents. The introduction of ozone significantly reduced the acute toxicity of wastewater. The integration of UVA photocatalysis showed a better detoxication than ozonation.[34] As a rule, the toxicity of samples increased at the beginning of the photocatalytic treatment, likely as a consequence of the accumulation of by-products or toxic intermediates, and then decreased. This result is in agreement with that reported for the removal of other organic pollutants by ozonation and solar photocatalytic oxidation with TiO_2.[80]

6.5.11.2 Bromate Issue

Ozone has been extensively used in water treatment for a long time due to its great oxidizing power, which enables it to selectively oxidize many organic and inorganic species in aqueous solution. The reactions between ozone and organic compounds, however, usually lead to the formation of intermediates, many of which are recalcitrant to ozone attack and therefore accumulate in water.[121] Further, one of the main drawbacks of ozonation is the induced oxidation of bromide to bromate ions, which is one ozonation by-product of main concern (reaction (6.28)) and which is suspected to be carcinogenic.[105]

$$Br^- + 3O_3 \rightarrow BrO_3^- + 3O_2 \quad (6.28)$$

Furthermore, other pathways have been reported in which bromate formation occurs by the action of the hydroxyl radicals produced by ozone decomposition. This latter mechanism is non-negligible only at relatively high pH values.[105] On the contrary, in the presence of bromide ions, photocatalysis does not induce the formation of bromate ions. In fact, the oxidation of bromide by $^{\bullet}OH$ radicals produces intermediates such as hypobromite ions, which are reconverted to bromide by photogenerated electrons according to reaction (6.29):[45]

$$BrO^- + 2e^- + H_2O \rightarrow Br^- + 2OH^- \quad (6.29)$$

When performed concurrently with ozonation, photocatalytic ozonation reduces the formed bromate ions to innocuous bromide ions (reaction (6.30)) at a rate that increases with the concentration of oxidized compounds (*i.e.* organic matter):[45]

$$BrO_3^- + 6H^+ + 6e^- \rightarrow Br^- + 3H_2O \quad (6.30)$$

Reaction (6.30) is of great importance because ozonation of bromide ions (reaction (6.28)) can produce unacceptable amounts of bromate if control of their formation is not effective. Thus the benefits of coupling photocatalysis and ozonation are not limited to the increase of the oxidation rate but also include the control of bromate ions. Indeed, as bromide ions are ubiquitous in ground and surface water, carcinogenic bromate ions may be almost quantitatively produced if the sole ozonation is used for purification

purposes.[63] This aspect is of paramount importance for marine aquaculture applications as bromide concentration in seawater is about 67 $mg\,L^{-1}$, and the high amount of bromate ions produced may be lethal for the living organisms. This is so by considering, for instance, that the suggested exposure safety value to protect aquatic organisms from long-term adverse effects is 3 $mg\,L^{-1}$. In this sense, it can be seen that PhCatOz offers the possibility of controlling bromate, the ozonation by-product of main concern.[45,63,105]

6.5.11.3 Disinfection

Disinfection processes aim at reducing the number of viable cells through the generation of damages in different cellular structures and molecules. The use of photocatalytic ozonation also has great potential in pathogen inactivation. Bacterial inactivation using photocatalytic ozonation is achieved through disrupting normal cellular functions by the reactive oxygen species (ROS), especially the $^{\bullet}OH$ radicals. These reactions result in oxidative damage to cellular components that lead to the loss of membrane potential, thereby leading to the death of the microorganisms.[58,65] In addition, when the stress conditions imposed by the water treatment processes are relieved, biological contaminants have the potential to regrow, and microbiological indicators should be monitored during storage of the treated wastewater. It has been shown that bacterial regrowth does occur after photocatalytic disinfection or disinfection by ozone. This is a major limitation in the individual application of these processes. Mecha *et al.*[58] demonstrated the synergistic effects of the combined photocatalytic ozonation process on the disinfection of municipal wastewater. Furthermore, this synergy led to a 50%–75% reduction in the contact time required for photocatalytic ozonation compared to photocatalysis or ozonation alone. Also, following the recovery period (24 h and 48 h in the dark), no bacterial regrowth is detected, showing that photocatalytic ozonation processes had caused irreversible damage to the bacterial cells.

6.6 Conclusions

From the review of works presented in this chapter, some conclusions can be drawn about UVA photocatalytic ozonation:

- It is an incipient AOP based on a strong synergism between ozonation and photocatalytic oxidation.
- However, for many cases, single ozonation has enough oxidizing power to remove many organics, especially those named as being of emerging concern (pharmaceuticals), that is without the contributing effect of catalyst and light.
- The synergism between both oxidation processes is clearly seen when the objective of the process is the removal of TOC or mineralization of the water content.

- There are up to five possible routes of hydroxyl radical formation during PhCatOz: (1) ozone decomposition in solution that can be accelerated with the formation of hydrogen peroxide after direct ozonation of organics, (2) ozone adsorption and decomposition on the catalyst surface, (3) electron–ozone reactions in the conduction band of the catalyst, (4) reactions of ozone with the superoxide ion radical formed from electron–oxygen reactions at the conduction band of the catalyst and (5) adsorption of water or hydroxyl anions on the catalyst surface and subsequent oxidation with positive holes at the valence band of the catalyst.
- The main material used is TiO_2 alone or combined with other non-metal, metal, metal oxides or carbon materials, such as MWCN, AC, carbon dots or graphene oxide.
- The intensity of oxidation increases with the decrease of the wavelength of incident radiation, but for environmental sustainability, radiation belonging to the UVA region (330–400 nm) or solar light is encouraged.
- Kinetic modeling of PhCatOz still has some gaps that need further investigation.
- Photoreactor geometry and catalyst separation are also still questions to be solved for the PhCatOz process to be of practical application.
- PhCatOz is also a way of increasing the disinfection of water and avoiding the formation of bromate in water containing bromide ions.

Facing these advantages, PhCatOz still presents the problems related to catalyst–water separation and to increasing the catalysts' absorption of photons. Therefore, studies on the synthesis of new catalysts that overcome these drawbacks are recommended.

Acknowledgements

The authors thank the Spanish State Agency of Investigation (project: PID2019/104429RB-I00/AEI/10.13039/501100011033) for their economic support.

References

1. J. Dębska, A. Kot-Wasik and J. Namieśnik, *Crit. Rev. Anal. Chem.*, 2004, **34**, 51.
2. S. A. Snyder, P. Westerhoff, Y. Yoon and D. L. Sedlak, *Environ. Eng. Sci.*, 2003, **20**, 449.
3. K. Kümmerer, *Chemosphere*, 2001, **45**, 957.
4. J. J. Rook, A. A. Gras, B. G. V. der Heijden and J. D. Wee, *J. Environ. Sci. Health A*, 1978, **13**, 91.
5. W. H. Glaze, *Environ. Health Perspect.*, 1986, **69**, 151.
6. T. A. Ternes, A. Joss and H. Siegrist, *Environ. Sci. Technol.*, 2004, **38**, 392A.

7. O. A. H. Jones, N. Voulvoulis and N. Lester, *Crit. Rev. Environ. Sci. Technol.*, 2007, **35**, 401.
8. S. Mompelat, B. Le Bot and O. Thomas, *Environ. Int.*, 2009, **35**, 803.
9. W. H. Glaze, J. W. Kang and D. H. Chapin, *Ozone: Sci. Eng.*, 1987, **9**, 335.
10. P. R. Gogate and A. B. Pandit, *Adv. Environ. Res.*, 2004, **8**, 501.
11. A. Vogelpohl and S. M. Kim, *J. Ind. Eng. Chem.*, 2004, **10**, 33.
12. M. Doré, Chimie des oxydants et traitement des eaux, *Technique et Documentation-Lavoisier*, Paris, 1989.
13. R. L. Kuczkowski, *In 1,3, Dipolar Cycloaddition Chemistry*, John Wiley and Sons., New York, 1984, vol. 2A, pp. 197–277.
14. J. Staehelin, R. E. Buhler and J. Hoigné, *J. Phys. Chem.*, 1984, **88**, 5999.
15. H. Tomiyasu, H. Fukutomi and A. Gordon, *Inorg. Chem.*, 1985, **24**, 2962.
16. F. J. Beltrán, *Ozone: Sci. Eng.*, 1997, **19**, 13.
17. G. R. Peyton and W. H. Glaze, *Environ. Sci. Technol.*, 1988, **22**, 761.
18. J. H. Baxendale and J. A. Wilson, *Trans. Faraday Soc.*, 1957, **53**, 344–356.
19. F. J. Beltrán, A. Aguinaco and J. F. García-Araya, *Appl. Catal., B*, 2010, **100**, 289.
20. B. Kasprzyk-Hordern, M. Ziółek and J. Nawrocki, *Appl. Catal., B*, 2003, **46**, 639.
21. F. J. Beltrán, J. Rivas and V. Montero-de-Espinosa, *Ind. Eng. Chem. Res.*, 2003, **42**, 3218.
22. A. Fujishima and K. Honda, *Nature*, 1972, **238**, 37.
23. A. Fujishima, K. Kobayakawa and K. Honda, *J. Electrochem. Soc.*, 1975, **122**, 1487.
24. A. Fujishima, T. N. Rao and A. D. Tryk, *J. Photochem. Photobiol., C*, 2000, **1**, 1.
25. S. Malato, J. Blanco, A. Vidal and C. Richter, *Appl. Catal., B*, 2002, **37**, 1.
26. M. NanChong, B. Jin, C. W. K. Chow and C. Saint, *Water Res.*, 2010, **44**, 2997.
27. M. M. Sein, M. Zedda, J. Tuerk, T. C. Schmidt, A. Golloch and C. von Sonntag, *Environ. Sci. Technol.*, 2008, **42**, 6656.
28. J. Xiao, Y. Xie and H. Cao, *Chemosphere*, 2015, **121**, 1.
29. M. Mehrjouei, S. Müller and D. Möller, *Chem. Eng. J.*, 2015, **263**, 209.
30. K. Tanaka, K. Abe and T. Hisanaga, *J. Photochem. Photobiol., A*, 1996, **101**, 85.
31. G. Matafonova and V. Batoev, *Water Res.*, 2018, **132**, 177.
32. I. Fuentes, J. L. Rodríguez, T. Poznyak and I. Chairez, *Environ. Sci. Pollut. R.*, 2014, **21**, 12241.
33. E. K. Radwan, L. Yu, G. Achari and C. H. Langford, *Environ. Sci. Pollut. R.*, 2016, **23**, 21313.
34. B. Liu, B. Chen, B. Zhang, X. Song, G. Zeng and K. Lee, *J. Hazard. Mater.*, 2021, **402**, 123456.
35. J. Gomes, J. Lincho, P. Mazierski, M. Miodyńska, A. Zaleska-Medynska and R. C. Martins, *Sci. Total Environ*, 2020, **743**, 140831.
36. A. M. Chávez, D. H. Quiñones, A. Rey, F. J. Beltrán and P. M. Álvarez, *Chem. Eng. J.*, 2020, **398**, 125642.

37. C. C. Tsoi, X. Huang, P. H. M. Leung, N. Wang, W. Yu, Y. Jia, Z. Li and X. Zhang, *J. Water Proc. Eng.*, 2020, **37**, 101501.
38. E. Asgari, M. Farzadkia, A. Esrafili, M. Y. Badi, S. F. Jokandan and H. R. Sobhi, Optik Internat, *J. Light Electron Opt.*, 2020, **212**, 164667.
39. E. Fernandes, R. C. Martins and J. Gomes, *Sci. Total Environ*, 2020, **718**, 137321.
40. M. Figueredo, E. M. Rodríguez, J. Rivas and F. J. Beltrán, *Environ. Sci.: Water Res. Technol.*, 2020, **6**, 1176.
41. A. M. Chávez, R. R. Solís and F. J. Beltrán, *Appl. Catal., B*, 2020, **262**, 118275.
42. D. H. Quiñones-Murillo, A. A. Ariza-Reyes and L. J. Ardila-Vélez, *Desalin. Water Treat.*, 2019, **170**, 61.
43. M. Gmurek, J. F. Gomes, R. C. Martins and R. M. Quinta-Ferreira, *Environ. Sci. Pollut. Res.*, 2019, **26**, 37174.
44. E. M. Rodríguez, A. Rey, E. Mena and F. J. Beltrán, *Appl. Catal., B*, 2019, **254**, 237.
45. G. Camera-Roda, V. Loddo, L. Palmisano and F. Parrino, *Appl. Catal., B*, 2019, **253**, 69.
46. U. S. Keerthi, M. Nithya and N. Balasubramanian, *J. Environ. Manage.*, 2019, **246**, 768.
47. C. A. Orge, O. Salomé, G. P. Soares, P. S. F. Ramalho, M. F. R. Pereira and J. L. Faria, *Catalysts*, 2019, **9**, 703.
48. D. B. Silva, A. Cruz-Alcalde, C. Sans, J. Giménez and S. Esplugas, *Appl. Catal., B*, 2019, **249**, 211.
49. Y. Zeng, D. Chen, T. Chen, M. Cai, Q. Zhang, Z. Xie, R. Li, Z. Xiao, G. Liu and W. Lv, *Chemosphere*, 2019, **227**, 198.
50. L. Pandian, R. Rajasekaran and P. Govindan, *Mater. Res. Express*, 2019, **6**, 85513.
51. A. M. Chávez, A. R. Ribeiro, N. F. F. Moreira, A. M. T. Silva, A. Rey, P. M. Álvarez and F. J. Beltrán, *Catalysts*, 2019, **9**, 472.
52. A. M. Chávez, O. Gimeno, A. Rey, G. Pliego, A. L. Oropesa, P. M. Álvarez and F. J. Beltrán, *Chem. Eng. J.*, 2019, **361**, 89.
53. F. Almomani, R. Bhosale, A. Kumar and M. Khraisheh, *Sol. Energy*, 2018, **172**, 128.
54. Y. Xie, Y. Chen, J. Yang, C. Liu, H. Zhao and H. Cao, *Chin. J. Chem. Eng.*, 2018, **26**, 1528.
55. M. Kete, O. Pliekhova, L. Matoh and U. L. Štangar, *Environ. Sci. Pollut. Res.*, 2018, **25**, 20453.
56. A. L. Oropesa, F. J. Beltrán, A. M. Floro, J. J. Pérez-Sagasti and P. Palma, *Environ. Sci. Pollut. Res.*, 2018, **25**, 1670.
57. J. F. Gomes, I. Leal, K. Bednarczyk, M. Gmurek, M. Stelmachowski, M. Diak, M. E. Quinta-Ferreira, R. Costa, R. M. Quinta-Ferreira and R. C. Martins, *Sci. Total Environ*, 2017, **609**, 329.
58. A. C. Mecha, M. S. Onyango, A. Ochieng and M. N. B. Momba, *Sci. Total Environ*, 2017, **601–602**, 626.

59. W. L. A. Kane, D. Wolbert, S. Rtimi and A. A. Assadi, *Chem. Eng. Process.*, 2017, **122**, 213.
60. J. Xiao, Q. Han, Y. Xie, J. Yang, Q. Su, Y. Chen and H. Cao, *Environ. Sci. Technol.*, 2017, **51**, 13380.
61. A. Kumar, A. Kumar, G. Sharma, M. Naushad, F. J. Stadler, A. A. Ghfar, P. Dhiman and R. V. Saini, *J. Cleaner Prod.*, 2017, **165**, 431.
62. C. A. Orge, J. L. Faria and M. F. R. Pereira, *J. Environ. Manage.*, 2017, **195**, 208.
63. F. Parrino, G. C. Roda, V. Loddo and L. Palmisano, *Lect. Notes Civil Eng.*, 2017, **4**, 319.
64. A. C. Mecha, M. S. Onyango, A. Ochieng and M. N. B. Momba, *Chemosphere*, 2017, **186**, 669.
65. C. Becerra-Castro, G. Macedo, A. M. T. Silva, C. M. Manaia and O. C. Nunes, *Sci. Total Environ*, 2016, **573**, 313.
66. E. K. Radwan, L. Yu, G. Achari and C. H. Langford, *Environ. Sci. Pollut. Res.*, 2016, **23**, 21313.
67. S. Cataldo, A. Iannì, V. Loddo, E. Mirenda, L. Palmisano, F. Parrino and D. Piazzese, *Sep. Purif. Technol.*, 2016, **171**, 101.
68. A. C. Mecha, M. S. Onyango, A. Ochieng, C. J. S. Fourie and M. N. B. Momba, *J. Catal.*, 2016, **341**, 116.
69. X. He, R. Chen, X. Zhu, Q. Liao, L. An, X. Cheng and L. Li, *Ind. Eng. Chem. Res.*, 2016, **55**, 8627.
70. J. C. Cardoso, G. Garcia-Bessegato and M. V. Boldrin-Zanoni, *Water Res.*, 2016, **98**, 39.
71. P. M. Alvarez, D. H. Quiñones, I. Terrones, A. Rey and F. J. Beltran, *Water Res.*, 2016, **98**, 334.
72. N. F. F. Moreira, J. M. Sousa, G. Macedo, A. R. Ribeiro, L. Barreiros, M. Pedrosa, J. L. Faria, M. F. R. Pereira, S. Castro-Silva, M. A. Segundo, C. M. Manaia, O. C. Nunes and A. M. T. Silva, *Water Res.*, 2016, **94**, 10.
73. O. Gimeno, J. F. García-Araya, F. J. Beltrán, F. J. Rivas and A. Espejo, *Chem. Eng. J.*, 2016, **290**, 12.
74. J. Xiao, Y. Xie, F. Nawaz, S. Jin, F. Duana, M. Li and H. Cao, *Appl. Catal., B*, 2016, **181**, 420.
75. M. Habibi, A. A. L. Zinatizadeh and M. Akia, *Desalin. Water Treat.*, 2016, **57**, 916.
76. A. Hassani, A. Khataee, S. Karaca and M. Fathinia, *RSC Adv.*, 2016, **6**, 87569.
77. R. R. Solís, F. J. Rivas, O. Gimeno and J. L. Pérez-Bote, *J. Chem. Technol. Biotechnol.*, 2016, **91**, 51.
78. N. F. F. Moreira, C. A. Orge, A. R. Ribeiro, J. L. Faria, O. C. Nunes, M. F. R. Pereira and A. M. T. Silva, *Water Res.*, 2015, **87**, 87.
79. L. Yu, D. Wang and D. Ye, *RSC Adv.*, 2015, **5**, 96896.
80. D. H. Quiñones, P. M. Álvarez, A. Rey and F. J. Beltrán, *Sep. Purif. Technol.*, 2015, **149**, 132.
81. A. Espejo, F. J. Beltran, F. J. Rivas, J. F. Garcia-Araya and O. Gimeno, *J. Environ. Sci. Health, Part A: Toxic*, 2015, **50**, 553.

82. T. Mano, S. Nishimoto, Y. Kameshima and M. Miyake, *Chem. Eng. J.*, 2015, **264**, 221.
83. M. Fathinia and A. Khataee, *Appl. Catal., A*, 2015, **491**, 136.
84. M. Fathinia, A. Khataee, A. Naseri and S. Aber, *Spectrochim. Acta A*, 2015, **136**, 1275.
85. D. H. Quiñones, P. M. Álvarez, A. Rey, S. Contreras and F. J. Beltrán, *Chem. Eng. J.*, 2015, **260**, 399.
86. D. H. Quiñones, A. Rey, P. M. Álvarez, F. J. Beltrán and G. LiPuma, *Appl. Catal., B*, 2015, **178**, 74.
87. E. Mena, A. Rey, E. M. Rodríguez and F. J. Beltrán, *Catal. Today*, 2017, **280**, 74.
88. M. A. Figueredo, E. M. Rodríguez, M. Checa and F. J. Beltran, *Molecules*, 2019, **24**, 1728.
89. A. M. Chávez, A. Rey, J. López, P. M. Álvarez and F. J. Beltrán, *Sep. Purif. Technol.*, 2021, **255**, 117660.
90. F. S. Souza, V. V. Da Silva, C. K. Rosin, L. Hainzenreder, A. Arenzon, T. Pizzolato, L. Jank and L. A. Feris, *J. Environ. Sci. Health, Part A: Toxic*, 2018, **53**, 213.
91. Y. Ye, Y. Feng, H. Bruning, D. Yntema and H. H. M. Rijnaarts, *Appl. Catal., B*, 2018, **220**, 171.
92. Y. Zhao, N. Hoivik and K. Wang, *Nano Energy*, 2016, **30**, 728.
93. D. H. Quiñones, A. Rey, P. M. Álvarez, F. J. Beltrán and P. K. Plucinski, *Appl. Catal., B*, 2014, **144**, 96.
94. F. J. Beltrán, P. M. Álvarez and O. Gimeno, *Molecules*, 2019, **24**, 3438.
95. S. Stankovich, D. A. Dikin, R. D. Piner, K. A. Kohlhaas, A. Kleinhammes, Y. Jia, Y. Wu, S. T. Nguyen and R. S. Ruoff, *Carbon*, 2007, **45**, 1558.
96. D. R. Dreyer, S. Park, C. W. Bielawski and R. S. Ruof, *Chem. Rev.*, 2010, **39**, 228.
97. M. Checa, M. Figueredo, A. Aguinaco and F. J. Beltrán, *J. Hazard. Mater.*, 2019, **369**, 70.
98. Y. Wang, X. C. Wang and M. Antonietti, *Ang. Chem., Int. Ed.*, 2012, **51**, 68.
99. S. T. Meek, J. A. Greathouse and M. D. Allendorf, *Adv. Mater.*, 2011, **23**, 249.
100. V. K. Sharma and M. Feng, *J. Hazard. Mater.*, 2019, **372**, 3.
101. F. J. Beltrán, *Ozone Reaction Kinetics for Water and Wastewater Systems*, Lewis Publishers, Boca Raton, USA, 2004.
102. M. Bilal and H. Iqbal, *Cosmetics*, 2020, **7**, 24.
103. M. Bilal and H. M. Iqbal, *Sci. Total Environ*, 2019, **670**, 555.
104. G. Pojana, A. Gomiero, N. Jonkers and A. Marcomini, *Environ. Int.*, 2007, **33**, 929.
105. F. Parrino, G. Camera-Roda, V. Loddo, V. Augugliaro and L. Palmisano, *Appl. Catal., B*, 2015, **178**, 37.
106. M. Kwon, H. Kye, Y. Jung, Y. Yoon and H. Kang, *Water Res.*, 2017, **122**, 172.
107. A. Cruz-Alcalde, S. Esplugas and C. Sans, *Chem. Eng. J.*, 2019, **170**, 1092.

108. M. S. Elovitz and U. von Gunten, *Ozone: Sci. Eng.*, 1999, **21**, 239.
109. M. D. Gurol and S. Nekouinaini, *J. Water Pollut. Control Fed*, 1985, **57**, 235.
110. T. Yang, J. Peng, Y. Zheng, X. He, Y. Hou, L. Wu and X. Fu, *Appl. Catal., B*, 2018, **221**, 223.
111. A. Tolosana-Moranchela, A. Manassero, M. L. Satuf, O. M. Alfano, J. A. Casas and A. Bahamonde, *Appl. Catal., B*, 2019, **246**, 1.
112. F. J. Beltrán, M. Checa, J. Rivas and J. F. García-Araya, *Catalysts*, 2020, **10**, 1256.
113. A. E. Cassano and O. M. Alfano, *Catal. Today*, 2000, **58**, 167.
114. A. Brucato, A. E. Cassano, F. Grisafi, G. Montante, L. Rizzuti and G. Vella, *AIChE J.*, 2006, **52**, 3882.
115. A. Tolosana-Moranchel, J. A. Casas, J. Carbajo, M. Faraldos and A. Bahamonde, *Appl. Catal., B*, 2017, **200**, 164.
116. Z. Wang, Y. Zhang, K. Li, Z. Sun and J. Wang, *J. Hazar. Mater.*, 2020, **391**, 122194.
117. A. Katsoyiannis, S. Canonica and U. von Gunten, *Water Res.*, 2011, **45**, 3811.
118. M. Gągol, A. Przyjazny and G. Boczkaj, *Ultrason. Sonochem.*, 2018, **45**, 257.
119. A. Fernandes, M. Gągol, P. Makoś, J. A. Khan and G. Boczkaj, *Sep. Purif. Technol.*, 2019, **224**, 1.
120. J. P. García-Cambero, F. J. Beltrán, A. Encinas, F. J. Rivas and A. L. Oropesa, *Environ. Sci.: Water Res. Technol.*, 2019, **5**, 2269.
121. A. M. Chávez, A. Rey, F. J. Beltrán and P. M. Álvarez, *J. Hazard. Mater.*, 2016, **317**, 36.

CHAPTER 7

Visible-light-driven Photocatalytic Ozonation of Aqueous Organic Pollutants

JIADONG XIAO,[a] ZHUANG GUO,[b] HONGBIN CAO[c] AND YONGBING XIE*[c]

[a] Research Initiative for Supra-Materials, Interdisciplinary Cluster for Cutting Edge Research, Shinshu University, Nagano 380-8553, Japan; [b] Beijing Institute of Aerospace Test Technology, Beijing 100072, China; [c] Division of Environment Technology and Engineering, Institute of Process Engineering, Chinese Academy of Sciences, Beijing 100190, China
*Email: ybxie@ipe.ac.cn

7.1 Introduction

Since the first establishment of a UV/O_3/TiO_2 system by Keiichi Tanaka in 1996,[1] photocatalytic ozonation (light/O_3/photocatalyst) has been developed for over 20 years and has demonstrated itself as a robust advanced oxidation process (AOP).[2–6] The primary advantage of this process is its strong oxidation power, surpassing the sum of photocatalytic oxidation and ozonation. As a result, it leads to efficient mineralization of a wide variety of organic contaminants (aliphatic acids, phenols, dyes, pesticides, pharmaceuticals, *etc.*) and real organic effluents.[2–6] This has been clarified and showcased in Chapter 6, discussing the UVA photocatalytic ozonation of water contaminants. The other advantage is the feasible utilization of sunlight and oxygen in air as the source of energy and O_3, respectively. Since visible light

Chemistry in the Environment Series No. 8
Advanced Ozonation Processes for Water and Wastewater Treatment: Active Catalysts and Combined Technologies
Edited by Hongbin Cao, Yongbing Xie, Yuxian Wang and Jiadong Xiao

Published by the Royal Society of Chemistry, www.rsc.org

(*ca.* 42%) takes a significantly larger portion of sunlight in energy compared to UV light (*ca.* 4%), visible-light-driven photocatalytic ozonation (vis/O_3/photocatalyst) is of greater interest and significance for achieving the ultimate goal of scalable sunlight- and air-based wastewater treatment plants. Hence, this chapter will focus on the visible-light photocatalytic ozonation process and particularly discusses the history of catalyst development, the reaction mechanism of the process, as well as the property–performance relationship and stabilities of the most representative catalysts. Finally, the present state and challenges for the practical application of this advanced oxidation process (AOP) are discussed.

7.2 Overview of the Catalysts and Their Performances

The types and numbers of catalysts reported for visible-light photocatalytic ozonation are quite limited due to its very short research history since 2010. Scheme 7.1 briefly illustrates the catalyst development history, and Table 7.1 lists the most representative catalysts and their main provenances. The first example of visible-light photocatalytic ozonation was given in 2010, in which WO_3[7] and Au/Bi_2O_3 nanorods[8] were used by Nishimoto *et al.* and Anandan *et al.*, respectively. They found significantly enhanced removal of organic contaminates and total organic carbon (TOC) in visible-light photocatalytic ozonation (vis/O_3/cat.) systems as compared to the ozonation or photocatalytic oxidation (vis/O_2/cat.) systems.[7,8] Since then, the coupling of ozone with visible light by a visible-light-responsive photocatalyst has been the research frontier of this field, and the exploration of active visible-light-responsive catalysts evolved as a focus for the scientists of this field.

The most widely studied metal-oxide-type catalyst so far has been WO_3 with a bandgap value of around 2.7 eV. As shown in Table 7.2, Mano and coworkers studied visible-light photocatalytic ozonation over different metal oxide photocatalysts for the mineralization of oxalic acid (OA), a refractory degradation intermediate of a wide variety of organic pollutants,[40,41] and

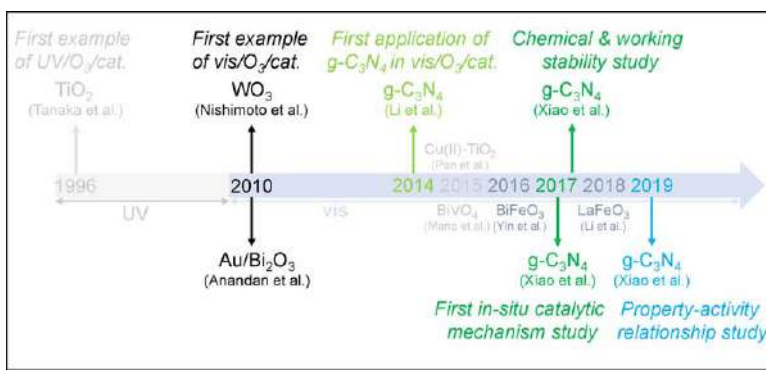

Scheme 7.1 Catalyst development history involving the representative visible-light photocatalytic ozonation catalysts and achievements.

Table 7.1 Representative visible-light photocatalytic ozonation catalysts reported in the literature.

Catalyst	Reference
g-C_3N_4-based	9–24
WO_3-based	7,25–30
Modified TiO_2	31–35
$BiVO_4$	30,36,37
Au/Bi_2O_3	8
$BiFeO_3$	38
$LaFeO_3$	39

Table 7.2 Comparison of activities of various metal oxide catalysts in visible-light photocatalytic ozonation for oxalic acid mineralization. Adapted from ref. 30 with permission from Elsevier, Copyright 2014.

			TOC removal by vis/O_3/cat. (%)		
Catalyst	Bandgap (eV)	S_{BET} ($m^2\,g^{-1}$)	60 min	120 min	240 min
WO_3	2.7	3.6	62	99	—
$BiVO_4$	2.3	1.7	31	62	94
In_2O_3	2.8	7.6	28	60	82
SnO_2	3.6	54.1	17	46	95
Fe_2O_3	2.0	12.2	11	20	42
TiO_2	3.1	52.3	8	22	45
Nb_2O_5	3.1	2.1	9	19	37

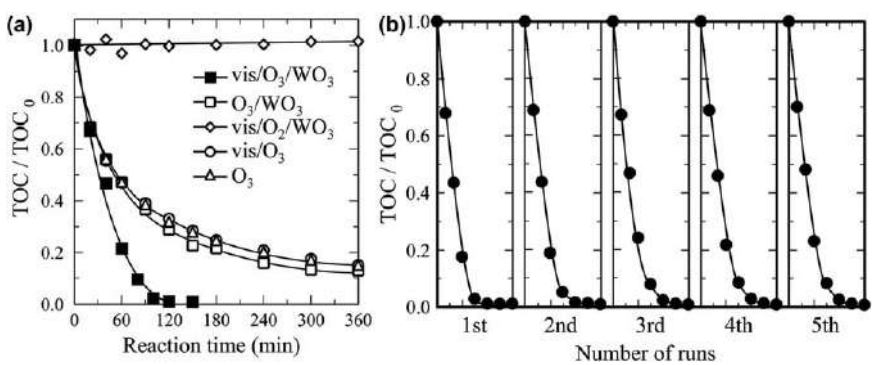

Figure 7.1 (a) TOC removal in a phenol solution ($TOC_0 = 130\ mg\,L^{-1}$) by different processes. (b) Repetitive TOC removal by vis/O_3/WO_3 process. Adapted from ref. 7 with permission from Elsevier, Copyright 2010.

found that WO_3 significantly outperformed other metal oxides with almost 100% TOC removal at 2 h. Follow-up with WO_3, $BiVO_4$ and In_2O_3 also showed considerable performance. Nishimoto *et al.* investigated the mineralization of aqueous phenol, a nonbiodegradable and light-stable pollutant, by visible-light photocatalytic ozonation using mixed-phase (monoclinic and triclinic) WO_3 catalyst.[7] As shown in Figure 7.1,

photocatalytic ozonation (vis/O_3/WO_3) showed significantly higher mineralization efficiency compared to photocatalytic oxidation (vis/O_2/WO_3) or (catalytic) ozonation (O_3(/WO_3)). The vis/O_3/WO_3 system removed about 100% TOC after 120 min of treatment, whereas 15%–20% of the initial TOC still remained in the vis/O_3, O_3 and O_3/WO_3 systems after 360 min. The remaining TOC in the latter systems were ozone-refractory compounds (*e.g.* pyruvic acid, ketomalonic acid and oxalic acid).[7] The worst of all is the vis/O_2/WO_3 system that was incapable of removing any total organic carbon (TOC), indicating extremely weak oxidizing power.

The vis/O_3/WO_3 system also demonstrated its efficiencies in the mineralization of emerging contaminants with increasing environmental concern, such as pharmaceutical and personal care products (PPCPs).[26,28,29] For example, Mena *et al.* studied the mineralization of *N,N*-diethyl-*meta*-toluamide (DEET), an active compound in insect repellents, under vis/O_3/WO_3 conditions.[26] Their best WO_3 catalyst completely removed DEET in less than 20 min with a mineralization level up to 70% in 2 h. Furthermore, a lumped kinetic model based on the reactions between TOC and hydroxyl radicals ($^{\bullet}$OH) was developed to simulate DEET, intermediates and short-chain organic acids evolution.[28] This simplified approach can be useful for understanding the mineralization kinetics of DEET by $^{\bullet}$OH formed in the photocatalytic ozonation process.

Recently, graphitic carbon nitride (g-C_3N_4) has become the most actively studied material in this field since the first example of vis/O_3/g-C_3N_4 was given by Liao *et al.* in 2014.[16] g-C_3N_4 is typically a melon-based, two-dimensional, polymeric semiconductor, composed of intralayer heptazine (tri-*s*-triazine) units connected by bridging NH/NH_2 groups that form hydrogen bonds (Figure 7.2a),[42,43] and has attracted great attention since its first appearance as a visible-light-responsive photocatalyst (bandgap $\approx$ 2.7 eV) in 2009.[42] Compared to WO_3, its advantages as a visible-light photocatalytic ozonation catalyst lies in (1) metal-free composition of nontoxic and earth-abundant C and N elements, (2) easy synthesis from direct calcination of cheap feedstocks such as urea,[16,17] thiourea,[10,11] dicyandiamide[10,12] or melamine[9,13] and (3) very negative conduction band edge potential (-1.3 V_{NHE} theoretically), which is considered as a beneficial property for photocatalytic ozonation.[6,16]

As shown in Figure 7.2b–d, g-C_3N_4 with diverse morphologies showed excellent performance for the mineralization of OA, a refractory degradation intermediate of a wide variety of organic pollutants,[40,41] and *p*-hydroxybenzoic acid (PHBA), a common pollutant in agroindustrial wastewater refractory to anaerobic biological treatment.[44] As shown in Figure 7.2b, 95% of initial OA molecules were decomposed in 20 min by a vis/O_3/bulk g-C_3N_4 system, while the vis/O_2/bulk g-C_3N_4 or O_3/bulk g-C_3N_4 processes caused negligible OA removal even up to 1 h. Note that vis/O_3 is incapable of decomposing OA because the ozone photolysis that generates hydroxyl radicals ($^{\bullet}$OH) occurs only under UV light well below 300 nm[4] and that g-C_3N_4 is catalytically inert for decomposing ozone into $^{\bullet}$OH (Figure 7.2b). The pseudo zero-order degradation rate constant of OA by

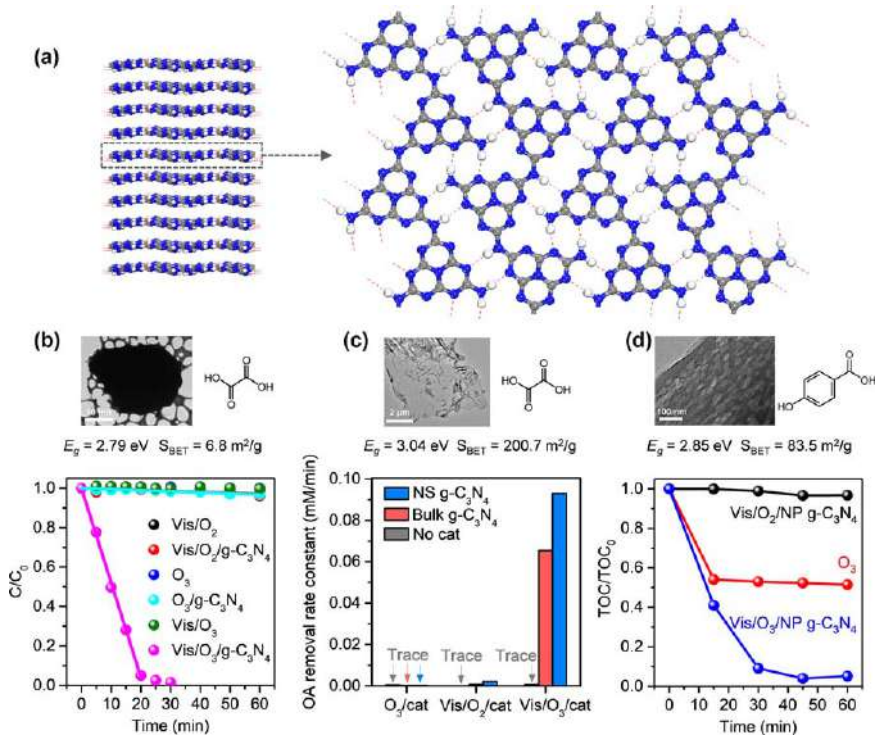

Figure 7.2 (a) Chemical structure of g-C_3N_4; (b–d) selected examples to show the efficiencies of visible-light photocatalytic ozonation for the mineralization of different organic pollutants with different g-C_3N_4 catalysts. (b) Bulk g-C_3N_4, OA; (b) g-C_3N_4 nanosheet, OA; (c) nanoporous g-C_3N_4, *PHBA.* Adapted from ref. 6 with permission from American Chemical Society, Copyright 2020.

vis/O_3/bulk g-C_3N_4 (4.79×10^{-2} mM min^{-1}) was 95.8 times higher than the sum of the rate constants in vis/O_2/bulk g-C_3N_4 (5.00×10^{-4} mM min^{-1}) and ozonation (~0 mM min^{-1}),[12] demonstrating the supersynergism between photocatalytic oxidation and the ozonation trigger by g-C_3N_4 as a catalyst. The bulk g-C_3N_4 outperformed, under the same experimental conditions WO_3 (2.89×10^{-2} mM min^{-1}), the most widely studied metal oxide catalyst of this AOP. This is the case because bulk g-C_3N_4 exhibits significantly more negative conduction band maximum (CBM) potential than WO_3 (−0.93 eV in comparison to 0.3 eV),[12] benefiting electron capture by O_3, a crucial step for separating surface electron–hole pairs as well as decomposing ozone in photocatalytic ozonation.[6] The vis/O_3/bulk g-C_3N_4 process was found to be more robust than some well-known carbocatalytic ozonation systems like O_3/reduced graphene oxide (2.86×10^{-2} mM min^{-1}) and O_3/multiwalled carbon nanotubes (3.86×10^{-2} mM min^{-1}) under the same operational conditions.[12] Nanosheet (NS) g-C_3N_4 made by exfoliating bulk g-C_3N_4 *via* a thermal oxidation etching method was found to be more active than the bulk

counterpart, as reflected by the larger degradation rate constant of OA on NS g-C_3N_4 (Figure 7.2c).[13] This is mainly due to the upshift of CBM by 0.10 eV.[13]

Figure 7.2d shows the mineralization efficiencies of PHBA by different (catalytic) oxidation methods using honeycomb-like nanoporous (NP) g-C_3N_4 as the catalyst.[11] Negligible total organic carbon (TOC) was removed under vis/O_2/nanoporous (NP) g-C_3N_4 conditions, indicating the very poor mineralization ability of the photocatalytic oxidation method. Ozonation caused the removal of TOC by about 48% at 15 min, but no further TOC removal was achieved afterward. This is due to the formation and accumulation of O_3-refractory intermediates such as OA.[11] Notably, photocatalytic ozonation (vis/O_3/NP g-C_3N_4) led to steady and robust removal of TOC, due to direct ozonation reactions with the initial pollutant and intermediates and, more importantly, to the *in situ* formation of •OH that further reacted with ozone-refractory intermediates until complete mineralization.[11] The mineralization pathway of PHBA was revealed by time-dependent electrospray ionization-mass spectrometry (ESI-MS) and is illustrated in Scheme 7.2a. This result is in agreement with the TOC removal behaviors in phenol

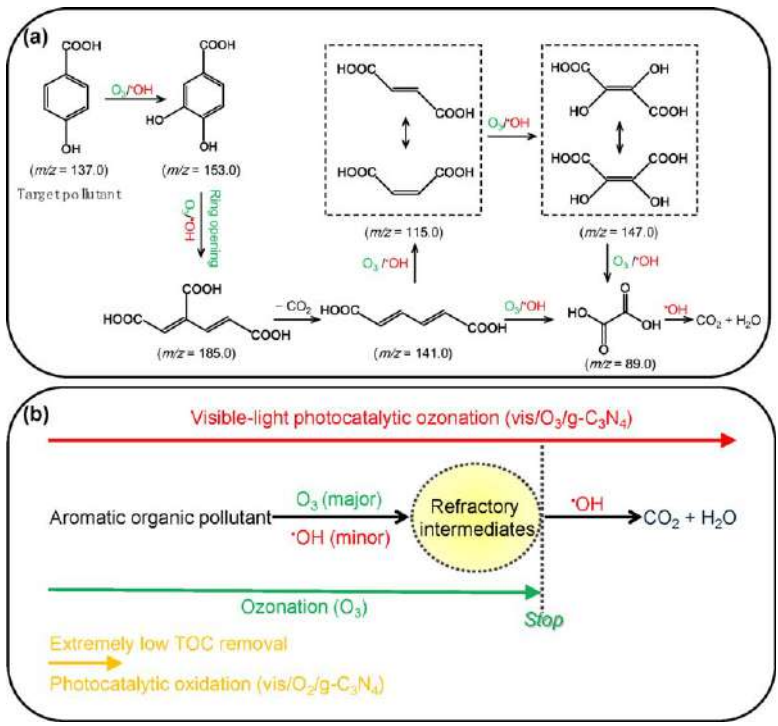

Scheme 7.2 (a) Mineralization pathway of PHBA by vis/O_3/nanoporous g-C_3N_4 process. Adapted from ref. 11 with permission from Elsevier, Copyright 2016. (b) Rule for the mineralization of aromatic compounds by different oxidation methods.

mineralization by different oxidation processes using WO_3 as catalyst (Figure 7.1a). Hence, the rule for mineralizing aromatic compounds by different oxidation methods could be summarized in Scheme 7.2b.

7.3 Reaction Mechanism

Hydroxyl radicals ($^{\bullet}OH$, $E^0 = 2.80\ V_{NHE}$), the most powerful reactive oxygen species (ROS), are able to unselectively and completely oxidize organic pollutants in atmosphere and water, of which the yield produced *in situ* governs the oxidation capacity of AOPs.[45] It is well-known that indirect oxidation by $^{\bullet}OH$ plays an essential role in photocatalytic ozonation rather than the direct oxidation by O_3. It is also generally accepted that the synergism between photocatalytic oxidation and ozonation arises from the more efficient photoelectron capture by O_3 than by O_2, which promotes not only charge separation upon charge transfer to the surface but also ozone decomposition.[2–5] This preliminary understanding is mainly based on the rate constants of related elementary reactions studied by the pulse radiolysis technique in the 1980s and quenching experiments mainly using *tert*-butyl alcohol (TBA) as a $^{\bullet}OH$ scavenger.[20,22,30] However, it remains insufficient particularly concerning the tiny details of how the electron transfer and reactive oxygen species (ROS) evolve in the presence of dissolved ozone.

To promote fundamental understanding, *in situ* electron paramagnetic resonance (EPR) spectroscopic study of vis/O_3/g-C_3N_4 as a model reaction was carried out in the group of Angelika Brückner.[13] The *in situ* EPR spectroscopic setup (Figure 7.3) was mainly composed of an ozone generator, an ozone analyzer, a 300 W Xe-arc lamp equipped with a cutoff filter GG420, a Bruker EMX CW-micro X-band EPR spectrometer equipped with an ER4119HS-WI high-sensitivity optical resonator, a specially designed flat cell (0.5 mm inner distance) and fused silica capillaries as the gas channel. Also, a self-modified syringe was used for the developed online DMPO (5,5-dimethyl-1-pyrroline *N*-oxide) spin trapping technique. With this method, the photoexcitation of electrons (CB-e^-) from the valance band (VB) to the conduction band (CB) of g-C_3N_4 and their further reaction with dissolved O_2 and O_3 to form ROS could be monitored under realistic aqueous conditions.[13] For example, the change in the relative number of CB-e^- inside aqueous g-C_3N_4 suspensions with visible-light irradiation and under N_2, O_2 and O_3 (2.1 mol% in O_2) saturated conditions (Figure 7.4a) or under consecutive bubbling of N_2, O_2 and O_3 (Figure 7.4b) can be semi-quantitatively measured. It was found that a mixture of O_3/O_2 (2.1 mol% O_3 in O_2) gas can trap approximately double to triple the number of CB-e^- in an aqueous g-C_3N_4 suspension than pure O_2. This is the case because the redox potential (1.03 V_{NHE} *versus* −0.18 V_{NHE}[46]) and water solubility (*ca.* 109 mg L^{-1} *versus* 8 mg L^{-1} at 1 atm and 298 K[47]) of O_3 are much higher.

Furthermore, an online DMPO spin trapping technique was developed to probe the ROS evolution under photocatalytic ozonation (vis/O_3/g-C_3N_4) conditions in comparison with under photocatalytic oxidation (vis/O_2/g-C_3N_4)

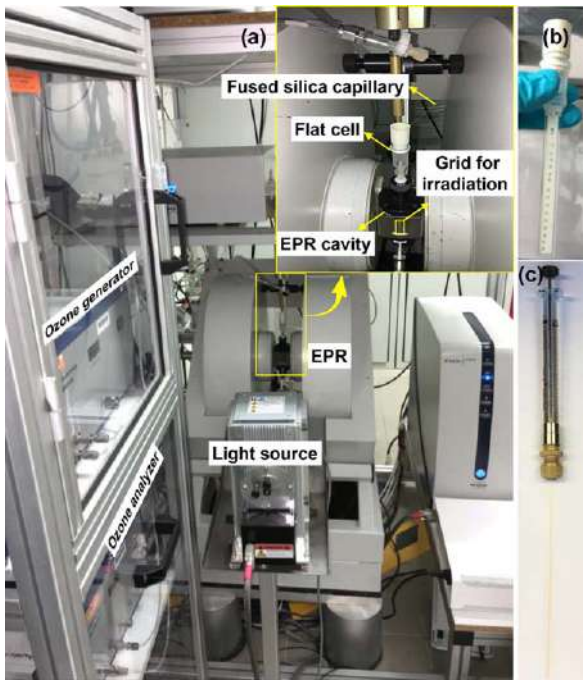

Figure 7.3 (a) *In situ* EPR spectroscopic setup. (b) Flat cell loaded with bulk g-C_3N_4 suspension under O_3 bubbling (0.5 mL min^{-1}). (c) Self-modified syringe. Reproduced from ref. 13 with permission from American Chemical Society, Copyright 2017.

conditions.[13] Figure 7.4c and d show the EPR spectra of DMPO–OH and DMPO–OOH (the adducts of DMPO with $^{\bullet}OH$ and $^{\bullet}O_2^-$, respectively) species under these two conditions, with and without OA (model pollutant). On the basis of the semi-quantitative analyses using the EasySpin/Matlab toolbox and double integration calculation,[13] the authors found that DMPO–OOH constituted almost 80% of the DMPO spin trapping adducts formed in vis/O_2/g-C_3N_4, while around 90% of the DMPO adducts in vis/O_3/g-C_3N_4 were DMPO–OH. This indicates that $^{\bullet}O_2^-$ and $^{\bullet}OH$ are the dominant ROS in vis/O_2/g-C_3N_4 and vis/O_3/g-C_3N_4 processes, respectively. Specifically, the yield of $^{\bullet}OH$ in vis/O_3/bulk g-C_3N_4 is about 18 times higher than that in vis/O_2/bulk g-C_3N_4, and. likewise, the vis/O_3/NS g-C_3N_4 system generated six times more $^{\bullet}OH$ than the vis/O_2/NS g-C_3N_4 system. These results demonstrate that feeding just a small portion of O_3 (*e.g.* 2.1 mol% O_3 in O_2) into a photocatalytic oxidation system could significantly improve the overall yield of ROS as well as the selectivity for $^{\bullet}OH$ formation.

$^{\bullet}OH$ were produced from the 1-electron reduction of O_3 under vis/O_3/g-C_3N_4 conditions, *i.e.* CB-e^- capture by O_3 *via* the intermediate formation of $^{\bullet}O_3^-$ (eqn (7.1)) and $HO_3^{\bullet}$ radicals (eqn (7.2)) that rapidly decompose into $^{\bullet}OH$ (eqn (7.3)). $E^0(O_{3aq}/^{\bullet}O_3^-)$ (1.03 V_{NHE}[17]) is theoretically much higher than

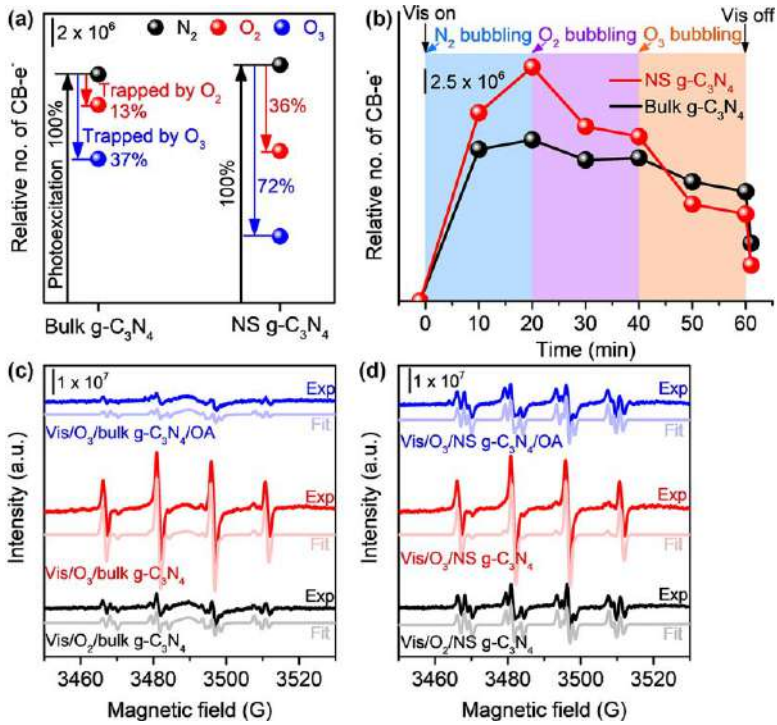

Figure 7.4 (a) Relative number of photoexcited CB-e^- in N_2-, O_2- or O_3-saturated aqueous suspension of bulk and NS g-C_3N_4, respectively. (b) Time-dependent change of the relative number of photoexcited CB-e^- in aqueous suspensions of bulk and NS g-C_3N_4 under consecutive bubbling of N_2 (20 min), O_2 (20 min) and O_3 (20 min) and irradiation of visible light. Comparison of DMPO spin trapping EPR spectra of (c) bulk and (d) NS g-C_3N_4 suspensions in the presence of O_2, O_3 or O_3/OA under visible-light irradiation. Reproduced from ref. 13 with permission from American Chemical Society, Copyright 2020.

$E^0(O_{2aq}/{}^\bullet O_2^-)$ (-0.18 V_{NHE}[17]), so O_3 can easily take an electron from ${}^\bullet O_2^-$ (eqn (7.4)) with an approximate rate constant of 1.5×10^9 $M^{-1}s^{-1}$ [49] and further convert it into ${}^\bullet OH$ *via* the ${}^\bullet O_3^-$-mediated route (eqn (7.2)–(7.3)), rather than *via* the original H_2O_2-mediated 3-electron reduction of O_2 (eqn (7.5)–(7.8)).

$$O_3 + \text{CB-e}^- \rightarrow {}^\bullet O_3^- \tag{7.1}$$

$${}^\bullet O_3^- + H^+ \overset{pK=8.2}{\longleftrightarrow} HO_3^\bullet \tag{7.2}$$

$$HO_3^\bullet \rightarrow O_2 + {}^\bullet OH \tag{7.3}$$

$$O_3 + {}^\bullet O_2^- \rightarrow {}^\bullet O_3^- + O_2 \tag{7.4}$$

$$O_2 + \text{CB-e}^- \rightarrow {}^\bullet O_2^- \tag{7.5}$$

$$^{\bullet}O_2^- + H^+ \overset{pK=4.8}{\longleftrightarrow} HO_2^{\bullet} \quad (7.6)$$

$$HO_2^{\bullet} + H^+ + CB\text{-}e^- \rightarrow H_2O_2 \quad (7.7)$$

$$H_2O_2 + CB\text{-}e^- \rightarrow {}^{\bullet}OH + OH^- \quad (7.8)$$

The authors also found that the DMPO–OOH signal intensity reflecting the $^{\bullet}O_2^-$ number decreased with an increase in the DMPO–OH number upon switching from vis/O_2/g-C_3N_4 to vis/O_3/g-C_3N_4. In keeping with this, the formation of H_2O_2 [a necessary intermediate for the three-electron reduction of O_2 (eqn (7.5)–(7.8))] was greatly inhibited, upon introduction of O_3 (2.1 mol% in O_2) into a vis/O_2/g-C_3N_4 system.[13] These observations point to the conversion of $^{\bullet}O_2^-$ into $^{\bullet}$OH in the presence of O_3, which is the additional way for enhanced $^{\bullet}$OH production. In the presence of OA (*i.e.* under the vis/O_3/g-C_3N_4/OA conditions, Figure 7.4c and d), the EPR signal intensity of DMPO–OH greatly dropped (Figure 7.4c and d), indicating the rapid reaction between OA and $^{\bullet}$OH, which is in line with the predicted high reaction rate between oxalate and $^{\bullet}$OH.[48] Moreover, a complete inhibition of OA degradation in the presence of *tert*-butyl alcohol (TBA, a well-known $^{\bullet}$OH scavenger[49]) was observed.[13] All these findings verified $^{\bullet}$OH as the sole oxidant able to decompose OA. OA oxidation by $^{\bullet}$OH directly produces CO_2 and H_2O since no stable intermediates were detected.[13] Hence, the removal of OA by $^{\bullet}$OH is equal to complete mineralization.

In summary, the key reason for the high oxidation ability of visible-light-driven photocatalytic ozonation is that ozone traps and converts photoelectrons into $^{\bullet}$OH far more efficiently than oxygen, *via* a 1-electron reduction pathway ($O_3 \rightarrow {}^{\bullet}O_3^- \rightarrow HO_3^{\bullet} \rightarrow {}^{\bullet}$OH), and reacts with $^{\bullet}O_2^-$ to form $^{\bullet}O_3^-$ that generates further $^{\bullet}$OH (Figure 7.5a). It is due to the fast electron capture by O_3 and further efficient conversion into $^{\bullet}$OH that CB-e^- can be

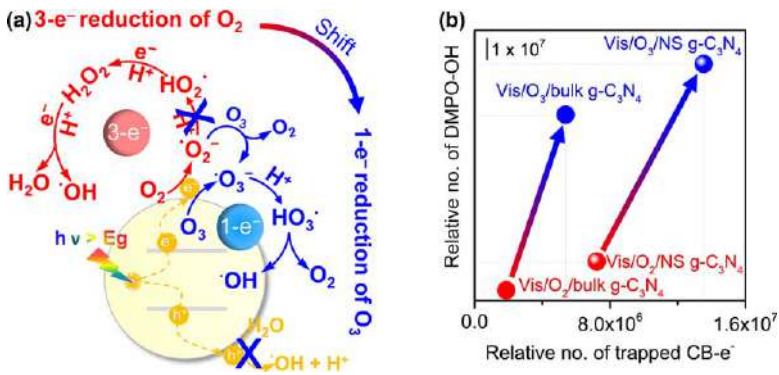

Figure 7.5 (a) Proposed pathways of $^{\bullet}$OH generation in vis/O_3/g-C_3N_4. (b) Relative number of DMPO–OH as a function of the number of trapped CB-e^-. Adapted from ref. 13 with permission from American Chemical Society, Copyright 2020.

Table 7.3 Selected properties of the studied WO_3. Adapted from ref. 26 with permission from Elsevier, Copyright 2014.

Catalyst	Synthesis	WO_3 phase	S_{BET} ($m^2\,g^{-1}$)
W-c	Commercial	Monoclinic	9.8
W1-500	Sol–gel; $T = 500$ °C	Orthorhombic	9.0
W1-600	Sol–gel; $T = 600$ °C	Monoclinic	8.1
W1-700	Sol–gel; $T = 700$ °C	Monoclinic	5.3
W2	Hydrothermal	Hexagonal	82.0
W2-t	Hydrothermal; treated ($O_3 + h\nu$)	Hexagonal	93.7
W2-500-t	Hydrothermal; $T = 500$ °C; treated ($O_3 + h\nu$)	Monoclinic	8.2
W2-600	Hydrothermal; $T = 600$ °C	Monoclinic	5.8
W2-600-t	Hydrothermal; $T = 600$ °C; treated ($O_3 + h\nu$)	Monoclinic	9.6
W2-700-t	Hydrothermal; $T = 700$ °C; treated ($O_3 + h\nu$)	Monoclinic	9.4

more adequately utilized for producing $^{\bullet}OH$ with a high yield and selectivity in photocatalytic ozonation (Figure 7.5b). It should be mentioned that the $^{\bullet}OH$ formation pathway in g-C_3N_4 is somewhat different from that in WO_3 due to their different band structures. For WO_3, $^{\bullet}OH$ forms *via* both CB-e^- reduction by O_3 and direct oxidation of H_2O by VB-h^+.[29] Unlike WO_3, VB-h^+ in g-C_3N_4 cannot oxidize H_2O directly to $^{\bullet}OH$ as proven by the experimental fact that no DMPO–OH signal was observed under vis/N_2/g-C_3N_4 conditions.[13] This is in line with the significantly lower VB edge potential of g-C_3N_4 compared with $E^0(^{\bullet}OH, H^+/H_2O)$.[50] However, the 1-electron reduction of O_3 dominates the g-C_3N_4 photocatalytic ozonation process and produces $^{\bullet}OH$ far more efficiently, so g-C_3N_4 behaves more actively than WO_3. VB-h^+ in g-C_3N_4 reacted with OA extremely slowly,[15] and thus the main consumption of the surviving VB-h^+ could be their reaction with H_2O directly to O_2, since their redox potential is more positive than $E^0(O_2, H^+/H_2O)$.[51] In order to confirm this, a further isotope experiment using $H_2{}^{18}O$ would be required since the feed gas contains O_2.

7.4 Structure–Performance Relationship of Catalysts

7.4.1 WO_3

There are very limited studies on the structure–performance relationship of WO_3, though WO_3 is the most widely investigated metal-oxide catalyst in visible-light photocatalytic ozonation. Mena *et al.* compared commercial and own-made WO_3 catalysts (Table 7.3) with different morphologies (spherical and irregular) and crystalline structures (orthorhombic, monoclinic and hexagonal) in photocatalytic ozonation of *N,N*-diethyl-*meta*-toluamide (DEET) (Figure 7.6), an active compound in insect repellents.[26] They found that the monoclinic and/or orthorhombic structure of WO_3 and the presence

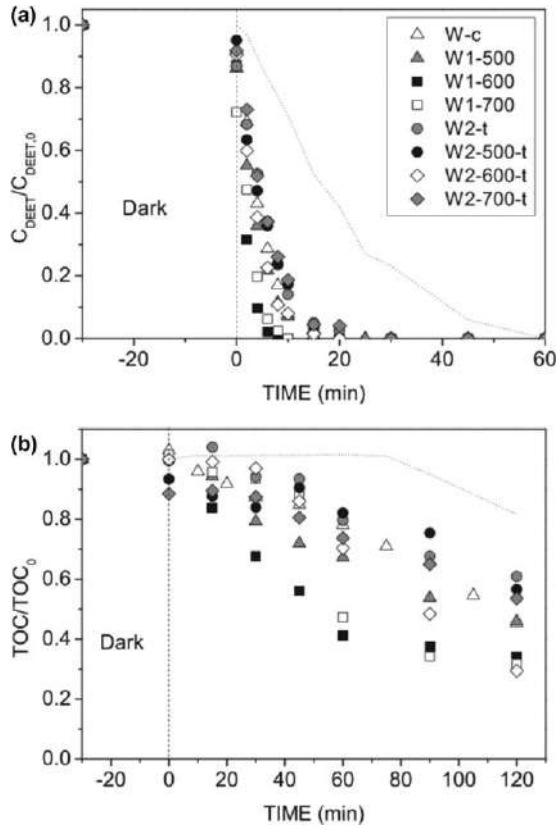

Figure 7.6 (a) DEET dimensionless concentration. (b) TOC dimensionless concentration during photocatalytic ozonation with different WO_3 catalysts listed in Table 7.3 (dotted lines show single ozonation results). Adapted from ref. 26 with permission from Elsevier, Copyright 2014.

of reduced W species were favorable properties, while a larger specific surface area (S_{BET}) was not important at all. The champion WO_3 catalyst led to a complete removal of DEET in less than 20 min with a mineralization level up to 70% in 2 h (Figure 7.6). Likewise, Rey *et al.* found that monoclinic crystalline structure, together with the presence of oxygen vacancies in WO_3, promoted electron migration on the catalyst surface to some extent, thus accelerating the photocatalytic ozonation reactions under visible-light irradiation.[27] The specific surface area (S_{BET}) was found to be of no importance to the activity either.[27]

Yang *et al.* synthesized three kinds of WO_3 materials (M-100, M-001 and H-100) with different morphologies, crystal phases and band structures, and compared their activities in visible-light photocatalytic ozonation of OA and cephalexin (a macromolecular antibiotic compound commonly found in pharmaceutical wastewater).[29] In keeping with the findings mentioned above,[26,27] monoclinic WO_3 (M-100 and M-002) were more active than the

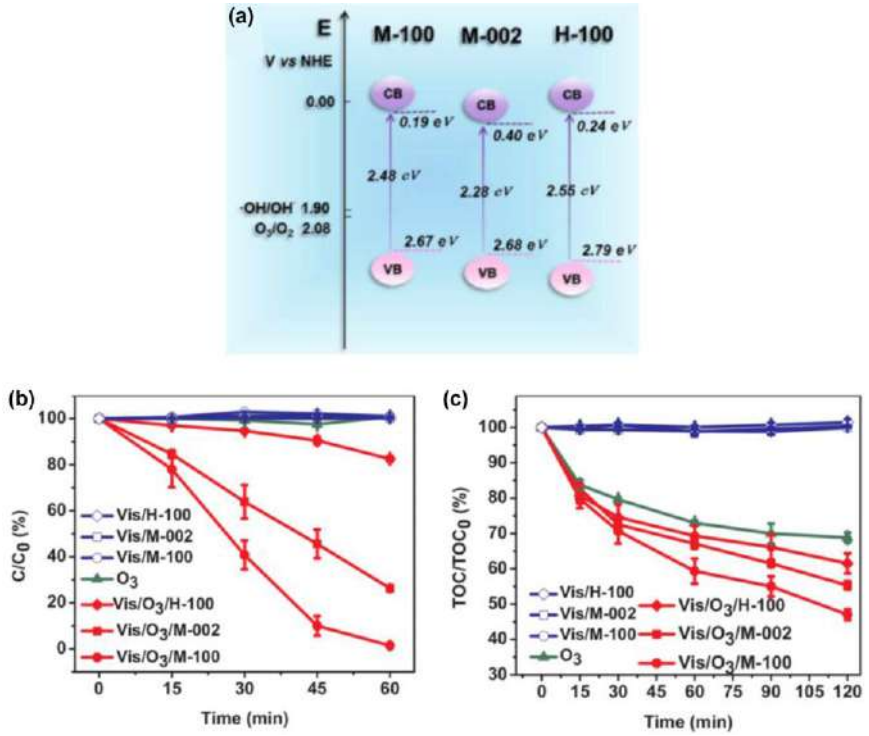

Figure 7.7 (a) Band structures of different WO_3. (b) Degradation of OA. (c) Mineralization of cephalexin in photocatalytic oxidation, ozonation and photocatalytic ozonation under visible-light irradiation. Adapted from ref. 29 with permission from Elsevier, Copyright 2018.

hexagonal WO_3 (H-100) (Figure 7.7), and S_{BET} was not an impacting factor either. Moreover, they demonstrated that the intrinsic charge separation ability of WO_3 particles (probed by the photoluminescence spectroscopy) is not of relevance to the photocatalytic ozonation performance, though it is important for photocatalytic oxidation. This does not mean that the charge separation is not crucial for photocatalytic ozonation. Rather, it does play a vital role, but the efficiency of charge separation should be assessed under realistic conditions, *i.e.* in the presence of reagents that actively affect the surface charge separation. Considering the role of ozone as a powerful electron trap, its presence causes the efficient separation of charge carriers upon diffusion to the catalytic particle surface, making the intrinsic charge separation property at a photocatalyst surface less important for the photocatalytic ozonation performance. The activity difference between M-100 and M-002 was assigned to their different band structures, particularly to the different CB edge positions.[29] CB-e^- formed upon M-100 had a larger reducing power due to its more negative CB edge potential (Figure 7.7a), and this causes more efficient electron capture by O_3, resulting in improved

surface charge separation and ozone decomposition. As a consequence, M-100 outperformed M-002 in the degradation of OA (Figure 7.7b) and mineralization of cephalexin (Figure 7.7c).

7.4.2 g-C_3N_4

The structure–performance relationship studies of g-C_3N_4 in visible-light photocatalytic ozonation are few, and the dominant contribution is from us in cooperation with the group led by Angelika Brückner.[15] In Figure 7.2, the performance of g-C_3N_4 follows the order of nanosheet g-C_3N_4 > bulk g-C_3N_4 > nanoporous g-C_3N_4, with the CB edge potential varying from the most to the least negative.[9,11,13] Also, it was due to the upshift of the CB edge by around 0.10 eV that bulk g-C_3N_4 synthesized by thermopolymerization of dicyandiamide outperformed that synthesized from thiourea.[10] In line with the studies on WO_3,[26,27] S_{BET} was of negligible importance to the activity of g-C_3N_4 in the photocatalytic ozonation of OA.[9–11,15] This was the case because $^{\bullet}$OH formation was not adsorption limited, and OA oxidation by $^{\bullet}$OH occurred in the liquid phase rather than on the g-C_3N_4 surface. The latter was supported by two facts: (1) OA adsorption on the g-C_3N_4 samples was negligible, and (2) *tert*-butyl alcohol (TBA, a liquid-phase $^{\bullet}$OH scavenger that is scarcely adsorbed on low-polarity carbon surfaces[52]) completely blocked the decomposition of OA.[13,15] In keeping with WO_3,[29] the suppression of radiative electron–hole recombination within g-C_3N_4 itself was also excluded as a factor, as g-C_3N_4 with less pronounced radiative charge recombination (reflected by lower photoluminescence intensity) was less active.[15] All these findings indicate that the band structure, *i.e.* the VB and CB edge positions and the corresponding bandgap, could be the main factor governing the photocatalytic ozonation activity of g-C_3N_4.

In order to reveal the relationship between band structure and catalytic performance, *in situ* electron paramagnetic resonance (EPR) spectroscopy was used to explore the number and reactivity of photoexcited charge carriers in various g-C_3N_4 specimens with well-tailored band structures for producing $^{\bullet}$OH radicals, as well as the efficiency of $^{\bullet}$OH in the degradation of OA used as a model pollutant.[15] As shown in Figure 7.8a and b, the OA removal rate constants under both photocatalytic ozonation (vis/O_3/g-C_3N_4, Figure 7.8a) and photocatalytic oxidation (vis/O_2/g-C_3N_4, Figure 7.8b) conditions were closely linked to the conduction band edge potential (CBEP) and bandgap values. The OA removal rate increased with the negative shift of CBEP and the enlargement of bandgap, reaching a maximum for the sample Ar-640-Air-550, but decreased further upon the sample Ar-640-Air-570.

The entire photoexcited CB-e^- as well as the reactive CB-e^- that can be trapped by O_2 or O_3 inside the selected g-C_3N_4 catalysts (*i.e.* bulk, Ar-640, Ar-640-Air-550 and Ar-640-Air-570 in Figure 7.8) under realistic aqueous conditions, were semi-quantified.[15] Furthermore, the formed $^{\bullet}$OH in these samples were also semi-quantified by using the EPR intensity of DMPO–OH

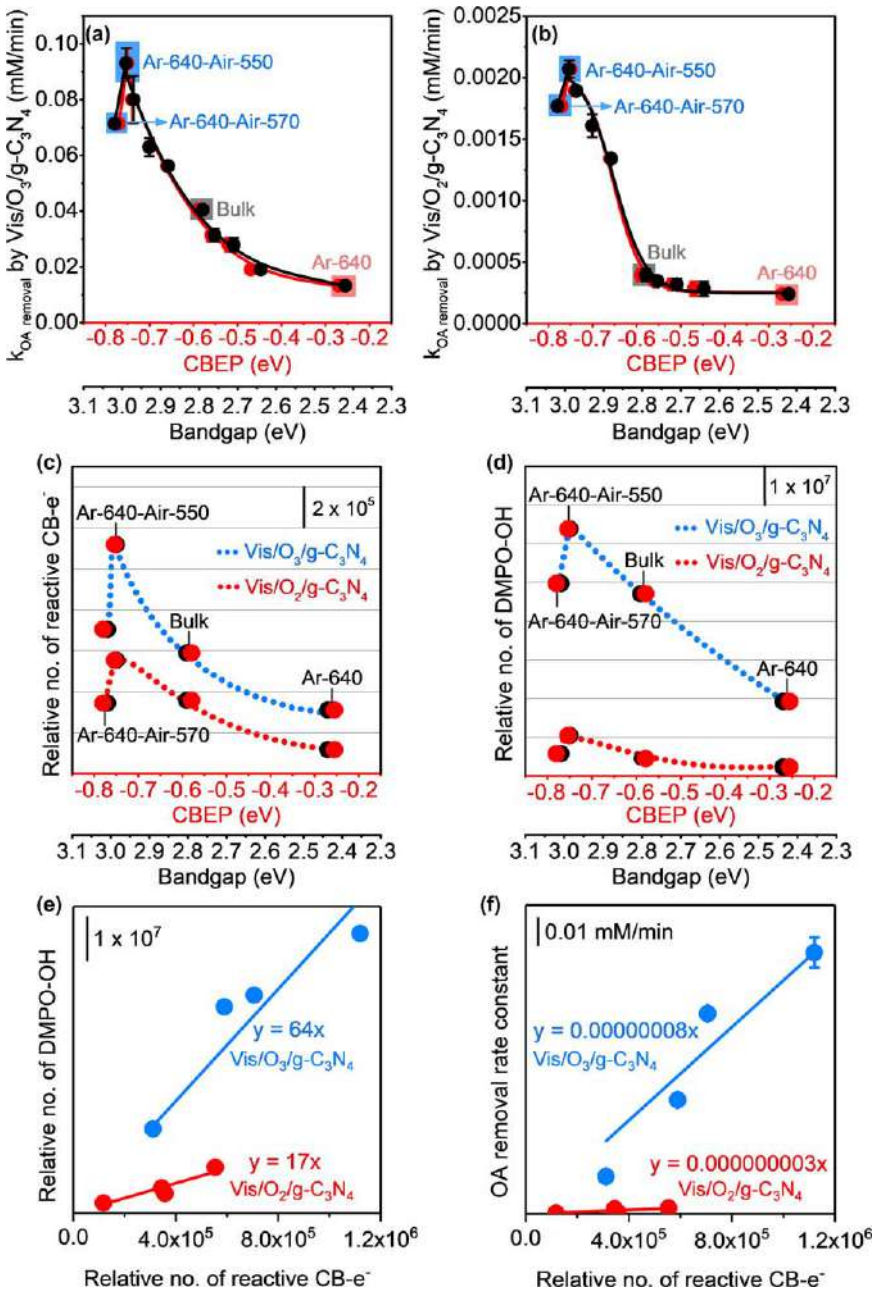

Figure 7.8 Relation of OA removal rate constant to CBEP and bandgap of g-C_3N_4 under (a) vis/O_3/g-C_3N_4 and (b) vis/O_2/g-C_3N_4 conditions. Relation of relative numbers of (c) reactive CB-e^- and (d) DMPO-OH to the CBEP and bandgap of selected g-C_3N_4. (e) Relative number of DMPO-OH adducts. (f) OA removal rate constant as a function of the relative number of reactive CB-e^- under vis/O_3/g-C_3N_4 and vis/O_2/g-C_3N_4 conditions. Reproduced from ref. 15 with permission from American Chemical Society, Copyright 2020.

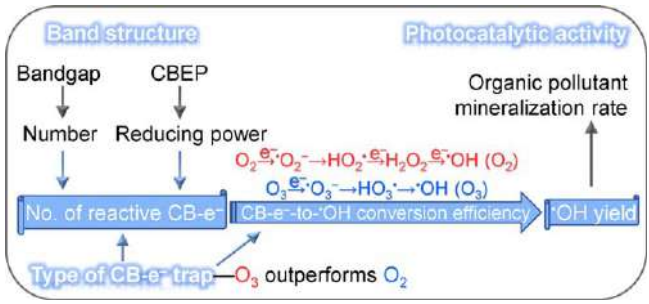

Scheme 7.3 The relationship among band structure, type of CB-e^- trap and photocatalytic activity. Reproduced from ref. 15 with permission from American Chemical Society, Copyright 2020.

adducts as a measure. The plot of the relative number of reactive CB-e^- as a function of the band structure (Figure 7.8c) showed the same trend as that of the relative number of DMPO–OH (Figure 7.8d) and of the OA decomposition rate constant (Figure 7.8a and b), under both vis/O_3/g-C_3N_4 and vis/O_2/g-C_3N_4 conditions. This indicates that it is the interplay between the bandgap and CBEP of g-C_3N_4 that governs the number of reactive CB-e^-, which is itself directly proportional to the yield of $^{\bullet}OH$ (Figure 7.8e) and to the rate of OA degradation (Figure 7.8f). This rule is independent of the type of the primary oxidant (*i.e.* the CB-e^- trap; O_2 or O_3) used.

Scheme 7.3 summarizes the relationship between the band structure, type of CB-e^- trap and photocatalytic performance of g-C_3N_4. An optimum balance between the number and reducing power of CB-e^- is a key factor for the catalytic performance of g-C_3N_4, and this depends on the interplay between the bandgap and CB edge potential. The authors proposed a new concept, the "number of reactive charge carriers" (CB-e^- in the present case, Scheme 7.3), to describe the collective effects of the bandgap and CB/VB edges. It should be noted that this concept virtually reflects the charge separation efficiency in the presence of reactants and under realistic conditions because reactive charge carriers refer to the CB-e^-/VB-h^+ that are separated and directly used for the photocatalytic reaction.

7.4.3 Future Design and Optimization of g-C_3N_4

Scheme 7.4 summarizes five main research directions for further improvement of the g-C_3N_4-based catalysts. First of all, three catalytic particle engineering strategies are suggested on the basis of the structure–performance relationship studies: (3) narrowing the bandgap and raising the CB edge (Scheme 7.4a), so as to increase the number of reactive CB-e^- in g-C_3N_4; (2) forming a Z-scheme heterojunction[53] with another visible-light-responsive semiconductor (S-II, *e.g.* WO_3,[54] modified $BiVO_4$,[55] modified TiO_2,[56] *etc.*) (Scheme 7.4b) having a VB edge potential more positive than $E^0(^{\bullet}OH, H^+/H_2O)$, so as to enable direct H_2O oxidation by VB-h^+ from S-II (New Pathway I) for $^{\bullet}OH$ production; (3) designing

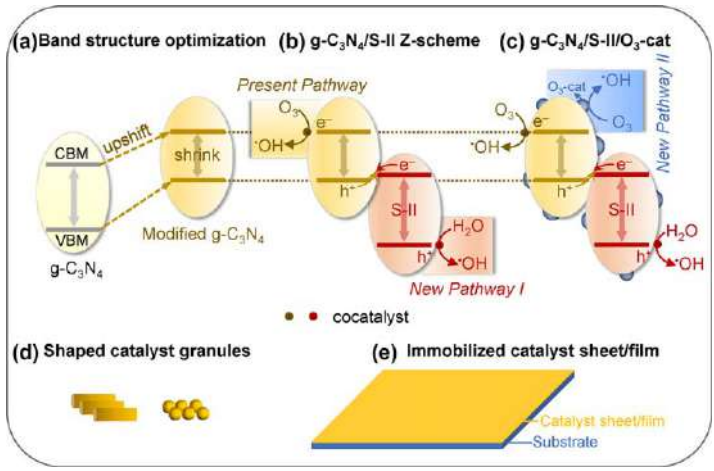

Scheme 7.4 Proposed directions for future optimization and design of g-C_3N_4-based catalysts. Adapted from ref. 15 with permission from American Chemical Society, Copyright 2020.

a bifunctional catalyst (Scheme 7.4c) by compositing g-C_3N_4 with other materials (*e.g.* MnO_2,[57] ZnO,[58] carbon nanotube,[12] reduced graphene oxide,[49] *etc.*) that can catalytically decompose surplus ozone into $^{\bullet}OH$ (New Pathway II), so as to take full advantage of ozone for $^{\bullet}OH$ production. Note that there may exist competition between the present pathway and new pathways for $^{\bullet}OH$ production and that some modification strategies (*e.g.* foreign element doping) may impact two or more reaction pathways, resulting in opposite outcomes. Therefore, great efforts are required to study the interplay between the present and additional $^{\bullet}OH$ production pathways, so as to achieve an ideal cooperation.

At the same time, it is important to explore useful co-catalysts to extract more CB-e^-/VB-h^+ from the catalyst bulk and to offer catalytically active sites for desired surface reactions, as well as to suppress unwanted charge recombination or side reactions. In addition, to harvest a larger portion of solar energy, active photocatalytic ozonation catalysts with narrower bandgaps are to be developed. To this end, it is suggested to have a systematic and careful examination of the widely studied narrow-band-gap semiconductors (*e.g.* (oxy)nitrides, (oxy)sulfides, *etc.*) in visible-light photocatalytic ozonation reactions. In terms of practical applications, the catalyst must be assembled into a shaped or immobilized form. Therefore, the other two strategies aim to explore and fabricate active-shaped catalyst granules (Scheme 7.4d) and catalyst sheet/film (Scheme 7.4e) using the optimized catalyst powder. These two such catalyst forms have never been examined in the field of photocatalytic ozonation. In terms of the preparation and assembling processes, we suggest to follow the work from Kazunari Domen's group.[59,60]

7.5 Stability of g-C_3N_4 Catalysts

The chemical and working stability of g-C_3N_4, the most actively studied visible-light photocatalytic ozonation catalyst, was studied by our group,[14] while there is, to the best of our knowledge, no such studies for other catalysts in photocatalytic ozonation. g-C_3N_4 was found to be chemically stable with O_3 or $^{\bullet}O_2^-$; in contrast, $^{\bullet}OH$ could tear the heptazine units from g-C_3N_4 to form cyameluric acid and further release NO_3^- into the aqueous environment (Scheme 7.5). Due to the high yield of $^{\bullet}OH$ under photocatalytic ozonation conditions, TOC and NO_3^- were detected, which gradually accumulated in initially ultra-pure water. In line with this, the fragmentation of g-C_3N_4 nanosheets (observed by TEM), as well as decreased surface C and N contents (analyzed by XPS), were found.[14] After treatment for 10 h, the ratios of released nitrogen from nanosheet-structured (NS) g-C_3N_4 and bulk g-C_3N_4 that finally existed in the form of NO_3^- reached 9.5 and 6.8 mol% in initially ultra-pure water, respectively. The decomposition of nanosheet g-C_3N_4 was more pronounced than that of bulk g-C_3N_4 because (1) more $^{\bullet}OH$ were formed on NS g-C_3N_4, and (2) less layer stacking in the nanosheet g-C_3N_4 decreased its structural stability.[14]

Fortunately, in the presence of organic pollutants that compete against g-C_3N_4 for $^{\bullet}OH$, the g-C_3N_4 decomposition was completely or partially blocked.[14] $^{\bullet}OH$ reacted with OA, benzene, phenol and thiophene in preference to g-C_3N_4 but attacked BPA, valproate or quinizarin with almost equal preference to g-C_3N_4. The degree of this protection effect varied from pollutant to pollutant, most likely due to the difference in structural stabilities between the organic pollutant and g-C_3N_4. This difference is minor for macro-molecular organics (bisphenol A, valproate and quinizarin) as compared with the micromolecular ones (OA, benzene, phenol and thiophene), so a pinch of $^{\bullet}OH$ still reacted with NS g-C_3N_4 in the presence of the former. To sum up, organic pollutants in wastewater protect g-C_3N_4 from decomposition by $^{\bullet}OH$, so the high activity of g-C_3N_4 is maintained while treating a model pollutant or wastewater.[6,12]

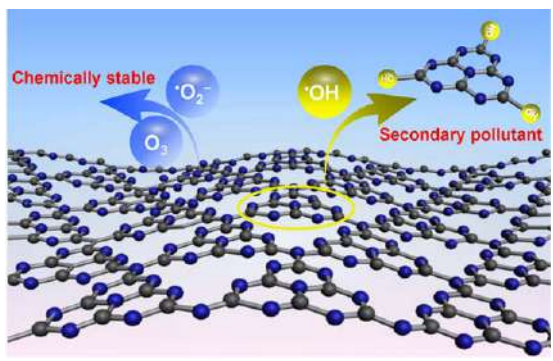

Scheme 7.5 Chemical stabilities of g-C_3N_4 toward O_3, $^{\bullet}O_2^-$ and $^{\bullet}OH$. Adapted from ref. 14 with permission from American Chemical Society, Copyright 2017.

7.6 Present State and Challenges for Practical Application

A pilot-scale plant (Figure 6.7) of solar photocatalytic ozonation was established in Badajoz, Spain (38°52′43″N, 6°58′15″W) in 2014, which successfully treated real-world wastewater using natural sunlight and air (source of ozone).[61,62] The system was mainly composed of a 45-degree-tilted compound parabolic collector (CPC) reactor equipped with 4 borosilicate glass tubes (32 mm external diameter, 1.4 mm thickness, 750 mm length), a broadband UV radiometer, an air compressor, an ozone generator and analyzer, gas flow controllers, tubes *etc.* The total collector surface was 0.25 m^2 and the volume of illuminated wastewater was 1.8 L. Ozone was generated from dry air by an ozone generator and fed through two porous plates located at the entrance of the tubes into the reactor. The gas flow rate and ozone concentration were controlled at about 45 $L\,h^{-1}$ and 20 $mg\,L^{-1}$, respectively. The wastewater to be treated was kept recirculating at a rate of 300–400 $L\,h^{-1}$. Such a system successfully treated the pharmaceutical compounds-containing secondary effluent from a municipal wastewater treatment plant, with high efficiencies of organics mineralization (~85%) and toxicity removal (~90%).[61]

This was a good start and demonstrated the great potential of solar photocatalytic ozonation for scalable applications. However, TiO_2, the catalyst used in the systems,[61,62] absorbs only UV light (*ca.* 4% of sunlight in energy), and the catalyst form of particulate suspension is not realistic for large-scale applications. Therefore, there are still many challenges on the way to the practical application of solar photocatalytic ozonation.

First of all, active bifunctional particulate catalyst (*e.g.* g-C_3N_4/S-II/O_3-cat, Scheme 7.4c) is to be made, which is the precondition for achieving the goal. Only with such a catalyst can $^{\bullet}OH$ be produced regardless of the weather or time. Under sunlight (*i.e.* during a sunny day), $^{\bullet}OH$ would be produced *via* photocatalytic and catalytic ozonation pathways; in the absence of sunlight (*i.e.* during a cloudy day or at night), $^{\bullet}OH$ would be produced *via* catalytic ozonation. Secondly, active catalyst granules (Scheme 7.4d) or immobilized catalyst sheet/film (Scheme 7.4e) are to be fabricated using the optimized catalyst powder. At the same time, the design and fabrication of devices, reactors and equipment related to the solar photocatalytic ozonation system are required to maximize photon absorption and the mass transfer of redox species under pilot-scale conditions. In this regard, in parallel with lab-scale experiments, outdoor wastewater treatment plants are to be established, and research on catalyst improvement, device/equipment manufacture and optimization of operational conditions should be carried out in these plants. We look ahead one day to a natural sunlight- and air-based wastewater treatment plant, as illustrated in Scheme 7.6, by continuous research and cooperation among scientists and engineers around the globe.

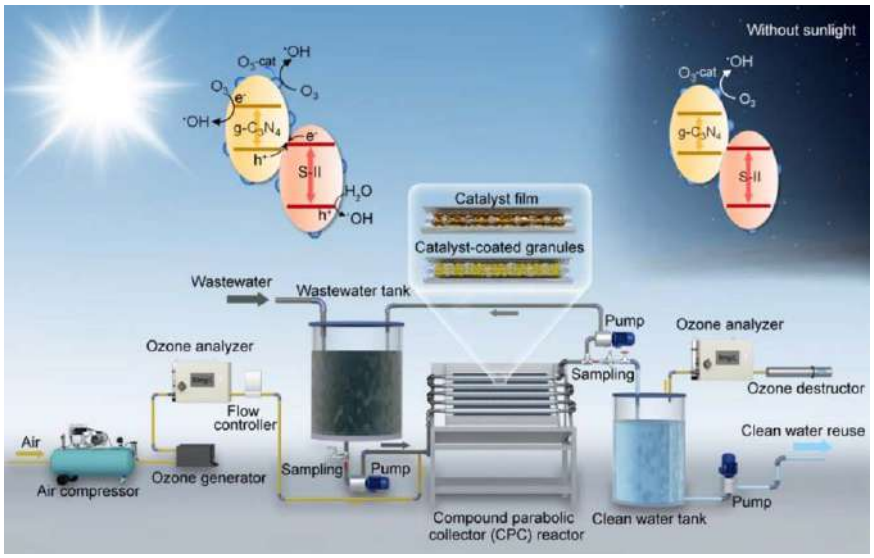

Scheme 7.6 Sunlight- and air-based water treatment plant combining solar photocatalytic ozonation and catalytic ozonation processes. Adapted from ref. 6 with permission from American Chemical Society, Copyright 2020.

7.7 Conclusions

This chapter summarizes the representative catalysts, the state-of-the-art understanding of the reaction mechanism and the catalyst structure–performance relationship and stability in visible-light photocatalytic ozonation, and discusses the future directions for catalyst improvement and how to advance the practical application of solar photocatalytic ozonation.

The key reason for the robust oxidation power of visible-light photocatalytic ozonation lies in the high yield of $^{\bullet}OH$. In this AOP, ozone plays a crucial role because it traps and converts photoelectrons into $^{\bullet}OH$ far more efficiently than oxygen, *via* a 1-electron reduction pathway ($O_3 \rightarrow {}^{\bullet}O_3^- \rightarrow HO_3^{\bullet} \rightarrow {}^{\bullet}OH$), and reacts with $^{\bullet}O_2^-$ to form $^{\bullet}O_3^-$, which generates further $^{\bullet}OH$. g-C_3N_4 has emerged as the most actively studied catalyst recently and has exhibited multiple advantages over WO_3, the second most popular catalytic material of this field. Band structure has been found to be the decisive factor to the activity of pristine g-C_3N_4 because it affects the number of reactive charge carriers, which is directly proportional to the yield of $^{\bullet}OH$. g-C_3N_4 is chemically stable with ozone and $^{\bullet}O_2^-$ but can be oxidatively decomposed by $^{\bullet}OH$. Fortunately, the decomposition of g-C_3N_4 could be inhibited in wastewater treatment because of the protection effect of organic pollutants that compete with g-C_3N_4 for $^{\bullet}OH$. Therefore, g-C_3N_4 photocatalytic ozonation treatment of wastewater remains robust and steady.

Further improvement of g-C_3N_4-based particulate catalysts is necessary. The main directions include (1) narrowing the bandgap and shifting up the CB edge of g-C_3N_4, (2) forming a Z-scheme heterojunction with another visible-light responsive semiconductor, whose VB-h^+ can directly oxidize H_2O to $^{\bullet}OH$, (3) building a bifunctional catalyst by compositing with materials that can catalytically decompose ozone into $^{\bullet}OH$, and (4) loading suitable co-catalysts to promote desired reactions while suppressing unwanted side reactions. To advance the scalable applications, active catalyst granules or immobilized catalyst sheets/films are to be fabricated. Also, fabrication of innovative devices, reactors and equipment is required to maximize photon absorption and the mass transfer of redox species, and outdoor pilot-scale examinations are also important in parallel with lab-scale experiments. Therefore, we need keep moving forward toward the ultimate goal, the establishment of sunlight- and air-based scalable wastewater treatment plants.

Acknowledgements

The authors appreciate the financial support from the National Science Fund for Distinguished Young Scholars of China (51425405) and the Beijing Natural Science Foundation (8172043).

References

1. K. Tanaka, K. Abe and T. Hisanaga, *J. Photochem. Photobiol. A*, 1996, **101**, 85–87.
2. T. E. Agustina, H. M. Ang and V. K. Vareek, *J. Photochem. Photobiol. C*, 2005, **6**, 264–273.
3. M. Mehrjouei, S. Müller and D. Möller, *Chem. Eng. J.*, 2015, **263**, 209–219.
4. J. Xiao, Y. Xie and H. Cao, *Chemosphere*, 2015, **121**, 1–17.
5. F. Beltrán and A. Rey, *Molecules*, 2017, **22**, 1177.
6. J. D. Xiao, Y. B. Xie, J. Rabeah, A. Bruckner and H. B. Cao, *Acc. Chem. Res.*, 2020, **53**, 1024–1033.
7. S. Nishimoto, T. Mano, Y. Kameshima and M. Miyake, *Chem. Phys. Lett.*, 2010, **500**, 86–89.
8. S. Anandan, G. J. Lee, P. K. Chen, C. Fan and J. J. Wu, *Ind. Eng. Chem. Res.*, 2010, **49**, 9729–9737.
9. J. D. Xiao, Y. B. Xie, H. B. Cao, Y. Q. Wang and Z. J. Zhao, *Catal. Commun.*, 2015, **66**, 10–14.
10. J. D. Xiao, Y. B. Xie, F. Nawaz, S. Jin, F. Duan, M. J. Li and H. B. Cao, *Appl. Catal., B*, 2016, **181**, 420–428.
11. J. D. Xiao, Y. B. Xie, F. Nawaz, Y. X. Wang, P. H. Du and H. B. Cao, *Appl. Catal., B*, 2016, **183**, 417–425.
12. J. D. Xiao, Y. B. Xie, H. B. Cao, Y. X. Wang, Z. Guo and Y. Chen, *Carbon*, 2016, **107**, 658–666.
13. J. D. Xiao, J. Rabeah, J. Yang, Y. B. Xie, H. B. Cao and A. Bruckner, *ACS Catal.*, 2017, **7**, 6198–6206.

14. J. D. Xiao, Q. Z. Han, Y. B. Xie, J. Yang, Q. Z. Su, Y. Chen and H. B. Cao, *Environ. Sci. Technol.*, 2017, **51**, 13380–13387.
15. J. Xiao, Q. Han, H. Cao, J. Rabeah, J. Yang, Z. Guo, L. Zhou, Y. Xie and A. Brückner, *ACS Catal.*, 2019, **9**, 8852–8861.
16. G. Z. Liao, D. Y. Zhu, L. S. Li and B. Y. Lan, *J. Hazard. Mater.*, 2014, **280**, 531–535.
17. G. Z. Liao, D. Y. Zhu, C. C. Li, B. Y. Lan and L. S. Li, *Ozone: Sci. Eng.*, 2016, **38**, 312–317.
18. J. Yin, G. Z. Liao, D. Y. Zhu, P. Lu and L. S. Li, *J. Photochem. Photobiol., A*, 2016, **315**, 138–144.
19. Y. Ling, G. Z. Liao, W. H. Feng, Y. Liu and L. S. Li, *J. Photochem. Photobiol., A*, 2017, **349**, 108–114.
20. Y. Ling, G. Z. Liao, P. Xu and L. S. Li, *Sep. Purif. Technol.*, 2019, **216**, 1–8.
21. Y. X. Huang, Y. F. Yang, J. W. Jiang, Z. H. Xu, C. L. Zhu and L. Li, *J. Environ. Eng.*, 2018, **144**, 04018063.
22. M. Jourshabani, J. A. Dominic, G. Achari and Z. Shariatinia, *Chem. Eng. Sci.*, 2019, **209**, 115181.
23. Z. Liu, C. Y. Lu, Q. C. Mo, Q. Z. Yan, J. L. Li and W. S. Guan, *Desalin. Water Treat.*, 2020, **202**, 355–363.
24. C. A. Orge, M. J. Sampaio, J. L. Faria, M. F. R. Pereira and C. G. Silva, *J. Environ. Chem. Eng.*, 2020, **8**, 104172.
25. T. Mano, S. Nishimoto, Y. Kameshima and M. Miyake, *J. Ceram. Soc. Jpn.*, 2011, **119**, 822–827.
26. E. Mena, A. Rey, S. Contreras and F. J. Beltran, *Catal. Today*, 2015, **252**, 100–106.
27. A. Rey, E. Mena, A. M. Chavez, F. J. Beltran and F. Medina, *Chem. Eng. Sci.*, 2015, **126**, 80–90.
28. E. Mena, A. Rey, E. M. Rodriguez and F. J. Beltran, *Appl. Catal., B*, 2017, **202**, 460–472.
29. J. Yang, J. D. Xiao, H. B. Cao, Z. Guo, J. Rabeah, A. Brückner and Y. B. Xie, *J. Hazard. Mater.*, 2018, **360**, 481–489.
30. T. Mano, S. Nishimoto, Y. Kameshima and M. Miyake, *Chem. Eng. J.*, 2015, **264**, 221–229.
31. Z. H. Pan, Q. H. Cai, Q. Luo and X. W. Li, *Synth. React. Inorg., Met.-Org., Nano-Met. Chem.*, 2015, **45**, 447–450.
32. S. Maddila, V. O. Ndabankulu and S. B. Jonnalagadda, *Global Nest J.*, 2016, **18**, 269–278.
33. M. Sheydaei, H. R. K. Shiadeh, B. Ayoubi-Feiz and R. Ezzati, *Chem. Eng. J.*, 2018, **353**, 138–146.
34. M. Sheydaei, D. Soleimani and B. Ayoubi-Feiz, *Environ. Technol. Innovation*, 2020, **17**, 100512.
35. L. Wu, Z. Zhao, H. Yu, M. Wang, G. Li, H. Li and J. Yan, *Catal. Sci. Technol.*, 2020, **10**, 7481–7485.
36. J. Yang, X. Liu, H. Cao, Y. Shi, Y. Xie and J. Xiao, *Front. Chem. Sci. Eng.*, 2019, **13**, 185–191.
37. X. L. Liu, Z. Guo, L. B. Zhou, J. Yang, H. B. Cao, M. Xiong, Y. B. Xie and G. R. Jia, *Chemosphere*, 2019, **222**, 38–45.

38. J. Yin, G. Z. Liao, J. L. Zhou, C. M. Huang, Y. Ling, P. Lu and L. S. Li, *Sep. Purif. Technol.*, 2016, **168**, 134–140.
39. J. L. Li, W. S. Guan, X. Yan, Z. Y. Wu and W. D. Shi, *Catal. Lett.*, 2018, **148**, 23–29.
40. K. Sehested, N. Getoff, F. Schwoerer, V. Markovic and S. O. Nielsen, *J. Phys. Chem.*, 1971, **75**, 749–755.
41. P. C. C. Faria, J. J. M. Órfão and M. F. R. Pereira, *Appl. Catal., B*, 2008, **79**, 237–243.
42. X. Wang, K. Maeda, A. Thomas, K. Takanabe, G. Xin, J. M. Carlsson, K. Domen and M. Antonietti, *Nat. Mater.*, 2009, **8**, 76.
43. Y. Wang, X. Wang and M. Antonietti, *Angew. Chem., Int. Ed.*, 2012, **51**, 68–89.
44. J. Beltran-Heredia, J. Torregrosa, J. R. Dominguez and J. A. Peres, *Chemosphere*, 2001, **42**, 351–359.
45. S. Gligorovski, R. Strekowski, S. Barbati and D. Vione, *Chem. Rev.*, 2015, **115**, 13051–13092.
46. W. H. Koppenol, D. M. Stanbury and P. L. Bounds, *Free Radical Biol. Med.*, 2010, **49**, 317–322.
47. http://www.ozonesolutions.com/ (last accessed July 2021).
48. G. V. Buxton, C. L. Greenstock, W. P. Helman and A. B. Ross, *J. Phys. Chem. Ref. Data*, 1988, **17**, 513–886.
49. Y. X. Wang, Y. B. Xie, H. Q. Sun, J. D. Xiao, H. B. Cao and S. B. Wang, *ACS Appl. Mater. Interfaces*, 2016, **8**, 9710–9720.
50. X. Dang, X. Zhang, W. Zhang, X. Dong, G. Wang, C. Ma, X. Zhang, H. Ma and M. Xue, *RSC Adv.*, 2015, **5**, 15052–15058.
51. K. Maeda, X. Wang, Y. Nishihara, D. Lu, M. Antonietti and K. Domen, *J. Phys. Chem. C*, 2009, **113**, 4940–4947.
52. Z.-Q. Liu, J. Ma, Y.-H. Cui and B.-P. Zhang, *Appl. Catal., B*, 2009, **92**, 301–306.
53. P. Zhou, J. Yu and M. Jaroniec, *Adv. Mater.*, 2014, **26**, 4920–4935.
54. D. Robert, *Catal. Today*, 2007, **122**, 20–26.
55. K. Ding, B. Chen, Y. Li, Y. Zhang and Z. Chen, *J. Mater. Chem. A*, 2014, **2**, 8294–8303.
56. D. Zhang, M. Wen, S. Zhang, P. Liu, W. Zhu, G. Li and H. Li, *Appl. Catal., B*, 2014, **147**, 610–616.
57. F. Nawaz, H. Cao, Y. Xie, J. Xiao, Y. Chen and Z. A. Ghazi, *Chemosphere*, 2017, **168**, 1457–1466.
58. H. Jung and H. Choi, *Appl. Catal., B*, 2006, **66**, 288–294.
59. T. Hisatomi and K. Domen, *Nat. Catal.*, 2019, **2**, 387–399.
60. Q. Wang, T. Hisatomi, Q. X. Jia, H. Tokudome, M. Zhong, C. Z. Wang, Z. H. Pan, T. Takata, M. Nakabayashi, N. Shibata, Y. B. Li, I. D. Sharp, A. Kudo, T. Yamada and K. Domen, *Nat. Mater.*, 2016, **15**, 611–615.
61. G. Márquez, E. M. Rodríguez, F. J. Beltrán and P. M. Álvarez, *Chemosphere*, 2014, **113**, 71–78.
62. D. H. Quiñones, P. M. Álvarez, A. Rey, S. Contreras and F. J. Beltrán, *Chem. Eng. J.*, 2015, **260**, 399–410.

CHAPTER 8

Catalytic Peroxone Process and the Coupled Processes

ZHUANG GUO,[a] YONGBING XIE[b,c] AND HONGBIN CAO*[b,c]

[a] State Key Laboratory of Environmental Criteria and Risk Assessment, Chinese Research Academy of Environmental Sciences, Beijing 100012, China; [b] Chemistry & Chemical Engineering Data Center, Chinese Academy of Sciences, Beijing 100190, China; [c] Beijing Engineering Research Center of Process Pollution Control, Institute of Process Engineering, Chinese Academy of Sciences, Beijing 100190, China
*Email: hbcao@ipe.ac.cn

8.1 Introduction

In 1982, Staehelin and Hoigne first proposed the peroxone process, generating hydroxyl radicals ($^{\bullet}OH$) through the reaction between O_3 and H_2O_2 to realize the efficient removal of refractory organics.[1] As it has the advantages of simplicity, rapid generation of radicals, low operation cost and negligible secondary pollution, this process has quickly become a hot pot.[2] However, the peroxone process mainly relies on the reaction between O_3 and HO_2^- (the deprotonated form of H_2O_2) to produce reactive oxygen species (ROS), and the high pK_a of H_2O_2 leads to the limited reaction rate under the acidic solution.[3,4] As a result, the application of the peroxone process is limited to acidic wastewater treatment. The establishment of the catalytic peroxone process using a catalytic material is a promising means of overcoming this long existing shortfall, and thus the application scope could be extended.[5] This chapter summarizes various homogeneous and heterogeneous catalysts

Chemistry in the Environment Series No. 8
Advanced Ozonation Processes for Water and Wastewater Treatment: Active Catalysts and Combined Technologies
Edited by Hongbin Cao, Yongbing Xie, Yuxian Wang and Jiadong Xiao

Published by the Royal Society of Chemistry, www.rsc.org

in the field, as well as their efficiencies for water contaminant removal and catalytic mechanism. In addition, some peroxone-coupled processes, including combination with photolysis, photocatalysis, ultrasonication and plasma, are summarized, which can enhance the treating efficiencies of peroxone process.

8.1.1 Mechanism

The peroxone process is comprised of several completed chain reactions. The reaction mechanism is gradually revealed with in-depth research; for example, HO_2^- can act as the initiator instead of H_2O_2. In general, the development of the mechanism has been divided into three phases: mechanism 1, mechanism 2 and mechanism 3.

Mechanism 1

Electron transfer is deemed the initial reaction between O_3 and H_2O_2, which generates $HO_2^{\bullet}$ and $^{\bullet}O_3^-$. $HO_2^{\bullet}$ can spontaneously decompose into $^{\bullet}O_2^-$. Relying on the fast reaction rate between $^{\bullet}O_2^-$ and O_3 ($k = 1.5\times10^9\ M^{-1}\ s^{-1}$), it produces $^{\bullet}O_3^-$. In final, $^{\bullet}OH$ is generated by the protonation and dissociation process of $^{\bullet}O_3^-$ (eqn (8.1)–(8.5)).[6]

$$O_3 + HO_2^- \rightarrow {}^{\bullet}O_3^- + HO_2^{\bullet} \tag{8.1}$$

$$HO_2^{\bullet} \leftrightarrow {}^{\bullet}O_2^- + H^+ \tag{8.2}$$

$$^{\bullet}O_2^- + O_3 \leftrightarrow O_2 + {}^{\bullet}O_3^- \tag{8.3}$$

$$^{\bullet}O_3^- + H^+ \rightarrow HO_3^{\bullet} \tag{8.4}$$

$$HO_3^{\bullet} \leftrightarrow {}^{\bullet}OH + O_2 \tag{8.5}$$

According to these chemical equations, it is found that the stoichiometry of O_3 and $^{\bullet}OH$ reaches 1 : 1; in other words, O_3 can be completely converted into $^{\bullet}OH$ (eqn (8.6)).

$$2O_3 + H_2O_2 \rightarrow 3O_2 + 2{}^{\bullet}OH \tag{8.6}$$

Mechanism 2

In 2004, Lesko proposed that the hydrogen transfer reaction was conducted first between O_3 and HO_2^- to produce HO_3^- (eqn (8.7)–(8.8)), according to the results of the kinetic isotope effect (KIE).[7] In the research, it was found that the KIE value of the peroxone process was only 19.6 ± 4.0, which was significantly lower than that of the formation process of radicals (eqn (8.1)). Therefore, the original chain reactions couldn't happen. However, this mechanism was quickly denied by Sein.[8] The reason was that the product H_2O_3 didn't have any characteristics of active radicals and couldn't match

the performance of $^{\bullet}OH$. Ultimately, it was confirmed to be an experimental illusion in KIE research.

$$O_3 + HO_2^- \rightarrow O_2 + HO_3^- \tag{8.7}$$

$$HO_3^- + H^+ \rightarrow H_2O_3 \tag{8.8}$$

Mechanism 3

According to the KIE data, Sein proposed that HO_5^- adduct was the initial product in the peroxone process (eqn (8.9)). Fischbacher found that the consumption of O_3 in the peroxone process was almost two times more than that in γ-radiolysis based on the same treatment efficiencies, when the organics in water were 4-chlorobenzoic acid, 4-nitrobenzoic acid or atrazine.[4] It is generally known that O_3 is completely converted into $^{\bullet}OH$ in γ-radiolysis. Therefore, the $^{\bullet}OH$ yield per O_3 is only 50% in the peroxone process. Considering the reaction paths, the HO_5^- adduct decomposes into $^{\bullet}O_3^-$ and $HO_2^{\bullet}$ in competition with O_2 and OH^- (eqn (8.10)–(8.13)). Although there is a big difference in the free energy of thermodynamics for the two reaction paths (eqn (8.10) $G^0 = 13.2$ kJ mol^{-1}, eqn (8.11) $G^0 = -197$ kJ mol^{-1}), the former only involves the fracture of single bond, and the latter includes the fracture and rearrangement of several bonds. Considering thermodynamics and quantum mechanics, it is rational to believe that the two reactions occur with a 50% probability, respectively.[9] So far, mechanism 3 has been widely recognized in the peroxone process.

$$O_3 + HO_2^- \rightarrow HO_5^- \tag{8.9}$$

$$HO_5^- \rightarrow {}^{\bullet}O_3^- \rightarrow HO_2^{\bullet} \tag{8.10}$$

$$HO_5^- \rightarrow 2^3O_2 + OH^- \tag{8.11}$$

$$^{\bullet}O_3^- \leftrightarrow O_2 + {}^{\bullet}O^- \tag{8.12}$$

$$^{\bullet}O^- + H_2O \leftrightarrow {}^{\bullet}OH + OH^- \tag{8.13}$$

8.1.2 Application

Over the past decades, the applied field of the peroxone process has been expanded from river water containing simple organic substances to chemical and pharmaceutical wastewater including a large amount of refractory organics. Witte *et al.* treated the ciprofloxacin with the peroxone process, which exhibited an obviously higher efficiency than the ozonation process.[10] Moreover, the effects of O_3 inlet concentration, H_2O_2 concentration, ciprofloxacin concentration, temperature and pH were explored. The results show that pH and the ratio of O_3 and H_2O_2 greatly affect the efficiencies, while the influence of temperature (6.0–62.0 °C) is negligible. Specifically, the

efficiencies are reduced with decreasing pH, and excessive H_2O_2 causes the competitive effect of promoting radical formation *versus* scavenging radicals. The oxidation of simazine, one of the herbicides with moderate toxicity, by the peroxone treatment was investigated.[11] It realized a high TOC removal rate of up to 82% under a O_3/H_2O_2 ratio of 0.6 and pH of 11. In addition, organic sulfurated compounds, potential hazards for atmosphere and water, were efficiently treated by the peroxone process.[12] The results showed that in the dibutylsulfide (DBS) oxidation process, the DBS degradation rate increased with the increase of H_2O_2 concentration (ranging from 0.1 to 1 mol L^{-1}) at pH 9, whereas it exhibited a slight change when the H_2O_2 concentration was lower than 0.1 mol L^{-1}. Therefore, appropriate operational parameters are vital for the treatment efficiency of the peroxone process.

It also can effectively improve the biodegradability of wastewater by increasing the concentration of assimilable organic carbon (AOC) with the role of O_3 and H_2O_2.[13] Additionally, the process is used to disinfect bacteria and degrade their secretion sustainably. Oh proved that the peroxone process not only eliminated the *Escherichia coli* but also removed the endotoxin released from *Escherichia coli*.[14] This study compared the degradation efficiencies of endotoxin by O_3 alone, UV/H_2O_2 and O_3/H_2O_2. Only 8% and 30% of the initial endotoxin were degraded, respectively, by O_3 alone and by UV/H_2O_2 under optimal conditions, whereas the removal ratio under O_3/H_2O_2 conditions was 70%. The outstanding performance of the peroxone process confirms its potential in biological applications.

Peroxone process is considered to be an alternative for reverse osmosis (RO) in the treatment of secondary effluents. Wu applied the peroxone process in a direct potable water reuse research treatment system.[15] The results showed that the Chemical Oxygen Demand (COD) value of secondary effluent could be reduced to less than the detection limit under optimized conditions (O_3 dosages > 4.6 mg L^{-1} h^{-1} and O_3/H_2O_2 mass ratio of 3.4–3.8). The secondary effluent is purified completely by the peroxone process. In comparison with RO, the peroxone process satisfies the permanent mineralization without extra processes and without the consumption needed for solving the membrane fouling and corrosion problems.

The peroxone process can be used to degrade the volatile organic compounds (VOCs) that are widely present at various industrial facilities. Fernandes compared the degradation efficiencies of 16 kinds of VOCs, including benzene, toluene, 2-ethylthiophene, phenol and so on, under O_3, H_2O_2 and O_3/H_2O_2 (peroxone process) conditions, respectively.[16] The results showed that the peroxone process significantly outperformed the processes involving O_3 or H_2O_2 alone, with complete degradation of the total organics in a short time. A basic economic evaluation on its cost was performed (Table 8.1). The study of the chemical and energy costs demonstrated that peroxone process (0.01\$ L^{-1}) was cheapest, compared with O_3 (0.3\$ L^{-1}) or H_2O_2 (0.12\$ L^{-1}), without considering the treatment time. Taking into account the expensive prices of $Na_2S_2O_8$, the cost of persulfate (PS) increases by

Table 8.1 Treatment cost calculations of O_3, UV/H_2O_2 and peroxone process. Reproduced from ref. 13 with permission from Elsevier, Copyright 2019.

Methods	Oxidant amount (min)	T (°C)	Effective time (min)	Effective amount (g)	Chemical cost ($)	Energy demand (kJ)	Energy cost ($)	Total cost ($)	Treatment cost ($\$L^{-1}$)
H_2O_2	62	40	181.5	62.23	0.09	871.2	0.03	0.12	0.02
O_3	70	40	357.6	69.38	–	9655.2	0.30	0.30	0.06
O_3/H_2O_2	O_3 61.5H_2O_2 127.5	40	30	O_3 5.82H_2O_2 12.05	0.02	954	0.03	0.05	0.01
$Na_2S_2O_8^-$	436	40	181.5	435.59	17.75	871.2	0.03	17.77	3.55

two orders of magnitude to 17.77$. Therefore, the implementation of peroxone process is viable in a real-world case scenario.

8.1.3 Drawbacks

The degradation efficiencies of organics in the peroxone process are affected seriously by the pH of the solution. The efficiencies are reduced with decreasing pH values. Because HO_2^- as the initiator reacts with O_3 in the peroxone process and the pK_a of H_2O_2 is up to 11.8, only limited quantities of HO_2^- are produced under acidic solution, thus restricting the rate constant seriously.[17] According to the equation of apparent rate constant, a huge difference in rate constants under alkaline and acidic conditions is observed (eqn (8.14)).[18]

$$k = k_{HO_2^- + O_3} \times 10^{(pH - pK_a)} \tag{8.14}$$

The k values are 9.6×10^6 and 0.01 $M^{-1} s^{-1}$ at pH of 11.8 and 3, respectively, with a difference of nine orders of magnitude. In addition, carboxylic acids are unavoidably generated as the degradation intermediates of refractory organic compounds, lowering the solution pH and thus limiting the mineralization efficiency. Therefore, it is an urgent problem to solve the inefficiencies of the technology in acidic solutions, which is of great importance in broadening the application scope of the peroxone process.

8.2 Catalysts in Peroxone Process

Catalytic processes are the most effective methods to promote the peroxone process. Due to the complexity of this process including the two kinds of active oxidants, only limited kinds of catalysts have been developed so far. According to the difference in catalytic components and mechanisms, the catalysts are divided into traditional metal catalysts and single-atom catalysts.

8.2.1 Traditional Metal Catalysts

(1) Fe^0 Catalyst

Fe^0 catalyst is comprised of Fe^0 powders (98%, 200 mesh). When the Fe^0 catalyst was introduced in the peroxone process for the treatment of landfill leachate, the treatment efficiencies were conspicuously enhanced.[19] Concretely, the COD, UV_{254} and CN removal efficiencies were improved from 22.5%, 42% and 24% to 43.4%, 59.5% and 93.2%, respectively.

According to XRD and XPS analyses, iron oxides were formed after the reaction. Based on the previous research in which Fe^0 was used to catalyze O_3 and also to react with H_2O_2 to form a Fenton-like system, it is believed that the Fe^0 catalyst promoted the peroxone process by catalytic activation of O_3 and H_2O_2 individually.

The catalytic mechanisms of Fe^0 are deemed to be as follows: (1) Fe^0 reacts with O_3 to generate Fe^{2+} in the presence of O_3/H_2O_2, (2) Fe^{2+} catalyzes the decomposition of O_3 and H_2O_2, (3) the iron oxides (Fe_2O_3, Fe_3O_4 and FeOOH) are formed and further catalyze O_3 and H_2O_2 to promote the generation of reactive oxygen species (eqn (8.15)–(8.21)).

$$Fe + 2O_3 \rightarrow Fe^{2+} + 2^{\bullet}O_3^- \tag{8.15}$$

$$Fe^{2+} + O_3 \rightarrow Fe^{3+} + {}^{\bullet}O_3^- \tag{8.16}$$

$$Fe^{2+} + H_2O_2 \rightarrow + {}^{\bullet}OH + OH^- + Fe^{3+} \tag{8.17}$$

$$H^+ + {}^{\bullet}O_3^- \rightarrow HO_3 \rightarrow {}^{\bullet}OH + O_2 \tag{8.18}$$

$$Fe^{2+} + O_3 \rightarrow (FeOH)^{2+} + O_2 \tag{8.19}$$

$$(FeO)^{2+} + H_2O \rightarrow Fe^{3+} + {}^{\bullet}OH + OH^- \tag{8.20}$$

$$Fe^{3+} + O_3 + H_2O \rightarrow (FeO)^{2+} + {}^{\bullet}OH + O_2 + H^+ \tag{8.21}$$

Strictly speaking, Fe^0 power can't be regarded as the catalyst of the peroxone process because it catalytically activates O_3 and H_2O_2 individually. In addition, Fe^0 catalyst gives rise to the problem of iron sludge due to the oxidation of Fe^0 and precipitation.

(2) Ti(IV) catalyst

The Tong Group found that Ti(IV) ions could accelerate the degradation of acetic acid in the peroxone system.[20] Only an acetic acid degradation efficiency of 5.6% was caused by the peroxone process due to the acidic condition (pH = 2.8). The addition of Ti(IV) can significantly increase the efficiency up to 52%, while negligible increased efficiencies were observed in the processes, including Ti(IV)/O_3 and Ti(IV)/H_2O_2. These results indicate that Ti(IV) ions had a catalytic activity in the peroxone process. The R_{ct} values reflecting the $^{\bullet}OH$ generation efficiency in the Ti(IV)-free peroxone system and Ti(IV)/O_3/H_2O_2 system were 5.548×10^{-9} and 2.128×10^{-7} respectively. The obviously increased R_{ct} value in Ti(IV)/O_3/H_2O_2 system indicated that Ti(IV) can promote the generation of $^{\bullet}OH$ in the peroxone process.

The catalytic mechanism of Ti(IV) has been revealed in analyses of experimental phenomena and physical characterization. First, Ti(IV) reacts with H_2O_2 to form complex ($Ti_2O_5{}^{2+}$). This complex, as the initiator, can promote the decomposition of O_3 to produce the $^{\bullet}OH$ continuously (eqn (8.22)–(8.24)).

$$O_3(Ti_2O_5{}^{2+}) \rightarrow {}^{\bullet}O_3^- \tag{8.22}$$

$${}^{\bullet}O_3^- + H_3O^+ \rightarrow HO_3{}^{\bullet} + H_2O \tag{8.23}$$

$$HO_3{}^{\bullet} \rightarrow {}^{\bullet}OH + O_2 \tag{8.24}$$

Ti(IV) ion catalysts eased the low efficiency problem of the peroxone process in an acidic solution to some extent, but the recovery of Ti ions is difficult, restricting its practical application. An effective way around the drawback is to prepare the heterogeneous catalysts by immobilizing the

Ti ions on substrates. The TS-MCM-41 and TS-1 catalysts, the typical titanium silicon molecular sieves, have been used to promote the peroxone process.[21,22] These catalysts possess a large specific surface area, with stably fixed Ti ions. However, it was found that the treatment efficiencies of TS-MCM-41 or TS-1 catalysts clearly decreased in comparison with Ti(IV) ions catalyst in reality. The decrease of Ti(IV) ions on catalysts and extra side reactions may directly or indirectly affect the treatment process. Therefore, developing Ti-containing catalysts with a balance between the density of active sites (Ti(IV) ions) and structural stability has become a research topic.

(3) SO_4^{2-}/ZrO_2–Fe_2O_3 catalyst

Iron oxide–promoted sulfated zirconia catalyst (SO_4^{2-}/ZrO_2–Fe_2O_3, abbreviated as SZF), discovered by the Tong Group, exhibited stable catalytic performance in the peroxone process even under strong acidic conditions.[23]

Sulfated zirconia (SO_4^{2-}/ZrO_2, abbreviated as SZ) is one kind of solid superacid that has higher acidity than that of 100% sulfuric acid. Compositing iron oxide with the sulfated zirconia can increase the surface area and Lewis and/or Brønsted acidity, which is favorable for catalytic activity. X-ray diffraction (XRD) characterization of the catalyst showed that the ZrO_2 and Fe_2O_3 existed in amorphous forms, indicating that the components interacted with each other in the SZF catalyst.

In the degradation experiment of acetic acid, the SZF catalyst exhibited limited activities for catalyzing the activation of O_3 or H_2O_2 individually. When O_3 and H_2O_2 exist simultaneously, SZF catalyst can markedly enhance the degradation efficiency, which is much higher than the sum of the efficiencies in the SZF/O_3 process and the SZF/H_2O_2 process. In addition, the experimental results showed that SZF catalyst exhibited a higher catalytic activity in comparison with titanium catalysts, with an order of SZF > Ti(IV) > SZ > TS-1.

There was a positive correlation between pH values and the degradation efficiencies of acetic acid in the SZF/O_3/H_2O_2 process (Figure 8.1). These results demonstrated that the SZF catalyst widened the pH range of

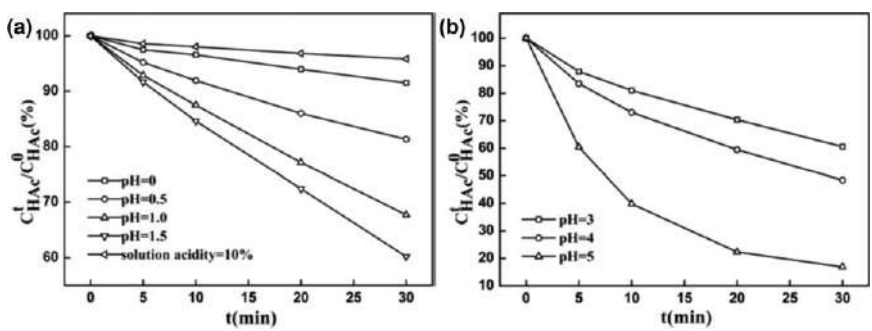

Figure 8.1 (a) and (b) Degradation rates of acetic acid in the SZF/O_3/H_2O_2 process at different pH values. Reproduced from ref. 19 with permission from American Chemical Society, Copyright 2016.

wastewater treatable by the peroxone process. However, the SZF catalyst was not applicable to all cases. For example, it had a negligible effect when the acidity of solution was above 10% (mass fraction of H_2SO_4).

It was proposed that the SZF catalyst promoted the generation of $^{\bullet}OH$ in the peroxone process by the S–Fe(III) peroxo complex (S–$[Fe^{III}OOH]^{2+}$) formed from the reaction between the catalyst and H_2O_2. The multifunctional complex not only produced some active species under light but could also initiate the decomposition of O_3 to generate $^{\bullet}OH$. Moreover, the existing Lewis and/or Brønsted acidity on the catalyst was considered to accelerate the O_3 decomposition. Therefore, the discovery of the SZF catalyst advances the treatment of strong acidic wastewater by the catalytic peroxone process.

(4) CeO_2 catalyst

CeO_2 is a rare earth material with the features of widely available sources, low price, environmental friendliness and easy synthesis. So far, CeO_2 has been extensively applied in numerous fields because of its unique Ce^{3+}/Ce^{4+} redox couple and the formed oxygen vacancies, which contribute to the occurrence of several inert reactions. Meanwhile, CeO_2 also exhibits good adsorption abilities and stability in water, making it feasible in wastewater treatment.[24]

In comparison with the catalysts discovered previously, CeO_2 exhibited the highest degradation efficiencies of acetic acid in the peroxone process (Figure 8.2). Moreover, there was a negligible contribution from individual catalytic processes by CeO_2/O_3 and CeO_2/H_2O_2. This indicated that CeO_2 had an excellent catalytic activity for the peroxone process.

The performance of CeO_2 is due to its distinctive oxygen vacancies. The presence of oxygen vacancies is demonstrated by the coexistence of Ce^{3+} and Ce^{4+} in CeO_2. Typically, the Ce^{3+} has a positive orrelation with oxygen

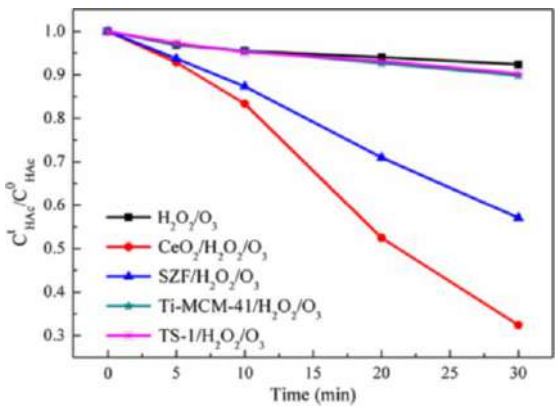

Figure 8.2 Degradation rates of acetic acid in the O_3/H_2O_2 process with different catalysts including CeO_2, SZF, Ti-MCM-41 and TS-1. Reproduced from ref. 20 with permission from Elsevier, Copyright 2018.

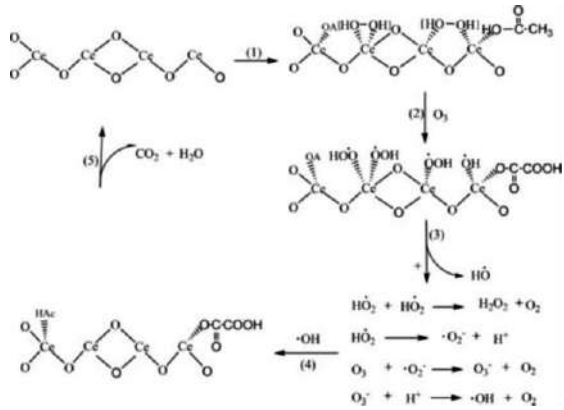

Figure 8.3 Catalytic mechanism of CeO_2 in the O_3/H_2O_2 process. Reproduced from ref. 20 with permission from Elsevier, Copyright 2018.

vacancies. The increased ratio of Ce^{3+} ions to the total Ce for the CeO_2 catalyst used indicates that the oxygen vacancies have been the potential active sites, according to the X-ray photoelectron spectroscopy (XPS) spectra of fresh CeO_2 and used CeO_2. Subsequently, the emerging peak in Raman spectrum, which is assigned to the stretching vibration of peroxide-like species, confirmed the interaction between oxygen vacancies and H_2O_2.

With the aid of oxygen vacancies, H_2O_2 can be absorbed on the surface of CeO_2 to form Ce(III)-H_2O_2 as a HO_2-like species, promoting the decomposition of O_3 to form Ce(III)–$^{\bullet}OH$ and Ce(III)–$HO_2^{\bullet}$. The former can directly react with the organics, and the latter can be converted into $^{\bullet}OH$ by the chain reactions. Meanwhile, the active sites are recovered to maintain the catalytic stability. In a word, these catalysts are characterized by the formed peroxide intermediates, which can accelerate the decomposition of O_3 instead of HO_2^- (Figure 8.3).

However, the CeO_2 catalyst was not always active in all acidic solutions, and its performance decreased with decreasing pH of the reaction solution. Ding discovered the *N*-graphene–CeO_2 catalyst, which could significantly improve the treatment efficiencies at a pH value of 1.[25] By studying the change of CeO_2 after incorporation of *N*-graphene, it was found that the ratio of Ce^{3+} ions increased from 10.28% to 30.21%. This confirmed the importance of oxygen vacancies in CeO_2 and indicated that compositing carbon materials with CeO_2 may be a feasible way to increase the amounts of Ce^{3+} ions.

8.2.2 Single-atom Catalysts

In recent years, single-atom catalysts (SACs), which are prepared by the uniform deposition of isolated metal atoms on a substrate *via* coordination bonds, have been a research focus owing to their utmost metal utilization,

excellent catalytic activity and structural stability. The optimized electronic property of metal atoms on SACs, benefiting from the strong interaction between metal atoms and substrate, may result in improvement of selectivity in a variety of reactions and may enable SACs to outperform their cluster and nanoparticle forms. Therefore, the use of SACs to promote the formation of •OH by the catalyzing peroxone process is promising. Guo discovered a Mn SAC (abbreviated as C_3N_4–Mn) that is characterized by atomically dispersed active Mn–N_4 sites on graphitic carbon nitride (g-C_3N_4), which significantly enhances the treatment efficiencies of organics in acidic wastewater.[5]

The C_3N_4–Mn was prepared by thermal condensation. Mn SAC showed structural information that is similar to g-C_3N_4 material, and no characteristic peaks of Mn chlorides or oxides were observed in the XRD spectrum. The as-obtained C_3N_4–Mn exhibited the typical block multilayer morphology of g-C_3N_4. The bright dots of atomic size in a high-angle annular dark-field

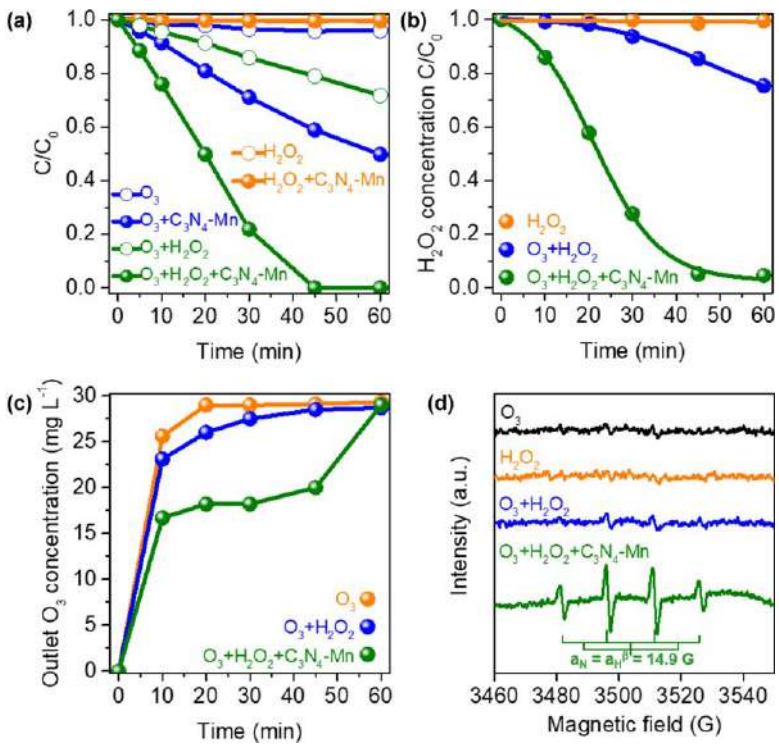

Figure 8.4 (a) Degradation curves of OA in ozonation, H_2O_2 process and peroxone process with or without the C_3N_4–Mn catalyst. (b) Corresponding H_2O_2 decay curves in different processes. (c) Corresponding outlet O_3 concentration in different processes. (d) EPR spectra of DMPO-•OH adduct in different processes. Reproduced from ref. 22 with permission from American Chemical Society, Copyright 2019.

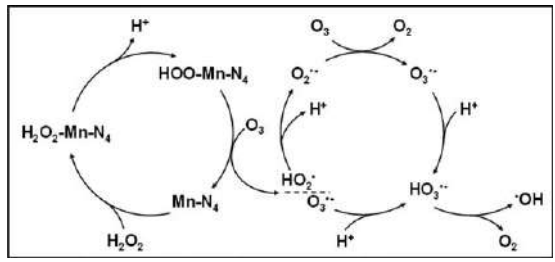

Figure 8.5 The catalytic mechanism of C_3N_4–Mn catalyst for peroxone process. Reproduced from ref. 22 with permission from American Chemical Society, Copyright 2019.

scanning transmission electron microscopy image (HAADF-STEM) confirmed the atomically dispersed Mn species.

The catalytic activity of the C_3N_4–Mn was investigated in the degradation of oxalic acid (OA), which is a common refractory intermediate in various advanced oxidation processes. The peroxone process caused a degradation efficiency of 28% after 60 min, while the initial OA was degraded completely within 40 min, when C_3N_4–Mn was added. In comparison, the ratios of removed OA were 0% and 50% after 60 min under H_2O_2/C_3N_4–Mn and O_3/C_3N_4–Mn systems, respectively (Figure 8.4a). Moreover, H_2O_2 and O_3 were both gradually consumed according to the detection of H_2O_2 and outlet O_3 concentrations (Figure 8.4b–c). The electron paramagnetic resonance (EPR) measurements with 5,5-dimethyl-1-pyrroline *N*-oxide (DMPO) as a spin-trapping agent revealed a strong DMPO–$^{\bullet}$OH signal in the C_3N_4–Mn/O_3/H_2O_2 process (Figure 8.4d). These results confirmed that C_3N_4–Mn had excellent catalytic activity in the peroxone process.

Mn–N_4 sites played an important part in the catalytic cycle. It could adsorb H_2O_2 to form the HOO–Mn–N_4 species and then reacted with O_3 molecules to produce $HO_2^{\bullet}$ and $^{\bullet}O_3^-$. As a conjugated base of $HO_2^{\bullet}$, a small amount of $^{\bullet}O_2^-$ would react with O_3 to generate $^{\bullet}O_3^-$. $^{\bullet}O_3^-$ would combine with H^+ in acidic solution to form $HO_3^{\bullet}$, which was quickly converted into $^{\bullet}$OH. The introduction of C_3N_4–Mn eliminated the restriction of HO_2^- as the essential initiator in the conventional peroxone reaction (Figure 8.5). Therefore, the discovery of C_3N_4–Mn paved a new way to explore novel catalysts for efficient water remediation based on the peroxone process.

8.3 Enhancement by Other Processes

Besides the catalysts just mentioned, the peroxone process can be enhanced by integration with other processes (*e.g.*, electrochemistry, UV light, ultrasonication, plasma, *etc.*) to promote the generation of $^{\bullet}$OH. The combined technique of peroxone with electrochemical processes will be introduced in the following chapter. Here, we summarize the results of the integrated processes of peroxone with photocatalysis, sonolysis and plasma.

8.3.1 Photolysis and Photocatalysis

As highly active oxidants, O_3 and H_2O_2 can be radiated under UV light to produce reactive oxygen species (eqn (8.25)–(8.27)). $O^{\bullet}$ is produced quickly by the decomposition of O_3 under UV light and then combines with H_2O to form $^{\bullet}OH$. The fast conversion rate can obviously enhance the oxidation efficiencies of organics in comparison with the single ozonation process. Also, the O–O bonds of H_2O_2 are fractured to form $^{\bullet}OH$ under UV light, in which the ratio of H_2O_2 to $^{\bullet}OH$ reaches 1 : 2, which is twice as high as that in the traditional Fenton process.[26] However, the conversion rate of H_2O_2 is relatively low because of the low molar absorption coefficient of H_2O_2 ($\varepsilon_{254} = 19.6\ M^{-1}\,cm^{-1}$).

$$O_3 + h\nu \rightarrow O^{\bullet} + O_2 \tag{8.25}$$

$$O^{\bullet} + H_2O \rightarrow 2^{\bullet}OH \tag{8.26}$$

$$H_2O_2 + h\nu \rightarrow 2^{\bullet}OH \tag{8.27}$$

With the help of UV light, the respective photolytic processes of O_3 and H_2O_2 will improve the generation rate of $^{\bullet}OH$ in the peroxone process. In addition, introducing semiconductor materials, such as TiO_2 and ZnO, will further promote the generation of $^{\bullet}OH$. When TiO_2 is irradiated under UV light, photogenerated electrons (e^-) transfer from the valence band (VB) of TiO_2 to the conduction band (CB), leaving behind positive holes (h_{VB}^{+}) in the VB. The photogenerated electron-hole pairs can initiate the decomposition of O_3, H_2O_2 and H_2O, which accelerate the generation of $^{\bullet}OH$ (eqn (8.28)–(8.31)).

$$h_{VB}^{+} + H_2O \rightarrow {}^{\bullet}OH + H^{+} \tag{8.28}$$

$$h_{VB}^{+} + OH^{-} \rightarrow {}^{\bullet}OH \tag{8.29}$$

$$O_3 + e_{CB}^{-} + H_2O \rightarrow {}^{\bullet}OH + OH^{-} + O_2 \tag{8.30}$$

$$H_2O_2 + e_{CB}^{-} \rightarrow {}^{\bullet}OH + OH^{-} \tag{8.31}$$

The adsorbed H_2O on the TiO_2 will be oxidized by photogenerated holes. Simultaneously, O_3 and H_2O_2, as e^- acceptors, react with photogenerated electrons to generate $^{\bullet}OH$. André Fernandes thoroughly summarized the mechanism of the photocatalytic process of $TiO_2/UV/O_3/H_2O_2$ in the treatment of VOCs (Figure 8.6).[27] The combination of TiO_2 and UV formed additional generation paths for $^{\bullet}OH$ generation in the peroxone system, which had a positive influence on the treatment of VOCs.

The results showed that the degradation efficiencies of VOCs were improved by adding TiO_2 and UV light in the peroxone system, but negligible improvement in efficiency was observed with the increase of TiO_2 concentration, demonstrating that TiO_2 had a limited contribution to make to the process. Owing to the numerous generation paths of radicals, the competition affected the production of $^{\bullet}OH$ in the $TiO_2/UV/O_3/H_2O_2$ system.

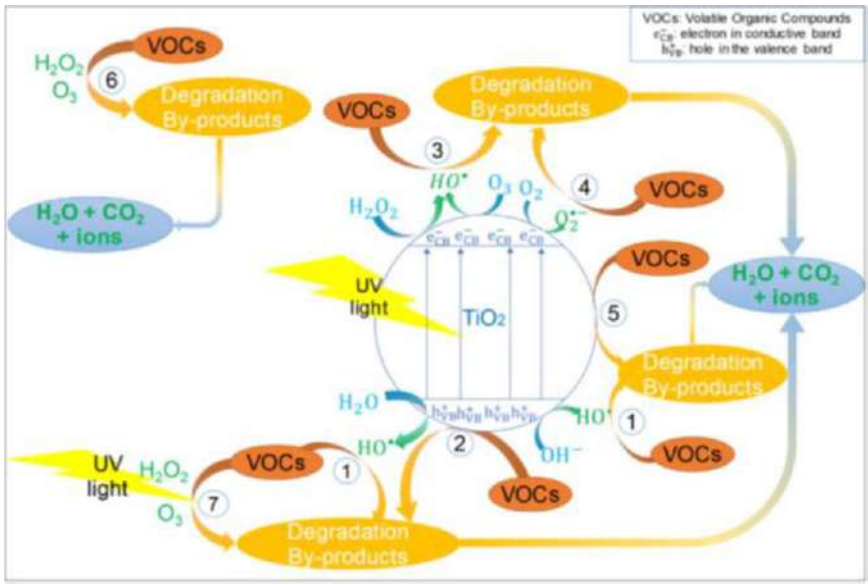

Figure 8.6 Mechanism of photocatalysis in O_3/H_2O_2 process. Reproduced from ref. 24 with permission from Elsevier, Copyright 2019.

Therefore, its degradation efficiency was lower than that in the $UV/O_3/H_2O_2$ system. In the $TiO_2/UV/O_3/H_2O_2$ system, it was important to design rational reactors to give full play to the synergies of various processes.

8.3.2 Sonolysis

An ultrasonic wave is a kind of sound wave whose frequency is more than 20 000 Hz. Ultrasonic technology has been a novel water treatment process because of the formation of the cavitation effect at a high frequency. The collapse of cavitation bubbles can release a large amount of energy and instantaneously construct a high-temperature and high-pressure environment. These not only contribute to the decomposition of H_2O to form $H^{\bullet}$ and $^{\bullet}OH$ but also help in the degradation of some organics.

Introducing an ultrasonic wave into the peroxone process has markedly improved the generation rate of radicals by means of the cavitation effect and its physicochemical effect. It has been speculated that the generation of radicals is not dependent on the complex chain reaction but on the direct decomposition of O_3 and H_2O_2 under the cavitation effect. The sonoperoxone process has been used to treat olive mill wastewater.[28] The addition of an ultrasonic wave could improve TOC removal efficiency and biodegradability in the peroxone system. However, this technology is still at the laboratory-scale stage at present, and there is a long way to go to realize its industrial applications.

8.3.3 Plasma

Plasma is the fourth state of matter, which differs from solid, liquid and gas. Non-thermal plasma technology is a novel water treatment process. With the help of a high-voltage discharge in gas–liquid environments, it can generate a great amount of highly reactive species, including several radicals ($^{\bullet}OH$, $HO_2^{\bullet}$, $O^{\bullet}$, $H^{\bullet}$), ions (O^+, O^-, H^+) and molecules (O_3 and H_2O_2). Concomitantly, UV irradiation is also formed in the excited-state transitions of species. Because of the *in situ* generation of O_3 and H_2O_2, plasma technology has been deemed an enhanced peroxone process.

In the degradation of atrazine, non-thermal plasma technology exhibited the most effective processing capacity in comparison with the UV/O_3 and UV/O_3/H_2O_2 processes.[29] As expected, 1 mg L^{-1} O_3 and 500 μmol L^{-1} H_2O_2 were detected in the plasma experiments, confirming their *in situ* generation. The degradation efficiency of the peroxone process was less than half of that in the plasma process using the same concentrations of O_3 and H_2O_2. The continuous generation of radicals and wide reaction space (including the plasma chamber and the solution reservoir) contributed to the enhancement.

Given the high-voltage discharge in the non-thermal plasma technology, the significantly increased treatment cost has to be considered. However, the practical cost was acceptable by evaluating the electrical energy per order (EE/O) values, which represented the electrical energy in kilowatt hours (kW h) required to degrade a certain contaminant by one order of magnitude in 1 m^3 of water.[29] The results showed that the EE/O of O_3/H_2O_2, UV/O_3, UV/O_3/H_2O_2 and plasma processes were 5.96, 65.3, 44.1 and 19.8 kW h m^{-3}, respectively. It was thus clear that the treatment cost of the plasma process was obviously lower than that of UV-based processes. In addition, the mass transfer improvement would enhance the treatment efficiencies in non-thermal plasma technology, leading to further reductions in treatment costs.

8.4 Conclusions

Peroxone process has been deemed the ideal water and wastewater treatment technology because of its simplicity, high efficiency and negligible secondary pollution. The key problem, *i.e.* the inefficiency under acidic conditions, could be solved by the use of catalysts, including Fe^0, Ti(IV), SO_4^{2-}/ZrO_2–Fe_2O_3, CeO_2, and C_3N_4–Mn single-atom catalysts. The combination with other techniques, such as photolysis, photocatalysis, ultrasonication and plasma, could further increase the yield of $^{\bullet}OH$, making the peroxone-coupled systems more competitive with the various advanced ozonation processes for water purification and wastewater treatment. It is anticipated that the design and fabrication of active catalysts in the near future will substantially improve the efficiencies of peroxone and peroxone-coupled processes in a wide pH scale range, eventually to the level required for scalable applications.

References

1. J. Staehelln and J. Holgne, *Environ. Sci. Technol.*, 1982, **16**, 676–681.
2. J. Cerkovnik and B. Plesnicar, *Chem. Rev.*, 2013, **113**, 7930–7951.
3. C. von Sonntag, *Water Sci. Technol.*, 2008, **58**, 1015–1021.
4. A. Fischbacher, J. von Sonntag, C. von Sonntag and T. C. Schmidt, *Environ. Sci. Technol.*, 2013, **47**, 9959–9964.
5. Z. Guo, Y. Xie, J. Xiao, Z. Zhao and Y. Wang, *J. Am. Chem. Soc.*, 2019, **141**, 12005–12010.
6. R. E. Buehler, J. Staehelin and J. Hoigné, *J. Phys. Chem.*, 1984, **88**, 2560–2564.
7. T. M. Lesko, A. J. Colussi and M. R. Hoffmann, *J. Am. Chem. Soc.*, 2004, **126**, 4432–4436.
8. M. M. Sein, A. Golloch, T. C. Schmidt and C. von Sonntag, *Chem. Phys. Chem.*, 2007, **8**, 2065–2067.
9. G. Merenyi, J. Lind, S. Naumov and C. v. Sonntag, *Environ. Sci. Technol.*, 2010, **44**, 3505–3507.
10. B. De Witte, J. Dewulf, K. Demeestere and H. Van Langenhove, *J. Hazard. Mater.*, 2009, **161**, 701–708.
11. E. C. Catalkaya and F. Kargi, *J. Environ. Eng.*, 2009, **135**, 1357–1364.
12. S. Popiel, T. Nalepa, D. Dzierżak, R. Stankiewicz and Z. Witkiewicz, *J. Hazard. Mater.*, 2009, **164**, 1364–1371.
13. P. A. Hacker, C. Paszko-Kolva and M. H. Stewart, *Ozone: Sci. Eng.*, 1994, **16**, 197–212.
14. B. T. Oh, Y. S. Seo and D. Sudhakar, *J. Hazard. Mater.*, 2014, **279**, 105–110.
15. T. Wu and J. D. Englehardt, *Water Res.*, 2015, **73**, 362–372.
16. A. Fernandes, P. Makoś, J. A. Khan and G. Boczkaj, *J. Cleaner Prod.*, 2019, **208**, 54–64.
17. M. M. Sein, M. Zedda, J. Tuerk, T. C. Schmidt, A. Golloch and C. von Sonntag, *Environ. Sci. Technol.*, 2008, **42**, 6656–6662.
18. C. Von Sonntag and U. Von Gunten, Chemistry of Ozone in Water and Wastewater Treatment: From Basic Principles to Applications, IWA Publishing, 2012.
19. F. Wang, Y. Luo, G. Ran and Q. Li, *Sci. Total Environ.*, 2020, **699**, 134371–134380.
20. W. Li, P. Liu, H. Zhang, R. Shi, S. Tong and C. Ma, *CIESC J*, 2010, **61**, 1790–1795.
21. R. Peng, T. Shen, S. Tong and C. Ma, *Ozone: Sci. Eng.*, 2016, **38**, 194–203.
22. Y. Chen, R. Peng, T. Shen, S. Tong and C. Ma, *Sep. Purif. Technol.*, 2015, **151**, 269–275.
23. Q. Wang, T. Shen and S. Tong, *Ind. Eng. Chem. Res.*, 2016, **55**, 10513–10523.
24. Y. Ding, J. Wang, S. Xu, K. Lin and S. Tong, *Sep. Purif. Technol.*, 2018, **207**, 92–103.

25. Y. Ding, H. Bao, R. Qian, T. Shen and S. Tong, *Sep. Purif. Technol.*, 2019, **225**, 80–87.
26. G. Wang, S. Hsieh and C. Hong, *Water Res.*, 2000, **34**, 3882–3887.
27. A. Fernandes, M. Gągol and P. Makoś, *Sep. Purif. Technol.*, 2019, **224**, 1–14.
28. M. R. Khani, H. Kuhestani and L. R. Kalankesh, *J. Taiwan Inst. Chem. E*, 2019, **97**, 47–53.
29. N. Wardenier, Z. Liu and A. Nikiforov, *Chemosphere*, 2019, **234**, 715–724.

CHAPTER 9

Promising Electrocatalytic Ozonation Processes for Water and Wastewater Treatment

HUIJIAO WANG,[a,b] WEIKUN YAO,[a] JUHONG ZHAN,[a] GANG YU[a] AND YUJUE WANG*[a]

[a] School of Environment, Tsinghua University, Beijing 100084, China;
[b] School of Chemical and Environmental Engineering, China University of Mining and Technology (Beijing), Beijing 100083, China
*Email: wangyujue@tsinghua.edu.cn

9.1 Introduction

Electrochemical technologies have been extensively investigated as appealing advanced oxidation processes (AOPs) for water and wastewater remediation.[1–3] During electrochemical treatment, contaminants can be degraded *via* direct electron transfer at the electrode and/or indirect reaction with various reactive species *in situ* generated in the treatment system. For instance, reactive oxidants such as the hydroxyl radical ($^{\bullet}OH$), chlorine (Cl_2), ozone (O_3) and sulfate radical ($SO_4^{\bullet-}$) can be electrogenerated at the anode (eqn (9.1)–(9.4)) during electrochemical processes, while hydrogen peroxide (H_2O_2) can be electrogenerated from cathodic oxygen (O_2) reduction at the cathode (eqn (9.5)).[3–6] These electrogenerated species can then participate in reactions leading to pollutant removal. For example, the electrogenerated H_2O_2 can react with ferrous ion (Fe^{2+}) *via* the Fenton reaction (eqn (9.6)–(9.7)) to generate $^{\bullet}OH$ for pollutant oxidation.[7,8] Major advantages of

Chemistry in the Environment Series No. 8
Advanced Ozonation Processes for Water and Wastewater Treatment: Active Catalysts and Combined Technologies
Edited by Hongbin Cao, Yongbing Xie, Yuxian Wang and Jiadong Xiao

Published by the Royal Society of Chemistry, www.rsc.org

electrochemical technologies include mild reaction conditions, the use of clean electricity as an energy source, easy operation and automation. Therefore, electrochemical technologies have been widely applied to abate organic pollutants, such as phenols, dyes and pharmaceuticals, in water and wastewater treatment.[1,9–14]

$$H_2O \rightarrow {}^{\bullet}OH + H^+ + e^- \quad (9.1)$$

$$2Cl^- \rightarrow Cl_2 + 2e^- \quad (9.2)$$

$$3H_2O \rightarrow O_3 + 6H^+ + 6e^- \quad (9.3)$$

$$SO_4{}^{2-} \rightarrow SO_4{}^{\bullet -} + e^- \quad (9.4)$$

$$O_2 + 2H^+ + 2e^- \rightarrow H_2O_2 \quad (9.5)$$

$$H_2O_2 + Fe^{2+} \rightarrow Fe^{3+} + {}^{\bullet}OH + OH^- \quad (9.6)$$

$$Fe^{3+} + e^- \rightarrow Fe^{2+} \quad (9.7)$$

However, for the practical implementation of electrochemical processes, some limitations still need to be improved.[15] Due to the development of the stagnant boundary layer at the electrode surface, direct electron transfer is often limited by the mass transfer of pollutants to the electrode surface during the electrochemical process. This limitation results in slow kinetics, low current efficiency and high energy consumption for pollutant abatement by electrolysis. To improve the process efficiency, electrodes with high electrocatalytic activity and good stability (*e.g.* boron-doped diamond (BDD)) are desired. Nevertheless, these potent electrodes are expensive (*e.g.* 12 000–18 000€ m^{-2} for BDD) and thus hardly applicable for large-scale applications.[16] Moreover, the formation of chloride-derived oxidation by-products (OBPs), *e.g.* chlorate, perchlorate and chlorinated organics, is also a major concern of electrochemical processes since chloride is ubiquitously present in all water matrices at concentrations of $mg\,L^{-1}$ to $g\,L^{-1}$.[17–22] Due to their toxicity and harmful effects on human health and ecosystems, these chloride-derived OBPs are strictly regulated in drinking water standards and/or wastewater discharge standards in many countries and should be effectively mitigated during electrochemical treatment.[23,24]

To enhance water treatment performance, electrochemical processes have been increasingly integrated with other technologies such as coagulation, membrane, ultraviolet (UV) and sonication.[1,25–29] Among these hybrid processes, the combination of electrochemical processes with ozonation (referred to as electrocatalytic ozonation hereafter) has shown great synergy and thus has been considered a promising alternative to the conventional electrochemical process for water and wastewater treatment.[30–36]

The first study on ozone electrochemistry dates back to the late 1960s, during which Johnson *et al.* investigated the reaction mechanism of electrochemical reduction of O_3 in acid media (eqn (9.8)).[37] In the following decades, studies mainly focused on the cathodic reduction of O_3 in acid or alkaline electrolytes.[38–40] In 2005, the research group of Kishimoto proposed

electrolysis–ozonation technology by combining ozonation with single electrolysis for water treatment.[33] During the electrolysis–ozonation treatment, metal electrodes (*e.g.* stainless steel and titanium) are used as the cathode, and the reduction of O_3 ($E^0 = 2.07$ V *versus* SHE) to $^{\bullet}O_3^-$ at the cathode can lead to the more powerful oxidant $^{\bullet}OH$ ($E^0 = 2.80$ V *versus* SHE, eqn (9.9) and (9.10)). Therefore, the electrolysis–ozonation process considerably enhanced the removal of O_3-refractory pollutants such as 1,4-dioxane and *p*-chlorobenzoic acid (*p*-CBA).[32,33,41–46] However, it was also found that when current density at the cathode exceeded 10 mA cm^{-2}, the electroreduction of O_3 to $^{\bullet}O_3^-$ (eqn (9.9)) would be limited by O_3 mass transfer, which decreases the efficiency of $^{\bullet}OH$ generation and pollutant degradation by the process.[33] Moreover, the electrolysis–ozonation process generates considerable amounts of potentially carcinogenic bromate during the treatment of bromide-containing water, which is undesired in water and wastewater treatment.[47]

$$O_3 + 2H^+ + 2e^- \rightarrow O_2 + H_2O \quad (9.8)$$

$$O_3 + e^- \rightarrow {}^{\bullet}O_3^- \quad (9.9)$$

$$^{\bullet}O_3^- + H_2O \rightarrow {}^{\bullet}OH + O_2 + OH^- \quad (9.10)$$

To overcome the drawbacks of the electrolysis–ozonation process, Wang's research group developed a novel electro-peroxone (E-peroxone) process by combining ozonation with *in situ* generation of H_2O_2 from cathodic O_2 reduction (eqn (9.5)) in 2013 (see Figure 9.1).[48] Unlike the electrolysis–ozonation process, the E-peroxone process uses carbon-based cathodes to electrogenerate H_2O_2 from O_2 present in excess in ozone-based processes.[49–51] The *in situ* generated H_2O_2 can then diffuse into the bulk solution and react with dissolved O_3 *via* the peroxone reaction to yield $^{\bullet}OH$ (eqn (9.11)) in the bulk solution, which avoids the mass transfer limitation of pollutants on their degradation during electrolysis.[30,31,52–54] Furthermore, the *in situ* generated H_2O_2 can quickly reduce hypobromite (BrO^-) and hypochlorite (ClO^-) to bromide (Br^-, eqn (9.12)) and chloride (Cl^-,

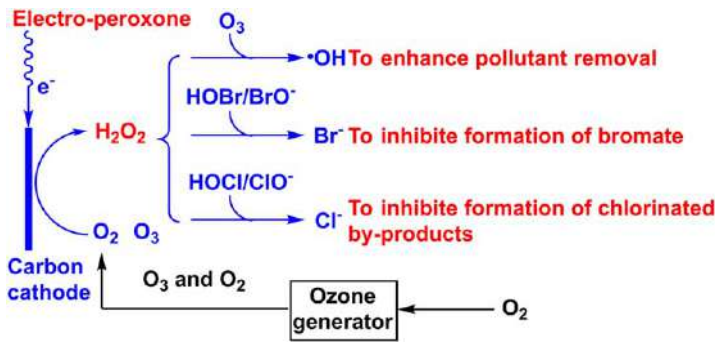

Figure 9.1 Schematic of the E-peroxone process.

eqn (9.13)), respectively.[17,18,55] Therefore, the E-peroxone process can effectively inhibit the formation of bromide- and chloride-derived harmful by-products (*e.g.* bromate and chlorinated organics),[18,47] which has been a major concern associated with ozone-based and electrochemical processes for water and wastewater treatment.[19,56] These promising results demonstrate that the E-peroxone process can overcome the main drawbacks of conventional ozone-based and electrochemical processes and thus offer a superior electrochemical advanced oxidation process (EAOP) for water and wastewater remediation.[30,31,54]

$$2O_3 + 2H_2O_2 \rightarrow {}^{\bullet}OH + HO_2^{\bullet} + 3O_2 + H_2O \tag{9.11}$$

$$BrO^- + H_2O_2 \rightarrow H_2O + O_2 + Br^- \quad k = 7.6\times10^8\ M^{-1}\,s^{-1} \tag{9.12}$$

$$ClO^- + H_2O_2 \rightarrow H_2O + O_2 + Cl^- \quad k = 3400\ M^{-1}\,s^{-1} \tag{9.13}$$

Because of its outstanding performance, the E-peroxone process has attracted increasing attention worldwide and been tested for various treatment purposes, *e.g.* the degradation of refractory organic pollutants (*e.g.* dyes, oxalate, diuron, and diethyl phthalate),[22,48–50,53,57–69] abatement of emerging contaminants (ECs, *e.g.* pharmaceuticals, pesticides, biocides, and tastes and odors),[21,31,70–86] control of harmful OBPs (*e.g.* perchlorate, bromate, chlorinated organics and polymers),[17,18,47,85,87,88] regeneration of spent activated carbon,[74,89–92] and reduction of bacteria and antibiotic resistance genes.[86,93,94] Furthermore, the E-peroxone process has been increasingly integrated with other technologies (*e.g.* UV and membrane) to enhance water treatment performance, develop more effective processes for specific applications (*e.g.* industrial wastewater treatment) and extend the application areas.[6,34–36,60,70,71,74,86,93,95–101] Simultaneously with the lab-scale investigations, efforts have been devoted to scale up the E-peroxone process for practical applications. In 2018, a pilot-scale E-peroxone system with a treatment capacity of 3 $m^3\,d^{-1}$ was developed and tested for micropollutant abatement in drinking water and municipal wastewater.[102] In addition, demonstration-scale E-peroxone equipment that could process ~200 m^3 of wastewater per day has been established for advanced wastewater treatment in full-scale facilities in 2020. These observations indicate that the E-peroxone process has emerged as an excellent alternative to the conventional AOPs for water and wastewater treatment and is now under fast development toward real applications.

This chapter aims to describe the mechanisms of electrocatalytic ozonation, review its recent progress, discuss the challenges that need to be overcome for its practical applications, and identify its niche applications in water and wastewater treatment systems. The main focus has been placed on the E-peroxone process because of its great potential for practical water and wastewater treatment applications.

9.2 Mechanisms of Electrocatalytic Ozonation

9.2.1 Mechanisms of •OH Generation

During conventional ozonation, •OH are mainly generated from natural O_3 decomposition with •OH-generating water constituents, *e.g.* electron-rich aromatic components of dissolved organic matter (DOM).[103,104] The •OH yield (moles of •OH generated per mole of O_3 consumed) from natural O_3 decomposition is only ~10%–30% during conventional ozonation of natural water and wastewater.[81,104] To enhance the •OH yield for efficient abatement of ozone-resistant pollutants, ozonation can be combined with electrochemical processes (*i.e.* electrocatalytic ozonation) to enhance the transformation of O_3 to •OH.[30]

Depending on the materials used to make the cathode, which plays a determining role in the mechanisms of •OH formation, electrocatalytic ozonation can be generally classified into two categories: (1) the electrolysis–ozonation process[33] and (2) the E-peroxone process.[48] During the electrolysis–ozonation process, metal (*e.g.* stainless steel) electrodes are used as the cathodes. Compared with conventional ozonation, the electrolysis–ozonation process can enhance •OH formation *via* two pathways: (1) O_3 decomposition under the high local pH near the cathode and (2) cathodic O_3 reduction to $^{\bullet}O_3^-$ (eqn (9.9)),[90] which then gives rise to •OH (eqn (9.10)).[33,104] Nevertheless, because the reaction of O_3 with OH^- is relatively slow ($k = 70\ M^{-1}\,s^{-1}$),[105] the contribution of pathway (1) to •OH generation can typically be neglected during electrocatalytic ozonation.[104] For instance, Kishimoto *et al.* reported that pathway (1) contributed only 0.1% to the enhanced •OH formation during the electrolysis–ozonation process, while pathway (2) contributed 99.9%.[33]

It should be noted that in parallel with cathodic O_3 reduction to $^{\bullet}O_3^-$, O_3 can also be reduced to O_2 at the cathode (eqn (9.14)).[37] Because the standard potentials of reactions (9.9) and (9.14) are nearly the same (1.23 V *versus* NHE and 1.25 V *versus* NHE, respectively), it has been estimated that the two reactions will proceed simultaneously at similar rates at the cathode.[33] Consequently, only about 50% of the O_3 reduced at the cathode can lead to •OH, while the other 50% is wasted to generate O_2. This is a considerable waste of energy as electricity is consumed to produce O_3 from O_2 feed gas in ozone generators and then consumed again to reduce O_3 back to O_2 at the cathode.[31]

$$O_3 + H_2O + 2e^- \rightarrow O_2 + 2OH^- \tag{9.14}$$

Unlike the electrolysis–ozonation process, the E-peroxone process uses carbon-based materials as the cathodes, *e.g.* carbon black,[34,35,48,57,59,78–81,101] carbon fiber,[50,52,91,92,94,106,107] graphite or graphite fiber,[65,66,86,93] vitreous carbon[49,71] and carbon nanotubes.[51,74,82,84] In contrast to metallic cathodes, where the oxygen reduction reaction (ORR) proceeds *via* the four-electron reduction pathway to H_2O (eqn (9.15)), carbon-based cathodes favor the two-electron ORR pathway to H_2O_2 (eqn (9.16)).[108,109] The reaction of H_2O_2 with O_3

(eqn (9.11)) can produce •OH with a yield of ~50%, which is considerably higher than those from natural O_3 decomposition in water. Thus, by utilizing O_2 that is always available at high concentrations in ozone-based processes to produce H_2O_2, the E-peroxone process can substantially enhance the •OH production from O_3 decomposition compared to conventional ozonation, especially during the treatment of water matrices that have insufficient •OH-generating moieties (*e.g.* electron-rich aromatic components).[81]

During the E-peroxone process, other reactions may occur simultaneously with ORR at the cathode, *e.g.* further reduction of electrogenerated H_2O_2 to H_2O (eqn (9.17)), hydrogen (H_2) evolution (eqn (9.18)) and O_3 reduction (eqn (9.9) and (9.14)).[52] These side reactions will decrease the current efficiency of H_2O_2 electrogeneration and thus should be minimized during the E-peroxone process.[52,110] Fortunately, carbon materials generally have a low catalytic activity for H_2O_2 decomposition and high overpotentials for hydrogen (H_2) evolution.[7,50,52] Therefore, the side reactions of H_2O_2 reduction (eqn (9.17)) and H_2 evolution (eqn (9.18)) are generally negligible at the carbon-based cathodes when sufficient O_2 is available in the cathode diffuse layer to accept the electrons transferred at the cathode.[52] Furthermore, by optimizing applied currents and O_3 doses, cathodic O_3 reduction can be controlled under mass-transfer limited conditions.[52] Under such conditions, O_3 reduction will be a negligible cathodic reaction as compared with ORR to H_2O_2.[52] Overall, the results of previous studies have demonstrated that by carefully selecting electrodes and optimizing the reaction conditions, side reactions such as H_2O, H_2O_2 and O_3 reduction can be minimized at the cathode, thus allowing H_2O_2 to be efficiently produced during the E-peroxone process.

$$O_2 + 2H_2O + 4e^- \rightarrow 4OH^- \tag{9.15}$$

$$O_2 + H_2O + 2e^- \rightarrow HO_2^- + OH^- \tag{9.16}$$

$$HO_2^- + H_2O + 2e^- \rightarrow 3OH^- \tag{9.17}$$

$$2H_2O + 2e^- \rightarrow H_2 + 2OH^- \tag{9.18}$$

Once electrogenerated at the cathode, H_2O_2 can diffuse into the bulk solution and then react with dissolved O_3 *via* the peroxone reaction to yield •OH (eqn (9.11)).[52,53,104] The second-order rate constant for the reaction of O_3 with H_2O_2 is pH dependent (eqn (9.19)) and approximately 150–4800 $M^{-1}\,s^{-1}$ within the typical pH range (7–8.5) of water and wastewater treatment. Therefore, electrogenerating H_2O_2 can remarkably accelerate the transformation of O_3 to •OH during the E-peroxone process.

$$k_{obs} = k_{\left(HO_2^- + O_3\right)} \times 10^{\left(pH - pK_a\right)} \tag{9.19}$$

where $k_{\left(HO_2^- + O_3\right)}$ is the second-order rate constant of HO_2^- with O_3, k_{obs} is the obvious second-order rate constant of the peroxone reaction at different pH, and the pK_a of H_2O_2 is 11.8.

9.2.2 Mechanisms of Pollutant Abatement

During electrocatalytic ozonation, pollutants can be abated *via* mainly three mechanisms: anodic oxidation, O_3 oxidation and $^{\bullet}OH$ oxidation.[81] Therefore, the kinetics of pollutant abatement can usually be reasonably simulated using the chemical kinetic model of eqn (9.20).[33,81]

$$-\frac{d[P]}{dt} = k_{O3}[O_3][P] + k_{\bullet OH}[^{\bullet}OH][P] + k_E[P] \quad (9.20)$$

where k_{O3} and $k_{\bullet OH}$ are the second-order rate constants of pollutant [P] with O_3 and $^{\bullet}OH$, respectively; k_E is the pseudo first-order rate constant during single anodic oxidation; $[O_3]$ and $[^{\bullet}OH]$ are the concentration of O_3 and $^{\bullet}OH$ in the treatment system.

Several studies have shown that due to the mass transfer limitation of pollutants to the electrode surface, the rate of pollutant abatement by anodic oxidation is usually significantly slower than that by O_3 and/or $^{\bullet}OH$ oxidation.[31,81] Thus the contribution of anodic oxidation to pollutant abatement can typically be neglected during electrocatalytic ozonation.[33,53,79] In addition, the results indicate that for pollutants with high ozone reactivity (*e.g.* $k_{O3} \geq 1000\ M^{-1}\ s^{-1}$), they are mainly abated by the direct oxidation with O_3 during electrocatalytic ozonation, whereas pollutants with low ozone reactivity (*e.g.* $k_{O3} \leq 100\ M^{-1}\ s^{-1}$) are primarily abated by $^{\bullet}OH$ oxidation (see Figure 9.2).

Due to the higher $^{\bullet}OH$ yield from O_3 decomposition with H_2O_2 (~50%) than with $^{\bullet}OH$-generating water constituents, *e.g.* 24–43% for phenols, 8–17% for alkoxybenzenes, 15% for tertiary amine and 28–30% for anilines,[81,85,111,112] more $^{\bullet}OH$ can be produced from the same O_3 dose during the E-peroxone process than during conventional ozonation. Therefore, the adaption of conventional ozonation to the E-peroxone process can usually increase the abatement efficiencies of ozone-resistant pollutants during water and wastewater treatment (see Figure 9.2).

9.3 Cathode Studies During the E-peroxone Process

9.3.1 Cathode Materials

Electrogenerating H_2O_2 efficiently and stably at the cathodes is vital for the E-peroxone process.[31,113] Due to their abundance, low cost, high selectivity for two-electron ORR to H_2O_2, nontoxicity and other favorable properties, carbonaceous materials are the most commonly used electrocatalysts for H_2O_2 production in electrochemical processes for water treatment, *e.g.* the electro-Fenton and electro-peroxone processes.[7,27,31,114,115] A variety of carbon-based electrodes have been tested in the E-peroxone process for water treatment, for example carbon black-polytetrafluoroethylene (carbon-PTFE),[34,35,48,57,59,78–81,101] carbon fiber (CF),[50,52,91,92,94,106,107] graphite,[65,66,86,93] reticulated vitreous carbon (RVC)[49,71] and carbon nanotube (CNT).[74,82,116] They generally showed good stability and catalytic activity for H_2O_2 production. In addition, the

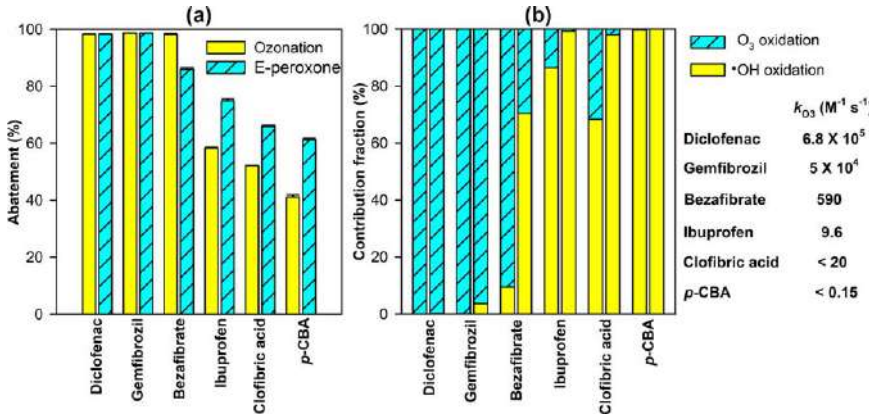

Figure 9.2 (a) Abatement of pharmaceuticals with different O_3 reactivities. (b) Contribution fraction of O_3 and $^{\bullet}OH$ oxidation to pharmaceutical abatement during ozonation and the E-peroxone process. Reaction conditions: groundwater, 150 $\mu g\,L^{-1}$ for each pharmaceutical, solution volume = 250 mL, specific O_3 dose = 1.5 mg O_3 (mg DOC)$^{-1}$, and current = 30 mA for E-peroxone. Reproduced from ref. 81 with permission from Elsevier, Copyright 2018.

results show that electrodes with higher electrocatalytic activity for H_2O_2 generation can usually achieve better pollutant removal performance during the E-peroxone process.[49,116] Therefore, carbon-PTFE electrodes, which usually show the highest current efficiency for H_2O_2 generation among the various carbon-based electrodes, are currently the most used cathodes in the E-peroxone process.

To further enhance $^{\bullet}OH$ generation, several researchers have recently tested modifying carbon-based electrodes (*e.g.* CNT) with ferrite, copper ferrite and nitride materials to induce catalytic O_3 decomposition and/or Fenton-like reactions during the E-peroxone process.[61,63,82,84] For instance, Guo *et al.* composited different kinds of graphitic carbon nitride materials with a multi-wall CNT (*e.g.* C_3N_4/CNT and C_3N_4-Mn/CNT).[61,63] Results show that because of the high pyrrolic-N content modified on the CNT surface and its high surface area, the C_3N_4/CNT composite exhibited relatively high activity for catalytic ozonation. Meanwhile, the high electron transfer ability of C_3N_4/CNT benefited the electroreduction of both O_2 and O_3 during the E-peroxone process.[61] In addition, Mn coordinated with nitrogen was deduced to be the active site for the peroxone reaction. Therefore, the use of C_3N_4-Mn/CNT composite as a heterogeneous catalyst in the E-peroxone process substantially promoted the peroxone reaction and pollutant removal in acid solution.[63]

9.3.2 Cathode Configuration

For the E-peroxone process, the carbon-based electrodes are conventionally used in two general setups: (1) submerged and aerated electrode (SAE) and

(2) gas diffusion electrode (GDE), which differs mainly in the way of oxygen supply.[48,113] The SAEs are directly submerged in the water where an O_2 and O_3 gas mixture (*i.e.* ozone generator effluent) is aerated. O_2 in the aerated gas is first dissolved in the solutions and then transferred from the bulk solution to the cathode surface, where it is reduced to H_2O_2.[48] In contrast, the GDEs are usually assembled electrodes that consist of a carbon-based electrode (typically carbon-PTFE), gas chamber, gaskets and other parts. During the E-peroxone process, O_2 is first fed to the gas chamber, and then it diffuses through the porous carbon-PTFE structure to the other side of the electrode in contact with electrolytes, where it reacts with H^+/H_2O and electrons to form H_2O_2.[113] In contrast to the SAEs, which can directly exploit O_2 in the aerated ozone generator effluent to produce H_2O_2, the GDEs require an extra oxygen source (*e.g.* O_2 in the off-gas of the ozone contactor). Moreover, the operation of GDEs is more complicated than that of SAEs. For example, the gas pressure and flow rates have to be carefully managed to prevent water flooding of the GDE cell.[113,117] Overall, because of the effective oxygen transfer in GDEs, high current densities can be applied to accelerate H_2O_2 production during electrolysis with the GDE cathodes; the current efficiencies for H_2O_2 production are usually higher than 85%.[34,101,113] Nevertheless, more studies are still needed to improve the GDE design and gas–water management for stable operation in long-term applications.

Compared with the GDEs, the SAEs have a simpler configuration and are easier to operate. Therefore, they are currently the most commonly used electrode setup in the E-peroxone process.[31] Nevertheless, due to the low solubility of O_2, the rate of H_2O_2 production is prone to be limited by the mass transfer of dissolved O_2 (DO) to the ORR active sites of SAE cathodes.[7,52] To enhance oxygen mass transfer, carbonaceous materials with large surface area (*e.g.* CF and RCV) can be used to make the SAE cathode.[49,50] In addition, our recent study shows that when superaerophilic electrodes (*e.g.* carbon-PTFE) are used as the SAEs, they can directly adsorb oxygen microbubbles aerated in the water, which greatly enhances oxygen mass transfer compared with DO diffusion.[118] Therefore, relatively high current densities (*e.g.* 10–20 $mA\,cm^{-2}$) can be applied to accelerate H_2O_2 production during the E-peroxone process with carbon-PTFE cathodes.[53]

In addition to the conventional GDEs and SAEs, flow-through electrodes made of porous carbon materials (*e.g.* graphite felt and RVC) have recently been used for the E-peroxone process.[71,86] During the treatment, a mixed stream of water and O_2/O_3 gas is forced to pass through the flow-through electrodes. Due to the favorable mass transport conditions inside the porous structure of the electrodes, large amounts of H_2O_2 can be efficiently electrogenerated from ORR to enhance O_3 transformation to $^{\bullet}OH$.[71] Consequently, the flow-through E-peroxone process can considerably increase the abatement efficiency of ozone-resistant pollutants (*e.g.* ibuprofen) compared to conventional ozonation.[71,119] In addition, the flow-through E-peroxone process has been shown to be an effective way of disinfection due

to the synergy of the different microbial inactivation mechanisms (*e.g.* O_3 disinfection, $^{\bullet}OH$ oxidation and electrochemical disinfection).[86]

9.3.3 Cathode Stability

For practical applications, the electrodes must be able to maintain high stability over long-term operation and varying conditions. Due to the strong oxidizing conditions in the E-peroxone system, the concern was that the carbon-based cathodes might be progressively oxidized by the oxidants introduced into or generated within the system (*e.g.* O_3, H_2O_2 and $^{\bullet}OH$). However, the results of several studies have suggested that because of the net electrons accumulated on the cathode surface upon cathodic polarization, the oxidation of carbon-based cathodes is usually insignificant during the E-peroxone process.[91,92,106,113] Nevertheless, the formation of mineral scale (*e.g.* $CaCO_3$(s)) on the cathode surface may gradually decrease the electrode efficiency for H_2O_2 production during long-term operation.[113] For instance, a recent study shows that during electrochemical H_2O_2 production in groundwater, calcium ions continuously precipitated on the cathode surface due to the high local pH of the cathode. Because of the covering of the cathode surface by the precipitations, the current efficiencies of H_2O_2 production decreased gradually from ~95% to ~80% over the 1000 h operation, while energy consumption increased from ~8.3 to 9.8 kW h kg^{-1} H_2O_2 (see Figure 9.3).[113] Moreover, the precipitation of $CaCO_3$ reduced the hydrophobicity of the carbon-PTFE electrode. As a result, water began to penetrate the GDE into the gas chamber after ~1000 h, resulting in a quick deterioration of H_2O_2 production performance in the following 4 days.[113]

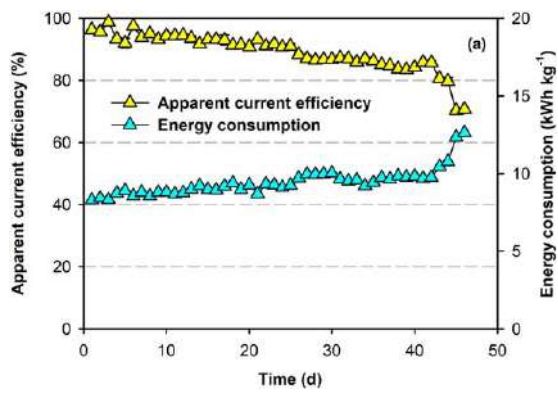

Figure 9.3 Evolution of apparent current efficiency and energy consumption during electrochemical H_2O_2 production with a GDE cathode. Reaction conditions: water flow rate = 20 mL min^{-1}, hydraulic residence time = 20 min, electrolyte = 0.1 M Na_2SO_4, and current density = 40 mA cm^{-2}. Reproduced from ref. 113 with permission from Springer Nature, Copyright 2021.

Overall, although several studies have already evaluated the stability of carbon-based electrodes for H_2O_2 production and pollutant removal during the E-peroxone process, the time frame of most studies is usually just several to several tens of hours, which is too short a period to draw convincing conclusions on the long-term stability of the cathodes for practical applications. Additional studies are needed to assess the long-term stability of the electrodes under varying operation conditions.

9.4 Water and Wastewater Treatment by the E-peroxone Process

9.4.1 Removal of Organic Pollutants

The E-peroxone process has been applied to abate a broad range of organic pollutants in various water matrices, including industrial chemicals, pesticides and herbicides, pharmaceuticals and personal care products, taste and odor compounds, and natural organic matter in drinking water, municipal wastewater, and industrial wastewater.[30,31,54] In general, the E-peroxone process shows high kinetics and energy efficiency for the abatement of the various pollutants. The results of representative studies are summarized in Table 9.1.

During the E-peroxone process, pollutants with high and moderate O_3 reactivity can be efficiently abated by direct O_3 oxidation, whereas pollutants with low O_3 reactivity are mainly abated by $^{\bullet}OH$ oxidation.[81] Due to the enhanced $^{\bullet}OH$ production from H_2O_2-induced O_3 decomposition, higher abatement efficiencies can usually be obtained for O_3-resistant pollutants during the E-peroxone process compared to conventional ozonation. In addition, compared with other conventional ozone-based AOPs (*e.g.* the UV/O_3 process), the E-peroxone process consumes significantly less amounts of energy because electrogeneration of H_2O_2 is energy efficient.[80,102] Furthermore, conventional ozonation systems can be easily retrofitted for the E-peroxone process by installing low-cost electrodes in ozone contactors.[47,102] Therefore, the E-peroxone process has been considered an attractive option to upgrade existing ozonation systems to enhance pollutant removal in water and wastewater treatment.

9.4.2 Control of Harmful Oxidation By-products

A prominent advantage of the E-peroxone process is that it can substantially reduce the formation of bromide- and chloride-derived harmful by-products (*e.g.* bromate, perchlorate and chlorinated organics) during water and wastewater treatment compared to conventional ozonation and electrochemical processes (*e.g.* anodic oxidation).[17,18,47,102] Chloride and bromide are two ubiquitous halide ions in various water matrices.[120] During ozone-based and electrochemical AOPs, chloride and bromide can be chemically or electrochemically oxidized to hypochlorite and hypobromite, which can then react

Table 9.1 Applications of the E-peroxone process for water and wastewater treatment (an updated literature review since 2018).

Research objects	Cell configuration	Reaction conditions	Major results
Removal of refractory pollutants in industrial wastewater			
Phenol[50]	Semi-batch reactor with continuous O_3/O_2 sparging, polyacrylonitrile-based carbon fiber cathode, and Ti/IrO_2 anode	Volume = 1 L, $[Na_2SO_4] = 0.1$ M, $[phenol]_0 = 200\ mg\ L^{-1}$, current = 400 mA, gaseous O_3 concentration = $90\ mg\ L^{-1}$, and gas flow rate = $0.4\ L\ min^{-1}$	After 30 cycles of the E-peroxone treatment (2 h per cycle), the carbon fiber cathode kept efficient on H_2O_2 electrogeneration, and complete phenol mineralization can be stably maintained.
Phenol[101]	Batch reactor with *in situ* generation of O_3 and H_2O_2, CNTs/carbon-PTFE cathode, and nickel-antimony doped tin oxide (NATO) anode	Volume = 200 mL, $[Na_2SO_4] = 0.1$ M, $[phenol]_0 = 200\ mg\ L^{-1}$, and current density = $10\ mA\ cm^{-2}$	O_3 was *in situ* generated at the NATO anode to drive the *in situ* peroxone process. Complete phenol and 95% TOC removal can be achieved, with 35.7% less energy being consumed during the process.
Acid orange 7[65,66]	Continuous circular flow reactor, and graphite as cathode and anode, with electrodes placed in a circular arrangement	$[Na_2SO_4] = 0.1$ M, $[dye]_0 = 500\ mg\ L^{-1}$, pH = 7.7, current = 500 mA, gaseous O_3 concentration = $25\ mg\ L^{-1}$, gas flow rate = $0.8\ L\ min^{-1}$, and water flow rate = $8.5\ L\ min^{-1}$	The E-peroxone process was able to remove 99% of the Acid Orange 7 after 10 min treatment at optimal conditions, with an energy demand of $8\ kW\ h\ kg^{-1}$ dye. After 99 min E-peroxone treatment, TOC and COD were removed by 92% and 99%, respectively.
Diuron[64]	Semi-batch reactor with continuous O_3/O_2 sparging, reticulated vitreous carbon cathode, and Pt anode	Volume = 100 mL, $[Na_2SO_4] = 0.05$ M, $[diuron]_0 = 40\ mg\ L^{-1}$, current = 25 mA, and gaseous O_3 flow rate = $17.4–260\ mg\ L^{-1}\ h^{-1}$	Compared with ozonation, the E-peroxone process can promote the decomposition of O_3 and thus the degradation of diuron.

Table 9.1 (*Continued*)

Research objects	Cell configuration	Reaction conditions	Major results
Leachate concentrates[34]	Batch reactor with *in situ* generation of O_3 and H_2O_2, CNTs/carbon-PTFE GDE cathode, and Ti/SnO_2-Sb_2O_5 anode	Volume = 200 mL, $[TOC]_0 = 246\ mg\,L^{-1}$, and current density = 10–40 $mA\,cm^{-2}$	The *in situ* E-peroxone process can save 17.7%–23.2% energy for effective treatment of leachate concentrates.
Pharmaceutical wastewater[90]	Semi-batch reactor with continuous O_3/O_2 sparging, three-dimensional (3D) electrodes, *i.e.* GAC loaded between metal electrodes	Volume = 500 mL, $[TOC]_0 = 13\,475\ mg\,L^{-1}$, current density = 21 $mA\,cm^{-2}$, gaseous O_3 concentration = 118 $mg\,L^{-1}$, and gas flow rate = 0.4 $L\,min^{-1}$	The combined 3D-ozonation process considerably enhanced TOC removal from 23% and 43% during ozonation and 3D-electrolysis, respectively, to 71% after 6 h treatment.
Oil field fracturing flowback water[125]	Semi-batch reactor with continuous O_3/O_2 sparging, 3D electrodes, *i.e.* GAC loaded between metal electrodes	Volume = 150 mL, $[COD]_0 = 6750\ mg\,L^{-1}$, current = 0–1000 mA, gaseous O_3 concentration = 0–80 $mg\,L^{-1}$, and gas flow rate = 0.15 $L\,min^{-1}$	The combined 3D-ozonation process considerably enhanced COD removal from 17% and 37% during ozonation and 3D-electrolysis, respectively, to 78% after 3 h treatment. COD removal can be stably maintained at >60% after multiple cycles.
Shale gas fracturing flowback water (SGFFW)[36]	Semi-batch reactor with continuous O_3/O_2 sparging, carbon-PTFE cathode, and Al anode	Volume = 150 mL, current = 200–600 mA, gaseous O_3 concentration = 8.25 $mg\,L^{-1}$, and gas flow rate = 0.6 $L\,min^{-1}$	Electrocoagulation was combined with E-peroxone for SGFFW treatment. This process can effectively enhance removal of COD and degradation of intermediates with large and medium molecular weight than individual electrocoagulation.

Shale gas fracturing flowback water (SGFFW)[126]	Divided semi-batch reactor with continuous O_3/O_2 sparging, carbon-PTFE cathode, and Al anode	Volume = 300 mL for each chamber, current = 200–600 mA, for cathode chamber: gaseous O_3 concentration = 20–80 mg L^{-1}, and gas flow rate = 0.5 L min^{-1}	The combined electrocoagulation-E-peroxone (EC-EP) process in divided reactor effectively removed ~95% of SGFFW TOC, with a specific energy consumption of 0.11–0.21 kW h g^{-1} TOC removed, which was more effective and energy-efficient than single EC, EP, and undivided EC-EP processes.
Oxalic acid[63]	Semi-batch reactor with continuous O_3/O_2 sparging, graphite cathode, and Pt anode	Volume = 250 mL, $[\text{oxalic acid}]_0 = 2$ mM, $[Na_2SO_4] = 0.05$ M, pH = 3, current = 20 mA, C_3N_4–Mn/CNT catalyst dosage = 0.1 g L^{-1}, gaseous O_3 concentration = 30 mg L^{-1}, and gas flow rate = 0.1 L min^{-1}	The C_3N_4–Mn/CNT catalyst in the E-peroxone process can obviously enhance oxalic acid removal at acid pH from 15% after 60 min treatment without catalyst to ~100% within 30 min treatment.
Sodium oxalate[61]	Semi-batch reactor with continuous O_3/O_2 sparging, graphite cathode coated with n-C_3N_4/CTN composite and Pt anode	Volume = 250 mL, $[\text{oxalic acid}]_0 = 2$ mM, $[Na_2SO_4] = 0.05$ M, pH = 9, current = 20 mA, gaseous O_3 concentration = 60 mg L^{-1}, and gas flow rate = 0.1 L min^{-1}	The n-C_3N_4/CNT composite during the E-peroxone treatment exhibited the highest efficiency on oxalate degradation.
Nitrobenzene[107,127]	Electrocatalytic membrane contactor (ECMC), composite membrane cathode, and RuO_2/Ti anode	Volume = 120 mL, $[\text{Nitrobenzene}]_0 = 30$ mg L^{-1}, $[Na_2SO_4] = 0.05$ M, current density = 0.4–3 mA cm^{-2}, gaseous O_3 concentration = 0–70 mg L^{-1}, and gas flow rate = 0.02–0.1 L min^{-1}	Electrocatalytic membrane was combined with the E-peroxone to enhance O_2 and O_3 mass transfer. After 120 min treatment, the combined process removed 85% of nitrobenzene, which was much higher than those by membrane contact ozonation and electrolysis (55% and 23%, respectively).

Table 9.1 (*Continued*)

Research objects	Cell configuration	Reaction conditions	Major results
Benzophenone-3[83]	Continuous flow reactor, carbon cloth cathode, Pt anode, and PVDF membrane fixed under cathode	$[Na_2SO_4] = 0.05$ M, river water, $[\text{benzophenone-3}]_0 = 10\ mg\,L^{-1}$, voltage = 0–4 V, inlet O_3 concentration = 0–48.6 $mg\,L^{-1}$, and gas flow rate = 0.2 $L\,min^{-1}$	The E-peroxone process was more efficient than ozonation and electrolysis on pollutant degradation and thus membrane fouling mitigation during the following microfiltration process.
Metanil yellow dye, benzotriazole, 4-chlorophenol, carmoisine and tetracycline[95]	Semi-batch reactor with continuous O_3/O_2 sparging, graphite felt cathode, and Pt anode	Volume = 300 mL, $[Na_2SO_4] = 0.1$ M, $[dye]_0 = 50\ mg\,L^{-1}$, UV density = 1.51 $mW\,cm^{-2}$, current = 100–400 mA, catalyst dose = 20-150 $mg\,L^{-1}$, gaseous O_3 concentration = 11.4–43.7 $mg\,L^{-1}$, and gas flow rate = 0.2 $L\,min^{-1}$	A hybrid photoelectron-peroxone/zero valent ion (PEP/ZVI) process was developed for organic pollutant removal. The PEP/ZVI process was effective for removal of metanil yellow and other contaminants.
Yellow F3R dye, and real field textile wastewater[98]	Semi-batch reactor with continuous O_3/O_2 sparging, graphite cathode, and Ti/TiO_2 anode	Volume = 1 L, $[Na_2SO_4] = 0.1$ M, $[\text{Yellow F3R}]_0 = 50\ mg\,L^{-1}$, pH = 2–9, UV lamp = 6 W, current = 300 mA, gaseous O_3 concentration = 2 $g\,h^{-1}$, and gas flow rate = 12 $L\,min^{-1}$	The PEP process could achieve 97.66% color and 84.64% TOC removal of the dye solution, which were 14 and 1.4 times greater than photolysis and E-peroxone, respectively.
Abatement of ECs from aquatic environment			
Diclofenac, naproxen, gemfibrozil, bezafibrate, ibuprofen, clofibric acid, chloramphenicol, *p*-CBA and bromate[102]	Continuous flow pilot system, carbon-PTFE cathode, and RuO_2/IrO_2-Ti anode	Three real waters (groundwater, surface water, and secondary effluent), water flow rate = 28–113 $L\,h^{-1}$,150 $\mu g\,L^{-1}$ for each EC, $[Br^-] = 150$-180 $\mu g\,L^{-1}$, current = 50–200 mA, and specific	Compared with ozonation, the E-peroxone process can enhance abatement of O_3-refractory ECs by 30–40%, shorten the hydraulic retention time by 50%–75%,

		O_3 dose = 1.0–2.0 mg O_3 mg^{-1} DOC	and reduce energy demand by 10%–50% at optimal reaction conditions. Furthermore, bromate formation was significantly reduced to below the 10 $\mu g\,L^{-1}$ drinking water standard during the E-peroxone process.
Levofloxacin[70]	A filter-press flow cell, 3D air-diffusion cathode (graphite felt and carbon cloth-PTFE), and Ti/IrSnSb-oxide anode	$[Na_2SO_4]$ = 0.05 M, pH = 3, $[TOC]_0$ = 20 mg L^{-1}, water flow rate = 2 L min^{-1}, current density = 20 mA cm^{-2}, gaseous O_3 mass flow rate = 17.5 mg min^{-1}	The E-peroxone achieved 63% removal of TOC with a specific energy consumption of 0.27 kW h $(g\ TOC)^{-1}$.
Thiamethoxam[80]	Semi-batch reactor with continuous O_3/O_2 sparging, carbon-PTFE cathode, and Pt anode	Volume = 780 mL, groundwater and surface water, $[thiamethoxam]_0$ = 500 $\mu g\,L^{-1}$, current = 100 mA, gaseous O_3 concentration = 14 mg L^{-1}, and gas flow rate = 0.35 L min^{-1}	At a transferred O_3 dose of 5 mg L^{-1}, thiamethoxam can be abated by 16–32%, >70%, and 100% from two real waters by ozonation, E-peroxone, and UV/O_3 processes, respectively. The energy demand to abate 90% thiamethoxam was comparable for E-peroxone and ozonation (0.14 ± 0.03 kW h m^{-3}), but higher for UV/O_3 process (0.21–0.22 kW h m^{-3}).
Fluconazole[82]	Semi-batch reactor with continuous O_3/O_2 sparging, CNTs-PTFE cathode, and Pt anode	Volume = 500 mL, $[Na_2SO_4]$ = 0.05 M, $[fluconazole]_0$ = 20 mg L^{-1}, catalyst dose = 0.1–0.8 g L^{-1}, current density = 10–60 mA cm^{-2},	Copper ferrite modified carbon nanotubes ($CuFe_2O_4$/CNTs) were employed as adsorbents/catalysts to

Table 9.1 (*Continued*)

Research objects	Cell configuration	Reaction conditions	Major results
		gaseous O_3 concentration $= 7.2–29.7\ mg\,L^{-1}$, and gas flow rate $= 0.2\ L\,min^{-1}$	assist the E-peroxone treatment, and this can enhance fluconazole removal by ~10% than E-peroxone without catalyst.
Ibuprofen[113]	Continuous flow reactor, carbon-PTFE GDE cathode, and Pt anode	$[Na_2SO_4] = 0.1$ M, groundwater, $[ibuprofen]_0 = 100\ \mu g\,L^{-1}$, current density $= 40\ mA\,cm^{-2}$, gaseous O_3 concentration $= 18.7\ mg\,L^{-1}$, gas flow rate $= 0.25\ L\,min^{-1}$, water flow rate $1.2\ m^3\,d^{-1}$	During a lifetime of 46 days, the GDE cathode can electrogenerate H_2O_2 at high current efficiencies (>70%) with an overall cost of 0.88$ kg^{-1} H_2O_2. The electrogenerated H_2O_2 considerably enhanced ibuprofen removal from 7% during ozonation to 43%-59% during the E-peroxone process.
Ibuprofen[71]	A flow-through E-peroxone reactor, RVC cathode, and $Ti/RuO_2/IrO_2$ anode	$[Na_2SO_4] = 0.05$ M, $[ibuprofen]_0 = 2.5\ mg\,L^{-1}$, current density $= 2.83–14.15\ mA\,cm^{-2}$, gaseous O_3 concentration $= 8\ mg\,L^{-1}$, gas flow rate $= 0.25\ L\,min^{-1}$, water flow rate $30–300\ mL\,min^{-1}$	Ibuprofen removal can be considerably enhanced from 59% and 64% by electrolysis and ozonation to ~100% by the E-peroxone process. At optimal conditions, the energy demand during E-peroxone was only 14.3% of that during ozonation.
5 antibiotics, 7 biocides, and 2 benzotriazoles[78]	Semi-batch reactor with continuous O_3/O_2 sparging,	Volume = 250 mL, synthetic water and secondary wastewater effulent,10 $\mu g\,L^{-1}$ for each EC,	Most of the biocides studied are moderately reactive or non-reactive with O_3, and

	carbon-PTFE cathode, and Pt anode	current = 35 mA, gaseous O_3 concentration = 4.5 mg L^{-1}, and gas flow rate = 0.35 L min^{-1}	the E-peroxone process can accelerate the removal of O_3-refractory ECs than ozonation.
Carbamazepine[35]	Semi-batch reactor with continuous O_2 sparging, carbon-PTFE cathode, and Ti/SnO_2–Sb anode	Volume = 100 mL, [Na_2SO_4] = 0.05 M, [carbamazepine]$_0$ = 10 mg L^{-1}, current density = 30 mA cm^{-2}, and O_2 gas flow rate = 0.1 L min^{-1}	O_3 and H_2O_2 were *in situ* generated at current efficiency of ~7% and ~70%, respectively. Consequently, the removal of carbamazepine and TOC reached 99.8% and 97.6% after 15 and 90 min of *in situ* E-peroxone treatment, respectively, with the treatment efficiencies remaining stable after multiple cycles.
Diclofenac, gemfibrozil, bezafibrate, ibuprofen, clofibric acid and *p*-CBA[79,81]	Batch reactor with addition of O_3 stock solution, carbon-PTFE cathode, and Pt anode	Volume = 250 mL, three real waters (groundwater, surface water, and secondary effluent), 150 μg L^{-1} for each EC, current = 30 mA, and specific O_3 dose = 0.5–1.5 mg O_3 mg^{-1} DOC	Compared with ozonation, abatement efficiencies of O_3-refractory ECs by the E-peroxone process were evidently enhanced in groundwater (up to 14%–18%), moderately enhanced in surface water (up to 6%–10%), and negligibly enhanced in secondary effluent.
Inhibition of harmful or toxic OBPs			
Trichloromethane (TCM), chloroacetic acids (CAAs) and 8 ECs	Semi-batch reactor with continuous O_3/O_2 sparging, carbon-PTFE cathode and RuO_2/IrO_2–Ti anode	Volume = 600 mL, surface water, 150 μg L^{-1} for each EC, [Cl^{-1}] = 100 mg L^{-1}, current density = 1.25–5 mA cm^{-2}, gaseous	Compared with ozonation, the E-peroxone process accelerated the abatement of O_3-refractory ECs.

Table 9.1 (*Continued*)

Research objects	Cell configuration	Reaction conditions	Major results
		O_3 concentration = 7 mg L^{-1}, and gas flow rate = 0.15 L min^{-1}	Meanwhile, formation of TCM and CAAs was significantly mitigated by converting electrolysis to E-peroxone.
Bromate, and 8 ECs[73]	Batch reactor with addition of O_3 stock solution, carbon-PTFE cathode, and Pt anode	Volume = 230 mL, groundwater, 100 μg L^{-1} for each EC, $[Br^-]$ = 176 μg L^{-1}, current = 30 mA, and specific O_3 dose = 0.5–1.5 mg O_3 mg^{-1} DOC	Abatement efficiencies of O_3-refractory ECs were enhanced by ~10%–40%, and bromate formation was considerably reduced by converting ozonation to peroxone or E-peroxone process, with the E-peroxone being a more convenient, flexible and safer operational means than peroxone.
Trihalomethanes, haloacetic acids, bromate, and brominated OBPs[88]	Semi-batch reactor with continuous O_3/O_2 sparging, carbon-PTFE cathode, and RuO_2/IrO_2-Ti anode	Volume = 500 mL, synthetic surface water, $[Cl^{-1}]$ = 51 mg L^{-1}, $[Br^{-1}]$ = 150 μg L^{-1}, current = 90 mA, gaseous O_3 concentration = 7.4 mg L^{-1} and gas flow rate = 0.24 L min^{-1}	Both ozonation and the E-peroxone process substantially reduced the formation of trihalomethanes and haloacetic acids during post-chlorination. Compared to ozonation, the E-peroxone process can effectively suppress bromide transformation to bromate, but it may lead to higher formation of brominated OBPs during post-chlorination.

Reduction of bacteria and ARGs			
ARGs in simulated hospital wastewater[94]	Semi-batch reactor with continuous O_3/O_2 sparging, activated carbon fiber cathode, and Pt anode	Volume = 2 L, simulated hospital wastewater, $[Na_2SO_4] = 0.05$ M, current = 400 mA, gaseous O_3 concentration = 2–5 g h^{-1}, and gas flow rate = 1 L min^{-1}	E-peroxone pre-treatment could largely reduce the numbers and contents of ARGs produced in the following biological treatment unit.
Escherichia coli (*E. coli*) and trihalomethanes (THMs)[93]	Continuous flow reactor, modified graphite felt cathode and dimension stable anode	Water flow rate 7–52.5 mL min^{-1}, simulated ballast water, $[E.\ coli]_0 = 6\times10^3$–$10^7$ CFU mL^{-1}, current = 20–150 mA, and aeration rate = 0.02–0.15 L min^{-1}	The E-peroxone process exhibited higher inactivation of *E. coli* than ozonation and electrolysis, with an energy consumption of 0.12–0.33 kW h m^{-3}. Besides, formation of THMs during the E-peroxone process can meet the WHO drinking water standard.
Escherichia coli (*E. coli*), tetracycline, and trihalomethanes (THMs)[86]	Continuous flow reactor, modified graphite felt cathode and dimension stable anode	Water flow rate 7–52.5 mL min^{-1}, $[Na_2SO_4] = 0.05$ M, $[\text{tetracycline}]_0 = 700$ μg L^{-1}, $[E.\ coli]_0 = 10^3$ CFU mL^{-1}, current = 50 mA, and aeration rate = 0.02–0.11 L min^{-1}	The E-peroxone could achieve simultaneous removal of tetracycline and disinfection, with the disinfection by-products THMs meeting the WHO drinking water standard.

with organics in the water matrix to form toxic chlorinated and brominated organics, *e.g.* trihalomethanes (THMs) and haloacetic acids (HAAs).[19,120] Moreover, hypochlorite and hypobromite can also be further oxidized to higher oxychlorine and oxybromine species, such as chlorate, perchlorate and bromate. Due to their harmful and toxic effects on human health, these chloride- and bromide-derived by-products are strictly regulated in the drinking water standards of many countries, for example 10 $\mu g\,L^{-1}$ for bromate, 80 $\mu g\,L^{-1}$ for THMs, and 60 $\mu g\,L^{-1}$ for HAAs.[23,121,122] Therefore, the formation of bromide- and chloride-derived by-products has been a major concern associated with conventional ozone-based and electrochemical processes, especially for drinking water treatment.

Interestingly, while the E-peroxone process is a combined process of ozonation and electrolysis, it generates insignificant amounts of chloride- and bromide-derived by-products during the treatment of chloride- and bromide-containing water (see Table 9.1).[17,18,47] This improvement can be mainly attributed to the fact that during the E-peroxone process, the *in situ* generated H_2O_2 can quickly reduce hypochlorite and hypobromite back to chloride and bromide (eqn (9.12) and (9.13)),[123,124] thus blocking the formation pathways of higher oxychlorine and oxybromine species, as well as chlorinated and brominated organics.[17,18,47] Consequently, the E-peroxone process can provide a safe AOP option for water and wastewater treatment.

9.4.3 Disinfection and Removal of Antibiotic Resistance Genes (ARGs)

In addition to pollutant abatement, the E-peroxone process can also be used for disinfection in water and wastewater treatment (see Table 9.1).[86,93,94] Recently, Zhang *et al.* (2018) developed a flow-through E-peroxone process by using carbon-PTFE-modified graphite felt as the cathode and perforated DSA electrode as the anode.[93] During water treatment, the flow-through E-peroxone process effectively eliminated tetracycline in the inflow water.[86] Meanwhile, it achieved one order of magnitude higher inactivation of *E. coli* than conventional ozonation and electrolysis, indicating that there is a significant synergy between chemical and electrochemical inactivation for disinfection.[86,93] These results demonstrate that the E-peroxone process can provide an effective method for simultaneous disinfection and pollutant abatement in water treatment.

In addition, the E-peroxone process has been tested as a pretreatment of biological process for the treatment of hospital wastewater.[94] It was found that the E-peroxone pretreatment effectively reduced the numbers and contents of ARGs production in the following sequencing batch reactor (SBR). Consequently, the probability of ARGs proliferation and horizontal gene transfer during biological treatment of hospital wastewater can be largely reduced. Furthermore, the E-peroxone pretreatment increased microbial abundance and reduced functional genus inhibition in the SBR,

which led to enhanced treatment performance and stability of subsequent biological treatment. These results suggest that the E-peroxone process can be used as a viable pretreatment to reduce the risks of ARGs proliferation and to enhance wastewater treatment performance of the biological process.

9.4.4 Pilot-scale Study

In 2018, a pilot-scale E-peroxone system was developed and compared with conventional ozonation and UV/O_3 process for micropollutant abatement and bromate control in drinking water and wastewater treatment (see Figure 9.4).[102] Both the E-peroxone and UV/O_3 processes considerably enhanced the abatement efficiencies of ozone-resistant micropollutants and decreased bromate formation compared with conventional ozonation. However, the E-peroxone process is significantly more energy-efficient than the UV/O_3 process. Due to its high energy efficiency, the E-peroxone process reduced ~10%–50% of the energy consumption that is required to abate the concentrations of micropollutants by ≥90% in the tested water matrices compared to conventional ozonation. In contrast, the UV/O_3 process consumed approximately one order of magnitude higher energy to achieve the same degree of micropollutant abatement. In addition, the E-peroxone process is also more effective at mitigating bromate formation than the UV/O_3 process. Bromate was almost undetected in the effluents of the E-peroxone process but was sometimes detected at concentrations higher than the drinking water standard (10 $\mu g\,L^{-1}$) in the effluents of the UV/O_3

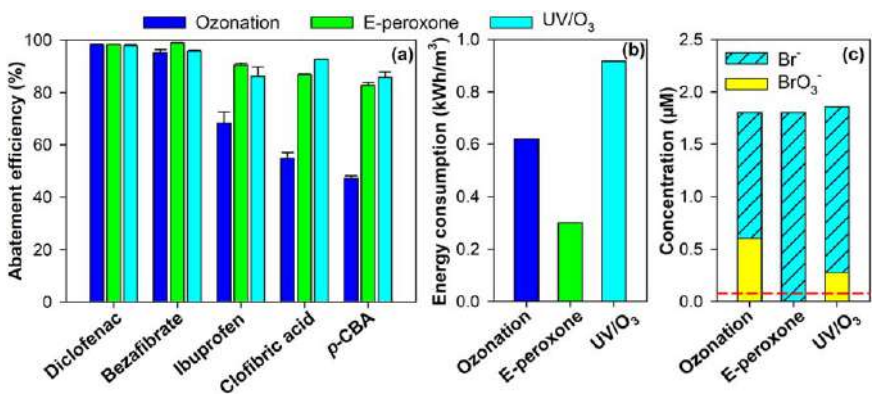

Figure 9.4 (a) Pharmaceutical abatement efficiency. (b) Energy consumption to abate selected pharmaceuticals by ≥90%. (c) Bromate formation during ozonation, E-peroxone and UV/O_3 process at pilot-scale. Reaction conditions: groundwater and 5 min hydraulic residence time for (a) and (b), surface water and 20 min hydraulic residence time for (c), 150 $\mu g\,L^{-1}$ for each pharmaceutical, 150–180 $\mu g\,L^{-1}$ for initial Br^{-1} concentration, specific O_3 dose = 1.5 mg O_3 (mg DOC)$^{-1}$, and current = 150 mA for E-peroxone. Reproduced from ref. 102 with permission from Elsevier, Copyright 2018.

process. Overall, the pilot-scale study confirms the feasibility and superiority of the E-peroxone process for micropollutant abatement and bromate control in water and wastewater treatment.

9.5 Integration of the E-peroxone Process with Other Technologies

To further enhance water and wastewater treatment performance, several research groups have developed novel hybrid processes by integrating the E-peroxone process with other technologies. The recent progress on these hybrid processes is described next.

9.5.1 Combination with UV Photolysis

In 2016, Frangos *et al.* proposed combining the E-peroxone process with UV photolysis and developed the photoelectro-peroxone (PEP) process (see Figure 9.5).[96] During the PEP process, H_2O_2 is electrogenerated at carbon-based cathodes in the same way as during the E-peroxone process (eqn (9.16)). The *in situ* generated H_2O_2 then goes through UV-induced photolysis (eqn (9.21)) and/or the peroxone reaction with O_3 (eqn (9.11)) to yield $^{\bullet}OH$.[96] In addition, UV photolysis of O_3 can also generate $^{\bullet}OH$ (eqn (9.22)).[99,128] Due to the multiple mechanisms of $^{\bullet}OH$ production, the PEP process significantly accelerates pollutant removal compared to the individual ozonation, electrolysis and UV process and their binary combinations. In addition, during the PEP process, pollutants can be degraded by many pathways, including electrochemical oxidation, O_3 and $^{\bullet}OH$ oxidation and UV photolysis. Therefore, the PEP process maintains high and stable pollutant

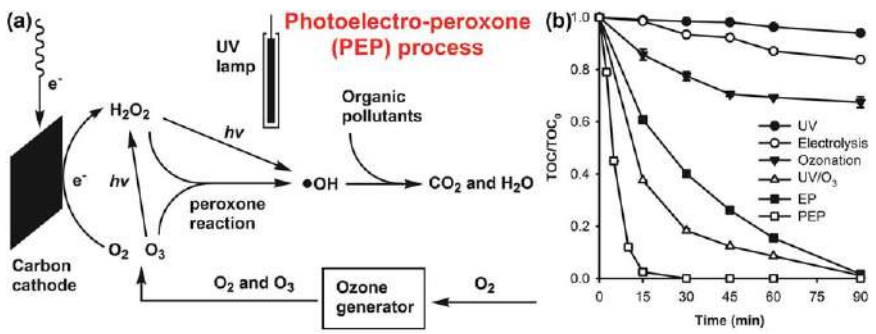

Figure 9.5 (a) Schematic of the photoelectro-peroxone process. (b) TOC mineralization from substituted benzene mixture solution by ozonation, UV, electrolysis, UV/O_3, E-peroxone, and photoelectro-peroxone (PEP) processes. Reaction conditions: 10 mg L^{-1} for initial concentration of nitrobenzene, chlorobenzene and benzaldehyde, solution volume = 700 mL, sparging gas flow rate = 0.25 L min^{-1}, inlet O_3 gas phase concentration = 110 mg L^{-1}, current = 400 mA, and UV fluence rate = 0.87 mW cm^{-2}. Reproduced from ref. 96 with permission from Elsevier, Copyright 2016.

mineralization efficiency under varying conditions that are unfavorable for the other processes.[95–100] The PEP process can thus serve as an effective and robust technology for the treatment of refractory wastewater, especially when other technologies are ineffective.

$$H_2O_2 + h\nu \rightarrow 2^{\bullet}OH \tag{9.21}$$

$$3O_3 + h\nu \rightarrow 2^{\bullet}OH \tag{9.22}$$

9.5.2 Combination with Adsorption

In addition to being used as the electrodes of electrocatalytic ozonation, carbon-based materials are also commonly used as adsorbents in water and wastewater treatment. Therefore, an increasing number of studies in recent years are aimed at combining the E-peroxone and adsorption process.[74,89–92,106] In 2016, Zhan *et al.* tested the regeneration of spent activated carbon fiber (ACF) by the E-peroxone process (see Figure 9.6).[91] After the ACF was saturated with phenolic compounds, it was attached to the carbon-PTFE cathode. The E-peroxone process was then initiated to drive both the cathodic desorption of adsorbed phenols and the bulk oxidation of desorbed phenols simultaneously. The results show that during the E-peroxone regeneration, the preloaded phenols can be quickly desorbed from the ACF and then mineralized by O_3 and $^{\bullet}OH$ oxidation in the bulk solution. The E-peroxone process can thus achieve the goal of adsorbent regeneration and pollutant mineralization simultaneously. In addition, due

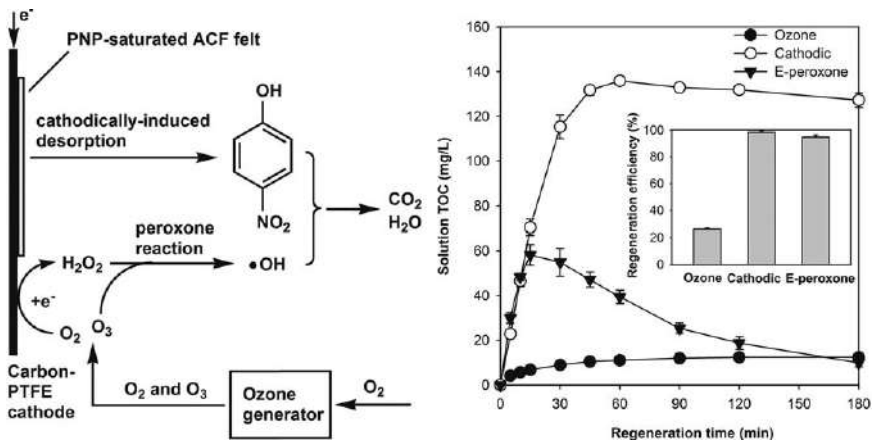

Figure 9.6 (a) Schematic of the E-peroxone regeneration of *p*-nitrophenol (PNP) saturated activated carbon fiber (ACF). (b) TOC evolution and regeneration efficiencies for ozone, cathodic, and E-peroxone regeneration. Reaction conditions: 400 mL of 0.05 M Na_2SO_4 electrolyte, 0.25 g ACF, current = 400 mA, inlet O_3 gas phase concentration = 65 mg L^{-1}, sparging gas flow rate = 0.4 L min^{-1}, and regeneration time = 3 h. Reproduced from ref. 91 with permission from Elsevier, Copyright 2016.

to the cathodic protection effect, the oxidation of ACF by O_3 and $^{\bullet}OH$ is negligible during the E-peroxone regeneration. Therefore, the ACF can retain high adsorption capacity and be reused for many cycles of adsorption and regeneration (see Figure 9.6). Compared with the conventional oxidation-based regeneration processes (*e.g.* ozone regeneration), the E-peroxone process can thus considerably extend the lifetime of ACF for adsorption applications.

9.5.3 Combination with Membrane

To enhance O_3 mass transfer and decomposition to $^{\bullet}OH$, a novel electrocatalytic membrane contactor has recently been designed (Figure 9.7).[107,127] The electrocatalytic membrane is prepared by compositing carbon fiber paper on a PTFE hydrophobic flat sheet membrane. The electrocatalytic membrane is then used to construct the GDE cathode for electrocatalytic ozonation, with the hydrophobic PTFE layer in contact with the gas phase and the catalytic layer of carbon fiber contacting the aqueous solution. During water treatment, an O_3/O_2 gas mixture is fed into the gas chamber of the GDE, which then diffuses through the membrane into the liquid phase. During the diffusion, O_2 in the O_2/O_3 mixture is electroreduced to H_2O_2 (eqn (9.16)), whereas O_3 will pass through the membrane and then react with electrogenerated H_2O_2 in the liquid phase to yield $^{\bullet}OH$ (eqn (9.11)). Due to the enhanced O_3 decomposition by electrogenerated H_2O_2, O_3 mass transfer was increased twofold during the electrocatalytic ozonation process compared to membrane contact ozonation. Consequently, nitrobenzene removal efficiencies were substantially increased from 23% and 55% during individual electrolysis and membrane contact ozonation to 85% during the electrocatalytic ozonation process.[107]

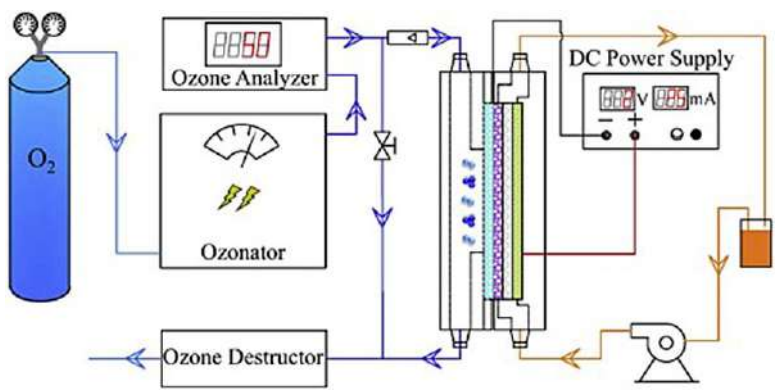

Figure 9.7 Example of combination of membrane with the E-peroxone process. Reproduced from ref. 107 with permission from Elsevier, Copyright 2020.

In addition, the E-peroxone process has been integrated with membrane technologies to mitigate membrane fouling and to enhance pollutant removal during filtration.[83] During microfiltration with the PVDF membrane, a carbon cloth was fixed above the membrane and used as the cathode for the E-peroxone process. Due to the enhanced $^{\bullet}OH$ production and the introduced electrostatic repulsion force, the E-peroxone process mitigated membrane fouling more effectively and resulted in >15% higher fluxes than ozonation and electrolysis. Meanwhile, the removal of benzophenone-3 was also enhanced in the E-peroxone-assisted microfiltration process. These results suggest that electrocatalytic ozonation may offer a viable assistive method for membrane filtration.

9.5.4 Combination with Electrocoagulation

The E-peroxone process has also been combined with electrocoagulation (EC) in different configurations recently (see Figure 9.8).[36,126] In 2019, Kong *et al.* developed a so-called ECP process by combining EC with the E-peroxone process in an undivided electrochemical reactor and tested its performance for organic removal in shale gas fracturing flowback water.[36] During the ECP process, an aluminum (Al) or iron (Fe) anode is used to generate Al^{3+} or Fe^{2+} from anodic oxidation and thus to drive the electrocoagulation process. Meanwhile, a carbon-based cathode is used to produce H_2O_2 from O_2 in the aerated O_2/O_3 gas mixture and thus drive the E-peroxone process. The results show that during the ECP process, high-molecular-weight (HMW) organics in the shale gas fracturing flowback water could be quickly removed by coagulation, while low-molecular-weight (LMW) organics that resist coagulation could be efficiently mineralized by $^{\bullet}OH$ generated in the system. Therefore, the ECP process considerably enhanced organic removal in the fracturing flowback water compared to the individual EC and E-peroxone process.

However, it was also found that, in the undivided reactor, the EC and E-peroxone process can have some negative effects on each other.[126] For

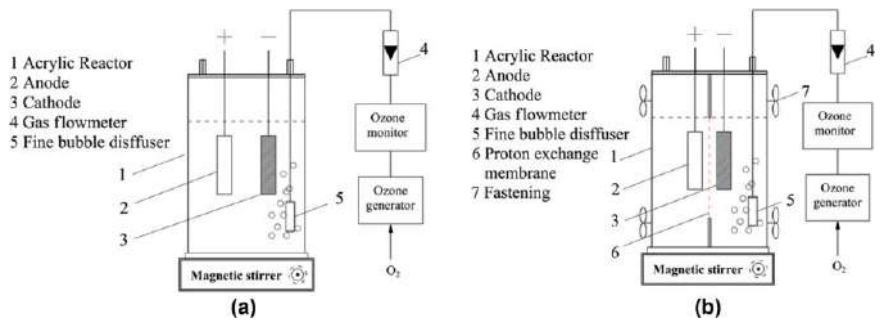

Figure 9.8 Combination of electrocoagulation with the E-peroxone process in (a) undivided and (b) divided reactor.

example, the oxidation of HMW organics by O_3 and $^{\bullet}OH$ consumes a significant fraction of the oxidants and generates smaller and more hydrophilic transformation products that are difficult to be removed by coagulation. To avoid these side effects, Zhang *et al.* proposed to combine the EC and E-peroxone process in a divided reactor as the EC-EP process, where the anodic and cathodic compartments are separated by a cation exchange membrane (Figure 9.8b).[126] During the EC-EP process, wastewater is first treated in the anodic compartment to remove HWM organics by EC. The supernatant from the anode chamber is then further treated in the cathodic compartment to remove LWM organics that resist coagulation by oxidation. The results demonstrate that the EC-EP process can avoid the mutual negative effects of the two processes on each other and thus further improve wastewater treatment performance compared to the previous ECP process. During the EC-EP process, electricity is efficiently utilized to drive both the anodically induced EC and cathodically induced E-peroxone process. In addition, the merit of the EC and E-peroxone process for the removal of HMW and LMW organics is well integrated in the EC-EP process. Therefore, the EC-EP process may provide an energy-efficient and cost-effective way to remove various organic pollutants in real wastewater.

9.6 Challenges and Prospects

9.6.1 Challenges

While many promising results have been reported for the E-peroxone process in laboratory-scale studies, more efforts are still needed for the scale-up of the process for practical applications. In particular, more attention should be paid to overcome the challenges that might be encountered during scaling up the electrodes for large-scale and long-term applications. For example, for practical applications, the rate of H_2O_2 production must be able to meet the required H_2O_2 doses in water and wastewater treatment (see eqn (9.23)). As shown in eqn (9.24), the rate of H_2O_2 production is directly proportional to the applied current density and current efficiency for H_2O_2 production. Therefore, high current density and efficiency are prerequisite for reducing the cathode surface area to construct compact electrochemical reactors for practical applications.

$$r = \frac{D_{H_2O_2} Q_W}{s} \times 10^3 \tag{9.23}$$

$$r = \frac{122400 j \eta}{n F} \tag{9.24}$$

where r is the mass of H_2O_2 produced per unit time and per unit cathode area ($mg\,h^{-1}\,cm^{-2}$), $D_{H_2O_2}$ is the required H_2O_2 dose for water treatment ($mg\,L^{-1}$), Q_W is the flow rate of water that needs to be treated ($m^3\,h^{-1}$), S is

the cathode area (cm^2), j is the current density ($mA\,cm^{-2}$), η is the apparent efficiency for H_2O_2 electrogeneration (%), n is the number of electrons consumed for H_2O_2 production (2 electrons), and F is the Faraday constant ($96\,485\ C\,mol^{-1}$).

Currently, most lab-scale studies on the E-peroxone process employed SAEs for H_2O_2 production because of their simple configuration and operation. However, due to the slow mass transfer of oxygen to SAEs, the rate of H_2O_2 production becomes mass transport limited at relatively low applied current densities (*e.g.* $<10\ mA\,cm^{-2}$).[113,129] Therefore, a large electrode surface area will be needed to produce sufficient H_2O_2 doses when scaling up the E-peroxone process with SAEs for practical applications. For example, it is estimated that with an applied current density of $10\ mA\,cm^{-2}$, at least a $1.6\ m^2$ cathode surface area will be needed to produce $10\ mg\,L^{-1}$ H_2O_2 in a $10\ m^3\,h^{-1}$ water flow (calculated according to eqn (9.23) and (9.24), assuming 100% current efficiency for H_2O_2 production). The requirement for a large electrode surface makes it problematic to construct compact electrochemical reactors for large-scale applications. Therefore, the SAE configuration may be applicable only in small applications, such as decentralized water treatment at a household level.

On the other hand, while GDEs allow higher current densities to be applied to accelerate H_2O_2 production and thus reduce electrode surface area required for water treatment, more studies are needed to evaluate the long-term stability of GDE, especially under conditions simulating real water and wastewater treatment. In a recent (2021) study, Li *et al.* found that the current efficiency of a GDE for H_2O_2 production decreased gradually from initially ~95% to ~85% after 1000 h operation in groundwater. Moreover, water began to penetrate the GDE into the gas chamber after ~1000 h, resulting in flooding of the GDE gas chamber.[113] It has been suggested that this deterioration is probably mainly caused by the continuous precipitation of calcium carbonate on the GED, which decreases the active sites of ORR and the hydrophobicity of the electrode. As a result, water progressively seeps into the pores of GDE under cathodic polarization conditions and eventually penetrates into the gas chamber. These observations suggest that future work should be carried out to investigate the mechanisms and control strategies of electrode fouling and thus extend the lifetime of GDEs for long-term applications.

9.6.2 Prospects

In general, the results obtained to date have clearly demonstrated the superiority and significant potential of the E-peroxone process for water and wastewater treatment. By electrogenerating H_2O_2 during conventional ozonation, the E-peroxone process can improve the overall treatment performance in many aspects, as compared with conventional ozone-based and electrochemical processes. For example, due to the significant $^{\bullet}OH$ production from the reaction of sparged O_3 with electrogenerated H_2O_2, the

E-peroxone process can considerably enhance the abatement kinetics and efficiency of pollutants, especially for ozone-resistant pollutants, compared to conventional ozonation and electrolysis. In addition, the formation of bromate and chlorinated by-products, which is a major concern associated with conventional ozonation and electrochemical processes, respectively, can be effectively inhibited during the E-peroxone process. During the E-peroxone process, H_2O_2 can be electrochemically produced from ORR with generally similar or even lower energy consumption compared to the sales price of H_2O_2 stock solutions. The E-peroxone process can thus not only eliminate the risks associated with the transport and storage of concentrated H_2O_2 stocks but also reduce the operation cost of water and wastewater treatment. Furthermore, the E-peroxone process can be easily retrofitted from conventional ozonation systems that are commonly used in water and wastewater facilities by installing low-cost carbon electrodes. Compared with other conventional ozone-based AOPs (*e.g.* O_3/H_2O_2 and UV/O_3), the E-peroxone process is thus a more convenient and cost-effective way to upgrade existing ozonation systems to enhance the performance of water and wastewater treatment.

As an electricity-driven process, the E-peroxone process is highly flexible and amenable to automation. In addition, during the E-peroxone process, all oxidants (O_3 and H_2O_2) can be produced on site and on demand using O_2 in the air, which avoids the transportation and storage of chemicals. These favorable characteristics make the E-peroxone process particularly suitable for decentralized treatment systems that are expected to be a vital component of future urban water systems. Furthermore, based on the combination of E-peroxone and other technologies, a variety of hybrid processes have been developed recently with the aim of further enhancing treatment performance in specific applications. Therefore, it is expected that the E-peroxone process will play an increasingly important role in future water treatment systems.

Acknowledgements

We appreciate the financial support from the NSFC (National Natural Science Foundation of China) project (51878370) and Tsinghua University–INDITEX Sustainable Development Fund (TISD201906).

References

1. E. Brillas and C. A. Martínez-Huitle, *Appl. Catal., B*, 2015, **166–167**, 603–643.
2. B. P. Chaplin, *Environ. Sci.: Processes Impacts*, 2014, **16**, 1182–1203.
3. C. A. Martínez-Huitle, M. A. Rodrigo and O. Scialdone, in *Electrochemical Water and Wastewater Treatment*, Butterworth-Heinemann, 2018, pp. 183–187.

4. D. Bejan, E. Guinea and N. J. Bunce, *Electrochim. Acta*, 2012, **69**, 275–281.
5. S. Trasatti, *Electrochim. Acta*, 2000, **45**, 2377–2385.
6. R. Amadelli, L. Samiolo, A. De Battisti and A. B. Velichenko, *J. Electrochem. Soc.*, 2011, **158**, P87–P92.
7. E. Brillas, I. Sires and M. A. Oturan, *Chem. Rev.*, 2009, **109**, 6570–6631.
8. P. V. Nidheesh and R. Gandhimathi, *Desalination*, 2012, **299**, 1–15.
9. Y. J. Wang, X. Y. Li, L. M. Zhen, H. Q. Zhang, Y. Zhang and C. W. Wang, *J. Hazard. Mater.*, 2012, **229**, 115–121.
10. S. L. Ambuludi, M. Panizza, N. Oturan, A. Ozcan and M. A. Oturan, *Environ. Sci. Pollut. Res.*, 2013, **20**, 2381–2389.
11. A. Y. Bagastyo, J. Radjenovic, Y. Mu, R. A. Rozendal, D. J. Batstone and K. Rabaey, *Water Res.*, 2011, **45**, 4951–4959.
12. C. Barrera-Díaz, P. Cañizares, F. Fernández, R. Natividad and M. Rodrigob, *J. Mex. Chem. Soc.*, 2014, **58**, 256–275.
13. J. Wang, D. Zhi, H. Zhou, X. He and D. Zhang, *Water Res.*, 2018, **137**, 324–334.
14. X. P. Zhu, S. Y. Shi, J. J. Wei, F. X. Lv, H. Z. Zhao, J. T. Kong, Q. He and J. R. Ni, *Environ. Sci. Technol.*, 2007, **41**, 6541–6546.
15. B. P. Chaplin, in *Electrochemical Water and Wastewater Treatment*, Butterworth-Heinemann, 2018, pp. 451–494.
16. P. Cañizares, A. Beteta, C. Saez, L. Rodriguez and M. Rodrigo, *J. Environ. Eng. Manage.*, 2008, **18**, 183–191.
17. Z. Lin, W. Yao, Y. Wang, G. Yu, S. Deng, J. Huang and B. Wang, *Water Res.*, 2016, **88**, 691–702.
18. W. Yao, J. Fu, H. Yang, G. Yu and Y. Wang, *Water Res.*, 2019, **157**, 209–217.
19. J. Radjenovic and D. L. Sedlak, *Environ. Sci. Technol.*, 2015, **49**, 11292–11302.
20. J. Radjenovic, A. Bagastyo, R. A. Rozendal, Y. Mu, J. Keller and K. Rabaey, *Water Res.*, 2011, **45**, 1579–1586.
21. W. Yao, X. Wang, H. Yang, G. Yu, S. Deng, J. Huang, B. Wang and Y. Wang, *Water Res.*, 2016, **88**, 826–835.
22. Z. X. Li, S. Yuan, C. C. Qiu, Y. J. Wang, X. J. Pan, J. L. Wang, C. W. Wang and J. A. Zuo, *Electrochim. Acta*, 2013, **102**, 174–182.
23. USEPA, *National Primary Drinking Water Regulations: Disinfectants and Disinfection Byproducts-final Rule*, 1998.
24. USEPA, *Interim Drinking Water Health Advisory for Perchlorate*, 2008.
25. D. Haaken, T. Dittmar, V. Schmalz and E. Worch, *Water Res.*, 2014, **52**, 20–28.
26. A. M. Zaky and B. P. Chaplin, *Environ. Sci. Technol.*, 2013, **47**, 6554–6563.
27. P. Frangos, W. H. Shen, H. J. Wang, X. Li, G. Yu, S. B. Deng, J. Huang, B. Wang and Y. J. Wang, *Chem. Eng. J.*, 2016, **291**, 215–224.
28. Y. Zhang, H. Wang, Y. Li, B. Wang, J. Huang, S. Deng, G. Yu and Y. Wang, *Water Res.*, 2020, **183**, 116115.

29. E. Fockedey and A. Van Lierde, *Water Res.*, 2002, **36**, 4169–4175.
30. Y. Wang, *Handb. Environ. Chem.*, 2018, **61**, 57–84.
31. Y. Wang, G. Yu, S. Deng, J. Huang and B. Wang, *Chemosphere*, 2018, **208**, 640–654.
32. N. Kishimoto, Y. Morita, H. Tsun and Y. Yasuda, *Water Environ. Res.*, 2007, **79**, 1033–1042.
33. N. Kishimoto, Y. Morita, H. Tsuno, T. Oomura and H. Mizutani, *Water Res.*, 2005, **39**, 4661–4672.
34. C. Qu, S. Lu, D. Liang, S. Chen, Y. Xiang and S. Zhang, *J. Hazard. Mater.*, 2019, **364**, 468–474.
35. B. Yang, J. Deng, G. Yu, S. Deng, J. Li, C. Zhu, Q. Zhuo, H. Duan and T. Guo, *Electrochem. Commun.*, 2018, **86**, 26–29.
36. F.-X. Kong, X.-F. Lin, G.-D. Sun, J.-F. Chen, C.-M. Guo and Y. F. Xie, *Chemosphere*, 2019, **218**, 252–258.
37. D. C. Johnson, D. T. Napp and S. Bruckenstein, *Anal. Chem.*, 1968, **40**, 482–488.
38. C. Fabjan, *Monatsh. Chem.*, 1975, **106**, 513–528.
39. C. Fabjan, *J. Electroanal. Chem.*, 1977, **76**, 91–99.
40. C. Fabjan and R. Movahedi, *Electrochim. Acta*, 1977, **22**, 185–189.
41. N. Kishimoto and N. Matsuda, *Environ. Sci. Technol.*, 2009, **43**, 2054–2059.
42. N. Kishimoto, T. Matsutani, Y. Yasuda, M. Asano and H. Mizutani, *Ozone: Sci. Eng.*, 2008, **30**, 282–289.
43. N. Kishimoto, T. Nakagawa, M. Asano, M. Abe, M. Yamada and Y. Ono, *Water Res.*, 2008, **42**, 379–385.
44. N. Kishimoto, T. Nakagawa, H. Okada and H. Mizutani, *Ozone: Sci. Eng.*, 2011, **33**, 463–469.
45. N. Kishimoto, Y. Yasuda, H. Mizutani and Y. Ono, *Ozone: Sci. Eng.*, 2007, **29**, 13–22.
46. C. C. Qiu, S. Yuan, X. Li, H. J. Wang, B. Bakheet, S. Komarneni and Y. J. Wang, *J. Hazard. Mater.*, 2014, **280**, 644–653.
47. Y. K. Li, W. H. Shen, S. J. Fu, H. W. Yang, G. Yu and Y. J. Wang, *Chem. Eng. J.*, 2015, **264**, 322–328.
48. S. Yuan, Z. X. Li and Y. J. Wang, *Electrochem. Commun.*, 2013, **29**, 48–51.
49. M. Hou, Y. Chu, X. Li, H. Wang, W. Yao, G. Yu, S. Murayama and Y. Wang, *J. Hazard. Mater.*, 2016, **319**, 61–68.
50. G. Xia, H. Wang, J. Zhan, X. Yin, X. Wu, G. Yu, Y. Wang and M. Wu, *Chem. Eng. J.*, 2020, **396**, 125291.
51. D. Wu, G. Lu, R. Zhang, Q. Lin, Z. Yan, J. Liu and Y. Li, *Environ. Sci. Pollut. Res.*, 2015, **22**, 15812–15820.
52. G. Xia, Y. Wang, B. Wang, J. Huang, S. Deng and G. Yu, *Water Res.*, 2017, **118**, 26–38.
53. H. Wang, S. Yuan, J. Zhan, Y. Wang, G. Yu, S. Deng, J. Huang and B. Wang, *Water Res.*, 2015, **80**, 20–29.
54. O. Turkay, Z. G. Ersoy and S. Barisci, *J. Electrochem. Soc.*, 2017, **164**, E94–E102.

55. U. Von Gunten and Y. Oliveras, *Water Res.*, 1997, **31**, 900–906.
56. U. von Gunten, *Environ. Sci. Technol.*, 2018, **52**, 5062–5075.
57. B. Bakheet, S. Yuan, Z. Li, H. Wang, J. Zuo, S. Komarneni and Y. Wang, *Water Res.*, 2013, **47**, 6234–6243.
58. L. Castaneda, O. Cornejo and J. L. Nava, in *Electrochemical Engineering General Session -and- Characterization of Electrochemical Reactors: Fluid Dynamics and Current Distribution*, 2018, ed. J. A. Staser, D. Riemer and J. L. Nava, 86, 129–138.
59. H. Wang, B. Bakheet, S. Yuan, X. Li, G. Yu, S. Murayama and Y. Wang, *J. Hazard. Mater.*, 2015, **294**, 90–98.
60. X. Li, S. Sun, X. Zhang, G. Liu, C. R. Zheng, J. Zheng, D. Zhang and H. Yao, *Sep. Purif. Technol.*, 2017, **178**, 189–192.
61. Z. Guo, H. Cao, Y. Wang, Y. Xie, J. Xiao, J. Yang and Y. Zhang, *Chemosphere*, 2018, **201**, 206–213.
62. Z. Guo, Y. Xie, Y. Wang, H. Cao, J. Xiao, J. Yang and Y. Zhang, *Chem. Eng. J.*, 2018, **337**, 733–740.
63. Z. Guo, L. B. Zhou, H. B. Cao, Y. B. Xie, J. D. Xiao, J. Yang and Y. Zhang, *Catal. Sci. Technol.*, 2018, **8**, 6241–6251.
64. I. Bavasso, D. Montanaro, L. Di Palma and E. Petrucci, *Electrochim. Acta*, 2020, **331**, 135423.
65. M. Ghalebizade and B. Ayati, *Chemosphere*, 2019, **235**, 1007–1014.
66. M. Ghalebizade and B. Ayati, *Sep. Purif. Technol.*, 2020, **251**, 117350.
67. L. Liu, K. Li, L. Xu, J. Wang, Q. Qin and J. Wang, *Technol. Water Treat.*, 2019, **45**, 89–93, 102.
68. O. Turkay, S. Barisci, B. Ozturk, H. Ozturk and A. Dimoglo, *J. Electrochem. Soc.*, 2017, **164**, E180–E186.
69. O. Turkay, S. Barisci and M. Sillanpaa, *J. Environ. Chem. Eng.*, 2017, **5**, 4282–4290.
70. O. M. Cornejo and J. L. Nava, *Sep. Purif. Technol.*, 2021, **254**, 117661.
71. X. Cui, Z. Lin, H. Wang, G. Yu and Y. Wang, *China Environ. Sci.*, 2019, **39**, 1619–1626.
72. W. Q. Guo, Q. L. Wu, X. J. Zhou, H. O. Cao, J. S. Du, R. L. Yin and N. Q. Ren, *RSC Adv.*, 2015, **5**, 52695–52702.
73. Y. Guo, E. Zhao, J. Wang, X. Zhang, H. Huang, G. Yu and Y. Wang, *J. Hazard. Mater.*, 2020, **389**, 121829.
74. Q. Huang, S. Deng, D. Shan, Y. Wang, B. Wang, J. Huang and G. Yu, *J. Colloid Interface Sci.*, 2017, **488**, 142–148.
75. X. Li, B. Wang, Y. Wang, K. Li and G. Yu, *Chem. Eng. J.*, 2019, **360**, 1111–1118.
76. X. Li, Y. Wang, S. Yuan, Z. Li, B. Wang, J. Huang, S. Deng and G. Yu, *Water Res.*, 2014, **63**, 81–93.
77. X. Li, Y. Wang, J. Zhao, H. Wang, B. Wang, J. Huang, S. Deng and G. Yu, *J. Hazard. Mater.*, 2015, **300**, 298–306.
78. H. Wang, M. Mustafa, G. Yu, M. Ostman, Y. Cheng, Y. Wang and M. Tysklind, *Chemosphere*, 2019, **235**, 575–585.

79. H. Wang, L. Su, S. Zhu, W. Zhu, X. Han, Y. Cheng, G. Yu and Y. Wang, *Molecules*, 2019, **24**, 2638.
80. H. Wang, J. Zhan, L. Gao, G. Yu, S. Komarneni and Y. Wang, *J. Hazard. Mater.*, 2020, **390**, 122180.
81. H. Wang, J. Zhan, W. Yao, B. Wang, S. Deng, J. Huang, G. Yu and Y. Wang, *Water Res.*, 2018, **130**, 127–138.
82. D. Wu, G. Lu, J. Yao, C. Zhou, F. Liu and J. Liu, *Chem. Eng. J.*, 2019, **370**, 409–419.
83. D. Wu, C. Zhou, G. Lu, Y. Zhou and Y. Shen, *Sep. Purif. Technol.*, 2019, **227**, 115715.
84. D. H. Wu, G. H. Lu, R. Zhang, Q. H. Lin, J. J. Yao, X. H. Shen and W. Wang, *Electrochim. Acta*, 2017, **236**, 389–398.
85. W. Yao, Q. Qu, U. von Gunten, C. Chen, G. Yu and Y. Wang, *Water Res.*, 2017, **108**, 373–382.
86. Y. Zhang, S. Zuo, Y. Zhang, G. Ren, Y. Pan, Q. Zhang and M. Zhou, *J. Hazard. Mater.*, 2019, **368**, 771–777.
87. B. Bakheet, C. C. Qiu, S. Yuan, Y. J. Wang, G. Yu, S. B. Deng, J. Huang and B. Wang, *Chem. Eng. J.*, 2014, **252**, 17–21.
88. Y. Mao, D. Guo, W. Yao, X. Wang, H. Yang, Y. F. Xie, S. Komarneni, G. Yu and Y. Wang, *Water Res.*, 2018, **130**, 322–332.
89. S. T. Liu, Y. J. Wang, B. Wang, J. Huang, S. B. Deng and G. Yu, *J. Cleaner Prod.*, 2017, **168**, 584–594.
90. J. Zhan, Z. Li, G. Yu, X. Pan, J. Wang, W. Zhu, X. Han and Y. Wang, *Sep. Purif. Technol.*, 2019, **208**, 12–18.
91. J. H. Zhan, H. J. Wang, X. J. Pan, J. L. Wang, G. Yu, S. B. Deng, J. Huang, B. Wang and Y. J. Wang, *Carbon*, 2016, **101**, 399–408.
92. J. H. Zhan, Y. J. Wang, H. J. Wang, W. H. Shen, X. J. Pan, J. L. Wang and G. Yu, *Carbon*, 2016, **109**, 321–330.
93. Y. Zhang, S. Zuo, Y. Zhang, M. Li, J. Cai and M. Zhou, *Chem. Eng. J.*, 2018, **348**, 485–493.
94. H. S. Zheng, W. Q. Guo, Q. L. Wu, N. Q. Ren and J. S. Chang, *Environ. Int.*, 2018, **115**, 70–78.
95. M. Ahmadi and F. Ghanbari, *J. Environ. Manage.*, 2018, **228**, 32–39.
96. P. Frangos, H. J. Wang, W. H. Shen, G. Yu, S. B. Deng, J. Huang, B. Wang and Y. J. Wang, *Chem. Eng. J.*, 2016, **286**, 239–248.
97. N. Jaafarzadeh, G. Barzegar and F. Ghanbari, *Process Saf. Environ.*, 2017, **111**, 520–528.
98. A. C. Joy, R. Gandhimathi, S. V. Niveditha, S. T. Ramesh and P. V. Nidheesh, *Sep. Sci. Technol.*, 2020, **55**, 2550–2559.
99. W. H. Shen, Y. J. Wang, J. H. Zhan, B. Wang, J. Huang, S. B. Deng and G. Yu, *Chem. Eng. J.*, 2017, **310**, 249–258.
100. N. Bensalah and A. Bedoui, *Environ. Technol.*, 2017, **38**, 2979–2987.
101. C. Qu, G. S. Soomro, N. Ren, D. W. Liang, S. F. Lu, Y. Xiang and S. J. Zhang, *J. Hazard. Mater.*, 2020, **384**, 121398.
102. W. Yao, S. W. Ur Rehman, H. Wang, H. Yang, G. Yu and Y. Wang, *Water Res.*, 2018, **138**, 106–117.

103. M. S. Elovitz and U. von Gunten, *Ozone: Sci. Eng.*, 1999, **21**, 239–260.
104. C. von Sonntag and U. von Gunten, *Chemistry of Ozone in Water and Wastewater Treatment: From Basic Principles to Applications*, IWA Publishing, 2012.
105. J. Staehelin and J. Hoigne, *Environ. Sci. Technol.*, 1982, **16**, 676–681.
106. X. K. Zhang, Y. Zhou, C. Zhao, Z. H. Sun, Z. G. Zhang, Z. A. Mirza, G. Saylor, J. Zhai and H. L. Zheng, *Chem. Eng. J.*, 2016, **304**, 129–133.
107. K. Li, Y. Zhang, L. Xu, L. Liu, Z. Wang, D. Hou, Y. Wang and J. Wang, *Appl. Catal., B*, 2020, **264**, 118512.
108. S. Yang, A. Verdaguer-Casadevall, L. Arnarson, L. Silvioli, V. Čolić, R. Frydendal, J. Rossmeisl, I. Chorkendorff and I. E. L. Stephens, *ACS Catal.*, 2018, **8**, 4064–4081.
109. Z. Lu, G. Chen, S. Siahrostami, Z. Chen, K. Liu, J. Xie, L. Liao, T. Wu, D. Lin, Y. Liu, T. F. Jaramillo, J. K. Nørskov and Y. Cui, *Nat. Catal.*, 2018, **1**, 156–162.
110. C. Paliteiro, A. Hamnett and J. B. Goodenough, *J. Electroanal. Chem. Interfacial Electrochem.*, 1987, **233**, 147–159.
111. T. Nothe, H. Fahlenkamp and C. von Sonntag, *Environ. Sci. Technol.*, 2009, **43**, 5990–5995.
112. Y. Lee, D. Gerrity, M. Lee, A. E. Bogeat, E. Salhi, S. Gamage, R. A. Trenholm, E. C. Wert, S. A. Snyder and U. von Gunten, *Environ. Sci. Technol.*, 2013, **47**, 5872–5881.
113. Y. Li, Y. X. Zhang, G. S. Xia, J. H. Zhan, G. Yu and Y. J. Wang, *Front. Environ. Sci. Eng.*, 2021, **15**, 1–15.
114. S. O. Ganiyu, M. Zhou and C. A. Martínez-Huitle, *Appl. Catal., B*, 2018, **235**, 103–129.
115. E. C. Paz, L. R. Aveiro, V. S. Pinheiro, F. M. Souz, V. B. Lima, F. L. Silva, P. Hammer, M. R. V. Lanza and M. C. Santos, *Appl. Catal., B*, 2018, **232**, 436–445.
116. A. R. Khataee, M. Safarpour, M. Zarei and S. Aber, *J. Electroanal. Chem.*, 2011, **659**, 63–68.
117. F. C. Moreira, R. A. R. Boaventura, E. Brillas and V. J. P. Vilar, *Appl. Catal., B*, 2017, **202**, 217–261.
118. G. Xia, Y. Tian, X. Yin, W. Yuan, X. Wu, Z. Yang, G. Yu, Y. Wang and M. Wu, *Appl. Catal., B*, 2021, **299**, 120655.
119. Q. Yang, H. Huang, K. Li, Y. Wang, J. Wang and X. Zhang, *Chem. Eng. J.*, 2021, **415**, 127618.
120. U. von Gunten, *Water Res.*, 2003, **37**, 1469–1487.
121. WHO, *Guidelines for Drinking-Water Quality*, Geneva, 2011.
122. European Union, *Council Directive 98/83/EC of 3 November 1998 on the Quality of Water Intended for Human Consumption*, 1998.
123. M. S. Siddiqui, *Water Res.*, 1996, **30**, 2160–2170.
124. U. von Gunten and J. Hoigne, *Environ. Sci. Technol.*, 1994, **28**, 1234–1242.
125. Y. Zhang, X. Cui, S. Liu, W. Zhu, X. Han and Y. Wang, *China Environ. Sci.*, 2020, **40**, 2270–2275.

126. Y. Zhang, E. Zhao, X. Cui, W. Zhu, X. Han, G. Yu and Y. Wang, *Sep. Purif. Technol.*, 2021, **265**, 118496.
127. K. Li, L. Xu, Y. Zhang, A. Cao, Y. Wang, H. Huang and J. Wang, *Appl. Catal., B*, 2019, **249**, 316–321.
128. O. Legrini, E. Oliveros and A. M. Braun, *Chem. Rev.*, 1993, **93**, 671–698.
129. W. Zhou, X. Meng, J. Gao and A. N. Alshawabkeh, *Chemosphere*, 2019, **225**, 588–607.

CHAPTER 10

Catalytic Ozonation with Ultrasound

LEI ZHAO

School of Civil Engineering, Harbin Institute of Technology, 202 Haihe Road, Nangan District, Harbin City 150090, People's Republic of China
Email: zhaolei999999@126.com

10.1 Introduction

During the last 20 years, we have witnessed an amazing increase in the application of ultrasound in different fields of science. In the field of environmental engineering, ultrasound is also widely used in the removal of organic matter in water. The removal of organic pollutants in water by the synergistic effect of ultrasound and ozone has a good effect.

Catalytic ozonation is a water treatment technology that can oxidize most organic compounds. Ozone is an important disinfection gas for drinking water treatment and is a suitable replacement for chlorination in that it reduces disinfection byproducts.[1] It is an unstable trioxygen molecule (O_3) that easily releases oxygen atoms in aqueous solutions and that subsequently reacts with hydrogen ions in water, leading to increased levels of hydroxyl radicals ($^{\bullet}OH$) in the medium.[2] In addition, as an emerging method of industrial wastewater treatment and advanced oxidation process, ultrasound has been widely used. Its degradation conditions are mild, degradation rate is fast, and it is also known as an environmentally friendly technology.

Chemistry in the Environment Series No. 8
Advanced Ozonation Processes for Water and Wastewater Treatment: Active Catalysts and Combined Technologies
Edited by Hongbin Cao, Yongbing Xie, Yuxian Wang and Jiadong Xiao

Published by the Royal Society of Chemistry, www.rsc.org

Previous investigations have found the combination of ozone and ultrasonic irradiation to be effective at enhancing the degradation and mineralization of various organic solutes in aqueous solution.[3] Oxidation treatment combining ozone and ultrasound ensures the ozone is fully dispersed, reducing the applied amount of ozone and improving its oxidation capacity and, with the help of the ultrasonic cavitation effect and physicochemical action to strengthen the decomposition of ozone, generating a large number of free radicals; the combination of ozone and ultrasound showing a synergistic effect.

10.2 Fundamental Characteristics of Ultrasound

10.2.1 Generation of Ultrasound

Ultrasound is a kind of sound wave, its vibration frequency is very high, higher than 2000 Hz. As a form of energy transmission, ultrasound and audible sound are the same in essence. In the generation process of ultrasound, the high-frequency oscillation signal from the ultrasound generator is converted into high-frequency mechanical oscillation by the transducer and propagated to the medium.

Ultrasonic waves create pressure differences within a solution for the enhancement of physical (mechanoacoustic) and chemical (sonochemical) processes. This occurs at frequencies beyond the audible range, typically between 20 and 1000 kHz. Ultrasound is generated by either piezoelectric or magnetostrictive transducers. Piezoelectric transducers are more commonly used today and manipulate the piezoelectric property of some ceramics. The piezoelectric material will respond to an alternating current with mechanical vibrations to produce ultrasound of a characteristic frequency. This creates a pressure wave, leading to the phenomenon that the bubbles in a sonication solution are subject to collapse during compression of the wave. This collapse is almost adiabatic and can result in localized temperatures of around 5000 K and pressures of 1000 atm. The collapse results in the formation of radicals through the dissociation of the molecules within and around the bubbles, luminescence due to excited molecules formed losing energy and microjets shooting out of the bubbles of speeds in the realm of hundreds of $km\,h^{-1}$.[4]

Ultrasound waves typically contain compression and expansion cycles. Positive pressure can push molecules together in the compression cycle, and the expansion cycle generates cavities because of a large negative pressure that overcomes the liquid's tensile strength.[5] With the ultrasonic processing progresses, the cavities keep absorbing acoustic energy. Upon reaching their critical size, the cavities implode, release high energy, generate a high-pressure condition (up to 50 MPa) and heat surroundings to an extremely high temperature (up to 5500 °C). Since ultrasonic waves are mechanical waves, strong agitation, shear stress and turbulence are also characterized during ultrasound processing.[6] Such a unique environment generated in ultrasound is favored by the food industries as a means of processing, cleaning and sanitizing.

Four types of ultrasound are classified according to frequency and intensity. Scientists normally define a frequency higher than 500 kHz as high-frequency ultrasound and an intensity higher than 1 $W\,cm^{-2}$ as high-intensity ultrasound. High-frequency ultrasound is normally utilized for soft tissue surgery (using high-frequency and high-intensity focused ultrasound) or for diagnostic imaging, increased drug delivery and simulation of tissue regeneration (using high-frequency and low-intensity ultrasound).[7] With a sufficiently low intensity of ultrasound, stable cavitation is produced without the violent collapsing of bubbles during the compression cycle. When the intensity of ultrasound is high enough, cavities implode after absorbing sufficient energy. The sudden reversal in the motion of the bubble wall produces a shock wave and high temperature that can fragment water and other molecules into free radicals.[8]

10.2.2 Typical Reactors Applied

In the field of water treatment, ultrasound combined with ozone can improve the oxidation capacity of the system notably. In order to achieve better degradation of pollutants, many researchers have designed different reactors. In this book, all reactors are divided into two categories: ultrasonic bath and ultrasonic probe.

10.2.2.1 Ultrasonic Bath

Figure 10.1 shows a typically ultrasonic bath. Researchers use it to produce ultrasound and then deliver O_3 into the degradation reactor inside the bath.

In the process of ultrasound and ozone designed for the degradation of the X-3B, ozone was generated by electrical discharge using oxygen in a laboratory ozone generator. Ozone was continuously bubbled into the solution, and the flux rate was kept unchanged. Therefore, the concentration of the ozone could be kept constant. Furthermore, the suitable ozone flux could be obtained by adjusting a glass rotameter. The ozone was placed in contact with the solution for reaction. At the same time, sonication was performed by an ultrasonic generator, which was equipped with a titanium probe

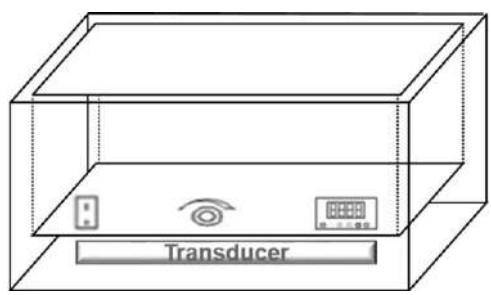

Figure 10.1 Device diagram of ultrasonic bath.

transducer. After sampling, the residual ozone was terminated by sodium sulfite (Na_2SO_3) so that the concentration of the target could be determined. Finally, the residual ozone in the off-gas was released into the KI absorption bottle and was absorbed by the mass fraction of 2% KI solution[9] (Figure 10.2).

The ultrasonic bath used in the work consisted of a single transducer with a frequency of 36 kHz and a rated power output of 150 W and was fitted longitudinally at the bottom of the reactor. The energy to this transducer was supplied by a generator. Using calorimetric studies, the actual power dissipated to the system at an operating capacity of 7 L was found to be 78.3 W, giving energy efficiency at 52.2%. It is important to understand that the energy efficiency of this configuration is much better than the one observed for the conventional design of ultrasonic horn.[10]

The ozone (O_3) treatment used was similar to the one reported in previous work, which is schematically illustrated in Figure 10.1. In short, 700 mL of starch suspension (10% m/m, wet basis) in distilled water was placed in a glass reactor and processed for 15 min at 25 °C. The ozone was generated from industrial oxygen (95% purity; constant flow at 1 $L\,min^{-1}$) using an ozone generator unit. The gas ($O_2 + O_3$) stream, with an ozone concentration of 42 mg $O_3\,L^{-1}$ of mixture, was introduced in the reactor, being bubbled in the starch suspension. After processing, the water was separated from the sample, and an air circulation oven (at 35 °C) was used to dry the starch (until ~12% of moisture content). The samples were sieved (250 μm) before the analyses.

To perform the physical modification using ultrasound (US), a starch suspension in distilled water (700 mL, 10% w/w) was prepared inside a glass beaker and processed in an ultrasonic bath. The US conditions were processing time of 8 h, temperature of 24–26 °C, frequency of 25 kHz and volumetric power of 72 $W\,L^{-1}$. The temperature was controlled using a heat exchanger inside the US bath (the recirculating water was provided by an

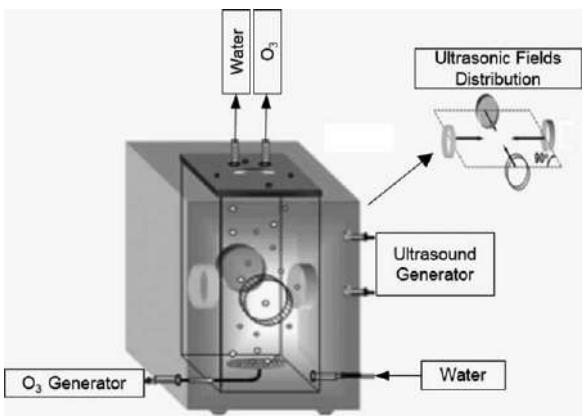

Figure 10.2 Device diagram of ultrasonic reactor with multifields.

external water bath). The ideal location of the samples inside the US bath was evaluated according to the good practices described in the literature, ensuring homogeneity and the exposure of the sample to the highest US intensity. The bath was filled with 6 L of distilled water mixed with 15 drops (~0.5 g) of dishwashing detergent, to decrease the surface tension of the solvent. To prevent decantation of the starch granules during the treatment, a mechanical stirrer was used. After processing, the water was separated from the sample, and an air circulation oven (at 35 °C) was used to dry the starch (until ~12% of moisture content). The samples were sieved (250 μm) before the analyses.[11]

There's a system like the ultrasound bath in principle that doesn't have a water bath but instead puts the ultrasonic transducer at the bottom of the reactor. A large-scale water treatment device from Ultrasonic Systems Gmbh, Thierhaupten, Germany, was employed to deliver ultrasound and ozone for water treatment using a technology known as US/O_3. The system consisted of an ozone generator, 20 ultrasonic transducers at maximum power setting (100 W each/[612 kHz]), a mixer and an external pump that was capable of treating up to a maximum capacity of 4 $m^3\,h^{-1} = 66.67\ L\,min^{-1}$. Internally, the system consisted of long steel tubes with a diameter of 108.3 mm, $L = 3.02$ m, $V = 28\ L = 0.028\ m^3$ and retention time = 0.8 min. The bacterial suspension was pumped into the USO_3 kit using an external pump (flow rate, 35 $L\,min^{-1}$). Experiments were performed at a constant flow rate of 35 $L\,min^{-1}$, delivering a constant ozone supply capable of generating a concentration that accumulated to 1 $mg\,L^{-1}$. The aqueous suspension of the bacteria was treated at this flow rate in a recycling system for 16 min with pulsed ultrasonic treatment on for 5 s and off for 5 s. The ozone concentration was measured using the indigo colorimetric method.[12]

Preliminary experiments with ozone alone were carried out in 250 mL glass chambers to estimate the ozone mass transfer coefficient at varying pH levels (3.0, 6.5 and 9.0) and ozone flow rates (3, 6 and 12 $mg\,min^{-1}$, corresponding to inlet concentrations of 2, 4 and 8 $g\,m^{-3}$, respectively). Ozone was generated onsite using an Ozonelab-100 Model generator and dry pure oxygen flowing at 1.5 $L\,min^{-1}$. Single experiments with solid catalysts alone were carried out at pH 3.0 and 6.5 to assess the degree of IBP adsorption and the extent of solids leaching into the sample solutions. The concentration of IBP, the mixing rate and the contact time were 50 M, 250 rpm and 24 h, respectively. The catalyst dose in each test was adjusted so as to maintain 5 $mg\,L^{-1}$ Fe in all samples.

Catalytic experiments with Fe-bearing species were run with 50 M IBP (10 $mg\,L^{-1}$) and 5 $mg\,L^{-1}$ Fe-equivalent of each catalyst during a gas flow rate of 12 $mg\,min^{-1}$ for 1 h at pH 6.5 unless stated otherwise. The experiments with ultrasound were carried out in a high-frequency plate-type ultrasonic reactor (500 mL) equipped with a 120 W generator (operated at 90% of capacity) and a piezoelectric transducer (22 cm^2) emitting 861 kHz. The reactor was operated at a specific power of 0.23 $W\,mL^{-1}$, cooled by circulating water to maintain constant temperature (20 ± 0.5 °C) and

occupied by a sample volume of 250 mL. The flow rate of O_3 into the reactor was 12 mg min^{-1} throughout the reaction time.[13]

The experiments were performed in a semicontinuous ultrasonic reactor depicted schematically in Figure 10.2, which was made entirely of stainless steel with a breadth of 11.5 cm, a depth of 11.5 cm and a height of 26.8 cm. The four flattened sides of the reactor were respectively mounted with the four same piezoelectric transducers, each of which was arranged on one side of the reactor and all of which were driven at 28 kHz (A, B, C and D fields). The emitting system was connected to a frequency generator and a power supply. The emphasis of the present study is located on the relationship investigation between accelerating •OH initiation and increasing the number of multiple ultrasonic fields under the same total ultrasonic power input condition; *i.e.* the total ultrasonic power input was controlled at 120 W either individually (A, the same as B, C or D field) or in combinations (AB [60 W + 60 W], ABC [40 W + 40 W + 40 W] or ABCD [30 W + 30 W + 30 W + 30 W] field). Therefore, typical power intensity and power density were same for the entire individual or combined multiple field, which were 0.39 W L^{-1} and 38.5 W L^{-1}, respectively, according to the method described by the previous study.[14]

10.2.2.2 Ultrasonic Probe

The ultrasonic probe is immersed directly into the sample container in this system. There are two differences between the ultrasonic probe and the ultrasonic bath: One is that the reactor is immersed in an ultrasonic bath, whereas an ultrasonic probe is immersed directly into the sample container; the other is that the ultrasonic probe can deliver much higher ultrasonication intensity (100 times greater) than the ultrasonic bath. The probe is generally used to attain effects that cannot be achieved with the ultrasonic bath. More and more researchers use the ultrasonic probe as the reaction system.

Figure 10.3 shows a typical system of the ultrasonic probe. The ultrasonic horn is the core in the ultrasonic probe. The frequency of the ultrasonic is

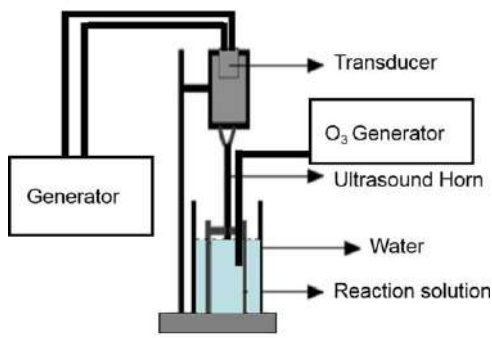

Figure 10.3 Device diagram of ultrasonic probe.

20 kHz, power dissipation is 120 W, tip diameter is 2.1 cm, depth into the liquid is 1 cm and the duty cycle is 80%. All the experiments have been performed in a glass beaker of capacity 250 ml. The beaker was always immersed in a water bath for maintaining a constant temperature (around 32 ± 2 °C), which was measured using a thermometer.

An ozone generator was used to generate ozone from air. Ozone was bubbled into the reactor as required using a bubble diffuser at a flow rate of 400 mg h^{-1}. To regulate the ozone flow into the reactor, a two-way bypass valve attached to the pipe was used as a controller. The calibration of ozone output was done using the standard iodometric titration method.[15] (see Figure 10.3).

There is a system that combines US and O_3. In this system, semibatch experiments were performed in a rectangular air-lift reactor made of plexy glass. The reactor consists of a square column (50 mm×50 mm) with the height of 120 mm, divided into a riser and a downcomer section by a plexy glass baffle (width: 50 mm; thickness: 4 mm; total height: 50 mm). The riser-to-downcomer cross-sectional area ratio is 1.3. The baffle was located at a distance of 12 mm from the bottom of the reactor. The gas distributor at the bottom of the riser was a perforated tube with six orifices of 1 mm diameter each. Ozone was generated by electric discharge using 99.9% oxygen in a laboratory ozone generator. A magnetic stirrer provided complete mixing of the solution in the reactor.

Sonication was performed with an ultrasonic generator equipped with a titanium probe transducer. The tip of the probe was 1 cm in diameter and was placed 1.5 cm into the liquid layer. The sonication was administered in a pulse mode of 2.5 s on and 2.1 s off. The acoustic power was determined calorimetrically. At preselected time intervals, samples were taken by a syringe and filtered through 0.45 cm membranes before the tetracycline concentration was measured.[16]

Some researchers investigated the scheme of ultrasound combined with ozone treatment on waste activated sludge (WAS). The ultrasonic apparatus was an ultrasonic homogenizer Autotune 950W that worked with a probe with a diameter of 8 mm and an operating frequency of 21 kHz. The ultrasonic probe was dipped 10 mm into the sludge. The ultrasonic energy output was adjusted between 40 and 600 W under various test conditions; ozone was generated from pure oxygen using an ozone generator, and ozone was released to the sludge by a microporous diffuser. The gas flow rate was adjusted from 1 to 4 L min^{-1} under various experimental conditions. For each batch experiment, 400 ml sludge was filled in a 7 cm×25 cm (diameter×height) bottle.[17]

The US/O_3 pretreatment was performed using the combined ozonation and sonolysis experimental set up as in Figure 10.3, but the ozone generator relied on a UV irradiation system. It produced ozone by splitting the oxygen molecules of the airflow provided by a compressor. The airflow containing ozone was introduced into the glass reactor containing the spiked solution; the exhaust gas was extracted from the reactor and forced to a trap, where a

2% KI solution captured the residual ozone, which could be determined by titration according to the Standard.

The ultrasonic device was equipped with a titanium horn with a 1.3 cm diameter tip and a temperature probe to monitor the temperature. The ultrasonic probe was positioned about 4 cm into the solution and fixed at the center of the reactor. The pretreatment was applied in batches, as an offline process prior to the membrane bioreactor (MBR) system.[18]

The experimental setup for treatment is comprised of an ultrasonic horn and a 250 mL beaker containing the pharmaceutical industry effluent (PIE) sample. The titanium horn with 2.1 cm tip diameter operates at a frequency of 22 kHz, with a maximum power output of 250 W, and was fitted with single piezoelectric ceramic material (PZT) transducer at the tip of the horn. The tip of the probe was dipped to a certain depth (typically 2 mm) below the surface level of the PIE sample in the beaker. The beaker was kept in a water bath with ice pellet introduction at regular intervals so as to maintain a constant temperature of the PIE sample throughout the experiment.[19]

All advanced oxidation process experiments were carried out in a high-frequency plate-type ultrasonic reactor equipped with a 120 W generator and a piezoelectric transducer emitting optionally at 577, 861 or 1145 kHz. The reactor was operated at 861 kHz and a specific power and was cooled by circulating water to maintain a constant temperature. Ozone was injected at a flow rate of 1.5 $L\,min^{-1}$, and the aqueous concentration of the gas was maintained at 2, 4 or 8 $mg\,L^{-1}$ depending on the operating conditions. The UV lamp was immersed vertically along the center of the reactor and turned on only in UV-combined applications.[20]

10.3 Reactivity of Compounds

The organic pollutants in water can be removed effectively by catalytic ozone in water treatment. The ultrasound, with ozone processes, can generate more $^{\bullet}OH$ and can improve the degradation of organic pollutants. As an attractive and promising AOP, ultrasound catalytic ozonation has been found to be effective for the degradation of a variety of environmentally hazardous pollutants. This combined process overcomes the drawbacks of ozonation alone and ultrasound alone, including high cost, only partial oxidation of contaminants and lesser extent of mineralization. The reactivity of compounds was divided into four categories in this book: phenols, aromatic, dyes and others.

10.3.1 Phenols

Phenol, commonly known as ArOH, is an aromatic compound in which the hydrogen on the aromatic hydrocarbon ring is substituted by the hydroxyl group (–OH). Phenolic compounds refer to the compounds formed when the hydrogen atoms on the benzene ring are replaced by hydroxyl groups in aromatic hydrocarbons.

Phenols are essential chemicals that are widely used in the chemical and allied industries. They are released in wastewater by the industries that handle, manufacture or use them. Phenolic wastewater is one of the most harmful and widely polluted industrial wastewater in the world. It is an important source of water pollution in the environment. In many industrial fields, such as gas, coking, oil refining, metallurgy, machinery manufacturing, glass, petrochemical industry, wood fiber, chemical organic synthesis industry, plastics, medicine, pesticides, paint and other industrial effluents contain phenol. This wastewater can pollute the air, water, soil and food if it is directly discharged and irrigated to farmland without further treatment.

Phenols abatement is possible by oxidation processes such as wet-air oxidation, ozonation, wet-peroxide oxidation and photocatalytic oxidation. Although individual oxidation processes are incomplete and impractical, the combination of ultrasonic and ozone oxidation technology can remove it effectively.

According to the reports in the literature, the application of ultrasound and ozone, operated individually and in combination with a catalyst (ZnO and CuO), establishes possible synergistic effects for the degradation of 2,4-dichlorophenol. The dependency of the extent of degradation on the operating parameters, like temperature (over the range of $30 \sim 36\ ^{\circ}C$), initial pH ($3 \sim 9$), catalyst as ZnO (loading of 0.025–0.15 $g\,L^{-1}$) and CuO (loading of 0.02–0.1 $g\,L^{-1}$) and initial concentration of 2,4-DCP ($20 \sim 50$ ppm), has been established to maximize the efficacy of ultrasound-induced degradation. Using only US, the maximum degradation of 2,4-DCP obtained was 28.85% under optimized conditions of initial concentration at 20 ppm, pH of 5 and temperature of 34 °C. The study of the effect of the ozone flow rate for the ozone-only approach revealed that maximum degradation was obtained at 400 $mg\,h^{-1}$ ozone flow rate. The combined approaches, such as $US + O_3$, $US + ZnO$, $US + CuO$, $O_3 +$ ZnO, $O_3 +$ CuO, $US + O_3 + ZnO$ and $US + O_3 + CuO$, have been subsequently investigated under optimized conditions and observed to be more efficient as compared to individual approaches. The maximum extent of degradation for the combined operation of $US + O_3$ (400 $mg\,h^{-1}$) + ZnO (0.1 $g\,L^{-1}$) and $US + O_3$ (400 $mg\,h^{-1}$) + CuO (0.08 $g\,L^{-1}$) has been obtained as 95.66% and 97.03%, respectively. The degradation products of 2,4-DCP have been identified using GC–MS analysis, and toxicity analysis has also been performed based on the antimicrobial activity test (agar well diffusion method) for the different treatment strategies. The present work has conclusively established that the combined approach of $US + O_3 +$ CuO was the most efficient treatment scheme, resulting in nearly complete degradation of 2,4-DCP with production of less toxic intermediates.[10]

Relevant experiments related to combining sonolysis and ozonation were performed at 10 ppm *p*-nitrophenol concentration and O_3 mixture ($O_3 + O_2$) flow rate of 25 $mL\,s^{-1}$. The concentration of ozone in the ozone-oxygen mixture was 10% by volume. It has been observed that the combined

operation results in 98.3% degradation, which clearly confirms that the combination approach is much better as compared to the use of ultrasonic or ozone alone. The extent of mineralization for 10 ppm *p*-nitrophenol was obtained to be 36% for the combined operation.

Similar results of enhancement of the extent of degradation of organic pollutants using a combination of ozone and ultrasound can be observed in the literature. Weavers studied the degradation of different aromatic compounds like nitrobenzene, 4-nitrophenol and 4-chlorophenol using the combination technique of sonolysis and ozonolysis. It has been reported that the degradation rates for the combination technique for nitrobenzene, 4-nitrophenol and 4-chlorophenol were all higher as compared to the individual operation. Weavers also obtained similar results with the degradation of pentachlorophenol.

Since phenol is a hydrophilic solute, the destruction pattern during combined ozonation and sonolysis is expected to be governed by $^{\bullet}OH$-mediated oxidation in the bulk liquid, although it may also react directly with molecular ozone and hydrogen peroxide. The probability of thermal and radical decomposition in the bubble–liquid interface is low but is likely to occur at high concentrations. In any case, the rate-limiting step is the mass transfer of ozone in solution and the diffusion of $^{\bullet}OH$ into the bulk liquid.

A comparison of phenol destruction in single and combined operations of ozonation and sonolysis was done at three pH levels. The negligible rate of decay by US at pH 10 is due to the relatively high distribution of phenolate ion in this condition, which remains far away from the bubble–liquid interface (due to extreme hydrophobicity), where $^{\bullet}OH$ are at a maximum.[21]

In addition, He *et al.* inspected the mineralization of *p*-aminophenol (PAP) by coupling sonolysis with ozonation. They noticed that the mineralization rate of PAP was enhanced in the coupled experiments (88% and 99% at 10 and 30 min, respectively) than that observed using individual techniques (72% and 90% efficiency in the presence of O_3 alone and 3% and 4% in the presence of US alone at 10 and 30 min).[22]

Using GC/MS, they detected intermediates such as 4-iminocyclo-hexa, 2-5-dien-1-one, phenol but also 2-enedioic acid and acetic acid. Destaillats *et al.* performed a reduction of the total organic carbon (TOC) with the coupled accomplishment of ultrasound and ozone quantities to elucidate the chemical synergism. They chose two rather persistent by-products, namely nitrobenzene and benzoquinone, which are formed upon sonolysis of azobenzene and methyl orange by the combined effect of sonolysis with ozone.

The decomposition was slow in the presence of ozone alone. A further advantage of coupling sonolysis with ozonolysis may exclude the formation of poisonous intermediates by the active species that provided an additional mineralization route. Many researchers have shown that ozonation coupled with ultrasonic irradiation is more efficient for the destruction of various pollutants.[23] For example, Martins *et al.* studied the combination and individual techniques (ozonation and/or sonolysis) for the degradation of pararosaniline colorant. They illustrated that the reaction follows the

second-order rate for the mineralization of pararosaniline. In addition, they also mentioned that sonolytic ozonation produces various intermediates compared to the individual ozonation process, which illustrates that mineralization by ozonation is a complex process.[24]

10.3.2 Aromatics

An aromatic is usually a hydrocarbon with a benzene ring structure in the molecule. It's one of the closed-chain classes. It has the basic structure of a benzene ring. Aromatics are toxic substances that can harm the human respiratory tract and skin. Consuming too many aromatics over a long period of time may cause cancer.

Sonolysis, ozonolysis and a combination process are used to remove aromatics in water treatment. The combination of ultrasound and ozone is used to investigate the degradation of nitrobenzene, BTA, nitroaromatics and so on.

Lei Zhao used the process of ozonation alone to remove nitrobenzene. The results indicated that 22.3% degradation efficiency of nitrobenzene is observed. The degradation efficiency of nitrobenzene increased to 95.4% by the combination of ultrasound and ozone. From the data mentioned, the work concluded that the introduction of ultrasound can enhance ozonation for the degradation of nitrobenzene, producing the synergetic effect between ozone and ultrasound. The total organic carbon (TOC) also exhibited the same trend of the enhancement on nitrobenzene degradation. That is to say, the introduction of ultrasound advanced the degradation efficiency of nitrobenzene as well as mineralization into carbon dioxide and water.[14]

A study investigated the degradation efficiency of benzotriazole (BTA) using a combination of ultrasound and ozone. The results showed that the highest removal efficiency was reached at neutral pH, ozone = 6.8 $mg\,L^{-1}$, PMS = 1.5 mM and US power = 200 W. Under these conditions, 40 $mg\,L^{-1}$ of BTA was completely degraded within 60 min, leading to almost 85% of chemical oxygen demand removal, 75% of TOC removal and 73.3% of organic nitrogen removal. Based on the scavenging tests, it was found that the hydroxyl radical was the main oxidizing agent in the system.[25]

The removal of nitroaromatics from polluted water is difficult due to their high stability in conventional treatment methods. Some researchers have used the application of ultrasound and ozonation in the electrochemical reaction. This system allows virtually complete destruction of the compounds in a short time. The effect is attributed to the ultrasonic enhancement of the electrochemical process, which gives intermediates that are susceptible to ozone oxidation.[26]

10.3.3 Dyes

Dyes are widely used in textile dyeing operations, but a significant portion of these dyes is wasted with spent dyebaths. The wasted dyes are mixed with

the rest of the dyeing mill effluent to be processed in the treatment facilities. However, most of the dyes are not removed entirely and are transmitted into receiving water bodies with properties of unesthetic color and a potential to produce carcinogenic amines.[27,28]

Although ozonation is one of the most common advanced oxidation processes for dye degradation, the mass transfer rate of ozone in the solution is the limiting parameter. Therefore, the combined operation of ultrasonic and ozone renders synergistic effects in dye degradation and accelerates the mass transfer of ozone in the solution due to ultrasonic effects. In the process of combining ultrasound and ozone, a part of the dissolved ozone may react directly with the dye molecules, and then the major part of the dissolved ozone is efficiently decomposed by ultrasound irradiation. The system produces $^{\bullet}OH$, O^{-2} and $^{\bullet}O_2H$ radicals so that the dyes and the by-products can be decomposed and mineralized.

The effect of dyes decomposing is influenced by many factors, such as the initial dye concentration, the pH of system, the ozone concentration and the frequency of ultrasound. According to the literature, the US/O_3 combined oxidation process is less responsive to an increase in dye concentration in the higher ranges. The dye degradation rate also increases as the pH values increase to a value of 8–10; ozone decomposition kinetics are not influenced by acidity in the pH range of 2.58–5.93 for dye degradation. Even so, some studies imply that the sonolytic ozonation process at acidic or basic pH levels shows no difference in the dye degradation rate. Similarly, ozone concentration and the frequency of ultrasound are also an important parameter in the sonolytic ozonation process; the removal of dyes increases with the increase of ozone concentration and the frequency of ultrasound within certain ranges.

The effectiveness of ozone combined with ultrasound techniques in degrading Reactive Red X-3B is evaluated. A comparison among ozone, ultrasonic, ozone/ultrasonic (US/O_3) for the degradation of Reactive Red X-3B has been performed. Results show that the US/O_3 system was the most effective and that the optimally synergetic factor reaches 1.42 in the US/O_3 system. The cavitation of ultrasound plays an important role during the degradation process. It is found that 99.2% of dye is degraded within 6 min of reaction at the initial concentration of 100 mg L^{-1}, pH of 6.52, ozone flux of 40 L h^{-1} and ultrasonic intensity of 200 W L^{-1}. Ozonation reactions in conjunction with sonolysis indicate that the decomposition followed pseudo first-order reaction kinetics but that the degradation efficiencies are affected by operating conditions, particularly initial pH and ultrasonic intensity. In addition, the main reaction intermediates, such as *p*-benzoquinone, catechol, hydroquinone, phthalic anhydride and phthalic acid, are separated and identified using GC/MS and a possible degradation pathway is proposed during the US/O_3 process.[9]

The degradation of a reactive dye by combined sonolysis (520 kHz) and ozonation was studied using CI Reactive Black 5 as a model dye. It was found that the joint action of ultrasound and ozone induced a synergistic effect on

both the decolorization of the dye and the overall degradation process. Due to the inefficiency of ultrasonic irradiation by itself to render any significant degradation under the conditions employed, the synergy was attributed mainly to the mechanical effects of ultrasound to enhance the mass transfer of ozone in solution. The radical chain reactions taking place during thermolysis of water and ozone in collapsing cavities may also have contributed chemically to the synergy by providing additional decomposition pathways for ozone and an excess of electron-deficient chemicals in solution.[29]

10.3.4 Antibiotics

An antibiotic is a kind of drug with inhibitory and killing effects on bacteria. It is a kind of pharmaceutical active compound (PhAC) with wide distribution range and high detection frequency in the environment. It has played an important role in the prevention and treatment of human and animal diseases for a long time. Although the application of antibiotics has brought great convenience to human beings, the vast majority of drugs will enter the environment with human and animal excrement, which poses a great threat to human health and the ecological environment.[30]

The results showed that the antibiotic was degraded by ultrasound enhanced catalytic ozonation. The antibiotics removal rate increased with increasing gaseous ozone concentration, pH, gas flow rate and power density (ultrasound-enhanced catalytic ozonation of tetracycline in a rectangular airlift reactor). Sulfamethoxazole (SMX) degradation was investigated using US, O_3 and US/O_3. It was proved that ultrasound significantly enhanced SMX ozonation by assisting ozone in producing more $^{\bullet}$OH in US/O_3.[31] The antibiotics tetracycline (TC) was degraded by US-enhanced catalytic ozonation using goethite catalyst (US/goethite/O_3).[16] The degradation of tetracycline was investigated using the ultrasound-enhanced magnetite catalytic ozonation process (US/Fe_3O_4/O_3).[32] It was proved that ultrasound significantly enhanced SMX ozonation by assisting ozone in producing more $^{\bullet}$OH UOOP. In these researches, it was proved that ultrasound significantly enhanced the antibiotic ozonation by assisting ozone in producing $^{\bullet}$OH in the ultrasound/ozone oxidation process.

10.3.5 Industrial Wastewater

Tremendous population growth and industrial development are responsible for the generation of a large quantity of wastewater containing toxic pollutants, which in turn increase the overall pollution load.[33] Treatment of actual industrial wastewater is a challenging task, and the combination of ultrasound and ozone is an efficient process for the treatment of industrial wastewater.

According to the literature, when using ultrasound alone, the frequency of ultrasound must be higher than 300 kHz, showing a reduction in chemical oxygen demand (COD, 18% reduction) and biological oxygen demand (BOD,

50% reduction). Combining ultrasound with ozone, on the contrary, led to a significant decrease in COD (44%) and BOD (78%) removal for the three frequencies under study. So we know that the combination of ultrasound and ozone can greatly increase the removal of COD and BOD.

10.4 Reaction Kinetics

The reaction kinetics is a subject in which the rate of a reaction is studied as certain parameters are varied, and it reflects how fast the chemical reaction is going on. The reaction kinetics rate constants of some pollutants in the process of combination of ultrasound and ozone are[3,9,10,16,25,34] are as seen in Table 10.1).

10.5 Influencing Factors

There are many influencing factors in the process of ultrasound and ozone, such as ultrasonic power density, the frequency of ultrasound, the concentration of ozone, the pH of system, the temperature of system and so on. The remove rate of the organic pollutants is greatly affected by these factors.

10.5.1 Ultrasonic Power Density

Ultrasonic power density is an important parament of ultrasound and an important influencing factor in the process of ultrasound and ozone. As we set an optimal condition and investigate the influence of ultrasonic power density, we find that with an increase in power intensity, the rate of degradation of the pollutants increases, and maximum degradation is observed at optimum power. According to the literature, the observed increase in pollutants reduction with an increase in power is attributed to the higher quantum of cavitation bubbles and hence enhanced cavitational activity. At higher power dissipation levels up to the optimum, the quantum of $^{\bullet}OH$ is higher due to an increase in cavitational activity, and hence a greater extent of pollutants reduction is obtained. Beyond optimum power, the rate of oxidation decreases due to acoustic decoupling effects obtained based on the formation of too many bubbles at the tip of the horn. Due to the decoupling, the magnitude of energy transferred is lowered, reducing the cavitational activity and hence less degradation is seen.[35]

10.5.2 Frequency

Frequency is the special property of ultrasound itself, and its settings influence the nature and severity of the ultrasonic effects. Studies looking for mass transfer improvement generally opt for the lower frequency range, and higher frequencies are used for increased sonochemical activity. At lower frequencies (under 100 kHz), the bubbles have more time to grow, and therefore the cavitational collapses are more violent. At higher frequencies,

Table 10.1 The reaction kinetics rate constants of some pollutants under different conditions in the combination process of ultrasound and ozone.

Pollutant	Reaction order	Rate	Density power	Frequency	Concentration of O_3	Concentration of pollutant	pH	Temperature
$H_2C_2O_4$	0	2.8×10^{-5}	100	358	340 μM	0.9 mM	3	15
		6.75×10^{-6}	83		150 μM			
		2.34×10^{-5}	83		350 μM			
Procion Red MX-5B-(24h)	1	0.8069	200	313	40 $L\,h^{-1}$	100 $mg\,L^{-1}$	6.52	25
Methyl *tert*-butyl ether	1	3.32×10^{-5}	200	205	0.30	0.01 mM	6.6	20
		3.13×10^{-5}			0.31	0.05 mM		
		1.49×10^{-5}			0.32	0.25 mM		
		1.22×10^{-5}			0.34	0.50 mM		
		0.63×10^{-5}			0.26	1.00 mM		
Tetracycline	1	0.096	0	20	13.8 $mg\,L^{-1}$	100 $mg\,L^{-1}$	3	20
		0.115	85.7	20	13.8 $mg\,L^{-1}$		3	20
2,4-Dichlorophenol	1	4.2×10^{-3}	150W	36	100 $mg\,h^{-1}$	20 ppm	7	30
		8.1×10^{-3}			200 $mg\,h^{-1}$			
		1.5×10^{-2}			300 $mg\,h^{-1}$			
		2.23×10^{-2}			400 $mg\,h^{-1}$			
Benzotriazole	1	0.0044	200 W	—	6.8 $mg\,L^{-1}$	250 $mg\,L^{-1}$	7	25

more bubbles are produced, which collapse, producing more radicals. The inverse effects of frequency were demonstrated with ultrasonic treatment of polyphenylene ether and through iodide dosimetry. At even higher frequencies, such as in the megahertz range, the rarefaction of the wave becomes too short for cavitation to occur. The studies shows that high-frequency conditions promote more oxidizing radicals, and low-frequency conditions promote the physical effects of ultrasound; however, both the physical and chemical effects are present across the frequency range generally used in ultrasound.[4,36]

10.5.3 The Concentration of Ozone

The concentration of ozone is the most important influencing factor in the process of ultrasound and ozone. The studies have shown that the degradation and mineralization of IBP were found to accelerate with increasing O_3 flow rates in the process of water treatment[13] and that the removal of COD increased with the increasing of the ozone concentration in the process of wastewater treatment.[13] The increase in the concentration of ozone improved the mass transfer of O_3 and increased the area of the gas–liquid interface, which resulted in an increase of ozone concentration and the formation of the free radicals in the solution.[37]

10.5.4 pH

During ozonation in liquid media, there are two decomposition rates: a low O_3 decomposition rate at $pH < 7$ and a lower O_3 decomposition rate at $pH < 4$. But there is a high O_3 decomposition rate at $pH > 7$. The studies show that oxidation can occur through direct reaction involving molecular O_3 and *via* an indirect pathway through $^{\bullet}OH$ formed during O_3 decomposition. That is, at pH values between 4 and 8, both $^{\bullet}OH$ and molecular O_3 take part in the oxidation process of compounds when O_3 is applied. At pH values above 8, $^{\bullet}OH$ is the main oxidizing agent, while at pH values of 4 or below, molecular O_3 is the leading agent in compound removal. During the present study, an increase in pH from 6.7 to 7.9 does not significantly affect $^{\bullet}OH$ generation.[38]

10.5.5 Temperature

It was observed that pollutants reduction increases with an increase in temperature in general. In a couple of works, the increased rate of the degradation is attributed to two points. On the one hand, the activation energy for the degradation of chemicals was independent of the change of temperature within a limited range. The higher the temperature was, the more energy was generated, and the more target molecules were decomposed. On the other hand, although the ozone concentration decreased as the temperature rose and its water solubility decreased with the increase

of reaction temperature, the system also generated more •OH as temperature went up because of the cavitation effect of US.[9] But in another theory, it was observed that pollutants reduction increases with an increase in temperature up to an optimum temperature. A marginal decrease in pollutants reduction was observed for a further increase in temperature. The enhanced degradation rate at the optimum temperature is due to the optimum balance between the cavitational activity and kinetic rates, but beyond the optimum temperature, the decreased rate of the degradation is attributed to the dominant negative effect of lower cavitational activity due to the cushioned collapse of cavities.[15]

10.6 Combined Processes

The combination of ultrasound and ozone can be conducted with a variety of other treatments. Based on the state of the reaction process in this book, the treatments are divided into two types: homogeneous and heterogeneous.

10.6.1 Homogeneous

10.6.1.1 UV

The combined operation of ultrasound, ozone and UV light was the most effective method of pollutants decay. The advantage over both of the dual combinations (US/O_3 and US/UV) arises from the reaction of ozone in the presence of UV irradiation to yield singlet-state oxygen, which is readily converted to hydrogen peroxide and •OH:[21]

$$O_3 + UV \rightarrow O(^1D) + O_2 \tag{10.1}$$

$$O(^1D) + H_2O \rightarrow H_2O_2 \rightarrow 2^{\bullet}OH \tag{10.2}$$

10.6.1.2 H_2O_2

The increase in the extent of pollutants reduction in the combined operation of ultrasound, O_3 and H_2O_2, as compared to the combination of ultrasound with only O_3/H_2O_2, is due to the combined effect of O_3 and H_2O_2. The introduction of H_2O_2 increases the probability of reaction of O_3 with H_2O_2 to generate •OH. •OH is a powerful oxidant, and has the potential to oxidize most organic pollutants. The increased rate of generation of •OH can also be due to the fact that ultrasonic irradiations result in turbulence, which further increased the mass transfer rate of O_3 and hence its utilization.[1] The reported illustration confirms the beneficial contribution of adding hydrogen peroxide and ozone to give the enhanced quantum of •OH.[19]

10.6.1.3 PMS

This study investigated the degradation efficiency of pollutants using a combination of US, peroxymonosulfate (PMS) and ozone. Based on the scavenging tests, it was found that •OH was the main oxidizing agent in the oxidation of pollutants by the PMS/ozone/US process. The PMS/ozone/US process was compared to US/peroxone, and the results showed the importance of US irradiation in both systems. Accordingly, the PMS/ozone/US process could be considered as an efficient and promising process for water treatment.[35]

10.6.2 Heterogeneous

The combination of the US and O_3 approach with a metallic oxide catalyst in separate experiments was applied for water treatment. Further improvement of the degradation rate was observed with the addition of the catalyst. Ultrasound in homogeneous systems is often used for sonochemical effects such as bond breakage and radical formation, which leads to chemical reactions. Conversely in heterogeneous systems, ultrasound is utilized for the enhancement of mass transport, erosion and mixing. Additionally, the augmentation of rates and yields is also explained by a chemical effect of the ultrasound in heterogeneous systems.[4] In part of the studies, it was observed that the only marginal synergetic effect of sonocatalysis using CuO or TiO_2 as the catalyst was mostly attributed to dominant oxidation by ozone.[15] In other studies, it can be said that TiO_2 and CuO gives better degradation of 37.2% compared to 30.5% using CuO at a similar loading from the results obtained for TiO_2 and CuO in combination with ultrasound and ozone. The observed trends can be attributed to the fact that the presence of CuO and TiO_2 provides an activated surface area in addition to providing nuclei for cavitation; these activated surface areas can accelerate the reactivity and generation of •OH by possible decomposition of the generated hydrogen peroxide in the system.[39] Above all, we can conclude that the degradation effect of organic pollution was enhanced with the addition of catalyst.

10.7 Enhanced Mechanism

According to the literature, the enhanced mechanism is divided into three parts in the process of combining ultrasound and ozone.

A part of the pollutants can be decomposed by ultrasound because of the energy of ultrasound. The ultrasound irradiation of aqueous solutions results in the formation and quasi-adiabatic collapse of vapor bubbles formed from preexisting bubble nuclei.

The •OH is generated by sonolysis alone through substrate pyrolysis inside the bubble or by reaction with the acoustically generated •OH. Then the •OH reacts with the pollutants to remove them from the water or wastewater.

Meanwhile, the radical reactions by ultrasound produce other oxidizing species such as the hydroperoxyl radical $HO_2^{\bullet}$ and superoxide $O_2^{\bullet -}$.

In the absence of ultrasound, ozonation can produce the $^{\bullet}OH$ by means of aqueous reactions, the produced $^{\bullet}OH$ could react with the pollutants, and the pollutants would be removed.

In the combination of ultrasound and ozone, ultrasound enhances the ozone mass transfer and improves the O_3-dissolved concentration. Subsequently, the O_3 is decomposed under the ultrasound and produces the $^{\bullet}OH$ and O_2 simultaneously. Although O_2 lose their oxidizing power, the $^{\bullet}OH$ react with the pollutants and decompose them. On the other hand, sonication enhances the mass transfer of O_3, which may result in additional O_3 being transferred to solution and decomposed. Thanks to its high solubility in water, O_3 at high concentrations in the aqueous phase may act as a quencher of active cavitation formation due to the high degree of bubble coalescence. This may be the reason for which negative synergy between US and O_3 was reported in many cases. Thus the threshold $[O_3]$, above which there is no inertial cavitation, should not be exceeded. The reaction of O_3 with the acoustically generated H_2O_2 in the aqueous phase is another possible pathway for increasing US/O_3 performance. Note that the occurrence of $^{\bullet}OH$ is to a great extent affected by operating conditions, that is, frequency, power and O_3-dissolved concentration, which control all the physical and chemical effects of acoustic cavitation.[40]

References

1. U. von Gunten, *Water Res.*, 2003, **37**, 1469.
2. A. Pascual, I. Liorca and A. Canut, *Food Sci. Technol.*, 2009, **18**, S29.
3. C. D. Vecitis, T. Lesko, A. J. Colussi and M. R. Hoffmann, *Phys. Chem. A*, 2010, **114**, 4968.
4. M. J. Bussemaker and D. Zhang, *Ind. Eng. Chem. Res.*, 2013, **52**, 3563.
5. H. Yua, Y. X. Seowa, P. K. C. Onga and W. Zhou, *Food Chem.*, 2018, **269**, 628.
6. H. Yua, Y. X. Seowa, P. K. C. Onga and W. Zhou, *Ultrason. Sonochem.*, 2017, **34**, 154.
7. M. Erriu, C. Blus, S. Szmukler-Moncler, S. Buogo, R. Levi, G. Barbato, D. Madonnaripa, G. Denotti, V. Piras and G. Orrù, *Ultrason. Sonochem.*, 2014, **21**, 15.
8. H. Yu, Y. Liu, L. Li, Y. H. Guo, Y. F. Xie, Y. L. Cheng and W. R. Yao, *Trends Food Sci. Technol.*, 2020, **96**, 91.
9. Y. J. Shen, Q. H. Xu, R. R. Wei, J. L. Ma and Y. Wang, *Ultrason. Sonochem.*, 2017, **38**, 681.
10. A. J. Barik and P. R. Gogate, *Ultrason. Sonochem.*, 2017, **36**, 517.
11. N. Castanha, D. C. Lima, M. D. M. Junior, O. H. Campanella and P. E. D. Augusto, *Int. J. Biol. Macromol.*, 2019, **139**, 63.
12. A. M. Al-Hashimi, T. J. Mason and E. M. Joyce, *Environ. Sci. Technol.*, 2015, **49**, 11697.
13. A. Ziylan and N. H. Ince, *Catal. Today*, 2015, **240**, 2.

14. L. Zhao, W. C. Ma, J. Ma, G. Wen and Q. L. Liu, *Ultrason. Sonochem.*, 2015, **22**, 198.
15. S. D. Ayare and P. R. Gogate, *Ultrason. Sonochem.*, 2019, **51**, 69.
16. Y. Wang, H. Zhang and L. Chen, *Catal. Today*, 2011, **175**, 283.
17. G. H. Xu, S. H. Chen, J. W. Shi, S. M. Wang and G. F. Zhu, *J. Hazard. Mater.*, 2010, **180**, 340.
18. M. Ibánez, E. Gracia-Lor, L. Bijlsma, E. Morales, L. Pastor and F. Hernández, *J. Hazard. Mater.*, 2013, **260**, 389.
19. S. Chandak, P. K. Ghosh and P. R. Gogate, *Process Saf. Environ. Prot.*, 2020, **137**, 149.
20. A. Ziylan and N. H. Ince, *Chem. Eng. J.*, 2013, **220**, 151.
21. R. Kidak and N. H. Ince, *Chem. Eng. J.*, 2007, **146**, 630.
22. Z. Q. He, S. Song, H. P. Ying, L. J. Xu and J. M. Chen, *Ultrason. Sonochem.*, 2007, **14**, 568.
23. S. Anandana, V. K. Ponnusamyb and M. Ashokkumar, *Ultrason. Sonochem.*, 2020, **67**, 105130.
24. A. O. Martins, V. M. Canalli, C. M. N. Azevedo and M. Pires, *Dyes Pigm.*, 2006, **68**, 227.
25. F. Ghanbari, M. Khatebasreh, M. Mahdavianpour and K. A. Lin, *Chemosphere*, 2020, **244**, 125326.
26. V. O. Abramov, O. V. Abramov, A. E. Gekhman, V. M. Kuznetsov and G. J. Price, *Ultrason. Sonochem.*, 2006, **13**, 303.
27. N. H. Ince, *Ultrason. Sonochem.*, 2018, **40**, 97.
28. R. Ganesh, G. D. Boardman and D. Michelsen, *Water Res.*, 1994, **28**, 1367.
29. N. H. Ince and G. Tezcanli, *Dyes Pigm.*, 2001, **49**, 145.
30. N. Liu, X. W. Jin, C. L. Feng, Z. J. Wang, F. C. Wu, A. C. Johnson, H. X. Xiao, H. Hollert and J. P. Giesy, *Environ. Int.*, 2020, **136**, 105454.
31. W. Q. Guo, R. L. Yin, X. J. Zhou, J. S. Du, H. O. Cao, S. S. Yang and N. Q. Ren, *Ultrason. Sonochem.*, 2015, **22**, 182.
32. L. W. Hou, H. Zhang, L. G. Wang and L. Chen, *Chem. Eng. J.*, 2013, **229**, 557.
33. S. Ibrahim, M. A. El-Liethy, A. L. K. Abia, M. Abdel-Gabbar, A. M. A. Zanaty and M. M. Kamel, *Total Environ.*, 2020, **703**, 134786.
34. J. W. Kang and M. R. Hoffmann, *Environ. Sci. Technol.*, 1998, **32**, 3194.
35. S. D. Ayarea and P. R. Gogate, *Sep. Purif. Technol.*, 2020, **233**, 115979.
36. N. M. Navarro, T. Chave, P. Pochon, I. Bisel and S. I. Nikitenko, *J. Phys. Chem. B*, 2011, **115**, 2024.
37. H. Destaillats, A. J. Colussi, J. M. Joseph and M. R. Hoffmann, *J. Phys. Chem. A*, 2000, **204**, 8930.
38. P. Alfonso-Muniozguren, M. H. Bohari, A. Sicilia, C. Avignone-Rossa, M. Bussemaker, D. Saroj and J. Lee, *Ultrason. Sonochem.*, 2020, **64**, 104986.
39. K. P. Mishra and P. R. Gogate, *Ind. Eng. Chem. Res.*, 2012, **51**, 1166.
40. S. Merouani and O. Hamdaoui, *Curr. Opin. Green Sustainable Chem.*, 2019, **18**, 98.

CHAPTER 11

Hybrid Ceramic Membrane Catalytic Ozonation

ZILONG SONG, RUIJUN REN, YUTING ZHANG, AO LI, JING LIU AND FEI QI*

Beijing Key Laboratory for Source Control Technology of Water Pollution, Beijing Forestry University, No. 35 Qinghua East Road, Beijing 100083, P.R. China
*Email: qifei@bjfu.edu.cn

11.1 Introduction

Generally, catalytic ozonation has shown good application potentials in drinking and wastewater purification in the removal of micropollutants or refractory organics. However, the reported powder active catalyst cannot be used directly in a water treatment plant due to the loss in the effluent. This loss not only increases the cost but also decreases the quality of effluent due to the presence of the powder, especially for the TSS and heavy metal exposure risk. Even though there were many methods to make powder catalyst by granulation, the catalytic activity is lost to a certain degree. Therefore, the granulation of powder catalyst is a limitation problem for the application of catalytic ozonation.

Recently, membrane filtration was also used widely in drinking and wastewater purification to remove particulates and bacteria. The application of membrane filtration in drinking water shortened the water treatment process and safely reclaimed water from municipal effluent. However, membrane fouling is an important problem for its application and the cost reduction.

Chemistry in the Environment Series No. 8
Advanced Ozonation Processes for Water and Wastewater Treatment: Active Catalysts and Combined Technologies
Edited by Hongbin Cao, Yongbing Xie, Yuxian Wang and Jiadong Xiao

Published by the Royal Society of Chemistry, www.rsc.org

Therefore, ozonation is an efficient pretreatment for membrane filtration, among all the reported methods. However, while polymeric membrane has shown worse chemical resilient property with ozone, ceramic membrane has shown more stability, longer life and higher physical integrity. In the literature, the combination of ozonation and ceramic membrane filtration has exhibited better performance in refractory organic degradation, the precursor degradation of disinfection by-products and membrane fouling migration. This coupling technology has been used for drinking water purification when alga-rich water was used as the source in a wastewater reclaiming process.

Due to the inorganic components in ceramic membrane, such as Al_2O_3, ZrO_2 and TiO_2, ceramic membrane showed potential catalytic ozonation activity. The bromate elimination in the coupling of ceramic membrane with ozonation confirmed this idea. On the other hand, ceramic membrane is a good supporter for active powder catalyst in catalytic ozonation. If this is achieved, the interface catalytic ozonation is able to remove refractory organic or microcontaminants and to degrade natural organic matter (NOM), achieving disinfection by-product (DBPs) precursor degradation and membrane fouling migration.

In this chapter, the application of the combination of ozonation and ceramic membrane is described first, and the key point is the membrane fouling migration mechanism derived by ozonation. After that, the progress of the catalytic ceramic membrane and its coupling with the interface of catalytic ozonation is shown, including novel catalytic ceramic membrane fabrication, its performance on refractory organics and DBP precursor degradation, membrane fouling migration.

11.2 Coupling of Ceramic Membranes with Ozonation

Membrane filtration integrated with ozonation has proven to be the most promising technique for purifying drinking water and wastewater treatment,[1–3] especially for removing natural organic matter (NOM),[4] emerging micro-organic pollutants[5] and disinfection by-product (DPB) precursors.[6] Ozone is a powerful oxidant with a redox potential of 2.07 V[7] and is able to reduce membrane fouling caused by NOM, secondary effluent organic matter (EfOM) and microorganisms in effluent by changing their molecular sizes or other characteristics.[6,8] For instance, Wei *et al.* reported that pre-ozonation-filtration (pre-O/F) with ceramic membranes mitigated hydraulically reversible fouling but could not alleviate irreversible fouling because of the selective oxidation of high-MW substances,[2] which was also reported by Tang *et al.*[9] In *in-situ*-ozonation filtration (*in-situ*-O/F), oxidized organic foulants deposited on the membrane surface improved filterability.[10] In drinking water and wastewater treatment, *in-situ*-O/F effectively mitigated reversible and irreversible fouling[10–12] that could not be alleviated by pre-O/F.[10] Song *et al.* reported that *in-situ*-O/F outperformed pre-O/F in terms of irreversible membrane fouling because the dissolved ozone and the resultant hydroxyl radical ($^{\bullet}OH$) oxidized

irreversible membrane fouling deposited on the membrane surface and in the membrane pores *in situ.*[13]

However, membrane fouling is a complex phenomenon that typically includes inorganic, organic and biofouling layers.[14] The role of ozonation in mitigating membrane fouling had been studied by Song *et al.*[15] in more detail to guide the application of coupled ozonation and ceramic membrane filtration, including coupling running modes such as *in-situ*-O/F and pre-O/F.

11.2.1 Effect of Ozone Coupling Mode on EfOM Removal

It has been found that the filtration removed 47.06% of chemical oxygen demand (COD), 40.79% of UV_{254} and 42.34% of total organic carbon (TOC). Ozonation removed more COD (55.88%), UV_{254} (72.36%) and TOC (50.67%) than filtration when the contact time was 40 min. The combination of ozonation and filtration performed best, depending on the reaction time. In pre-O/F mode, the removal performance for COD, UV_{254} and TOC increased to 64.71%, 40.89% and 53.93%, after pre-ozonation for 8 min, while for *in-situ*-O/F, these removal performances were 55.88%, 42.85% and 55.12%, respectively.

Fluorescence excitation and emission matrix (EEM) spectra were used to characterize the EfOM in the effluent of a wastewater treatment plant (WWTP) and ozonation and in the permeates obtained from filtration. Coupling ozonation and filtration improved the removal efficiency of EfOM, which was further enhanced by increasing the reaction time from 8.0 to 40 min. When reaction time was 8 min in pre-O/F mode, the removal efficiency followed the order fulvic-acid-like substances (rejection efficiency was 43.16%) > humic-acid-like substances (41.89%) > soluble microbial products (36.29%) > aromatic protein substances (18.97%). These removal efficiencies were higher than those observed for either ozonation or filtration alone, but no cooperative or synergistic effects were observed. For example, filtration had a 15.71% rejection efficiency for aromatic protein substances, while ozonation had a 3.56% removal efficiency. The pre-O/F removal efficiency was simply the sum of the removal efficiencies of filtration and ozonation (18.97%).

However, in *in-situ*-O/F mode, the order of the removal efficiencies of the components of EfOM changed to humic-acid-like substances (63.47%) > fulvic-acid-like substances (44.07%) > soluble microbial products (40.37%) > aromatic protein substances (20.85%). *In-situ*-O/F mode rejected more EfOM than pre-O/F mode, especially for humic-acid-like and fulvic-acid-like substances. The performance of *in-situ*-O/F mode was obviously better than that of either filtration or ozonation alone. Unlike in pre-O/F mode, synergistic effects were clearly observed in *in-situ*-O/F mode including between oxidation and membrane rejection. Simultaneous oxidation and filtration enhanced the interfacial mass transfer and led to improved EfOM removal.[16]

Overall, coupling filtration and ozonation resulted in higher EfOM removal efficiency than either filtration or ozonation alone. *In-situ*-O/F performed better than pre-O/F in removing protein-like substances that easily clogged the membrane pores.

11.2.2 Effects of Pre-O/F and *In-situ*-O/F on Membrane Fouling

The specific flux (J/J_0) was employed to evaluate membrane permeate flux and membrane fouling. In pre-O/F mode, J/J_0 gradually decreased in the initial 20 min as the ozonation time increased. When the pre-ozonation times were 8, 20 and 40 min, the values of J/J_0 were 1.16, 1.42 and 2.18 times the value for filtration alone, respectively. In *in-situ*-O/F mode, the value of J/J_0 decreased rapidly even after the introduction of ozone. Because of the shorter contact time in *in-situ*-O/F mode, the EfOM cannot be oxidized completely. However, after 20 min, *in-situ* ozonation gradually began to decrease the quantity of membrane fouling. This efficiency increased with the *in-situ* ozonation time. In summary, the flux in pre-O/F mode was higher than in *in-situ*-O/F mode, suggesting that the former performed better in mitigating fouling.

In addition, after filtration, the thickness of the layer formed from the foulants was 38.2 ± 1.21 μm based on SEM cross-sectional images of the tubular ceramic membranes (TCMs). This value decreased to 9.58 ± 1.09 μm in pre-O/F because of the ozonation. The foulant layer formed after combined ozonation and filtration had more loose fragments than that obtained from filtration alone. These loose fragments can be flushed away more easily by crossflow to mitigate membrane fouling [33]. The reduction of the fouling load before filtration was the primary mechanism of membrane fouling mitigation in pre-O/F mode. In *in-situ*-O/F mode, the thickness of the foulant layer was 16.67 ± 0.47 μm, which was thicker than that obtained in pre-O/F mode and which resulted in poor flux recovery in this mode.

11.2.3 Membrane Fouling Mitigation Mechanism

The membrane fouling layer formed in the filtration mode was mainly composed of inorganic, organic and biofouling fouling layers. Among them, the organic and biofouling layers were classified either as reversible membrane fouling, such as protein-like substances in EfOM and extracellular polymeric substances (EPS) or microbes in biofouling fouling layers, or as irreversible membrane fouling, such as humic-acid-like substances in EfOM and EPS or microbes in biofouling fouling layers (Figure 11.1).

For inorganic membrane fouling, three aspects should be considered: (1) The degradation and structural transformation of EfOM in ozonation decreased the precipitation of Ca/Mg on the membrane surface. (2) The ozonation made the fouling layer smoother, which led to the hard formation of inorganic membrane fouling on the surface. (3) The effect of concentration polarization decreased, and the inorganic membrane fouling was mitigated substantially when the crossflow velocity increased.

For organic membrane fouling, in pre-O/F mode, EfOM was degraded or transformed in pre-ozonation, which decreased the EfOM load in filtration and eliminated membrane fouling. In *in-situ*-O/F mode, organic membrane

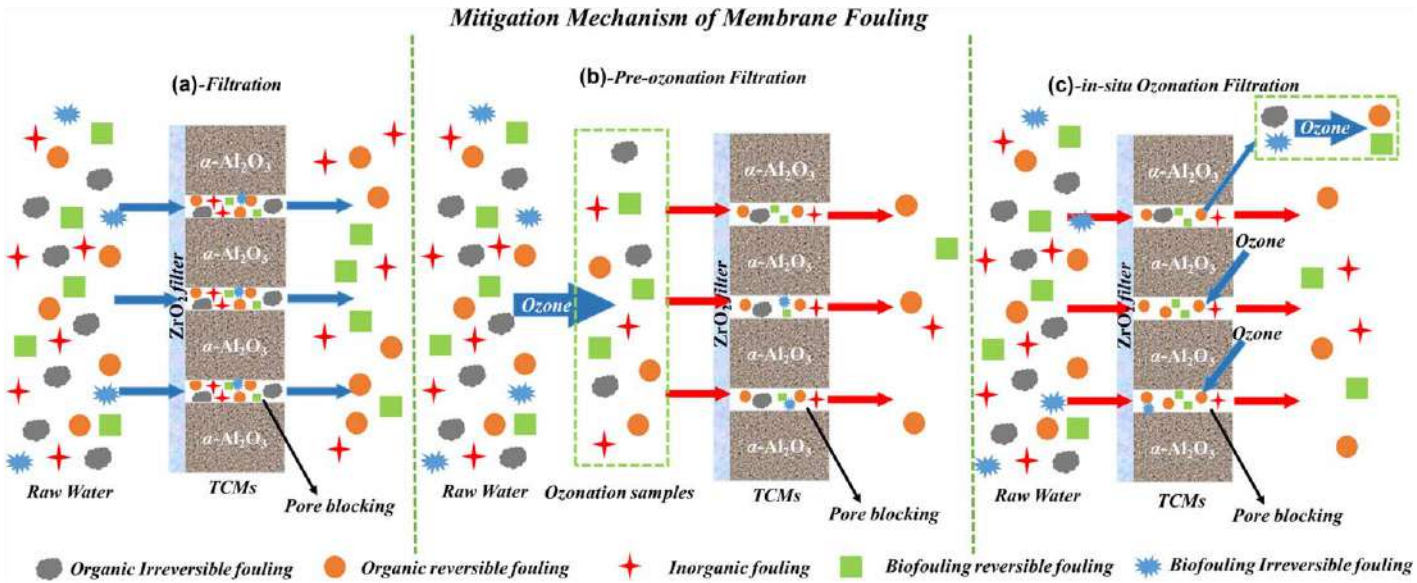

Figure 11.1 Mechanism of membrane fouling mitigation in (a) filtration, (b) pre-O/F and (c) *in situ* O/F. Reproduced from ref. 15 with permission from Elsevier, Copyright 2020.

fouling mitigation was mainly the consequence of lower adhesion between irreversible membrane fouling and the pores/surfaces of the TCMs. At the same time, part of the organic fouling was destroyed by *in-situ* ozonation.

For biofouling, in pre-O/F mode, the structures of α-polysaccharides, proteins and β-polysaccharides were destroyed and the microorganisms in the effluent were killed by ozonation. This phenomenon was also observed in *in-situ*-O/F mode. Microorganisms on the surface of the membrane were also killed by ozonation, and the adhesion between the biofouling foulants and membrane channels or pores was destroyed by *in-situ* ozonation. The quantity of biofouling foulants clogging the membrane pores also diminished.

11.3 Coupling of Catalytic Ceramic Membranes with Ozonation

11.3.1 Kinds of Catalytic Ceramic Membranes and Corresponding Fabrication Methods

11.3.1.1 Physical Coating Techniques

(i) Physical Vapor Deposition

Physical vapor deposition (PVD) includes a variety of deposition methods in which the target material is evaporated from a condensed phase to vapor and then transmitted to an ambient substrate for condensation under a vacuum in a low-pressure gas or plasma environment. PVD is a versatile technique to prepare thin films of pure metals, alloys or compounds.[17] As for catalyst immobilization, this technique has been primarily utilized to prepare palladium (Pd) or Pd alloy membranes for hydrogenation and dehydrogenation processes.[18] For example, Lin *et al.* used the magnetron sputtering technique to coat a γ-Al_2O_3 membrane with 75% Pd–25% Ag alloy and Pd(II) acetylacetonate,[19] which is atomized by collisions of Ar plasma and deposited on the ceramic membrane. The catalyst film thickness on the porous substrates was adjusted by changing substrate temperature (25–400 °C), plasma power (10–60 W) and coating time (5–20 min). By contrast, Dittmeyer *et al.* prepared Pd composite membranes by evaporating Pd in a vacuum chamber and subsequently condensing it on porous stainless steel tubes inside a vacuum chamber.[20]

(ii) Dip Coating

Dip coating involves the immersion of a membrane substrate into a solution containing coating substances, followed by removal and drying of the coated substrate. The dip coating technique can be normally divided into five separate steps: immersion, start-up, deposition, drainage and evaporation, with the first three steps sequential and last two concomitant. The coating layer thickness can

be controlled by adjusting different process parameters such as immersion time, withdrawal speed, solution composition, dipping cycles. For example, the photocatalytic membranes were fabricated by dip-coating a TiO_2 sol onto a filtration membrane, followed by calcination to achieve a desired TiO_2 crystalline phase.[21] Dionysious *et al.* prepared a TiO_2/Al_2O_3 composite photocatalytic membrane by dip coating organic/inorganic sol containing isopropanol, acetic acid, Tween 80 and titanium tetraisopropoxide, followed by calcination at 500 °C.[22]

Organic catalysts such as Amberlyst 15,[23] styrene–divinylbenzene copolymer,[24] and perfluorosulfonic acid[25] have also been successfully immobilized on membrane substrate by dip coating. For example, Benes *et al.* prepared a dip coating suspension with Amberlyst 15, Aculyn (as rheology modifier) in water, which was used to immerse (16 mm s^{-1}) a pre-wetted PVA pervaporation membrane for 2 min before drying in air at 90 °C for 2 h.[23] An Amberlyst 15 layer (~ 25 mm of thickness) was coated on the PVA membrane surface. This layer offered catalytic activity on conventional pervaporation membranes and simultaneously enabled esterification catalysis and water removal for superior ester yield.

(iii) Spin Coating

The spin coating technique uses centrifugal forces to spread uniformly thin films on flat substrates. In particular, a small amount of coating substances in a liquid form is applied on the substrate center, which is fixed on a spinning device, followed by a high-speed rotation of the substrate to spread the coating substances. A number of studies have successfully used the spin coating technique for catalytic membrane fabrication.[26] For example, Godbert *et al.* fabricated a porous TiO_2/α-alumina membrane by first spin coating a TiO_2 precursor solution at 1000 rpm for 1 min on an α-Al_2O_3 membrane,[27] followed by calcination at over 350 °C. A uniformly TiO_2-coated alumina surface was obtained, facilitating a promoted pollutant adsorption on the membrane surface (a key requirement for enhanced catalytic degradation). The membrane showed effective methylene blue degradation under sunlight. In a more recent example, Ma *et al.* prepared a $CuFe_2O_4$-decorated ceramic membrane for treating humic acid *via* peroxymonosulfate (PMS) activation.[28]

(iv) Casting

Casting is one of the most commonly used techniques to produce flat polymeric membranes[29] and has also been extensively applied for catalyst coating on dense or porous membrane substrates. A number of studies utilized the casting technique to coat homogeneous catalysts on membrane substrates.[30] For instance, Li *et al.* developed a catalytically active composite membrane for esterification enhancement in pervaporation reactors.[30] They cast a catalytic solution containing poly (styrene sulfonic acid) (catalyst) and poly (vinyl alcohol)

(hosting polymer) onto a traditional pervaporation membrane and evaporated it in atmosphere at room temperature to form the catalytic membrane *via* a vapor-induced phase separation mechanism. The dense composite membrane combined the catalytic activity and pervaporation separation functions and enhanced the reactant (propionic acid) conversion rate to 92.8% within 12 h. Alternatively, the casting technique can also be used to immobilize heterogeneous catalyst such as solid acid[24] and enzymes.[31] For example, Qing *et al.* cast a solution with lipase suspension, poly (vinyl alcohol) (PVA) and glutaraldehyde (act as cross-linking agent) onto a PVA pervaporation membrane[32] and immersed the solution into a coagulation bath (an ammonium sulfate aqueous solution) for nonsolvent-induced phase separation.

(v) Filtration

Filtration for catalyst immobilization refers to the process where a catalyst-loaded solution or suspension is filtrated through a porous membrane, during which the catalysts are attached on the membrane surface[33] or the inner channel.[34] Either covalent bonding or noncovalent bonding (hydrophobic/hydrophilic or electrostatic interactions) exists between the catalyst and the membrane surface. Owing to its facile and straightforward operation, filtration has widely been applied to immobilize either homogeneous or heterogeneous catalysts on both inorganic and polymeric porous membranes for water treatment. For example, Molinari *et al.* deposited photocatalysts (TiO_2) on a flat sheet polyacrylonitrile membrane by filtrating the TiO_2 aqueous suspension.[33] The resulting membrane removed 40 $mg\,L^{-1}$ 4-nitrophenol after 5–6 h in a membrane photoreactor. However, poor mechanical stability was also evidenced due to noncovalent bonding of the photocatalyst with the polyacrylonitrile membrane. Likewise, Qi *et al.* filtrated a Cu-MOF nanosheets catalyst suspension onto a commercial nylon porous membrane,[35] followed by reducing the membrane with an aqueous $NaBH_4$ solution to form a Cu/Cu_2O/nylon composite catalytic membrane for continuous *p*-nitrophenol reduction. The membrane efficiently converted >95% of *p*-nitrophenol to *p*-aminophenol in 8 h without obvious membrane structure changes or catalyst deactivation.

(vi) Layer-by-layer Assembly

Layer-by-layer (LBL) assembly was first proposed by R. K. Iler to prepare multilayered films *via* alternating coatings of oppositely charged colloidal particles[36] and now has evolved to be a pervasive technique for coating substrates with nanoparticles, colloids, polymers, biomolecules with superior versatility and controllability.[37] LBL assembly has also been widely used to fabricate catalytic membrane for a variety of applications, including energy production,[38] water treatment[39] and chemical synthesis.[40] Remarkably, several studies explored the use of LBL assembly to fabricate membrane electrodes

for membrane fuel cell applications. Membrane electrodes have attractive features in the facile incorporation of conductive nanofillers, high ionic contents, conformal coating of surfaces with any complex geometry and nanoscale control of film thickness and porosity. Different nanoparticles (Au,[41] Pt,[42] Pd,[43] SiO_2,[44] ZrO_2[45]) carbon nanotubes (single wall[46] and multiwall[47]) have been successfully employed on Nafion membranes through LBL assembly for promising proton exchange membrane fuel cell development.

11.3.1.2 Chemical Coating Techniques

(i) Coupling Agents

"Coupling agents" refers to any chemicals that can act as "molecular bridges" to establish strong chemical binding or adhesion between dissimilar coating materials and substrate materials.[48] Polydopamine (PDA) is the most notable coupling agent in recent years for catalyst coating.[49] PDA is a novel bio-inspired material containing catechol, amine and imine functional groups, which offers attractive mussel-like adhesive properties and can firmly attach to different substrates with robust binding strength. PDA was first reported by Messersmith *et al.*,[50] who reported that dopamine mimics the composition of adhesive proteins and is able to self-polymerize in water to form adhesive PDA thin films. The PDA film from this pioneering work provides a versatile platform for secondary reaction and has attracted considerable research interest for surface modification.[51]

Silane coupling agent (SCA) has a general formula, RnSiX(4-n), where R is a non-hydrolytic organic group that reacts with different polymers,[52] and X is a hydrolytic group with good reactivity with hydroxyl groups on inorganic surfaces such as metals, ceramics, oxides and semiconductors. The binding principle follows three basic steps: First is hydrolysis of the X group into hydroxyl group, which then forms a hydrogen bond with a hydroxyl group on the inorganic surface or is dehydrated into an ether bond. Finally, the R group is bonded to the organic materials. Sun *et al.* coated goethite (α-FeOOH) catalysts on a zirconia/titanium-aluminum membrane with the bis-(3-[trimethylsilyl]-propyl]-tetrasulfide coupling agent to prepare a photo-Fenton ceramic membrane.[53] The results showed that the photo-Fenton reaction slowed down membrane fouling. At the same time, the degradation rate of HA and BSA in the light Fenton flat ceramic membrane in 60 min were 76% and 86%, respectively.

(ii) Sol–Gel Method

The solution–gelation (sol–gel) technique is a well-studied technique to synthesize solid materials from small molecules, which generally starts with the hydrolysis of a liquid precursor (sol), which undergoes poly-condensation to form a gel.[54] A typical sol–gel process

consists of four stages: (1) hydrolysis, (2) monomers condensation to form chains and ions, (3) growth of particles and (4) tight aggregation of the polymer.[55] For example, Mamane *et al.* coated N-doped TiO_2 photocatalytic film on commercial α-Al_2O_3 photocatalytic membranes using the sol–gel technique for concurrent bottom-up filtration and photocatalytic oxidation.[56] About eighty percent of the membrane surface was covered by the N-doped TiO_2 film, which unfortunately reduced over 50% of the permeability for membrane substrates.

(iii) Chemical Vapor Deposition

Chemical vapor deposition (CVD) is a popular surface coating technique for a variety of applications, during which a volatile coating precursor is vaporized in an inert atmosphere by heat, light and/or plasma discharge and is then reacted on a solid substrate surface to produce a desired deposit.[57] CVD has been one of the most promising and well-studied methods for deposition of catalysts onto membranes.[58] For example, noble metal catalytic films including palladium, rhodium, ruthenium, iridium and platinum acetylacetonates were deposited on porous inorganic membranes for various reactions,[17] such as methane steam reforming,[59] hydrogenation and dehydrogenation,[60] hydroxylation of benzene,[61] and water–gas shift.[62] Itoh *et al.* reported a catalytic palladium membrane fabricated by CVD for reductive oxidation of benzene to phenol.[61]

(iv) Surface Grafting

Surface grafting is a chemical coating method that involves the covalent conjugation of polymer chains (in some cases a small molecular chain) to a target surface to change its surface properties. For example, Szekely *et al.* reported the surface covalent grafting of organ catalysts on nanofiltration (NF) membranes for synthesis-separation coupling.[63] They first synthesized an azido-derivatized cinchona squaramide bifunctional catalyst for asymmetric Michael additions and then grafted it on a polybenzimidazole- (PBI-) based NF membrane through an azide–alkyne cycloaddition. The catalysis/separation integrated membrane realized 98% product recovery and 99% unreacted substrate recovery, respectively, for the asymmetric Michael and azaMichael reactions of 1,3-dicarbonyl and pyrazole, indole and triazole derivatives to β-nitrostyrene.

(v) *In-situ* Growth

In-situ growth of coating materials on specific substrate surfaces has become increasingly popular due to the generation of uniform surface coating with tunable properties (thickness, porosity and catalyst morphology). It inherently eliminates the daunting aggregation problem that most heterogeneous catalysts (especially small particles) face in many other coating processes. *In-situ* growth is generally realized by surface chemical reactions (*e.g.* hydrothermal, catalytic initiation and anodic oxidation), during which a growth center (seed) is usually required as a core on the surface followed by crystallization on the

matrix. For example, Zhang *et al.* deposited titanium silicalite-1 zeolite films on porous α-Al_2O_3 tubes using nano-sized silicalite-1 particles as seeds by a hydrothermal growth technique.[64] The catalytic membrane was successfully used in a phenol hydroxylation reaction. More recently, Zhan *et al.* synthesized Mn_3O_4 nanodots ($Mn(CH_3COO)_2{\cdot}4H_2O$ as precursor) on graphitic carbon nitride membrane support through hydrothermal synthesis for catalytic degradation of 4-chlorophenol.[65]

11.3.2 Reaction Mechanism

The reaction mechanism of catalytic membrane is closely related to the type of catalytic membrane, such as metal-based catalytic membrane, carbon-based catalytic membrane and so on. But in the final analysis, the reaction mechanism of catalytic membrane is still the electron transfer mechanism, leading to the formation of reactive oxygen species (ROS). For instance, Lee *et al.* proposed the reaction mechanism of heterogeneous catalytic ozonation by cerium oxide–modified CM. In the presence of water, the surface of the metal oxides is generally covered with surface hydroxyl groups (S–OH) due to the interaction between water molecules and the metal oxide surface. The protonated surface hydroxyl groups ($S\text{–}OH_2^+$) could serve as Brønsted acid sites for reaction with $O_{3(aq)}$ and H_2O (eqn (11.1) and (11.2)) to produce $HO^\bullet$ and $HO_3^\bullet$. The $HO^\bullet$ generated could further react with O_3 and initiate the chain reactions (eqn (11.3)–(11.5)) in bulk solution to generate $O_2^{\bullet-}$. The $O_2^{\bullet-}$ could then react with O_3 and H^+ to generate $HO_3^\bullet$ (eqn (11.6) and (11.7)), whereby the $HO_3^\bullet$ generated could further self-decompose into $HO^\bullet$ (eqn (11.8)). Besides, cerium oxide exhibited high oxygen storage capacity with rapid formation and elimination of oxygen vacancy defects. The $O_{3(aq)}$ could be adsorbed and accept electron transferred from the surface Ce^{3+}, producing $O_3^{\bullet-}$ as a precursor of $HO^\bullet$ generation (eqn (11.7) and (11.8)). Then the Ce^{4+} could be reduced back to Ce^{3+} *via* electron transfer from O_{lat}, creating oxygen vacancies for oxygen species adsorption.[8]

$$S\text{–}OH_2^+ + O_3 \rightarrow S\text{–}OH^+ + HO_3^\bullet \quad (11.1)$$

$$S\text{–}OH^+ + H_2O \rightarrow S\text{–}OH_2^+ + {}^\bullet OH \quad (11.2)$$

$$HO^\bullet + O_3 \rightarrow HO_4^\bullet \quad (11.3)$$

$$HO_4^\bullet \rightarrow HO_2^\bullet + O_2 \quad (11.4)$$

$$HO_2^\bullet \leftrightarrow H^+ + {}^\bullet O_2^- \quad (11.5)$$

$${}^\bullet O_2^- + O_3 \rightarrow {}^\bullet O_3^- + O_2 \quad (11.6)$$

$$O_3^{\bullet-} + H^+ \leftrightarrow HO_3^\bullet \quad (11.7)$$

$$HO_3^\bullet \leftrightarrow HO^\bullet + O_2 \quad (11.8)$$

In addition, Song *et al.* proposed the reaction mechanism of carbon-based catalytic membrane.[66]

(1) The role of oxygen-containing functional groups (eqn (11.9)–(11.16)):

$$6\text{Carbon–(HC=O)} + 2O_3 \rightarrow 6\text{Carbon–(COOH)} \quad (11.9)$$

$$2\text{Carbon–(COOH)} + O_3 + H_2O \rightarrow 2\text{Carbon} + 2H_2O_2 + 2O_2 \quad (11.10)$$

$$O_3 + \text{Carbon–OH} \rightarrow {}^{\bullet}O_3\text{–Carbon} + HO^{\bullet} \quad (11.11)$$

$${}^{\bullet}O_3\text{–Carbon} \rightarrow {}^{\bullet}O\text{–Carbon} + O_2 \quad (11.12)$$

$$O_3 + {}^{\bullet}O\text{–Carbon} \rightarrow {}^{\bullet}O_2^- + \text{Carbon} + O_2 \quad (11.13)$$

$$\text{Carbon-}\pi + 2H_2O \rightarrow \text{Carbon–}H_3O^+ + OH^- \quad (11.14)$$

$$O_3 + OH^- \rightarrow {}^{\bullet}HO_2 + {}^{\bullet}O_2^- \quad (11.15)$$

$${}^{\bullet}HO_2 \rightarrow {}^{\bullet}O_2^- + H^+ \quad (11.16)$$

(2) The role of free electrons (as shown in eqn (11.17)–(11.19)):

$$O_3 + e^- \rightarrow {}^{\bullet}O_3^- \quad (11.17)$$

$${}^{\bullet}O_3^- + H^+ \rightarrow HO_3^{\bullet} \quad (11.18)$$

$$HO_3^{\bullet} \rightarrow O_2 + HO^{\bullet} \quad (11.19)$$

As shown in Figure 11.2, these formed ROS could effectively increase the removal efficiency of target pollutants, resulting in reduced effluent toxicity.

Meanwhile, these formed ROS could effectively eliminate the formation membrane fouling. For inorganic membrane fouling, the degradation and structural transformation of EfOM by these formed ROS decreased the precipitation of Ca/Mg on the catalytic membrane surface. Also, the fouling

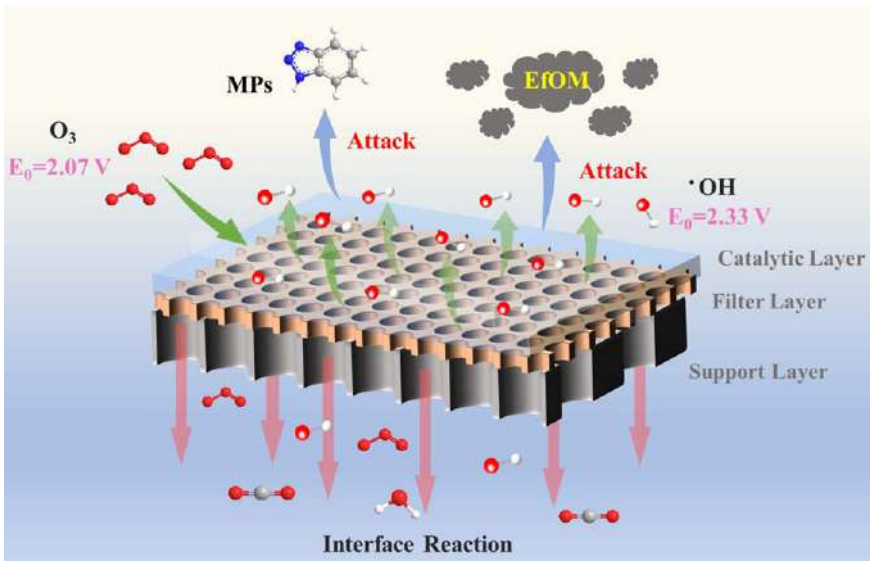

Figure 11.2 Reaction mechanism of catalytic membrane.

layer became smoother after ROS treatment, which led to the hard formation of inorganic membrane fouling on the surface. The crossflow velocity also increased, which led to the decrease of concentration polarization, and the inorganic membrane fouling was mitigated substantially (Figure 11.3).

For organic membrane fouling, high exposure to the catalytic layer on the CM surface led to the formation of considerable amounts of $^{\bullet}OH$ *via* rapid catalytic ozone decomposition, and the fouled membrane was cleaned *in situ*. This superior *in-situ* interfacial catalytic activity enhanced the ozonation efficiency in reversible membrane fouling, and $^{\bullet}OH$ species formed close to contaminants were more likely to attack these molecules. This enhanced the alleviation of reversible membrane fouling. The $^{\bullet}OH$ species produced *in-situ* on the CM surfaces/pores promoted *in-situ* attack of irreversible foulants, which led to their release and degradation. Therefore, irreversible membrane fouling was greatly decreased (Figure 11.4).

11.3.3 Fe-based Catalytic Ceramic Membranes

11.3.3.1 Preparation and Performance of Membranes

Park *et al.*[67] proposed the active ceramic membrane (RM) was synthesized by dipping titanium-dioxide-and-zirconia-mixed ceramic membrane into dispersed iron oxide nanoparticle (IONS) solution and sintering at high temperature. To evaluate catalytic ozonation in the hybrid ceramic membrane process, *p*CBA removal tests were conducted using *p*CBA ($1\ mg\,L^{-1}$) by a hybrid ceramic membrane process with RM and CM. Using the crossflow membrane filtration system, the system temperature was maintained at $20 \pm 1\ ^{\circ}C$, and the transmembrane pressure (TMP) and feed flow rate were kept at 0.8 bar and $0.02\ L\,min^{-1}$, respectively. The RM-ozonation process showed the highest *p*CBA removal efficiency ($C/C_0 = 0.54$) compared to those in CM with ozonation process ($C/C_0 = 0.72$) and without ozonation process ($C/C_0 = 0.92$), indicating that the surface-catalyzed reaction of ozone in the presence of IONs on RM generates hydroxyl radicals. Clémentine *et al.*[68] proposed that a ceramic commercial nanofilter with a very low molecular weight cutoff of 200 Da was functionalized by sol–gel deposition of a mesoporous maghemite (γ-Fe_2O_3) thin layer. Preliminary experiments determined that the maximum temperature was usable for the thermal strengthening of the catalytic layer without significant permeance change. Permeation measurements were done both on pristine and on functionalized membranes, with a transmembrane pressure equal to 10 bar and continuous weighting of the collected permeate during 1 h. Experiments were carried out with *p*CBA ($[p\text{CBA}] = 2\ \mu mol\,L^{-1}$) in the feed tank. The concentration of the injected gaseous ozone was $\sim 28\ g\ Nm^{-3}$. The dissolved concentration of ozone in the transfer reactor and in all the experimental setup was $\sim 3.5\ mg\ O_3\ L^{-1}$. To quantify the catalytic performance of the functional membrane, the R_{ct} value was determined by plotting the *p*CBA elimination as a function of O_3 exposure; as a reference, a configuration

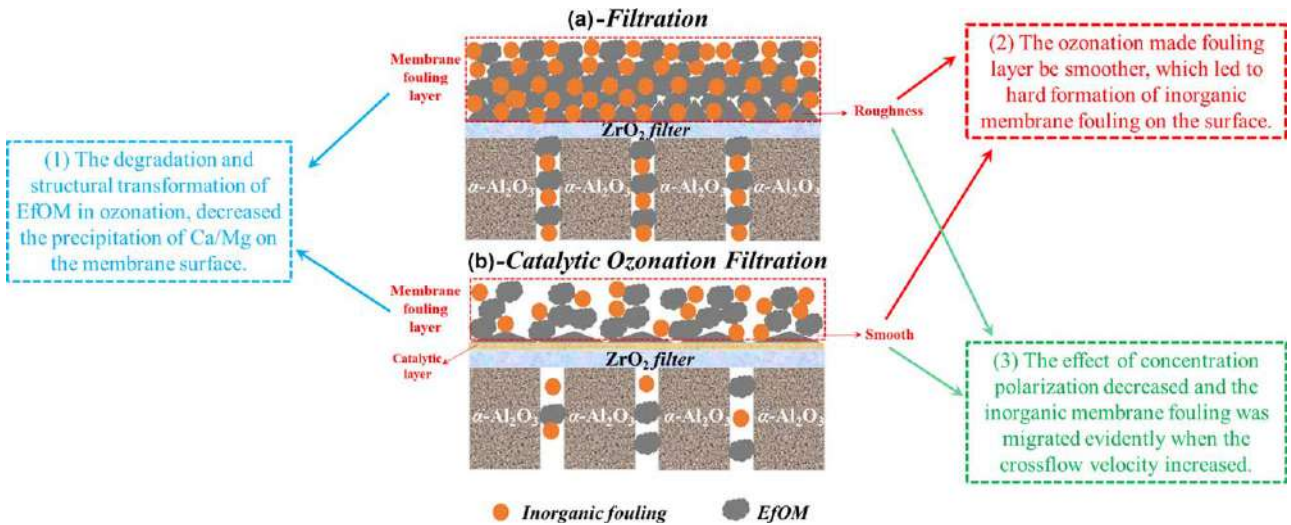

Figure 11.3 Mechanism of inorganic membrane fouling elimination. Adapted from ref. 15 with permission from Elsevier, Copyright 2020.

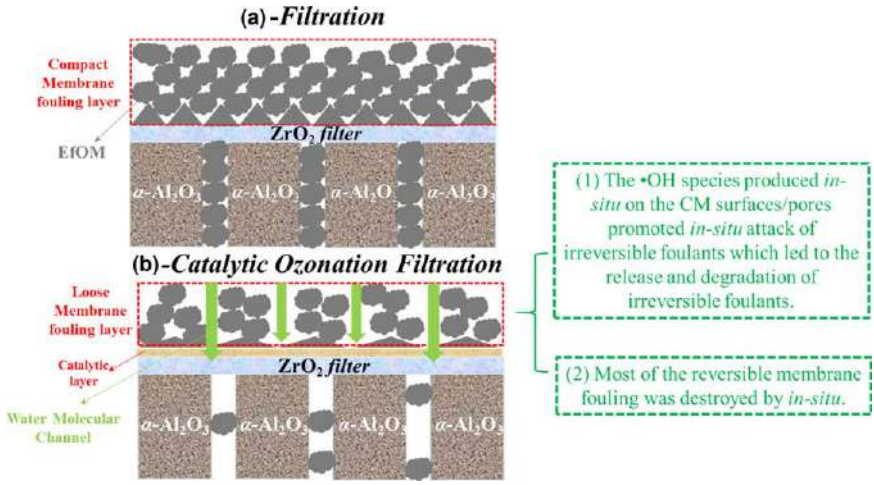

Figure 11.4 Mechanism of organic membrane fouling elimination. Adapted from ref. 15 with permission from Elsevier, Copyright 2020.

without membrane was also implemented. In such a case, R_{ct} was quite low (2.58×10^{-10}). With the pristine membrane, the value of R_{ct} increased to 4.26×10^{-10}. The pristine membrane thus exhibited a weak catalytic activity. These results undoubtedly demonstrated the significant enhancement of the catalytic ozonation due to the presence of the added mesoporous maghemite thin layer.

11.3.3.2 Removal of DBP Precursors

Karnik *et al.*[69] utilized the layer-by-layer technique to coat the membranes, which made a ceramic membrane with catalytic performance by impregnating the titanium dioxide ceramic membrane in ferric chloride solution and subjecting it to calcination at 500 °C or 900 °C. The experiments were performed with a membrane crossflow velocity of 0.6 m s^{-1}; a constant water temperature of 20 °C was maintained using a recirculating water bath. The ozonation–membrane filtration experiments were carried out at TMP 0.5 bar and with gaseous ozone concentration and flow rate kept at 2.5 g m^{-3} and 100 mL min^{-1}. Water samples were dosed with a chlorine concentration that ensured a residual chlorine concentration in the range of 0.5 mg L^{-1} after 48 h of incubation at room temperature. The concentrations of total trihalomethanes (THMs) and haloacetic acids (HAAs) were reduced by up to 90% and up to 85%, respectively, with ozonation combined with an iron oxide–coated 5 kDa membrane. With the use of a 5 kDa MWCO (molecular weight cutoff) membrane, coated 20 times and sintered at 900 °C, the concentrations of TTHMs and HAAs after chlorination were approximately 25–30 μg L^{-1} and 20–25 μg L^{-1}, respectively. Even better-quality water was achieved using a 5 kDa MWCO membrane, coated 40 times and sintered at 900 °C.

After chlorination, the concentration of TTHMs was approximately 15–20 $\mu g\,L^{-1}$, and the concentration of HAAs was approximately 7–15 $\mu g\,L^{-1}$. Byun *et al.* prepared the active ceramic membranes by the layer-by-layer assembly method to deposit iron oxide nanoparticles according to previous reports[69] and proposed that the removal of the trihalomethanes (THMs) and HAAs precursors by the hybrid ozonation filtration system be studied to gain a better understanding of how the coating of the membrane affected the performance of the system.[70] Simulated distribution system (SDS) THMs and SDS HAAs were measured after chlorination to simulate the formation of these DBPs in the distribution system. Water samples were dosed with chlorine at a concentration ensuring that the residual chlorine concentration was in the range 0.5–2 $mg\,L^{-1}$ after 48 h incubation at room temperature. With the use of a 5 kDa MWCO membrane, coated 40 times and sintered at 900 °C, the addition of ozone significantly enhanced the removal of THMS precursors, and the removal efficiency was improved by nearly 10% compared with the ceramic membrane without iron oxide nanoparticle coating. At the same time, compared with the uncoated ceramic membrane, the ceramic membrane coated with iron oxide particles improved the HAA removal effect by about 50%. Karnik *et al.* proposed that the membrane be coated with colloidal iron oxide, prepared by Sorum's method and used for coating the membranes following the layer-by-layer technique developed by the previous research reported. The membranes were coated with 40 layers of iron oxide nanoparticles and sintered at 900 °C. A fresh stock solution of SA (20 $mg\,L^{-1}$) was prepared daily for the experiments, under the operating conditions with TMP of 5×10^4 Pa, water temperature of 20 °C and ozone gas flow rate of 2.5 $g\,m^{-3}$. The concentrations of the by-products are reported as a total by-products concentration derived by adding up the molar concentrations of the individual compounds. The ratio of the concentration of the by-products formed to the initial salicylic acid (SA) concentration ($C_{\text{By-products}}/C_{\text{SAacid}}$) represents the generation of by-products. At pH 2.5–3.0, SA by-products were not detected in the treated water from either ozonation or membrane filtration alone. However, with the hybrid process, SA by-products were formed at low concentrations with $C_{\text{By-products}}/C_{\text{SAacid}} < 0.2$. This supports the proposed hypothesis that the decomposition of ozone on the membrane surface leads to the formation of hydroxyl radicals, which react with SA to form the observed by-products. With the hybrid process using uncoated/unsintered or coated/sintered membranes, the $C_{\text{By-products}}/C_{\text{SAacid}}$ ratio was ~0.55 and ~0.75 after 240 min, respectively. With ozonation alone at pH 8.1, the ratio was ~0.33.

11.3.3.3 Membrane Fouling

P. Hosik *et al.*[67] designed flux decline tests that were conducted using Suwannee River NOM (SRNOM) contained in water by hybrid ceramic membrane processes with reactive ceramic membrane (RM) and CM to observe the changes in the permeate flux against filtration time. A flat-sheet-type of

cell for crossflow filtration was used in this study. The flux of a CM process without ozonation using SRNOM as a feed water source decreased by 30% of the initial flux during 360 min of filtration. However, there was a noticeable enhancement in the membrane flux when continuous ozonation was applied to the hybrid ceramic membrane process (CM-ozonation process: 25%, RM-ozonation process: 15%); thus it is clear that the hybrid ceramic membrane process was found to be very effective in controlling NOM fouling. These results indicate that the hybrid ceramic membrane process with continuous ozonation reduced fouling through the decomposition/mineralization of NOM and also by altering the characteristics of NOM due to the reaction of NOM with ozone and/or hydroxyl radicals produced by the catalytic decomposition of ozone by IONs on the RM surface. The fouling behavior of membrane surface was further studied by Byun *et al.*[70] The fouled membranes were cleaned with DDI water using ozonation filtration with 10 g m^3 gaseous ozone at a flow rate of 10 mL min^{-1} for 3–5 h until the initial clean water flux was restored. Experiments were conducted with and without ozone under the conditions of feed TOC of 10.4 mg C L^{-1}, TMP of 1.24 bar, with the initial flux 90 ± 4 L m^{-2} h^{-1}, crossflow velocity of 0.47 m s^{-1}, temperature of 22.3 °C and ozone dosage 1.67 mg O_3 s^{-1}. In all cases, the flux rapidly declined over the first 1–2 h due to fouling. No recovery of the permeate flux was observed without ozone. In the presence of ozone, the permeate flux begins to increase after approximately 2 h. This recovery is believed to be due to the catalytic ozonation of the foulants at the membrane surface.

11.3.4 Mn-based Catalytic Ceramic Membranes

11.3.4.1 Preparation and Performance of Membranes

Ceramic membranes can be used in combination with ozone, as they are resistant to ozone.[71] Coating the ceramic membranes with catalytic materials has been shown to enhance their performance when used in combination with ozone. Manganese-containing catalysts have been shown to increase the rate of decomposition of ozone. Manganese oxide is also known to catalyze the oxidation of organic compounds by ozone.[72] Thus coating a membrane with manganese oxide is expected to produce a catalytic surface, which in the presence of ozone will reduce fouling. Corneal *et al.*[73] prepared manganese oxide (MnO_x) nanoparticles *via* the ozonation of $MnCl_2$ or the mixing of $KMnO_4$ and allylamine hydrochloride, then used a novel layer-by-layer (LbL) technique to coat the ceramic membranes with MnO_x nanoparticles. The results indicated that when the membranes were used in a hybrid ozonation and membrane filtration system, the coated membrane removed 56% of the organic carbon (OC), whereas the uncoated membrane only removed 43% of the OC. Similarly, Byun *et al.*[74] also employed the LbL technique to produce catalytic membranes by coating commercial ceramic ultrafiltration membranes with MnO_x nanoparticles. The performance of the

manganese oxide–coated membrane was superior to that of the other membranes tested. It showed the least degree of fouling and the greatest reduction of TOC in the permeate. The low degree of fouling observed with this membrane is due to the fact that its surface is negatively charged.

In Cheng *et al.*'s study,[75] commercial available MnO_2 (C-MnO_2), $KMnO_4$ (M-MnO_2) and $Na_2S_2O_3$ (S–MnO_2) were utilized to prepared MnO_2, respectively, and three types of MnO_2 incorporated ceramic membranes were further synthesized by vacuum drying, which was employed in catalytic ozonation system toward *p*-chloronitrobenzene removal. And the 48.6%, 51.7%, 61.5% and 68.0% of the *p*-CNB removal efficiencies were achieved in the virgin, C-MnO_2, M-MnO_2 and S–MnO_2 incorporated membranes in the hybrid ozone-membrane process, respectively. Obviously, the presence of MnO_2 enhanced the catalytic ozonation performance of *p*-CNB degradation. In addition, a kind of citrate sol–gel-assisted wet impregnation method was utilized by Lee *et al.*[8] to deposit MnO_x nanocatalyst into the ceramic membranes (CMs). Subsequently, the performance of the obtained catalytic ceramic membranes (CCMs) that were used in a custom-made hybrid oxidation separation technology (HOST) system was investigated by comparing the degradation of bisphenol A (BPA). There were relatively low adsorptions of MPs (<5%) with insignificant TOC removal observed for the original CM. However, Mn-CCM was able to remove up to 55% BPA by adsorption throughout 1 h of operation, resulting in 11% TOC removal.

Nowadays, asymmetric multichannel tubular ceramic membranes dominate over other membrane geometries. Flat-sheet ceramic membranes are mostly configured in immersed units for industrialization, facilitating the replacement of the membrane elements and membrane cleaning through air sparging.[76] Flat disk membranes find limited applications in the laboratory due to their low packing density; thus their configuration needs further design and improvement. He *et al.*[77] integrated 3D MnO_2 hollow microsphere ozone catalysis with flat-plate membrane filtration. In their work, the polyvinylidene fluoride (PVDF) flat-plate membrane module was submerged in the slurry catalytic ozonation reactor to form a heterogeneous catalytic ozonation/membrane filtration (HCOMF) reactor for treating wastewater containing bisphenol A (BPA). The influences of permeation flux and humic acid (HA) on BPA degradation efficiency were analyzed. Here, 15 $L\,m^2\,h^{-1}$ was selected as the optimal permeation flux after considering combined factors such as water treatment capacity and treatment cost. Compared to the BPA degradation efficiency of the ozonation/membrane filtration (OMF) system (68.3%), the final degradation efficiency of BPA in HCOMF system was 92.2%, with an increase of 23.9%. Furthermore, the presence of HA in HCOMF system could enhance the degradation efficiency of BPA.

11.3.4.2 Removal of DBP Precursors

Since chlorine residual must be provided in the distribution system to control the biostability of water, the formation of disinfection by-products

(DBPs), undesired compounds, is unavoidable. Among several hundred of DBP compounds, THMs and HAAs are two major groups found in drinking water.[78] Byun *et al.*[74] has evaluated the formation of THMs and HAAs in the permeate samples under conditions that simulate those typically found in water distribution systems. The addition of ozone clearly enhanced the removal of THM precursors, except in the case of the uncoated (TiO_2) membrane. The greatest removal of THM precursors was observed for the membrane coated 20 times with MnO_x nanoparticles. The removal of HAA precursors was greatest for the membrane coated 40 times with MnO_x nanoparticles. And in this study, although up to 39% removal of THM precursors and 55% removal of HAA precursors were achieved, Byun *et al.* did not meet the regulatory limits for THMs and HAAs after chlorination using the membrane.

11.3.4.3 Membrane Fouling

One of the most significant challenges to the operation of membrane filtration for the treatment of surface water is the fouling of membranes by natural organic matter. Manganese oxides are also an effective catalyst for the decomposition of ozone and the oxidation of organic compounds by ozone. As such, the application of a manganese oxide coating to a membrane should produce a membrane that is capable of degrading foulants when used in a hybrid ozonation-membrane system. Corneal *et al.*[79] fabricated Mn oxide–coated catalytic membranes for hybrid ozonation-membrane filtration and studied the effect of the number of coating layers on the structure of the resulting catalytic coating and the filtration performance of the coated membrane. They reported that when the coated membranes were used in the hybrid system, the initial flux decrease that occurred over the first hour was followed a steady recovery of the flux. The membrane coated with 20 layers achieved approximately a 95% recovery after 5.5 h, while the membrane coated with 30 layers achieved approximately an 85% recovery after 5.5 h, and the membrane coated with 40 layers achieved approximately an 80% recovery after 5.5 h. The improved flux recovery for the coated membranes, as compared to the uncoated membrane, is the result of the catalytic activity of the coating, which results in the improved oxidation of the foulants deposited on the membrane surface. Moreover, the phenomena of membrane fouling in the membrane filtration (MF) and HCOMF system was also studied by He *et al.*[77] It could be seen that the membrane resistance caused by the membrane itself (R_m), caused by pore (R_p) and caused by cake layer (R_c) in a membrane filtration (MF) system was calculated to be 2.97, 0.15 and 0.6×108 m^{-1}, respectively, accounting for 80%, 4% and 16% of the total membrane resistance (R_t) respectively. By contrast, in a HCOMF system, the membrane resistance of R_p and R_c decreased to 0.03 and 0.11×108 m^{-1}, respectively, with a proportion of 1% and 4% to R_t, respectively. The results reveal that membrane fouling can be solved in the HCOMF system. Simultaneously, the

contact angle of PVDF membrane after treatment in an MF system and MnO_2-PVDF membrane after treatment in a HCOMF system were 69.4° and 55.9°, respectively, revealing that the hydrophilicity of MnO_2-PVDF membrane was enhanced confirming the preferable property of membrane fouling control.

11.3.5 Ce-based Catalytic Ceramic Membranes

11.3.5.1 Preparation and Performance of Membranes

In Jie *et al.*,[8] cerium oxide (CeO_x) was deposited on catalytic ceramic membranes (CCMs) that were fabricated *via* citrate a sol–gel-assisted wet impregnation method. Ce-CCM was selected to study the effect of catalyst loading on MP degradation, owing to its better mineralization ability and stability. The removals of individual MPs and their combined TOC were removed by the hybrid process with HRT of 13.7 s. There were relatively low adsorptions of MPs (<5%) with insignificant TOC removal observed for both the original CM and 1×Ce-CCM. 1×Ce-CCM exhibited stronger mineralization capability with ~38% TOC removal with 13.7 s contact time, throughout 1 h of operation. It has been reported that Ce/MCM-41 was more active than Mn/MCM-41 in oxalic acid degradation *via* catalytic ozonation in a batch study conducted by Jeirani and Soltan.[80] By repeating the impregnation cycle, higher catalyst loadings of Ce-CCMs were obtained, which introduced higher densities of surface-active sites across the Ce-CCMs for catalytic reaction. The $O_{3(aq)}$ decomposition was improved from 86% to complete decomposition when increasing the number of impregnation cycle from 1 to 5.

11.3.5.2 Membrane Fouling

Furthermore, AFM was used to characterize the topography and surface roughness of the CCMs. The three-dimensional AFM surface images were made of the outer surface of CCMs, and the results showed that Ce-CCMs surface topographies were similar to that of the original CM. The average surface roughness obtained from AFM also showed no statistical difference in the surface roughness before and after impregnation. These results demonstrated that the impregnation of metal oxides did not significantly alter the membrane surface morphologies and porous structure. Notably, both metal oxide–impregnated CCMs showed improved surface hydrophilicity over the original CM as the water contact angles decreased in both cases. Furthermore, with the increase in catalyst loading of Ce-CCM from 1× to 5× impregnation cycles, the surface hydrophilicity of Ce-CCM was enhanced, whereby the water contact angle decreased from 26.0 to 23.3 °C. Meanwhile, the permeability of the 1×Ce-CCM was maintained at >95% of the initial permeability in each filtration cycle, indicating insignificant membrane fouling during the hybrid process.

11.3.6 Cu-based Catalytic Ceramic Membranes

11.3.6.1 Preparation and Performance of Membranes

Scaratti *et al.*[81] prepared the CuO suspension and deposited the CuO layer into the CM with a vacuum pump. The catalytic ceramic membrane of stable CuO deposition was further synthesized on the ceramic membrane by heat treatment. The aim was to evaluate 1,4-dioxane mineralization on applying an innovative hybrid treatment coupling catalytic ozonation and ultrafiltration using a CuO-coated ceramic membrane. The tests were performed in a closed (deadend filtration with recirculation) or open system (deadend filtration with no recirculation). The operation pressure was 0.25 bar. The TOC and 1,4-dioxane removal (municipal water containing 1,4-dioxane) using the 0.90 mg cm^{-2} CuO-coated CM or CM in the presence of ozone. As expected, the CuO coating promoted both the mineralization and 1,4-dioxane removal, since the noncatalytic ozonation of this organic compound is slow at acid pH values.[82] In addition, the catalyst loading influenced the performance significantly, and the CM coated with 0.9 mg cm^{-2} of CuO showed the best performance due to the increase in the active component content. The 0.9 mg cm^{-2} coated CM increased the mineralization and 1,4-dioxane degradation efficiency by 11.4% and 45%, respectively, when compared with the CM. The pseudo first-order kinetics constants of 1,4-Dioxane were determined; the pseudo first-order kinetics constants for 1,4-dioxane degradation and mineralization increased by factors of 4.21 and 2.98, respectively, when compared with the uncoated hybrid process. When comparing the results obtained for 1,4-dioxane diluted in the WTP water and in deionized water, it was noticed that the highest 1,4-dioxane removal was obtained for the 1,4-dioxane solution in deionized water after 360 min of reaction. When the ozone concentration reached the steady state, the reactions followed second-order kinetics; the second-order kinetic constants for 1,4-dioxane removal and TOC removal increased by factors of 8.19 and 5.78, respectively, when compared with the uncoated CM-hybrid process. An increase in the catalyst load on the CM surface favored the decomposition of ozone as shown by the lower equilibrium concentration of ozone in the system. The enhanced production of free radicals increased the removal of 1,4-dioxane and its products in CO_2 and water.

11.3.6.2 Membrane Fouling

Further, the effect of ozone on the permeate flux for the hybrid system using the uncoated CM and CuO-coated CM in a closed system was studied. In the absence of ozone, the permeability declined rapidly during the first 180 min for the uncoated CM and the 0.9 mg cm^{-2} CuO-coated CM, with no significant difference between them. In this stage, a fouling cake begins to form at the membrane surface. After 180 min, in a closed system, all of the foulants are attached to the membrane. The total amount of foulant reduced the

flux to 60% of the initial value. Modifying CM with CuO did not change the CM permeability, in agreement with reports in the literature. Meanwhile, the effect of the ozone flow rate (0.064 $m^3 h^{-1}$) on the permeate flow was also researched. Initially, the permeate flux through CuO-coated or uncoated membrane decreases due to the fouling effect. However, the permeate flow through the 0.9 $mg\,cm^{-2}$ CuO-coated CM was completely reestablished after 60 min ($J/J_0 = 1$), while reestablishing the permeate flow of the uncoated CM is not complete even after 360 min. These results confirmed that the fouling caused by NOM and 1,4-dioxane in the municipal water is efficiently avoided and or decreased by applying ozone dissolved in the water. In addition, the permeation flux and fouling resistance of coated and uncoated films in the absence and presence of ozone were compared in the open system. The membrane fouling in the continuous experiment was expected to be more serious than that of the closed system. However, the values of J/J_0 after 180 min and absence of ozone in the closed system ($J/J_0 = 0.625$) are quite similar to that measured in the open system ($J/J_0 = 0.633$), within the experimental error (5%). In the absence of ozone, the permeability declined rapidly during the first 180 min for the uncoated and 0.9 $mg\,cm^{-2}$ CuO-coated CM, with no significant difference between them. However, when the ozone generator was turned on, the permeate flux recovered faster for the 0.9 $mg\,cm^{-2}$ CuO-coated CM when compared with the uncoated CM.

11.3.7 Hybrid Metal-oxide-based Catalytic Ceramic Membranes

11.3.7.1 MnO_2–Co_3O_4 Coated Ceramic Membrane

Guo *et al.* used a layer-by-layer technology to coat the surface of ceramic membrane with hybrid MnO_2–Co_3O_4 nanoparticles.[83] The uncoated ceramic membrane showed only slight activity as increased efficiency as 4.2%, compared with sole ozonation. The combination of coated ceramic membrane with ozonation significantly increases the removal efficiency of BP-3 over sole ozonation (47.4%) and the process with an uncoated ceramic membrane (51.6%). The coating times influenced the performance significantly, and ceramic membrane coated with MnO_2–Co_3O_4 nanoparticles 80 times (74.8%) shows the highest performance over that coated 30 times (61.0%), 40 times (69.4%) and 60 times (72.3%). Increasing the coating times increased the content of active components, resulting in the development of the performance.

The researchers also investigated the effects of process parameter and water quality on BP-3 removal efficiency. BP-3 cannot be efficiently removed at the ozone concentration of 0.5 $mg\,L^{-1}$, and its removal efficiency was only 55.8%. When the initial ozone concentration increased to 2.0 $mg\,L^{-1}$, the degradation of BP-3 was significantly improved to 92.0%. The removal efficiency of BP-3 decreased as the initial concentration of BP-3 continually increased over the range of 0.5–3.0 $mg\,L^{-1}$. The degradation of BP-3

increased as water pH increased from 2 to 10. Both nitrate and phosphate were not the quenchers of radicals, but they can be adsorbed on the surface of metal oxide by the surface hydroxyl group.[84] Phosphate and nitrate have different complexation affinities for Me^{n+} on the surface of metal oxides. As the anion complexion capacity increased, the negative effect on catalytic ozonation increased. Generally, the adsorption capacity of metal oxides for nitrate was much lower than that for phosphate as the pH varies from 7 to 8,[85,86] which might explain the insignificant influence on the performance in the presence of nitrate. As the anion complexion capacity increased, the negative effect increased. The inhibiting effect of phosphate or nitrate on membrane catalytic ozonation indicates that the surface hydroxyl group of coated ceramic membrane plays a role in the catalytic ozonation of BP-3. Additionally, the pore size of membrane affected BP-3 degradation. The removal efficiency of BP-3 decreased from 76.0% (Φ30-19-4-20) to 69.5% (Φ30-19-4-50), when membrane with pore size from 50.0 nm to 20.0 nm was used. Smaller membrane pore size meant fewer MnO_2–Co_3O_4 nanoparticles coating on ceramic membrane. The decreasing of activity component resulted in the poor performance.

The stability and safety of MnO_2–Co_3O_4 nanoparticles coating on a ceramic membrane were estimated. No remarkable change was observed on the catalytic activity of the MnO_2–Co_3O_4 nanoparticles coating on the ceramic membrane, after being used several times and the BP-3 removal efficiency was the most decreased by only 6.0%, and the performance kept similar after being used for successive seven runs. Moreover, the concentrations of leached metal irons from membrane into the solution along with the successive runs were investigated. Only alumina, manganese and cobalt ions leaching were observed. Alumina was not the dominating active component and came from the support of the ceramic membrane. During the first use, the concentration of leached ions showed the maximum and decreased as reaction time passed. However, the leached ions were too low compared with the coated MnO_2–Co_3O_4 nanoparticles. All concentrations of leached ions were lower than the National Standards for the Integrated Wastewater Discharge Standard in China ($C_{Mn} < 2$ mg L^{-1} and no limitation for alumina and cobalt ions),[87] indicating that the leaching of ions did not show the negative effect on the safety of membrane catalytic ozonation. More importantly, the leached manganese and cobalt irons suggested no catalytic activity for removing BP-3. The results suggested that the interface reaction was the dominant one in the membrane catalytic ozonation process. The leached ions did not show a homogeneous catalytic reaction.

Guo *et al.* also measured the acute toxicity of the BP-3 and the solution after sole ozonation, as well as membrane catalytic ozonation process with uncoated or coated ceramic membrane. The unicellular green microalgae *Chlorella vulgaris* (*C. vulgaris*) was used to assay algae toxicity. The toxicity assessment for EC_{50-72h} of BP-3 (2.0 mg L^{-1}) without any oxidation was 64.73%. After sole ozonation, membrane catalytic ozonation with uncoated or coated ceramic membrane, the EC_{50-72h} value increased to 70.97%,

71.99% and 74.99%, respectively. This increase of the EC_{50-72h} value indicated a decrease in toxicity. The membrane catalytic ozonation process with coated ceramic membrane showed the best detoxification performance.

11.3.7.2 $CuMn_2O_4$ Coated Ceramic Membrane

Guo *et al.* coated $CuMn_2O_4$ particles on ceramic membrane and estimated the effect of the coating quantity of $CuMn_2O_4$ particles on BP-3 removal in CMCO.[88] The BP-3 removal efficiency with MCO using the virgin CM increased by 4.2% as compared with that achieved with ozonation alone (47.4%). The removal efficiency of BP-3 increased when the soaking time of CM in $CuMn_2O_4$ precursor solution increased. The BP-3 removal increased to 76.6% with the soaking time of 180 min. A longer soaking time led to more active component adsorption onto the CM surface and a higher BP-3 removal.

The stability of the BP-3 degradation performance during lengthy recycling was evaluated. The modified membrane coated with $CuMn_2O_4$ particles (ϕ30-19-4-50) was reused 30 times (30 min per cycle). There were small fluctuations in BP-3 removal efficiency, ranging from 75.3% to 68.8%. Ions leaching results showed that alumina ions were relatively low and that the concentration was stable at 11.0–12.0 $\mu g\,L^{-1}$. Leaching of the two active components (*i.e.* copper and manganese ions) was higher, and their leaching equilibrium concentrations were approximately 32.0 and 230.0 $\mu g\,L^{-1}$, respectively. However, no catalytic activity and interfacial reactions dominated BP-3 degradation in CMCO. From the AFM images and the roughness data, it was clearly indicated that the CM membrane surface was smoother and that the average roughness of used CM was slightly decreased from 187 ± 17 nm to 155 ± 9 nm. These results all suggested that the modified CM with $CuMn_2O_4$ particles could maintain a high BP-3 removal efficiency and showed lower metal ion leaching and stable structure during lengthy operation. The cute toxicity of BP-3 and its solution after different treatments were compared to evaluate the detoxification ability of CMCO, showing that coating CM with $CuMn_2O_4$ particles for catalytic ozonation significantly reduced the aqueous toxicity of BP-3 to the microorganisms.

Guo *et al.* also evaluated membrane fouling through normalized permeate fluxes (J/J_0), when the effluent of a WWTP was used as the matrix (Figure 11.5). Results showed that the normalized permeate fluxes (J/J_0) of the virgin and modified CM decreased significantly to 34.2% and 36.1%, respectively, in the first operation cycle. The membrane fouling was significantly reduced by adding ozone to the reaction. The normalized permeate flux of the virgin CM over 120 min stabilized at about 65.9%, indicating that membrane fouling was well eliminated by the introduction of ozone. This effect was greater when $CuMn_2O_4$-coated CM was used, as the normalized permeate flux was 95.8%. Effluent organic matter (EfOM) in the effluent of WWTP could be degraded or changed by sole or catalytic

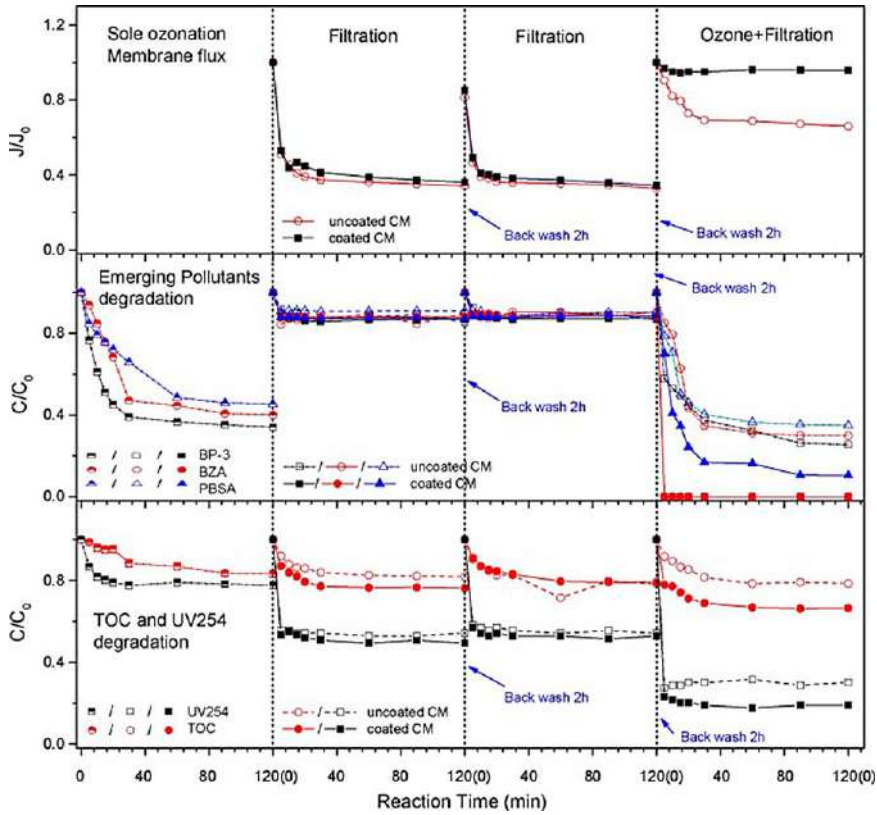

Figure 11.5 Performance of CMCO on water quality development (organic removal, UV_{254} and DOC reduction) and permeate flux of the modified membrane, in which the effluent of the wastewater treatment plant was used as the matrix. Reaction conditions: $[O_3]_0 = 2.0$ mg L^{-1}, $[BP\text{-}3]_0 = 0.5$ mg L^{-1}, $[BZA]_0 = 0.5$ mg L^{-1}, $[PBSA]_0 = 0.5$ mg L^{-1}, Φ30-19-5 and pH = 7.11 ± 0.19. Reproduced from ref. 5 with permission from Elsevier, Copyright 2018.

ozonation; this decreased the fouling of virgin CM. The surface coating of $CuMn_2O_4$ on CM greatly reduced membrane fouling because of surface catalytic ozonation by $CuMn_2O_4$. A higher normalized permeate flux and shorter recovery time were achieved with $CuMn_2O_4$-modified CM, suggesting a greater enhancement in the antifouling ability.

PPCPs (2-hydroxy-4-methoxybenzophenone [BP-3], benzotriazole [BZA], 2-phenylbenzimidazole-5-sulfonic acid [PBSA]) removal was investigated in WWTP effluent (Figure 11.5). The removal efficiencies of BP-3, BZA and PBSA were 66.0%, 60.1% and 54.6%, respectively, in the sole ozonation process, which increased to 74.5%, 70.1% and 65.1%, respectively, when the virgin CM was combined with ozonation. The performance was significantly improved as the modified CM was used. BP-3 and BZA could be completely degraded. The removal efficiency of PBSA was 89.5% using modified CM

with ozonation after 120 min. Thus $CuMn_2O_4$-modified CM showed higher catalytic ozonation ability due to the promotion of •OH.

Furthermore, UV_{254} and DOC in permeate samples were used to evaluate the performance of CMCO in EfOM degradation (Figure 11.5). Sole ozonation did not effectively degrade UV_{254} and DOC. The reductions in UV_{254} and DOC obtained with the modified CM were slightly better than those obtained with the unmodified membrane, indicating that surface coating with $CuMn_2O_4$ particles did not improve the filtration performance. Adding ozone into filtration showed a positive effect on the reduction of UV_{254}. The removal efficiencies of UV_{254} in CMCO with virgin and modified CM were 69.9% and 81.1%, respectively. Use of a combination of ozone and the CM coated with $CuMn_2O_4$ particles enhanced the degradation of EfOM containing unsaturated groups from the large-molecular-weight compounds to the small ones. The improvement in DOC removal achieved using the virgin CM was insignificant. About 10% reduction of DOC was observed in the modified CM. The combination of the ozone and surface particles coating improved the removal of trace organic chemicals and EfOM.

11.3.8 Carbon-based Catalytic Ceramic Membranes

11.3.8.1 GO/rGO-based Catalytic Ceramic Membrane

Nitrogen-doped reduced graphene oxide (N-rGO) is a type of two-dimensional (2D) large-sized lateral-layered nanoporous carbon material. In principle, this unique structural characteristic can reduce the influence of the coating catalytic layer on CM permeability.[89] Owing to differences in electronegativity, incorporating nitrogen into the carbon framework results in the redistribution of charge density and allows tailoring of the band structure of sp^2 carbons.[90] This induces N-rGO to exhibit superior catalytic performance without metal ion leaching. Furthermore, theoretical calculations have confirmed that edge quaternary N and adjacent C atoms exhibit superior adsorption energy (E_{ads}, eV) toward ozone molecules.[91] Therefore, N-rGO-based catalytic membranes show potential for improved performance. A high-activity N-rGO was assembled uniformly by Song *et al.*[92] and firmly on the surface of CM using pneumatic and vacuum suction methods. N-rGO was coated on the inner or outer surfaces of the CM (N-rGO-CM-I and N-rGO-CM-O, respectively) using pneumatic[93] or vacuum suction method,[94] respectively.

(i) MPs Degradation

The formation of •OH from the molecular ozone decay was supported by the degradation results for *p*-CBA, which is known to react rapidly with •OH (5×10^9 $M^{-1}\,s^{-1}$) but slowly with molecular ozone (0.15 $M^{-1}\,s^{-1}$).[95] As expected, less than 90% of *p*-CBA was destroyed by sole ozonation after 30 min (Figure 11.6). The extent of *p*-CBA degradation after ozonation in the presence of CM was slightly higher

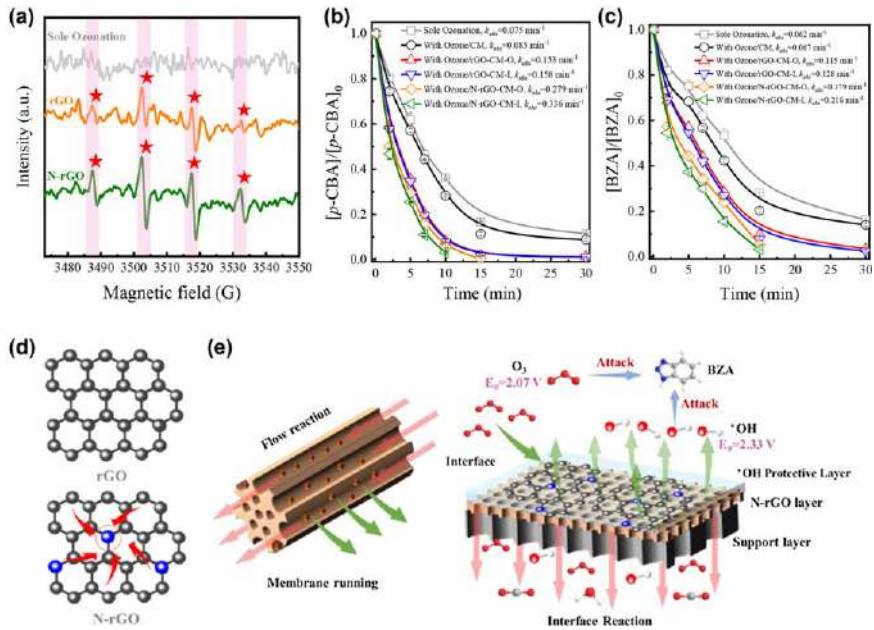

Figure 11.6 (a) DMPO spin trapping EPR spectra of sole ozonation, and rGO and N-rGO with ozone ([ozone gas] = 20 mg L^{-1}, [O_3] = 2 mg L^{-1}, [DMPO] = 10 mM [catalyst] = 0.25 g L^{-1}). (b) *p*-CBA and (c) BZA removal by sole ozonation, and CM, rGO-CM-O, rGO-CM-I, N-rGO-CM-O, and N-rGO-CM-I with ozone ([ozone gas] = 20 mg L^{-1}, [O_3] = 2 mg L^{-1}, TMP = 0.3 bar, crossflow velocity = 1200 mL min^{-1}, [BZA] = [*p*-CBA] = 0.084 mM). (d) Diagrammatic representation of clustering effect of free electrons. (e) Mechanism of interfacial catalytic reaction. Reproduced from ref. 66 with permission from Elsevier, Copyright 2021.

than that obtained by conventional ozonation. This result indicated that the presence of the CM did not significantly improve oxidation efficiency. There was 97.72% or 99.83% *p*-CBA removed in catalytic ozonation by rGO-CM-O and rGO-CM-I within 30 min; the mineralization efficiency of *p*-CBA was enhanced from 39.5% to 51% or 55.8% after 2 h, respectively. N-doping significantly enhanced catalytic activity. N-rGO-CM-O showed greater catalytic activity in catalytic ozonation than rGO-CM-O, resulting in a *p*-CBA removal efficiency of 98.71% within 15 min and 70% of TOC mineralization after 2 h. Complete *p*-CBA removal was observed at 10 min in N-rGO-CM-I catalytic ozonation and the corresponding mineralization efficiency was 77.8% after 2 h, suggesting N-rGO-CM-I effectively activated ozone molecules to generate reactive species. In summary, the •OH productive capacity was in the order N-rGO-CM-I > N-rGO-CM-O > rGO-CM-I > rGO-CM-O.

Another toxic and nonbiodegradable molecule, BZA, was used to evaluate the superior catalytic performance of the as-synthesized

catalytic membrane (Figure 11.6). Predictably, the best BZA removal performance and mineralization were achieved by N-rGO-CM-I, which afforded 99.89% removal efficiency of BZA within 15 min and 77.2% of mineralization efficiency after 2 h. The other three catalytic membranes showed removal performances in the order N-rGO-CM-O > rGO-CM-I > rGO-CM-O, which was consistent with the order of $^{\bullet}OH$ production capacity.

(ii) Synergistic Self-Cleaning Process Induced by Interfacial Catalytic Reaction

Without ozone dosing, the flux of CM or catalytic membrane declined sharply initially and then tended to decline more slowly and stably afterward during one filtration cycle (a ''fast–slow decline'' pattern). The flux decreased to 51.19%, 62.25% and 62.19% of the initial values in CM, rGO-CM-O and rGO-CM-I without ozone dose, and the normalized water permeance (J/J_0) of N-rGO-CM-O and N-rGO-CM-I remained at 69.64% and 74.40%, respectively. An increase in hydrophobicity was an important reason for these differences.[96] Uniformly inlayed N-rGO regulated the inherent interface properties of CM to provide better antifouling activity, which was important for permeate stability. Furthermore, the rejection efficiencies of SA in N-rGO-CM-O and N-rGO-CM-I were 53.21% and 51.18% after processing for 30 min. However, rGO-CM showed a significantly greater rejection ability than N-rGO-CM, resulting in 58.49% (rGO-CM-O) and 56.11% (rGO-CM-I) rejection efficiency of SA, owing to the physical sieving of membrane. This performance was further enhanced by the thicker rGO catalytic layer.[89]

The J/J_0 values of CM, rGO-CM-O and rGO-CM-I with ozone appeared to decline continuously, with reductions of 30.29%, 19.81% and 18.80%, respectively, while the J/J_0 values of N-rGO-CM-O and N-rGO-CM-I with ozone remained at 91.81% and 97.29%, respectively. Therefore, N-rGO-CM-I exhibited the best self-cleaning performance, when combined with ozone. The SA removal efficiency was the most direct evidence of this self-cleaning performance. The SA mineralization efficiency of CM with ozone was 23.16%, which increased to 39.25% and 37.38% for rGO-CM-I and rGO-CM-O with ozone, respectively. N-rGO-CM-I clearly showed the best SA mineralization efficiency (69.98%) when ozone was introduced, followed by N-rGO-CM-O (59.02%). This superior property should be primarily due to the high exposure of doped N atoms on the catalytic membrane surface, which results in the generation of more considerable amounts of $^{\bullet}OH$ *via* rapid catalytic decomposition of ozone to oxidize and mineralize membrane fouling *in-situ*. The higher SA oxidation and mineralization capacity led to the further reduction of TOC in the permeate.

(iii) Effect of Interface Characterization of N-rGO Catalytic Membrane on Performance

The interface characteristics (such as thickness, roughness and hydrophilicity) of the skin layer determined the synergistic performance of the catalytic membrane, comprising MP degradation and self-cleaning *in-situ*. N-rGO-CM-I containing skin layers with different interface characteristics were fabricated by varying the number of coatings from 1 to 3. The results indicated that the N-rGO layer thickness was well controlled by simple number manipulation. Increasing the number of coatings from 1 to 3 caused a notable increment in the average surface roughness from 249.6 ± 6.5 to 531.2 ± 16 μm. The surface hydrophobicity of N-rGO-CM-I was also enhanced, with the water CA increasing from $66.6 \pm 0.1^{\circ}$ to $75.9 \pm 0.1^{\circ}$, owing to the coverage of interfacial –OH groups on the surface of CM by adequate N-rGO.[97,98]

To study the impact mechanisms of interface characteristics on N-rGO-CM-I catalytic activity and self-cleaning performance, multiple linear relationships were established. The k_{obs} values of *p*-CBA and BZA improved almost linearly when increasing the preceding three interface characteristics (thickness, roughness, and hydrophobicity), indicating that they contributed to interface catalytic activity. A thicker catalytic layer in N-rGO-CM introduced more intricate electronic states and spin features of the covalent carbon system,[99] leading to $^{\bullet}$OH enrichment (*p*-CBA removal results illustrate this well from catalytic ozone decomposition). However, these results were contrary to the theory published by Byun *et al.*,[100] where a higher catalyst loading (Mn oxide) did not significantly improve the catalytic activities of CM. This result indicated that no more active sites were exposed to derive increased probe degradation. These studies also found no statistically significant change in roughness after increasing the loading amount of powder catalyst, suggesting that the newly coated catalytic layer completely covered the original active sites. Therefore, there was no performance enhancement. In contrast, in the present study, increased roughness indicated intricate surfaces with more exposed active sites, such as doped N, which helped improve catalytic activities. Therefore, the thickness and the roughness exhibited a synergistic effect on the regulation of catalytic activities for N-rGO-CM-I. Furthermore, the more hydrophobic N-rGO-CM-I surface was favorable for *p*-CBA or BZA adsorption;[101] moreover, the amount of *p*-CBA (Log K_{ow} of *p*-CBA was 2.3) adsorbed on hydrophobic N-rGO-CM-I surface was slightly more than that of BZA (Log K_{ow} of BZA was 1.44), also confirming this conclusion. Therefore, the interface adsorption shortened the distance between target molecules and oxidants, resulting in increased catalytic activity,[102] which depended on the hydrophobicity of the target probe.

Antifouling activity was another manifestation of catalytic membrane synergistic performance. The results showed that J/J_0 was negatively correlated with the preceding three interface

characteristics in N-rGO-CM-I without ozone, suggesting that increasing these interface characteristics in the as-obtained novel N-rGO-CM-I had a negative effect on the antifouling activity. The thicker and denser catalytic layer led to increased mass transfer resistance between water and SA, causing reduced antifouling activity. Our previous studies showed that a smoother surface decreased contaminant accumulation on the CM surface and reduced membrane fouling.[103,104] Therefore, the rougher surface of N-rGO-CM-I led to decreased antifouling activity. Interestingly, previous studies showed that increasing membrane hydrophobicity was expected to reduce fouling caused by the adsorption of hydrophilic SA on the membrane surface.[96] Therefore, the expected result was a positive correlation between hydrophobicity and J/J_0. This contradiction was attributed to the decrease in antifouling activity, which was caused by the increase in both layer thickness and roughness being larger than that in hydrophobicity, at least for the catalytic membrane and experimental conditions investigated herein.

When ozone was introduced, a higher J/J_0 was observed compared with N-rGO-CM-I without ozone. Herein, most SA molecules were transported onto the surface of the N-rGO catalytic layer by a flowing stream and then were decomposed by ozone and formed $^{\bullet}OH$. Therefore, this process also significantly alleviated membrane fouling. When N-rGO-CM-I and ozone were combined, a decrease in J/J_0 was still observed with increasing thickness, roughness and hydrophobicity. The effects of both catalytic layer thickness and roughness were still stronger than that of increased hydrophobicity. The improved efficiency of *in-situ* N-rGO-CM-I self-cleaning performance with catalytic ozonation was speculated to be insufficient to overcome the negative influences of increased mass transfer resistance caused by the thicker catalytic layer and easier accumulation, which contaminated the rough CM surfaces, under these test conditions ($[O_3] = 2.0\ mg\ L^{-1}$). Notably, the slope value of N-rGO-CM-I with ozone was lower than that of N-rGO-CM-I without ozone. Although catalytic ozonation was unable to completely overcome these negative effects on self-cleaning performance, it did achieve a reduction. Therefore, the permeate flux in N-rGO-CM-I with ozone could be controlled by maintaining a sufficiently high ozone concentration in the retentate.

(iv) Synchronous Removal of Multiple MPs and Elimination of Toxic Byproducts

In wastewater treatment, inorganic anions and NOM are widely present at various concentrations, leading to competitive reactions with reactive species against target MPs that result in decreased decomposition efficiency.[105] Eight MPs (BZA, ACLV, SMX, CBZ, ABEE, *p*-CBA, PTA and BP-4) were efficiently removed by N-rGO-CM-I with ozone. However, CM with ozone failed to achieve complete degradation of SMX, CBZ, and *p*-CBA. This result indicated that N-rGO-CM

overcame the insufficient abatement of ozonation refractory MPs.[106] Meanwhile, the apparent energy consumption of MPs removal (E_C, kW h mM^{-1}) was calculated, N-rGO-CM-I with ozone could reduce energy consumption to 1.119, 1.032 and 0.787 kW h mM^{-1} for the removal of SMX, CBZ and *p*-CBA, respectively, from 1.543, 1.427 and 1.490 kW h mM^{-1} in CM with ozone. The self-cleaning performance of N-rGO-CM-I with ozone was 2.2 times that of CM with ozone. Similarly, apparent energy consumption of permeation fluxes (E_L, kW h L^{-1}) was also calculated. The E_L of CM with ozone was 0.069 kW h L^{-1}, while the E_L of N-rGO-CM-I with ozone was notably decreased by 55.07%. In conclusion, N-rGO-CM-I could effectively reduce energy consumption while achieving higher permeation flux and better removal efficiency of MPs.

Introducing ozone increased the synergistic decontamination and self-cleaning performance of membranes but might have increased the formation of toxic by-products (such as ketoaldehydes).[107] The sum concentration of 14 kinds of ketoaldehydes identified as being formed after sole ozonation was 746.87 μg L^{-1} when using WWTP effluent as the matrix. The dominant by-products were FA (183.21 μg L^{-1}), Ace (292.71 μg L^{-1}) and But (111.27 μg L^{-1}), followed by Hex (42.85 μg L^{-1}) and Cyclo (71.18 μg L^{-1}). These five ketoaldehydes together constituted >90% of this class of by-products. Both Gly (1.29 μg L^{-1}) and Mgly (11.33 μg L^{-1}), possible mutagenic compounds,[108] were also identified. A substantial decrease in the formation of ketoaldehydes ([total ketoaldehydes] = 243.90 μg L^{-1}) was observed for N-rGO-CM-I with ozone, owing to the advanced interfacial catalytic performance of N-rGO-CM-I. This decrease was predominantly driven by reductions of ~98.5% in Hex, ~97.7% in Ace, ~62.1% in But, and ~60.0% in Cyclo.

Halogenated DBP formation following the disinfection of WWTP effluent was identified, with sum concentrations of 100.57 μg L^{-1} for all identified halogenated hydrocarbons and 1628.24 μg L^{-1} of HAAs. CM with ozone clearly decreased the formed halogenated hydrocarbons (total concentration of 37.07 μg L^{-1}) and HAAs (total concentration of 624.58 μg L^{-1}), owing to the removal of DBP precursors, such as fulvic-like or humic-like substances, from the EfOM.[109] The greatest removal efficiency for identified DBP precursors was observed for N-rGO-CM-I with ozone. The formation potentials of halogenated hydrocarbons and HAAs were reduced by 96.37% and 99.11%, respectively, and highly toxic TCAN, DCAN and DCAcAm were not detected after using N-rGO-CM-I with ozone, owing to the increased oxidation power of this novel N-rGO-CM-I.

(v) N-rGO-CM-I Maintained Long-Term Operational Stability

N-rGO-CM-I exhibited superior stability for both MP removal and membrane self-cleaning. N-rGO-CM-I, used 18 times, still retained high self-cleaning performance (>85% of initial water flux) and >91%

BZA removal efficiency. After backwashing with water, the water flux of N-rGO-CM-I recovered to almost the initial flux from the first use (>97% of initial water flux), providing high water flux in the next filtration cycle. The catalytic activity toward MP degradation was mostly recovered (>95% of BZA removal performance) after backwashing, owing to the removal of degradative products adsorbed by active sites in the backwash.[110] Furthermore, the fastness between the catalytic layer and CM could not be neglected. The SEM image allowed for observing the preservation of N-rGO, with no apparent variation in the thickness of catalytic layer compared with the virgin sample identified. Therefore, N-rGO-CM-I showed stable and efficient synergistic performance in MP removal and membrane self-cleaning, indicating its practicability for tackling contaminants in advanced wastewater treatment sustainably, while toxic by-products formation was strictly mitigated during treatment by N-rGO-CM with ozone.

11.3.8.2 Hybrid Metal Oxides and Carbon-based Catalytic Ceramic Membranes

The combination of membrane filtration with catalytic ozonation was established in this study in order to develop *in-situ* self-cleaning of membrane fouling and micropollutants degradation. Herein, a novel $CuMn_2O_4$/g-C_3N_4 catalytic ceramic membrane (CG/CM) was fabricated *via* the vacuum negative pressure method, and a catalytic ozonation membrane reactor was established. The active catalytic ceramic membrane was fabricated, where the thickness, roughness and hydrophilicity/hydrophobicity of $CuMn_2O_4$/g-C_3N_4 deposition on CG/CM was adjustable by changing the number of coating procedures. As for increasing the coating times, the thickness increased, but the roughness and hydrophobicity decreased, as first reported in the catalytic membrane synthesis process; this has become the favored for interface catalytic ozonation. SEM characterization showed the surface and cross-section of CM and CG/CM with different numbers of coating (CG-1/CM, CG-2/CM and CG-3/CM). After being coated by CMO/g-C_3N_4 particles, the membrane surface appeared smoother, and surface particles were more densely packed compared with uncoated CM. This smoother surface will greatly enhance retention ability and membrane antifouling.[111] A ZrO_2 filter layer (thickness, 15.31 μm) was observed in CM, and its thickness was unchanged after CMO/g-C_3N_4 particles were coated on the surface. The particle catalyst layer (CMO/g-C_3N_4) thickness varied from 9.75 to 29.30 μm, according to the number of surface coatings. As the number of coatings increased, the thickness of the active layer increased, with a linear relationship observed between them. This result confirmed that the thickness of the active layer could be adjusted by changing the number of coatings. Furthermore, Al_2O_3 (JCPDS#10-0173) and ZrO_2 (JCPDS#49-1642) were observed in samples of both CM and CG-3/CM as the membrane matrix. The XRD

peak at 28.5° of CG-3/CM matched with CMO/g-C_3N_4 powder. This indicated the presence of CMO/g-C3N4 on the CM inner surface. However, no obvious crystalline peak of CMO/g-C3N4 was detected in samples of CG-1/CM and CG-2/CM, which might be due to the greater intensity of the Al_2O_3 and ZrO_2 layer masking the presence of CMO/g-C_3N_4 loaded on the membrane. Three-dimensional AFM surface images showed that CM with a CMO/g-C_3N_4 particle coating was smoother than the original CM. The roughness parameter of each sample was calculated for five different AFM scanning areas of 5.0 μm×5.0 μm, showing a strong dependence on the number of coatings and the active layer thickness. Coating with CMO/g-C_3N_4 particles decreased the average roughness from 321 ± 160.5 nm to 97.3 ± 22.2 nm, implying that particles filled the pores in the filter layer and valleys on the membrane surface. This was consistent with SEM results. Furthermore, the smoother surface will decrease foulant accumulation in valleys on the rough membrane surface, thus reducing membrane fouling, which enables a constant permeate flux and better catalytic ozonation performance on deposited foulants and MPs on the membrane surface.[112] With an increasing number of coatings, the membrane water contact angle gradually decreased from 39.88 ± 0.59° to 0°, which was attributed to the enhanced hydrophilicity of CMO/g-C3N4. Development of the hydrophilic properties of CG/CM will greatly affect membrane flux. More adsorbed water molecules will effectively inhibit the adhesion of pollutants to the membrane surface, making it easier to remove pollutants in filtration and leading to less flux decline. These results were in accordance with the work of Zhao, who postulated that the repulsion force from the hydrated layer on the membrane surface was conducive to mitigating pollutant adsorption.[113]

All CG/CMs were used to investigate the synergetic performance of the combination of separation and catalytic ozonation in COMR. The concentration of ozone and transmembrane pressure (TMP) showed a significant influence on CG/CM performance. Compared with ozone concentration and TMP, the membrane surface velocity had little effect on CG/CM performance. When ozone was absent, BP-4 removal efficiency was only approximately 20%, as provided by filtration. When ozone concentration was 5 mg L^{-1}, the degradation performance of BP-4 was increased to 86.1%. As ozone concentration continued to increase, the degradation performance of BP-4 improved significantly. When ozone concentration was 30 mg L^{-1}, the k_{obs} value was 8.8 times that obtained without ozone. Furthermore, higher ozone concentration resulted in greater BrO_3^- formation in the permeate, which was consistent with a previous study.[114] However, BrO_3^- concentration formed in the COMR was much lower than that observed in sole ozonation. As for TMP, the removal efficiency of BP-4 increased first when the TMP was increased from 0.05 to 0.1 bar and then decreased as the TMP was further increased from 0.10 to 0.30 bar. Increasing the TMP might form a thicker foulant layer covering the catalytic active layer of CG-2/CM, leading to decreasing catalytic performance. When the TMP was 0.1 bar, the best BP-4 degradation performance was achieved. CF velocity has a slight influence

on BP-4 removal efficiency. The k_{obs} value of BP-4 degradation efficiency increased from 0.33 to 0.39 min^{-1} when the CF velocity ranged from 0.026 to 0.106 $m\,s^{-1}$. When the CF velocity was 0.085 $m\,s^{-1}$, the best BP-4 degradation performance was obtained.

Furthermore, the concentration effects of SA on performance were studied. In CM filtration, the flux was 131.82 LMH when the SA concentration was 30 $mg\,L^{-1}$, which decreased to 86.75 LMH when CG-2/CM was used. The J/J_0 value of CM under these conditions was 0.45 and reached 0.48 when CG-2/CM was used, which indicated that CG-2/CM was less likely to be blocked than CM during the filtration of the SA solution. This was an advantage of this catalytic CM. Meanwhile, when the SA concentration increased from 6.0 to 60 $mg\,L^{-1}$, the flux of CG-2/CM decreased from 117.61 to 29.50 $L\,m^{-2}\,h^{-1}$(LMH), and the J/J_0 value of CG-2/CM decreased from 0.65 to 0.16. This downtrend trend for J/J_0 may be due to the membrane surface being blocked by the increase in SA at a higher concentration. Surface catalytic ozonation in the COMR reasonably improved the normalized flux. When SA concentration was 30 $mg\,L^{-1}$, the J/J_0 value of CG-2/CM in the COMR was 0.87, which was much higher than that in the filtration with CM ($J/J_0 = 0.45$), CG-2/CM ($J/J_0 = 0.48$), or CM-O_3 ($J/J_0 = 0.48$). In this process, the molecular ozone and formed ROS depolymerized SA molecules by reacting with glycosidic linkages,[115] which converted high-MW SA fractions into smaller molecules (such as monosaccharides). When CG-2/CM was used, CMO/g-C3N4 on the ceramic membrane surface helped derive more ROS to take part in the reaction. Therefore, the interface catalytic ozonation in the COMR effectively prevented cake/gel formation on the membrane surface and mitigated membrane fouling. However, when SA was high, its presence inhibited interface catalytic ozonation in the COMR. Therefore, when SA concentration increased from 6 $mg\,L^{-1}$ to 60 $mg\,L^{-1}$, the J/J_0 value of CG-2/CM in the COMR decreased from 1.00 to 0.71. This result favored *in-situ* self-cleaning performance, which improved from 53.84% to 343.75% and which depended on SA concentration. This result was significantly better than reported values in other catalytic ceramic membranes, which were also influenced by reaction parameters. BP-4 degradation efficiency increased slightly in the first 7.0 min with increasing the SA concentration from 6.0 to 30 $mg\,L^{-1}$, and the pseudo first-order reaction kinetic constant increased from 0.36 to 0.39 min^{-1}. The competitive reaction between BP-4 and SA did not result in reduced catalytic activity, indicating that interface catalytic ozonation in the COMR was very strong for organics degradation.

11.4 Conclusions and Outlook

In 2005, Karnik *et al.* firstly fabricated a CM with catalytic ozonation properties using a layer-by-layer method to deposit iron oxide particles on a titania-coated membrane.[69] Research focuses on the application of these membranes in a combined ozonation-ultrafiltration process to remove DBPs and their precursors. A series of subsequent studies focused on the removal

of DBPs by metal oxide modified CM coupled with ozonation, such as Fe oxide CM,[116] Mn oxide CM,[103] Ti oxide CM[100] and so on. After that, a number of researchers began to focus on NOM removal performance and the mechanism of catalytic ozone membranes.[67,100] For example, Choi *et al.* studied the membrane fouling mitigation mechanisms by analyzing the structural transformation mechanism of NOM on the surface of a catalytic membrane.[67] In 2016, Guo *et al.* fabricated a novel CM coated with MnO_2–Co_3O_4 nanoparticles by catalytic ozonation for the degradation of benzophenone-3, a typical MP, from water.[83] After that, most studies focused on the preparation of novel catalytic membranes for MPs removal.[8,88,117]

However, many studies tend to simplify and pay too much attention to the preparation of new membrane materials, where only the removal efficiency of MPs as the evaluation index of catalytic ozonation membrane was selected and the membrane cleaning efficiency was ignored. In a catalytic ozonation membrane reactor, the transformation of membrane fouling components and the mitigated mechanism of membrane fouling is still unclear. As a result, it is necessary to develop new NOM characterization techniques to resolve the membrane fouling mitigation mechanism, such as microscope-infrared spectroscopy (microFTIR) analysis, microscope-Raman spectroscopy (microRaman) analysis, matrix-assisted laser desorption (MALDI)-TOF-MS and so on.

In addition, the influence of the inorganic membrane fouling upon the mitigation of catalytic membrane fouling has been neglected: for example, after Ca^{2+}/Mg^{2+} complexation with organic fouling, whether the active sites of the catalytic membrane would be masked, resulting in the decline of catalytic performance. Furthermore, the influence mechanism of particulates on catalytic membrane has not been revealed, especially for new catalytic membrane in the drinking water treatment process. Based on the classical membrane fouling model, the membrane fouling model of catalytic ozone membrane also needs to be developed to predict the formation type of membrane fouling, which will facilitate the development of membrane antifouling strategies.

Acknowledgements

We thank the Beijing Natural Science Foundation (Grant Nos. L182027, L160006 and 8132033), the National Natural Science Foundation of China (Grant Nos. 51878047 and 22076012), the National Key Research and Development Program of China (2021YFE0100800), and the Beijing Forestry University Outstanding Young Talent Cultivation Project (2019JQ03008) for financial support.

References

1. S. Tang, Z. Zhang and X. Zhang, *J. Membr. Sci.*, 2018, **555**, 30.
2. D. Wei, T. Yi, Z. Zhang and X. Zhang, *Chem. Eng. J.*, 2016, **294**, 157.

3. J. Zhang, T. Lin and W. Chen, *Chem. Eng. J.*, 2017, **325**, 160.
4. B. Harman, H. Koseoglu, N. Yigit, M. Beyhan and M. Kitis, *Desalination*, 2010, **261**, 27.
5. Y. Guo, Z. Song, B. Xu, Y. Li, F. Qi, J. P. Croue and D. Yuan, *J. Hazard. Mater.*, 2018, **344**, 1229.
6. S. Byun, J. S. Taurozzi, A. L. Alpatova, F. Wang and V. V. Tarabara, *Sep. Purif. Technol.*, 2011, **81**, 270.
7. V. Camel and A. Bermond, *Water Res.*, 1998, **32**, 3208.
8. W. J. Lee, Y. Bao, X. Hu and T.-T. Lim, *Chem. Eng. J.*, 2019, **378**, 121670.
9. S. Tang, Z. Zhang and X. Zhang, *Chem. Eng. J.*, 2017, **314**, 670.
10. S. Tang, Z. Zhang, J. Liu and X. Zhang, *J. Membr. Sci.*, 2017, **533**, 112.
11. X. Fan, Y. Tao, L. Wang, X. Zhang, Y. Lei, Z. Wang and H. Noguchi, *Desalination*, 2014, **335**, 47.
12. D. Wei, Y. Tao, Z. Zhang, L. Liu and X. Zhang, *J. Membr. Sci.*, 2016, **498**, 116.
13. S. Jia, Z. Zhang and X. Zhang, *J. Membr. Sci.*, 2017, **538**, 50.
14. L. Zheng, D. Yu, G. Wang, Z. Yue, C. Zhang, Y. Wang, J. Zhang, J. Wang, G. Liang and Y. Wei, *J. Membr. Sci.*, 2018, **563**, 843.
15. Z. Song, Y. Li, Z. Wang, M. Wang and F. Qi, *Chem. Eng. J.*, 2020, **394**, 124935.
16. M. Kukuzaki, K. Fujimoto, S. Kai, K. Ohe, T. Oshima and Y. Baba, *Sep. Purif. Technol.*, 2010, **72**, 347.
17. S. Yun and S. T. Oyama, *J. Membr. Sci.*, 2011, **375**, 28.
18. J. J. Conde, M. Maroño and J. M. Sánchez-Hervás, *Sep. Purif. Rev.*, 2017, **46**, 152.
19. G. Xomeritakis and Y. Lin, *J. Membr. Sci.*, 1997, **133**, 217.
20. P. Quicker, V. Höllein and R. Dittmeyer, *Catal. Today*, 2000, **56**, 21.
21. X. Zhang, D. K. Wang and J. C. D. da Costa, *Catal. Today*, 2014, **230**, 47.
22. H. Choi, E. Stathatos and D. D. Dionysiou, *Appl. Catal., B*, 2006, **63**, 60.
23. T. A. Peters, N. E. Benes and J. T. Keurentjes, *Appl. Catal., A*, 2007, **317**, 113.
24. W. Zhang, W. Qing, N. Chen, Z. Ren, J. Chen and W. Sun, *J. Membr. Sci.*, 2014, **451**, 285–292.
25. X.-H. Ma, Z.-L. Xu, Y. Liu and D. Sun, *J. Membr. Sci.*, 2010, **360**, 315.
26. S.-L. Chen, A.-J. Wang, C. Dai, J. B. Benziger and X.-C. Liu, *Chem. Eng. J.*, 2014, **249**, 48.
27. T. F. Mastropietro, C. Meringolo, T. Poerio, F. Scarpelli, N. Godbert, G. Di Profio and E. Fontananova, *Ind. Eng. Chem. Res.*, 2017, **56**, 11049.
28. Y. Zhao, D. Lu, C. Xu, J. Zhong, M. Chen, S. Xu, Y. Cao, Q. Zhao, M. Yang and J. Ma, *Water Res.*, 2020, **171**, 115387.
29. E. Drioli and L. Giorno, *Encyclopedia of Membranes*, Springer, 2018, pp. 1–72.
30. S. Han, Y. Li, S. Bai, L. Zhang, W. Li and W. Xing, *J. Appl. Polym. Sci.*, 2018, **135**, 46514.
31. Z. Cao, C. Xia, W. Jia, W. Qing and W. Zhang, *J. Membr. Sci.*, 2020, **595**, 117485.

32. W. Zhang, W. Qing, Z. Ren, W. Li and J. Chen, *Bioresour. Technol.*, 2014, **172**, 16.
33. R. Molinari, L. Palmisano, E. Drioli and M. Schiavello, *J. Membr. Sci.*, 2002, **206**, 399–415.
34. X. Cao, J. Luo, J. M. Woodley and Y. Wan, *ACS Appl. Mater. Interfaces*, 2016, **8**, 30511.
35. X.-J. Bai, D. Chen, Y.-N. Li, X.-M. Yang, M.-Y. Zhang, T.-Q. Wang, X.-M. Zhang, L.-Y. Zhang, Y. Fu and X. Qi, *J. Membr. Sci.*, 2019, **582**, 30.
36. R. Iler, *J. Colloid Interface Sci.*, 1966, **21**, 569.
37. J. J. Richardson, J. Cui, M. Björnmalm, J. A. Braunger, H. Ejima and F. Caruso, *Chem. Rev.*, 2016, **116**, 14828.
38. S. Wang, M. Hou, Q. Zhao, Y. Jiang, Z. Wang, H. Li, Y. Fu and Z. Shao, *J. Energy Chem.*, 2017, **26**, 168.
39. Y. Gao, M. Hu and B. Mi, *J. Membr. Sci.*, 2014, **455**, 349.
40. M. Liu, X. Zhu, R. Chen, Q. Liao, D. Ye, B. Zhang, J. Liu, G. Chen and K. Wang, *Chem. Eng. J.*, 2018, **354**, 35.
41. S. Mu, H. Tang, Z. Wan, M. Pan and R. Yuan, *Electrochem. Commun.*, 2005, **7**, 1143.
42. L. Li, Z. Liu, M. Pan and H. L. Tang, *Electrochem. Solid-State Lett.*, 2005, **8**, A574.
43. H. Tang, M. Pan, S. Jiang, Z. Wan and R. Yuan, *Colloids Surf., A*, 2005, **262**, 65.
44. H. Tang, Z. Wan and M. Pan, *Electrochem. Commun.*, 2007, **9**, 2003.
45. K. Li, G. Ye, J. Pan, H. Zhang and M. Pan, *J. Membr. Sci.*, 2010, **347**, 26.
46. M. Michel, A. Taylor, R. Sekol, P. Podsiadlo, P. Ho, N. Kotov and L. Thompson, *Adv. Mater.*, 2007, **19**, 3859.
47. D. Wang and S. Lu, *Chem. Commun.*, 2010, **46**, 2058.
48. D. Kregiel, *Food Control*, 2014, **40**, 32.
49. Q. Huang, J. Chen, M. Liu, H. Huang, X. Zhang and Y. Wei, *Chem. Eng. J.*, 2020, **387**, 124019.
50. H. Lee, S. M. Dellatore, W. M. Miller and P. B. Messersmith, *Science*, 2007, **318**, 426.
51. N. Li, G. Chen, J. Zhao, B. Yan, Z. Cheng, L. Meng and V. Chen, *J. Membr. Sci.*, 2019, **591**, 117341.
52. A. Idris, Z. Man, A. S. Maulud, H. A. Mannan and A. Shafie, *Polym. Test.*, 2019, **73**, 159.
53. S. Sun, H. Yao, W. Fu, L. Hua, G. Zhang and W. Zhang, *Water Res.*, 2018, **144**, 690.
54. J. Livage and D. Ganguli, *Sol. Energy Mater. Sol. Cells*, 2001, **68**, 365.
55. S. Dervin and S. C. Pillai, in *Sol-Gel Materials for Energy, Environment and Electronic Applications*, Springer, 2017, pp. 1–22.
56. I. Horovitz, D. Avisar, M. A. Baker, R. Grilli, L. Lozzi, D. Di Camillo and H. Mamane, *J. Hazard. Mater.*, 2016, **310**, 98.
57. H. Demiral and İ. Demiral, *Adv. Powder Technol.*, 2018, **29**, 3033.
58. G. L. Puma, A. Bono, D. Krishnaiah and J. G. Collin, *J. Hazard. Mater.*, 2008, **157**, 209.

59. G. Barbieri, V. Violante, F. P. Di Maio, A. Criscuoli and E. Drioli, *Ind. Eng. Chem. Res.*, 1997, **36**, 3369.
60. T. Ioannides and G. Gavalas, *J. Membr. Sci.*, 1993, **77**, 207.
61. N. Itoh, S. Niwa, F. Mizukami, T. Inoue, A. Igarashi and T. Namba, *Catal. Commun.*, 2003, **4**, 243.
62. A. S. Augustine, in *Supported Pd and Pd/Alloy Membranes for Water-gas Shift Catalytic Membrane Reactors*, Doctoral Dissertations, 2013.
63. C. Didaskalou, J. Kupai, L. Cseri, J. Barabas, E. Vass, T. Holtzl and G. Szekely, *ACS Catal.*, 2018, **8**, 7430.
64. X. Wang, X. Zhang, H. Liu, K. L. Yeung and J. Wang, *Chem. Eng. J.*, 2010, **156**, 562.
65. C. Chen, M. Xie, L. Kong, W. Lu, Z. Feng and J. Zhan, *J. Hazard. Mater.*, 2020, **390**, 122146.
66. Z. Song, J. Sun, W. Wang, Z. Wang, Y. Zhang, B. Xu and F. Qi, *Appl. Catal., B*, **283**, 119662.
67. H. Park, Y. Kim, B. An and H. Choi, *Water Res.*, 2012, **46**, 5861.
68. C. Mansas, L. Atfane-Karfane, E. Petit, J. Mendret, S. Brosillon and A. Ayral, *J. Environ. Chem. Eng.*, 2020, **8**, 104043.
69. B. S. Karnik, S. H. Davies, M. J. Baumann and S. J. Masten, *Environ. Sci. Technol.*, 2005, **39**, 7656.
70. S. Byun, S. H. Davies, A. L. Alpatova, L. M. Corneal, M. J. Baumann, V. V. Tarabara and S. J. Masten, *Water Res.*, 2011, **45**, 163.
71. S. Lee, K. Lee, W. M. Wan and Y. Choi, *Desalination*, 2005, **178**, 287.
72. X. Cheng, D. Wu, H. Liang, X. Zhu, X. Tang, Z. Gan, J. Xing, X. Luo and G. Li, *Water Res.*, 2018, **145**, 39.
73. L. M. Corneal, S. J. Masten, S. H. R. Davies, V. V. Tarabara, S. Byun and M. J. Baumann, *J. Hazard. Mater.*, 2010, **360**, 292.
74. S. Byun, S. H. Davies, A. L. Alpatova, L. M. Corneal, M. J. Baumann, V. V. Tarabara and S. J. Masten, *Water Res.*, 2011, **45**, 163.
75. X. Cheng, H. Liang, F. Qu, A. Ding, H. Chang, B. Liu, X. Tang, D. Wu and G. Li, *Chem. Eng. J.*, 2017, **308**, 1010.
76. C. Li, W. Sun, Z. Lu, X. Ao and S. Li, *Water Res.*, 2020, **175**, 115674.
77. Z. He, D. Xia, Y. Huang, X. Tan, C. He, L. Hu, H. He, J. Zeng, W. Xu and D. Shu, *J. Hazard. Mater.*, 2018, **344**, 1198.
78. M. A. Shannon, P. W. Bohn, M. Elimelech, J. G. Georgiadis, B. J. Marinas and A. M. Mayes, *Nature*, 2008, **452**, 301.
79. L. M. Corneal, M. J. Baumann, S. J. Masten, S. H. R. Davies, V. V. Tarabara and S. Byun, *J. Membr. Sci.*, 2011, **369**, 182.
80. Z. Jeirani and J. Soltan, *J. Water Process Eng.*, 2016, **12**, 127.
81. G. Scaratti, A. De Noni Junior, H. J. Jose and R. D. F. Peralta Muniz Moreira, *Environ. Sci. Pollut. Res.*, 2020, **27**, 22144.
82. W. Shen, Y. Wang, J. Zhan, B. Wang, J. Huang, S. Deng and G. Yu, *Chem. Eng. J.*, 2017, **310**, 249.
83. Y. Guo, B. Xu and F. Qi, *Chem. Eng. J.*, 2016, **287**, 381.
84. A. Ikhlaq, D. R. Brown and B. Kasprzyk-Hordern, *Appl. Catal., B*, 2015, **165**, 408.

85. H. Jiang, P. Chen, S. Luo, X. Tu, Q. Cao and M. Shu, *Appl. Surf. Sci.*, 2013, **284**, 942.
86. A. Sowmya and S. Meenakshi, *Int. J. Biol. Macromol.*, 2014, **69**, 336.
87. Y. Jiang, B. Cheng, M. Liu and Y. Nie, *Bull. Environ. Contam. Toxicol.*, 2016, **96**, 186.
88. Y. Guo, Z. Song, B. Xu, Y. Li, F. Qi, J.-P. Croue and D. Yuan, *J. Hazard. Mater.*, 2018, **344**, 1229–1239.
89. Q. Zhang, S. Chen, X. Fan, Y. Haiguang and Q. Hongtao, *Appl. Catal., B*, 2018, **224**, 204–213.
90. Z. Song, Y. Zhang, C. Liu, B. Xu, F. Qi, D. Yuan and S. Pu, *Chem. Eng. J.*, 2019, **357**, 655.
91. Y. Wang, L. Chen, C. Chen, J. Xi and S. Wang, *Appl. Catal., B*, 2019, **254**, 283.
92. Z. Song, J. Sun, Z. Wang, Y. Zhang, B. Xu and F. Qi, *Appl. Catal., B*, 2020, **283**, 119662.
93. K. Huang, J. Yuan, G. Shen, G. Liu and W. Jin, *Chin. J. Chem. Eng.*, 2017, **25**, 752.
94. M. Zhang, K. Guan, S. Jie, G. Liu and W. Jin, *AIChE J.*, 2017, **63**, 5054.
95. Y. Yuan, G. Xing, S. Garg, J. Ma, X. Kong, P. Dai and T. D. Waite, *Water Res.*, 2020, 115785.
96. M. Sun, I. Zucker, D. M. Davenport, X. Zhou, J. Qu and M. Elimelech, *Environ. Sci. Technol.*, 2018, **52**, 8674.
97. F. Xu, M. Wei, X. Zhang, Y. Song, W. Zhou and Y. Wang, *Res.*, 2019, **2019**, 2581241.
98. B. Liu, R. Wu, J. A. Baimova, H. Wu, A. W.-K. Law, S. V. Dmitriev and K. Zhou, *Phys. Chem. Chem. Phys.*, 2016, **18**, 1886.
99. H. Sun, S. Liu, G. Zhou, H. M. Ang, M. O. Tadé and S. Wang, *ACS Appl. Mater. Interfaces*, 2012, **4**, 5466.
100. S. Byun, S. Davies, A. Alpatova, L. Corneal, M. Baumann, V. Tarabara and S. Masten, *Water Res.*, 2011, **45**, 163–170.
101. Y. Wang, Z. Ao, H. Sun, X. Duan and S. Wang, *Appl. Catal., B*, 2016, **198**, 295.
102. L. Yu, G. Zhang, C. Liu, H. Lan, H. Liu and J. Qu, *ACS Catal.*, 2018, **8**, 1090.
103. L. M. Corneal, S. J. Masten, S. H. Davies, V. V. Tarabara, S. Byun and M. J. Baumann, *J. Membr. Sci.*, 2010, **360**, 292.
104. H. Song, J. Shao, Y. He, B. Liu and X. Zhong, *J. Membr. Sci.*, 2012, **405**, 48.
105. R. Yuan, S. N. Ramjaun, Z. Wang and J. Liu, *J. Hazard. Mater.*, 2011, **196**, 173.
106. L. Xing, Y. Xie, H. Cao, D. Minakata, Y. Zhang and J. C. Crittenden, *Chem. Eng. J.*, 2014, **245**, 71.
107. H. Vatankhah, A. Szczuka, W. A. Mitch, N. Almaraz, J. Brannum and C. Bellona, *Environ. Sci. Technol.*, 2019, **53**, 2720.
108. H. Matsuda, Y. Ose, T. Sato, H. Nagase, H. Kito and K. Sumida, *Sci. Total Environ.*, 1992, **117**, 521.

109. Y. Zhang, Y. An, C. Liu, Y. Wang, Z. Song, Y. Li, W. Meng, F. Qi, B. Xu and J.-P. Croue, *Water Res.*, 2019, 115026.
110. P. Duan, T. Ma, Y. Yue, Y. Li, X. Zhang, Y. Shang, B. Gao, Q. Zhang, Q. Yue and X. Xu, *Environ. Sci. Nano*, 2019, **6**, 1799.
111. L. M. Corneal, S. J. Masten, S. H. R. Davies, V. V. Tarabara, S. Byun and M. J. Baumann, *J. Membr. Sci.*, 2010, **360**, 292.
112. H. Song, J. Shao, Y. He, B. Liu and X. Zhong, *J. Membr. Sci.*, 2012, **405–406**, 48–56.
113. Q. Zhao, D. Lu, H. Jiang, Y. Zhao, Y. Sun, Z. Li, M. Yang, P. Wang and J. Ma, *J. Membr. Sci.*, 2019, **573**, 210.
114. M. Moslemi, S. H. Davies and S. J. Masten, *Water Res.*, 2011, **45**, 5529.
115. Y. Wang, R. I. Hollingsworth and D. L. Kasper, *Carbohydr. Res.*, 1999, **319**, 141.
116. B. S. Karnik, S. H. Davies, M. J. Baumann and S. J. Masten, *Environ. Eng. Sci.*, 2007, **24**, 852.
117. X. Cheng, H. Liang, F. Qu, A. Ding, H. Chang, B. Liu, X. Tang, D. Wu and G. Li, *Chem. Eng. J.*, 2017, **308**, 1010.

CHAPTER 12

Ozonation Nanobubble Technology

XIAONAN SHI, TAHA MARHABA AND WEN ZHANG*

John A. Reif Jr., Department of Civil and Environmental Engineering, New Jersey Institute of Technology, Newark, New Jersey 07102, United States
*Email: wen.zhang@njit.edu

12.1 Introduction to Water Disinfection and Ozonation Disinfection

12.1.1 Principles of Ozonation Disinfection

Ozone, due to its potential oxidizing capacity, has widely been used to inactivate bacteria, fungi, viruses, protozoa and bacterial or fungal spores.[1,2] Ozone generally exhibits strong antimicrobial effects without inducing microbial resistance.[3,4] Ozonation is also commonly used in pharmaceutical,[5] food,[6,7] cosmetic[8] and medical treatment of skin/nails/dental infections[4,9,10] and surgical site infections.[11] For example, both gaseous and aqueous forms of ozone are clinically used to kill oral pathogens or endodontic infections.[12–14] Ozone therapy considerably reduces the growth of common pathogens in chronic periodontitis *Aggregatibacter actinomycetemcomitans*, *P. gingivalis* and *T. forsythia*.[15,16]

The oxidation power of ozone is contributed to by molecular ozone and/or reactive radical species formed during the self-decomposition or

Chemistry in the Environment Series No. 8
Advanced Ozonation Processes for Water and Wastewater Treatment: Active Catalysts and Combined Technologies
Edited by Hongbin Cao, Yongbing Xie, Yuxian Wang and Jiadong Xiao

Published by the Royal Society of Chemistry, www.rsc.org

decay of ozone.[17] The ozone oxidation half-reactions of ozone in water include:

$$O_3 + 2H^+ + 2e^- \rightarrow O_2 + H_2O \ (E^0 = 2.076 \text{ V})$$

$$O_3 + H_2O + e^- \rightarrow O_2 + 2OH^- \ (E^0 = 1.24 \text{ V})$$

Besides this direct electron transfer or acquisition, indirect ozone reactions may involve ozone decay and the production of various reactive oxygen species such as superoxide radicals ($^{\bullet}O_2^-$), hydroperoxide radicals ($HO_2^{\bullet}$) and ozonide radicals ($^{\bullet}O_3^-$) that may also react with water pollutants:[18–23]

$$O_3 + OH^- \rightarrow HO_2^{\bullet} + {}^{\bullet}O_2^- \ (k_1 = 70 \text{ mol s}^{-1})$$

$$O_3 + OH^- \rightarrow HO_2^- + O_2 \ (k_2 = 40 \text{ mol s}^{-1})$$

$$O_3 + HO_2^- \rightarrow HO_2^{\bullet} + {}^{\bullet}O_3^- \ (k_3 = 2.2 \times 10^6 \text{ mol s}^{-1})$$

The efficiency of microbial inactivation generally depends on the susceptibility of the specific microbes, contact time and concentrations of ozone or radicals.[24] Ozone can disrupt the cell membrane (disruption of carbon–nitrogen bonds of proteins leading to depolymerization) and key components such as lipoproteins and polysaccharides, resulting in the rupture and damage of bacterial wall.[24] Ozone could then oxidize the interior cytoplasm such as nucleic acid and protein and ultimately disable the metabolic and reproductive capabilities of bacteria.[11,25,26] As opposed to chlorine, ozone has many advantages. First, ozone has high oxidation potential and is more reactive on disinfectant and is a more effective bactericide and viricide at comparable doses.[27] Second, ozone leaves far less residual products than chlorination, which causes formation of chlorinated DBPs.[17]

12.1.2 Limitations of Traditional Ozonation Disinfection

Despite the advances, ozone disinfection still has some disadvantages,[27] such as high capital, operation and maintenance costs (*ca.*, 10 kW kg^{-1} O_3) in many ozonation contacting systems (*e.g.* bubble columns, injectors, spray chambers or diffusers), the corrosive nature of ozone and safety concerns for human health, and formation of bromate and *N*-nitrodimethylamine (NDMA).[28,29] Also, the large footprint treatment unit and limited transfer or dispersion efficiencies of O_3 bubbles in water,[30] largely due to relatively poor solubility and stability,[31] are drawbacks. Thus enhancing the ozone–water mass transfer is necessary and often achieved by designing different reactor configurations or operations such as increasing the stirring,[32] surface areas[33] and exposure time.[34] For instance, oscillatory flow reactors (OFRs) were demonstrated to intensify multiphase mixtures with high efficiency,[34–37] by forcing the fluid to oscillate with variable geometric baffles and thus increasing retention and contact time.[36]

Another major limitation is the short life of ozone in water (*e.g.* the half-life is only about 20 min).[38] This rapid decay often results in relatively low concentrations of dissolved ozone (*e.g.* less than 10 mg L^{-1} at 25 °C when injecting 3% ozone gas into water) and therefore reduced performance. The decay of ozone results from direct reactions of ozone with other compounds in water and from indirect reactions of self-decay that converts ozone into hydroxyl radicals and oxygen. The decay of ozone can be described in the following general form (eqn (12.1)):[39]

$$-\frac{d[O_3]}{dt} = k_d \cdot [O_3]^n \tag{12.1}$$

where O_3 is the concentration of ozone in water (mol L^{-1}) at reaction time, t (s); the exponent n is a reaction order, and k_d is the ozone decay constant (*e.g.* s^{-1} when n is 1 and in mol L^{-1} s^{-1} when n is 2).

Ozone decay kinetics in water has been reported to depend on many factors, such as the dissolved ozone concentration,[40,41] solution temperature,[42] pH,[39] alkalinity,[42] hydrodynamic conditions,[43] light exposure[39,44] and the presence of organic and inorganic carbons.[39,41,44] For example, high solution pH could speed up ozone decay.[39] Inorganic carbons act as a scavenger for hydroxyl radicals and thus increase ozone decay.[44] Yurteri and Gurol proposed eqn (12.2) to estimate the decay rate constant (s^{-1}) that considers the effects of pH, DOC and alkalinity.[45] Laplanche *et al.* further incorporated the UV absorbance that speeds up the destruction of ozone in eqn (12.3).[46]

$$\log k_d = -7.116 + 0.66 \cdot \mathrm{pH} + 0.61 \cdot \log[\mathrm{DOC}] - 0.42 \cdot \log[0.1 \cdot \mathrm{ALK}] \tag{12.2}$$

$$\log k_d = -3.93 + 0.24 \cdot \mathrm{pH} + 0.7537 \cdot \log[\mathrm{UV}_{254}] + 1.08 \cdot \log[\mathrm{DOC}] - 0.19 \cdot \log[\mathrm{ALK}] \tag{12.3}$$

where DOC is the concentration of dissolved organic carbon (mg L^{-1}), UV_{254} is the UV absorbance at 254 nm (dimensionless) and ALK is alkalinity expressed as mg of $CaCO_3$ L^{-1}.

12.2 Nanobubbles and Generation Principles of Ozone Nanobubbles

12.2.1 Nanobubbles and Their Applications

Nanobubbles (NBs) are ultrafine bubbles with a size or diameter typically smaller than 1 μm,[47] which exhibit valuable characteristics (*e.g.* long residence times in water due to their low buoyancy, high stability against coalesces, collapse or burst).[48,49] Thus NBs are expected to have a higher

efficiency of mass transfer compared to bulk scale bubbles (macrobubbles) due to the high specific surface areas.[48,50,51] NBs have proven useful in many industrial and engineering applications, such as emulsion technology for chemical processing, detergent-free cleaning,[52] intracellular drug delivery,[53] water and wastewater treatment,[54–56] as well as agricultural fields (pathogen control and irrigation).[57–60]

12.2.2 Ozone Nanobubble Generation Methods

Most ozone NB generation combines different NB generation systems and ozone generation to generate ozone NBs.[4,31,61–63] Generation of NBs can be achieved with a wide range of hydrodynamic methods, such as spiral liquid flow (also known as rotary liquid flow) *via* Venturi nozzles, pressurization–depressurization, porous-membranes, ultrasonication and laser or optical ablation.[64] For example, Figure 12.1(a) shows that in a spiral liquid flow generator, water is pumped through a side hole to produce a tangent flow in the cylinder.[65–67] The tangent flow sucks in the gas through an orifice on the bottom of the cylinder and converts it into fine bubbles at the second orifice due to the centrifugation effect.

Ejectors in Figure 12.1(b) consist of a cylindrical channel that water flows through to produce high-pressure fluctuations.[67,68] Gas is sucked in where the channel expands and consequently the pressure is reduced. A high number of micro/nanobubbles are generated due to cavitation.[68,69] In a pressurization–depressurization method (Figure 12.1(c)),[70] gas solubility is first enhanced by increasing the gas pressure and then rapidly decreasing it to induce micro/nanobubbles in liquid similar to ejectors.[71–73] However, this method usually does not produce a monodisperse bubble size distribution, due to the dynamic and nonuniform rate of pressure change in the solution.[70]

Figure 12.1(d) shows the Venturi nozzle–based generation, where water is presaturated with gas to form millibubbles (*i.e.* bubbles with diameters of a few millimeters).[74] This presaturated water goes through the throat of Venturi tube and undergoes a drastic pressure variation that results in millibubble collapse and formation of NBs.[49,74–76]

Lastly, ultrasonication is the most common method to produce NBs by using ultrasound waves to induce cavitation in water.[77,78] Kim *et al.* employed an ultrasonic cleaner as shown in Figure 12.1(e) to produce a bimodal distribution of NBs using 42 kHz and 70 W.[79] The study indicates the dependence of bubble size on the solution pH. For pH 12, over 50% of bubbles had diameters under 100 nm (in the range of 50–90 nm), whereas for pH 3 most of bubble diameters were in the range 150–350 nm. Moreover, when surfactants were used, the bubble sizes were reduced to the decrease of the solution surface tension.

As shown in Figure 12.1(f),[80,81] NBs may also be produced on the membrane surface when the pressurized gas permeates the membrane pores, a

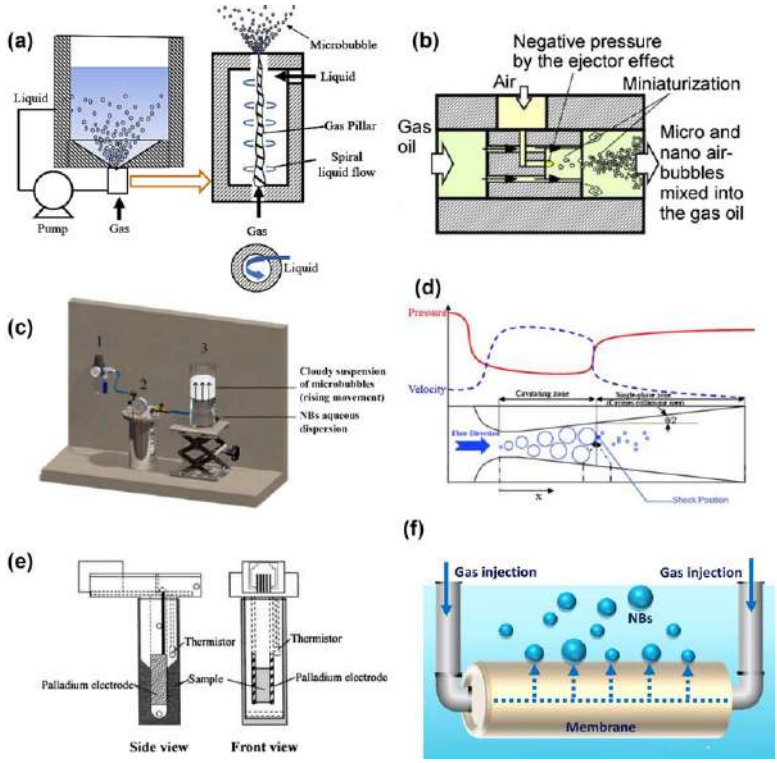

Figure 12.1 Schematic examples for different nanobubble generators. (a) Spiral liquid flow generator. (b) Ejector-type generator. The figure is reproduced from (c) Pressurization–depressurization generation process. (d) Venturi-type generator. (e) Ultrasonication generator. (f) Formation process of NBs through the hydrophobized ceramic membranes' pores by injection of a pressurized gas. (b), (c), (d) and (e) reproduced from ref. 68 with permission from Elsevier, Copyright 2013; ref. 70 with permission from Elsevier, Copyright 2016; ref. 74, https://doi.org/10.5277/ppmp170220, under the terms of the CC BY 4.0 license https://creativecommons.org/licenses/by/4.0/; and ref. 79 with permission from Elsevier, Copyright 2000, respectively.

process called membrane ozonation. The water surface tension and adhesion between bubbles and membrane surface largely prevent bubble detachment from the membrane surface. The size of NBs will grow until the buoyancy and or the built-up pressures overcome the forces of surface tension and adhesion.[82,83] The recent studies reported by Zhang's group indicate that the size of generated bubbles is governed by the gas–liquid–solid contact angles, the surface hydrophobicity of the membrane pores and liquid solvent, and the injection pressure of the gas.[80]

12.3 Ozone Nanobubble Properties and Applications

12.3.1 Stability and Disinfection Characteristics of Ozone Nanobubbles

Ozone NBs, a new form of dispersion in water (besides dissolved ozone or nondissolved ozone gas), could potentially increase the longevity and stability of ozone as well as the effective dissolved ozone concentration compared to regular dissolved ozone. Due to its complex internal states (*e.g.* pressures and phases), it remains largely debatable in the scientific community whether and how NBs are stabilized in liquid.[84–88] To date, different stability mechanisms have been proposed to explain its existence and stability by accounting for different potential factors including formation of surface barriers,[89–91] high zeta potentials,[92,93] electric double layer[94,95] and high-density mechanisms.[96,97] However, it remains unclear how the internal gas pressure and solution temperature affect the NBs' properties such as bubble size and stiffness. As illustrated in Figure 12.2, NBs may act as a storage package of gas molecules that may progressively release or leach the gaseous molecules *via* dissolution and collapse. Besides pressure waves and heat, the collapse of NBs may generate radical species and degrade the contaminants.[51,98–100] The high concentration of dissolved ozone in aqueous solution (either acidic or alkaline) leads to the formation of $^{\bullet}OH$ radicals.[100] Generation of free radicals through the collapse of the NBs has been observed by electron spin resonance spectroscopy.[101] Meanwhile, the type of gases affects the quantity or quality of free radicals that are generated. For example, oxygen NBs promote the formation of $^{\bullet}OH$ radicals compared to inert gases such as nitrogen NBs.[102]

Although the oxidizing power of ozone (2.07 eV) is lower than that of $^{\bullet}OH$ radicals (2.85 eV), ozone still yields higher reactivity and selectivity toward organic compounds[103] than other common oxidants such as hydrogen peroxide (1.77 eV) and hypochlorous acid (1.49 eV).[104] Recent applications of NBs in ozonation entail water treatment,[105] oral treatment[106–108] and food processing.[109] Previous studies showed the application of ozone

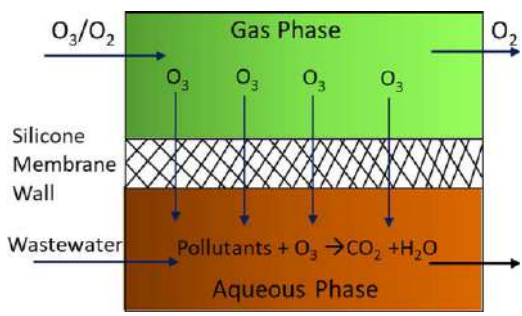

Figure 12.2 Schematics of membrane-based ozonation process.

micro/nanobubbles for disinfection of various kinds of microorganisms including *Fusarium oxysporum*, *Pectobacterium carotovorum* subsp. *carotovorum*,[110] Coliform group,[111] and *Bacillus subtilis* spores,[112] demonstrating that ozone NBs were efficient for use as a disinfectant against those microorganisms. In addition, exposure to ozone NBs in water for 0.5 min reduced the bacterial counts below the lower limit of detection (<10 CFU mL^{-1}).[38] Some researchers reported that NBs could accelerate the formation of $^{\bullet}OH$ radicals in ozonation processes.[113,114] Specifically, NBs could increase the mass transfer of ozone, and hence promote utilization rate and oxidation reactions of pollutants in water and wastewaters.[115] Enhancing ozone utilization will potentially reduce the supplied ozone dose and the off-gas ozone concentration, which reduces energy consumption and safety concerns.[116]

12.3.2 Mass Transfer of Ozonation

Mass transfer of ozone into water and its stability in liquid determine the reactivity and performance of ozonation for water disinfection and other reactions. Dissolved ozone concentrations in water often reduce rapidly since ozone is an unstable molecule, especially at higher temperatures, leading to lower reaction efficiencies and reduced disinfection efficacy. Also, ozone is about 12 times less soluble in water than chlorine, which limits its effectiveness at equivalent doses against target water pollutants or persistent microorganisms, such as persistent bacterial spores or cysts. Clearly, ozonation with NBs holds great promising potential to address these technical barriers for full commercialization or industrialization of NB-based ozonation.[38] Due to the small bubble sizes, ozone NBs are expected to significantly increase the mass transfer efficiencies of ozone, oxygen and other reacting species such as hydrophobic pollutants that adsorb to and migrate at the bubble–liquid interface.[117]

The mass-transfer coefficient ($k_{aq}{\cdot}a, \mathrm{min}^{-1}$) in liquid can be calculated by eqn (12.4):

$$\frac{dO_3}{dt} = k_{aq} \cdot a \cdot (O_3{}^{*} - O_3) - k_d \cdot O_3 \tag{12.4}$$

where $O_3{}^{*}$ and O_3 are the steady-state dissolved ozone concentrations ($mg\,L^{-1}$) and at time t, respectively.[35] k_d is the first-order decay rate constant of dissolved ozone (min^{-1}). $k_{aq}{\cdot}\alpha$ (s^{-1}) is the mass transfer rate constant or volumetric liquid mass transfer coefficient that can be then determined by multiplying the mass transfer coefficient (k_{aq}, $m\,s^{-1}$) with the geometric surface area (α) of the ozone bubble per volume of solution (m^{-1}), which is calculated by eqn (12.5):

$$\alpha = \frac{\text{Total surface area}}{\text{Total volume}} = \frac{N \times 4 \cdot \pi \cdot r^2}{N \times \frac{4}{3} \cdot \pi \cdot r^3} = \frac{3}{r} \tag{12.5}$$

where N is the total number of ozone NBs in liquid, and r is the radius of the ozone bubble. This formula assumes a uniform size or radius of ozone NBs in water and thus enables this simplified calculation of this geometric surface area (α). The $k_{aq}\cdot\alpha$ level is affected by the ozone concentration in the gas phase, the feed gas flow rate, liquid temperature and pH, as well as the ozone bubble characteristics such as bubble size and concentrations. The reported $k_{aq}\cdot\alpha$ values varied from 0.2×10^{-3} s^{-1} to 25×10^{-3} s^{-1} in water.[118,119] $k_{aq}\cdot\alpha$ was shown to slight decrease from 6.9×10^{-3} s^{-1} to 4.3×10^{-3} s^{-1} when the solution pH increased from 1.5 to 9.[118] One of the plausible reasons of the improved reactivity of ozone NBs is that, due to the bubble shrinkage and surface tension force at the water–gas interface, ozone NBs may present high internal pressures, which significantly elevate the gas solubility and the level of O_3*.[66] Moreover, the mass transfer coefficient (k_{aq}) does not change with the forms or sizes of ozone bubbles or NBs, as k_{aq} is a measure of the mass transport rate of the gaseous molecules across the liquid and gas film layers (two-film theory) and a characteristic that is governed by the properties of gas and liquid or the gas–liquid interface. Thus the second reason is clearly owing to the geometric surface area (α) that increases with the reduced bubble size of ozone.

The mass transfer efficiency (MTE), which is a ratio of the mass of ozone that is transferred to the liquid from the gas phase, can be calculated in eqn (12.6):

$$\mathrm{MTE} = \frac{Q_L \cdot [O_3]_L}{Q_G \cdot [O_3]_G} \cdot 100\,\% \tag{12.6}$$

where Q_L is the input liquid flow rate ($mL\,min^{-1}$), Q_G is the input gas flow rate ($cm^3\,min^{-1}$), and $[O_3]_L$ and $[O_3]_G$ are the ozone concentrations in liquid

Table 12.1 Summary of the literature-reported membrane ozonation systems.

Membrane materials	Pore size	Ozone bubble diameter (nm)	Reported or calculated MET	Ref.
Shirasu porous glass (SPG) membranes	510 nm	Bubbleless	0.1% (hydrophilic) 0.3% (hydrophobic)	121
PVDF membrane	420 nm	Bubbleless	0.21%	122
PVDF membrane	0.1–1 μm	Bubbleless	NA	123
PVDF membrane	0.2 μm	Bubbleless	NA	124
PVDF membrane/Ni foam	0.2 μm	Bubbleless	NA	125
Non-porous PDMS Membrane	NA	Bubbleless	0.35%	126
Polytetrafluoroethylene (PTFE)	0.2–1 μm	10–90 μm	NA	127
Alumina capillary membrane	0.6 μm	100 μm	NA	128
Al_2O_3 ceramic membranes	100–900 nm	Bubbleless	NA	129

and gaseous phases ($mg\,L^{-1}$), respectively. As mentioned, a rationale ozone contactor or reactor design is important for improving mass transfer. As Table 12.1 shows, very few studies report or provide sufficient data to calculate the MET values, which was found to be around 0.1%–0.3%. Previous studies indicated that the MTE for oxygen[36,120] and ozone[34,37] in OFRs are several orders of magnitude higher than in other contactors. The ozone–water mass transfer in the OFR under continuous flow was found to increase with the increasing oscillatory frequencies and amplitudes. This oscillation is expected to increase $k_L a$ as ultrafine bubbles may evolve, which provides larger surface areas for mass transfer.[35]

12.3.3 Enhanced Reactivity of Ozone Nanobubbles

Enhanced reactivity and the oxidation power or duration of ozone NBs may be attributed to the continuous release of ozone molecules from NBs and radical formation from bubble collapse. Moreover, the improved degradation of water pollutants may also be attributed to the high adsorption capability and mass transfer of NBs offering a large surface area to facilitate the reaction. For example, NBs were combined with vacuum ultraviolet (VUV) irradiation (185–254 nm) to enhance the degradation of the sodium dodecylbenzenesulfonate (SDBS) surfactant in aqueous solution.[130] The penetration of the incident 185 nm UV light in water is very short because of its high absorption coefficient in water (1.8 cm at 298 K).[131] Thus the rate-determining step in VUV reactor is the diffusion of the SDBS to the UV-irradiated reaction site, where both $OH^{\bullet}$ radicals and direct photolysis result in the surfactant degradation. The presence of NBs allows surfactants to rapidly diffuse to the interface of bubbles from bulk solution.[130] Moreover, the degradation rate of surfactants (SDBS) was found faster than that of nonsurfactants (*e.g.* benzene sulfonate) with the presence of NBs under UV irradiation, possibly because surfactants can effectively adsorb at the water–gas interface of micro/nanobubbles and then stabilize the micro/nanobubbles as degradation reaction sites.[132]

12.3.4 Applications of Ozone Nanobubbles

The worldwide market for ozone generation technology is expected to grow at a compound annual growth rate (CAGR) of approximately 6.0% over the next five years and will reach US$20 million in 2024, from US$14 million in 2019, according to a new research study. As a result of the need to destroy and avoid the formation of substances of concern, typically enforced with recent legal regulations, the International Ozone Association (IOA) predicted that the U.S. market for oxygen/ozone used in drinking water applications is accelerating exponentially. Global ozone CAPEX spending is a significant part of overall disinfection technology spending, which is at US$6.14 billion for 2019.

Ozonation is a common advanced oxidation process (AOP) that is applied mostly for enhancing degradation of target substances (*e.g.* refractory pollutants, microbial pathogens, color and odor) in air, drinking water, industrial water, wastewater, medical applications and food treatment or processing.[1,2] With improved solubility and stability of ozonated water, ozone micro/nanobubbles have a great potential as a disinfectant for water treatment,[105] for oral cleaning or teeth treatment[106–108] and for food processing.[109] Both oxygen and ozone NBs were shown to reduce COD,[133] decolorize the wastewater from the textile industry,[134] and reduce the concentration of pesticides.[135] Ozone microbubbles caused 99.99% inactivation of *E. coli* cells with a lower ozone dose and a smaller volume of the water disinfection systems.[99,136] In addition, ozone NBs are effective against other types of bacteria such as *Bacillus subtilis* spores and *Cryptosporidium parvum*.[137] The persistent pathogens such as norovirus in oysters or *E. coli* bacteria in frozen vegetables (*e.g.* spinach or listeria) pose catastrophic health implications around the world. During food disinfection or storage, chemical treatments are often not desirable or practical as they may negatively affect the taste and quality of the food products. Ozone and oxygen NBs are thus considered holding potential to make a change. For example, ozone NBs may largely reduce the dosage of ozone, off-gas consumption and human exposure. Moreover, ozone NBs in water, after application on food, are expected to sustain disinfection power much longer than regular ozonated water. The surface coating of food by negatively charged NBs help remove and destroy most organics and pathogens from the surface of the food. Bacteria inactivation and removal are also anticipated due to the formation of hydroxyl radicals or other reactive species by ozone NBs (*e.g.* during collapse or burst).[137,138] Furthermore, combinations of NBs with UV irradiation or ultrasonication may boost radical formation and improve the disinfection power of NBs.[51,139,140]

12.4 Future Research Directions

12.4.1 Industrialized Ozone Nanobubble Generator Development

In the research areas of enhancing the transfer efficiency of gases into liquids, developing a highly scalable nanobubble (NBs) production method that enables the efficient, industrial-scale production of saturated ozone NB solutions is still at infancy stage. Early commercial deployment has demonstrated the value and potential of NBs as a hyperefficient gas transfer and chemical-free water quality remediation method in a broad set of new and existing processes including surface water remediation, horticulture, aquaculture and water treatment applications.

Further, industry standard ozone injection methods such as Venturi nozzles or contact bubble chambers often inefficiently transfer ozone, resulting in off-gassing. Off-gassed ozone reduces ozone utilization rates and

creates a health and safety hazard for drinking water operators due to the low exposure limits. Conversion into ozone NBs may present the opportunity to minimize or eliminate ozone off-gassing resulting in increased utilization rates and to reduce health and safety concerns. Increased ozone utilization rates directly impact the capital and operational costs of ozone injection, reducing the cost of ozone treatment. However, due to the lack of suitable instrumentation for the characterization of NBs and inadequate knowledge in the formation and stability of NBs in water, there are many notable barriers for commercialization or industrialization of ozone NB technology. Novel experimental and model approaches need to be integrated to evaluate the promising properties of ozone NBs widely claimed in the literature: enhanced reactivity (*e.g.* higher radical generation and higher dissolved ozone levels) and the resulting higher potency in pollutant degradation or disinfection. For example, stability of bubble size and distribution, concentrations and zeta potentials of ozone NB water must be rigourously examined to evaluate water chemistry changes after injection of ozone NBs into environmentally relevant water matrixes, to characterize reactive radical species generation and concentrations and to establish a new modeling and experimental assessment framework for ozone NB stability and collapse dynamics.

12.4.2 Safety Concerns of Ozone Nanobubbles

The development and industrialization of ozone NBs in the drinking water matrix will be critical for guiding dose control and application strategies (spatial and temporal) to ensure sufficient NBs for specific treatment goals. NB ozonation represents a potentially game-changing water treatment and disinfection technology that significantly increases contaminant degradation efficiencies and the sustainability of ozone treatment. It combines the benefits of ozone, as a highly powerful oxidant capable of removing some of the most intractable emerging contaminants and of leaving no chemical residual after treatment, with the various benefits of nanobubble gas injection. For the disinfection and remediation of drinking water plants, ozone NBs are poised to yield greater efficacies of pollution and pathogen removal than regular ozonation (with fine and coarse bubbles in contact chambers).

It is also very important to develop a nanobubble generator specifically designed for ozone NB generation in drinking water treatment applications. Core technology research is critical to maximize ozone NB production while eliminating the off-gassing of ozone and to minimize the liquid pumping requirements (the primary source of electrical consumption) of NB production to ensure market-competitive operational cost. As part of maximizing NB production, the elimination of larger coarse bubble production is essential to maximize ozone transfer efficiency and ozonation utilization and to eliminate process safety hazards. It is required to characterize the advantages of ozone and NB oxidation by comparing the effectiveness of dissolved ozone and NB-suspended ozone on common target contaminants in

clean water and real-world water matrices. Model contaminants such as perfluorinated substances, taste and odor compounds, natural organic matter (NOM) and medicinal substances will be used to compare the effectiveness of dissolved ozone and ozone NBs and inform a go-to-market strategy based on contaminant removal performance. Systematic and intensive study of ozone NBs will need to be conducted, ranging from laboratory proof-of-concept studies, the design and field validation of a modular ozone NB generator designed for drinking water disinfection and other broad applications.

Lastly, ozone is a known phytotoxic gas, and its ecological risk has been well-known in agricultural and food-related applications.[141–143] Overhead spray irrigation of aqueous ozone (3 $mg\,L^{-1}$ and 6 $mg\,L^{-1}$) was shown to negatively affect plant growth,[143] while low ozone concentrations (up to 1.5 $mg\,L^{-1}$) did not present measurable risk. Thus it is also imperative determine the upper tolerance limits of foliar spray so that peak pathogen control efficacy is achieved without posing significant adverse risks on ecological systems and even human health.

Acknowledgements

This research is partially supported by the United States Department of Agriculture (USDA), the National Institute of Food and Agriculture, AFRI project [2018-07549] and the United States Environmental Protection Agency (US EPA) under Assistance Agreement No. 83945101 and 84001901 (EPA P3 phase I and II). The USDA and the EPA have not formally reviewed this study. The views expressed in this document are solely those of authors and do not necessarily reflect those of the agencies. The USDA and EPA do not endorse any products or commercial services mentioned in this publication.

References

1. M. V. Selma, A. M. Ibáñez, M. Cantwell and T. Suslow, *Food Microbiol.*, 2008, **25**, 558–565.
2. A. Pérez, T. Poznyak and I. Chairez, *Ozone: Sci. Eng.*, 2015, **37**, 119–126.
3. J.-G. Kim, A. E. Yousef and S. Dave, *J. Food Prot.*, 1999, **62**, 1071–1087.
4. S. Hayakumo, S. Arakawa, Y. Mano and Y. Izumi, *Clin. Oral Invest.*, 2013, **17**, 379–388.
5. J. Bing, C. Hu and L. Zhang, *Appl. Catal., B*, 2017, **202**, 118–126.
6. V. Prabha, R. D. Barma, R. Singh and A. Madan, *Trends Biosci.*, 2015, **8**, 4031–4047.
7. R. Pandiselvam, S. Sunoj, M. Manikantan, A. Kothakota and K. Hebbar, *Ozone: Sci. Eng.*, 2017, **39**, 115–126.
8. J. Tessier, P. N. Rodriguez, F. Lifshitz, S. M. Friedman and E. J. Lanata, *Acta Odontol. Latinoam.*, 2010, **23**, 84–89.
9. P. Barone, *Ozone Ther.*, 2017, **2**, 19–25.
10. R. Manjunath, D. Singla and A. Singh, *J. Adv. Oral Res.*, 2015, **6**, 5–9.

11. M. T. Buhmann, D. Abt, S. Altenried, P. Rupper, P. Betschart, V. Zumstein, K. Maniura-Weber and Q. Ren, *Front. Microbiol.*, 2018, **9**, 1470.
12. K. C. Huth, M. Quirling, S. Maier, K. Kamereck, M. Alkhayer, E. Paschos, U. Welsch, T. Miethke, K. Brand and R. Hickel, *Int. Endod. J.*, 2009, **42**, 3–13.
13. R. Hems, K. Gulabivala, Y. L. Ng, D. Ready and D. Spratt, *Int. Endod. J.*, 2005, **38**, 22–29.
14. M. Arita, M. Nagayoshi, T. Fukuizumi, T. Okinaga, S. Masumi, M. Morikawa, Y. Kakinoki and T. Nishihara, *Oral Microbiol. Immunol.*, 2005, **20**, 206–210.
15. K. C. Huth, M. Quirling, S. Lenzke, E. Paschos, K. Kamereck, K. Brand, R. Hickel and N. Ilie, *Eur. J. Oral Sci.*, 2011, **119**, 204–210.
16. K. C. Huth, F. M. Jakob, B. Saugel, C. Cappello, E. Paschos, R. Hollweck, R. Hickel and K. Brand, *Eur. J. Oral Sci.*, 2006, **114**, 435–440.
17. K. Verma, D. Gupta and A. Gupta, *J. Environ. Chem. Eng.*, 2016, **4**, 3021–3032.
18. K. Ikehata and Y. Li, in *Advanced Oxidation Processes for Waste Water Treatment*, Elsevier, 2018, pp. 115–134.
19. S. Jasim, M. Uslu, R. Seth and N. Biswas, *Ozone: Sci. Eng.*, 2020, **42**, 461–468.
20. K. Loganathan, *Desalin. Water Treat.*, 2016, **59**, 65–71.
21. G. Ponnusamy, L. Francis, K. Loganathan, O. O. Ogunbiyi, S. Jasim and J. Saththasivam, *J. Water Supply: Res. Technol.--AQUA*, 2019, **68**, 655–665.
22. M. Schneider and L. Bláha, *Environ. Sci. Eur.*, 2020, **32**(1), 1–24.
23. C. Wei, F. Zhang, Y. Hu, C. Feng and H. Wu, *Rev. Chem. Eng.*, 2017, **33**, 49–89.
24. J. Alexander, G. Knopp, A. Dötsch, A. Wieland and T. Schwartz, *Sci. Total Environ.*, 2016, **559**, 103–112.
25. J. Zheng, C. Su, J. Zhou, L. Xu, Y. Qian and H. Chen, *Chem. Eng. J.*, 2017, **317**, 309–316.
26. N. Miranda, E. Oliveira and G. Silva, *Water Sci. Technol.*, 2014, **70**, 108–113.
27. C. Somerlot and D. Davis, *Clearwaters*, 2015, **45**, 18.
28. L. W. Gassie and J. D. Englehardt, *Water Res.*, 2017, **125**, 384–399.
29. J. Hollender, S. G. Zimmermann, S. Koepke, M. Krauss, C. S. McArdell, C. Ort, H. Singer, U. von Gunten and H. Siegrist, *Environ. Sci. Technol.*, 2009, **43**, 7862–7869.
30. K. L. Rakness, *Ozone in drinking water treatment: process design, operation, and optimization*, American Water Works Association, 2011.
31. H. He, L. Zheng, Y. Li and W. Song, *Ozone: Sci. Eng.*, 2015, **37**, 78–84.
32. Y. Qiu, C.-H. Kuo and M. E. Zappi, *Environ. Sci. Technol.*, 2001, **35**, 209–215.

33. N. F. Moreira, J. M. Sousa, G. Macedo, A. R. Ribeiro, L. Barreiros, M. Pedrosa, J. L. Faria, M. F. R. Pereira, S. Castro-Silva and M. A. Segundo, *Water Res.*, 2016, **94**, 10–22.
34. A. Al-Abduly, P. Christensen, A. Harvey and K. Zahng, *Chem. Eng. Process. Process Intensif.*, 2014, **84**, 82–89.
35. C. A. Graça, R. B. Lima, M. F. R. Pereira, A. M. Silva and A. Ferreira, *Chem. Eng. J.*, 2020, **389**, 124412.
36. A. Ferreira, J. A. Teixeira and F. Rocha, *Chem. Eng. J.*, 2015, **262**, 499–508.
37. M. S. Lucas, N. M. Reis and G. L. Puma, *Chem. Eng. J.*, 2016, **296**, 335–339.
38. S. Hayakumo, S. Arakawa, M. Takahashi, K. Kondo, Y. Mano and Y. Izumi, *Sci. Technol. Adv. Mater.*, 2014, **15**, 055003.
39. D. Gardoni, A. Vailati and R. Canziani, *Ozone: Sci. Eng.*, 2012, **34**, 233–242.
40. L. V. Tkhi, V. Tarasov and Y. I. Popov, *Theor. Found. Chem. Eng.*, 2009, **43**, 846.
41. I. Fábián, *Pure Appl. Chem.*, 2006, **78**, 1559–1570.
42. C. Gottschalk, J. A. Libra and A. Saupe, *Ozonation of water and waste water: A practical guide to understanding ozone and its applications*, John Wiley & Sons, 2009.
43. E. Paul and H. Debellefontaine, *Ozone: Sci. Eng.*, 2007, **29**, 415–427.
44. J. Hoigné and H. Bader, *Water Res.*, 1994, **28**(1), 45–55.
45. C. Yurteri and M. D. Gurol, *Ozone: Sci. Eng.*, 1988, **10**(3), 277–290.
46. A. Laplanche, M. T. Orta de Velasquez, V. Boisdon, N. Martin and G. Martin, *Ozone: Sci. Eng.*, 1995, **17**(1), 97–117.
47. M. Alheshibri, J. Qian, M. Jehannin and V. S. Craig, *Langmuir*, 2016, **32**, 11086–11100.
48. T. Uchida, S. Oshita, M. Ohmori, T. Tsuno, K. Soejima, S. Shinozaki, Y. Take and K. Mitsuda, *Nanoscale Res. Lett.*, 2011, **6**, 1.
49. F. Y. Ushikubo, T. Furukawa, R. Nakagawa, M. Enari, Y. Makino, Y. Kawagoe, T. Shiina and S. Oshita, *Colloids Surf., A*, 2010, **361**, 31–37.
50. W. W. Bowley and G. L. Hammond, *Ind. Eng. Chem. Process Des. Dev.*, 1978, **17**, 2–8.
51. A. Agarwal, W. J. Ng and Y. Liu, *Chemosphere*, 2011, **84**, 1175–1180.
52. J. Zhu, H. An, M. Alheshibri, L. Liu, P. M. Terpstra, G. Liu and V. S. Craig, *Langmuir*, 2016, **32**, 11203–11211.
53. Z. Gao, A. M. Kennedy, D. A. Christensen and N. Y. Rapoport, *Ultrasonics*, 2008, **48**, 260–270.
54. O. C. Thomas, R. E. Cavicchi and M. J. Tarlov, *Langmuir*, 2003, **19**, 6168–6177.
55. M. Żbik and R. G. Horn, *Colloids Surf., A*, 2003, **222**, 323–328.
56. T. Marui, *The 14th World Multi-Conference on Systemics, Cybernetics and Informatics*, International Social Science Council, Orlando, 2010.

57. A. K. A. Ahmed, X. Shi, L. Hua, L. Manzueta, W. Qing, T. Marhaba and W. Zhang, *J. Agric. Food Chem.*, 2018, **66**, 5117–5124.
58. S. Liu, S. Oshita, Y. Makino, Q. Wang, Y. Kawagoe and T. Uchida, *ACS Sustainable Chem. Eng.*, 2015, **4**, 1347–1353.
59. S. Liu, S. Oshita, S. Kawabata and D. Q. Thuyet, *Langmuir*, 2017, **33**, 12478–12486.
60. S. Liu, S. Oshita, S. Kawabata, Y. Makino and T. Yoshimoto, *Langmuir*, 2016, **32**, 11295–11302.
61. S. Aluthgun Hewage, J. H. Batagoda and J. N. Meegoda, *Environ. Eng. Sci.*, 2020, **37**, 521–534.
62. K. Chiba and M. Takahashi, *US Pat.*, US8137703B2, 2012.
63. J. H. Batagoda, S. D. A. Hewage and J. N. Meegoda, *J. Environ. Eng. Sci.*, 2019, **14**, 130–138.
64. R. Parmar and S. K. Majumder, *Chem. Eng. Process. Process Intensif.*, 2013, **64**, 79–97.
65. H. Li, L. Hu and Z. Xia, *Materials*, 2013, **6**, 3676–3687.
66. L. Hu and Z. Xia, *J. Hazard. Mater.*, 2018, **342**, 446–453.
67. K. Terasaka, A. Hirabayashi, T. Nishino, S. Fujioka and D. Kobayashi, *Chem. Eng. Sci.*, 2011, **66**, 3172–3179.
68. Y. Nakatake, S. Kisu, K. Shigyo, T. Eguchi and T. Watanabe, *Energy*, 2013, **59**, 233–239.
69. Y. Nakatake, T. Watanabe and T. Eguchi, *J. Energy Power Eng.*, 2013, **7**, 827.
70. A. Azevedo, R. Etchepare, S. Calgaroto and J. Rubio, *Miner. Eng.*, 2016, **94**, 29–37.
71. R. Etchepare, A. Azevedo, S. Calgaroto and J. Rubio, *Sep. Purif. Technol.*, 2017, **184**, 347–353.
72. R. Etchepare, H. Oliveira, M. Nicknig, A. Azevedo and J. Rubio, *Miner. Eng.*, 2017, **112**, 19–26.
73. Q. Wang, H. Zhao, N. Qi, Y. Qin, X. Zhang and Y. Li, *Sci. Rep.*, 2019, **9**, 1–9.
74. Z. Pourkarimi, B. Rezai and N. Noaparast, *Physicochem. Probl. Miner. Process.*, 2017, **53**, 920–942.
75. Y. Xiong and F. Peng, *Int. J. Min. Sci. Technol.*, 2015, **25**, 523–529.
76. F. Maoming, T. Daniel, R. Honaker and L. Zhenfu, *Min. Sci. Technol.*, 2010, **20**, 1–19.
77. T. Makuta, F. Takemura, E. Hihara, Y. Matsumoto and M. Shoji, *J. Fluid Mech.*, 2006, **548**, 113–131.
78. T. Makuta, R. Suzuki and T. Nakao, *Ultrasonics*, 2013, **53**, 196–202.
79. J.-Y. Kim, M.-G. Song and J.-D. Kim, *J. Colloid Interface Sci.*, 2000, **223**, 285–291.
80. A. K. A. Ahmed, C. Sun, L. Hua, Z. Zhang, Y. Zhang, W. Zhang and T. Marhaba, *Chemosphere*, 2018, **203**, 327–335.
81. A. Khaled Abdella Ahmed, C. Sun, L. Hua, Z. Zhang, Y. Zhang, T. Marhaba and W. Zhang, *Environ. Eng. Sci.*, 2018, **35**, 720–727.
82. M. Kukizaki and Y. Baba, *Colloids Surf., A*, 2008, **326**, 129–137.

83. W. B. Zimmerman, V. Tesar, S. Butler and H. C. Bandulasena, *Recent Pat. Eng.*, 2008, **2**, 1–8.
84. K. Ulatowski, P. Sobieszuk, A. Mróz and T. Ciach, *Chem. Eng. Process. Process Intensif.*, 2019, **136**, 62–71.
85. S. H. Oh, J. G. Han and J.-M. Kim, *Fuel*, 2015, **158**, 399–404.
86. J. H. Weijs and D. Lohse, *Phys. Rev. Lett.*, 2013, **110**, 054501.
87. A. Marchand, J. H. Weijs, J. H. Snoeijer and B. Andreotti, *Am. J. Phys.*, 2011, **79**, 999–1008.
88. P. S. Epstein and M. S. Plesset, *J. Chem. Phys.*, 1950, **18**, 1505–1509.
89. A. A. Kalmes, S. Ghosh and R. L. Watson, *J. Am. Coll. Cardiol.*, 2013, **61**, E106.
90. X. Zhang, X. Liu, Y. Zhong, Z. Zhou, Y. Huang and C. Q. Sun, *Langmuir*, 2016, **32**, 11321–11327.
91. J. H. Weijs, J. R. Seddon and D. Lohse, *Chem. Phys. Chem.*, 2012, **13**, 2197–2204.
92. S. H. Oh and J.-M. Kim, *Langmuir*, 2017, **33**, 3818–3823.
93. J. C. Millare and B. A. Basilia, *ChemistrySelect*, 2018, **3**, 9268–9275.
94. A. Srinivas and P. Ghosh, *Ind. Eng. Chem. Res.*, 2011, **51**, 795–806.
95. A. Khaled Abdella Ahmed, C. Sun, L. Hua, Z. Zhang, Y. Zhang, T. Marhaba and W. Zhang, *Environ. Eng. Sci.*, 2017, 720–727.
96. T.-W. Huang, S.-Y. Liu, Y.-J. Chuang, H.-Y. Hsieh, C.-Y. Tsai, W.-J. Wu, C.-T. Tsai, U. Mirsaidov, P. Matsudaira and C.-S. Chang, *Soft Matter*, 2013, **9**, 8856–8861.
97. M. Zhang, Y.-S. Tu and H.-P. Fang, *Appl. Math. Mech.*, 2013, **34**, 1433–1438.
98. T. Kimura and T. Ando, *Ultrason. Technol.*, 2002, **14**, 7–8.
99. M. Sumikura, M. Hidaka, H. Murakami, Y. Nobutomo and T. Murakami, *Water Sci. Technol.*, 2007, **56**, 53–61.
100. S. Khuntia, S. K. Majumder and P. Ghosh, *Chem. Eng. Res. Des.*, 2015, **98**, 231–239.
101. M. Takahashi, K. Chiba and P. Li, *J. Phys. Chem. B*, 2007, **111**, 1343–1347.
102. P. Li, M. Takahashi and K. Chiba, *Chemosphere*, 2009, **75**, 1371–1375.
103. M. S. Lucas, J. A. Peres and G. L. Puma, *Sep. Purif. Technol.*, 2010, **72**, 235–241.
104. T. A. Kurniawan, W.-H. Lo and G. Chan, *Chem. Eng. J.*, 2006, **125**, 35–57.
105. S. Saijai, V. Thonglek and K. Yoshikawa, *Int. Plasma Environ. Sci. Technol.*, 2019, **12**, 55–58.
106. M. Seki, T. Ishikawa, H. Terada and M. Nashimoto, *In Vivo*, 2017, **31**, 579–583.
107. K. Hayashi, T. Onda, H. Honda, N. Ozawa, H. Ohata, N. Takano and T. Shibahara, *Biochem. Biophys. Rep.*, 2019, **20**, 100697.
108. S. Arakawa, M. Sugisawa and A. Leewananthawet, *Dentistry*, 2017, **7**, 1–5.
109. Y. Inatsu, T. Kitagawa, N. Nakamura, S. Kawasaki, D. Nei, M. L. Bari and S. Kawamoto, *Food Sci. Technol. Res.*, 2011, **17**, 479–485.

110. F. Kobayashi, H. Ikeura, S. Ohsato, T. Goto and M. Tamaki, *Crop Prot.*, 2011, **30**, 1514–1518.
111. A. Tekile, I. Kim and J.-Y. Lee, *Korean Soc. Water Wastewater*, 2017, **31**, 481–490.
112. W. Ding, W. Jin, S. Cao, X. Zhou, C. Wang, Q. Jiang, H. Huang, R. Tu, S.-F. Han and Q. Wang, *Water Res.*, 2019, **160**, 339–349.
113. M. Takahashi, K. Chiba and P. Li, *J. Phys. Chem. B*, 2007, **111**, 11443–11446.
114. L.-B. Chu, S.-T. Yan, X.-H. Xing, A.-F. Yu, X.-L. Sun and B. Jurcik, *Chemosphere*, 2008, **72**, 205–212.
115. T. Zheng, Q. Wang, T. Zhang, Z. Shi, Y. Tian, S. Shi, N. Smale and J. Wang, *J. Hazard. Mater.*, 2015, **287**, 412–420.
116. P. Li and H. Tsuge, *J. Chem. Eng. Jpn.*, 2006, **39**, 1213–1220.
117. H. Li, L. Hu, D. Song and A. Al-Tabbaa, *Int. J. Environ. Res. Public Health*, 2014, **11**, 473–486.
118. R. Ratnawati, D. A. Kusumaningtyas, P. Suseno and A. Prasetyaningrum, *MATEC Web of Conferences*, 2018.
119. G. Tiwari and P. Bose, *Chem. Eng. J.*, 2007, **132**, 215–225.
120. N. Reis, R. N. Pereira, A. A. Vicente and J. A. Teixeira, *Ind. Eng. Chem. Res.*, 2008, **47**, 7190–7201.
121. M. Kukuzaki, K. Fujimoto, S. Kai, K. Ohe, T. Oshima and Y. Baba, *Sep. Purif. Technol.*, 2010, **72**, 347–356.
122. J. Phattaranawik, T. Leiknes and W. Pronk, *J. Membr. Sci.*, 2005, **247**, 153–167.
123. R. Jansen, J. De Rijk, A. Zwijnenburg, M. Mulder and M. Wessling, *J. Membr. Sci.*, 2005, **257**, 48–59.
124. T. Leiknes, J. Phattaranawik, M. Boller, U. Von Gunten and W. Pronk, *Chem. Eng. J.*, 2005, **111**, 53–61.
125. K. Li, L. Xu, Y. Zhang, A. Cao, Y. Wang, H. Huang and J. Wang, *Appl. Catal., B*, 2019, **249**, 316–321.
126. G. A. Zoumpouli, R. Baker, C. M. Taylor, M. J. Chippendale, C. Smithers, S. S. Ho, D. Mattia, Y.-M. Chew and J. Wenk, *Water*, 2018, **10**, 1416.
127. B. Wang, X. Xiong, Y. Shui, Z. Huang and K. Tian, *Chem. Eng. J.*, 2019, **357**, 678–688.
128. S. Heng, K. L. Yeung, M. Djafer and J.-C. Schrotter, *J. Membr. Sci.*, 2007, **289**, 67–75.
129. S. K. Stylianou, M. Kostoglou and A. I. Zouboulis, *Ind. Eng. Chem. Res.*, 2016, **55**, 7587–7597.
130. T. Tasaki, T. Wada, Y. Baba and M. Kukizaki, *Ind. Eng. Chem. Res.*, 2009, **48**, 4237–4244.
131. W. Han, P. Zhang, W. Zhu, J. Yin and L. Li, *Water Res.*, 2004, **38**, 4197–4203.
132. M. Kukizaki and M. Goto, *Colloids Surf., A*, 2007, **296**, 174–181.
133. S. Kutty, F. Winarto, S. Gilani, A. Anizam, W. Karimah and M. Isa, *Waste Management and the Environment V*, *Southampton, UK*, 2010: *WIT Press*, pp. 415–423.

134. L.-B. Chu, X.-H. Xing, A.-F. Yu, Y.-N. Zhou, X.-L. Sun and B. Jurcik, *Chemosphere*, 2007, **68**, 1854–1860.
135. H. Ikeura, F. Kobayashi and M. Tamaki, *J. Food Eng.*, 2011, **103**, 345–349.
136. L. Mezule, S. Tsyfansky, V. Yakushevich and T. Juhna, *Desalination*, 2009, **248**, 152–159.
137. T. Temesgen, T. T. Bui, M. Han, T.-I. Kim and H. Park, *Adv. Colloid Interface Sci.*, 2017, 40–51.
138. K.-K. Chen, *US Pat.*, US7488416B2, 2009.
139. Y. Ikeda-Dantsuji, L. B. Feril, K. Tachibana, K. Ogawa, H. Endo, Y. Harada, R. Suzuki and K. Maruyama, *Ultrason. Sonochem.*, 2011, **18**, 425–430.
140. T. Zheng, T. Zhang, Q. Wang, Y. Tian, Z. Shi, N. Smale and B. Xu, *RSC Adv.*, 2015, **5**, 77601–77609.
141. A. C. Hill and N. Littlefield, *Environ. Sci. Technol.*, 1969, **3**, 52–56.
142. J. Fuhrer and F. Booker, *Environ. Int.*, 2003, **29**, 141–154.
143. T. Graham, P. Zhang, Y. Zheng and M. A. Dixon, *HortScience*, 2009, **44**, 774–780.

Subject Index